

AD-A097 668

MASSACHUSETTS INST OF TECH CAMBRIDGE DEPT OF CIVIL E--ETC F/G 8/13
THE CREEP OF FROZEN SANDS: QUALITATIVE AND QUANTITATIVE MODELS.(U)
MAR 81 J M TING

UNCLASSIFIED

R81-5

ARO-14725.2-6S

DAAG29-77-C-0016

NL

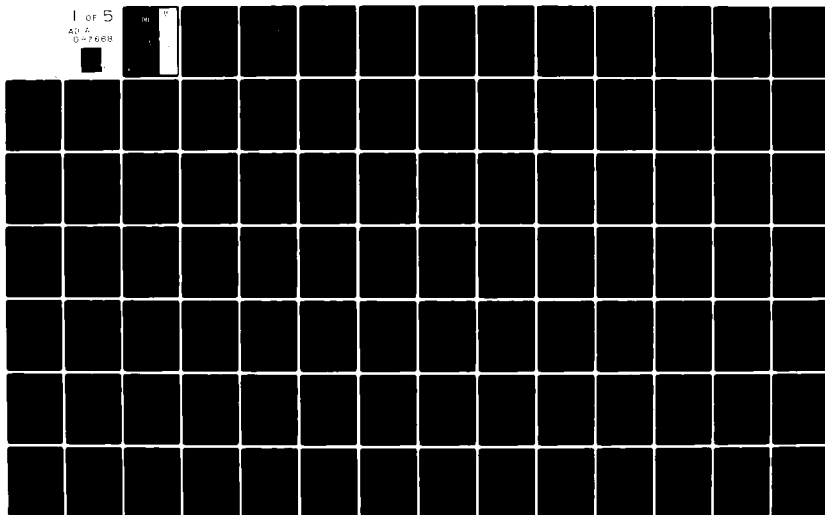
1 OF 5

AD-A
0-7668

NL

1

1



ARO 14725.2-GS

LEVEL

12

**THE CREEP OF FROZEN SANDS:
QUALITATIVE AND QUANTITATIVE MODELS**

FINAL REPORT PART II

by
John M. Ting

DTIC
ELECTED
APR 8 1981
C

March 1981

U.S. ARMY RESEARCH OFFICE
Contract Number
DAAG29-77-C-0016

Constructed Facilities Division
Research Report No. R81-5
Order Number 692

Approved For Public Release;
Distribution Unlimited

81 4

MIT

**DEPARTMENT
OF
CIVIL
ENGINEERING**

SCHOOL OF ENGINEERING
MASSACHUSETTS INSTITUTE OF TECHNOLOGY
Cambridge, Massachusetts 02139

AD A097 663

DTIC FILE COPY

**THE FINDINGS IN THIS REPORT ARE NOT TO BE CONSTRUED
AS AN OFFICIAL DEPARTMENT OF THE ARMY POSITION,
UNLESS SO DESIGNATED BY OTHER AUTHORIZED DOCUMENTS**

Unclassified

SECURITY CLASSIFICATION OF THIS PAGE (When Data Entered)

REPORT DOCUMENTATION PAGE		READ INSTRUCTIONS BEFORE COMPLETING FORM
1. REPORT NUMBER	2. GOVT ACCESSION NO.	3. RECIPIENT'S CATALOG NUMBER
	AD-A097 668	
4. TITLE (and Subtitle)	5. TYPE OF REPORT & PERIOD COVERED	
6 The Creep of Frozen Sands: Qualitative and Quantitative Models,	9 Final Report, Feb 79-Mar 1981	
	6. PERFORMING ORG. REPORT NUMBER	
	R81-5 Order No. 692	
7. AUTHOR(s)	8. CONTRACT OR GRANT NUMBER(s)	
10 John M. Ting	35 DAA G29-77-C-0016	
9. PERFORMING ORGANIZATION NAME AND ADDRESS	10. PROGRAM ELEMENT, PROJECT, TASK AREA & WORK UNIT NUMBERS	
Massachusetts Institute of Technology 77 Massachusetts Ave. Cambridge, MA 02139	12 433	
11. CONTROLLING OFFICE NAME AND ADDRESS	12. REPORT DATE	
U.S. Army Research Office P.O. Box 12211 Research Triangle, NC 27709	11 Mar 1981	
14. MONITORING AGENCY NAME & ADDRESS (if different from Controlling Office)	13. NUMBER OF PAGES	
18 AR3 1019 17-2-5-6	432	
	15. SECURITY CLASS. (of this report)	
	Unclassified	
	15a. DECLASSIFICATION/DOWNGRADING SCHEDULE	
	NA	
16. DISTRIBUTION STATEMENT (of this Report)		
Approved for public release; distribution unlimited		
17. DISTRIBUTION STATEMENT (of the abstract entered in Block 20, if different from Report)		
NA		
18. SUPPLEMENTARY NOTES		
The findings in this report are not to be construed as an official Department of the Army position, unless so designated by other authorized documents.		
19. KEY WORDS (Continue on reverse side if necessary and identify by block number)		
mechanics of frozen soil; creep models; tertiary creep; mechanisms of strength and deformation; soil/ice adhesion; creep of wetting and nonwetting glass beads;		
20. ABSTRACT (Continue on reverse side if necessary and identify by block number)		
<p>This Report develops better qualitative and quantitative models for the time-dependent mechanical behavior of frozen soils. By drawing upon an extensive literature survey, unconfined creep data for frozen sand, and a series of creep tests on glass beads made wetting and nonwetting, various physical mechanisms controlling the behavior of frozen soil are proposed: ice strength, soil strength, and mechanical interaction through structural hindrance and dilatancy effects.</p> <p>The nature of the linear relationship between the logarithm of the minimum creep (over)</p>		

Unclassified

SECURITY CLASSIFICATION OF THIS PAGE(When Data Entered)

20. (cont'd)

rate and the logarithm of the time to minimum observed from creep tests on ice, soil and frozen soil is shown to be due to the existence of an approximately constant strain at the minimum, and the relative insensitivity of this log-log plot to small deviations from a constant value of strain.

Two quantitative models for fitting and predicting the minimum strain rate and time to minimum for unconfined creep are developed and evaluated. Each can typically predict the minimum strain rate and time to minimum to within ± 4 times the actual value using data from only a relatively few tests.

New empirical creep models capable of describing the entire creep curve from primary through tertiary are also developed. Through a simple technique for parameter evaluation, the models can yield excellent fits of the data and reliable predictions of the creep behavior. Typically, the models predict the minimum strain rate to within ± 3 times and the strain at the minimum to within 70% of the actual values.

Accession For	
NTIS GRA&I	<input checked="checked" type="checkbox"/>
DTIC TAB	<input type="checkbox"/>
Unannounced	<input type="checkbox"/>
Justification	
By	
Distribution/	
Availability Codes	
Dist	Avail and/or Special
A	

Unclassified

SECURITY CLASSIFICATION OF THIS PAGE(When Data Entered)

ACKNOWLEDGEMENTS

There are many people whom I wish to thank for their part in making this thesis possible. I would like to express my gratitude to the U.S. Army Cold Regions Research and Engineering Laboratory and the U.S. Army Research Office for their generous funding of this research. Special thanks go to all the staff of USA CRREL, who provided the technical support and scientific interaction during my stay in Hanover, N.H.

I would especially like to thank (alphabetically): David Carbee, for his help anytime that something needed fixing; David Cole, for his assistance in running strength tests during the initial research project, and for supplying ice samples for our testing program; Gary DeKoff, for his aid in programming and helping me use the CRREL computers; Dr. Malcolm Mellor, for his constructive comments on the initial literature review; William Quinn, for his thoroughly congenial administrative supervision and aid; Frank Sayles, for his constructive review of the initial literature survey, and for his support throughout the project; and Al Tice, for carrying out the NMR unfrozen water content determinations. Also, I thank the undergraduate students who assisted in running many of the creep tests on Manchester Fine Sand for the initial research project: John Benedict, John Currier, Jim Metherall, John Quackenbush and Mike Woodward.

I also wish to express my sincere gratitude to each of my thesis supervisors, who were initially responsible for my working on this project. Prof. Charles Ladd provided a great deal of guidance and encouragement, especially through his extremely thorough and constructive comments on all of the drafts of this thesis. Dr. Martin was responsible for helping shape many of my ideas and concepts in this thesis during our many talks. Working with each has sincerely been a rewarding, enjoyable and treasured experience.

Thanks go especially to Dr. and Mrs. Martin for generously allowing me to stay with them while in Hanover (truly an act above and beyond the call of duty for each of them).

Finally, I wish to thank my parents, who raised me in an environment which allowed me to develop in the fullest (and who saved me months of additional drudgery by allowing me the use of their computer), and to my wife Christine, for her patience and understanding throughout my experience at M.I.T.

TABLE OF CONTENTS

TITLE.....	1
ABSTRACT.....	2
ACKNOWLEDGEMENTS.....	3
TABLE OF CONTENTS.....	4
LIST OF FIGURES.....	6
LIST OF TABLES.....	13
LIST OF COMMONLY USED SYMBOLS.....	15
 1. INTRODUCTION.....	 17
2. REVIEW OF THE NATURE AND MECHANICS OF ICE.....	20
2.1 Nature of Ice.....	20
2.2 Mechanics of Ice.....	29
2.2.1 Mechanisms of deformation.....	31
2.2.2 Strength of Ice... ..	34
2.2.3 Ductile-to-brittle transition.....	44
2.2.4 Deformation of ice.....	48
2.2.5 Quantitative models of ice strength and deformation.....	63
Rate Process Theory.....	64
Quantitative models of strength.....	69
Quantitative models of deformation.....	71
2.3 Summary of the Nature and Mechanics of Ice.....	77
3. REVIEW OF THE NATURE AND MECHANICS OF UNFROZEN SOIL.....	80
3.1 Nature of the Unfrozen Soil System.....	80
3.2 Mechanics of Unfrozen Soil.....	81
4. REVIEW OF THE NATURE AND MECHANICS OF FROZEN SOIL.....	88
4.1 Nature of the Frozen Soil System.....	88
4.1.1 Nature of ice nucleation and interaction in frozen soil.....	88
Frost heaving.....	90
Ice adhesion.....	94
4.1.2 Structure of the frozen soil system.....	97
4.2 Mechanics of Frozen Soil.....	103
4.2.1 Strength of frozen soil.....	104
Effect of confining stress.....	104
Effect of temperature.....	111
Effect of time.....	115
4.2.2 Deformation of frozen soil.....	121
Effect of stress level.....	123
Effect of temperature.....	125
Effect of confining stress.....	132
Other factors.....	134
4.2.3 Qualitative models of strength and defor- mation.....	139
Summary of the mechanics of frozen soil... ..	140
Qualitative models of behavior.....	143
4.2.4 Quantitative models of strength and defor-	

mation.....	148
4.3 Summary of the Nature and Mechanics of Frozen Soil.....	160
5. QUALITATIVE MODELS FOR THE MECHANICS OF FROZEN SAND....	164
5.1 The Linear $\log \dot{\epsilon}_m - \log t_m$ Correlation.....	164
5.2 Mechanisms of Strength and Deformation.....	172
5.2.1 Proposed mechanisms.....	172
5.2.2 Discussion of the mechanisms of strength and deformation.....	177
5.2.3 Summary and implications of testing program.	194
5.3 Proposed Qualitative Model for Frozen Sand Behavior.....	208
5.4 Conclusions.....	214
6. QUALITATIVE MODELS FOR THE CREEP OF FROZEN SAND.....	218
6.1 Prediction of the Minimum Strain Rate.....	223
6.2 Prediction of t_m	237
6.3 Proposed Creep Models.....	241
6.4 Conclusions.....	260
7. SUMMARY AND CONCLUSIONS.....	266
APPENDICES	
A.1 Properties of Glass Beads.....	272
A.2 Sample Preparation and Testing for Unconfined Creep of Saturated Frozen Glass Beads.....	283
A.3 Results of Creep Tests on Glass Beads.....	296
A.4 Results of Unfrozen Water Content Determinations of MS-M Glass Beads.....	309
A.5 Results of Testing on Frozen Manchester Fine Sand.....	314
A.6 Results of Creep Testing on Ice.....	340
B.1 Details on the Nature of the Linear $\log \dot{\epsilon}_m - \log t_m$ Correlation.....	344
B.2 Details of $\dot{\epsilon}_m$ Prediction for Manchester Fine Sand....	355
B.3 Details of t_m Prediction for Manchester Fine Sand....	383
B.4 Details on the Proposed Creep Models.....	391
REFERENCES.....	419
Ice.....	420
Unfrozen Soil and Particulate Composites.....	426
Frozen Soil.....	428
BIOGRAPHICAL NOTE.....	432

LIST OF FIGURES

2.1	Phase diagram for Ice.....	21
2.2	Structure of Ice Ih.....	22
2.3	Corte's experiment: a particle floating on a heavy- ing ice surface.....	25
2.4	Deformation mechanism map for polycrystalline ice of 1 mm grain size.....	33
2.5	Uniaxial compressive strength of ice at -9.5°C	35
2.6	Uniaxial compressive strength of ice as a function of temperature.....	37
2.7	Typical stress-strain curves for granular ice at -9.5°C	38
2.8	Effect of sand concentration on the strength of a sand-ice system.....	40
2.9	Triaxial strength of polycrystalline ice.....	42
2.10	Typical creep data for ice.....	49
2.11	Effect of sand concentration on the creep of a sand- ice system.....	57
2.12	Strain rate dependence of the yield and brittle strength and stress dependence of the "secondary" strain rate of ice.....	59
2.13	Linear $\log \dot{\epsilon}_m - \log t_m$ correlation for ice.....	61
2.14	Components of the Andrade equation.....	74
3.1	The physico-chemical effective stress equation.....	82
3.2	Components of strength of sand as determined by Rowe (1962).....	85
4.1	Two-dimensional schematic of the proposed structure of the frozen sand system.....	101
4.2	Effect of confining stress on the strength of ice and frozen soils.....	105
4.3	Results of strength testing on frozen soils at low confining stresses.....	108
4.4	Stress-strain curves for frozen Ottawa Sand.....	109
4.5	Mohr envelopes for Ottawa sand 20-30 and columnar- grained ice at -3.8°C	110
4.6	Effect of temperature on the uniaxial compressive and tensile strengths of silt and sand.....	112
4.7	Effect of confining stress on the temperature dep- endence of strength.....	114
4.8	Effect of strain rate on the uniaxial compressive strength of frozen soils.....	116
4.9	Effect of strain rate on the triaxial strength of frozen soils.....	118
4.10	Linear $\log \dot{\epsilon}_m - \log t_m$ correlation for frozen Man- chester Fine Sand.....	120
4.11	Strain rate vs. applied stress ratio for various materials.....	122
4.12	Stress dependence of creep for ice and Manchester Fine Sand at various degrees of ice saturation....	124

4.13	Effect of minor fluctuations in applied stress on the creep of frozen soils.....	126
4.14	Effect of temperature on the uniaxial creep of frozen Manchester Fine Sand.....	127
4.15	Determination of the apparent activation energy E for frozen partially saturated MFS.....	129
4.16	Variation of E with stress level.....	130
4.17	Effect of confining stress on the creep of frozen sand.....	133
4.18	Effect of relative density on the creep of frozen MFS.....	136
4.19	Effect of ice saturation on the creep of frozen MFS..	137
4.20	Typical creep models.....	149
4.21	Variation of failure envelopes with time for Ottawa Sand.....	155
4.22	Strength and creep data for frozen soils as a function of strain rate and stress.....	157
4.23	Energy surface for frozen silt.....	157
5.1	Summary of $\dot{\epsilon}_m - t_m$ correlations for various materials.....	165
5.2	Lines of constant strain based on secondary creep model.....	167
5.3	Lines of constant strain based on Singh-Mitchell (1968) creep model.....	168
5.4	Minimum creep data for 40% Si 55% Dr MFS with constant strain contours from Singh-Mitchell creep model.....	170
5.5	Buckling of a slender column in air and with an elastic foundation.....	176
5.6	Comparison of frozen and unfrozen soil strength for Ottawa Sand 100-200.....	181
5.7	Effect of surface treatment on the creep behavior of MS-M size glass beads.....	196
5.8	Results of creep testing on MS-M (wetting) glass beads.....	197
5.9	Comparison of creep behavior of frozen saturated MS-XPX size glass beads (wetting and nonwetting) and fine polycrystalline snow ice.....	198
5.10	Effect of a change in friction angle on the observed axial strength.....	202
5.11	Tentative mechanism maps for uniaxial compression of frozen sands.....	209
6.1	Results of creep testing on 40% Si MFS at 0.3 stress level.....	220
6.2	Typical uniaxial (unconfined) creep behavior for frozen sand.....	222
6.3	Comparison of fitted and actual $\dot{\epsilon}_m$ using the modified RPT equation for 55% Dr MFS at various levels of saturation.....	226
6.4	Frequency histogram indicating quality of fit using	

one modified RPT equation for describing $\dot{\epsilon}_m$, σ_1 and T variation.....	227
6.5 Use of ultimate strength for fitting constant load creep data for 40% Si and 100% Si MFS.....	229
6.6 Frequency histogram of data fits using ultimate strength.....	230
6.7 Frequency histogram of quality of fit using ultimate strength to account for temperature dependence, data at varying degrees of ice saturation Si.....	232
6.8 Comparison of predicted and actual $\dot{\epsilon}_m$ using modified RPT and stress ratio methods.....	235
6.9 Histograms of fitted t_m using $\log \dot{\epsilon}_m - \log t_m$ correlations.....	238
6.10 Proposed determination of parameters for Assur-Ting model.....	243
6.11 Comparison of actual and fitted creep curves for 40% Si 55% Dr MFS data at $\sigma_1 = 4.8$ MPa from Assur-Ting model.....	245
6.12 Comparison of actual and computed strain-time curves for 40% Si 55% Dr MFS at $\sigma_1 = 4.78$ MPa.....	246
6.13 Comparison of Assur-Ting, Singh-Mitchell creep models with actual test data.....	247
6.14 Comparison of predicted and actual $\dot{\epsilon}_m$ and ϵ_m using Assur-Ting model for 40% Si 55% Dr MFS using data from 8 creep tests.....	250
6.15 Comparison of $\log \dot{\epsilon}_m - \log t_m$ curves from Assur-Ting model predictions and actual data.....	251
6.16 Comparison of strain-time curves from predictions and actual data.....	252
6.17 Results of creep testing on saturated 55% Dr MFS at $\sigma_1 = 10.6$ MPa, various temperatures.....	253
6.18 Determination of parameters for modified creep model for saturated frozen MFS.....	255
6.19 Comparison of modified creep model and actual data for saturated Manchester Fine Sand.....	256
6.20 Comparison of strain-time curve from modified creep model with actual test for saturated MFS.....	257
6.21 Comparison of predicted and actual $\dot{\epsilon}_m$ and ϵ_m using modified creep model for saturated MFS using 10 tests to predict others.....	259
A.1.1 Grain sizes of tested materials.....	276
A.1.2 Results of CIDC tests on MS-M glass beads.....	277
A.1.3 Results of CIDC tests on MS-M WP glass beads.....	278
A.1.4 Scanning electron micrographs of MS-M glass beads.....	279
A.1.5 Scanning electron micrographs of MS-M WP (non-wetting) glass beads.....	280
A.1.6 Scanning electron micrographs of MS-XPX glass beads.....	281
A.1.7 Scanning electron micrographs of MS-XPX WP (non-wetting) glass beads.....	282

A.2.1	Schematic of compaction mold.....	289
A.2.2	Schematic of evacuation/saturation apparatus.....	290
A.2.3	Schematic of apparatus for freezing samples.....	291
A.2.4	Schematic of creep testing apparatus.....	292
A.2.5	Schematic of cold stage apparatus.....	293
A.2.6	Typical plots of creep data from one test.....	294
A.2.7	Water content profiles of frozen glass bead samples.....	295
A.3.1	Results of constant load creep testing on glass beads.....	300
A.3.2	Results of creep testing on MS-M (wetting) glass beads.....	301
A.3.3	Results of creep testing on MS-M WP (nonwetting) glass beads.....	302
A.3.4	Results of creep testing on MS-XPX (wetting) glass beads.....	303
A.3.5	Results of creep testing on MS-XPX WP (nonwetting) glass beads.....	304
A.3.6	Results of creep testing on MS-M (wetting) glass beads.....	305
A.3.7	Results of creep testing on MS-M WP (nonwetting) glass beads.....	306
A.3.8	Results of creep testing on MS-XPX (wetting) glass beads.....	307
A.3.9	Results of creep testing on MS-XPX WP (nonwetting) glass beads.....	308
A.4.1	Unfrozen water contents of MS-M glass beads from pulsed NMR.....	311
A.4.2	Unfrozen water contents of MS-M wetting and MS-M WP nonwetting glass beads from pulsed NMR (warming curves).....	312
A.4.3	Unfrozen water content as a function of ice content for MS-M wetting glass beads.....	313
A.5.1	Results of creep testing on 40% Si 55% Dr MFS at $\sigma_1 = 4.78$ MPa, various temperatures.....	328
A.5.2	Results of creep testing on 40% Si 55% Dr MFS at $\sigma_1 = 4.78$ MPa, various temperatures.....	329
A.5.3	Results of creep testing on 40% Si 55% Dr MFS at -18.8°C , various stresses.....	330
A.5.4	Results of creep testing on saturated 55% Dr MFS at $\sigma_1 = 10.6$ MPa, various temperatures.....	331
A.5.5	Results of creep testing on saturated 55% Dr MFS $T = -18.4^\circ\text{C}$, various stresses.....	332
A.5.6	Summary of minimum creep data for 55% relative density Manchester Fine Sand at various degrees of ice saturation.....	333
A.5.7	Results of creep testing on 40% Si MFS at varying Dr.....	334

A.5.8	Results of creep testing on saturated MFS at varying Dr.....	335
A.5.9	Results of creep testing on 40% Si MFS at varying Dr.....	336
A.5.10	Results of creep testing on saturated MFS at varying relative density.....	337
A.5.11	Water content profiles of MFS at 55% relative density.....	338
A.5.12	Unconfined strength tests on saturated MFS at 55% relative density.....	339
A.5.13	Unconfined strength tests on 40% Si 55% Dr MFS.....	339
A.6.1	Results of creep testing on fine polycrystalline snow ice.....	343
B.1.1	Summary of $\dot{\epsilon}_m - t_m$ correlations for various materials.....	349
B.1.2	Lines of constant strain based on secondary creep model.....	350
B.1.3	Lines of constant strain based on Singh-Mitchell (1968) creep model.....	351
B.1.4	Minimum creep data for 40% Si 55% Dr MFS with constant strain contours from Singh-Mitchell creep model.....	352
B.1.5	Comparison of actual creep data with ϵ_m prediction with $\dot{\epsilon}_m - t_m$ correlation and Singh-Mitchell creep model.....	353
B.1.6	Use of the Singh-Mitchell creep model for fitting actual creep data.....	354
B.2.1	Fit of constant load single stage creep test data for 40% Si 55% Dr MFS with variable apparent activation energy E fits.....	366
B.2.2	Fit of constant load single stage creep test data for 40% Si 55% Dr MFS with constant apparent activation energy E.....	367
B.2.3	Use of exponential function to describe stress dependence.....	368
B.2.4	Use of power function to describe stress dependence.....	369
B.2.5	Quality of fits of $\dot{\epsilon}_m$ data.....	370
B.2.6	Quality of fits of 100% Si 55% Dr data.....	371
B.2.7	Frequency histogram indicating quality of fit using one modified RPT equation for describing Si, Dr, σ_1 and T variation.....	372
B.2.8	Fit of selected constant load single stage creep test data for 100% Si 55% Dr MFS with constant apparent activation energy.....	373
B.2.9	Fit of selected constant load single stage creep test data for 40% Si 55% Dr MFS with constant apparent activation energy.....	374

B.2.10	Fit of selected constant load single stage creep test data for 20% Si 55% Dr MFS with constant apparent activation energy.....	375
B.2.11	Summary of stress dependence of creep for selected constant load creep tests at varying degrees of ice saturation Si.....	376
B.2.12	Frequency histogram of quality of predictions using one modified RPT equation and the results from 25 tests to predict all single stage constant load creep test data.....	377
B.2.13	Use of ultimate strength for fitting constant load creep data for 40% Si and 100% Si Mfs.....	378
B.2.14	Frequency histogram of data fits using ultimate strength.....	379
B.2.15	Frequency histogram of quality of fit using ultimate strength to account for temperature dependence, data at varying degrees of ice saturation Si.....	380
B.2.16	Frequency histogram of quality of fit using σ_{ult} and results from 18 tests to predict all MFS data.....	381
B.3.1	Histograms of fitted t_m using $\log \dot{\epsilon}_m - \log t_m$ correlation.....	387
B.3.2	Correlation between $\dot{\epsilon}_m$ and ϵ_m	388
B.3.3	Histograms of t_m fit using ϵ_m model with $\dot{\epsilon}_m$ fits.....	389
B.3.4	Histograms of t_m prediction using results from 8 tests to predict others, with $\log \dot{\epsilon}_m - \log t_m$ correlation.....	390
B.4.1	Typical normalized creep curves for 40% Si 55% Dr MFS.....	405
B.4.2	Proposed determination of parameters for Assur-Ting model.....	406
B.4.3	Comparison of actual and fitted creep curves for 40% Si 55% Dr MFS at $\sigma_1 = 4.8$ MPa.....	407
B.4.4	Comparison of actual and computed strain-time curves for 40% Si 55% Dr MFS at $\sigma_1 = 4.78$ MPa.....	408
B.4.5	Comparison of actual, Singh-Mitchell and Assur-Ting creep curves.....	409
B.4.6	Comparison of predicted and actual $\dot{\epsilon}_m$ and ϵ_m using Assur-Ting model for 40% Si 55% Dr MFS using data from 8 creep tests.....	410
B.4.7	Comparison of $\log \dot{\epsilon} - \log t$ curves from Assur-Ting model predictions and actual data.....	411
B.4.8	Comparison of strain-time curves from predictions and actual data.....	412
B.4.9	Determination of parameters for modified creep model for saturated frozen MFS.....	413
B.4.10	Comparison of modified creep model and actual data for saturated Manchester Fine Sand.....	414
B.4.11	Comparison of strain-time curves from modified creep model with actual test for saturated MFS.....	415
B.4.12	Correlations between ϵ_o and (σ_1/σ_{ult})	416

B.4.13	Correlations between slopes of $\log \dot{\epsilon}$ - $\log t$ curves for saturated MFS and stress ratio.....	417
B.4.14	Comparison of predicted and actual $\dot{\epsilon}_m$ and ϵ_m using modified creep model for saturated MFS using 10 tests to predict others.....	418

LIST OF TABLES

2.1	Unfrozen water content and estimated film thickness in various soils.....	27
2.2	Possible creep mechanisms in ice.....	68
2.3	Values of n and Q from constant strain rate tests....	70
2.4	Values of n and E from constant stress creep tests...	72
5.1	Results of testing on glass beads.....	199
6.1	Summary of modified RPT model parameters for MFS....	225
6.2	Summary of $\dot{\epsilon}_m$ prediction methods.....	236
A.1.1	Properties of glass beads.....	274
A.1.2	Summary of CIDC loading triaxial tests on unfrozen glass beads.....	275
A.3.1	Results of creep testing - MS-M series glass beads.....	297
A.3.2	Results of creep testing - MS-XPX series glass beads.....	298
A.3.3	Summary of creep testing on glass beads.....	299
A.5.1	Results of constant load creep testing on saturated MFS samples, nominal $w = 25\%$	318
A.5.2	Results of constant load creep testing on partially saturated MFS samples, nominal $w = 10\%$	319
A.5.3	Results of constant load creep testing on partially saturated MFS samples, nominal $w = 5, 3\%$..	320
A.5.4	Results of constant load creep testing on varying Dr MFS samples.....	321
A.5.5	Results of temperature stage creep tests on saturated MFS with computed experimental activation energy.....	322
A.5.6	Results of temperature stage creep tests on partially saturated MFS with computed experimental activation energy.....	323
A.5.7	Results of temperature stage creep tests on partially saturated MFS with computed experimental activation energy.....	324
A.5.8	Results of stress stage creep tests on saturated and partially saturated MFS.....	325
A.5.9	Summary of observed and computed quantities for MFS at 55% Dr.....	326
A.5.10	Summary of unconfined strength testing on MFS at 55% Dr.....	327
A.6.1	Results of creep testing on fine polycrystalline snow ice, $\phi = 0.6$ mm.....	342

B.2.1	Parameters for equation B.2.7 for 55% Dr MFS.....	364
B.2.2	A parameters for 55% Dr MFS using avg. $n = 10$, - (E/R) = 30000.....	364
B.2.3	Summary of tests used for determining model parameters for predictions.....	365
B.4.1	Summary of Assur-Ting model parameters for individual constant load creep tests for 40% Si MFS....	400
B.4.2	Summary of Assur-Ting model parameters using creep data from 8 tests only for 40% Si MFS.....	401
B.4.3	Summary of modified model parameters for individual constant load creep tests for 100% Si MFS creep data.....	402
B.4.4	Summary of modified model parameters for saturated MFS.....	403
B.4.5	Summary of modified model parameters using creep data from 10 tests only for saturated MFS.....	404

LIST OF COMMONLY USED SYMBOLS

a	unit area
a	contact area
A	long range attractive force
A	fitting constant for various models, including Singh-Mitchell (1968), Assur-Ting, modified RPT, etc.
B	Skempton's (1954) pore pressure parameter ($\Delta u/\Delta \sigma_c$)
c	cohesion intercept
D _r	relative density (also D _r)
e	void ratio
E	experimental activation energy based on creep testing (kJ/mole)
E	elastic modulus
f	applied shear force on a flow unit
ΔF	free energy of activation (kJ/mole)
G	specific gravity of mineral
h	Planck's constant ($6.624 \times 10^{-34} \text{ J-s}$)
k	Boltzmann's constant ($1.38 \times 10^{-23} \text{ J/}^\circ\text{K}$)
m	slope of $\log \dot{\epsilon} - \log t$ curve ($-\partial \ln(\dot{\epsilon})/\partial \ln(t)$)
m	fitting constant in SM, AT, modified AT models
n	fitting constant in mod. RPT, stress ratio models describing stress dependence
N	Avagadro's number (6.02×10^{23})
p	mean normal stress ($\sigma_1 + \sigma_3/2$)
q	shear stress ($\sigma_1 - \sigma_3/2$)
Q	experimental activation energy based on strength testing
r ²	coefficient of determination
R	long range repulsive force
R	Universal Gas constant ($8.30 \text{ J/}^\circ\text{K-mole}$)
S	number of flow units per unit area
S	degree of saturation of pores with water
S _i	degree of saturation of pores with ice (also S _i)
t	time
t _Δ	time of break Δ
t _m	time to the minimum strain rate (min)
t _o	arbitrary initial time
T _o	temperature ($^\circ\text{C}$ or $^\circ\text{K}$)
u	pore pressure (also u _p)
w	water content
w _u	unfrozen water content (weight of unfrozen water/weight solids)
α	$\tan^{-1}(q_f/p_f)$
α	stress dependence of creep ($\partial \ln \dot{\epsilon}/\partial \ln \sigma$)
β	fitting constant in SM, AT, stress ratio models
β	stress dependence of creep ($E = \Delta F - \beta \sigma$)
β	fitting constant in AT, mod. RPT, Andrade models
γ	fitting constant
γ _d	dry density
ε	strain

ϵ_{Δ} strain at break Δ
 ϵ_m strain at minimum strain rate
 ϵ_0 strain at initial time t
 $\dot{\epsilon}$ strain rate
 $\dot{\epsilon}_{\Delta}$ strain rate at break Δ
 $\dot{\epsilon}_m$ minimum strain rate
 $\dot{\epsilon}_0$ strain rate at time t_0
 Δ_0 indicates break in $\log \dot{\epsilon} - \log t$ curve; also time of stress
 or temperature change in stage test
 λ displacement of flow unit
 ν frequency of activation
 ϕ friction angle
 ϕ grain size diameter
 ϕ_{μ} sliding friction
 ϕ_{cv} friction angle at constant volume
 ρ_i specific gravity of ice
 σ normal stress
 σ' effective normal stress ($\sigma' = \sigma - u$)
 σ_1 major principal stress (deviator stress when $\sigma_3 = 0$)
 σ_3 minor principal stress
 σ_c confining stress
 σ_c effective confining stress
 σ_f normal stress at failure
 σ_{oct} octahedral normal stress
 σ_{ult} ultimate strength (also σ_u)
 σ_a contact attractive stress
 σ_r contact repulsive stress
 θ temperature ($-T$ in $^{\circ}C$)
 τ shear stress
 τ_f shear stress at failure

$(\frac{\dot{\epsilon}_f}{\dot{\epsilon}_{act}})_m$ ratio of fitted to actual minimum strain rate
 $(\frac{\dot{\epsilon}_{pr}}{\dot{\epsilon}_{act}})_m$ ratio of predicted to actual minimum strain rate
 $(\frac{t_f}{t_{act}})_m$ ratio of fitted to actual time to minimum
 $(\frac{t_{pr}}{t_{act}})_m$ ratio of predicted to actual time to minimum

CHAPTER 1 - INTRODUCTION

Knowledge of the time-dependent stress-strain-strength behavior of frozen soil is of great importance for civil engineering construction involving naturally and artificially frozen ground. This field has received increasing attention due to the heightened oil-related construction activity in North America and from the use of artificial ground freezing for soil stabilization under difficult conditions. Much of the recent research has centered on empirical engineering solutions rather than theoretically based models, with relatively little work devoted to the fundamental mechanisms controlling the mechanical behavior of frozen soils. Among the notable exceptions to this are the papers by Goughnour and Andersland (1968) and Chamberlain et al. (1972), as well as by Sayles (1974) and Vyalov (1973), each of which attempted to provide some fundamental explanation for their observed behavior.

This Report, in a broad sense, attempts to provide a better qualitative understanding of the mechanics of frozen soil. In addition, various quantitative models for the behavior are proposed. Specifically, the Report focuses on the physical mechanisms controlling the strength and deformation behavior of frozen soil systems and proposes methods for quantifying various aspects of creep behavior.

Frozen soil is a complex multiphase system consisting of soil, ice, unfrozen water and air. In order to properly understand the mechanics of the frozen soil composite, one must

first examine the nature and behavior of its various components. Chapters 2, 3 and 4 summarize the results of an extensive evaluation of the literature on the mechanics of ice, soil and frozen soil. Chapter 4 also reviews and evaluates the available explanations and models for frozen soil behavior.

Based on the information in Chapters 2 through 4, Chapter 5 presents a physical model developed to provide a qualitative picture of the principal physical mechanisms controlling the time-dependent strength-deformation characteristics of frozen sand. Some conclusions are made concerning the validity and relative importance of the proposed mechanisms by drawing upon: (a) the previously described synthesis of the known behavior of frozen soil systems, (b) data obtained from the extensive creep testing program performed on Manchester Fine Sand (Martin et al. 1981), and (c) results from creep tests conducted on glass beads of various sizes which were made wetting or non-wetting. The resulting probable mechanisms of strength and deformation are discussed in Chapter 5. Appendix A presents details of the testing procedures and results of pertinent creep tests carried out on the glass beads, MFS and ice, together with the accompanying support data on the glass beads.

While these qualitative models of deformation and strength should be considered in any theoretically based constitutive relationship, it was not possible to incorporate this knowledge into proposed new quantitative creep models. Instead, emphasis was placed on developing relatively simple empirical models for

fitting and predicting important aspects of creep behavior, specifically the minimum strain rate, $\dot{\epsilon}_m$, and the time to the minimum strain rate, t_m . New simple creep models capable of describing the strain - time behavior from the primary through the tertiary stages of creep are proposed and evaluated for saturated and partially saturated frozen sand. These quantitative models are described in Chapter 6 and are developed in greater detail in Appendix B. Both Chapters 5 and 6 contain suggestions for additional avenues of research for qualitative and quantitative modelling. The summary and conclusions for Chapters 5 and 6 are reiterated in Chapter 7.

CHAPTER 2 - REVIEW OF THE NATURE AND MECHANICS OF ICE

2.1 Nature of Ice

Ice forms an important, possibly controlling, structural component of the frozen soil system. At temperatures between 0°C and -130°C and at ordinary pressures, the thermodynamically stable form of water is Ice Ih (see Figure 2.1). Overall, this ice is slightly less dense than liquid water, with a specific gravity of about 0.91, and hence has a greater average molecular spacing than the liquid phase. The crystal structure of ice Ih is distinctly planar with H_2O molecules forming puckered sheets consisting of hexagonal rings, as shown in Figure 2.2. The plane of the sheets is termed the basal plane, with the axis perpendicular to this plane called the c-axis.

Slip occurs most readily along the basal plane, referred to as basal or easy glide. Slip not along these planes, termed non-basal or hard glide, can only be induced at stresses greater than ten times that for easy glide (Higashi 1969). One such nonbasal mechanism is dislocation climb, in which a line defect climbs from one glide plane to the next. However, it has been shown that when attempts are made to produce slip in nonbasal plane directions, the ice often fractures before slip occurs (Gold 1962, 1966(b), Weeks and Assur 1969).

As with most crystalline solids, ice does not necessarily form under favorable thermodynamic conditions. Nucleation is first required, possibly with the aid of existing ice crystals, chemical impurities or foreign particles. Nucleation

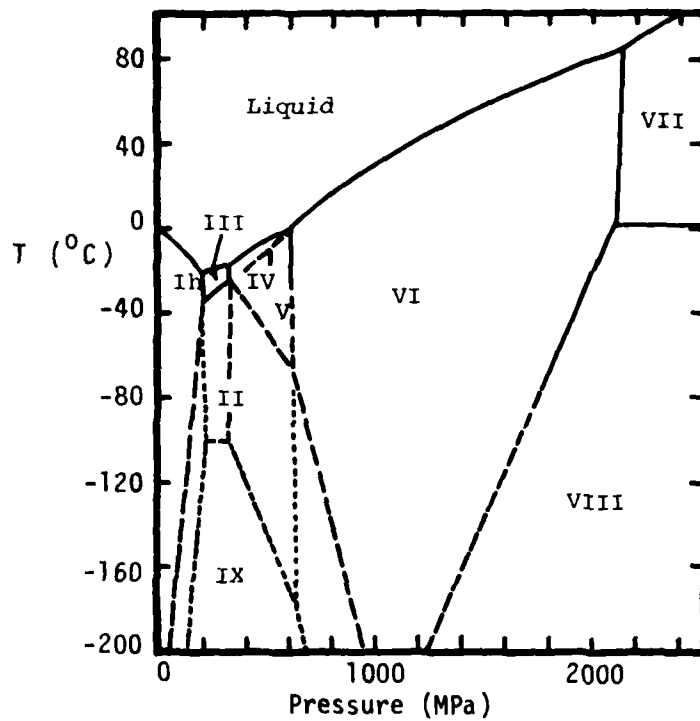


FIGURE 2.1 Phase diagram for Ice (after Whalley et al. 1968)

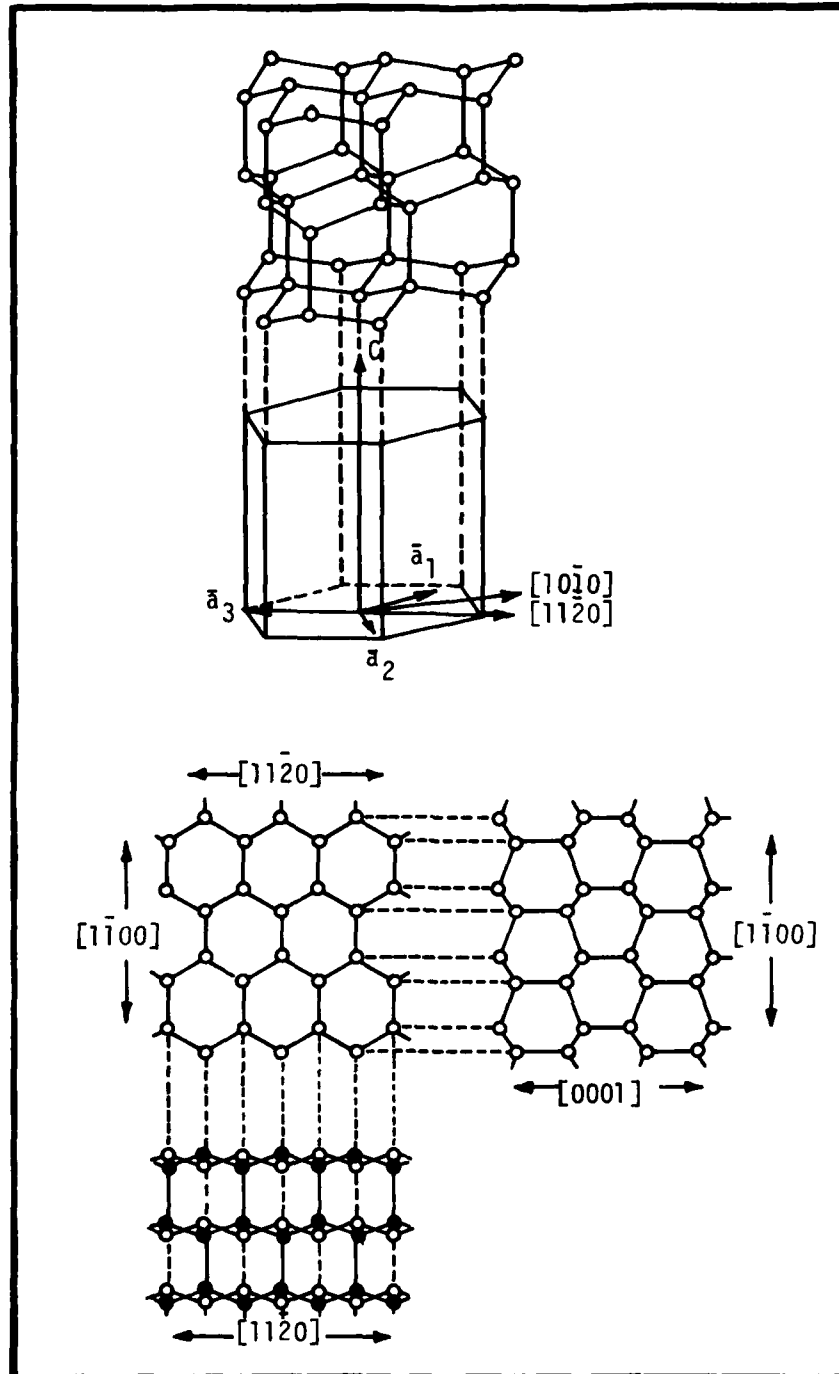


FIGURE 2.2 Structure of Ice Ih (in Weeks and Assur 1969)

may also be induced by mechanical agitation, sonic waves or electrical fields. If no foreign particles or pre-existing ice are present, then pure water can undergo a great deal of supercooling before ice forms. Experimentally, temperatures as low as -40°C have been obtained before homogeneous nucleation occurred. However, if foreign particles or ice are present, heterogeneous nucleation occurs at temperatures far closer to 0°C .

Ice typically exists in nature in polycrystalline form. The various types of naturally occurring ice have been described and classified by Michel and Ramseier (1971). One common form is granular or snow ice, which is associated with freezing under turbulent conditions and the freezing of slush. The individual grains in snow ice are roughly equidimensional and randomly oriented, resulting in generally isotropic mechanical behavior. Because of the polycrystalline nature of such naturally occurring ice systems, the deformational mechanisms are vastly different from monocrystalline ice.

The nature of ice in frozen soils is generally not well known. While it is possible to distinguish between general types of frozen soil structures (Tsyтовich 1975), such as fused, laminar and cellular, details of the nature of the ice in frozen soil are difficult to obtain. For example, the relative hardness of soil particles compared with ice makes it very difficult to obtain clean thin sections (Rein and Sliepcevich 1978). However, some thin section data by Gow (1975) for

a silt-ice system appear to indicate that pore ice is polycrystalline in nature.

Nevertheless, it is possible to infer that the nature of this ice and the structure of the frozen soil system are dependent on:

- (1) soil properties, such as pore size, grain size, permeability, specific surface area, surface activity and surface charge,
- (2) pore water properties, such as degree of saturation and amount of impurities, and
- (3) nature of the freezing process, such as magnitude of the freezing temperature and rate of freezing relative to the rate of possible pore water migration in the soil.

It is generally accepted that a liquid-like layer of unfrozen water exists at the ice to soil mineral interface. Strong indirect evidence suggests this interfacial water to be fluid and continuous. This evidence includes observed solute movement under an electrical field, conductance measurements within samples of frozen soil and ion diffusion (Anderson 1968). Corte (1962) also observed that ice growing upward can carry soil particles "floating" on the surface of the freezing front. This observation suggests that a thin layer of unfrozen water exists around the soil particles, whose molecules are constantly replenished by the water in the adjacent reservoir (see Figure 2.3).

The total amount of unfrozen water content for a given soil can be determined by a variety of methods, such as dila-

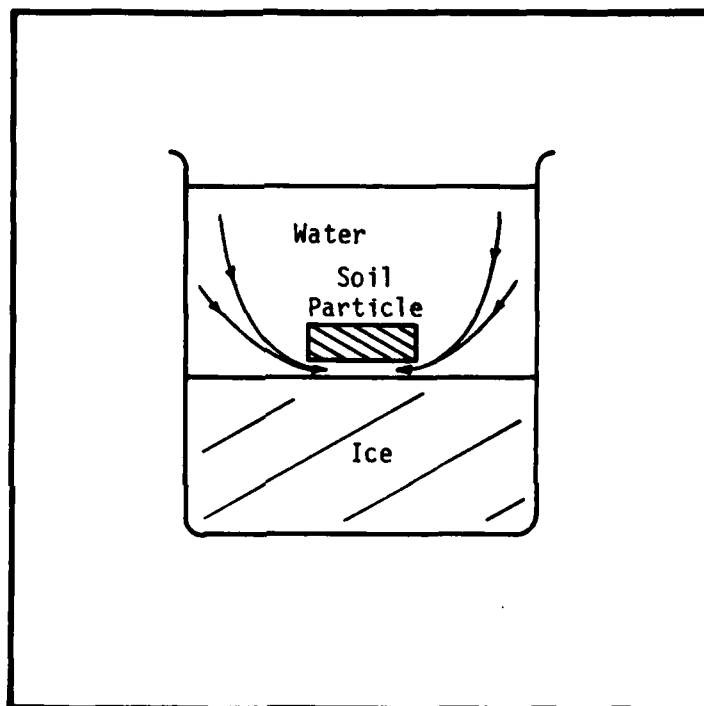


FIGURE 2.3 Corte's experiment: a particle floating on a heaving ice surface (Corte 1962)

tometry, adiabatic calorimetry, x-ray diffraction, heat capacity, differential thermal analysis and nuclear magnetic resonance. The results obtained from different methods on similar soils yield reasonably consistent values (Anderson and Morgenstern 1973). For each soil, the amount of unfrozen water typically decreases between 0° and about -5°C . At lower temperatures, the amount of unfrozen water remains approximately constant but is finite and appreciable in quantity.

If all of the unfrozen water at low temperatures exists in this soil interfacial layer, then the thickness of this liquid-like layer equals the unfrozen water content, w_u , divided by the specific surface area, SSA, of the soil. Based on data for several soils (Anderson and Tice 1972, Tice et al. 1978), this procedure yields estimated thicknesses in the tens of Angstroms, as seen in Table 2.1. However, recent work by Martin, Ting and Ladd (1981) indicates that a significant portion of the total unfrozen water may in fact be associated with the ice phase, rather than solely with the soil particles. Consequently, the computed thicknesses of the unfrozen water films in Table 2.1 represent upper bounds.

The nature of the ice in frozen soil is undoubtedly influenced by this unfrozen water layer, together with other structural factors such as the nature of the freezing process and soil structure. For example, the nature of the freezing process in a soil system determines the location and structure of the ice within the pores. Although the exact mechanism of freez-

SOIL TYPE	SSA(m ² /g)	*w _u (%)		estimated unfrozen + layer thickness (A°)	
		T=-1°C	T=-10°C	T=-1°C	T=-10°C
West Lebanon Gravel <100μ	18	3.82	0.87	21.2	4.8
Fairbanks Silt	40	4.81	2.27	12.0	5.7
Dowfield Silty Clay	50	10.35	2.52	20.7	5.0
Kaolinite	84**	23.80	10.30	28.3	12.3
Suffield Silty Clay	140	13.92	6.75	9.9	4.8
Hawaiian Clay	382	32.42	18.53	8.5	4.8
Wyoming Bentonite	800†	55.99	28.66	7.0†	3.6†
Umat Bentonite	800†	67.55	30.66	8.4†	3.8†
Manchester Fine Sand	0.1††	3.33†††	1.57†††	-	-

+upper bound values

*SSA and w_u from Anderson and Tice (1972); SSA mainly from direct ethylene glycol retention measurements or grain size computations from method described by Dillon & Andersland (1966); w_u using isothermal calorimetry.

**Mitchell (1976) reports SSA for Kaolinite as 10-20 m²/g; this gives a thickness of 159A at -1°C and 69A at -10°C.

†Values of SSA are secondary values; for primary SSA (with domain formation), Mitchell (1976) gives 50-120 m²/g; this results in a 10x increase in unfrozen layer thickness.

††Computed from grain size curves using method by Dillon and Andersland (1966), without due consideration of any clay fraction.

†††w_u from Tice et al (1978) using pulsed NMR techniques.

Table 2.1 - Unfrozen Water Content and Estimated Film Thickness in Various Soils.

ing is not fully understood, considerable insight can be obtained by studying the nucleation phenomenon as viewed in cloud physics, as well as the mechanism of frost heaving in soil. Details of the results from such studies are presented later in this Chapter.

Generally, the results from such studies indicate that ice nucleates initially in areas away from the silicate surface, probably adjacent to the adsorbed water layer (Anderson 1968). This information, together with the thin section data on a silt-ice system, suggest that the ice in a frozen soil is polycrystalline in nature and exists within the pores of the soil adjacent to the adsorbed water layer, not directly in contact with the soil particles. This topic will also be discussed in greater detail later in this Chapter.

2.2 Mechanics of Ice

Although the mechanical behavior of ice is similar to that of most crystalline materials, ice is unusual in that it commonly occurs in nature at temperatures near its melting point. Consequently, the bulk of engineering and scientific interest centers on the behavior of ice at very high homologous temperatures. The effect of temperature in the typical range of interest (0° to -20°C) is very important because of its large influence on the deformational mechanisms and amount of unfrozen water present.

Ice exhibits a very time dependent mechanical behavior; it will creep continuously under very low deviatoric stress levels but presumably possesses a finite, albeit small, limiting longterm strength. Typically, the multiplicity of experimental problems which occur with longterm testing of a frozen material limits the effective length of time over which a test can be carried out. As a result, the actual limiting longterm strength of ice remains unknown.

In addition, the behavior of ice is very dependent on the level of applied stress or strain rate. At sufficiently high levels of either, brittle failure modes can be induced, whereas at lower levels, apparently ductile failures occur. The structure of the ice also greatly affects its mechanical behavior.

Depending on the nature of the granular structure of the ice, the overall sample behavior can be isotropic or anisotropic, with widely varying rates and modes of deformation.

To better understand the mechanical behavior of ice, researchers have used a variety of different tests. These include uniaxial (unconfined) and multiaxial compression and tension tests, Brazil (diametral compression), indentation and beam tests, and ring shear and torsion tests. Of these, the most common are the uniaxial compression and tension tests. Multiaxial testing (such as triaxial, plane strain and biaxial) has recently increased as experimental techniques and apparatus become increasingly sophisticated. The remaining tests each have the advantage of convenience, but possess serious interpretation problems.

While it is desirable to formulate one generalized equation of state relating strain rate, stress, temperature, deformation, time and structural parameters, this has not yet been accomplished. Instead, an arbitrary division between strength and deformation is usually made. Typically, strength data are generated from strain or stress rate controlled tests. Time dependent effects and long term strengths are usually determined from constant load creep tests. In addition, various rheological models of creep have been evaluated from stress relaxation, stress stage and temperature stage tests.

In order to examine the mechanics of ice, the mechanisms of deformation in ice mono- and polycrystals will first be presented. Then, the strength and deformation behavior of ice will be discussed, together with the effects of various factors such as temperature, stress system, strain rate, im-

purities and structure. Attempts at quantifying this behavior are also presented.

2.2.1 Mechanisms of deformation

A variety of deformational mechanisms occur in polycrystalline ice. The relative importance of each depends on the applied stress or strain rate, temperature and ice structure. The mechanisms may be loosely grouped into the following categories.

(i) Microcreep (movement of defects). At low temperatures, stress and strain rates, the movement of point and line defects are important mechanisms of deformation. These mechanisms include the diffusion of point vacancies and defects, and the dislocation of line defects along basal and nonbasal directions. These mechanisms dominate below about -10°C and 0.50 MPa (Shoji and Higashi 1978). At higher temperatures and stresses, these mechanisms are probably still present, but no longer as rate-controlling processes.

(ii) Microcracking. At stresses or strain rates slightly higher than present in (i), microcracking can occur. This cracking results from dislocation pileups at the grain boundaries and stress concentrations within the crystal due to defects or impurities. These cracks are primarily transcrystalline and intercrystalline in nature and usually involve only one or two grains at a time (Gold 1966(b), 1970, Hawkes and Mellor 1972). This mechanism is essentially a brittle

phenomenon, but can result in an overall behavior which is ductile in appearance. This mechanism is considered to be the primary deformational mechanism for ice, and can be detected by viewing the ice sample through crossed polarizers and by pickup of the accompanying acoustical emissions. For polycrystalline snow ice, Hawkes and Mellor (1972) report that initial cracking activity occurs at between 2 and 4 MPa at -7°C , while Gold (1977) reports that cracking occurs at stresses above about 1 MPa.

(iii) Grain boundary effects. These include grain boundary sliding, formation of unfrozen water at the grain boundaries, grain boundary migration and growth, and pressure melting and surface regelation. In the region above -10°C , Barnes et al. (1971) suggest that the first four grain boundary mechanisms may occur. Above -3°C , pressure melting and surface regelation are also present at the grain boundaries.

Based on data from various sources, it is possible to construct a deformational mechanism map for a given ice as a function of stress level, temperature and strain rate. Such a mechanism map is shown in Figure 2.4 as constructed by Goodman (1977) for polycrystalline ice.

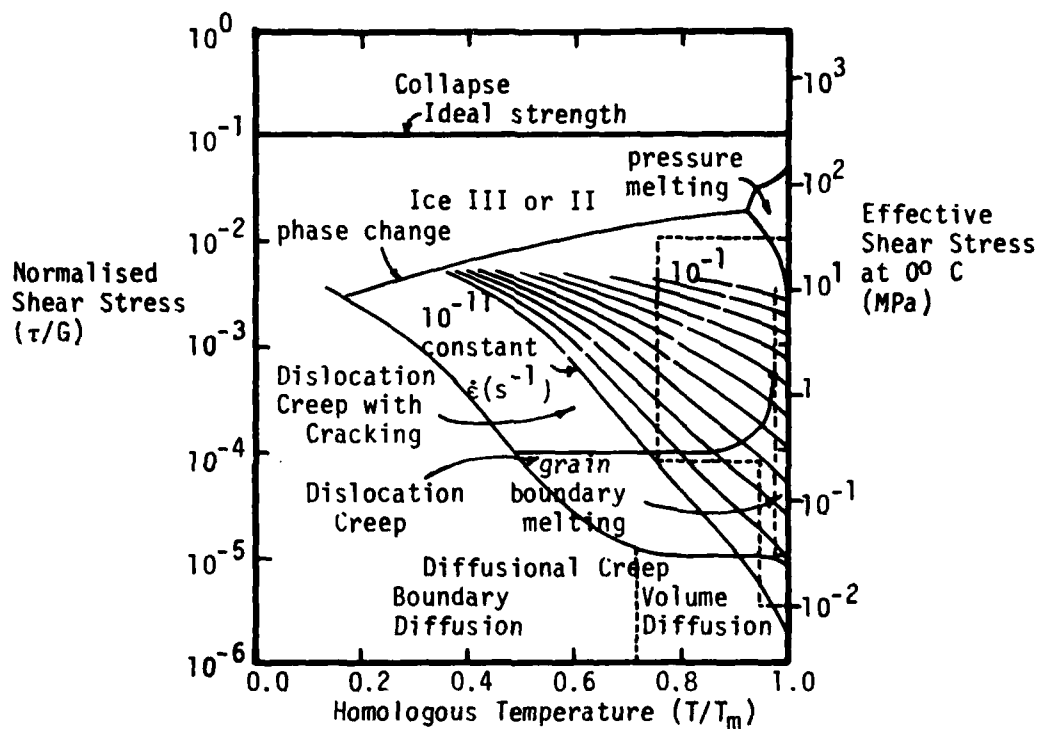


FIGURE 2.4 Deformation-mechanism map for polycrystalline ice of 1 mm grain size (after Shoji and Higashi 1978, Goodman 1977)

2.2.2 Strength of Ice

The most common tests employed for determining the strength of ice are the uniaxial unconfined compression and tension tests. Due to the importance of strain rate and temperature on strength, these are usually the test parameters varied in any test program. However, the apparently minor testing details such as end restraint conditions and end cap compliance, sample shape and aspect ratio often affect the results. The same applies to the sample variables such as the nature of the ice structure, grain size and the type and amount of impurities. These typically cause a large scatter in strength values and make it difficult to compare data from different researchers.

Results from deformation rate controlled compression tests on bubbly snow ice at -9.5°C reported by various researchers are plotted in Figure 2.5 and indicate a strong dependence of the uniaxial compressive strength on the applied strain rate. The exact numerical value of this dependence at a given temperature varies with the test procedures used, as well as the strain rate level.

Similarly, the uniaxial compressive strength of ice exhibits a large temperature dependence. As before, difficulty exists in attempting to determine the exact numerical value of this dependence, as the strength values at each temperature are functions of the applied deformation rate, testing apparatus and the nature of the ice specimen. Kovacs et al. (1977)

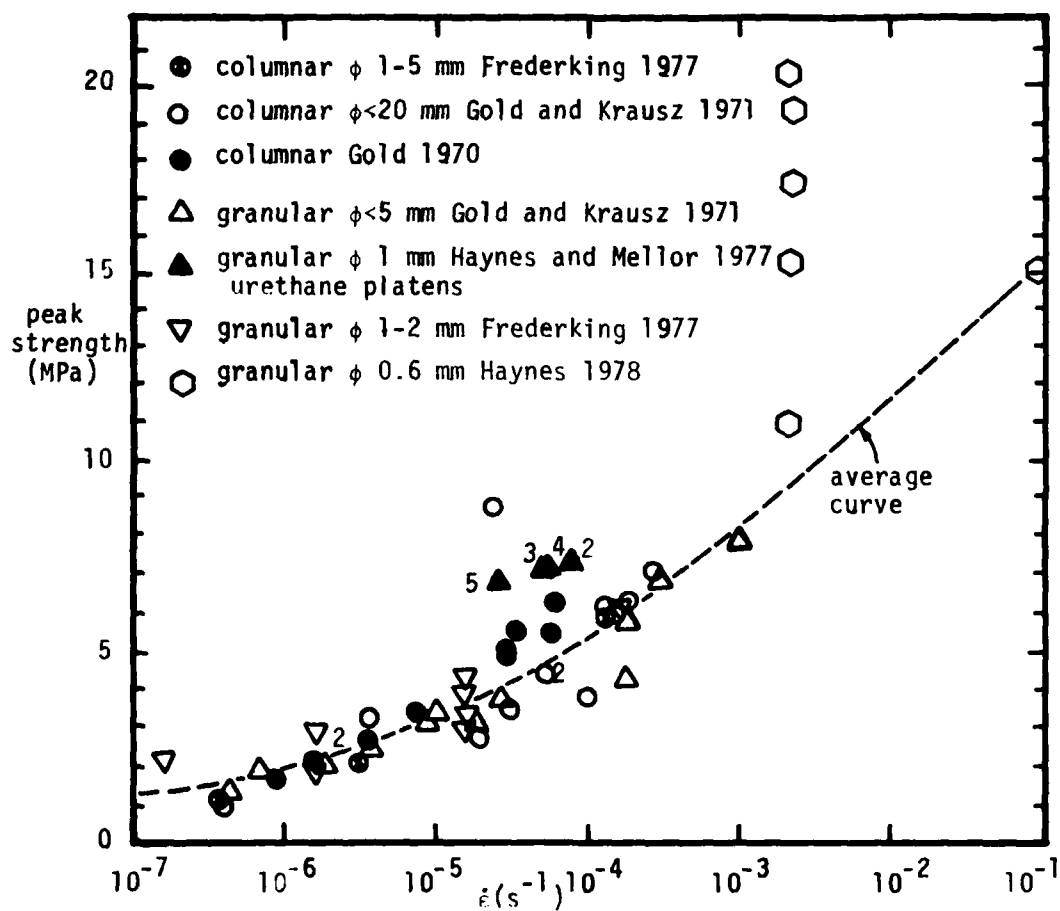


FIGURE 2.5 Uniaxial compressive strength of ice at $-9.5^{\circ}C (\pm)$
 (Note: numbers beside data points indicate duplicate results;
 large variation in results by Haynes 1978 attributed to
 experimental problems)

estimate the temperature coefficient of uniaxial compressive strength for snow ice to be about $0.076 \text{ MPa}/^{\circ}\text{C}$ in the range -20° to -40°C , based on data from several researchers. Data from Goughnour and Andersland (1968) indicate a rate of increase of ice strength of $0.14 \text{ MPa}/^{\circ}\text{C}$ between -4° and -12°C at an applied strain rate of $4.4 \times 10^{-6} \text{ /sec}$. Data from Haynes (1978), plotted in Figure 2.6, indicate rates of increase of about $0.7 \text{ MPa}/^{\circ}\text{C}$ for the relatively high applied strain rates of 2×10^{-3} and $1 \times 10^{-1} \text{ /s}$. This variation in the reported temperature coefficient of ice strength can be attributed to several factors. For example, it is possible that past attempts at high strain rate tests resulted in lower strength values due to problems with sample alignment and end restraint; the more recent data of Haynes (1978) suggest that the previously thought drop-off in strength at the large strain rates may not exist.

The various types of naturally occurring ice each possess slightly different strength and deformation behavior. Of these, polycrystalline granular (snow) ice is probably the most representative of the ice in frozen soil. Figure 2.7 illustrates typical stress-strain curves for snow ice at -9.5°C subjected to unconfined compression at fairly low strain rates. These curves indicate a typically ductile behavior, with peak strengths at around 1 % axial strain.

The effect of impurities depends on their type and amount. Work by Peyton (1966) on the compressive strength of single

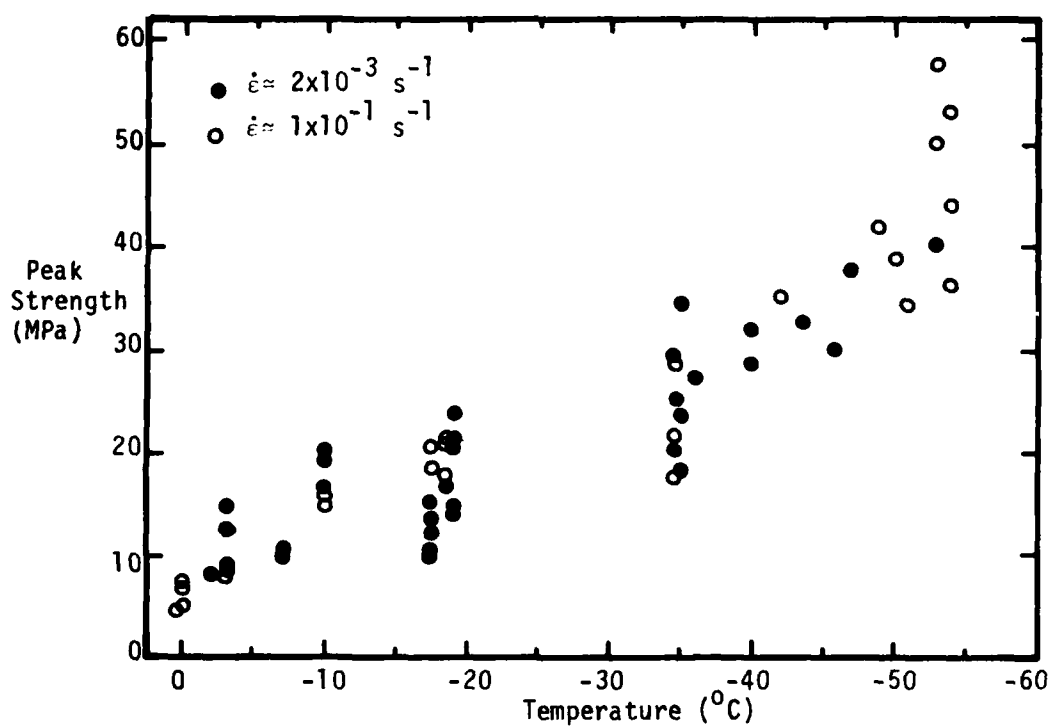


Figure 2.6 Uniaxial compressive strength of ice as a function of temperature (from Haynes 1978)

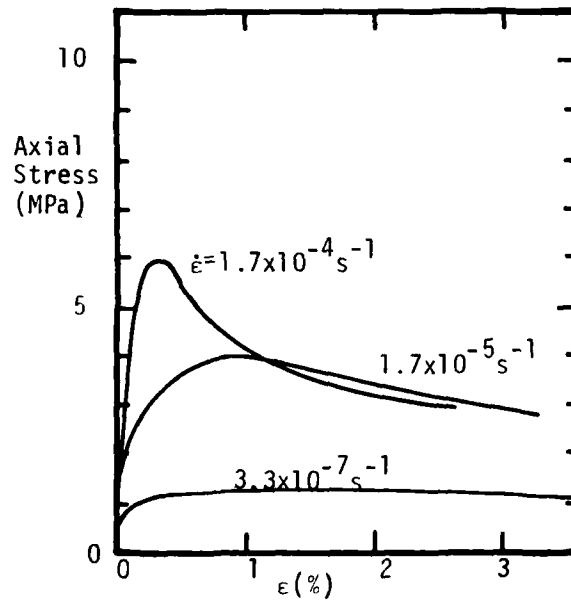


FIGURE 2.7 Typical stress-strain curves for granular ice at -9.5°C
(from Gold and Krausz 1971)

crystals of sea ice indicates that as the brine volume increases, the strength decreases. The effect of particulate impurities contrasts with that of chemical impurities. Goughnour and Andersland (1968) found that the peak strength of 20-30 Ottawa sand imbedded in a polycrystalline ice matrix increases with increasing sand concentration, as shown in Figure 2.8. Above a critical level (42% in the case of Ottawa sand), the rate of increase of strength rises sharply, most likely due to direct interaction between the sand grains. In effect, the sand-ice mixture becomes a frozen soil, rather than impure ice. Volumetric measurements during shear confirm this hypothesis as they indicate that the samples above this level dilate similar to dense unfrozen sand.

Unlike the behavior of ice under compressive loading, the tensile strength of ice is almost independent of temperature and strain rate above 10^{-5} /sec, although a slight increase in strength does occur with decreasing temperature. Failure is essentially a brittle event, with little evidence of internal cracking prior to fracture and separation. The results of various researchers indicate that bubbly snow ice with an average grain size of 1 mm has an uniaxial tensile strength of about 2 MPa in the temperature and strain rate ranges of interest. Note that this value is lower than for compressive loading under the same conditions.

As with compressional behavior, the presence of impurities can influence the tensile behavior of ice. Of the various

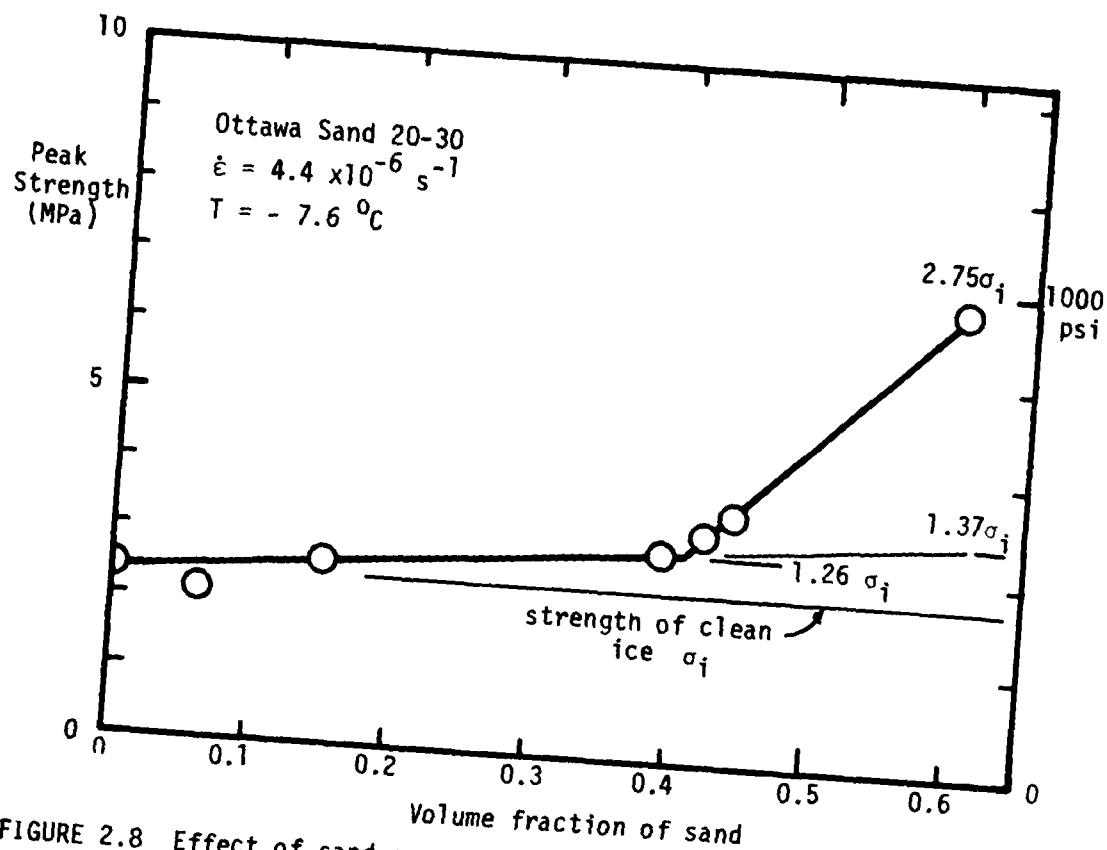


FIGURE 2.8 Effect of sand concentration on the strength of a sand-ice system (from Goughnour and Andersland 1968)

chemicals in a study by Nakumura and Jones (1973), only HF demonstrated any significant effect on the observable behavior of the ice. At -11°C , an applied strain rate of 1.6×10^{-6} , and with a 0.8 ppm concentration, the observed peak strength for the HF-doped ice was about half that of the pure ice crystal. Jones and Glen (1969(b)) also reported similar trends.

While the bulk of conventional strength testing in ice has used uniaxial (unconfined) loading, some workers have studied the influence of confining stress. Figure 2.9 plots data from Haynes (1973), Sayles (1974), Smith and Cheatham (1975) and Jones (1978). The triaxial compression data, when considered collectively, indicate an initial increase in strength with confining stress up to a maximum. Jones (1978) reports that above a confining stress of about 40 MPa, the strength decreased with further confinement.

At the lower stresses, confinement reduces cracking activity and compresses any existing air bubbles. Jones reports that for his tests at 0.1 MPa and 33.5 MPa carried out to 60% true strain, the sample at atmospheric pressure was very highly cracked, opaque and chipped, whereas the high pressure sample was uncracked and even clearer than at the start of the test. At the higher confining stresses, localized pressure melting probably explains the measured decrease in compressive strength with increasing confinement. Global pressure melting, associated with the water-ice phase transition, is expected above a confining stress of about 110 MPa at -10°C .

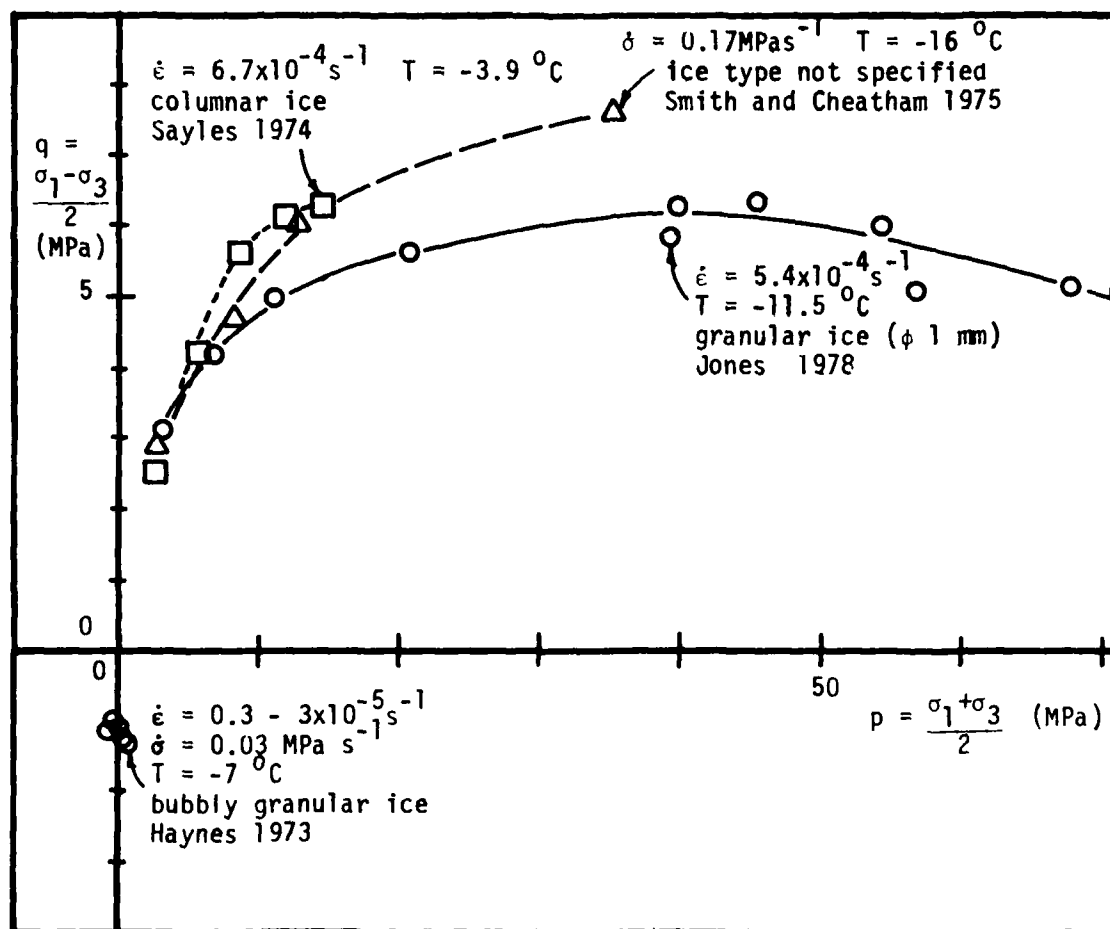


FIGURE 2.9 Triaxial strength of polycrystalline ice

Triaxial tensile testing results from Haynes (1973), also plotted in Figure 2.9, were used to indicate that polycrystalline ice follows neither the Mohr-Coulomb nor Griffith's failure criteria.

Frederking (1977) carried out plane strain tests on columnar and snow ice. For polycrystalline snow ice, his data indicate little difference between uniaxial and plane strain strengths as a function of strain rate.

Other tests that have been used to test ice in the laboratory and field include the Brazil (diametral compression), ring tension and beam tests. Each of these possess severe interpretation problems, associated with non-uniform stress states, large stress gradients, and the use of elasticity theory for a non-elastic material. Consequently, they are not valid as accurate strength tests, but should be regarded as strength index tests at best.

2.2.3 Ductile-to-brittle transition

According to the classical descriptions of mechanical behavior, ductile failure occurs after appreciable plastic deformation, whereas brittle fracture occurs after little or no plastic deformation. While it is not clear what amount of plastic deformation constitutes "appreciable" plastic deformation for ice, it is possible to qualitatively differentiate between these types of observed failures. The transition from ductile to brittle behavior for the shear of polycrystalline ice has been noted by various workers, and is useful in defining a reference strength for a given deformational mode, ie. ductile behavior.

In tension, Gold (1977) states that this transition occurs abruptly at the strain rate which does not allow sufficient time for dislocations to contribute significantly to the strain prior to the initiation of fracture.

For compressive loading, the ductile to brittle transition is much more gradual. While many researchers have discussed a ductile yield to brittle fracture transition zone, it is often difficult to ascertain the criterion used to determine this transition in each case. In the range of compressive stresses and strain rates of engineering interest, the primary mechanism of deformation, cracking, is a brittle event. However, the overall behavior is ductile for ice loaded in uniaxial compression at reasonably low strain rates (below 10^{-3} /s). Shear zones develop in areas approximately parallel to

the planes of maximum shear stress. This is usually associated with a barrelling failure (Gold 1970). However, if the ends are laterally restrained, cataclastic failure usually results, with conical wedges retained at the ends (Hawkes and Mellor 1972). At high applied strain rates, more abrupt failures occur, usually by the formation of a fault zone with little plastic straining.

Based on the observed change-over in overall stress-strain behavior, Gold and Krausz (1971) quote a ductile-to-brittle transition at about 2×10^{-4} /s for a type of columnar-grained ice. It should be noted that granular ice does not exhibit well-defined overall brittle behavior due to its inherent structure. At comparable strain rates, Gold and Krausz were not able to obtain brittle mechanical behavior for granular ice. It is possible that at higher strain rates, a change in mechanical behavior can be observed; however, data from Hawkes and Mellor (1972) indicate that even at 2×10^{-3} /s, a substantial amount of ductility still exists. Consequently, it may be difficult to determine a ductile-to-brittle transition for granular ice based on an observed change-over in mechanical behavior.

By observing the failure mode, one can also attempt to classify the behavior as brittle or ductile. Gold (1970) reported that brittle failure occurred by the abrupt development of a fault zone, while ductile failure was associated with barrelling or of the development of zones of crack concentration. In practice, however, it may be difficult to discern the different

failure types. As the applied strain rates increase, the times to failure decrease, as does the ability to identify the failure mode. Also, it is sometimes difficult or impossible to determine the exact mode of failure based on the remains of a ruptured sample.

When the ends are not laterally restrained, failure may occur by axial cleavage. In this case, the remains of the failed specimen differs greatly from one which failed by a ductile mode, and this can be used to differentiate between the failure modes. However, it is not altogether clear whether axial cleavage necessarily represents a truly brittle event characteristic of the ice sample. Instead, it may merely reflect the amount of restraint provided at the ends and the nature of the contact stresses at the platen/sample interface. Hawkes and Mellor (1972) took this position and disregarded all of their data exhibiting axial cleavage.

Hawkes and Mellor used a third method for determining the ductile-to-brittle transition. Basing their criterion on the belief that strength initially increases with strain rate, then reaches a maximum at the ductile-to-brittle transition, and thereafter possibly decreases to some asymptotic limit for very high strain rates, they plotted their peak strengths against applied strain rate. Because of the apparent maximum in strength at about 10^{-3} /s, this was cited as possibly being the ductile to brittle transition zone. However, preliminary data from Haynes (unpublished) seem to indicate that no

drop-off in strength or in strength increase with increasing strain rate occurs at strain rates up to 10^{-1} /s.

Slight errors in sample alignment and deficiencies in end restraint become magnified at higher strain rates. Also, experimental difficulties exist with measurement, loading and control systems. Consequently, some researchers have reported decreases in strength at high strain rates which subsequently disappeared with improved testing techniques.

With all of this uncertainty, it is difficult to arrive at a unique ductile to brittle transition value for a given ice type based on the results of different researchers. For columnar-grained ice, Gold and Krausz (1971) report the beginning of the transition at 2×10^{-3} /s, with the transition for granular ice probably at a higher rate. Jones (1978) observed a change in mechanical behavior for granular ice at 10^{-3} /s, together with a measured slope change in the peak strength vs. strain rate plot at this strain rate. With a 33.5 MPa confining stress, however, this transition disappeared, as the cracking activity was suppressed and only ductile behavior resulted. Nevertheless, a fairly consistent ductile-to-brittle transition zone has been reported for granular ice tested in unconfined compression by various researchers at a strain rate of 10^{-3} /s.

2.2.4 Deformation of Ice

Ice exhibits significant instantaneous recoverable (elastic) deformation as well as instantaneous permanent and recoverable time-dependent deformations under load. By far the greatest portion of the total deformation, however, is the time-dependent irrecoverable deformation. Typically, polycrystalline ice under constant stress exhibits a deformation-time behavior similar to that shown in Figure 2.10(a). Classically, the initial or primary stage of creep denotes decreasing strain rate, the secondary or "steady state" stage reflects a constant strain rate, and the tertiary stage an increasing strain rate. The tertiary stage of creep terminates by the failure of the sample due to "creep rupture". As will become evident, in most cases the secondary stage is not a "steady state" condition, but merely a point of inflection in the strain-time plot. This is particularly evident when the data are plotted using log strain rate and log time, as in Figure 2.10(b).

Creep deformation behavior exhibiting all stages of creep is typical also of monocrystalline ice constrained to deform in hard glide orientations (Butkovich and Landauer 1959, Higashi 1966). For monocrystalline ice deforming along basal planes, recent data indicate that primary (strain hardening) creep is also present at strain levels less than 0.25% (Ramseier 1971).

Almost all of the mechanisms of deformation described in Section 2.2.1 on deformational mechanisms exhibit some time dep-

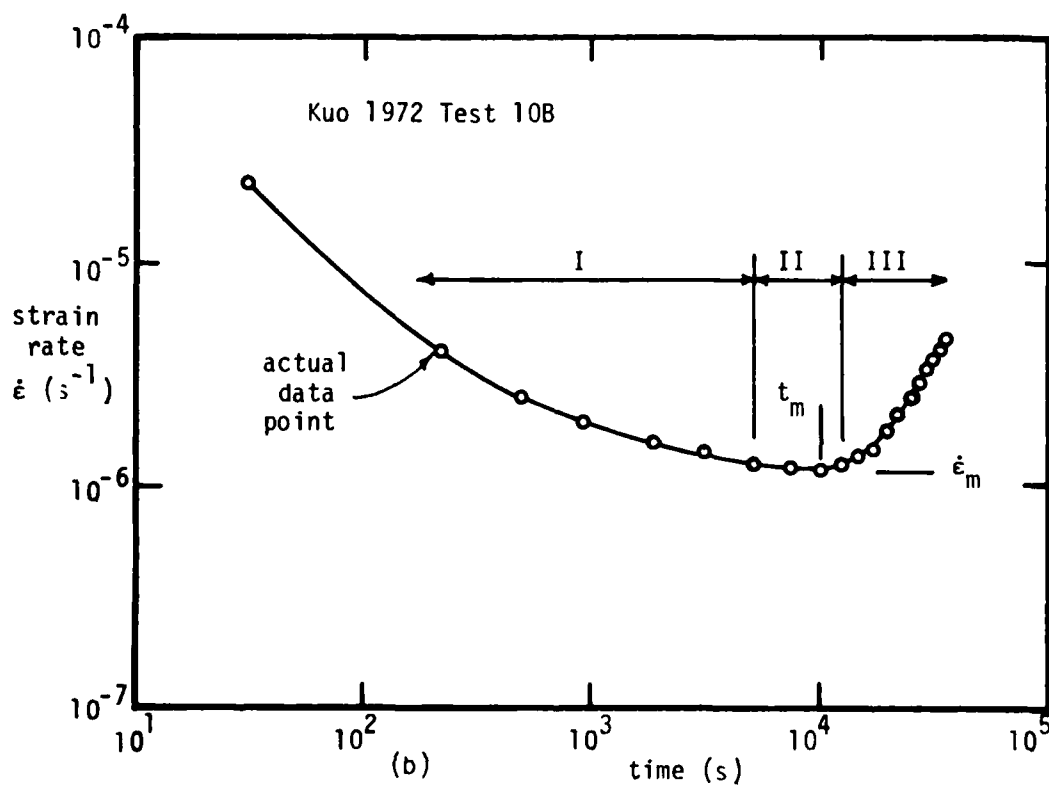
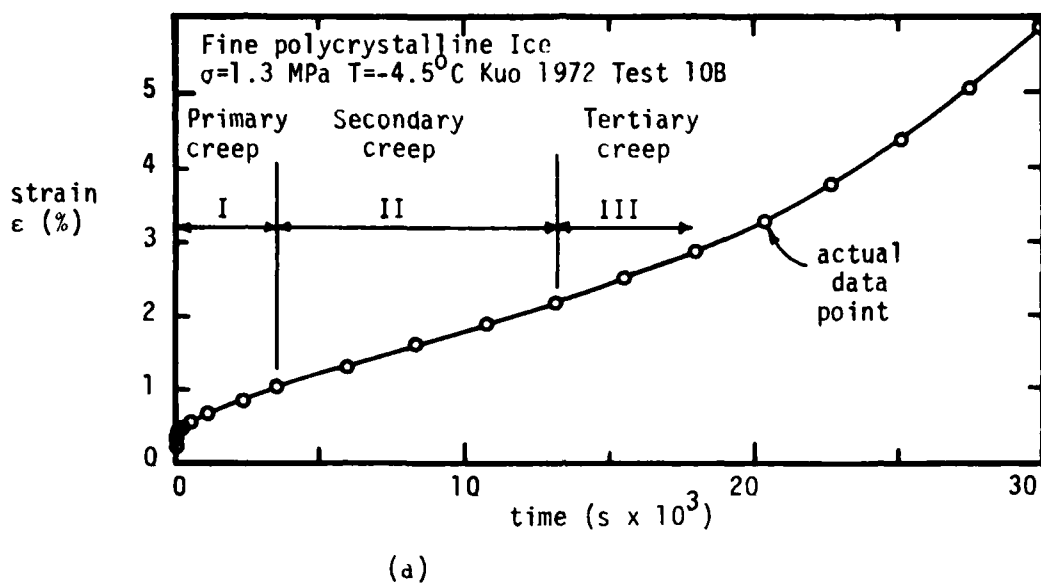


FIGURE 2.10 Typical creep data for ice

endence. Point and line defect motions are controlled by time dependent diffusion and dislocation processes. Grain boundary sliding may involve viscous shear mechanisms. Formation, transport and regelation of unfrozen water require time dependent liquid transport and heat flow. Cracking, while itself not a time dependent phenomenon, is the result of a time dependent buildup of dislocations at the grain boundaries and other points of stress concentration. Only the limited elastic compression and extension of the ice crystal lattice itself might truly be considered to be time independent phenomena.

Of these deformational mechanisms, some tend to soften the structure of the ice crystal, while others tend to harden the crystal. In a single crystal of pure ice, dislocation and point defect motion along the basal planes will marginally reduce the strength of the crystal by reducing the number of bonds acting along a given glide plane. Similarly, at higher stresses, microcracking in a pure ice monocrystal would also decrease the sample strength and cause an increase in the observed strain rate.

For monocrystals which possess impurities or are constrained to deform in hard glide, however, strain hardening does occur. The presence of certain chemicals, such as NH_3 , or particulate impurities serves as a barrier to dislocation motion, resulting in a strain hardening behavior (Jones and Glen 1969(b), Hooke et al. 1972). Tensile tests of ice monocrystals which were oriented so that the resolved shear stress on the basal planes was zero

indicated that strain hardening occurs only when hard glide motion is induced (Butkovich and Landauer 1959, Higashi 1966). This phenomenon has been reported in the metallurgical literature and is a feature exhibited by crystals with fewer than five slip planes, such as zinc (Freudenthal 1950). For ice Ih, with only one glide plane and hence two slip directions, non-basal defect motion results in distortion in the crystal structure. This leads to a more energetic structure which actually resists further defect movement. It can be inferred that a monocrystal with limited slip directions which deforms in other than these preferred directions is in actuality no longer a single crystal. If these sites of hard glide are thought of more as grain boundaries, then the hardening effect is easier to visualize. In each case, lattice mismatches in adjacent ice "crystals" result in a zone of reduced defect motion.

For polycrystalline ice, the processes in the monocrystal are combined with the effect on the grain boundaries. As previously mentioned, the effect of the granular structure is to induce deformational mechanisms other than easy glide. These include hard glide, accommodation cracking, crystal reorientation and grain boundary phenomena such as sliding, pressure melting and grain boundary migration. Of these mechanisms, most tend to weaken the resistance of the structure to shear. Reorganization of the crystal structure in individual grains due to an imposed stress, such as the melting of ice in high stress zones, liquid transport and resulting recrystallization at low-

er stressed regions tend to result in crystals more favorably oriented to easy glide. Microcracking, as in monocrystals, serves to relieve stress concentrations but also results in a weakened structure, with possibly new points of stress concentration.

While strengthening of the ice can occur by the healing of microcracks due to the formation of new bonds across the cracks, the major sources of strain hardening occur from the presence of grain boundaries and impurities in the ice. As already stated, each of these has been shown to individually cause apparent strain hardening in ice. Their combined effect results in considerably reduced creep behavior in polycrystalline ice compared to monocrystalline ice.

However, this apparent strengthening of the ice is done at the expense of the creation of additional stress concentrations in zones along the grain boundaries, around impurities and at the sites of major defects in the ice crystals. These zones of stress concentration serve as sites for the various strain softening mechanisms previously described, such as cracking, melting and grain boundary reorientation.

Consequently, the typical observed creep behavior of polycrystalline ice under constant stress can be explained as follows.

As the load is applied, elastic deformation of the crystals occurs, along with some cracking at initial points of stress concentration. Due to the granular structure of the ice,

hard glide mechanisms are induced in the ice. Easy glide mechanisms, while tending to soften the ice structure are not sufficient to be rate controlling. Instead, the rate of defect movement across grain boundaries and along hard glide directions tends to control the rate of creep. As a consequence, the strain rate decreases with time during this period. However, as deformation continues, stress concentrations build up at the grain boundaries, impurities and at large defects in the ice crystals. These serve to initiate softening mechanisms, primarily microcracking. When sufficient weakening of the overall structure occurs, the strain rate increases, resulting in accelerating creep. Rupture finally occurs when the sample is sufficiently weakened so as to be incapable of supplying the shear strength necessary to resist the applied load.

This hypothesis is supported in part by crack density and acoustical emissions studies such as carried out by Gold (1972). Preliminary results by St. Lawrence and Cole at CRREL indicate that the rate of acoustical emissions is proportional to the strain rate. Initially, some emissions are observed upon loading; thereafter, emissions activity decreases, until, at some point, acoustical activity increases corresponding to an increase in the strain rate.

From this treatment of the subject, it is clear that one unique deformational mechanism does not appear to control the creep of ice during the entire time period from initial load-

ing to final rupture. Instead, one would expect that the strain rate at any given time to be an aggregate of the strain rates due to numerous mechanisms. This is particularly true at the higher stresses, when more mechanisms occur in a short period of time. Consequently, the existence of a "steady state" stage of creep which corresponds to one unique dominant mechanism during secondary creep is considered to be unlikely.

While ice is known to creep continuously at fairly low stresses, it is not known if there exists a stress below which the creep rate of ice will not eventually accelerate. This problem concerns the existence of a limiting long term strength (LLTS) for ice. Typically, experimental problems with maintaining stress, temperature, sample quality and precision measurement systems over extended periods of time preclude valid longterm tests on ice at sufficiently low stresses. Lile (1977) reported uniaxial test results at -10°C which reached an observed minimum strain rate in 15 hr. at 0.6 MPa octahedral shear stress, but which did not reach a minimum (ie. it continued to decelerate) after 2000 hr at 0.005 MPa. Kuo (1972) reported that tests on fine polycrystalline ice at -4.5°C and 0.69 MPa axial stress increased in creep rate after 40 hr.

Studies on the effect of temperature on the creep of ice by many workers, such as Glen (1955), Mellor and Smith (1966 (a),(b)), Mellor and Testa (1969(a)) and Barnes et al. (1971), have shown that the creep rate of ice is very temperature sen-

sitive, especially above -10°C . Barnes et al. postulate that for low stresses, microcreep mechanisms such as point and line defect movements dominate below -10°C , while above this, grain boundary mechanisms are important. Above -3°C , pressure melting and recrystallization become significant.

Typically, the quoted strain rate at a given temperature and stress level is the observed "secondary" (minimum) strain rate. However, due to the previously cited problems concerning longterm testing of ice, the experimental minimum strain rate is often unavailable, particularly at lower stresses. Consequently, attempts at estimating the minimum strain rate have been made by empirical methods such as the use of the Andrade equation (Glen 1955, Barnes et al. 1971, Hooke et al. 1972, Baker 1978), or use of the strain rate at a specified strain level. Since the use of the Andrade equation for prediction of the minimum strain rate has been shown to be unreliable (Ting and Martin 1979), the results of analyses using this method should be viewed with caution. Also, from the previous discussion of the mechanisms of deformation, the minimum strain rate $\dot{\epsilon}_m$ probably does not represent a true "steady state" condition for a sample at a given temperature and stress level. However, in spite of these drawbacks, the bulk of the existing analyses of the temperature dependence of the creep of ice involve the use of this "secondary" strain rate. These analyses of the temperature dependence have also involved the assumption that the deformational processes in creep are ther-

mally activated. By the use of the Rate Process Theory, various values of the apparent activation energy of deformation have been computed. Details of such analyses are discussed later in this Chapter.

Hooke et al. (1972) and Goughnour and Andersland (1968) studied the effect of varying quantities of particulate impurities on the creep and strength of ice. Hooke et al. found that within the scatter of their data, as the amount of sand increased, the creep of the ice-sand decreased. Since tertiary creep was not achieved in each test, the minimum strain rate ($\dot{\epsilon} = 0$) was not observed. Instead, the "secondary" strain rates were approximated by the minimum values achieved during each test. These values are plotted in Figure 2.11 against sand fraction. From these results, the estimated minimum strain rate decreased considerably from 3×10^{-8} to 1.5×10^{-9} /s from pure ice to ice with 0.35 volume fraction of sand. This result is closely related to that of Goughnour and Andersland (1968) from Figure 2.8 where their peak strengths increased with increasing sand concentration. Above 0.42 sand volume, their data indicate a considerable increase in peak strength corresponding to the change in structure from a sandy ice to a frozen soil where the particles are in contact.

The effect of the grain size of ice on creep has been examined by Baker (1978), Goodman (1977) and others. Above a grain size of 1mm, the secondary creep rate increases approximately with the square of the grain size, as shown by Sherby

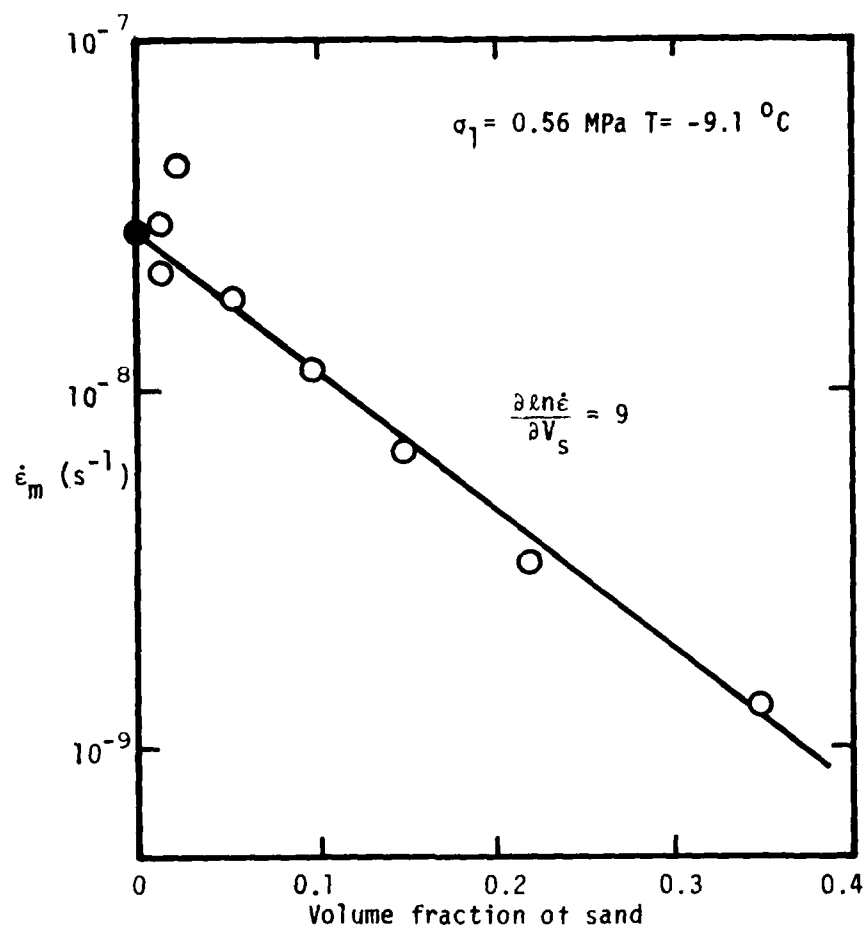


FIGURE 2.11 Effect of sand concentration on the creep of a sand-ice system (from Hooke et al. 1972)

(1962) for the creep of coarse-grained metals at high homologous temperatures. This result is to be expected, since the specific surface area decreases with increasing grain size. Since the grain boundary alone has been shown to decrease the creep in ice (Homer and Glen 1978), one would expect that when the grain boundary surface decreases, the strain rate increases. Below 1mm, however, Baker indicates that the strain rate increases markedly with decreasing grain size. This controversial result has been disputed (Hooke et al. unpubl.) and is currently the subject of ongoing research at USA CRREL.

Various other experimental observations have been made concerning the creep of ice. Among these is the so-called "correspondence principle" between constant stress creep tests and constant strain rate strength tests. By plotting the peak strength against applied strain rate from a strength test together with the minimum strain rate against applied stress in a creep test, Hawkes and Mellor (1972) observed that a smooth transition occurred between creep and strength test results. This correspondence has been implicitly assumed by by other researchers, without explicit justification. However, this correspondence does appear to have an experimental basis, as shown in Figure 2.12 by Gold (1977). This correspondence has also been shown to be valid, within limitations, for frozen soil by O'Connor and Mitchell (1978). To account for the slight discrepancies in the applied stress/minimum strain rate and peak

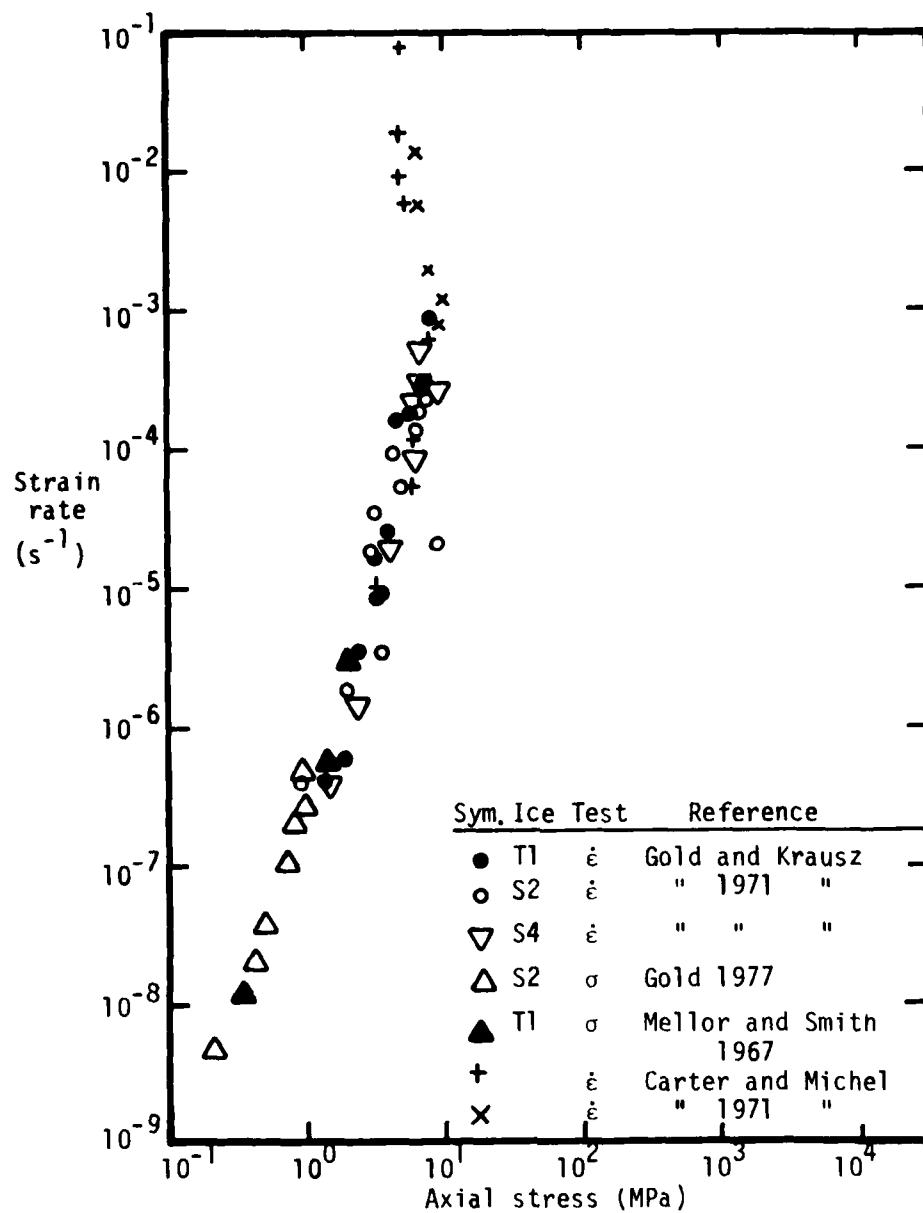


FIGURE 2.12 Strain rate dependence of the yield and brittle strength and stress dependence of the "secondary" strain rate of ice (from Gold 1977)

strength/applied strain rate values between the two tests, they postulated that the unifying factor was the applied strain energy in each test.

Preliminary results from an extensive study of this correspondence principle carried out at USA CRREL using constant stress creep tests, constant strain rate strength tests and multimodal tests appear to confirm its validity for polycrystalline snow ice.

A power relation has been observed for ice between the minimum strain rate and the time to this minimum strain rate (Jacka, in Lile 1977). By plotting creep data on double logarithmic scales, the linear relationship between minimum strain rate and the time to minimum is clear (see Figure 2.13(a) and (b)). This relation has also been observed in unfrozen clays (eg. Campanella and Vaid 1972, Mitchell 1976) and frozen soils (Martin, Ting and Ladd 1981). While this relation appears to be prevalent in many materials, very little work has been carried out to determine the theoretical basis for this behavior. A possible explanation is presented in Chapter 5.

Finally, an unusual but often observed phenomenon in the creep of ice has been a jerky, step-like movement at low creep rates (Baker 1978 and Kuo 1972). This may be due to stickiness in the loading system at cold temperatures, an error band due to the measurement system, a consequence of a small sample size in combination with very low strain rates, or it may be due to an actual slip-stick deformation in the ice.

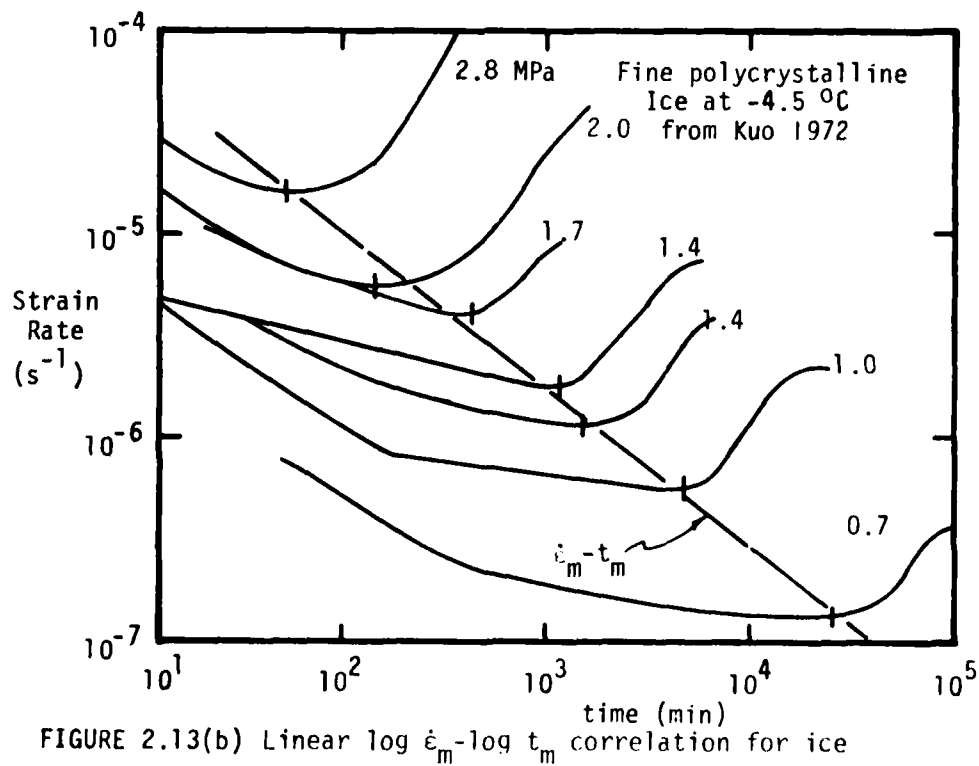
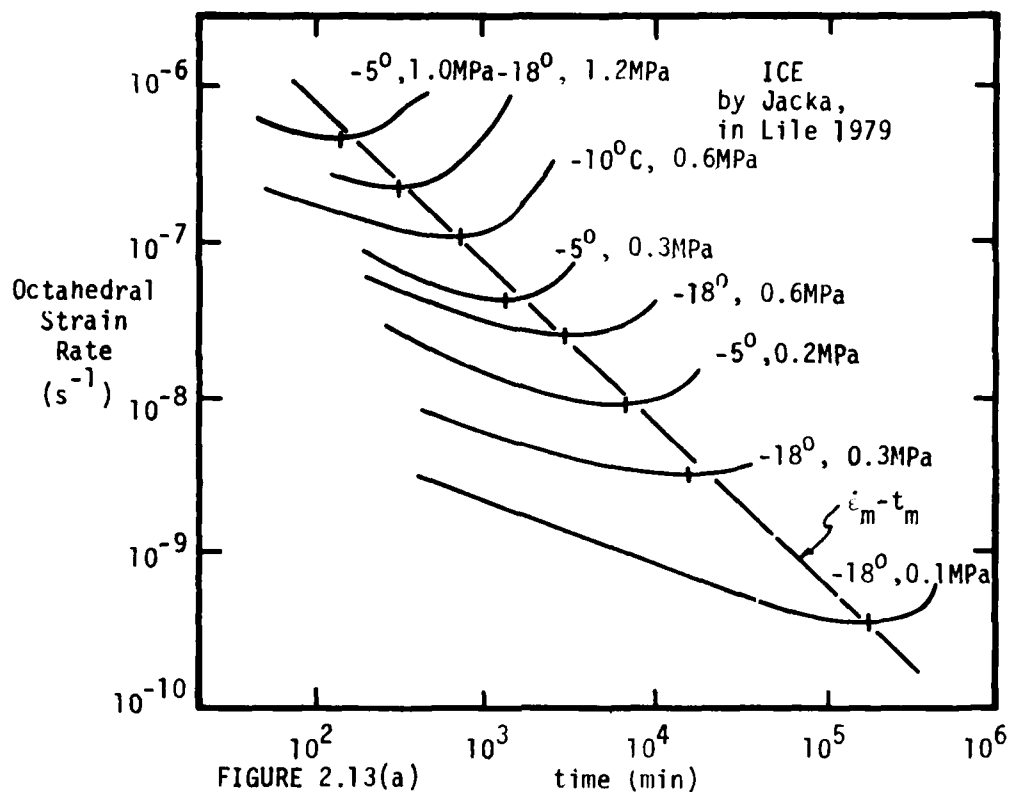


FIGURE 2.13(b) Linear $\log \dot{\epsilon}_m - \log t_m$ correlation for ice

The stickiness in the system may be checked by placing a load cell directly in-line with the sample; the size of error band expected may be estimated by analysis of the stability and resolution of each measuring device; the effect of sample size/low strain rate may be checked by varying the size of the samples tested.

2.2.5 Quantitative models of ice strength and deformation

Quantification of the strength and deformational behavior of ice is extremely difficult, primarily due to its existence in nature at temperatures near its melting point. Also, attempts at generalizing the results from several researchers are difficult due to the large effect of minor testing details and sample preparation techniques. In addition, tremendous scatter exists in strength and deformation data on nominally identical samples tested under similar conditions. Consequently, a unifying constitutive relation has not yet been developed which can adequately predict the stress-strain-time-temperature behavior of ice.

The observed scatter may be attributed to a variety of reasons. Problems with grain-size control, quantity, shape, size and location of air bubbles and amount and type of impurities hinder efforts in making perfectly uniform ice samples. Also, at stresses or strain rates high enough to induce crack phenomena, failure is usually controlled by the development of weakened shear zones or outright fracture through the development of a "critical crack". Since the brittle fracture of any material is governed by the statistics of the imperfections present, it can be expected that the strengths obtained at higher strain rates would be statistical, rather than deterministic, in nature. Also, increased scatter should be present at the higher strain rates as the effects of slight sample imperfections, slight sample misalignment and end restraint conditions

become magnified.

In spite of all the difficulties cited, numerous attempts have been made at quantifying strength and deformation behavior for ice. These have included the use of theoretical dislocation models, mechanistic theories such as Rate Process Theory and Griffith's fracture criteria, to empirical curve fitting relations.

Rate Process Theory

One model, Rate Process Theory (RPT) has been utilized to link the strain rate, temperature and the stress level of ice. This theory was originally formulated by Eyring (1936) and is summarized by Mitchell (1976), Mitchell et al.(1968), Andersland and Douglas (1970), Martin et al.(1981) and others.

The theory is based on the assumption that units participating in a deformation process (termed flow units) are constrained from movement relative to each other by virtue of energy barriers separating adjacent equilibrium positions. The displacement of flow units to new positions requires their activation through the acquisition of sufficient energy to overcome this energy barrier. The minimum energy required to overcome this barrier when the body is at rest is termed the free energy of activation, ΔF . From statistical mechanics, it is possible to describe the frequency of activation as:

$$\nu = kT/h \exp (-\Delta F/NkT) \quad (2.1)$$

where k = Boltzman's constant (1.38×10^{-23} joule/ $^{\circ}$ K)

h = Planck's constant (6.624×10^{-34} joule-s)

N = Avagadro's number (6.02×10^{23})

T = temperature ($^{\circ}\text{K}$)

In the absence of applied potentials, barriers are crossed with equal frequency in all directions and hence no observed consequences of periodic activation exists. However, if a directed potential such as an external shear stress is applied, then the barrier heights become distorted. For a force f acting on a flow unit, the net frequency of activation in the direction of the force becomes:

$$\dot{\bar{v}} - \bar{v} = \frac{2kT}{h} \exp\left[-\frac{\Delta F}{RT}\right] \sinh\left[\frac{f\lambda}{2kT}\right] \quad (2.2)$$

where R = Universal Gas constant ($8.31 \text{ J}/^{\circ}\text{K-mole}$)

λ = displacement of flow unit

At this point, Mitchell et al. (1968) introduce the term X which accounts for the proportion of activated flow units which successfully surmount the energy barrier and the distance λ travelled by each successful flow unit. Since the component of λ in the direction of motion times the number of successful jumps per unit time yields the deformation rate, then by using the X term to also account for some original length, the strain rate can be expressed as:

$$\dot{\epsilon} = 2X \frac{kT}{h} \exp\left[-\frac{\Delta F}{RT}\right] \sinh\left[\frac{f\lambda}{2kT}\right] \quad (2.3)$$

where X is both time and structure dependent.

For higher stress levels where $(f\lambda/2kT) > 1$,

$$\sinh\left[\frac{f\lambda}{2kT}\right] \approx \frac{1}{2}\exp\left[-\frac{E}{RT}\right] \quad (2.4)$$

and (2.3) becomes

$$\dot{\epsilon} = X \frac{kT}{h} \exp\left[-\frac{E}{RT}\right] \quad (2.5)$$

where $E = \Delta F - \beta\sigma$ is the experimental activation energy, σ is some measure of deviatoric stress level and β is an experimentally determined constant. Then for $XkT/h = \text{constant}$, equation (2.5) becomes the experimental Arrhenius equation for chemical reactions.

To evaluate the various parameters of the Rate Process Theory, numerous techniques and several types of tests have been used. These include running series of constant stress creep tests at different temperatures and stresses, stress stage tests and temperature stage tests. The detailed procedures for each method are described in Martin et al. (1981) and Ting (1981).

Various workers in ice, while accepting the form of the Arrhenius equation, have modified the basic equation to more accurately account for the stress dependence of the strain rate. Barnes et al. (1971) used the form

$$\dot{\epsilon}_{\text{steady state}} = A (\sinh \alpha \sigma)^n \exp\left(-\frac{E}{RT}\right) \quad (2.6)$$

where A , E , α , n are constants

In this case, it is not clear whether any physical significance can be attributed to the value of E , an "apparent activation energy".

Others have modified the RPT equation by including a power function to describe the stress dependence:

$$\dot{\epsilon} = C\sigma^n \exp\left(-\frac{E}{RT}\right) \quad (2.7)$$

(Glen 1955, Weertman 1973, Langdon 1973, Gold 1973, Homer and Glen 1978). This is by far the most popular deformational model, and is actually a combination of RPT and dislocation creep models. Equation (2.7) may be expanded to account for numerous creep mechanisms in polycrystals and monocrystals at high temperatures:

$$\dot{\epsilon} = \frac{AGb}{kT} D_0 \exp\left(-\frac{E_d}{kT}\right) \left(\frac{b}{d}\right)^m \left(\frac{\sigma}{G}\right)^n \quad (2.8)$$

where A = dimensionless constant

D_0 = frequency factor

E_d = activation energy for diffusion

G = shear modulus

b = Burger's vector (4.523×10^{-6} mm for ice)

d = average grain size

m, n = constants which depend on the operating creep mechanism

Since the constant A is not well defined, it is easier to compare the measured E_d , m and n with the theoretical values for each mechanism. These were reported by Langdon (1973) and are summarized in Table 2.2.

RPT as written in equation (2.3) and (2.5) adequately accounts for the temperature dependence of the creep of mono- and polycrystalline ice. However, the implicit (and widespread)

Mechanism	m	n	E
1. Point Defect Mechanisms			
Vacancy diffusion through lattice	2	1	E_l
Vacancy diffusion along grain boundaries	3	1	E_{gb}
2. Line Defect Mechanisms			
Dislocation glide/climb controlled by climb	0	4.5	E_l
Dislocation glide/climb controlled by glide	0	3	E_l
Dislocation climb without glide	0	3	E_l
Overcoming of Peierls stress on prismatic plane	0	2.5	E_{pe}
Cross-slip of basal dislocations into prismatic plane	0	2	E_{pr}
Viscous dislocation damping	0	3	E_{if}
3. Grain Boundary Shearing Mechanisms			
Viscous shear at grain boundaries	1	1	E_{gb}
Grain boundary sliding by a dislocation process	1	2	E_l (or E_{gb})

Table 2.2 Possible creep mechanisms in ice
(from Langdon 1973)

use of the modified forms of the RPT as in equations (2.6) to (2.8) strongly suggests that RPT is not strictly applicable for describing the stress dependence of the creep of polycrystalline ice. This result is in accordance with an extensive evaluation of the Rate Process Theory for ice and frozen soil by Martin et al. (1981), who found that the original RPT equation as written in (2.3) successfully describes the creep of monocrystalline ice, is less successful for polycrystalline ice, and cannot describe the creep of frozen sand.

Quantitative models of strength

Based on the modified rate process theory, Muguruma (1969) rewrote equation (2.7) in terms of stress:

$$\sigma = C\dot{\epsilon}^{1/n} \exp\left(-\frac{Q}{nRT}\right) \quad (2.9)$$

The values of n and Q for single crystals of ice from unconfined strength test data have been summarized by Weertman (1973) and are presented in Table 2.3, together with results for uniaxial and plane strain tests on polycrystalline ice from Frederking (1977) and Gold and Krausz (1971).

Note, however, that the original equation (2.7) was formulated in terms of applied stress and "steady-state" creep rate, whereas in (2.9) the interpretation is peak strength and applied strain rate. Since both equations are semi-empirical, this apparent inconsistency in the interpretation of the variables is not relevant. However, the usage of essentially the same equation to describe both test types, with similar values of

n	Q (kjoule/mole)	Reference	Comments
1.3	46	Muguruma (1969)	** chemically polished
1.7	63	" "	** mechanically polished
2.3	42-75	Jones and Glen (1968) *	**
1.5	66	Higashi et al (1964) *	**
2		Ramseier (1972) *	**
1.8	75	Nakamura / Jones (1973)	**
3	67	Muguruma (1969)	Columnar polycrystalline -10° to -30°C
4		Gold and Krausz (1971)	Columnar polycrystalline -10°C
3.3		Frederking (1977)	Columnar, uniaxial, -10°C
5.2		" "	" plane strain
6.7		" "	granular, plane strain
4.9		" "	" uniaxial

* references found in Weertman (1973)

** single crystals oriented for easy glide

Table 2.3 - Values of n and Q from constant strain rate tests on ice

n and E (see Table 2.4), implicitly suggest the existence of the correspondence principle previously described.

Numerous attempts at using other theories to describe the strength behavior of ice under different loading conditions, such as the Mohr-Coulomb failure criterion (Smith and Cheatham 1975) and fracture theory (Haynes 1973, Nevel and Haynes 1976, Gold 1977), have met with at best only limited success. Consequently, no unifying theory can at present adequately describe the strength behavior of a given ice type under a specific confining stress and temperature loading condition.

Although equation (2.9) does a reasonable job of empirically describing the data, considerable scatter is evident in Figures 2.5 and 2.6. This scatter can be partially attributed to the difficulty in obtaining reproducible samples of mono- and polycrystalline ice and the various reasons previously cited.

Quantitative models of deformation

Numerous attempts have been made to quantify the time dependent deformation of ice. These include purely empirical models which describe only the primary stage of creep, such as the Andrade's $1/3$ power law and the rheological model of Sinha (1978). Models such as Rate Process Theory and dislocation creep models/RPT describe only secondary creep as a function of the applied stress and temperature. A recently developed empirical relationship (Assur 1979) can model the entire

Reference	stress exponent n	Activation energy E kJ/mole	Temperature °C	Comments
Monocrystals				
Tripps, and Coles (1954)	2	-		
Steinemann (1958)	1.5-4.0	-		$n = 2.3-4.0, \dot{\gamma} < 0.2; \dot{\gamma} > 0.2$
Butkovich and Landauer (1958)	2.49	-		easy glide
	2.70	-		hard glide
Hidashi and others (1965)	1.58	66		
Glen and Jones (1967)	-	65.4	-10 to -50	
Jones and Glen (1968)	2.3	39.5	-50 to -90	
Ramseier (1967)	-	57.0		hard glide
Mellor and Testa (1969[a], [b])	-	64.0		hard glide
Homer & Glen (1978)	1.9	78		
Ramseier (1971)	1.9			
Poly crystals				
Maquruma (1969)	3	67	-10	constant strain-rate test columnar ice
Steinemann (1958)	3.1-3.6	83	-10	random orientation
Mellor (1959)	4.2	-	-10	Antarctic ice shelf
Bowden and Tabor (1964)	-	50	-10	friction experiments
Mellor and Smith (1967)	3.5	45	-10	random orientation
Weertman (1968)	3.5	42	-10	random orientation
	3.5	42	-10	D ₂ O ice
Mellor and Testa (1969[a], [b])	-	67.5	-10	random orientation
Nayar and others (1971)	-	62.5	-10	probably not random orientation
Ramseier (unpublished)	2.5-5	60	-10	
	4.0	60	-10	
	3.0-5	60	-10	
	3.1-5	60	-10	
Barnes and others (1971)	3.1	72	-10	
Leh (1971)	-	65	-10	frazil ice
Hawkes and Mellor (1972)	3	-	-10	random
Thomas (1973)	3	-	-10	Antarctic
Butkovich and Landauer (1960)	1	60	-10	commercial and natural glacier ice
Bromer and Kinverly (1968)	1	80	-13 to -4	random orientation
Mellor and Testa (1969[a], [b])	1.8	-	-	random
Glen (1955)	3.2	135	-10	random orientation
Steinemann (1958)	2.8-3.2	135	-10	
Butkovich and Landauer (1959)	3	-	-10	
Barnes and others (1971)	3.2	120	-10	
Colbeck and Evans (1973)	1.3	-	-0.01	natural glacier ice
Wadhams (1974)	3.0	-	-10	floating pack ice
Homer & Glen	2.9	75	-4 to -30	bi-crystal

TABLE 2.4
Values of n and E from constant stress creep tests.
References found in Homer and Glen (1978)

creep curve, from primary through tertiary creep.

The Andrade power law is a purely empirical equation which enjoys some success in fitting the primary stage creep data of metals for a given testing condition (Conway 1967), ice (Glen 1955, Barnes et al. 1971) and frozen soil (Ting and Martin 1979). Written in terms of natural strain, this model states:

$$\epsilon = \epsilon_0 - \beta t^{1/3} - kt \quad (2.10)$$

for $|\beta t^{1/3}| \ll 1$

where t = time after load application

ϵ_0 = sample strain at time t

ϵ, β, k = fitting constants

Using (2.10) the primary stage creep strain can be described as the sum of three components: (1) an instantaneous strain ϵ_0 , (2) a portion kt which increases linearly with time, and (3) a portion which is proportional to $t^{1/3}$. These components are plotted in Figure 2.14.

In addition to using this equation to fit the data, Glen (1955) and Barnes et al (1971) used this equation to predict the secondary strain rate $\dot{\epsilon}_m$ in tests where the secondary stage had not been reached. By interpreting k in equation (2.10) to represent $\dot{\epsilon}_m$, they reduced their data for tests which terminated in the primary stage of creep to obtain apparent secondary stage creep rates. While the Andrade equation may model data during primary creep under certain conditions, it cannot be used to predict the secondary strain rate in tests which terminated during primary creep (Ting and Martin 1979).

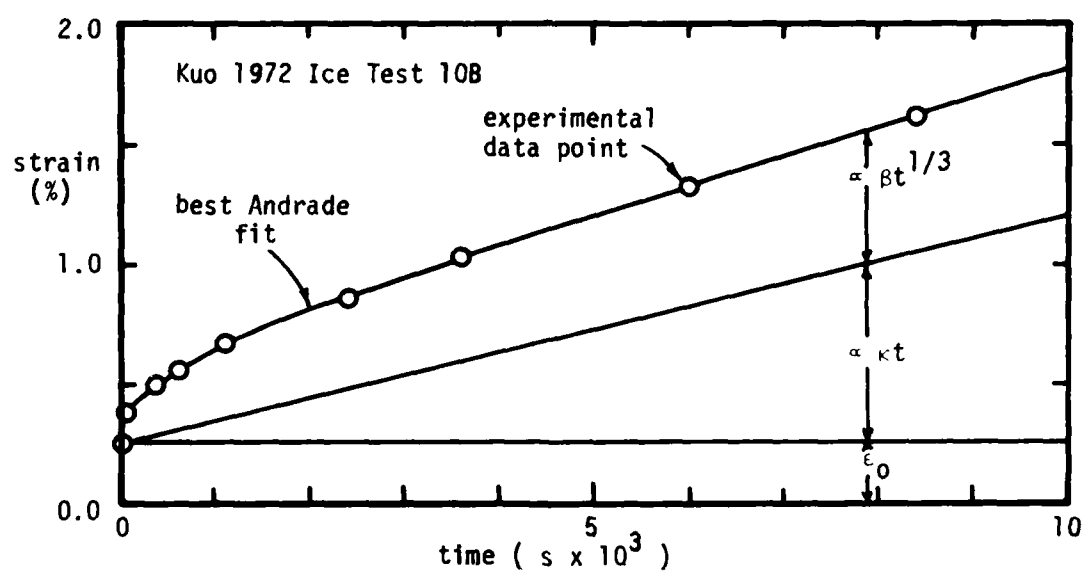


FIGURE 2.14 Components of the Andrade equation

As already stated, the most common deformational model in ice combines the rate process theory and dislocation creep models (equation 2.7). The values of n and E for ice obtained for the model from various researchers are summarized in Table 2.4. It is difficult to draw firm conclusions from the results quoted. Some of the data yielding $n = 1$ at low stresses (Butkovich and Landauer 1960, Bromer and Kingery 1960) have been discounted due to inadequate strain during the determination of the "steady state" strain rate. Some of the researchers used the Andrade equation prediction to evaluate the secondary strain rate (Barnes et al. 1971) or used a strain rate at a fixed strain level (Homer and Glen 1978, Mellor and Testa 1969 (a),(b)). None actually achieved a true minimum strain rate.

The previously described equations can model creep only in the primary or secondary stages. A recently developed empirical relationship by Assur (1979) can describe the creep of ice through the tertiary stage as well. The model states:

$$\dot{\epsilon} = Ae^{\beta t} t^{-m} \quad (2.11)$$

where A , β , m are constants.

Details of this equation are found in Chapter 6. While work must be done on this model to account for the loading conditions and for developing procedures for parameter evaluation, this equation shows considerable promise for modelling the creep behavior of ice.

In conclusion, it can be seen that although significant effort has been made towards quantifying the deformation beha-

behavior of ice under load, the current state of knowledge is not adequate to accurately predict the entire deformation-time behavior of ice as a function of stress level and temperature. The semi-empirical Rate Process Theory/dislocation models consider stress and temperature, but are only capable of predicting a steady state strain rate. Moreover, a quasi-steady strain rate is in fact only rarely present in ice. A promising new relationship (equation 2.11) appears capable of modelling the complete creep deformation behavior of a given sample of ice from primary through tertiary creep. However, since it is entirely empirical, further research is required in order to incorporate terms to account for the stress and temperature dependence.

2.3 Summary of the Nature and Mechanics of Ice

Important concepts presented in the previous sections on ice include:

- (1) the ice crystal lattice possesses only one plane of easy glide and hence only two independent slip directions;
- (2) ice typically exists in nature in some polycrystalline form;
- (3) ice possesses unfrozen liquid-like water even at temperatures down to -25°C , probably at the grain boundaries (Hosler et al.1957, Barnes et al.1971, Tice et al.1978);
- (4) ice exists in nature at temperatures very close to its melting point; consequently many high temperature phenomena exist, ie. pressure melting and regelation at stress concentrations, crystal reorientation and grain growth;
- (5) many deformational mechanisms are potentially applicable for ice, depending on the temperature and applied stress or strain rate: at temperatures below -10°C , stresses below 0.5 MPa and low strain rates, microcreep mechanisms dominate; below -10°C , above 1 MPa applied stress and at strain rates higher than for microcreep, microcracking is the dominant deformational mechanism; above -10°C , grain boundary effects dominate (see Figure 2.4);
- (6) time dependent deformation is the major component of the total deformation of ice under sustained load;
- (7) the uniaxial (unconfined) compressive strength of ice is very temperature and strain rate dependent (see Figures 2.5

and 2.6);

(8) the presence of sand in ice serves to strengthen the resulting composite; as the sand concentration is increased above a critical concentration corresponding to particle-to-particle contact in the sand, the rate of increase of strength increases significantly (see Figures 2.8 and 2.11);

(9) for the strain rates of interest ($> 10^{-6}$ /s), the uniaxial tensile strength of ice is not very temperature or strain rate dependent; this value is about 2 MPa for granular ice (Gold 1977);

(10) the influence of confining stress on the compressive strength of ice depends on the magnitude of the confining stress level: at low confining stresses, the strength increases with confining stress, probably due to the inhibition of cracking activity; at high stresses (> 40 MPa), strength decreases with increasing confining stress (see Figure 2.9);

(11) other means of ice testing such as ring shear testing, diametral compressive testing of rings and cylinders and beam testing should be treated as strength index tests due to interpretation problems and the complex stress conditions imposed;

(12) in spite of the many difficulties in defining a consistent transition point, a ductile-to-brittle transition for ice tested in unconfined compression appears to be present at a strain rate of 10^{-3} /s (Gold 1977);

(12) time dependent deformation is the major component of the total deformation of ice under sustained load;

(13) all ice, including monocrystals, probably exhibits decelerating (primary stage) creep behavior under constant stress loading immediately after stress application (Ramseier 1971);

(14) the effect of grain size on the behavior of ice may be significant; for granular (snow) ice above 1 mm grain size, an increasing grain size increases the creep behavior and decreases the strength; below this size, the effect of grain size is not clear (Baker 1978, Hooke et al. unpubl.);

(15) a correspondence between [peak stress/applied strain rate] and [applied stress/minimum strain rate] appears to exist (see Figure 2.12).

(16) a strong correlation exists between minimum strain rate and the time to minimum ($\dot{\epsilon}_m / t_m$) for creep testing at varying temperatures and stresses (see Figure 2.13).

(17) common methods for explaining and/or modelling the creep behavior of ice include Rate Process Theory, fracture theories, dislocation theories and rheological and empirical modelling; although none are currently capable of fully predicting the stress-strain-time-temperature behavior of ice, an equation (2.7) combining RPT and dislocation creep theories appears to adequately describe the relationship between applied stress and minimum strain rate for creep testing and peak strength and applied strain rate for strength testing.

CHAPTER 3 - REVIEW OF THE NATURE AND MECHANICS OF UNFROZEN SOIL

Together with ice, soil forms a prominent part of the frozen soil system. Several major references present detailed descriptions of the nature and mechanical behavior of unfrozen soil, such as Mitchell (1976), Lambe and Whitman (1969) and Ladd et al.(1977). This Chapter briefly emphasizes those aspects considered essential to an understanding of the behavior of a frozen soil system.

3.1 Nature of the Unfrozen Soil System

Unfrozen soil is composed of soil particles and voids, with the voids containing water and/ or air. For coarse grained soils under an applied load, grain to grain contact is assured due to the high contact stresses present, often sufficient to crush quartz particles. Solid particle contacts also probably exist for all but ideally dispersed clays. Experiments by Hofmann (1952) on freeze-dried clay gels and indirect data by Mitchell et al.(1968) using Rate Process Theory support this hypothesis.

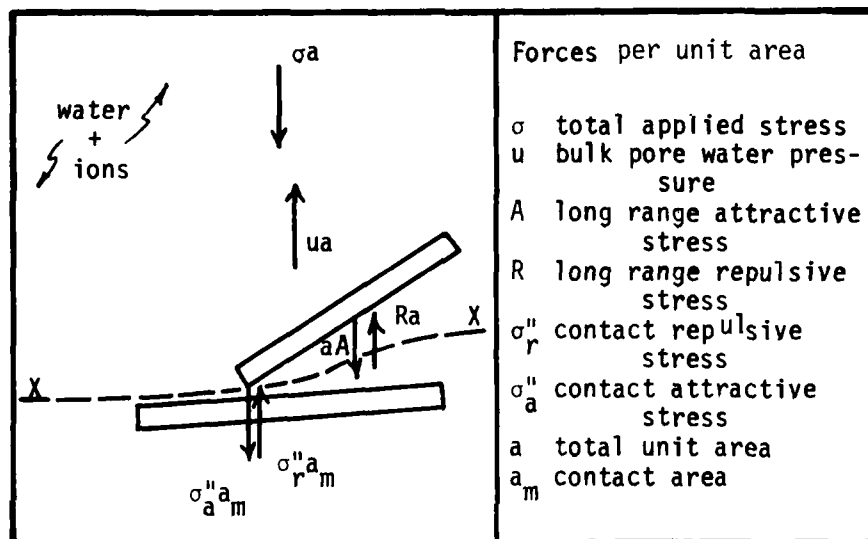
The water in unfrozen soil may be grouped into three categories: (a) adsorbed water adjacent to the soil surfaces, typically several molecular layers thick; (b) double layer water associated with the negatively charged mineral surface, up to several hundred Angstroms thick; and (c) bulk (normal) water, not influenced by soil-water forces. The adsorbed water film is strongly attracted to silicate surfaces, requiring in ex-

cess of 400 MPa to squeeze the last molecular layer of water away from a clay surface (Steinfink and Gebhart 1962, van Olphen 1963). The adsorbed water in unfrozen (and frozen) soils is continuous, completely surrounding the mineral surfaces except at the soil contacts, and does not behave like bulk water. It is capable of significant freezing point depression. While the nature and structure of this film are not completely clear, it probably is not "ice-like", probably exhibits Newtonian viscous flow parallel to the mineral surface (p. 107 Mitchell 1976) and hence probably does not generate significant shear strength at particle "contacts".

The physico-chemical effective stress equation (as seen in Figure 3.1) is generally accepted as describing the various components of stress believed to act in unfrozen soil systems. The average effective (intergranular) normal stress, σ , defined as the total stress minus the pore water pressure, may be expressed as the sum of the contact stresses and the double layer stresses. For coarse grained soils, the contact forces dominate and the surface (double layer) forces are negligible. For clays, however, the surface forces can strongly influence the overall mechanical behavior.

3.2 Mechanics of Unfrozen Soil

Due to the particulate nature of unfrozen soils, the mechanisms of strength and deformation include components which are not normally encountered in continuous materials. Some



Physico-chemical effective stress equation:

$$\sigma' = \sigma - u = (R - A) + (\sigma''_r - \sigma''_a) \frac{a_m}{a}$$

double layer contact
stresses stresses

FIGURE 3.1 The physico-chemical effective stress equation

of these mechanisms involve: elastic deformations of the particles, both axially and flexurally; particle crushing at the contacts; sliding and rolling at the contacts; changes in average interparticle spacing including reduction of the double layer thickness; and particle rearrangement and reorientation. Some of these mechanisms can be reversible, such as the elastic deformations and the changes in double layer spacing, while the others are not. Consequently, an altered structure results from shearing which can greatly affect future behavior. Moreover, most of the mechanisms also exhibit time-dependent (creep) behavior, especially those associated with relative deformation at the contacts.

Rowe (1962) proposed that the strength of a dry cohesionless particulate material consists of three basic components. Using the Mohr-Coulomb failure criterion (with $\sigma = \sigma'$),

$$\tau_f = c + \sigma_f \tan \phi \quad (3.1)$$

where τ_f = shear stress at failure on the failure plane

σ_f = normal stress at failure on the failure plane

ϕ = friction angle

c = apparent cohesion, equal to zero for cohesionless sands

Rowe postulated that the total frictional resistance as measured in triaxial tests is composed of the following:

(1) interparticle friction. This forms the bulk of the resistance, and is due to particle sliding friction at the contacts. It has since been shown by Skinner (1969) that

rolling friction should also be included within this category;

(2) dilation effect. For soils which exhibit positive dilation, ie. increased sample volume during shear, such as dense sands and overconsolidated clays, additional work must be expended due to the expansion of the soil against its confining stress;

(3) particle interference and reorientation. This occurs under all conditions except with very dense sands at small strains.

The three components of strength are shown in Figure 3.2 as a function of relative density. Quantitatively, Rowe presents:

$$\left(\frac{\sigma_1}{\sigma_3}\right)_{\max} = \left(1 + \frac{dV}{d\varepsilon}\right) \tan^2\left(45 + \frac{\phi_f}{2}\right) = \frac{1 + \sin\phi}{1 - \sin\phi} \quad (3.2)$$

where ϕ_μ = sliding friction

$\phi_f = \phi_\mu$ for very dense sands

$\phi_f = \phi_{cv}$ for very loose sands

$\frac{dV}{d\varepsilon}$ = rate of volume change with respect to strain.

When water is present, the mechanisms of strength as presented by Rowe are still applicable, provided the loading is drained, ie. no excess pore water pressure develops during shear, and the stresses are expressed in terms of the effective stresses $\sigma' = \sigma - u$. With these constraints, equation (3.2) has been used by several workers to describe the drained strength of sands (eg. Lee and Seed 1967). For example, the curved Mohr-Coulomb envelope exhibited by most granular soils mainly

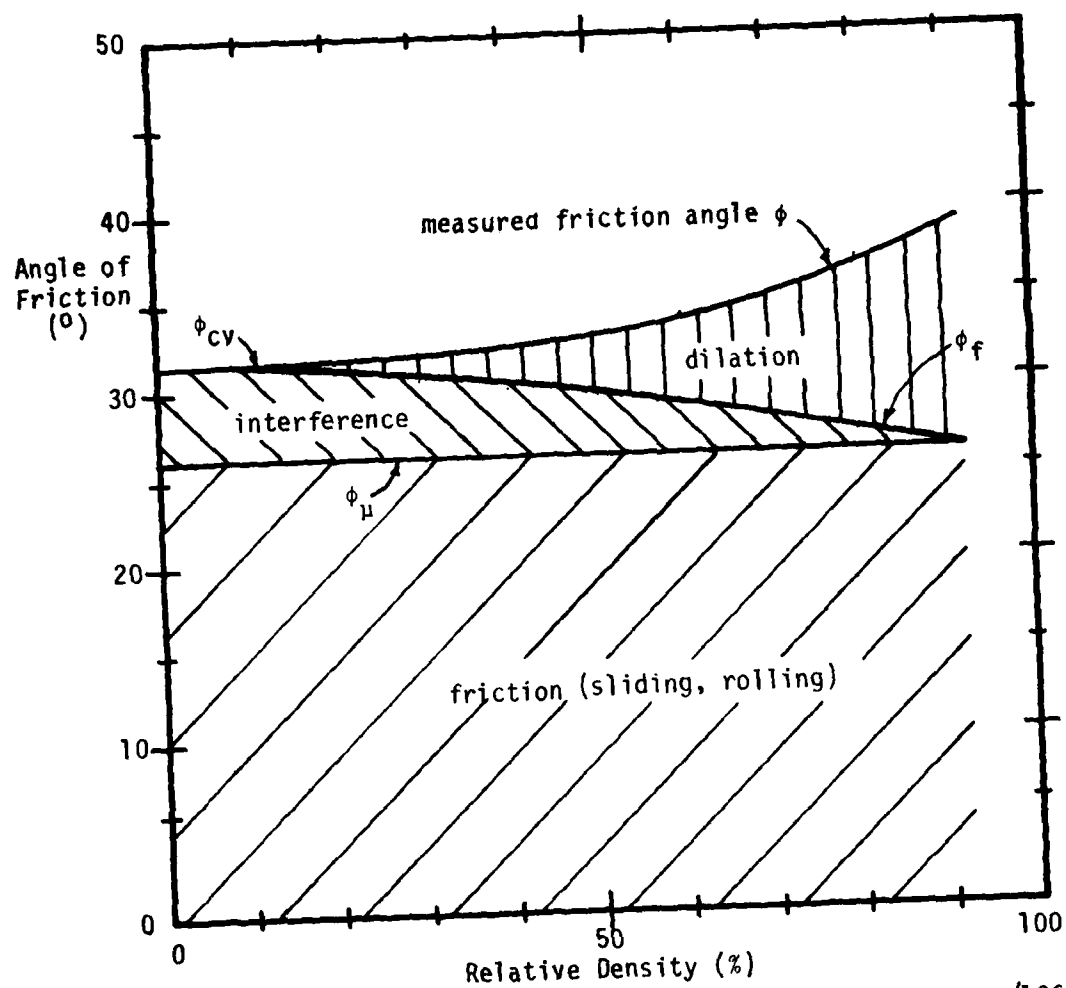


FIGURE 3.2 Components of strength of sand as determined by Rowe (1962)

results from a decrease in the dilation rate with increasing confining stress.

The effective stress principle and the Mohr-Coulomb failure criterion predict that additional strength will be generated in "wet" soils by the presence of negative pore water pressure. When a negative pore water pressure exists in soil, a positive effective stress results, even when the applied total stress is zero. This may occur due to capillarity (e.g. due to drying of the external soil surfaces) or due to dilation of the pore spaces during undrained shear. Regardless, an "apparent cohesion" results. For example, moist beach sands exhibit some strength at zero total confining stress.

For fine-grained soils, slow shearing rates are required to prevent the generation of excess pore pressures due to the low permeability of clays and silts. When drained conditions prevail, the concepts presented in the previous paragraphs still apply, provided the stresses are expressed in terms of the effective stresses. However, additional strength can be generated due to "true cohesion" caused by physical cementation and/or the existence of net interparticle attractive stresses (e.g. $A > R$ or $\sigma_a'' > \sigma_r''$ in Figure 3.1). Also, the magnitude of negative pore pressure (capillary tension) that can be generated in clays and silts is far greater than in sands. Consequently, the magnitude of the apparent cohesion can be far greater in fine-grained soils than in sands.

For undrained loading, excess pore pressures develop during

shear. This occurs in sands when drainage is not permitted, and in silts and clays due to their low permeability relative to usual rates of loading. The overall mechanical behavior of an undrained sample differs from a similarly loaded drained sample depending upon the magnitude of the excess pore pressures developed during shear. Thus, while the same basic mechanisms control deformation and strength in both cases, the resultant stress-strain-strength characteristics vary due to differences in effective stress acting in the drained and undrained cases.

For a medium-dense sand which normally exhibits positive dilational behavior during shear, for example, undrained shearing at constant volume results in a substantial induced negative pore pressure. The magnitude of the pore tension may approach the cavitation level for pore water, and results in a positive effective confining stress in the soil system. This causes a fairly large increase in measured axial strength. Such a mechanism may also exist during the shearing of frozen soil systems.

CHAPTER 4 - REVIEW OF THE NATURE AND MECHANICS OF FROZEN SOIL

Frozen soil has a very complex mechanical behavior; it is typically stronger than normal ice or soil at low confining stresses, but possesses very time dependent creep behavior, similar to ice. From the previous sections on ice and unfrozen soil, it can be seen that the main components of frozen soil are themselves very complex systems. Frozen soil retains these complexities, plus the additional complications arising from the interface between the soil and ice phases. This Chapter examines the nature of the frozen soil system by drawing upon the fields of cloud physics, frost heaving, ice adhesion, clay mineralogy and colloidal chemistry. The mechanical behavior of frozen soil is then described, together with available qualitative and quantitative explanations for the observed mechanical behavior.

4.1 Nature of the Frozen Soil System

4.1.1 Nature of ice nucleation and interaction in frozen soil

As previously mentioned, it is generally agreed that a film of unfrozen, liquid-like water exists around soil particles in frozen soil. Results from conductance measurements, ion diffusion and observed solute movement under an electric field (Anderson 1968) have shown that this layer is mobile, continuous and capable of mass transport. In addition, work in the field of cloud physics suggests that ice nucleates in the presence of silicate particles adjacent to the unfrozen adsorbed

water film, rather than directly on the particle surface (Roberts and Hallett 1968, Edwards et al. 1970). This hypothesis is further reinforced by Anderson's (1968) work on the freezing of clay mineral pastes at varying total water contents, in which the spontaneous nucleation temperature decreased abruptly at very low water contents. Anderson proposed that since the thickness of the unfrozen water film apparently decreases with decreasing water content up to a limit, this suggests that ice nucleates near the unfrozen adsorbed water film.

Corte (1962) observed that ice growing upward can carry with it soil particles "floating" on the heaving ice surface, as already shown in Figure 2.3. This phenomenon is possible only if an unfrozen water film completely surrounds the soil particle. This unfrozen film is then constantly being replenished from the adjacent water reservoir as freezing occurs. If any direct ice to soil contact existed, then the particle would become enveloped by the ice rather than be carried by the ice front.

A related phenomenon occurs when frost susceptible wet soil is subjected to freezing temperatures at ground level. Instead of a downward advancing freezing front, often ice is drawn upwards through the pores of the soil to form long, slender columns of "needle ice". These may often be observed in the early morning in the fall, when the ground is not frozen but is subjected to subfreezing air temperatures overnight. The mechanism by which the forces are generated to draw up the ice through

the pores are similar to that in Corte's experiment, and is closely related to that for frost heaving. As with Corte's experiment, this phenomenon can best be explained if some liquid-like film exists between the ice and soil particles.

Frost heaving

The phenomenon of frost heaving occurs in many fine-grained soils subjected to subfreezing temperatures. As the freezing front advances into a fine-grained soil, horizontally oriented ice lenses periodically form, resulting in a net soil heaving at the ground surface often greatly in excess of the volume increase associated with the freezing of the pore water. This frost heaving can generate very large heaving pressures above the freezing front, while developing large suction forces in the pore water below the freezing front. Freezing of coarser-grained materials such as sands and gravels does not result in frost heaving.

The occurrence of ice lensing requires a delicate balance between heat and water supply. For the freezing rates normally found in nature, frost heaving is most prominent in nonplastic silts with ready access to a water supply. If a plastic clay is frozen under similar conditions, heaving does not usually occur, as the water supply to the ice lens is not adequate, and the freezing front advances past the area of potential lensing without significant volume increase. However, if an abnormally slow freezing rate is imposed on a clay, such that sufficient

water migration to the ice lens is possible, very large heaving results (Wissa and Martin 1968).

Many theories have been advanced to explain the phenomenon of frost heaving. These have included explanations based on capillarity (Everett and Haynes 1965), nonsteady-state heat flow (Martin 1959) and the freezing of a portion of the adsorbed water films (Tagaki 1978). In each case, a key must be to explain the generation of the suction force which causes the drawing up of water to the ice lens.

Based on these theories, the following hypothetical model for ground freezing and frost heaving may be established:

As the air temperature is lowered, heat is extracted from the soil, lowering the soil temperature. In the soil, zones of potential ice nucleation and growth exist within the pore water at impurities and next to the adsorbed water films of the soil particles. As the temperature is continually lowered, supercooling occurs in the pores until nucleation occurs at some of the possible sites. The ice crystals grow within the fluid until growth is halted next to an adsorbed water film, by the ice crystal from an adjacent pore, or due to a lack of water supply. In coarse-grained soils, as the freezing zone progresses downward, the "front" is fairly well defined, as relatively little freezing point depression occurs due to the overlapping of adsorbed water films and water is readily available for freezing. For fine-grained soils where this overlapping does occur, a

great deal of freezing point depression occurs. As further cooling continues, the temperature is lowered at the ice crystal/water interface, causing the creation of a tension in the water, resulting in further freezing point depression. Alternatively, or concurrently, the external layers of the adsorbed water film freezes, resulting in a tension in this layer. These mechanisms both result in a "suction" force which draws the water to the ice crystal. For nonplastic silts, with a large percentage of fines but an appreciable permeability, water supply to the growing ice crystal is adequate to sustain significant ice lens growth. For clays, the permeability is usually so low that for normal freezing rates, sufficient supercooling occurs in the next pore to cause nucleation in that pore, rather than for water to be transported through the pore up to the ice lens. For silts, ice lensing continues as long as the unsteady state heat flow conditions exist at the ice/water interface. If heat is no longer being extracted, then the supercooling is insufficient to create the tension at the interface and/or freeze part of the adsorbed layer. If the water supply were so large that significant quantities of the water were frozen, as in sands and gravels, then the released heat of fusion could raise the temperature sufficiently to prevent further freezing. For frostheave susceptible silts, significant ice growth continues in a given pore until one of two conditions are met: insufficient water flow to the lens, or

insufficiently low temperatures for freezing in the existing pore. Thereafter, if heat is continually extracted, the temperature will continue to be lowered until nucleation occurs below the existing ice lens at some location where the thermodynamic and nucleation criteria are again met.

From this discussion of frost heaving, the exact role of the unfrozen water film in the frost heave phenomenon is not absolutely clear. However, it appears probable that transport of the pore water to the ice crystal occurs through this film, and it is possible that this film generates at least a portion of the suction force present during ice lensing.

Ice adhesion

The existence of a liquid-like layer on the surface of ice was postulated by Faraday as early as 1850. This concept has since undergone considerable scrutiny, particularly in the late 19th century. It is currently agreed that liquid-like unfrozen water exists in ice down to at least -25°C (Jelinek 1967, Barnes et al. 1971). However, it has been difficult to unequivocally determine the nature, location and properties of the unfrozen water.

Experiments carried out by Nagaya and Matsumoto (1953) and Hosler et al. (1957) offer strong evidence for the existence of an unfrozen liquid-like film down to at least -25°C . Ice spheres were suspended from threads to form pendulums, and were moved laterally into contact with a very slight force. The suspension points were then moved laterally until separation occurred. Quite frequently, the spheres started to slide and roll over each other before finally separating. This rotation occurred most frequently near the melting point, but was observed down to -7°C by Nagaya and Matsumoto, the strength of the contact tending to decrease with increasing temperature. For ice spheres made from 0.1% salt solution, rotation was more pronounced and frequent, and occurred at temperatures down to -14°C . In a water-saturated environment, adhesion was observed down to -25°C by Hosler et al. (1957), while in a dry atmosphere, adhesion practically ceased at -3°C .

These results are best explained by the presence of an un-

AD-A097 668

MASSACHUSETTS INST OF TECH CAMBRIDGE DEPT OF CIVIL E--ETC F/G 8/13
THE CREEP OF FROZEN SANDS: QUALITATIVE AND QUANTITATIVE MODELS.(U)

MAR 81 J M TING

DAAG29-77-C-0016

UNCLASSIFIED

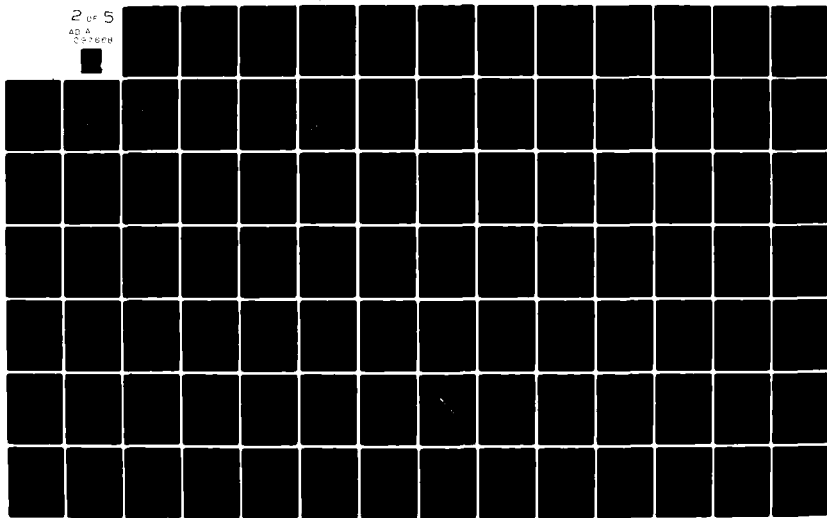
R81-5

ARO-14725.2-6S

NL

2 OF 5

AD A
C-0016



frozen transition film on the surface of the ice which has an increased thickness in the case of the salt solution and of the water saturated environment. During separation, a certain amount of force is required to break the ice bond between the spheres. However, instead of immediate separation, a rolling action takes place due to surface tension effects in the film, and final separation occurs at some greater angle. The salt solution spheres would have a thicker transitional film, and hence increased rolling activity. The film is thinner in the dry environment, and hence exhibits a decreased adhesion.

Jellinek (1957(a),(b),1960(b),(c),1962) carried out tensile and shear adhesion experiments on ice frozen to various surfaces, such as stainless steel and fused quartz of varying surface roughness. Cohesive-type breaks (ie. within the ice crystals) were observed only in the tensile experiments, however finely polished the surface. Adhesive-type breaks (ie. at the interface between the ice and solid) were observed in the shear experiments, with the measured strength a function of the rate of shear, surface finish and temperature. This adhesive shear strength is a linearly increasing function of decreasing temperature down to -13°C . Below -13°C , the strength is practically temperature independent. This adhesive shear strength is also strongly dependent on surface finish, with strength decreasing greatly with decreasing roughness. The adhesive tensile strength tests indicate an adhesive strength fifteen times greater than the adhesive shear strength.

To explain these results, Jellinek proposed that a continuous liquid-like transition layer exists between the ice and the substrate material. For the shear experiments, the adhesive strength is a function of the interfacial strength, and consists of a viscous contribution from this thin film, as well as contributions due to particulate impurities in the film and roughness of the surface. As the surface roughness decreases, down to the minimum of a few hundreds of Angstroms ($1/5$ th waveband) for optically flat fused quartz, so does the measured adhesive shear strength. It should be noted, however, that even in the smoothest surface, the thickness of the unfrozen layer is undoubtedly less than the maximum asperities present, and hence some degree of ice/quartz interlocking is bound to occur.

For the tensile adhesion tests, the measured strength is controlled by the ice strength, due to the nature of the observed failure breaks. Jellinek proposed that the ice/solid interfacial strength is increased in the tensile mode due to the reinforcing effect of surface "tension" at the perimeter of the interfacial transitional water.

Assuming the existence of this transitional film throughout the ice/solid interface, the mechanical properties of this film may be inferred. If the adhesive shear strength is primarily due to surface asperity interlocking, then the shear resistance of the film itself is probably quite low, less than 0.02 MPa at -4.5°C (Jellinek 1960(c)). The tensile strength, however, is at

least 1 MPa at -4.5°C . As noted above, Jellinek attributed the greatly increased tensile strength to surface tension effects at the perimeter of the ice. However, if one adopts the two-dimensional liquid model for adsorbed water in unfrozen soil (Martin 1960), then these adhesive properties may be readily explained: while it is relatively easy to induce motions laterally parallel to the surface, it is very difficult to displace the adsorbed water normal to the surface. By referring to the "ball-bearing on a magnetized surface" analogy, it is not necessary to invoke "surface tension" to explain the observed behavior. Instead, the adhesion data in ice agree very well with Martin's hypothesized behavior of adsorbed water in unfrozen soil.

Other tests and analyses relating to the nature of the unfrozen transitional film in ice have been carried out. These include experiments with wire/ice loading, sintering of ice spheres and quantitative analyses of the nature of the transition film in ice and water. This work is summarized by Barnes et al. (1971) and Jellinek (1967). Generally, the results from these investigations are consistent with the concept of a liquid-like surface transition film in ice.

4.1.2 Structure of the frozen soil system

In previous sections, the structure of unfrozen soil systems, the nature of adsorbed water and the nature of ice nucleation, growth and interaction with silicates have been described. In this section, the results from the investigations in each of

these areas are brought together in an attempt to understand the structure of the frozen soil system. The pertinent facts and hypotheses from each topic are first summarized. Based on this information, a possible structure of frozen soil is then presented. Where necessary, possible divergences from the proposed structure are discussed.

Pertinent facts about the unfrozen soil system include:

(1) the physico-chemical effective stress equation is applicable for all soils; however, for coarse-grained materials the mass forces dominate and the double-layer forces are negligible;

(2) for coarse-grained soils under an applied load, grain-to-grain contact is assured due to the high contact stresses present; these contact stresses can be sufficient to crush quartz;

(3) for all but ideally dispersed clays, solid inter-particle contacts effectively exist; data by Hofmann (1952) on freeze-dried clay gels and indirect data by Mitchell (1976) support this hypothesis.

Pertinent facts about adsorbed water in soil and ice include:

(1) water is strongly adsorbed by all siliceous materials; it requires in excess of 100°C to remove all water from soil, and greater than 400 MPa to squeeze the next-to-last molecular layer of adsorbed water from clay minerals (Steinfink and Gebhart 1962);

(2) adsorbed water is continuous, completely surrounds

the mineral surfaces, and is very mobile parallel to the mineral surfaces;

(3) adsorbed water does not behave like bulk water, and is capable of supercooling, freezing point depression, ice nucleation and "preactivation";

(4) the exact structure of adsorbed water is not clear; however, it apparently exhibits Newtonian viscous flow (Mitchell 1976, p.107);

(5) unfrozen water is present in ice at least down to -25°C in a vapor saturated environment, and probably exists on the external ice surface and at the ice grain boundaries;

(6) based on computations by Martin et al.(1981) using unfrozen water content data on Manchester Fine Sand from NMR, the amount of unfrozen water attributed to the ice phase is about the same as or greater than that portion which can be attributed to the soil phase.

Pertinent facts on the ice in frozen soil are:

(1) the structure and location of the ice in frozen soil depend on the initial water content, soil permeability, freezing rate, freezing temperature, the soil pore and grain size distributions and the location of the water supply;

(2) nucleation of ice in a soil pore can occur from ice propagation from an adjacent pore or within the pore at an ice nucleation site; this site may either be next to the adsorbed water film or may be a site within the bulk pore fluid;

(3) ice is not in direct contact with soil during the

freezing process (Corte 1962);

(4) direct ice to soil contact, even if possible, cannot exist over the entire ice/soil interface, based on Jellinek's adhesional shear and tension test results;

(5) ice in soil is polycrystalline in nature (Gow 1975); for in situ freezing where no frost heaving (segregation freezing) occurs, the maximum ice grain size is the pore size; unpublished data by Colbeck on the freezing of glass beads suggests that the number of ice grains in a pore is equal to the number of particles adjacent to the pore.

Based on these facts and hypotheses, a structure for frozen sand may be postulated. This is shown in Figure 4.1 and is based on the following points:

- (1) effectively solid contacts exist between soil grains;
- (2) probably no direct ice-to-soil contacts exist;
- (3) unfrozen water exists at the soil/ice interface and at the grain boundaries in the ice phase.

For fine-grained frozen soil systems, no significant differences from this model are anticipated, though much smaller ice grains would be expected due to the smaller pore sizes. For soils subjected to segregation freezing, an altered soil structure and larger ice grain sizes could result.

One point of potential controversy concerns the nature of the ice/soil interface. It is probable that no actual contact exists during freezing, based on Corte's experiments. Jellinek's experiments demonstrate that continuous ice/soil bonding is not

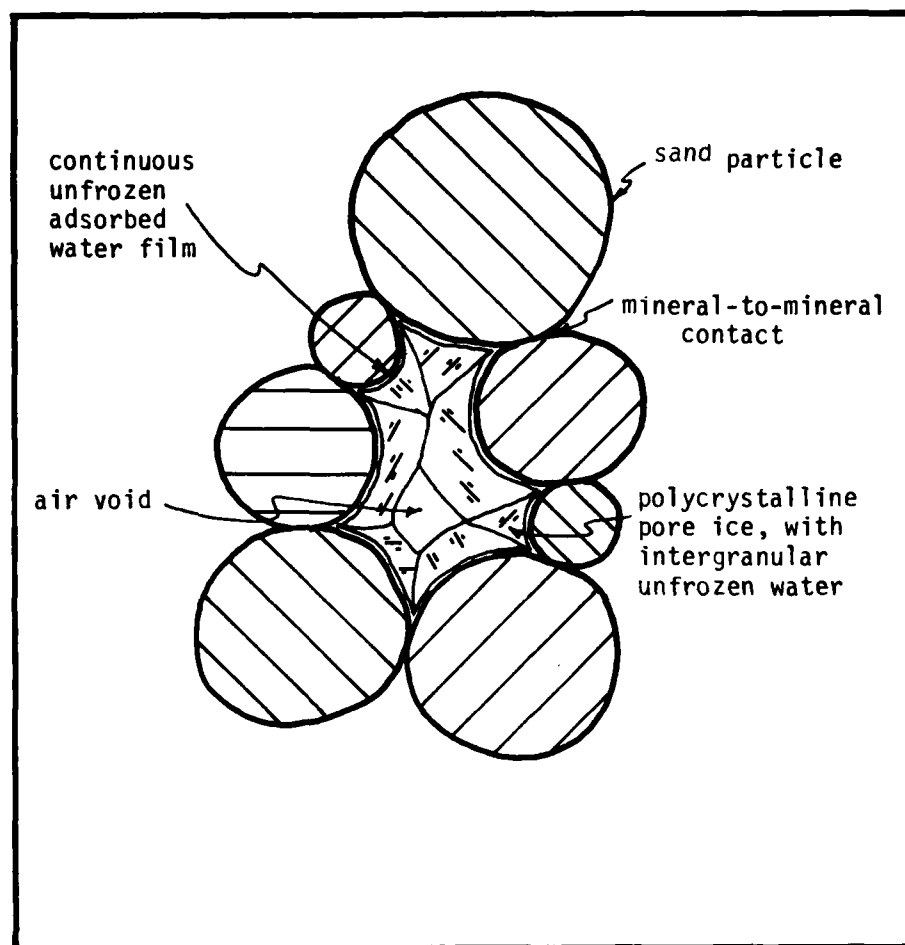


FIGURE 4.1 Two dimensional schematic of the proposed structure of the frozen sand system

likely due to the large discrepancy between the tensile and shear adhesive strengths. Thus, the bulk of the indirect experimental evidence indicates that no direct ice to soil contact exists, although this has yet to be proven conclusively.

4.2 Mechanics of Frozen Soil

As seen in the previous sections, frozen soil is an extremely complex system, composed of components which themselves possess very complex mechanical behavior. The mechanical behavior of frozen soil reflects this structural and mechanical complexity. While frozen soil exhibits considerable time, temperature and strain rate dependent behavior similar to ice, it also possesses frictional behavior as in unfrozen soil. However, its behavior cannot be modeled merely by combining the behavior of the components linearly, as with some composite materials. Instead, the components of the frozen soil system appear to interact synergistically; for example, the unconfined compressive strength of medium to dense frozen sand exceeds the sum of the strengths of the major structural components, ice and unfrozen soil.

Because of the complexity of the soil-water-ice system, the nature of this strong interaction between the ice and soil constituents has not been adequately determined. However, extensive work has been carried out in attempts to quantify and model the strength and deformation behavior of frozen soil. In the following sections, the existing experimental data on the mechanics of frozen soil are summarized. Although the strength and deformation behavior of frozen soil are intimately related, these topics are arbitrarily divided in the following sections for convenience.

Based on these results and the discussions in the previous

sections on the nature of the frozen soil system, numerous qualitative and quantitative explanations for the observed mechanical behavior are presented.

4.2.1 Strength of frozen soil

Effect of confining stress

The effect of confining stress on the strength of frozen soils has been extensively studied by Chamberlain et al. (1972), Alkire and Andersland (1973), Perkins and Ruerdrich (1973), Sayles (1974), Simonson et al. (1975), Smith and Cheatham (1975) and Roggensack and Morgenstern (1978). The results of Chamberlain et al. on 100-200 mesh Ottawa sand (OWS) and a nonplastic well-graded glacial till (WLT) are plotted in Figure 4.2 together with data on granular ice from Jones (1978). Note that of necessity, total stresses are used instead of the more meaningful effective stresses. Several interesting features are evident from this figure. It can be seen that each frozen soil possesses three distinct zones:

(1) the low stress region, in which the shear strength of the dilatant OWS increases with confining stress, while the nondilatant WLT has approximately the same shear strength;

(2) the intermediate stress region, where both OWS and WLT exhibit decreasing shear strength with increasing confining stress;

(3) the high confining stresses above about 100 MPa, where both OWS and WLT exhibit slightly increasing shear strength

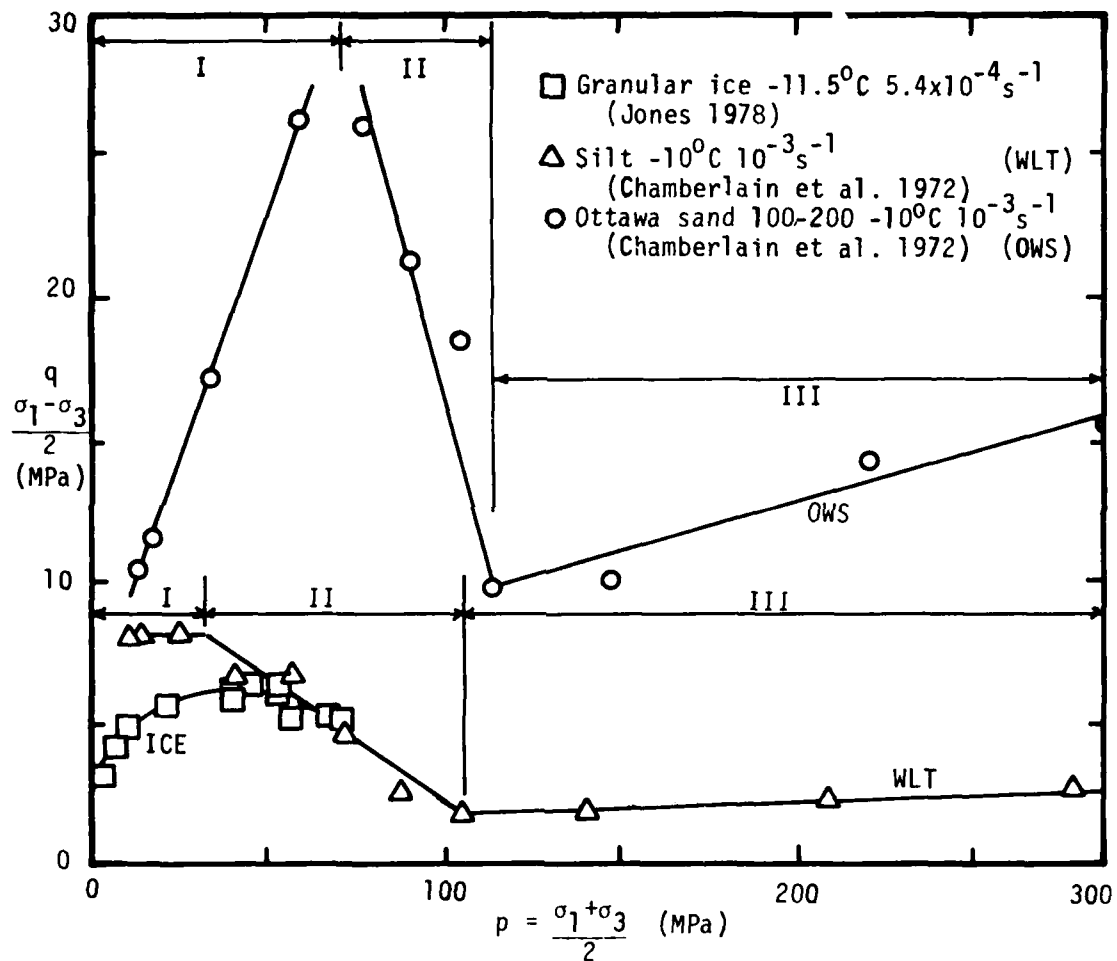


FIGURE 4.2 Effect of confining stress on the strength of ice and frozen soils

with increased confinement.

Note that the low stress region is the one of primary engineering concern.

Chamberlain et al. postulate that in region I, the strengthening of the OWS is due to particle interlocking and interparticle friction while the shear strength of the WLT is controlled by the unfrozen water films. In region II, the shear strength of both soils is controlled by the onset of pressure melting due to stress concentrations. In this region, the dilation of the OWS is completely suppressed, and some particle crushing occurs. The breakpoint between regions II and III occurs at $\sigma_{oct} = 110$ MPa. This corresponds closely with the pressure at which the ice/water phase transformation occurs at -10°C (see Figure 2.1). Significant particle crushing occurs in the sand, especially in Regions II and III, as might be expected at these high confining stress levels.

In the low stress region tested by Chamberlain et al., the frozen sand strength (plotted using total stresses) is greater than (or approximately equal to) the drained strength of the unfrozen sand. At the higher confining stresses, the strength of the frozen sand at a given level of total stress is much less than the drained strength of the unfrozen sand at the corresponding effective stress. Since global pressure melting occurs above about 110 MPa, the tested material is analytically similar to an unfrozen soil in this range. Due to the low strengths measured, the observed quantity must be an undrained

shear strength at effective stresses much less than the total stresses.

A summary of the results of strength testing by various researchers at low confining stresses is found in Figure 4.3. Note that the apparent friction angle of the frozen sands is similar to that of the unfrozen sand; however, a significant apparent cohesion exists in the frozen sand, even at ice contents less than 100% saturation.

From the stress-strain plots shown in Figure 4.4 it can be that a definite two peak behavior exists for OWS. An initial peak occurs at about 0.5 % to 1.0% strain and a second one between 8 % and 10 % strain. The first peak is considered to correspond to the yielding of the ice matrix, while the second one corresponds to the strength developed within the sand-ice composite. Sayles (1974) separated these two peaks in his experimental program on Ottawa sand and plotted the stress associated with each peak. As seen in Figure 4.5, the envelope of the first resistance peaks closely resembles that for columnar ice, while the envelope of the second peaks yields an apparent friction angle of 31° , similar to unfrozen OWS. Note that since the envelope of the second peaks also possesses a significant apparent cohesion, this indicates that the ice matrix contributes significantly to the strength of the composite system.

Direct shear tests on natural and laboratory-prepared silts and clays were reported by Roggensack and Morgenstern (1978). In each case, the apparent friction angle of the frozen soil

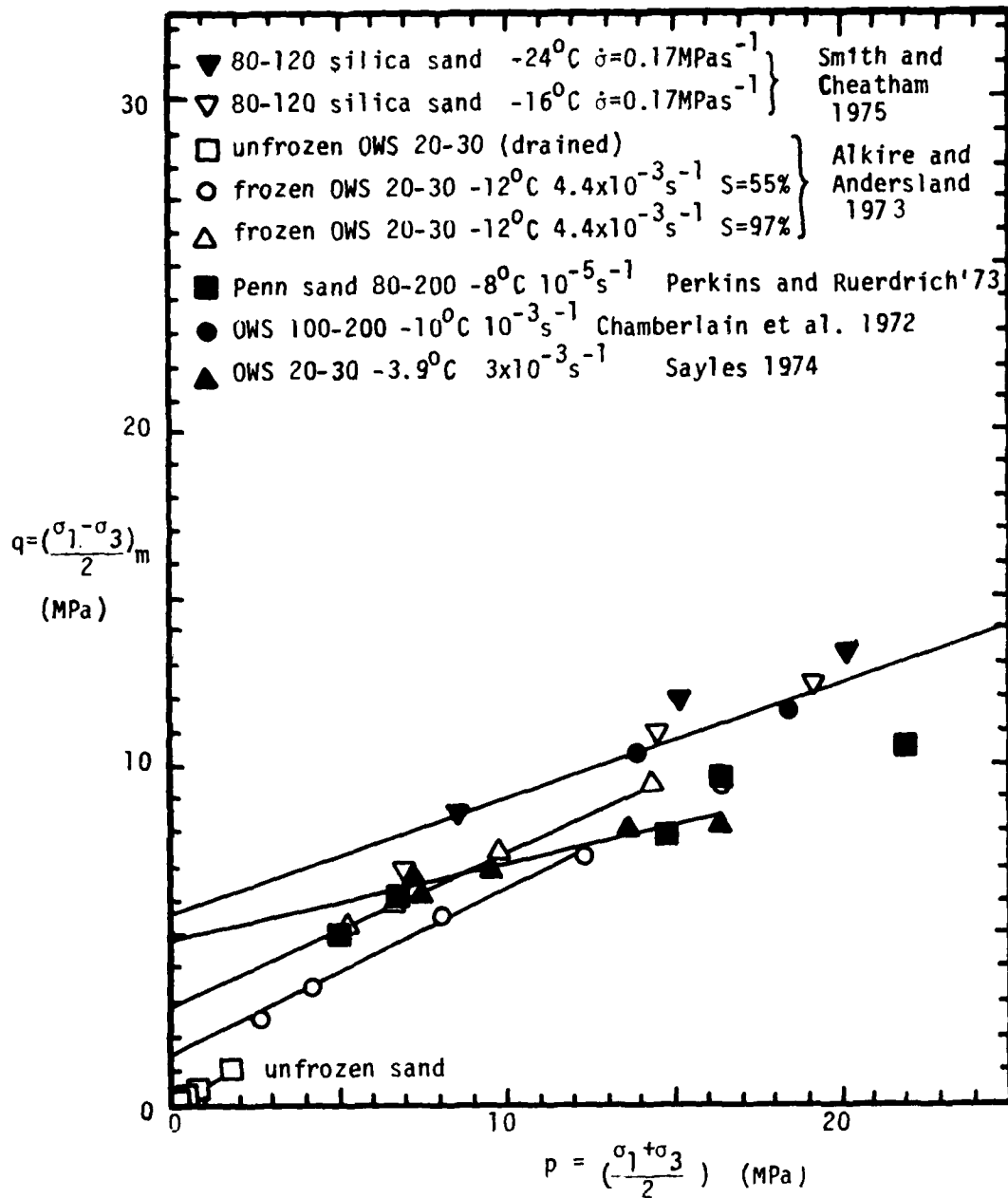


FIGURE 4.3 Results of strength testing on frozen soils at low confining stresses

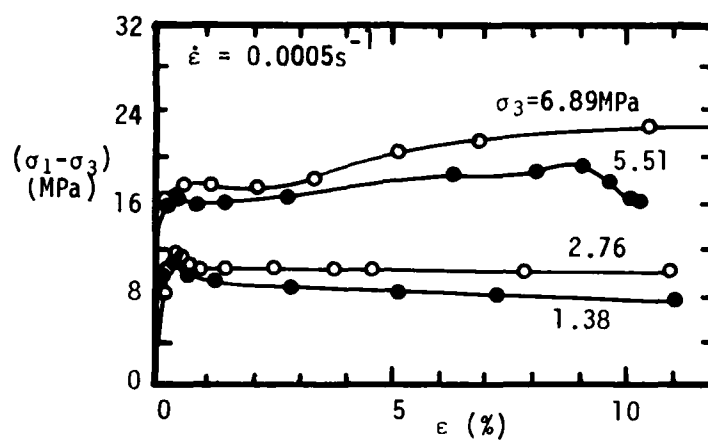
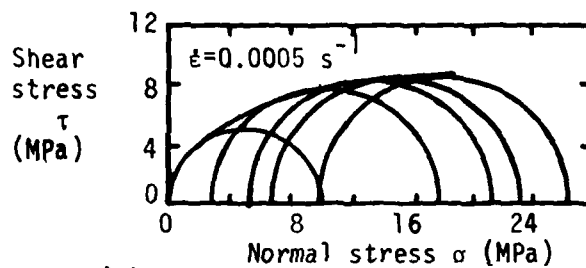
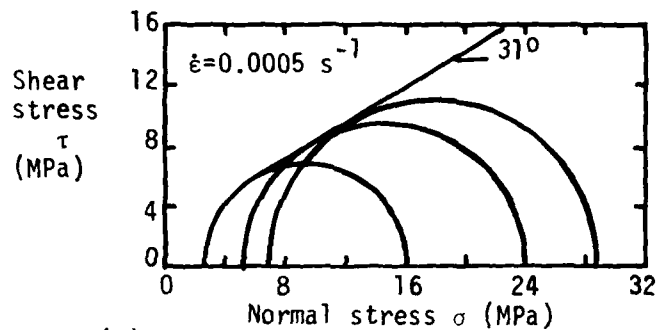


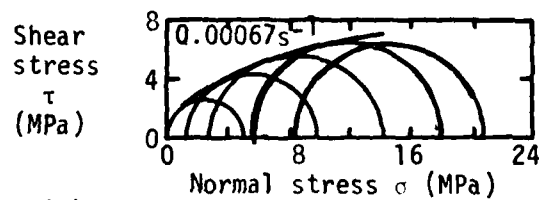
FIGURE 4.4 Stress-strain curves for frozen Ottawa Sand (from Sayles 1974)



(a) Ottawa 20-30 sand first resistance peak



(b) Ottawa 20-30 sand second resistance peak



(c) Columnar grained ice $T = -3.8^\circ\text{C}$

FIGURE 4.5 Mohr envelopes for Ottawa sand 20-30 and columnar-grained ice at -3.8°C (from Sayles 1974)

was the same as in the unfrozen soil. However, the frozen samples possess a much larger cohesion intercept. Tests carried out at several different rates indicate that as the deformation rate increases, the strength increases, especially at the low confining levels. Roggensack and Morgenstern interpret this to mean that at low strain rates or long times to failure, an increasing proportion of the shear strength can be attributed to frictional mechanisms.

Effect of Temperature

As with ice, frozen soil possesses a large temperature dependent behavior. Haynes and Karalius (1977) and Perkins and Ruerdrich (1973) present data from uniaxial compression and tension tests on silt and sand, respectively. These results are presented in Figure 4.6. For unconfined compressive strength, the silt and sand both possess an apparently linear temperature dependence. The sand exhibited little strain rate dependence between 8.3×10^{-5} and 4.2×10^{-3} /s and had a temperature coefficient of about $1 \text{ MPa}/^{\circ}\text{C}$. The silt, of the other hand, exhibited a large strain rate dependence between 4×10^{-3} and 4×10^{-1} /s, and had a significant non-linearity at the high temperatures and lower strain rate. This can possibly be attributed to significant time-dependent effects at the high temperature and lower strain rates. In this case, the temperature coefficient down to -60°C for the high strain rate was about $1.4 \text{ MPa}/^{\circ}\text{C}$, while for the lower strain rate, the temperature coefficient

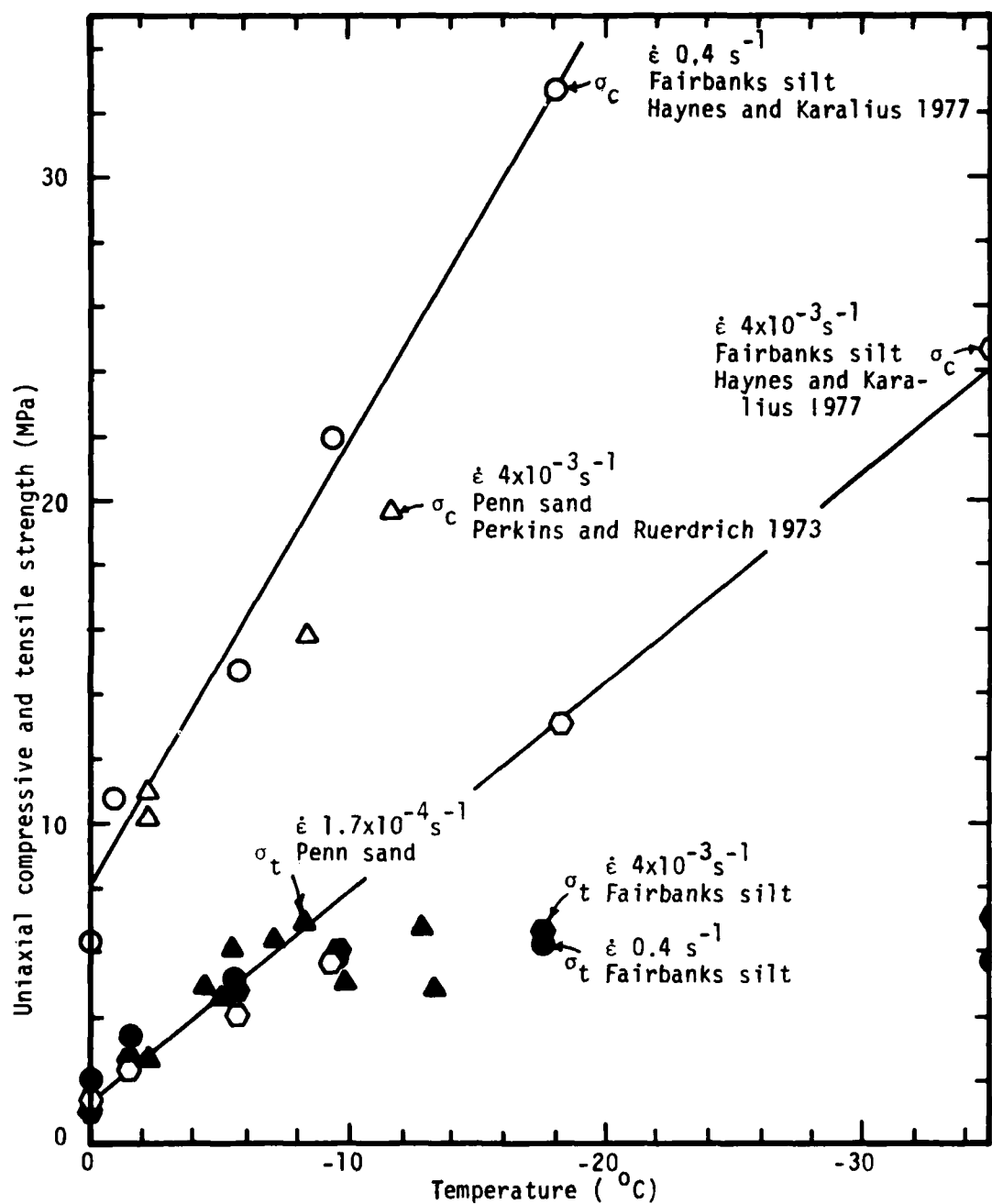


FIGURE 4.6 Effect of temperature on the uniaxial compressive and tensile strengths of silt and sand

was about $0.5 \text{ MPa}/^{\circ}\text{C}$ between 0° and -10°C . For comparison, the temperature coefficient for the uniaxial compressive strength of ice was quoted in Chapter 2 as being between 0.1 and $0.8 \text{ MPa}/^{\circ}\text{C}$.

The uniaxial tensile strength of each soil also exhibited a large temperature dependence in the range between 0° and -10°C . But as seen in Figure 4.6, the increase in the tensile strength below -10°C is slight in comparison.

The effect of temperature on the triaxial strength of frozen soil has not been extensively studied. Goughnour and Andersland (1968) carried out some triaxial tests at different temperatures, but only at a confining stress of 0.69 MPa . This stress level is not sufficient to significantly alter the strength behavior of frozen soil. Work done by Smith and Cheatham (1975) include higher confining stress levels, and are plotted in Figure 4.7. Based on these data, it can be seen that as the confining stress is increased, the temperature dependence of the strength decreases considerably. This may possibly be due the domination of ice on the behavior of frozen soil at the lower confining levels. At the higher levels, the interactive mechanical behavior of the sand and ice is more important, resulting in a much reduced temperature dependence. Further study is required, however, to confirm the trends found in Figure 4.7.

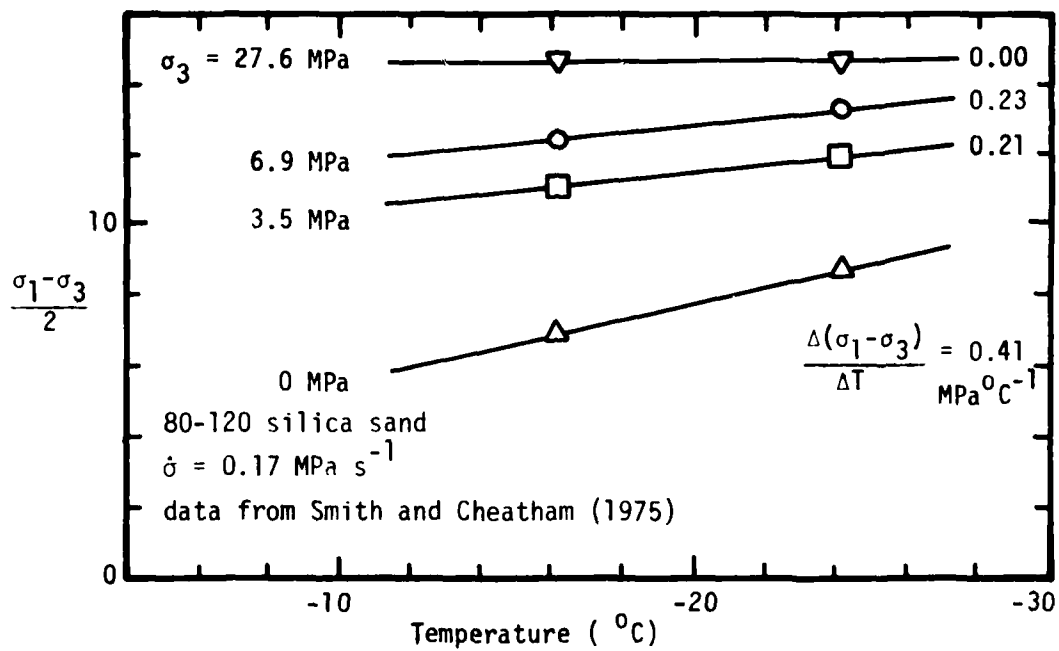


FIGURE 4.7 Effect of confining stress on the temperature dependence of strength

Effect of time

The effect of time on the strength of frozen soil from deformation rate controlled tests has been studied by numerous researchers under unconfined (Haynes et al. 1975, Perkins and Ruerdrich 1973, Sayles unpublished) as well as triaxial loading conditions (Sayles 1974, Roggensack and Morgenstern 1978). The results of uniaxial compression tests on various sands and silts at about -10°C are plotted in Figure 4.8 together with the average ice strength from Figure 2.5. As is evident from this Figure, the uniaxial strength of frozen soil is greatly dependent on the applied strain rate. The rate of increase in strength for frozen soils is similar to that for ice, and is much greater than for unfrozen soils.

Of interest is the fact that the uniaxial strength of the ice is apparently greater than for frozen silt and very loose sands. It is possible that differences in ice structure between the polycrystalline ice and the ice in the frozen soils account for this behavior. The possibility that a greater quantity of unfrozen water in the silt accounts for its lower strength is not plausible, as data from NMR studies on the Manchester Fine Sand and Fairbanks Silt indicate that at -10°C , the unfrozen water content for each soil is between 1 and 2 %. Consequently, other reasons are responsible for the great disparity in strength between the sand and silt.

As confining stresses are applied, the strength of the frozen soil continues to increase with increasing applied strain rate.

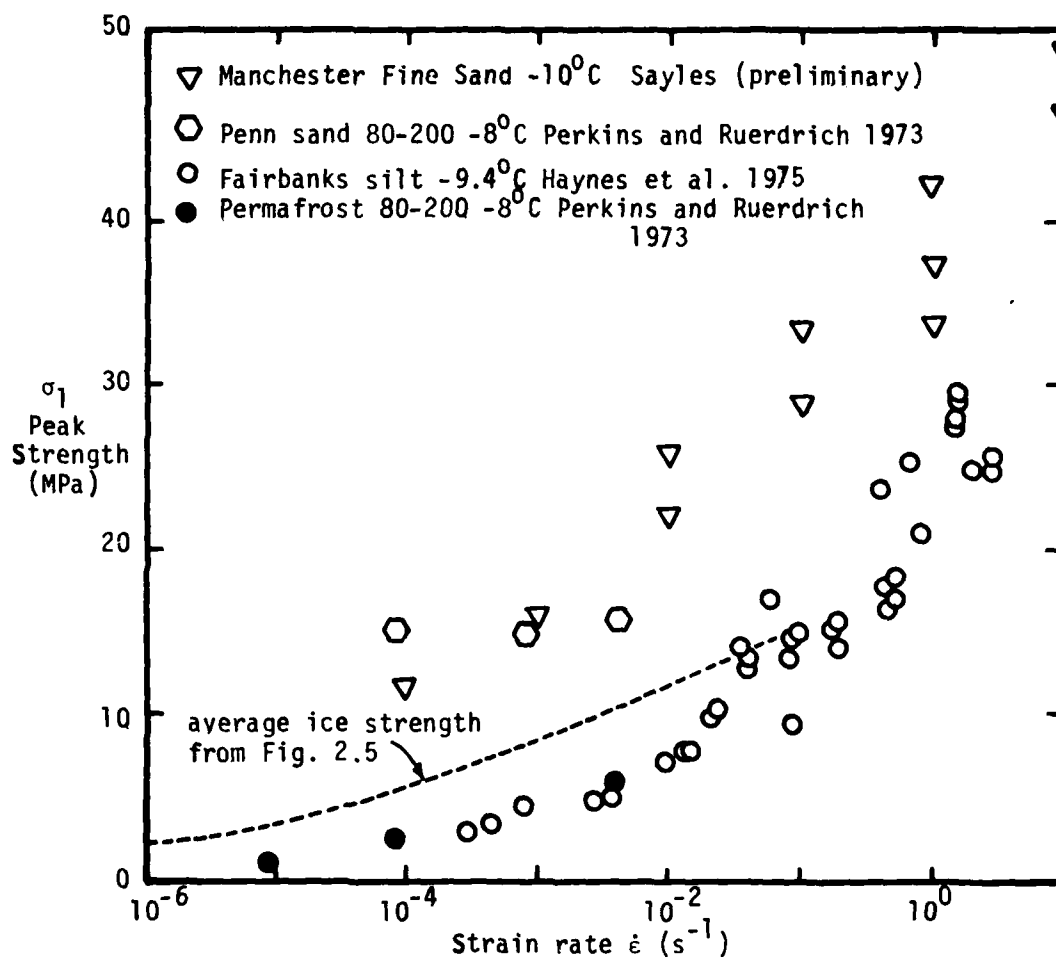


FIGURE 4.8 Effect of strain rate on the uniaxial compressive strength of frozen soils

Roggensack and Morgenstern (1978) report that the friction angle ϕ decreases with increasing strain rate, while the cohesion intercept increases with increasing strain rate, based on direct shear testing on frozen silt. Data from Sayles (1974) based on triaxial compression tests indicate that the strain dependence of strength does not change appreciably as the confining stress is increased, as seen in Figure 4.9.

Sayles at CRREL recently investigated the ductile-to-brittle transition zone for frozen MFS under unconfined stress conditions at several temperatures. Although a change in failure mode was observed at the larger strain rates, no apparent drop-off in strength or rate of strength increase was measured at rates up to 10 /s. The preliminary data are plotted in Figure 4.8. It should be noted that at the higher strain rates ($>10/s$) inertial effects become significant and can contribute to the measured resistance, hence giving a misleading measure of the true strength of the frozen soil (Whitman and Healy 1963).

The longterm strength of frozen soils has also been studied. Typically, the onset of accelerating creep in a constant load creep test indicates impending creep rupture or at least very large levels of deformation. Since the parameter $\dot{\epsilon}_m$, the minimum strain rate, is usually easy to determine, it has been used to characterize the "failure" strain rate, and the accompanying time to $\dot{\epsilon}_m$ has been used as a measure of the time to failure of the material for the specific temperature and stress conditions. As with ice and unfrozen soils, the correlation between the

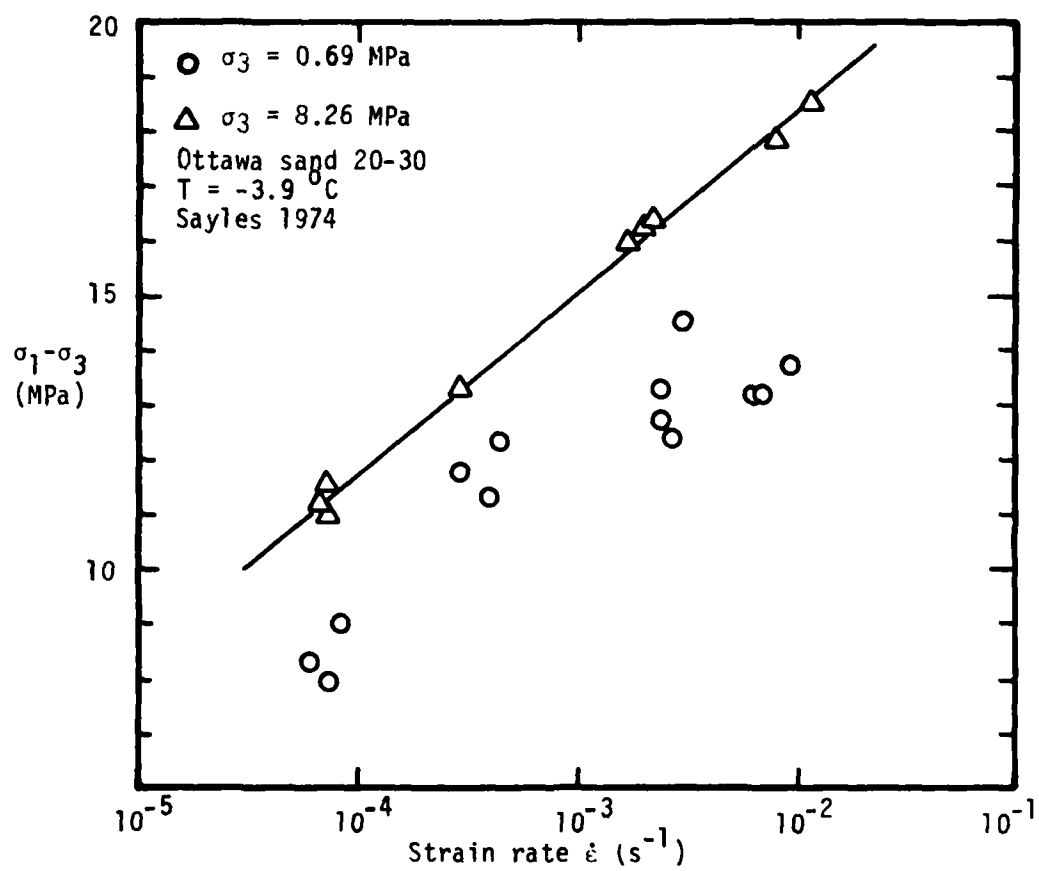


FIGURE 4.9 Effect of strain rate on the triaxial strength of frozen soils

minimum strain rate and the time to minimum is very good. Uniaxial compression data on partially saturated Manchester Fine Sand by Martin, Ting and Ladd (1981) at various temperatures between -11° and -21°C and axial stresses between 2.7 and 7.0 MPa are plotted in Figure 4.10.

The question arises, as with ice, of whether a true limiting long term strength (LLTS) exists for the uniaxial (unconfined) compression of frozen soil. The time-dependent deformation of frozen soil may represent a "consolidation" effect of the soil structure due to compression and creep in the pore ice, together with the shearing, rearrangement and flow of the ice to accommodate the stresses and deformations imposed by the soil particles during shear. Since the ice itself possesses a nominal long term strength, it would be expected that the limiting longterm strength of the frozen soil aggregate should be bounded by the drained strength of the unfrozen soil itself. Since the drained strength of unfrozen saturated soil is typically much lower than the strength of the same soil in the frozen state, for low confining stresses, some form of interaction between the ice and soil doubtless exists. A variety of possible explanations for this behavior are presented in Chapter 5. For example, a tension between the ice and soil would result in a positive effective confining stress, and hence generate shear strength.

Also, it is likely that some form of adhesion ("ice cementation") between the ice and soil exists in spite of (or as

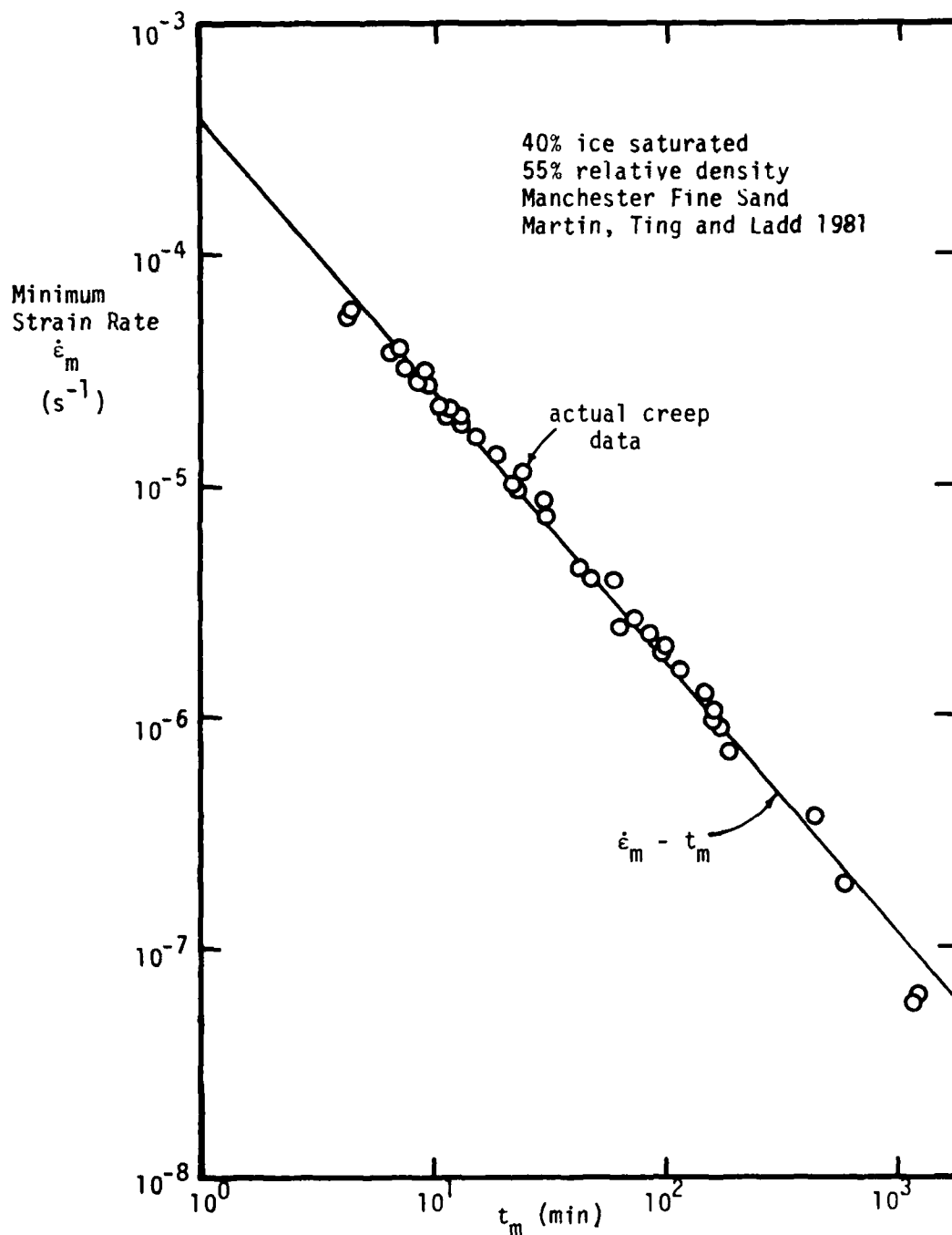


FIGURE 4.10 Linear $\log \dot{\epsilon}_m - \log t_m$ correlation for frozen Manchester Fine Sand (from Martin et al. 1981)

a result of) the unfrozen adsorbed water layer previously mentioned. This adhesion may be important if some "synergetic" mechanical interaction exists between the ice and soil, leading to a significant longterm limiting strength. However, due to the previously described problems with longterm testing of frozen materials and the time scale involved in these tests, no reliable data exist which can confirm the existence of a LLTS. This topic is discussed further later in this Chapter.

4.2.2 Deformation of frozen soil

Frozen soil, as with ice, possesses a very large creep susceptibility, much larger than for unfrozen soil. This can be seen from Figure 4.11, which shows that ice and frozen saturated sands have creep susceptibilities, much larger than a very creep susceptible unfrozen soil such as levee clay.

Since the time dependent deformation of frozen soil constitutes an overwhelming proportion of the total deformation under load, most of the research in the mechanics of frozen soils has focused on creep. The experimental data accumulated to date are summarized in the following sections, together with the various theories which have been presented in attempts at quantifying the stress-strain-time-temperature behavior of frozen soils.

Researchers have reported values of dynamic modulus (Vinson et al. 1978), tangent and secant moduli (Sayles 1974, Haynes et al. 1975, Haynes and Karalius 1977) and isothermal compres-

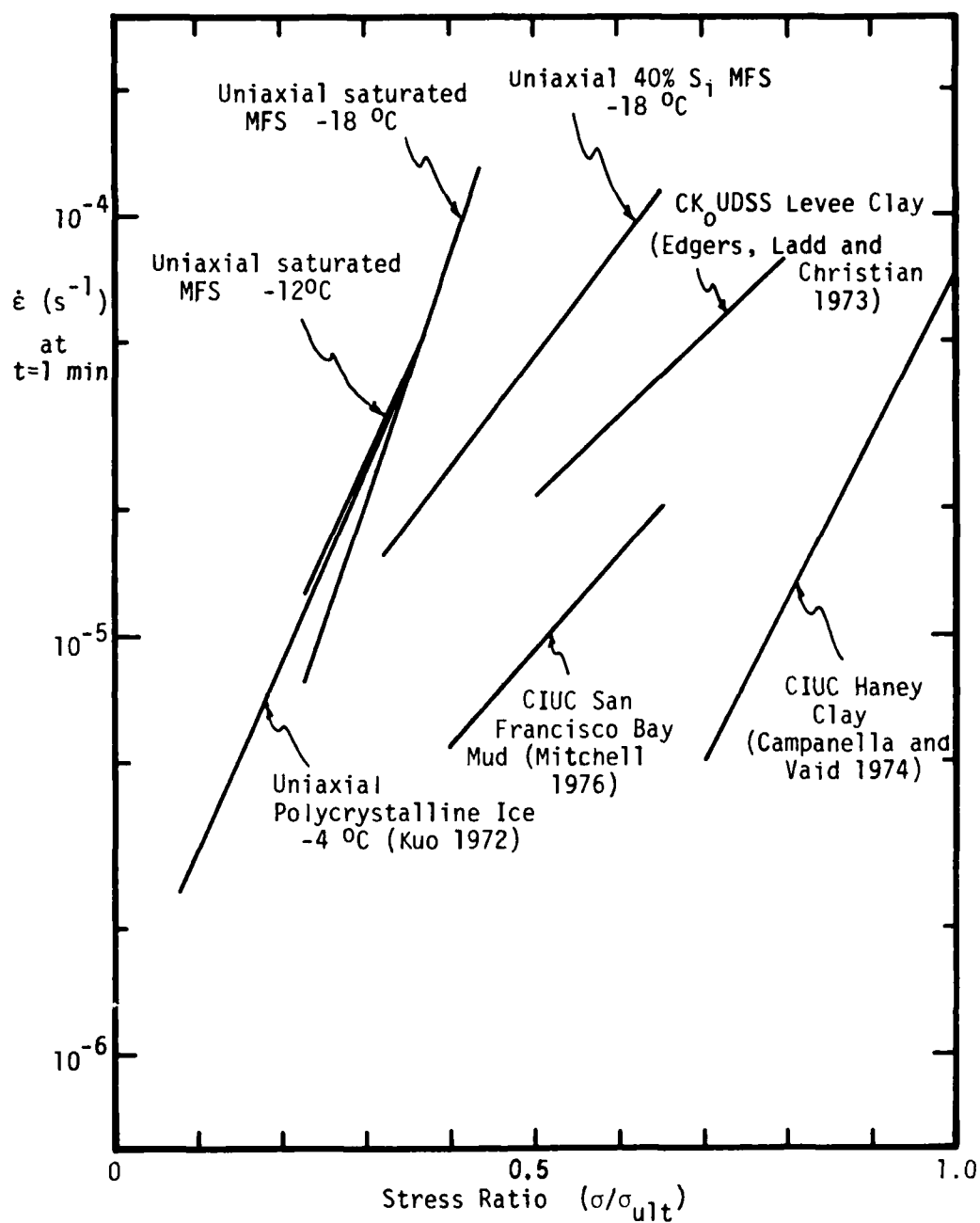


FIGURE 4.11 Strain rate vs. applied stress ratio for various materials

sibility (Chamberlain and Hoekstra 1970). However, these values should not be taken to represent any true elastic response of the material. Indeed, it is likely that at the slower loading rates, significant time-dependent deformation is present, contributing to lower moduli values. Instead, these observed moduli should be used only as tools for estimating the response during rapid loading.

Effect of stress level

Figure 4.12 demonstrates the very significant influence of stress level on the minimum strain rate, $\dot{\epsilon}_m$, for snow ice and partially and fully saturated Manchester Fine Sand (MFS) subjected to uniaxial compressive loading. As is evident from this Figure, the ice has a stress exponent of between 1.5 at the lower stresses and 6 at the higher stresses. 40 and 100% saturated frozen MFS, however, have a stress exponent of 10. In other words, the unconfined uniaxial creep of frozen sands is extremely sensitive to the level of applied deviator stress, far greater than the stress dependence of ice. It is possible to decrease the stress exponent by considering the existence of a "limiting longterm strength" (LLTS). Then, if the strain rate is plotted against the applied stress over and above this LLTS, the exponent decreases significantly. However, attempts at such analyses result in greatly increased scatter in the data.

One example of the influence of this high stress sensitivity

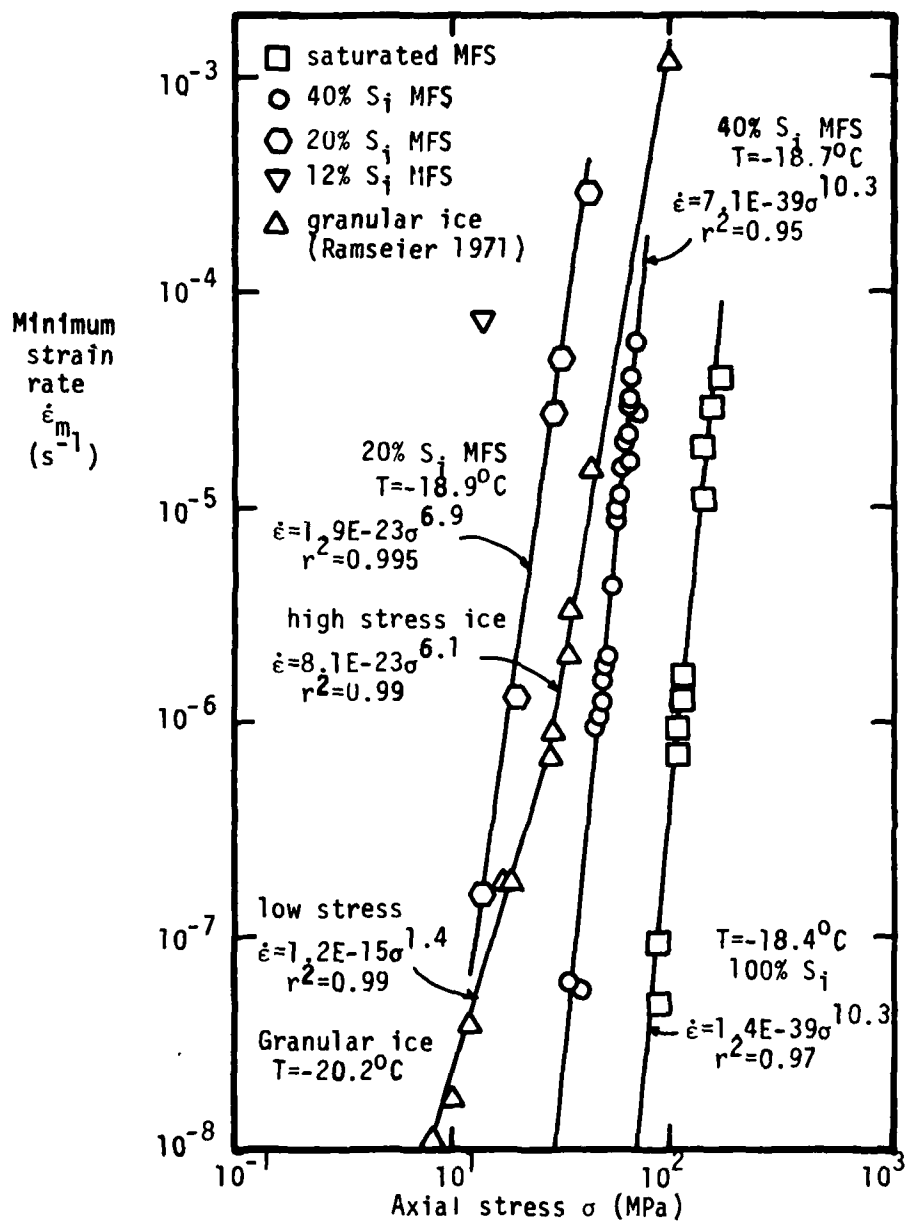


FIGURE 4.12 Stress dependence of creep for ice and Manchester Fine Sand at various degrees of ice saturation

on behavior is exhibited in Figure 4.13. An increase in stress fluctuation from 0.03% of applied load to 0.6% greatly increases the scatter in the measured strain rate. This suggests that even minute stress variations during creep testing can greatly affect the observed strain rate, particularly at low creep rates.

Effect of temperature

Similar to the behavior of ice, the creep of frozen soils is extremely temperature sensitive. The results of uniaxial creep testing at various temperatures on partially saturated MFS at an applied stress of 4.78 MPa are plotted in Figure 4.14. Analogous to the stress dependence of frozen soil, the temperature dependence of frozen soil is far greater than for ice.

By taking the minimum strain rate at varying temperatures and plotting $\dot{\epsilon}_m/T$ against $1/T$ as in Figure 4.15, the apparent activation energy can be determined for each level of applied stress from the slope of the resulting lines by equation (2.5). By obtaining the apparent activation energy at different stress levels, the true free energy of activation, ΔF , can be determined. This has been done for the data shown in Figures 4.14 and 4.15 and yields a ΔF of about 480 kJ/mole, as seen in Figure 4.16. Similar analysis of data on saturated MFS also yields a free energy of activation of about 480 kJ/mole. Notice that this is far in excess of the 59 kJ/mole reported for the free energy of activation for ice or the 125 kJ/m reported as an

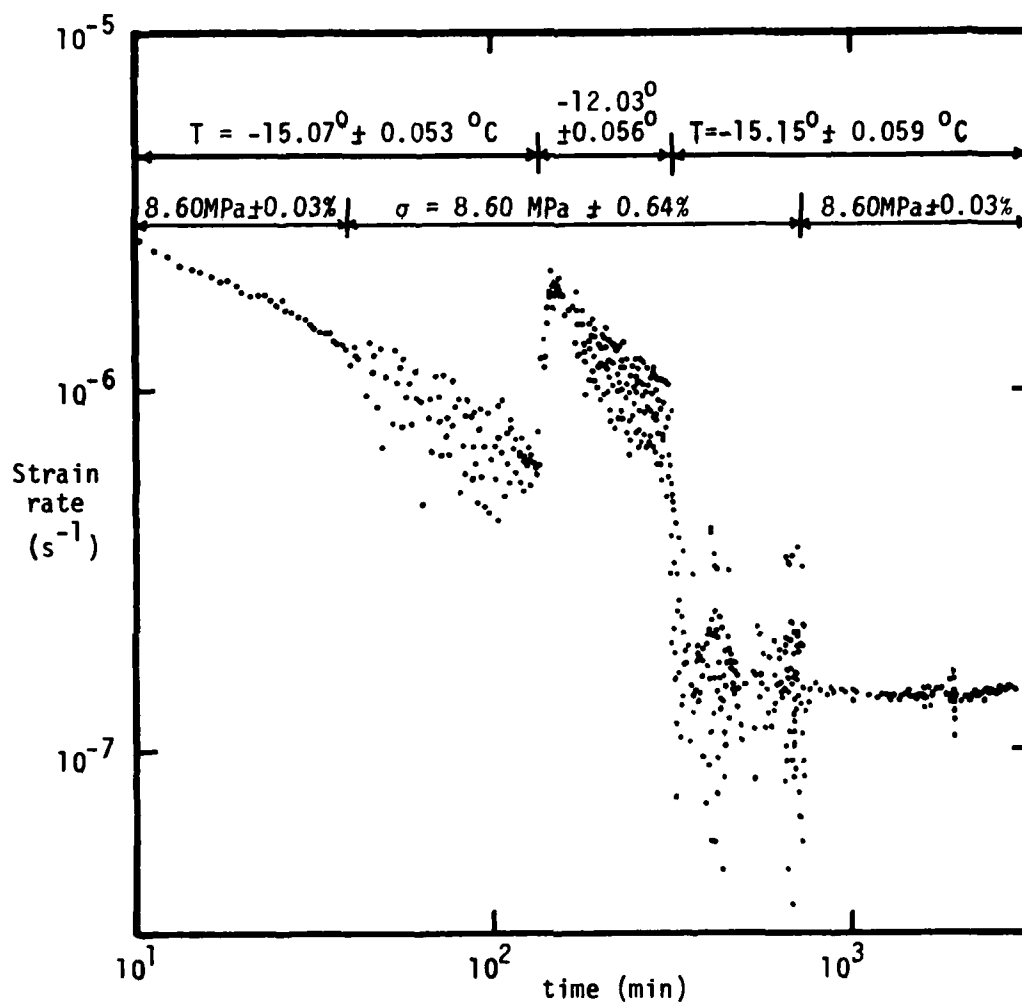


FIGURE 4.13 Effect of minor fluctuations in applied stress on the creep of frozen soils (from Martin, Ting and Ladd 1981)

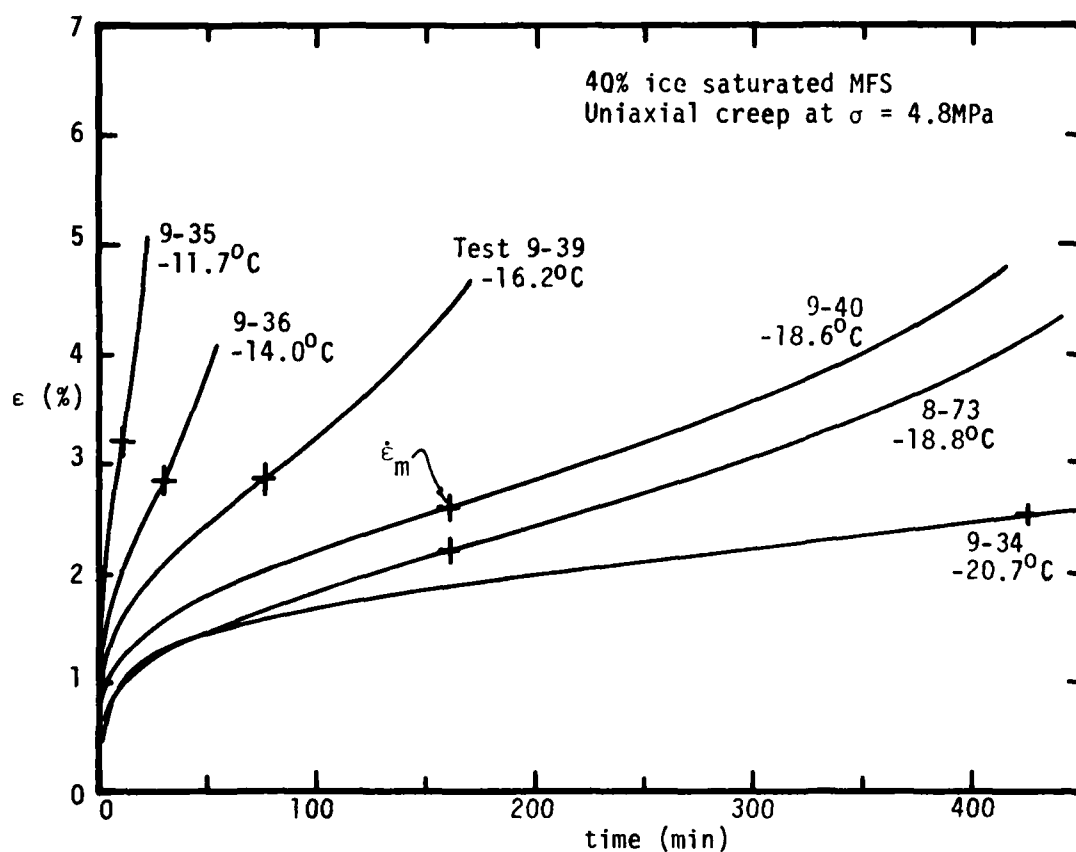


FIGURE 4.14(a) Effect of temperature on the uniaxial creep of frozen Manchester Fine Sand (from Martin et al. 1981)

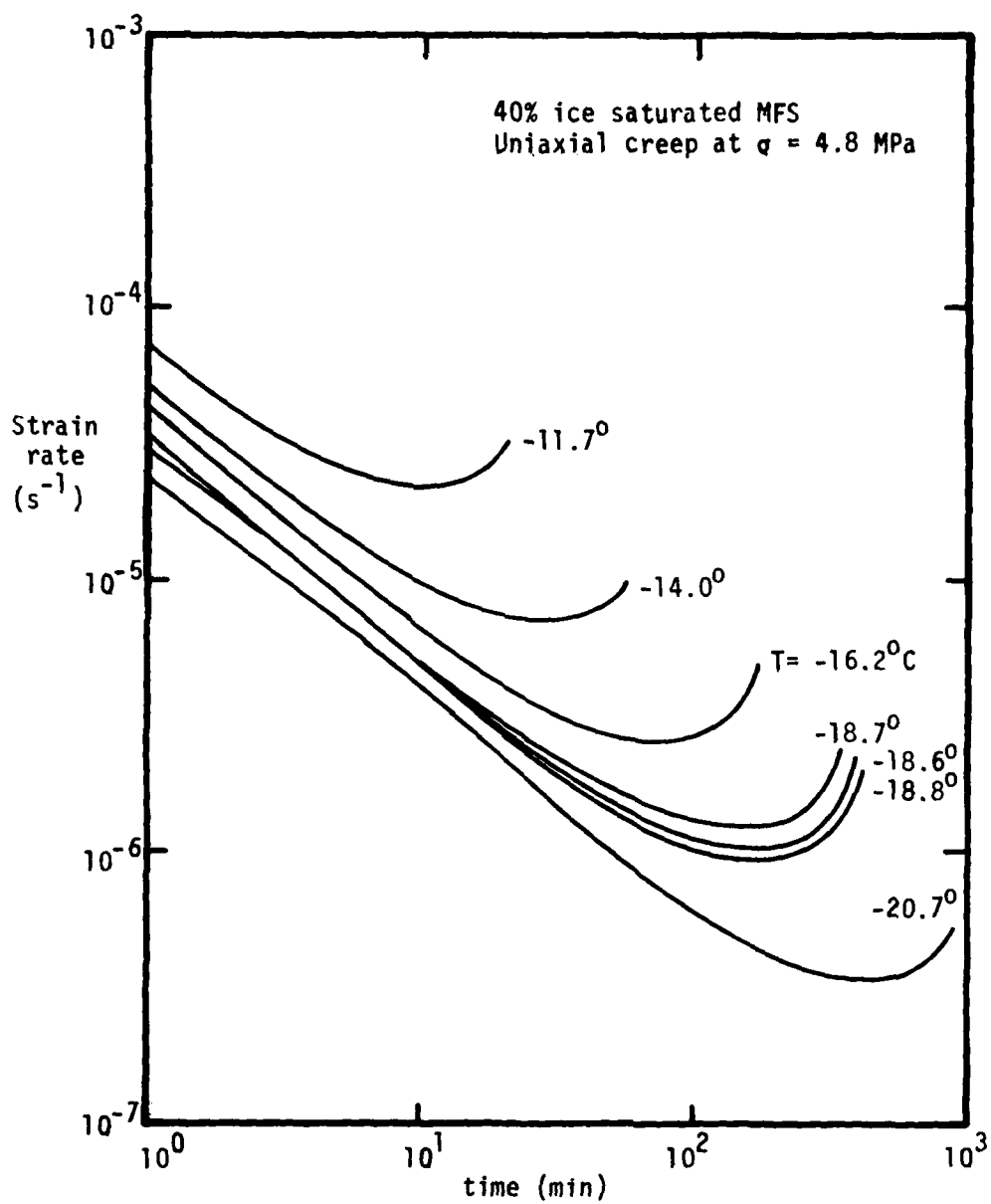


FIGURE 4.14(b) Effect of temperature on the uniaxial creep of frozen Manchester Fine Sand (from Martin et al. 1981)

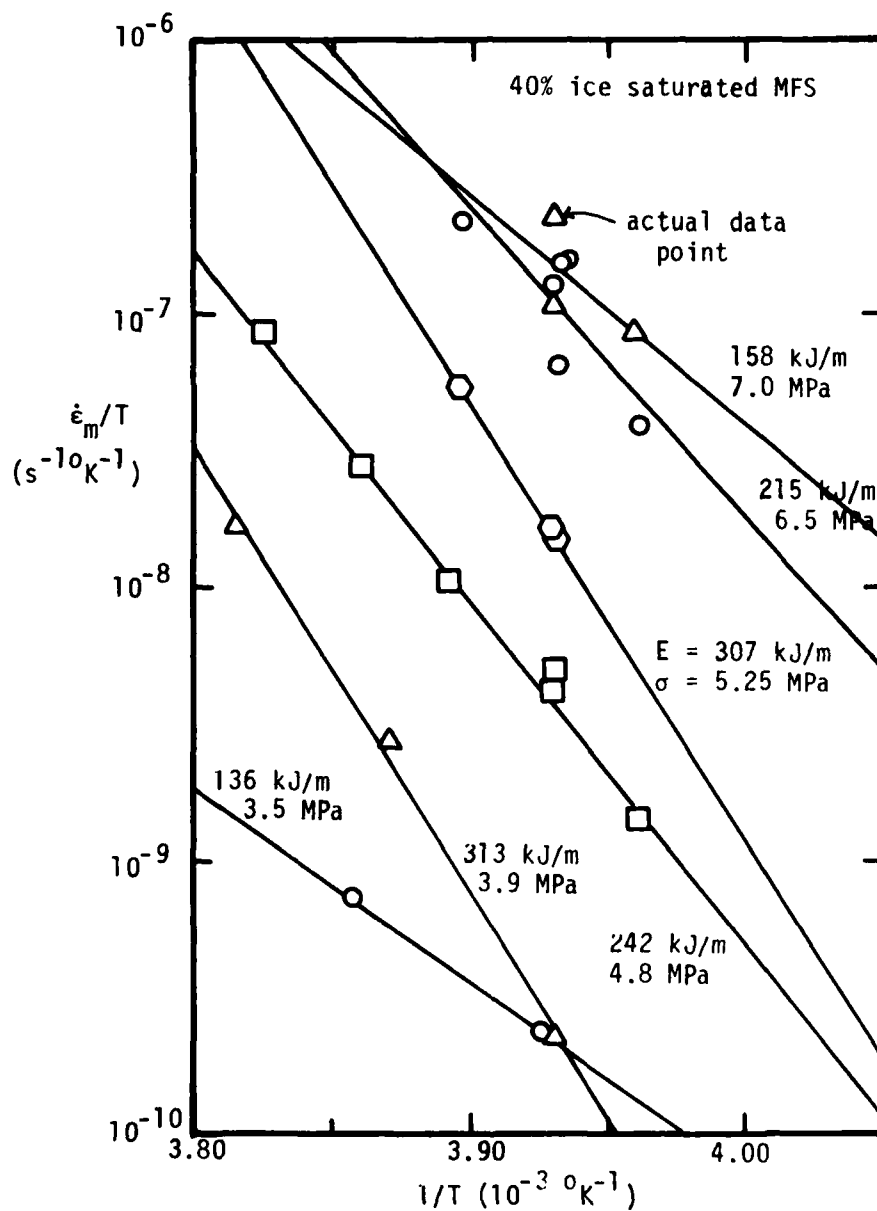


FIGURE 4.15 Determination of the apparent activation energy E for frozen partially saturated MFS (from Martin et al. 1981)

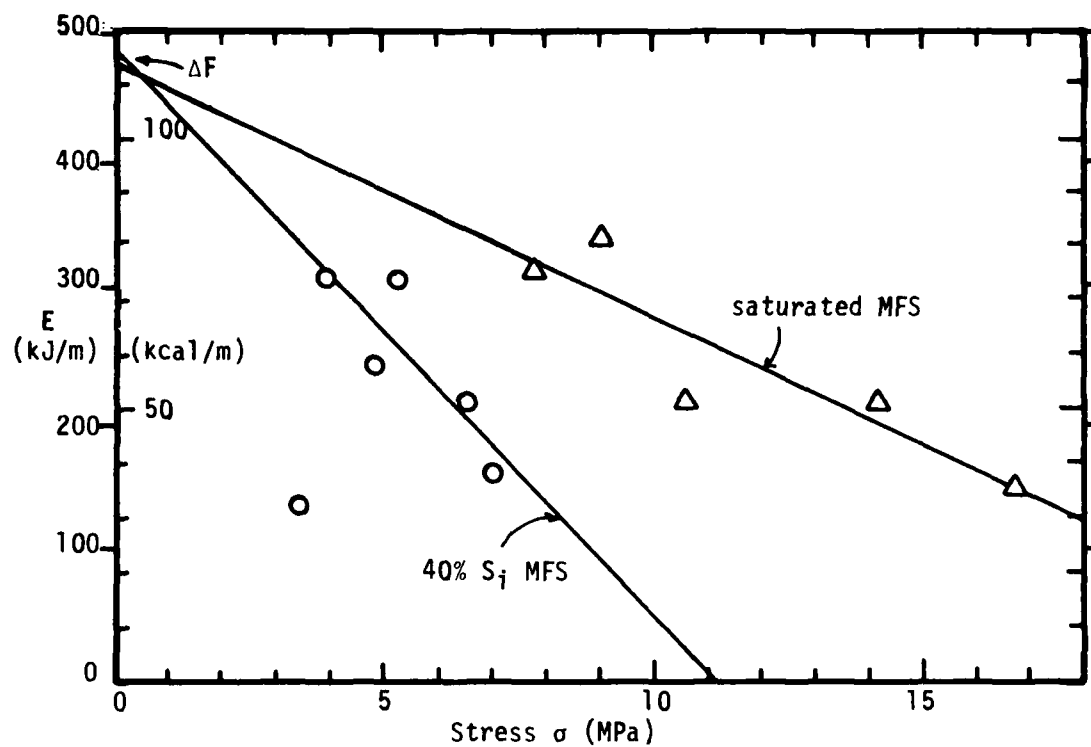


FIGURE 4.16 Variation of E with stress level (data from Martin et al. 1981)

apparent activation energy for unfrozen soil (Mitchell 1976). In general, for materials tested at approximately the same absolute temperature range which may be modelled empirically by the original or modified rate process theories (equations 2.5 or 2.7), the greater the observed activation energy, the greater the temperature sensitivity of the creep of the material.

By way of comparison, consider the following example: an ice sample is loaded to yield an $\dot{\epsilon}_m$ of 10^{-6} /s at -15°C ; another such sample similarly loaded will yield a strain rate of 9.23×10^{-7} /s at -16°C for $E = 42$ kJ/mole. For frozen sand loaded to yield an $\dot{\epsilon}_m$ of 10^{-6} /s at -15°C , another similarly loaded sand sample at -16°C would yield a strain rate of 6.33×10^{-7} for an E of 250 kJ/mole. Consequently, it is evident that the creep of frozen soil is far more temperature sensitive than for ice, and this extreme sensitivity to temperature results in experimental problems with temperature control during testing similar to the stress control problems previously noted.

It is difficult to compare this temperature dependence with unfrozen soil, since no free energy of activation has been reported. If unfrozen soil may be modelled adequately by equations (2.5) or (2.7), however, a comparison of the reported apparent activation energies indicates that frozen soil exhibits a greater temperature dependence sensitivity than unfrozen soil.

Effect of confining stress

Consistent with the effect of confining stress on the strength of frozen soil, an increasing confining stress level tends to decrease the creep rate of a loaded sample. Test results from triaxial creep tests on OWS 20-30 by Sayles (1974) at various levels of confining stress and constant deviator stress are plotted in Figure 4.17. As is evident from this Figure, the creep of frozen soils is quite dependent on the confining stress. However, it is not possible to compare this effect to the triaxial creep behavior of ice due to the lack of such data for ice.

Andersland and AlNouri (1970) and Alkire and Andersland (1973) also studied the effect of confining stress on the creep of OWS 20-30 by carrying out a series of stress stage tests where the confining stress was changed while the deviator was held constant. However, although they referred to their observed strain rates at each level of confining stress as "secondary strain rates", these rates were definitely not "steady-state" nor minimum strain rates due to the short duration of each stage. By postulating that the effect of the confining stress could be separated from the effect due to the deviator stress and the temperature, they proposed that:

$$\dot{\epsilon} = C \exp(\sigma_1 - \sigma_3) \exp[-(m\sigma_{oct})] \quad (4.1)$$

where $\sigma_{oct} = 1/3(\sigma_1 + \sigma_2 + \sigma_3)$

and $m = 0.01206$ (1/psi) for 64.7% OWS by volume

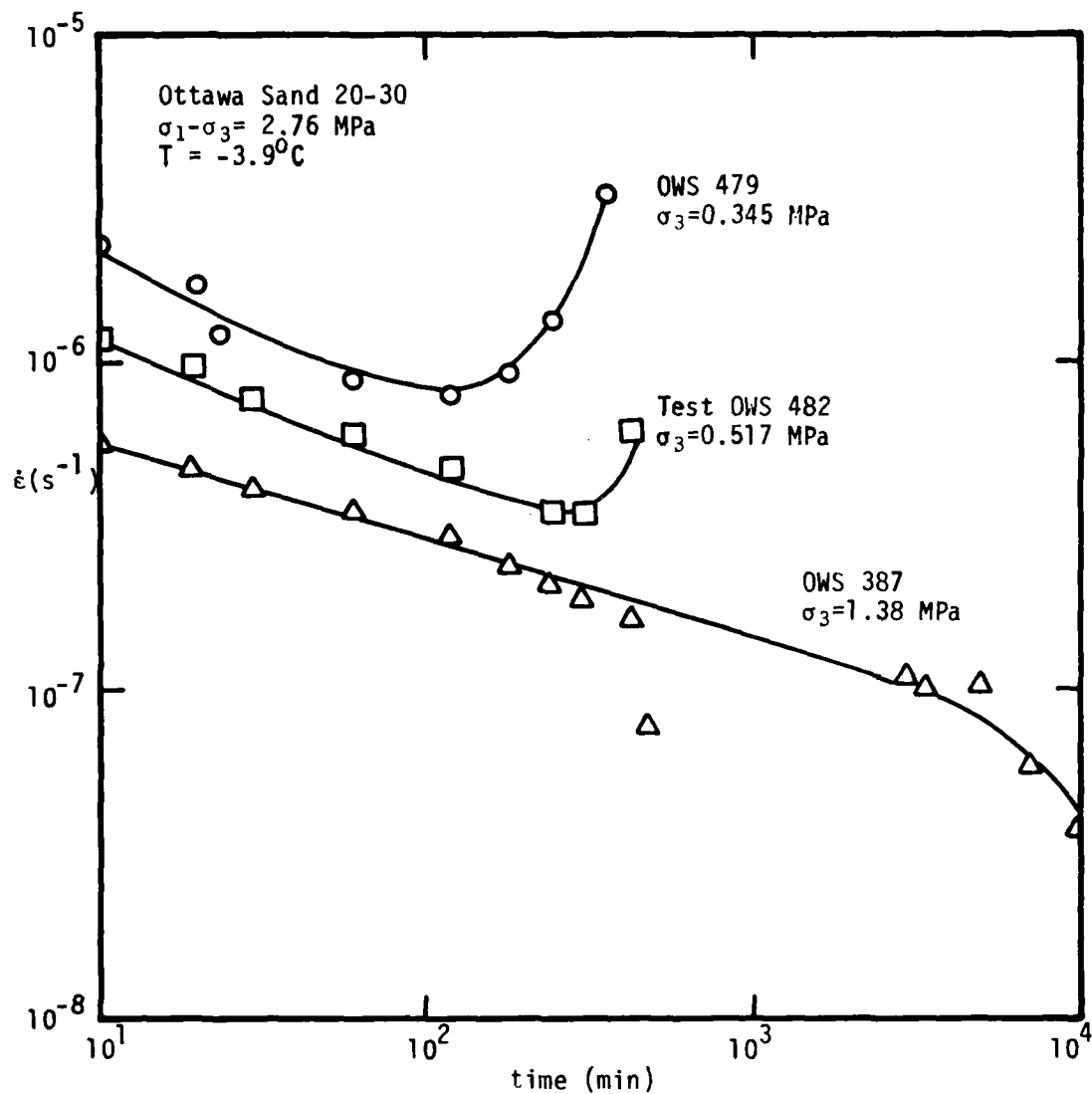


FIGURE 4.17 Effect of confining stress on the creep of frozen sand
 (from Sayles 1974)

Other factors

The previous sections described the major parameters which affect the strength and deformation of frozen soils, ie. the stress level, confining stress, temperature and strain rate. Many other factors also affect the measured mechanical behavior of frozen soil. Some of these are related to experiental techniques; others are a function of the properties of frozen soil.

Some of the properties which affect the mechanical behavior of frozen granular materials are: (1) relative density, (2) degree of ice saturation, and (3) structure and distribution of the ice in the frozen soil. As previously mentioned, Goughnour and Andersland (1968) showed that as the sand concentration in a saturated sand-ice mixture increases, the strength of the composite increases. In other words, as the relative density of the soil structure increases, so does the strength of the composite. Although this strength increase is due in part to the increased sand/sand particle contacts and the resistance of the ice matrix to the dilation of the sand structure, an effective strengthening of the ice is also present independent of the sand particle contacts. This is evident from the strengthening at low sand concentrations before sand-to-sand contacts exist (see Figure 2.8).

Similarly, a decreasing creep susceptibility is observed at increasing relative density. For partially and fully saturated MFS, Martin et al. (1981) show that a very large decrease in minimum strain rate occurs in the medium dense to dense range

of relative density (Figure 4.18). However, loose saturated MFS shows less effect of relative density, while partially saturated samples exhibit a large density dependence at all relative densities. The large density dependence in the loose range for partially saturated Manchester Fine Sand is probably indicative of a collapse of the ice structure. In the dense zone, however, the large dependence on density of both partially and fully saturated samples is probably due to the resistance of the ice matrix to dilation of the sand. The decreasing creep behavior with increasing relative density is analogous to the increasing strength with decreasing void ratio reported by Alkire and Andersland (1973), where small changes in void ratio were observed to greatly affect the measured strength.

The amount of ice saturation also greatly affects the mechanical behavior of frozen soil (Alkire and Andersland 1973, Martin et al. 1981, Sayles and Carbee 1980). Uniaxial creep tests have been carried out on frozen MFS at 12, 20, 40, 60 and 100 % nominal ice saturation levels by Martin et al. These data, partly summarized in Figure 4.12, clearly demonstrate the tremendous effect of ice content. By taking several strain rates from Figure 4.12, the effect of ice saturation on the applied stress yielding a given minimum strain rate can be plotted as in Figure 4.19.

Other important soil parameters include the type, distribution and structural integrity of the pore ice. The apparent

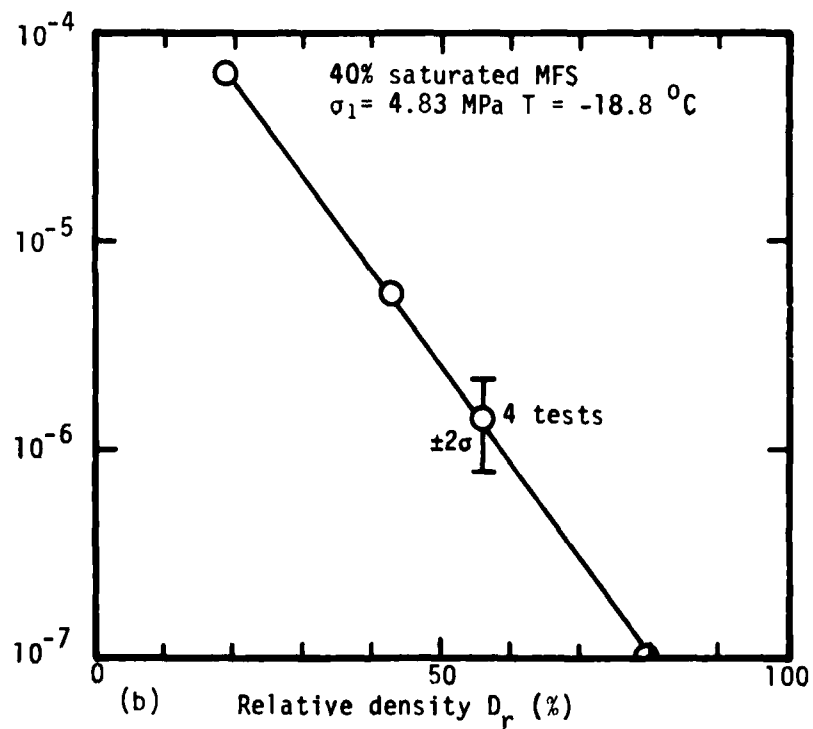
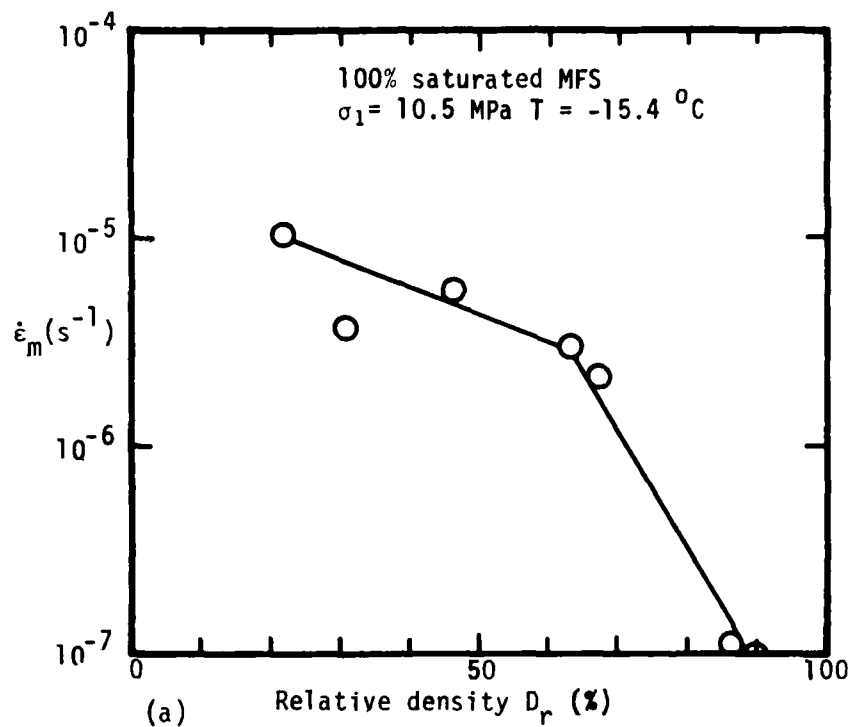


FIGURE 4.18 Effect of relative density on the creep of frozen MFS

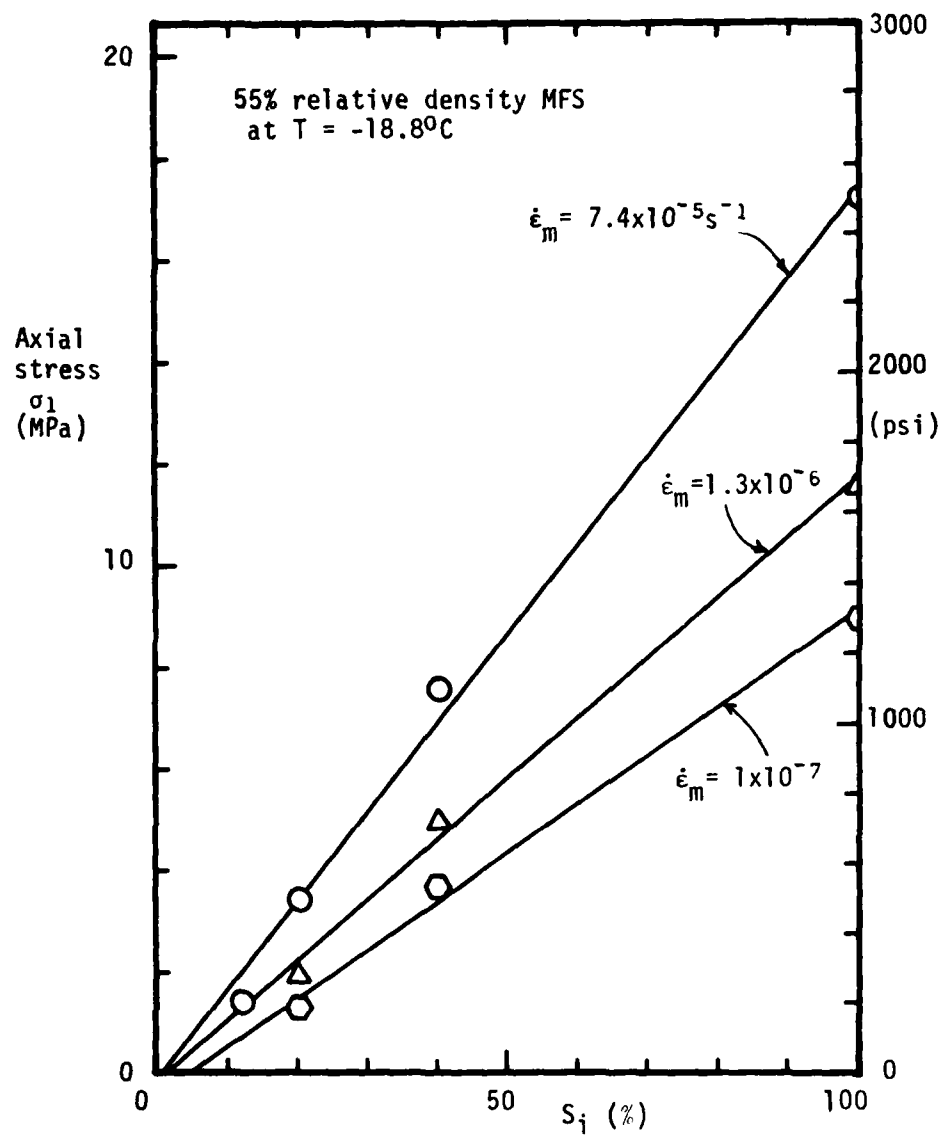


FIGURE 4.19 Effect of ice saturation on the creep of frozen MFS
(data from Martin et al. 1981)

strengthening effect of particulate and chemical impurities on ice could be due to an altered ice structure or grain size induced by the impurities. Distribution and location of the ice in the frozen soil can significantly affect the gross mechanical behavior. In silts, for example, ice lensing could cause extreme anisotropy and heterogeneity. The structural integrity of the ice can be affected by the stress history of the sample, whether it be due to pretest disturbance or sample preparation techniques. Those properties of the frozen soil samples related to the nature of the pore ice are particularly important during the preparation of test specimens. Careful control of the freezing rate, time and temperature and the method, temperature and length of storage and ensuring proper drainage conditions during freezing are all required to ensure sample reproducibility.

Experimentally, careful choice of the loading and temperature control systems is required to ensure minimal stress and temperature fluctuations during longterm testing. Sensitive measurements are needed to detect these potential fluctuations, especially at very low deformation rates. Other experimental factors which can affect the creep are improper alignment of the sample and the choice of the endcaps (T.H.W. Baker 1978).

4.2.3 Qualitative models of strength and deformation

A qualitative understanding of the mechanisms of strength and deformation is desirable for a better comprehension of the mechanical behavior of frozen soil. The many mechanisms of strength and deformation for ice and unfrozen soil have been described in the previous Sections. Because of the composite nature of frozen soil, the mechanisms for frozen soil reflect the component materials as well as the interaction between them. However, owing to the complexity of the physico-chemical and mechanical interaction between the ice and soil, it is not always clear how this interaction affects the mechanisms of the individual components.

Various researchers have attempted to provide qualitative mechanistic explanations of their experimental data, notably Sayles (1968, 1974), Goughnour and Andersland (1968), Hooke et al. (1972), Chamberlain et al. (1972) and Vyalov (1973), Alkire and Andersland (1973) and Roggensack and Morgenstern (1978). While these explanations may be adequate in describing the specific case examined, a comprehensive qualitative model for the mechanical behavior of frozen soil does not exist.

This Section first summarizes various aspects of the mechanical behavior of frozen soils. Available explanations for this behavior are then described. In this initial discussion, the view of each researcher is presented together with other possible explanations for the same behavior.

Summary of the mechanics of frozen soil

Some of the pertinent aspects of frozen soil behavior that any successful qualitative model should seek to explain are briefly summarized:

(1) frozen soil is generally very strong compared to its main structural components, ice and unfrozen soil; typically, short term strengths for frozen soil at low confining stress levels are up to two or three times greater than for conventionally tested ice and up to an order of magnitude greater than for unfrozen soil; at very high confining stresses, however, the drained strength of unfrozen soil substantially exceeds that of frozen soil (see Figures 4.2 and 4.3);

(2) frozen soil possesses very time dependent strength and deformational characteristics; the uniaxial strength may increase up to four times for a strain rate increase from 10^{-4} to 10^{-1} /s (Figures 4.8 and 4.9), and will eventually creep rupture at stress levels exceeding about 0.3 of its "instantaneous strength" (Martin et al. 1981);

(3) the failure envelopes for frozen soil at varying times to failure indicate that the "frictional" component of strength remains about the same, while the "cohesive" component decreases with increasing times to failure (Sayles 1974, Roggensack and Morgenstern 1978, Andersland and AlNouri 1970);

(4) some researchers report a substantial limiting longterm strength value for frozen cohesionless soils under uniaxial compressive loading (Rein et al. 1975); For triaxial loading at

low confining stress levels, the longterm "frictional" component of strength is similar to the corresponding component in the unfrozen soil at the same relative density; while the "cohesion" intercept decreases with increasing times to failure, and is probably bounded by the drained strength of the unfrozen soil, the overall longterm strength of the frozen soil is significantly greater than for the unfrozen soil (see Figure 4.21).

(5) the mechanical behavior of frozen soils is very temperature dependent, much more so than ice and unfrozen soil; this temperature dependence appears to decrease with increasing confining stress level (Figure 4.7);

(6) the creep behavior of frozen soils is very sensitive to the level of applied stress, much more so than ice (Figure 4.12);

(7) triaxial loading of frozen soils can result in volume changes even though "drainage" is not explicitly provided (Goughnour and Andersland 1968, Chamberlain et al. 1972); initially contractive, then dilatant behavior typically occurs for medium to dense sands at low confining stress levels; at higher confining stress levels, and for nondilatant silts, dilation is not observed;

(8) undrained triaxial compression of frozen soils at varying confining stress levels indicate that three distinct zones exist (Figure 4.2): a low stress region where dilatant sand exhibits an increasing strength with confining stress and nondilatant nonplastic silt exhibits essentially constant shear strength;

an intermediate stress region where both the sand and silt exhibit decreasing strength with increasing confining stress; and a high confining stress region where both sand and silt exhibit slightly increasing shear strength with increased confinement;

(9) at the lower confining stress levels, two stress peaks may be observed during strength testing (Figure 4.4); the first peak occurs at about 0.5 %, compatible with fracture of the ice matrix, while the second peak typically occurs after 8 % strain, compatible with the mobilization of the internal sand friction (Sayles 1974, Chamberlain et al. 1972); typically, the strain at which the ultimate strength is achieved increases with increasing confining stress;

(10) the relative density of the soil skeleton has a very pronounced effect on the mechanical behavior of frozen soils; increasing soil relative density increases the frozen soil strength (see Figure 2.8) and decreases creep (Figure 4.18);

(11) the strain at minimum strain rate during creep testing at the same applied stress and temperature typically decreases with increasing relative density (Martin et al. 1981); the strain at peak stress during strength testing may increase or decrease with increasing relative density of the soil skeleton (Alkire and Andersland 1972, Goughnour and Andersland 1968);

(12) the effect of ice content is very pronounced; increasing ice saturation of the pores at essentially constant soil relative density increases the frozen soil strength (Alkire and Andersland 1973) and decreases creep susceptibility (Figure 4.12).

Qualitative models of behavior

Sayles (1968, 1974) proposed that the strength of frozen soils depends upon the cohesion and internal friction of the component materials. The "cohesive" component is attributed to the ice matrix and depends on the amount and strength of the ice, and the area of contact between the ice and soil, each of which is a function of the temperature. Vyalov (1963) postulated that this cohesive component of strength consists of intermolecular solid/solid contacts, "structural" cohesion, and ice cementation. Note that although it is known that particles in frozen soil are completely surrounded by unfrozen water, substantial ice/silicate surface "cementation", or adhesion, can exist, based on Jellinek's experiments (1957(a),(b), 1960(b),(c) 1962). However, the exact nature of the "structural" cohesion is not specified.

The frictional component of strength is attributed primarily to the soil phase, and is a function of soil grain size, distribution, shape, arrangement and relative density. This hypothesis is confirmed by the observance of two apparent peaks in the stress-strain curves for the triaxial compression of frozen soils and the fact that the frictional component of the longterm strength of frozen soil reportedly approaches the frictional component of the drained unfrozen soil strength. For uniaxial compressive testing of frozen soils, however, a sizeable limiting longterm strength has been reported (Rein et al. 1975, Martin et al. 1981).

For higher confining stress levels, the initial peak may be absent, with the maximum resistance occurring at large strains. Sayles suggests that at the higher confining stresses, interparticle friction is relatively more important than at the lower stresses. However, this model does not entirely explain the generation of frozen soil strength, since the overall strength of frozen soil is greater than the sum of the unfrozen soil and ice strengths alone. Instead, some nonlinear interaction exists between the ice and soil, which needs to be clarified for a better understanding of frozen soil behavior.

Goughnour and Andersland (1968) proposed that the strengthening of frozen soil over pure ice may be due to three mechanisms. At the lower sand concentrations where no continuous soil skeleton exists, deformations occur primarily in the ice matrix. Since soil particles are much less deformable than ice, a larger deformation rate is imposed upon the ice with increasing soil concentration. Since ice strength increases with increasing applied strain rate, a higher overall strength is observed. However, once a continuous soil skeleton is established at the higher sand concentrations, the applied load is primarily carried by the sand. Consequently, this first mechanism of strengthening is probably not a significant factor at the higher soil concentrations.

A second mechanism is the result of interparticle friction at the contacts between sand particles, as also proposed by Sayles (1968). Goughnour and Andersland consider this mechanism to

be a function of the frictional characteristics of the solid material, "degree of suspension of the solids", and normal stresses at the interparticle contacts.

The third mechanism concerns the sample volume change. Dilatancy of the sand skeleton during shear is impeded by the ice matrix. Adhesion between the sand particles and the ice matrix during dilation may create an effect analogous to higher effective stresses in unfrozen soil. This results in an increased shear strength at interparticle contacts. This strength increase due to dilatancy continues to until the volume increase ceases, or until the limiting strength of the ice matrix is exceeded.

Hooke et al. (1972) report that for low sand concentrations the strengthening of sand-ice systems occurs in part due to dislocation impedance by the sand particles.

Chamberlain et al. (1972) postulated that the triaxial compressive strength behavior of frozen sands at low confining stresses is controlled by interparticle interlocking and friction. In the intermediate confining stress levels, Chamberlain et al. propose that local pressure melting at stress concentrations is responsible for the strength decrease with increasing confining stress levels. In the high stress region, a phase change is observed from ice to water, and the strength increases slightly with increasing confining stress level. Chamberlain et al. attribute the low friction angle in this region to the observed particle crushing due to the high stresses.

However, Chamberlain et al. do not specify whether their high pressure tests are drained or undrained. While volume change was observed at the lower stresses, no drainage was explicitly provided in the test setup. For the higher stresses where a complete phase change from ice to water has occurred, it is reasonable to assume that undrained conditions prevail. At low confining stress levels, the undrained shear strength of saturated unfrozen soils should be independent of confining stress. However, at the high levels of confining stress in region III, the Skempton (1954) pore pressure parameter "B" relating the increment of pore pressure to an increment of applied confining stress is probably less than unity (ie. $\Delta u < \Delta \sigma_c$) and hence a slight increase in effective confining stress with increasing total confining stress is expected. This is discussed later in greater detail.

For frozen silt, Chamberlain et al. (1972) observed essentially the same behavior as for the frozen sand. However, in the low confining stress region, no strength increase was observed with increasing confining stress level. Chamberlain et al. postulate that while interparticle friction should be important for the silt, it is perhaps obscured by "changing cohesive properties resulting from the increase in unfrozen water content".

Vyalov (1963) postulated the following schematic model for frozen soil:

As an external load is applied to a frozen soil sample, stress

concentrations exist at the contact points, resulting in plastic flow and pressure melting of the ice. The melted water migrates to zones of lower stress and refreezes. Simultaneously, structural and ice cementation bonds in weak locations yield and mineral particles slip. This is accompanied by ice crystal reorientations and mineral rearrangements and reorientations. The ice reorientations tend to weaken the system, as the crystals tend to realign with their basal planes in the direction of slip. Soil rearrangements may serve to weaken or strengthen the system; when the strengthening mechanisms in the system exceed the weakening ones, then damped creep behavior is observed for creep loading, and increasing strength is observed in strength testing.

Vyalov's model provides a nice qualitative explanation of the various events which occur during the loading of frozen soil. As with each of the models of behavior already presented, however, it is not completely satisfactory. To be fair, the individual models presented have sought for the most part to explain a particular set of data. While some of the models are consistent with the others, some are not entirely correct in their conclusions. None are completely thorough in their treatment of the possible mechanisms controlling the strength and deformation of frozen soils.

4.2.4 Quantitative models of strength and deformation

From the previous discussion, it is obvious that difficulties exist in merely describing the behavior of frozen soils conceptually. Any attempts at mechanistically based quantitative modelling must of necessity be exceedingly complex; consequently, empirical modelling is by far the most popular approach. Various empirical models proposed to describe the deformation and strength behavior of frozen soils have been summarized by Andersland and Anderson (1978) and are briefly described here.

To describe the time-dependent deformation of frozen soils, three types of mathematical models have been used. These may be termed "primary", secondary, and "tertiary" models, and are illustrated in Figure 4.20.

Vyalov (1962) proposed a primary creep model which has been popular in frozen soils and has been successfully applied to various frozen soils by Sayles (1968, 1974). In this model, strain is expressed as:

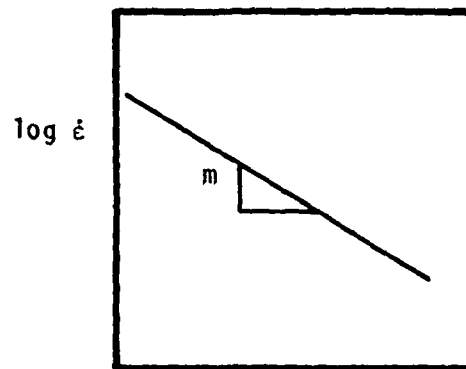
$$\begin{aligned}\epsilon &= \epsilon_0 + \epsilon(t) \quad \text{where for negligible initial strain } \epsilon_0, \\ \epsilon &= \epsilon(t) = \left[\frac{\sigma t^\lambda}{\omega (\theta + \theta_0)^k} \right]^{1/m} \quad (4.2)\end{aligned}$$

where $\theta = -T$ ($^{\circ}\text{C}$)

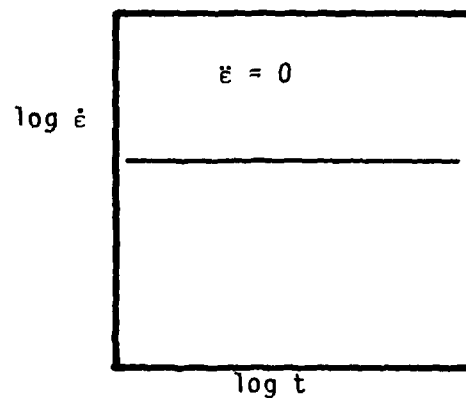
θ_0 = reference temperature, usually -1°C

ω, k, λ, m = soil parameters

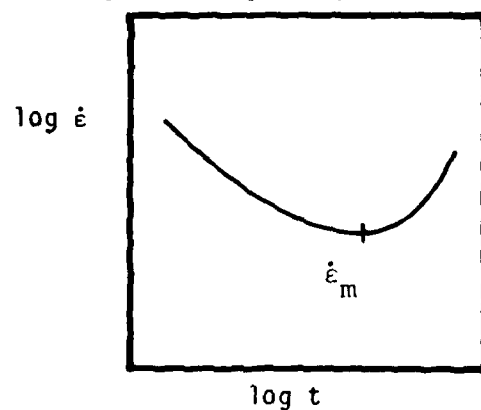
By differentiating (4.2) with respect to time, the strain rate may be obtained:



(a) "primary" creep model



(b) secondary creep model



(c) "tertiary" creep model

FIGURE 4.20 Typical creep models

$$\dot{\epsilon} = \frac{\lambda}{m} \left[\frac{\sigma}{\omega(\theta + \theta_0)^k} \right]^m t^{\frac{\lambda-m}{m}} \quad (4.3)$$

Note that the strain rate $\dot{\epsilon}$ continuously decreases with time, hence confirming the fact that (4.2) is a primary (strain hardening) creep model. In addition, a linear relation results between $\log \dot{\epsilon}$ and $\log t$. In this respect, the model is similar in form to the three-parameter creep model proposed by Singh and Mitchell (1968) for unfrozen soils and the Andrade $t^{1/3}$ law for ice and frozen soils (Ting and Martin 1979).

The parameters for the Vyalov model may be obtained by a series of log-log curve fits. First $\dot{\epsilon}$ and σ are plotted to yield $A(t)$ and m , where $A = t^\lambda / \omega(\theta + \theta_0)^k$. Then, $A(t)$ and t are plotted at different temperatures to yield R and λ , where $R = At^\lambda$. Finally, R and $(\theta + \theta_0)$ are plotted to yield ω and k . Sayles (1968) determined the various parameters for frozen Ottawa sand 20-30 and Manchester Fine Sand 40-200 with some success.

Secondary creep models for frozen soils have been proposed by Ladanyi (1972) based on work in metals by Hult (1966). In addition, secondary creep models based on the quasi-mechanistic Rate Process Theory have been advanced (Andersland and Akili 1967, Andersland and AlNouri 1970) and examined (Martin, Ting and Ladd 1981). At a constant temperature and stress, Ladanyi (1972) expressed the strain as:

$$\epsilon = \epsilon_i + \epsilon_c \quad (4.4)$$

where ϵ_i = pseudo-instantaneous strain = $F(\sigma, T)$ and can be expressed as the sum of a recoverable portion and an irrecov-

erable portion. The creep strain ϵ_c may be described from:

$$\frac{d\epsilon_c}{dt} = G(\sigma, T) = \dot{\epsilon}_c \left(\frac{\sigma}{\sigma_c(T)} \right)^{n(T)} \quad (4.5)$$

where $\dot{\epsilon}_c$ is an arbitrary strain rate corresponding to a proof stress, $\sigma_c(T)$, and n is a constant. Then, for a given material at a constant temperature,

$$\epsilon = \frac{\sigma}{E} + \epsilon_k \left(\frac{\sigma}{\sigma_c} \right)^k + t \dot{\epsilon}_c \left(\frac{\sigma}{\sigma_c} \right)^n \quad (4.6)$$

where E is the elastic modulus

For engineering applications, the third term in (4.7) gives good approximations of the total strain.

The basis for Rate Process Theory has been described in Chapter 2 and its application to frozen soils has been mentioned in Section 4.2.2. Basically, RPT predicts a "steady-state" creep rate corresponding to a specific temperature and stress level. While the theory has fundamental significance when applied to reaction rates in pure chemical systems, its application in the creep of frozen soils is primarily empirical in nature. Further discussion of its validity as a model for frozen soil is found in Chapter 6.

Care must be exercised in the use of these primary and secondary creep models, since they are applicable only in the time range for which they were formulated. For secondary creep models, for example, creep strain during primary creep is overestimated, while strain during tertiary creep is underestimated.

A more sophisticated "tertiary" model which does account

for accelerating creep was proposed by Goughnour and Andersland (1968). In this model, the plastic strain rate is composed of the sum of a strain hardening term and a softening term which is dependent on the absorbed strain energy. Since integration of their strain-based empirical model is quite difficult, Goughnour and Andersland proposed a separate empirical relation in terms of time:

$$\dot{\epsilon} = \frac{K_1}{t^{n_1}} \exp(-n_1 t^{1/2}) + K_2 \exp(n_2 t) \quad (4.7)$$

where n_1, n_2 are soil parameters which are functions of T

and K_1, K_2 are functions of stress and temperature:

$$K = \frac{C}{T^n} \left(\frac{\sigma}{\sigma_C} \right)^m$$

and σ_C = a normalizing constant

Goughnour and Andersland (1968) report excellent correlations between their model and data on Ottawa Sand 20-30.

While the deformation models which have been described can describe a variety of creep behavior, even including tertiary creep in one case, none consider creep rupture, the eventual failure of a sample during creep loading. Separate strength models exist to describe this phenomenon and are described in the following paragraphs.

The strength of frozen soils may take on various meanings depending upon the nature of the loading problem. Limiting longterm or creep strength refers to the stress below which creep rupture or excessive creep deformations do not occur. Short-term strength usually refers to the peak stress achieved during load or strain application. For uniaxial (unconfined)

compressive creep tests, failure is usually defined as the beginning of tertiary creep. For triaxial creep testing where large deformations may occur without actual creep rupture, an arbitrarily large strain, say 20%, is defined as the failure condition.

Vyalov (1959) suggests that the variation of the longterm creep strength of frozen soil with time may be represented by:

$$\sigma_f = \frac{\sigma_o}{\ln\left(\frac{t_f + t^*}{t_o}\right)} \approx \frac{\sigma_o}{\ln\left(\frac{t_f}{t_o}\right)} \quad (4.8)$$

where σ_o , t_o = temperature dependent soil parameters

t_f = failure time

σ_f = longterm strength

$t^* = t_o \exp(\sigma_o / \sigma_i)$

σ_i = instantaneous reference strength

For the temperature dependence of strength, power or exponential functions are typically employed.

For short-term strength analyses, various models based on the Mohr-Coulomb theory and plasticity have been proposed. Due to the difficulties in determining an actual effective (intergranular) stress in frozen soils, total stresses and quasi-single-phase models are used. Based on a series of triaxial compression tests with different times to failure, a sequence of Mohr-Coulomb failure envelopes may be constructed. Triaxial data from Sayles (1973) and direct shear data from Roggensack and Morgenstern (1978) suggest that the envelope for the frozen soil at large times to failure, expressed in

terms of total stress, approaches that for the unfrozen condition under drained loading. The friction angles for the frozen and unfrozen soils were approximately equal, while the apparent cohesion intercept for the frozen soil decreased with increasing time to failure. Although this cohesion intercept decreased with time, it remained significantly greater than the unfrozen soil intercept.

This type of data suggests that the following failure model may be used:

$$\tau_f = c(T, t_f \text{ or } \dot{\epsilon}) + \sigma_f \tan \phi \quad (4.9)$$

where $c = \left(\frac{\sigma_1 - \sigma_3}{2} \right)_f = c(T) \left(\frac{\dot{\epsilon}}{\dot{\epsilon}_0} \right)^{\frac{1}{n}}$ = "cohesion" intercept

$\tan \phi$ = component of frictional strength

τ_f = shear strength

σ_f = normal stress at failure

$\dot{\epsilon}_0$ = reference strain rate

A sequence of such envelopes is shown in Figure 4.21. Note, however, that since total stresses are used in this formulation, it is difficult to infer any physical significance from the relative magnitudes of the parameters in (4.9).

For ice-rich fine-grained soils, Ladanyi (1972) assumes that the strength is relatively independent of total stress changes. Based on this concept, Ladanyi used the von Mises yield criteria and plasticity theory assuming constant volume during shear to describe the strength of such a "nonfrictional" soil. While relatively little experimental data exist to confirm the existence of such behavior, data by Chamberlain et al.

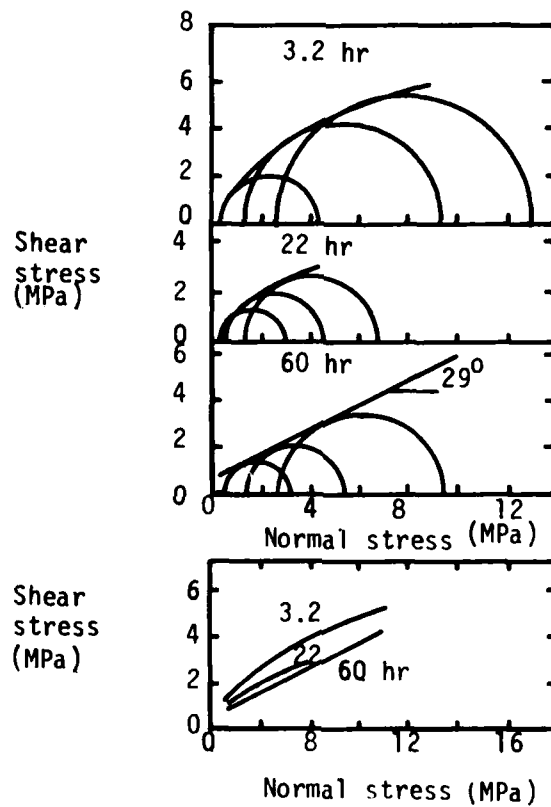


FIGURE 4.21 Variation of failure envelopes with time for Ottawa Sand (from Sayles 1974)

(1972) on a nondilatant silt indicated that little change in strength occurred for confining stresses up to about 20 MPa. However, it has been shown that even clean polycrystalline ice demonstrates a strength increase with increasing confining stress (Smith and Cheatham 1975, Jones 1978).

For individual creep tests, prediction of "failure" usually involves prediction of the time to failure t_m as a function of the secondary strain rate, $\dot{\epsilon}_m$, failure strain, ϵ_m , and loading conditions.

The simplest model is based on the secondary creep model, as proposed by Ladanyi (1972). Assuming a constant secondary creep rate, the time to failure for a given temperature and stress is:

$$t_m = \frac{\epsilon_m - \epsilon_i}{\dot{\epsilon}_m} \quad (4.10)$$

For large times and high ice content soils, $\epsilon_i \ll \epsilon_m$; then, the strain at failure ϵ_m is approximately constant, yielding

$$t_m = C / \dot{\epsilon}_m.$$

Use of equation (4.10) still requires prediction of the minimum strain rate as a function of the loading conditions, such as by the use of equation (4.1) or some RPT-based relationship. Such predictions are described further in Chapter 6.

In an attempt to unify the results from strain rate controlled and constant stress creep tests, O'Connor and Mitchell (1978) proposed an "energy surface" concept. Based on the creep and strength data on frozen silt in Figure 4.22, O'Connor and Mitchell tried to reconcile the slight differences between

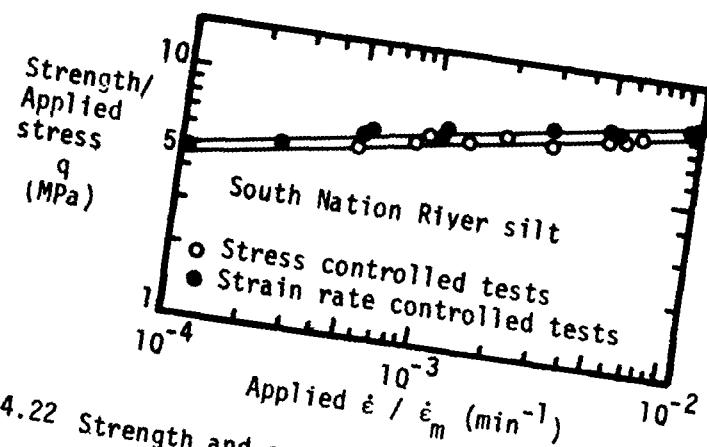


FIGURE 4.22 Strength and creep data for frozen soils as a function of strain rate and stress (from O'Connor and Mitchell 1978)

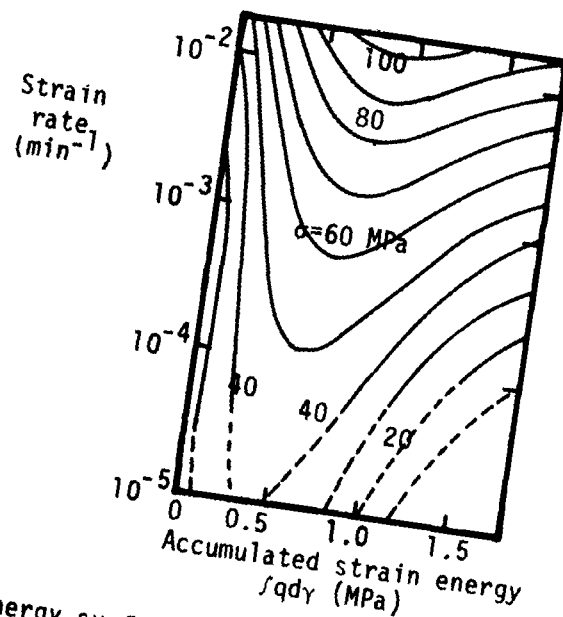


FIGURE 4.23 Energy surface for frozen silt (from O'Connor and Mitchell 1978)

the peak stress in a constant applied strain rate strength test with the minimum strain rate in a constant stress creep test. Note that the data in Figure 4.22 tend to suggest that a "correspondence principle" exists in frozen soil, as has been proposed in ice mechanics. This principle was discussed in Chapter 2 for ice. Based on a computer trend analysis, O'Connor and Mitchell postulated that the unifying concept between the two types of tests is the amount of absorbed strain energy. By combining the results for each type of test in one plot, they obtained an "energy surface" plot, as shown in Figure 4.23.

As a consequence of this concept, it should be possible to run any type of stress or strain rate controlled test, and be able to predict the resulting strain rate or stress, respectively, at a given level of strain energy. The testing need not be restricted to one mode, i.e. constant stress or strain rate, but may even include multimodal loading such as stress stage creep testing or combinations of stress/applied strain rate loading.

While such a concept would greatly enhance the understanding and modelling of frozen soil behavior, attempts at applying this concept to the Manchester Fine Sand data of Martin et al. (1981) have proven to be futile. Instead, the behavior seems to be a function of the level of strain, rather than the absorbed strain energy, as proposed by O'Connor and Mitchell. Further evaluation of this concept, together with testing on the "correspondence principle" for frozen soils, is underway at

USA CRREL, and includes multimodal testing using strain rate and stress controlled stages.

While the engineering models for the strength and deformation of frozen soils are varied and often fairly complex, the reliability of these models is generally quite poor due to the extremely complex nature of the frozen soil system. In addition, reproducibility of tests on frozen soils is usually poor. This is due to poor sample preparation and freezing techniques, inadequate temperature and stress control during testing, as well as the extreme sensitivity of the mechanical behavior to small variations in sample structure and testing conditions.

4.3 Summary of the Nature and Mechanics of Frozen Soil

Although Sections 4.1.2 and 4.2.3 already summarized the structure and mechanical behavior of frozen soil, the most important aspects are again presented for convenience and added emphasis:

(1) effectively solid contacts exist between most particles in frozen soil, especially for coarse-grained materials;

(2) unfrozen water exists at the ice to soil interface and at the grain boundaries in the ice, even at fairly low temperatures;

(3) this unfrozen water film is continuous and completely surrounds the mineral surfaces except at the minute mineral-mineral contacts;

(4) the amount of unfrozen water existing in the ice phase in frozen soil may be about the same or even greater than that portion associated with the soil's adsorbed water and double layer;

(5) probably no direct ice to soil contact exists;

(6) although the unfrozen water film is probably very mobile parallel to the mineral surface, strong tensile and shear adhesional strength exists between silicate surfaces and ice;

(7) the ice in frozen soil is polycrystalline in nature; for in situ freezing where no segregation freezing (ice lensing) occurs, the maximum grain size of the ice is the pore size;

(8) frozen soil is generally very strong compared to its main structural components, ice and unfrozen soil; typically,

short term strengths for frozen soil at low confining stress levels are up to two or three times greater than for conventionally tested ice and up to an order of magnitude greater than for unfrozen soil; at high confining stresses, local, and eventually global pressure melting of the pore ice causes a large strength reduction to values less than those corresponding to the drained strength of the unfrozen soil;

(9) frozen soil possesses very time dependent strength and deformational characteristics; the uniaxial strength may increase up to four times for a strain rate increase from 10^{-4} to 10^{-1} /s (Haynes et al. 1975), and will eventually creep rupture at stresses exceeding about 0.3 of its "instantaneous" strength (Martin et al. 1981);

(10) the failure envelopes for frozen soil at varying times to failure indicate that the "frictional" component of strength remains about the same with varying times, while the "cohesive" component decreases with increasing times to failure (Sayles 1974, Roggensack and Morgenstern 1978, Andersland and AlNouri 1970);

(11) some researchers report a substantial limiting long-term strength for cohesionless sands subjected to uniaxial compressive loading (Rein et al. 1975); for triaxial loading at low confining stress levels, the longterm "frictional" component of strength is similar to the corresponding component in the unfrozen soil at the same relative density, while the "cohesion" intercept decreases with increasing times to failure; the overall

longterm triaxial strength of frozen soil remains significantly greater than the drained strength of the unfrozen soil, for low confining stresses;

(12) the mechanical behavior of frozen soils is very temperature dependent, much more so than ice and probable unfrozen soil; this temperature dependence appears to decrease with increasing confining stress level (Smith and Cheatham 1975);

(13) the mechanical behavior of frozen soils is very sensitive to the level of applied stress; the creep behavior is especially sensitive, much more so than ice and unfrozen soil (Martin et al. 1981);

(14) triaxial loading of frozen soils can result in volume changes even though "drainage" is not explicitly provided (Goughnour and Andersland 1968, Chamberlain et al. 1972); initially contractive then dilatant behavior typically occurs for medium to dense sands at low confining stress levels; at higher confining stress levels, and for nondilatant silts, dilation is not observed;

(15) undrained triaxial compression of frozen soils at varying confining stress levels indicate that three distinct zones exist: a low stress region where dilatant sand exhibits an increasing strength with confining stress and nondilatant nonplastic silt exhibits essentially constant shear strength; an intermediate stress region where both the sand and silt exhibit decreasing strength with increasing confining stress; a high confining stress region where both sand and silt exhibit slightly

increasing strength with increased confinement;

(16) at the lower confining stress levels, two stress peaks may be observed during strength testing; the first peak occurs at about 0.5 %, compatible with fracture of the ice matrix, while the second peak typically occurs after 8 % strain, compatible with the mobilization of the internal sand friction (Sayles 1974, Chamberlain et al 1972);

(17) the relative density of the soil skeleton has a very pronounced effect on the mechanical behavior of frozen soils. Increasing soil relative density increases the frozen soil strength (Goughnour and Andersland 1968) and decreases creep susceptibility (Martin et al. 1981);

(18) the strain at peak stress during strength testing may increase or decrease with increasing relative density of the soil skeleton (Goughnour and Andersland 1968, Alkire and Andersland 1973); however, the strain at minimum strain rate for a given applied stress and temperature typically decreases with increasing relative density (Martin et al. 1981);

(13) the effect of ice content is very pronounced; increasing ice saturation of the pores at essentially constant soil relative density increases the frozen soil strength (Alkire and Andersland 1973) and decreases creep susceptibility (Martin et al. 1981).

CHAPTER 5 - QUALITATIVE MODELS FOR THE MECHANICS OF FROZEN SAND

A major purpose of this Report is to provide a better qualitative understanding of the mechanics of frozen soil. A significant portion of the research therefore concentrated on developing and evaluating the various mechanisms controlling the strength and deformation of frozen soil, based on the thorough literature review presented in Chapters 2 through 4, and on experimental testing programs (summarized in Appendices A.1 through A.6) carried out on Manchester Fine Sand (MFS), ice, and various types of glass beads. From these various mechanisms of strength and deformation, a comprehensive qualitative model for frozen soil is developed, together with new insight into the basis of the power relationship between the minimum strain rate, $\dot{\epsilon}_m$, and the time to the minimum, t_m .

5.1 The Linear $\log \dot{\epsilon}_m - \log t_m$ Correlation

As seen in Figure 5.1, creep tests performed on various materials all produce linear $\log \dot{\epsilon}_m - \log t_m$ correlations; eg. results from uniaxial loading on ice (data from Figure 2.13) and frozen MFS at various degrees of ice saturation (from Martin et al. 1981 as summarized in Appendix A.5) and undrained triaxial compression of isotropically and K_0 consolidated unfrozen Haney clay (Campanella and Vaid 1974, Mitchell 1976). While the existence of these linear correlations is widely recognized, the basis for this apparent linearity has not been explained. This Section examines the underlying reasons for

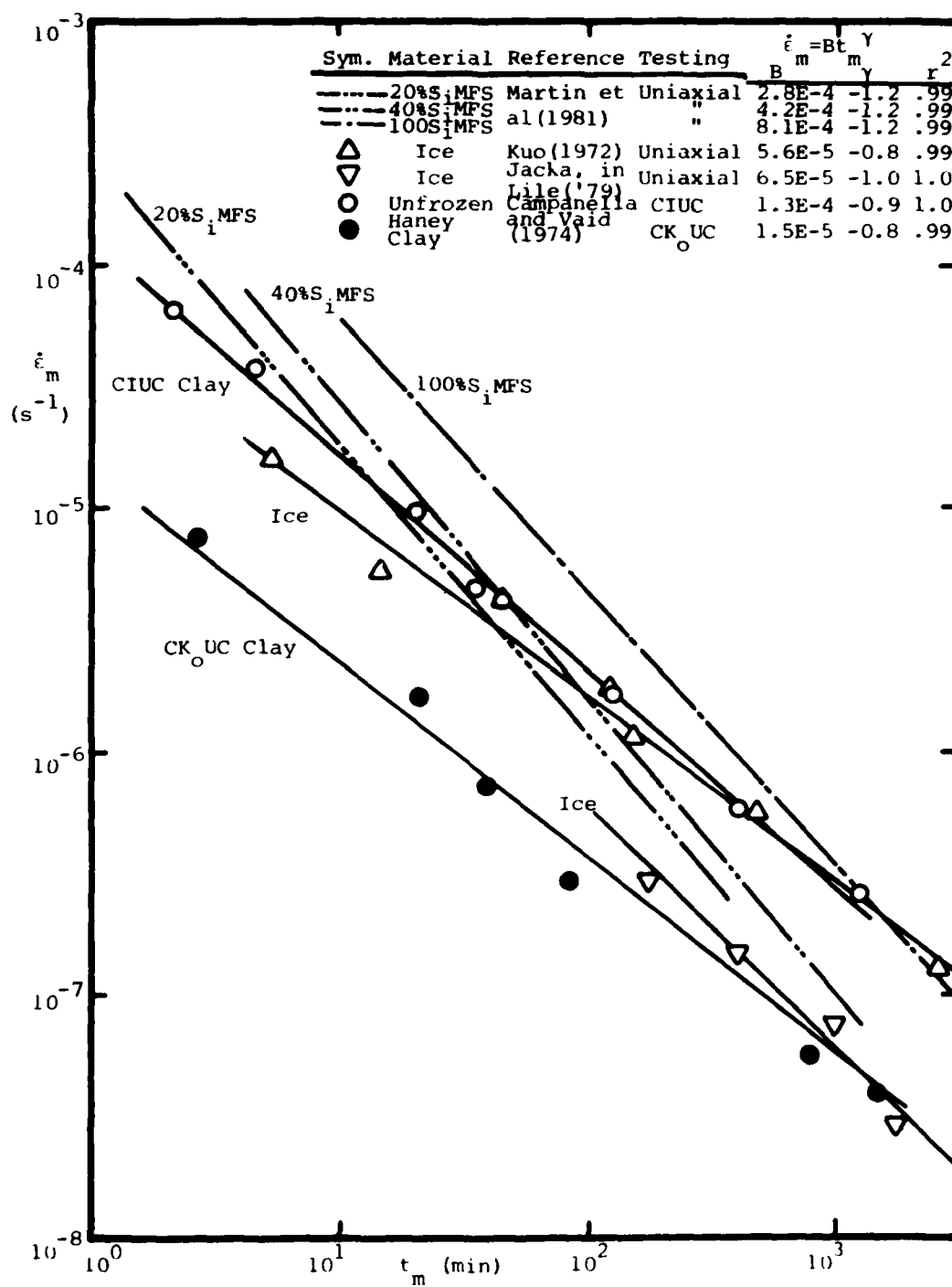


FIGURE 5.1 Summary of $\dot{\epsilon}_m$ - t_m correlations for various materials

this apparent linearity, in the hope that such an understanding will lead to better qualitative and quantitative models for creep. Details of the analyses for this Section are found in Appendix B.1.

Simple creep models, such as the secondary creep model proposed by Ladanyi (1972) or the Singh-Mitchell (1968) "primary" creep model yield simple expressions for the strain as a function of time. When the contours of constant strain are plotted on a $\log \dot{\epsilon} - \log t$ plot, the slope of the contours is -1 for the secondary creep model and approaches -1 at large times for the Singh-Mitchell model, as plotted in Figures 5.2 and 5.3, respectively. Note that the separation between these contours decreases at large strains.

Since the actual data for the materials in Figure 5.1 exhibit a slope between -0.8 and -1.2, this suggests that the strain ϵ_m at the minimum strain rate is approximately a constant for each material. However, the slope is not exactly -1, nor is the strain at $\dot{\epsilon}_m$ absolutely constant. Instead, for frozen MFS, the slope is between -1.1 and -1.2, and the strain at $\dot{\epsilon}_m$ typically decreases with decreasing minimum strain rate. For unfrozen Haney clay, with a slope greater than -1 (ie. a flatter slope), the strain at the minimum strain rate increases slightly with decreasing minimum strain rate. Both of these trends are consistent with the results from the secondary creep and Singh-Mitchell creep models plotted in Figures 5.2 and 5.3.

When actual ϵ_m data are plotted in Figure 5.2, the results

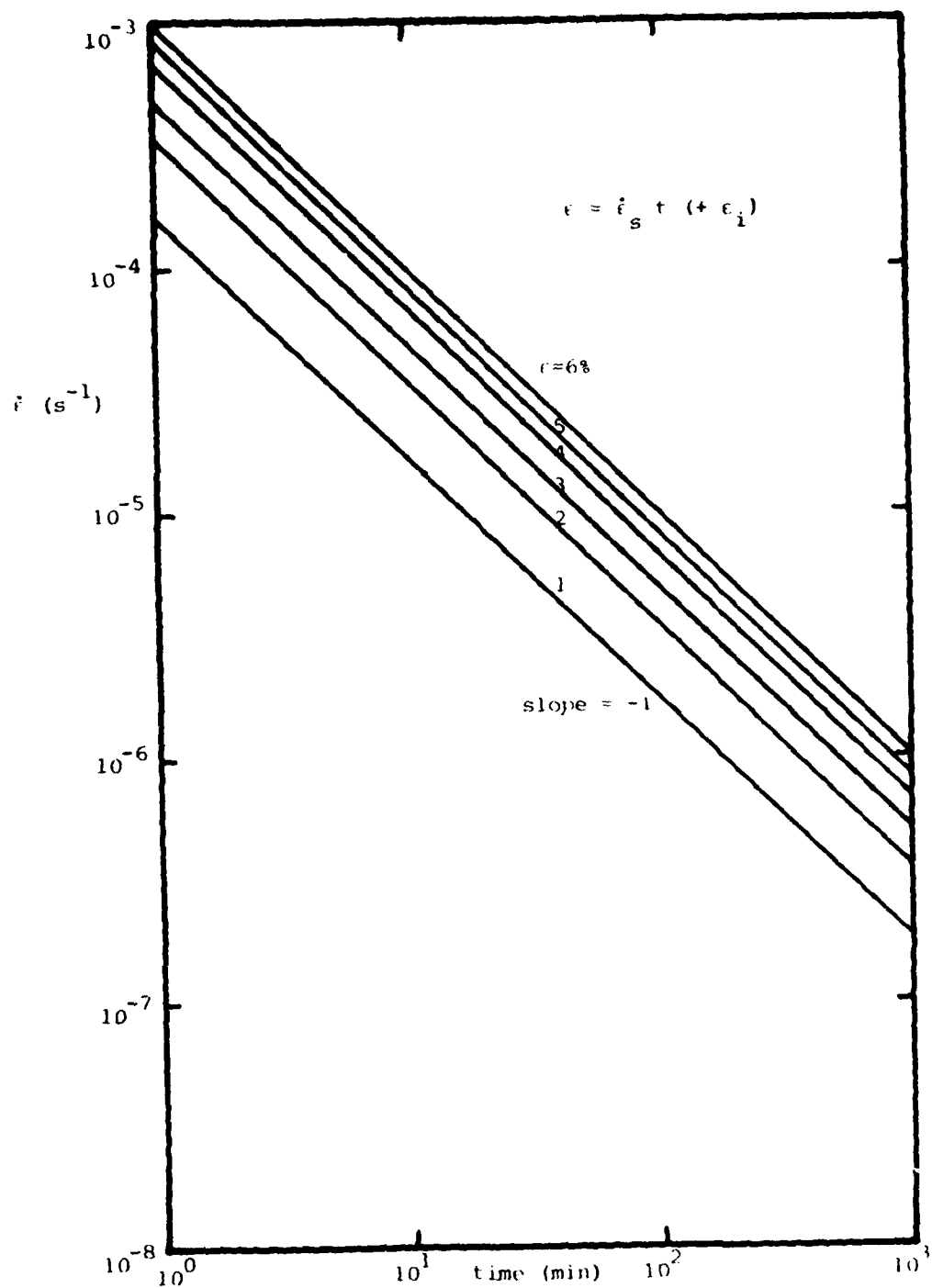


FIGURE 5.2 Lines of constant strain based on secondary creep model

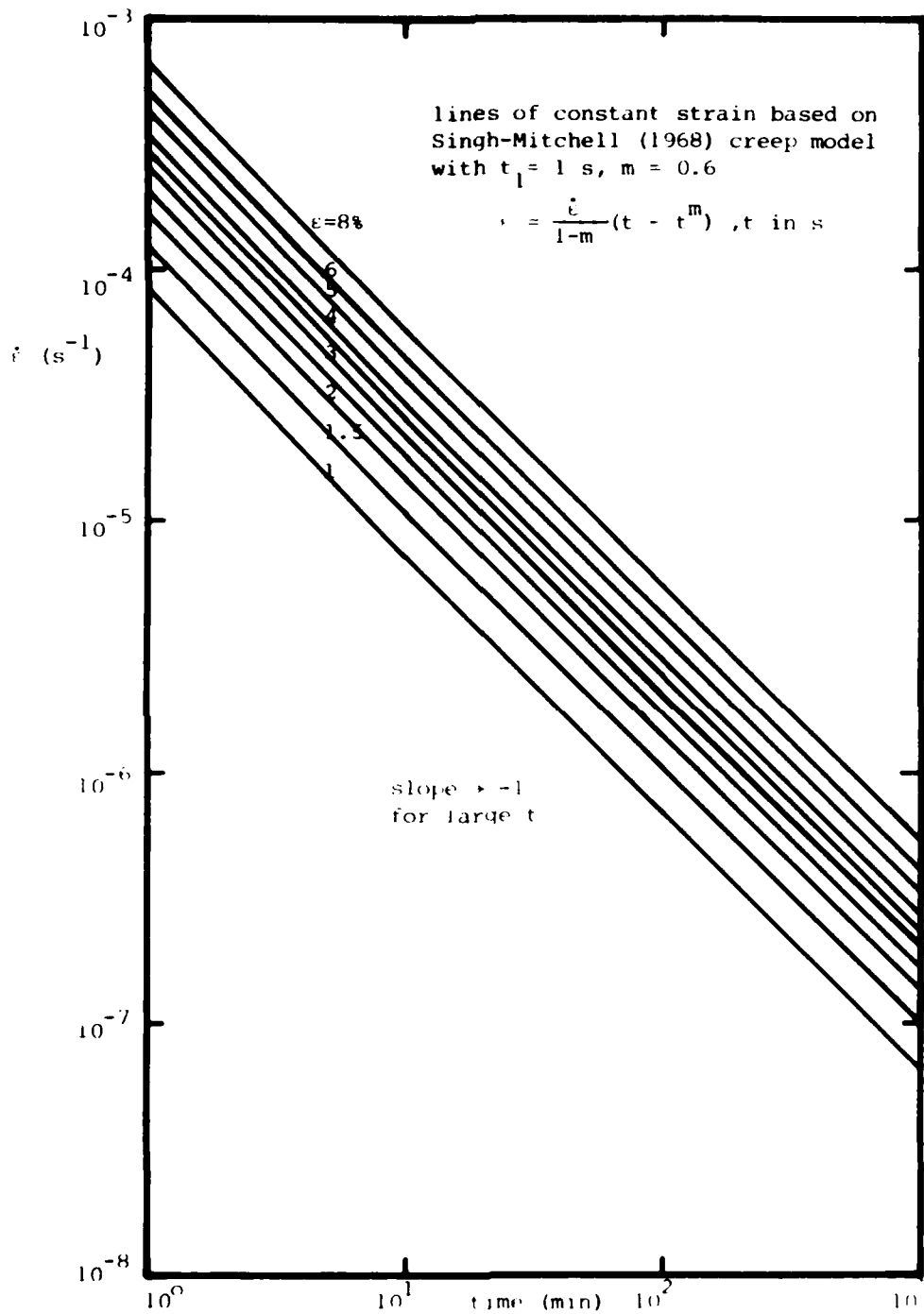
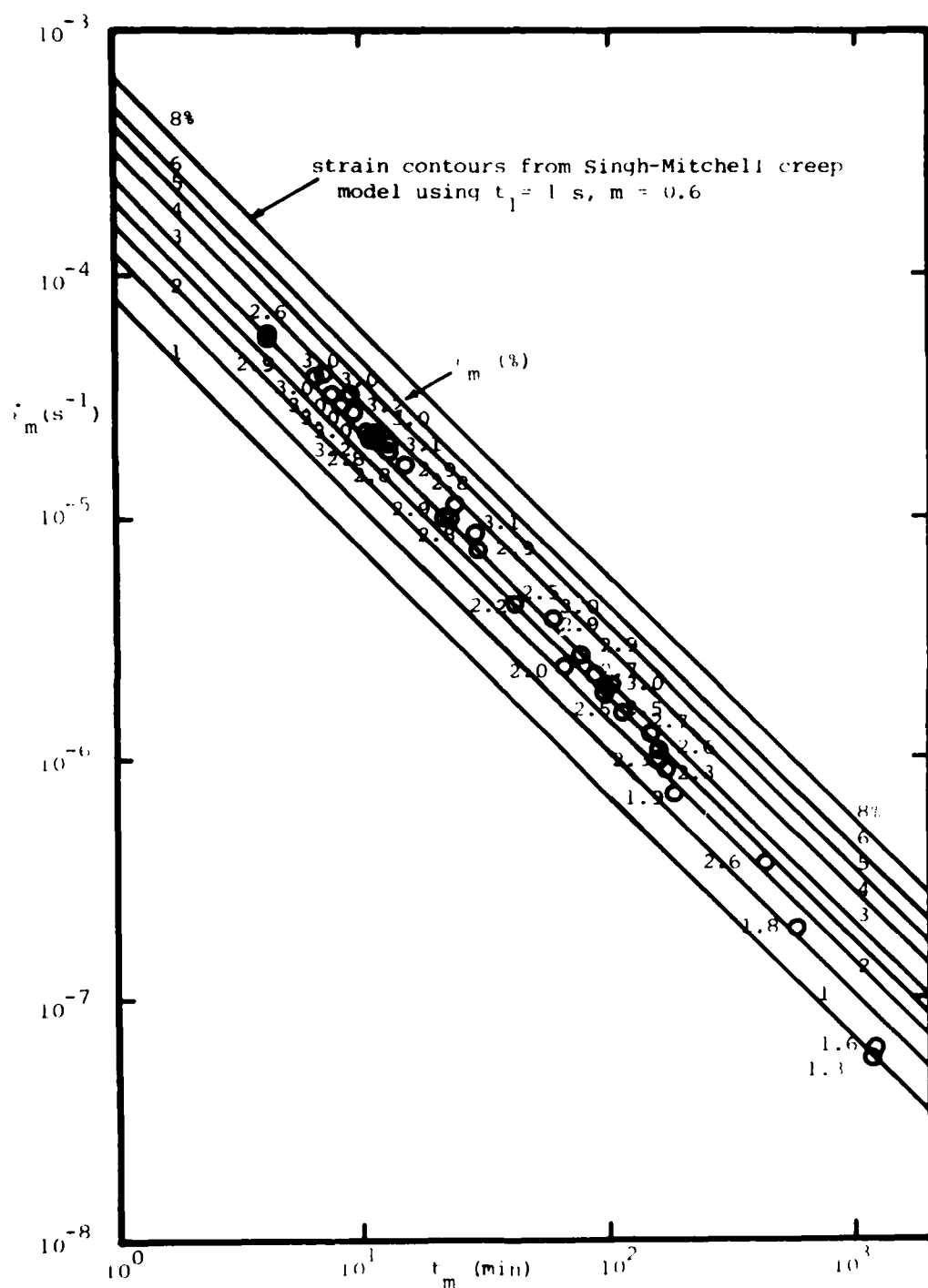


FIGURE 5.3 Lines of constant strain based on Singh-Mitchell (1968) creep model

do not fit well within the strain contours predicted by the secondary creep model since the actual shape of the $\dot{\epsilon} - t$ creep curve is poorly represented by the secondary creep model. However, when actual data for MFS are compared with the contours from the Singh-Mitchell model for an average m , most of the data fall within the predicted contours, as shown in Figure 5.4. While a fairly good fit exists at the lower strain rates, a slight overestimation of ϵ_m occurs for $\dot{\epsilon}_m$ greater than 10^{-5} /s. Two factors probably cause this: firstly, the actual $\log \dot{\epsilon}_m - \log t_m$ data are not truly linear for the higher strain rates, but exhibit some downward concavity. Since the actual data fall below the best linear least squares fit in this strain rate range, use of the fitted relation results in a higher predicted ϵ_m . The second reason is related to a change in the value of m with varying $\dot{\epsilon}_m$. Since the Singh-Mitchell model only approximates the actual creep curves, an average slope m is used for the entire family of curves. However, at the higher strain rates, the value of m decreases. The predicted ϵ_m could be improved in this range by using a reduced m consistent with the actual data, rather than an average m .

From this discussion, it can be seen that the linear $\log \dot{\epsilon}_m - \log t_m$ correlation for the creep of various materials is due to the existence of an approximately constant strain at the minimum strain rate, and the relative insensitivity of the $\log \dot{\epsilon}_m - \log t_m$ correlation to small deviations from constant ϵ_m , especially for materials having a relatively large ϵ_m .



Deviations from linearity at the higher strain rates and trends in the strain with varying strain rate can be explained by using simple creep models such as the secondary and Singh-Mitchell creep models.

5.2 Mechanisms of Strength and Deformation

5.2.1 Proposed mechanisms

In order to better understand the mechanical behavior of frozen soils, a comprehensive qualitative model needs to be formulated. Some of the explanations for frozen soils as presented in the literature were summarized in Section 4.2.3. However, it is necessary to understand all of the possible mechanisms controlling strength and deformation behavior in frozen soils. Based on an evaluation of the physical nature of the frozen soil system and the various factors that affect its behavior, the author developed the following list of physical mechanisms that collectively might provide a qualitative explanation of the strength of frozen soils.

(1) ICE STRENGTH. Section 2.2.2 described the factors affecting the strength of ice, which is very strong at high strain rates. It is also a function of temperature, applied confining stress and stress state, grain size, shape and orientation and deformational mechanism (i.e. cracking, easy glide or hard glide). For longterm load application, ice creeps continuously even at relatively low stresses. Since it is currently not possible to reliably predict whether a sample will creep rupture at a given stress and temperature, it is not easy to define a limiting longterm strength for ice.

(2) SOIL STRENGTH. For cohesionless sands, Rowe (1962) postulated that strength results from a frictional component (sliding between grains), dilatancy effects (volume increase against

a confining stress) and particle interference effects. The latter two components are functions of the soil relative density and the effective confining stress level. For cohesive soils, true particle cementation may also exist, but is usually small in comparison with the frictional and interference components of strength. A difficulty in assessing the amount of strength of frozen soil that can be attributed to the soil phase is the current inability to measure the effective (intergranular) stresses in frozen materials.

(3) INTERACTION BETWEEN ICE AND SOIL

(a) - Effective Increase in Ice Strength. This could be due to a variety of mechanisms: (i) the ice in the frozen soil may possess a higher strength than normally tested ice because of an altered ice structure; (ii) stress states acting on ice in the pores differ from the uniaxial or triaxial states commonly used in ice testing; (iii) deformational and volume constraints imposed in each pore may induce different deformational mechanisms, such as cracking and hard glide, in the ice in frozen soil; (iv) the strain rate applied to the ice matrix is possibly greater than the average applied strain rate in the entire sample, and may result in a higher component of ice strength. While each of the above four mechanisms may yield an increased ice strength, the last mechanism should only be prominent when the solid particles are in sufficiently low concentration such that a continuous soil skeleton does not exist.

(b) - Effective Increase in Soil Strength due to an Increase

in Effective Confining Stress: Dilatancy Effects.

For dense sands and heavily overconsolidated clays, the dilatational behavior of the soil skeleton during undrained shearing should create a tension in the ice in the pores. Assuming sufficient tensile adhesional strength between the ice and soil phases, the ice reacts against the tension with an effect analogous to that for unfrozen soils. A decreased or even a negative "pore pressure" results, which translates into a positive increment of effective confining stress. This would cause a strength increase similar to that observed during the shearing of heavily overconsolidated unfrozen saturated clays and dense sands.

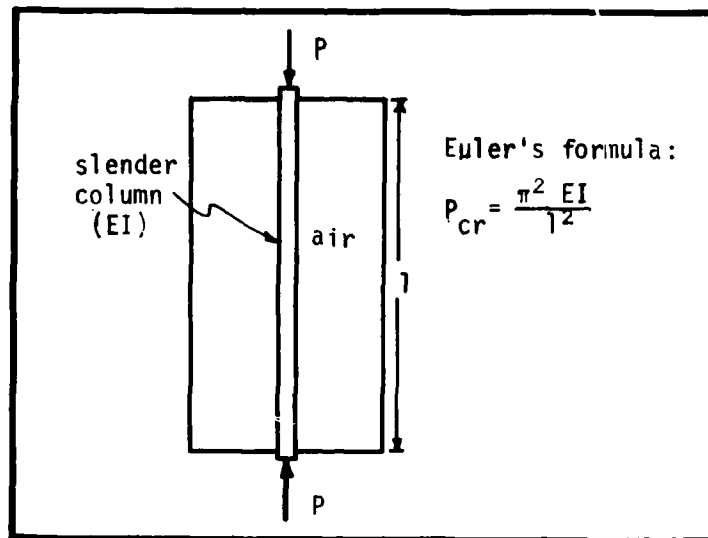
(c) Effective Increase in Soil Strength due to the Creation of a Negative Pressure in the Pores by other than Mechanical Means.

It is possible that a tension exists in the pores due to the nature of the interaction between the ice, the unfrozen water associated with the soil grains and soil. While the extensive literature in the fields of ice nucleation and frost heaving indicate that a substantial suction force can be generated in the adsorbed water film of a silicate particle during the freezing process under certain conditions, no data exist to substantiate its existence after the sample has equilibrated to the ambient temperature and applied stress. If this tension existed, a negative pressure would be exerted on the ice and the soil particle, resulting in an increased effective

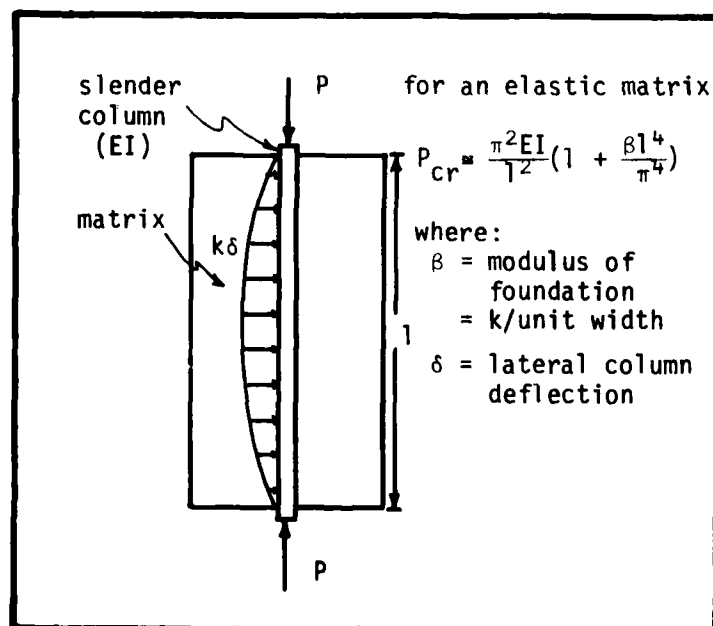
(intergranular) stress, with an associated increased shear strength. However, the existence of a tension in the film is totally hypothetical at this point in time.

(d) Effective Increase in Soil Strength due to a Structural Interaction between Ice and Soil.

The structural hindrance between the ice and soil may result in a strong mechanical interaction producing a composite far stronger than the sum of the individual component strengths, ie. a synergistic interaction. As a load is applied to a frozen soil, both the soil skeleton and ice matrix carry a portion of total load and attempt to deform accordingly. The load is transferred between particles in the soil skeleton at the contacts. Resistance to movement of the particles is provided by interparticle friction at the contacts, particle interference and structural impedance by the ice matrix. The structural impedance of the ice may greatly increase the shear resistance of the soil skeleton. A mechanical analogy to the proposed scheme is that of an axially loaded slender column embedded in a matrix with a finite shear resistance. As seen in Figure 5.5, a small resistance in the matrix greatly stabilizes the column. Similarly, it is proposed that a relatively small resistance (compared to the average applied stress) is required in the ice to stabilize the soil skeleton from "collapse". Such a synergistic mechanical interaction would make the frozen soil to be stronger than the sum of its major structural components, ice and soil.



(a) column in air



(b) column in an elastic matrix

FIGURE 5.5 Buckling of a slender column in air and with an elastic foundation (after Timoshenko and Gere 1961)

5.2.2 Discussion of the mechanisms of strength and deformation

The foregoing mechanisms of strength have been arbitrarily separated into three broad categories for convenience only, and should not imply that they are mutually exclusive. Some are well known and documented, while others are purely hypothetical and require experimental verification. However, each is considered to be a viable mechanism at this point in the discussion. By carefully examining the prerequisite requirements and experimental consequences of each mechanism, the relative importance and probable existence of each may be estimated.

Mechanisms 1 and 3(a) - Ice Strength and Ice Strengthening

The strength of the ice in frozen soil is no doubt quite substantial. Test results on ice indicate that it is affected by varying grain size, confining stress level, stress state, strain rate, etc. However, it is difficult to analytically assess the magnitude of these effects for ice in frozen soil. The loading conditions in each pore are difficult to evaluate; efforts to integrate the effect in each pore into an overall sample behavior would probably prove intractable. Consequently, any attempted analysis using the results from testing ice of varying grain size, structure, stress state, confining stress level and strain rate would probably be futile.

However, the tests by Goughnour and Andersland (1968) and Hooke, Dahlin and Kauper (1972) on sand-ice systems at low sand

concentrations provide reasonable estimates of the effect of ice strengthening mechanisms. These results are found in Figures 2.8 and 2.11, respectively. Strength data by Goughnour and Andersland indicate that at 42% sand concentration by volume and at -7.6°C , the strength of the saturated sand-ice systems is increased by only 26 % over that for pure ice. A 42% sand concentration corresponds to less than zero relative density for the sand, and is indicative of an extremely loose soil where the particles are barely in contact. Creep data by Hooke et al. at -9.6°C indicate that the minimum creep rate reduced by about 20 times for 35 % sand concentration compared with pure ice. These two sets of data provide a reasonable quantification of the ice strengthening due to the presence of the sand particles.

The altered ice structure, altered stress state, altered strain rate and deformational constraints present in frozen soil should be closely modelled in the 42 % sand-ice system. If one assumes that the strengthening effect in the ice continues linearly with sand concentration, this implies that the increase in strength due to ice strengthening in a 60% sand concentration system is approximately 37% over pure ice. By comparison, the actual strength increase for the 60% system, corresponding to a very dense sand of relative density near 100% is about 175 % over pure ice (see Figure 2.8). Consequently, the effect of ice strengthening should be significant for frozen soils, but still relatively small in comparison to the net effect

of the other mechanisms at high relative densities. Note, however, that while the relative effect on creep may also be small, the absolute magnitude of the effect of ice strengthening on creep rates is quite substantial.

Data by Sayles (1974) indicate that the ice matrix dominates the behavior of frozen soils at low strains and confining stresses. Strain-rate controlled triaxial compression tests on 20-30 Ottawa Sand possess twin stress peaks, one at less than 1 % strain, and the other at greater than 8 % strain. Since ice typically exhibits peak strengths at less than 1% strain, while soils usually require larger strains to mobilize its strength, Sayles proposes that the two peaks observed correspond to ice matrix strength and overall soil strength, respectively.

The above hypotheses regarding the relative importance of the ice matrix and soil strength components is supported by the creep behavior observed for the testing program on Manchester Fine Sand reported in Appendix A.5. For medium-dense saturated MFS, a change in slope of the $\log \dot{\epsilon} - \log t$ curves typically occurs at about 1.2 % strain, which coincides approximately with the strain at the minimum strain rate and the strain at peak stress for fairly low strain rate controlled strength testing for ice alone (see Figures A.5.4 and A.5.5 in Appendix A.5). For times prior to the change, the slope m of the $\log \dot{\epsilon} - \log t$ curve is similar to that for ice alone, while the slope after the change is similar to that for par-

tially saturated MFS. The data imply that the ice matrix dominates at the low strains for unconfined compression, while the behavior at the larger strains is dominated by the effect of soil friction and interaction effects.

Since the strength of frozen soils decreases with time at low confining stresses, reportedly approaching the drained unfrozen soil strength, Sayles proposes that the ice matrix dominates behavior at low confining stress levels, and is responsible for the "cohesional" component of strength. However, although it is clear that the "cohesion" certainly would not exist without the ice, it is equally clear that the magnitude of the "cohesion" would not be so great without the soil. Hence it may be overly simplistic (although possibly useful from an empirical point of view) to attribute the "cohesion" component of strength entirely to ice and the "friction" component entirely to the soil.

Mechanism 2 - Soil Strength

The contribution of sand strength is difficult to assess without the benefit of effective stress determinations and drainage condition assessments. At the high confining stress levels, it can be seen from Figure 5.6 that the strength of the "frozen" sand system plotted using total stresses is much less than the drained strength of the unfrozen soil system plotted using effective stresses. At the high confining stress levels where global pressure melting prevails, the "frozen" soil

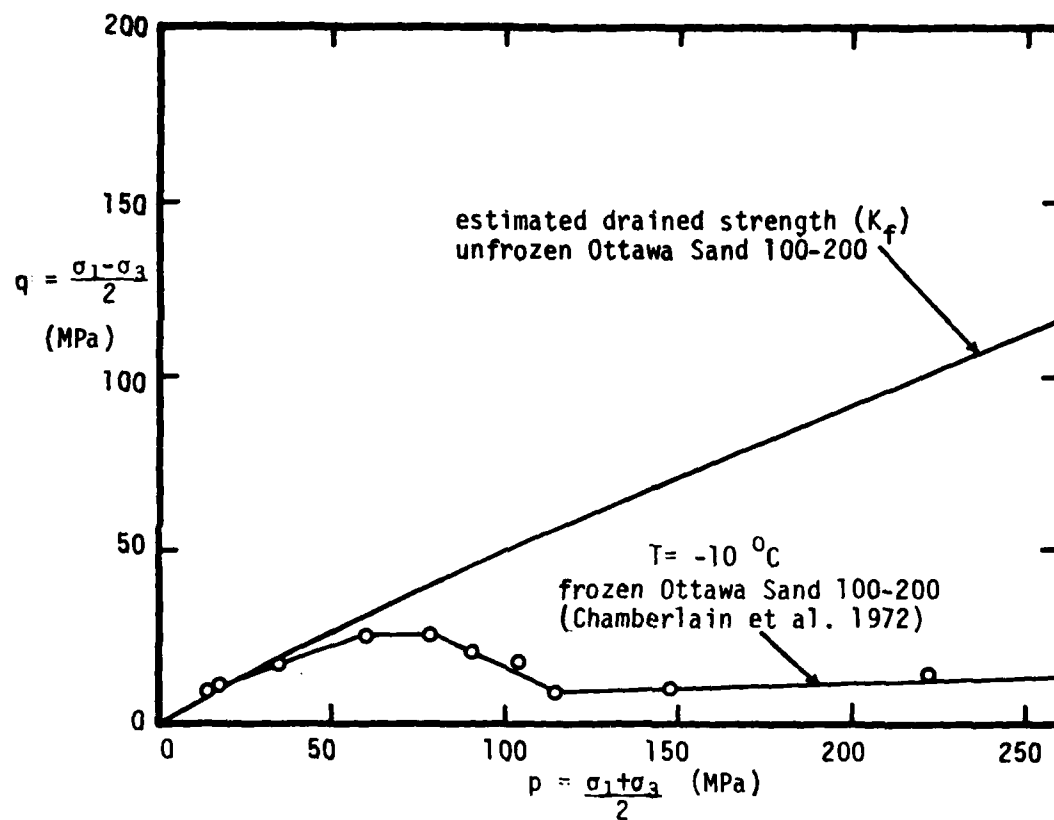


FIGURE 5.6 Comparison of frozen and unfrozen soil strength for Ottawa Sand 100-200 (data from Chamberlain et al. 1972)

can be analyzed as an unfrozen soil. The measured strength in this stress region is a reflection of the undrained shearing of an essentially unfrozen soil consolidated to some finite effective confining stress.

The low stress region is of primary engineering interest. In this region, the increase in measured strength with increasing confining stress is similar to that for the unfrozen soil, as shown in Figure 4.3. However, it is difficult to assess whether this similarity in "friction angle" (slope of the total stress envelope) is due to the same reasons as in unfrozen soil (i.e. interparticle friction, interference, dilatancy effects), whether it is due to interactions peculiar to frozen soil or whether it is merely coincidence.

Although the longterm strength of frozen soils at a given confining stress level reportedly approaches the drained unfrozen soil strength at the corresponding effective confining stress, the existing measured longterm strengths are still significantly greater than the drained unfrozen soil strengths for low confining stress levels.

As already mentioned, it is difficult to divorce the soil strength from the other mechanisms of strength, since the soil is such an integral part of the entire composite, and since the behavior of the system is necessarily greatly affected by the mechanical interaction between the individual phases. In this presentation, this separation has been attempted for the purposes of convenience only.

**Mechanism 3(c) - Effective Increase in Soil Strength Due to the
the Creation of a Negative Pressure in the Pores by Other
than Mechanical Means**

If a tension exists at the soil/water/ice interface due to some physico-chemical interaction, this would lead to a strengthening of the system due to the positive effective confining stress, and hence produce an apparent cohesion for shear in unconfined compression. As the ambient temperature of a frozen soil sample is reduced, the thickness of the unfrozen water layer also decreases. It is reasonable to assume that as the film thickness decreases, the tension in the layer increases, and hence the strength of the sample would increase. This is consistent with observed frozen soil behavior. Accepting the original hypothesis of tension in the film, this suggests that the strength of frozen soil is a function of the equilibrium temperature, not the temperature of freezing, although the freezing conditions could certainly affect the structure of the frozen soil system.

One would expect the thickness of the unfrozen water film to be a function of the mineralogy of the soil particles and the equilibrium temperature. Assuming sufficient water, the thickness of the film in a partially saturated frozen soil should be the same as for a saturated frozen system. This would imply that partially saturated and saturated frozen samples of the same soil and structure at the same equilibrium

temperature should behave similarly under unconfined loading conditions and have the same apparent "cohesion" intercept. However, this is clearly not the case, as indicated in the strength testing by Alkire and Andersland (1973) (Figure 4.3) and creep testing by Martin et al.(1981) (Figure 4.11). This indicates that if a tension does exist in the unfrozen water film due to some physico-chemical interaction, it is probably does not contribute significantly to the overall behavior of the frozen soil (except perhaps at stresses approaching the LLTS).

Mechanism 3(b) - Effective Soil Strengthening due to an Increase in Effective Confining Stress: Dilatancy Effects

Since the soil component of the frozen soil system carries a portion of the applied load, an increased sand relative density increases the number of interparticle contacts, probably decreases the resulting load on the ice, and hence results in a stronger, less creep susceptible system. At the higher relative densities corresponding to dilatant behavior, tensions are imposed on the ice by the soil skeleton during shear. Assuming that the tensile adhesional strength between the ice and soil exceeds the interfacial stress (ie. cleavage does not occur between the ice and soil), the tension in the pores creates an effect analogous to that in dense unfrozen sands and heavily overconsolidated clays, where a negative pore pressure is created during dilation which in turn results in a further increase in strength.

Based on this mechanism, one would expect the strength of frozen sand to increase greatly with increasing relative density from the very loose up to the medium density condition. For dilatant behavior in the medium to dense range, an even more rapid increase in strength should occur. The data by Goughnour and Andersland (1968) confirm the general trend of rapid strength increase with increasing relative density, but are not of sufficient detail to confirm or reject the latter hypothesis concerning the effect of dilatancy.

Similarly, one should see a reduced creep behavior with

increasing relative density in the nondilatant range, and a greater decrease in creep behavior in the dilatant range. Creep data by Martin et al.(1981) on saturated Manchester Fine Sand at varying relative density appear to exhibit such behavior, but are not sufficiently detailed to absolutely confirm this hypothesis. As seen in Figure 4.18, the rate of decrease in the minimum strain rate increases above a relative density of 60% for the saturated frozen sand system, as would be expected according to this hypothesis.

Mechanism 3(d) - Effective Soil Strengthening due to Structural Interaction

Mechanical interaction must exist between the ice and soil phases. What need to be determined are the nature of this interaction and the magnitude of its effects on the overall mechanical behavior of the frozen soil system. In particular, does a synergistic interaction occur?

As the degree of ice saturation increases, the ice matrix is strengthened due to an increased ice volume. Consequently, it can supply a greater structural hindrance to the deformations of the soil skeleton. This is confirmed by the strength data by Alkire and Andersland (1972) and the creep data by Martin et al.(1981). As the temperature is decreased, a stronger system is expected, due to the strengthening of the ice matrix. Increasing the applied strain rate reduces load transfer from the ice to the soil, and induces deformational mechanisms such

as hard glide and cracking, rather than easy glide mechanisms which are easier to induce but require more time. Each of these changes in test conditions should result in a stronger, less creep susceptible system, within the framework of the mechanisms discussed. Experimental data confirm this "predicted" behavior.

Increasing the confining stress results in increased load in both the soil and ice components. Strengthening in the ice occurs due to crack inhibition and closure while an increased magnitude in non-isotropic stresses in the pores causes a weakening. At higher confining stresses where local pressure melting occurs resistance to soil deformation by the ice is obviously reduced. Also, mobility of the ice is increased, as melted ice in the highly stressed regions may flow to areas of lesser stress. Since the load is shared by the ice and soil at all levels of confining stress, a portion of the applied confining stress results in an effective (intergranular) stress in the soil. This possibility is discussed further later in this Section.

One of the key questions regarding the structural hindrance mechanism is: can it explain the large apparent cohesion of frozen soil (ie. the large uniaxial compressive strength)? The behavior described in the previous two paragraphs may be explained by mechanical interaction, ie. structural hindrance in combination with dilatancy effects for dense sands, regardless of whether a "synergistic" mechanical interaction exists. However, if the synergistic interaction does exist such as in a form analogous to the buckling column, then very little resis-

tance is needed in the ice to stabilize the soil skeleton. Hence, this mechanism could account for the high observed unconfined strengths in frozen soil and hence the large cohesion intercept.

If such a synergistic interaction occurs, then it is possible that a true limiting long term strength exists for low confining stresses which exceeds the drained strength of the unfrozen soil (at a corresponding effective confining stress level). This is difficult to ascertain due to the previously mentioned problems with extreme longterm testing of frozen soils. Data by Rein et al. (1975) and Martin et al. (1981) indicate that a practical, and perhaps actual, longterm uniaxial compressive strength does exist. Although Sayles (1974) reports that the longterm triaxial strength approaches the drained strength of the unfrozen soil, his data indicate longterm frozen soil strengths significantly higher than the drained unfrozen soil strengths.

When an increment of isotropic confining stress is applied undrained to a saturated unfrozen soil at a given initial effective stress, the soil skeleton deforms very slightly, until the change in pressure in the incompressible water equals the increment of applied confining stress. This reflects a Skempton (1954) "B" parameter, defined as $\Delta u / \Delta \sigma_c$, equal to unity. No overall shear stress or shear deformation is induced, and no increase in effective (intergranular) stress occurs during undrained

application of an isotropic stress when $B \approx 1$. Upon undrained application of a deviatoric load or deformation, slippage occurs at the particle contacts. For medium to dense sands under moderate confining stresses, the pore volume initially compresses, and then dilates. As a result, positive pore pressures are initially generated, then become negative during dilation. These pore pressure changes translate into changes in the effective stress and hence affect the strength and deformation behavior of the unfrozen soil. No volume change occurs, however, as long as B remains equal to unity.

The behavior of an ice-saturated frozen soil during application of isotropic stresses should be identical to that of an unfrozen saturated soil since the compressibility of ice is of the same order of magnitude as water. Such should be the case until the magnitude of σ_c is sufficient to cause pressure melting in the ice, resulting in a substantial pore volume decrease (ie. greatly increasing the effective "compressibility").

During shortterm deviatoric loading of the frozen sample, part of the load is carried by the soil and part by the ice matrix. The contribution of the soil skeleton depends partly upon the level of initial intergranular stresses. However, the bulk of the strength generated by the soil skeleton is hypothesized as due to the resistance of the pore ice to soil particles deformations; ie. structural hindrance. With slower loading, or during long term creep testing, the ice deforms both both from the applied external load and the load due to defor-

mations of the sand skeleton such that more of the load is carried by the soil skeleton. Under these conditions, an increased portion of the total resistance of the system is controlled by the soil components of strength (ie. mechanisms 2, 3(b) and 3(d)).

At the higher confining stresses (Region II in Figure 4.2), where local pressure melting occurs, a decreased effective ice resistance to soil particle motion exists, resulting in a decreased overall frozen soil resistance for both the sand and silt. Note that this decrease in overall strength closely approximates the decrease in shear resistance for ice above about 40 MPa as seen in Figure 2.9.

For the very large confining stresses (Region III in Figure 4.2), a slight increase in "frozen" soil strength is observed with increasing confinement. Since a solid to liquid phase change is expected for ice Ih at about $\sigma_{oct} = 110$ MPa, the soils in Region III are probably better characterized as unfrozen soils. If Chamberlain et al.'s tests were indeed undrained, then the measured quantities were essentially undrained unfrozen soil strengths. Since the sand possesses no cohesion, the measured strength is entirely due to the existence of a positive effective confining stress. Although some effective stress may have existed due to sample preparation, it probably resulted primarily from the volume decrease of the sample during the phase change of the pore ice.

By backcalculating the effective confining stress neces-

AD-A097 668

MASSACHUSETTS INST OF TECH CAMBRIDGE DEPT OF CIVIL E--ETC F/G 8/13
THE CREEP OF FROZEN SANDS: QUALITATIVE AND QUANTITATIVE MODELS.(U)
MAR 81 J M TING

DAAG29-77-C-0016

UNCLASSIFIED

R81-5

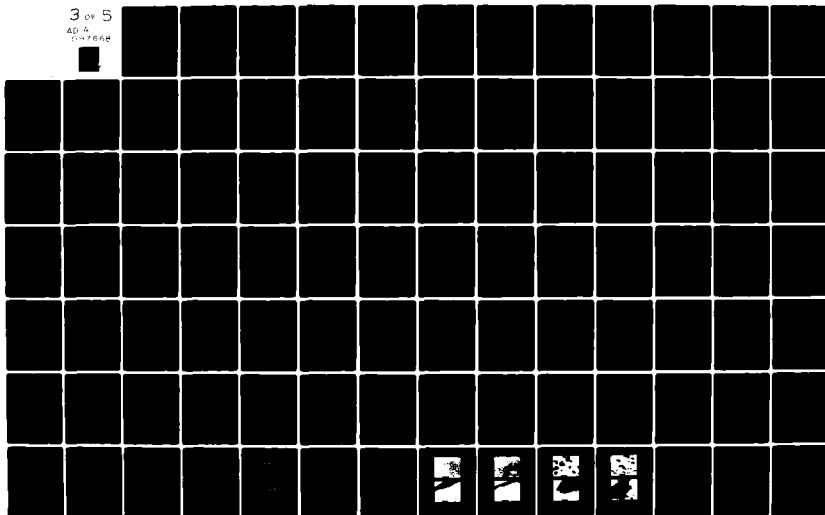
ARO-14725.2-GS

NL

3 OF 5

AD-A

COVER



sary to yield the measured strength of the sand ($\sigma'_c > 15$ MPa) and observing that substantial particle crushing occurred in Region III, the effective confining stress must be quite substantial. In this effective stress range, the compressibility of the soil skeleton is no longer orders of magnitude greater than for water, and hence B becomes less than unity. Consequently, an increase in the total confining stress also causes a slight increase in effective confining stress. This results in the observed slight increase in strength with increasing confinement.

The mechanisms of structural hindrance and tension in the pores due to dilational effects (3(d) and (b)) should be greatly affected by the amount of tensile adhesional strength at the soil/ice interface. Although it is known that an unfrozen water layer exists between ice and soil, Jellinek showed that substantial tensile adhesion can develop between ice and silicate surfaces. However, whether this adhesional strength is significant in comparison with the strength of the pore ice in frozen soil remains unknown. If the adhesion is low, then synergistic interaction probably cannot exist. If the tensile adhesion is less than the strength of the pore ice, failure will probably occur by cleavage between the ice and soil. If the adhesion is higher than the strength of the pore ice, then failure will probably occur by deformation within the entire soil skeleton-ice matrix system. Consequently, the nature of the ice/soil interface should be studied to develop a better understanding of the

behavior of frozen soils.

From this discussion, the following points may be made:

(1) the contribution to frozen soil strength due to the strength of the ice in the pores is significant; the portion due to the strengthening of the ice over and above conventionally tested ice is difficult to quantify analytically; however, data by Goughnour and Andersland suggest that the effect of ice strengthening is relatively small (say less than 15%) in comparison with the other mechanisms of strength;

(2) the existence of tension in the pore ice due to other than mechanical means is hypothetical and unsubstantiated from any experimental data; available indirect evidence suggests that the contribution to frozen soil strength from any such tension is negligible;

(3) the existence of tension in the pore ice due to dilation of the soil during shear is likely for dilatant soils such as dense sands and heavily overconsolidated clays, and should contribute to frozen soil strength; however, the amount of soil strengthening depends on the magnitude of the adhesional tensile strength between the pore ice and soil and the dilatational tendency of the soil skeleton;

(4) the structural hindrance component of mechanical interaction between the ice and soil serves to strengthen the system over and above that for the soil and ice alone; however, the amount and nature of the interaction depend on the soil system,

ice strength and the adhesional bonding between the ice and soil that exists in spite of the presence of the unfrozen water film between the ice and soil;

(5) for certain conditions, the mechanical interaction between the ice and soil may be synergistic; at low confining stresses, the strength of fairly dense frozen sands is far greater than for the unfrozen state (using total stress for the frozen soil and effective stress for the unfrozen soil) and up to two or three times the strength of ice at the same testing conditions. At very high confining stresses (say >40 MPa), the resistance supplied by the ice matrix is reduced due to local pressure melting, and the overall strength of the system eventually becomes smaller than the drained strength of the unfrozen soil.

5.2.3 Summary and implications of testing program

To help clarify the nature of the various possible mechanisms of strength and deformation in frozen soil, several test programs were conducted. Creep tests were carried out on Manchester Fine Sand (MFS) as part of the testing program reported by Martin et al. (1981) and are summarized in Appendix A.5. Of particular interest to this discussion are the tests on MFS samples at varying relative density and at different levels of ice saturation. Some of these results are plotted in Figures 4.17 and 4.18, and have already been incorporated into the previous discussions on these mechanisms. In particular, the large effect of ice saturation on mechanical behavior suggests that mechanism 3(b) involving tension in the pores due to physico-chemical interaction is not significant under normal testing conditions.

In order to gather insight into the nature of the ice-soil mechanical interaction and adhesional properties, several test sequences were carried out on nominally spherical glass beads with two gradations, MS-M (60-200 mesh) and MS-XPX (20-40 mesh). Each gradation was tested with a wetting and nonwetting (WP) surface treatment. It was hoped that by varying the surface properties, the thickness of the unfrozen water film and the adhesional properties between the ice and soil would be altered. Thus, the nature of the mechanical and physico-chemical interaction between the ice and soil would be clarified. Appendix A presents details and results from the entire test program on

the glass beads, Manchester Fine Sand and fine polycrystalline snow ice. The results of the creep tests on the four types of glass beads are summarized in Appendix A.3. Typical data for the MS-M size beads are plotted in Figures 5.7 and 5.8. As part of this creep test program, drained triaxial compression tests, grain size analyses and scanning electron microscopy were performed on the unfrozen glass beads. The results from these are found in Appendix A.1. Details on the sample preparation and testing procedures are found in Appendix A.2. Further insight into the nature of the unfrozen water film and the effectiveness of the nonwetting surface treatment was gained by unfrozen water content determinations by pulsed nuclear magnetic resonance (NMR) of MS-M size beads. Appendix A.4 summarizes these results. Some creep tests were conducted on fine polycrystalline snow ice at the same testing conditions as for the glass beads for comparison purposes (see Figure 5.9). These results, together with the data from tests carried out on ice as part of the testing program reported by Martin et al. (1981), are summarized in Appendix A.6.

Results and comparisons based on the testing program on the glass beads are summarized in Table 5.1. From these data, the following may be noted:

(1) the friction angle for the MS-M size beads, obtained from CIDC triaxial tests on unfrozen samples run both wet and dry, is 36.5° for the wetting beads and 34° for the non-wetting beads;

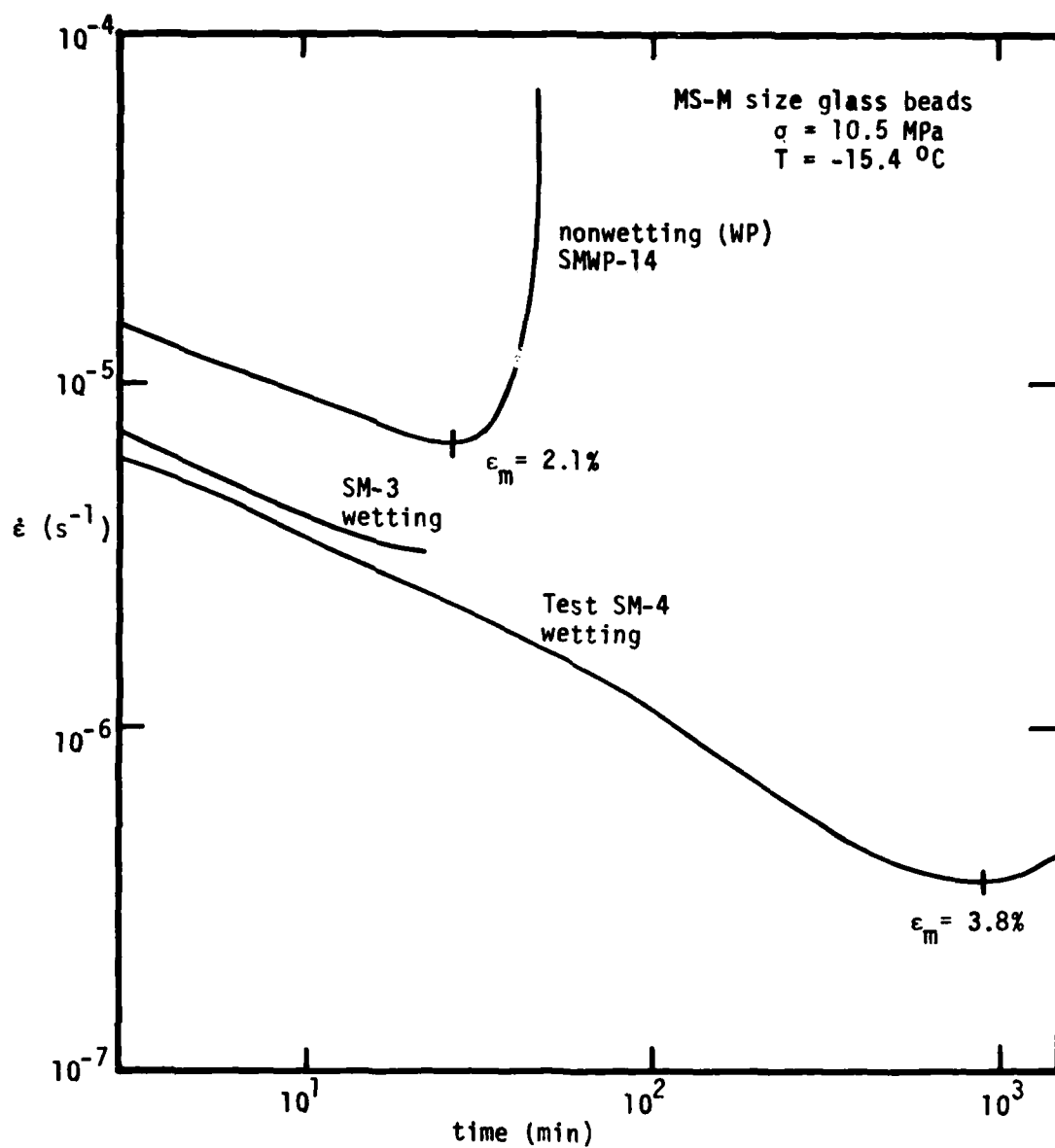


FIGURE 5.7 Effect of surface treatment on the creep behavior of MS-M size glass beads

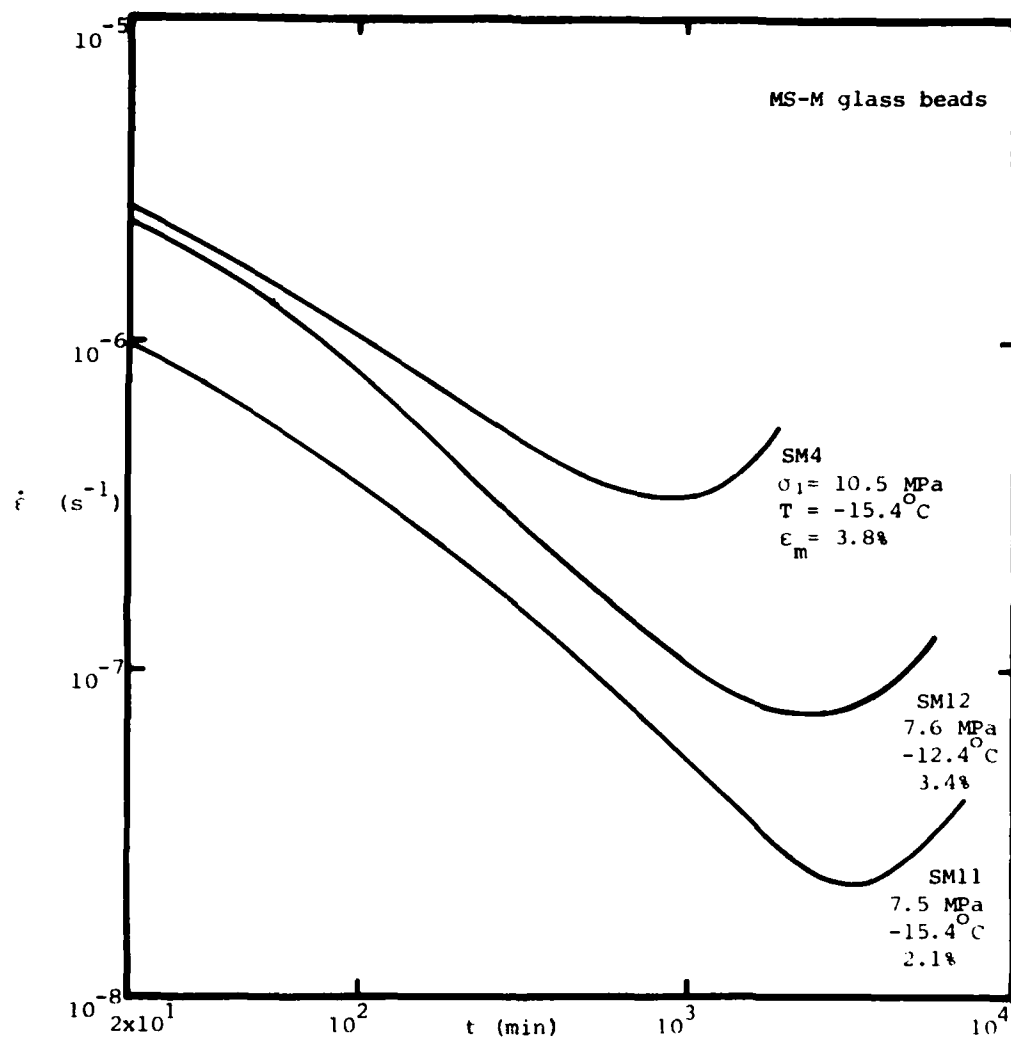


FIGURE 5.8 Results of creep testing on MS-M (wetting) glass beads

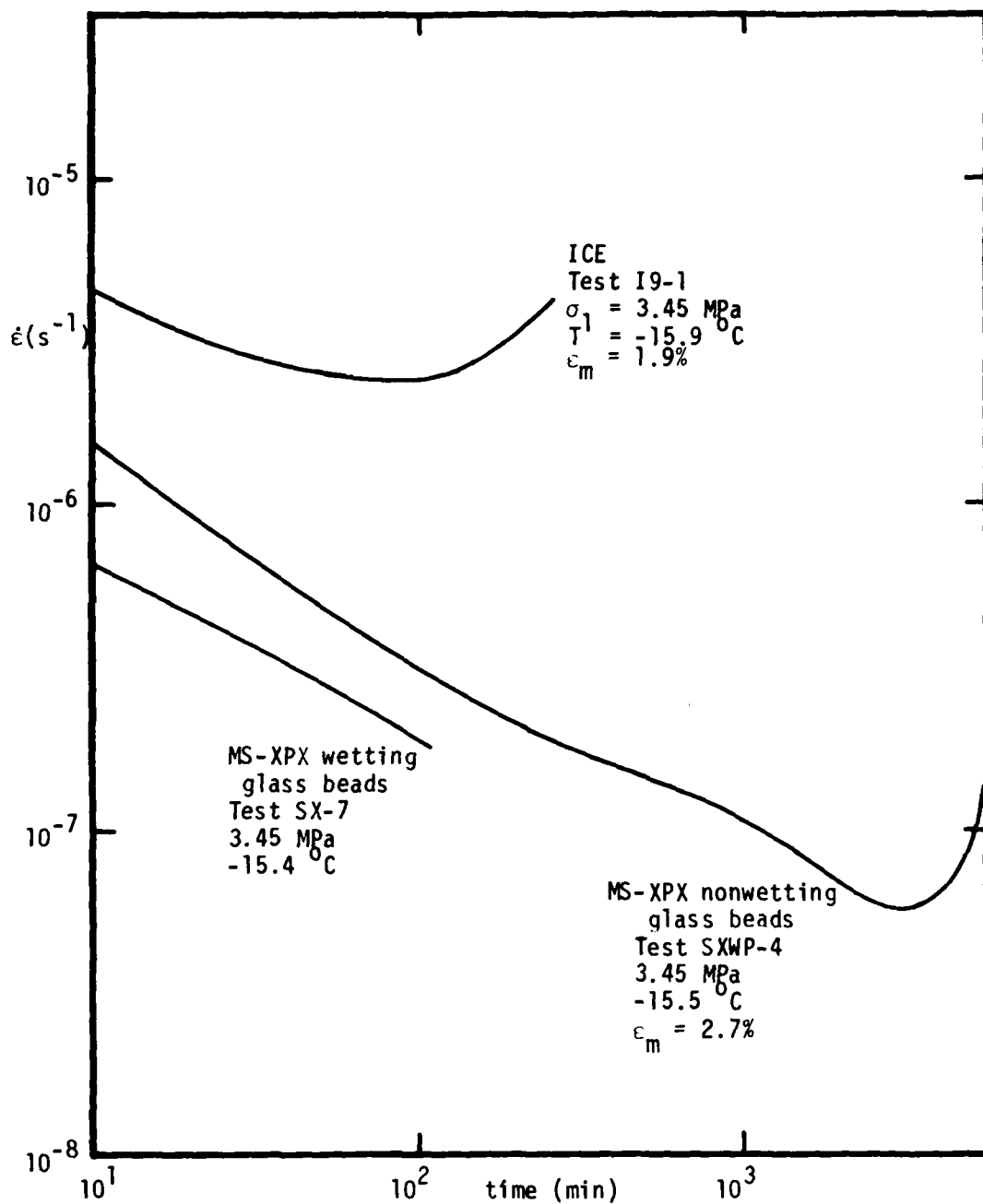


FIGURE 5.9 Comparison of creep behavior of frozen saturated MS-XPX size glass beads (wetting and nonwetting) and fine polycrystalline snow ice

Bead Type	MS-M	MS-MWP	MS-XPX	MS-XPXWP
sieve size	60-200	60-200	20-40	20-40
surface treatment	none	waterproofed	none	waterproofed
triaxial testing, unfrozen samples (σ'_3 between 0.2-0.6MPa):				
drained friction angle $\phi(^{\circ})$	36.6	33.9	-	-
ϵ at peak stress (%)	2.2	2.7		
avg D_r (%)	64	70	-	-
uniaxial creep testing, frozen saturated samples:				
avg ϵ_m (%)	3.1	1.6	1.9	1.6
avg D_r (%)	100	100	-	-
$\frac{\partial \ln \dot{\epsilon}_m}{\partial \sigma}$ (MPa $^{-1}$)	0.93	3.26	0.78	2.38
$E = \frac{-R \partial \ln(\frac{\dot{\epsilon}_m}{T})}{\partial (\frac{1}{T})}$ (kJ/m)	229	164	361	260
unfrozen water content w_u (%)	1.9	1.1	-	-
avg $\log_{10} \frac{\dot{\epsilon}_m \text{ treated}}{\dot{\epsilon}_m \text{ untreated}}$		1.65	-	
avg $\log_{10} \frac{t_m \text{ untreated}}{t_m \text{ treated}}$		1.70	>4.8	
avg $\log \frac{\dot{\epsilon}_m \text{ XPX}}{\dot{\epsilon}_m \text{ M}} \text{ treated}$			0.10	
avg $\log \frac{t_m \text{ M}}{t_m \text{ XPX}} \text{ treated}$			0.13	

TABLE 5.1

Results of testing on glass beads

(2) the strain at peak stress from the CIDC tests on the unfrozen MS-M beads is 2.2% for the wetting beads and 2.7% for the nonwetting beads;

(3) the frozen saturated samples made from the nonwetting beads exhibit greater creep than the wetting beads at the same applied stress and temperature;

(4) the strain at $\dot{\epsilon}_m$ for the wetting beads is greater than for the nonwetting beads;

(5) the frozen samples made from nonwetting beads exhibit greater stress dependence than the wetting beads;

(6) for the stress levels used, the frozen samples made from wetting beads possess a greater apparent activation energy E than for the nonwetting beads;

(7) the larger beads (MS-XPX, 20-40 mesh size) exhibit a greater creep than the smaller beads (MS-M, 60-200 mesh size) at the same applied stress and temperature;

(8) the frozen saturated nonwetting glass beads possess less unfrozen water than the wetting glass beads.

In addition, a comparison of tests on fine polycrystalline ice and glass beads indicates that even the most creep susceptible of the glass beads tested, the coarse, nonwetting MS-XPX WP beads were considerably less creep susceptible than the ice for similar testing conditions. Figure 5.9 plots a typical comparison.

From these results, various inferences may be made regarding the mechanisms of strength and deformation in frozen soils. By

comparing the creep behavior of the wetting and nonwetting beads of the same gradation, it is obvious that the nonwetting surface treatment results in a weaker, more creep susceptible behavior. This could be due to several possible reasons, as presented below.

(1) A change in the friction angle of the beads due to the surface coating would cause an altered creep behavior. A decrease in friction angle was observed in drained triaxial compression tests run wet and dry on the MS-M size glass beads. A decrease in friction angle from 36.5° to 34° should corresponds to about a 12% decrease in axial strength, as indicated in Figure 5.10. Assuming a stress dependence for $\dot{\epsilon}_m$ similar to Manchester Fine Sand, and assuming correspondence between creep test $\dot{\epsilon}_m$ vs. σ_1 and strength test $\dot{\epsilon}$ vs. σ_1 , this leads to at most a 3 X expected increase in $\dot{\epsilon}_m$ for the nonwetting beads. However, this is much less than the observed 45 to greater than 10^4 increase actually observed and hence should not be wholly responsible for the observed differences in creep.

(2) The surface treatment of the beads may cause changes in the ice structure. However, although the different surface coatings may alter the ice nucleation temperature, they should not greatly affect the granular structure nor grain size of the pore ice. In any case, the change in ice structure should be less drastic than for Goughnour and Andersland's (1968) sand-ice systems, where for an increase in sand concentration from 0 to 42% they observed only a 26% increase in strength. Since

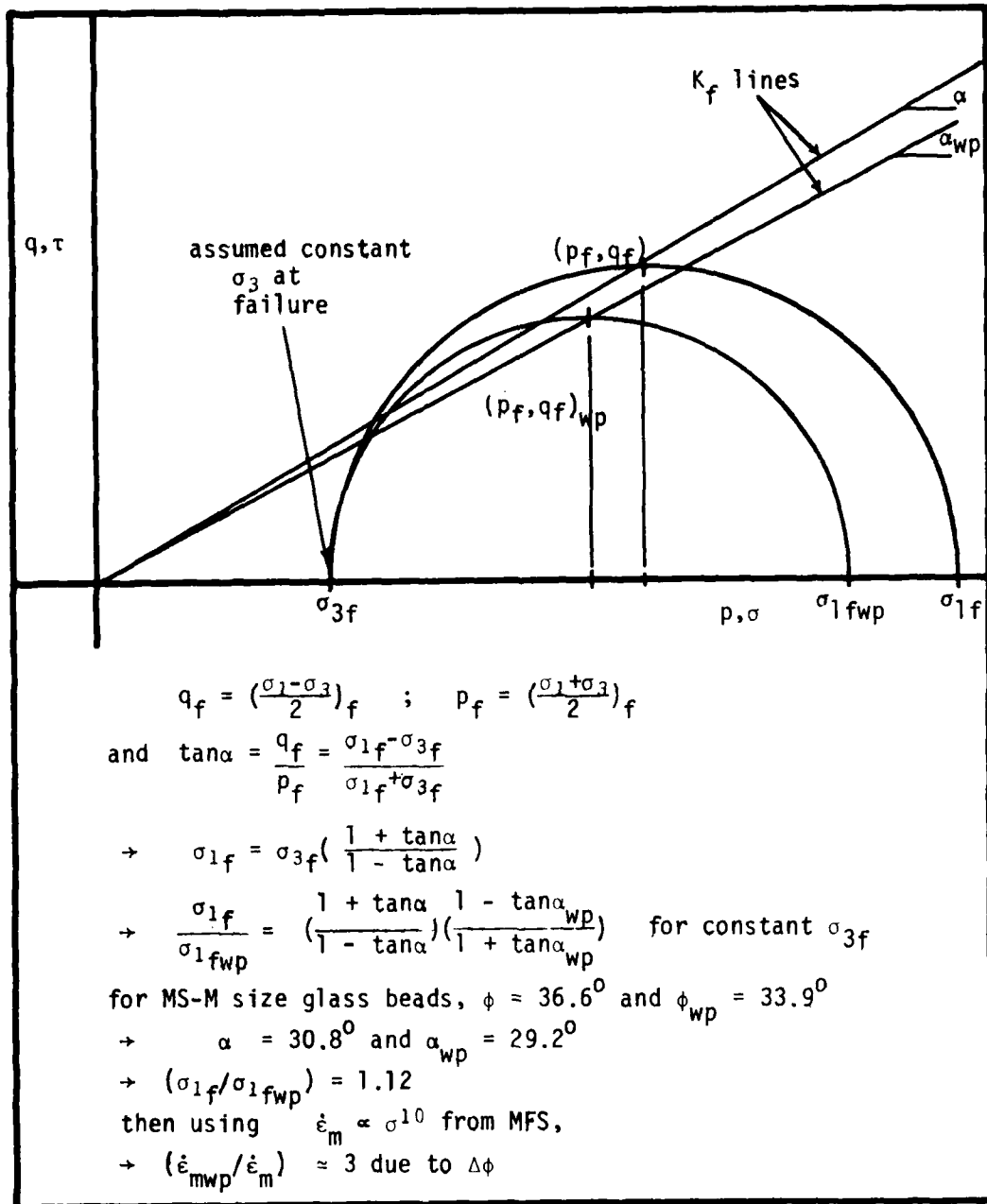


FIGURE 5.10 Effect of a change in friction angle on the observed axial strength

an altered ice structure is only partly responsible for the observed strength increase, this 26% represents an upper bound on the effect of an altered ice structure for the wetting and nonwetting beads. Consequently, this should not be responsible for the large difference in observed ϵ_m for the two different surface treatments.

(3) A difference in the unfrozen water film between the ice and glass bead most probably exists in the two cases. Pulsed NMR determinations of the unfrozen water content indicate that the nonwetting bead samples possess less unfrozen water than the wetting bead samples. Assuming that relatively small differences exist in the unfrozen water attributable to the pore ice phase in each case, this leads to the conclusion that the nonwetting bead samples have a decreased amount of unfrozen water in the film between the ice and glass beads. Since the specific surface area (SSA) of the differently treated beads of the same gradation are the same, this implies that the thickness of the unfrozen water film at the glass/water/ice interface is decreased for the nonwetting beads compared to that for the wetting bead samples.

Several consequences could arise from this altered interface. Assuming the presence of the previously described hypothetical physico-chemical tension in the film between the ice and the soil (glass beads), a decreased thickness in this film suggests a less tightly bound water layer, hence a decreased tension in the film. This result is consistent with strength

mechanism 3(c), as a decreased tension would result in a decreased positive effective confining stress, and hence a weaker, more creep susceptible sample. However, mechanism 3(c) is considered to be unlikely due to the other indirect arguments based on the creep behavior of frozen soils at varying degrees of ice saturation.

A change in the ice/water/glass interface could cause a decrease in the adhesional strength between the ice and soil (glass bead). While the exact mechanism of adhesion between the ice and glass is not clear, possible mechanisms may be proposed. Due to the two-dimensional nature of the unfrozen water film, with relative mobility parallel to the mineral surface and poor mobility normal to the mineral surface, strong tensile bonding between the ice and mineral can occur through the unfrozen water film. This is confirmed by work on adhesional tensile strength done by Jellinek (1957(a),(b), 1960(c)). The decreased water film thickness for the WP (non-wetting) beads results from less attraction between the glass interface and the adsorbed water and hence could be expected to cause less adhesional tensile strength between the beads and the pore ice. The adhesional shear strength, parallel to flat mineral surfaces, tends to be a function of the amount of interlocking between the ice and mineral substrate, and hence the roughness of the mineral surface. This also is confirmed by Jellinek's work. Although the scanning electron microscopy (SEM) of the beads appears to indicate that the treated, non-

wetting beads are surficially rougher than the wetting beads (see Figures A.2.4 to A.2.7 in Appendix A.2), it seems likely from a comparison of the creep behavior that any increase in adhesional shear strength is more than offset by a decrease in adhesional tensile strength.

This hypothesis is supported by the fact that the strain ϵ_m at $\dot{\epsilon}_m$ is decreased for the nonwetting beads. Assuming that the "effective confining stress" and the pore ice behavior are the same in each case, this suggests that the nonwetting beads have a weaker, less integral system since the gradation is the same in each case. Also, the larger gradation bead samples are slightly weaker (more creep susceptible), with a decreased ϵ_m . Since a larger gradation in particulate materials leads to larger forces at particle contacts and between the particles and the pore matrix, a larger adhesional strength between the ice and glass is required to maintain the same behavior as for the finer grained beads. For the larger gradation beads, ice-to-bead forces may exceed the adhesional strength of the interface, resulting in cleavage between the ice and bead. For example, a series of frozen saturated samples made from wetting, uniform spherical glass beads of increasing grain diameter yielded decreasing strength. For bead diameters above about 5 mm, samples could no longer be ejected from the compaction molds described in Appendix A.2 without breaking. Consequently, the weaker sample behavior for the larger gradation also supports the hypothesis that the

adhesional strength between the ice and glass beads is altered by the nonwetting surface coating.

From this discussion, it appears likely that the wetting and nonwetting glass beads possess differing ice/glass adhesional strengths. By assuming that the nonwetting beads possess a decreased adhesional strength, all of the observed creep behavior at the different gradations may be consistently explained. While other effects are present in the differently treated bead samples, such as an altered friction angle, perhaps an altered pore ice structure and possibly an altered (hypothetical) film tension, these are not considered to be of sufficient magnitude to cause the large differences in observed creep behavior.

Since most soils are silicates, they should exhibit an affinity for water similar to the wetting glass beads. In addition, most soils should possess a mineral surface roughness in excess of that for the glass beads tested. Hence, it is expected that frozen sand should exhibit an overall (shear and tensile) adhesional strength greater than that for the frozen wetting glass beads.

From this line of reasoning, the testing program verifies the existence of significant adhesional strength between the ice and soil in frozen soils, in spite of (or perhaps because of) the existence of an unfrozen water film at the interface. This adhesional strength is shown to significantly affect the overall mechanical behavior of the frozen soil system. This infers that mechanisms 3(b) and (d) - Effective soil streng-

thening by interaction : dilation and structural hindrance - are both very important mechanisms, as the pore ice is probably strongly "bonded" to the soil, especially for the finer-grained granular soils. Consequently, "synergistic" mechanical interaction between the ice and soil is considered to be a dominant strength mechanism under normal (low confining stress) conditions.

5.3 Proposed Qualitative Model for Frozen Sand Behavior

Based on the test results, discussions and conclusions presented in the previous sections, it is possible to propose a probable model for frozen sand behavior. The key mechanisms controlling the strength behavior for this model are:

(1) ice strength, which is greater than that in normally tested ice due to an altered structure, deformational constraints and different stress states and strain rates; the strength increase of the ice in frozen soils compared to pure ice is significant, but small in comparison with the effect of the soil contribution, as represented by its relative density;

(2) soil strength, which consists of interparticle friction, particle interference, dilatancy effects and is mainly a function of the confining stress level and the drainage conditions;

(3) structural hindrance between the soil and ice matrix, which can be synergistic in nature, ie. the strength of the composite is greater than the sum of the strengths of the individual components;

(4) dilatancy effects, in which an increase in the effective stress due to dilation of the soil skeleton increases the observed strength for dense sands.

Based on these mechanisms of strength for frozen sand, it is possible to construct mechanism "maps" for both strength and creep testing as a function of volume fraction of sand. Figure 5.11 presents such maps for uniaxial (unconfined) compression data, and indicates the relative importance of each mechanism:

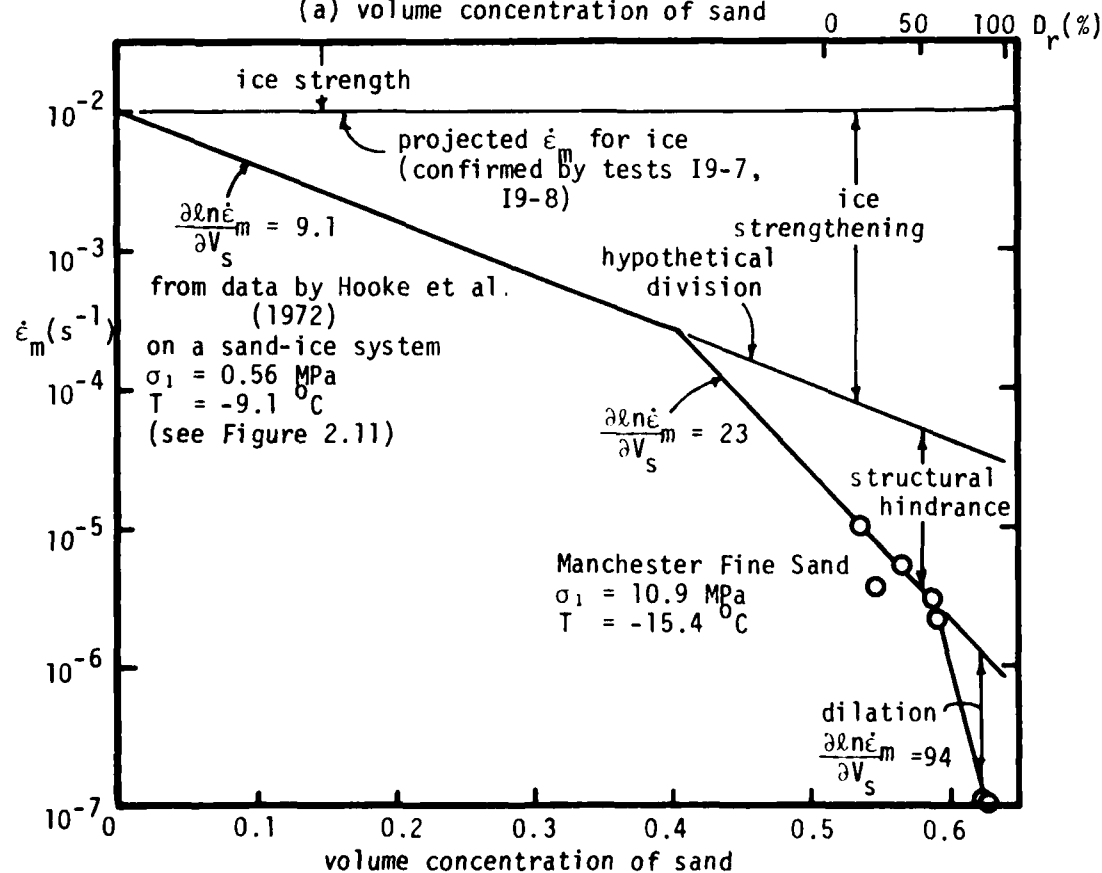
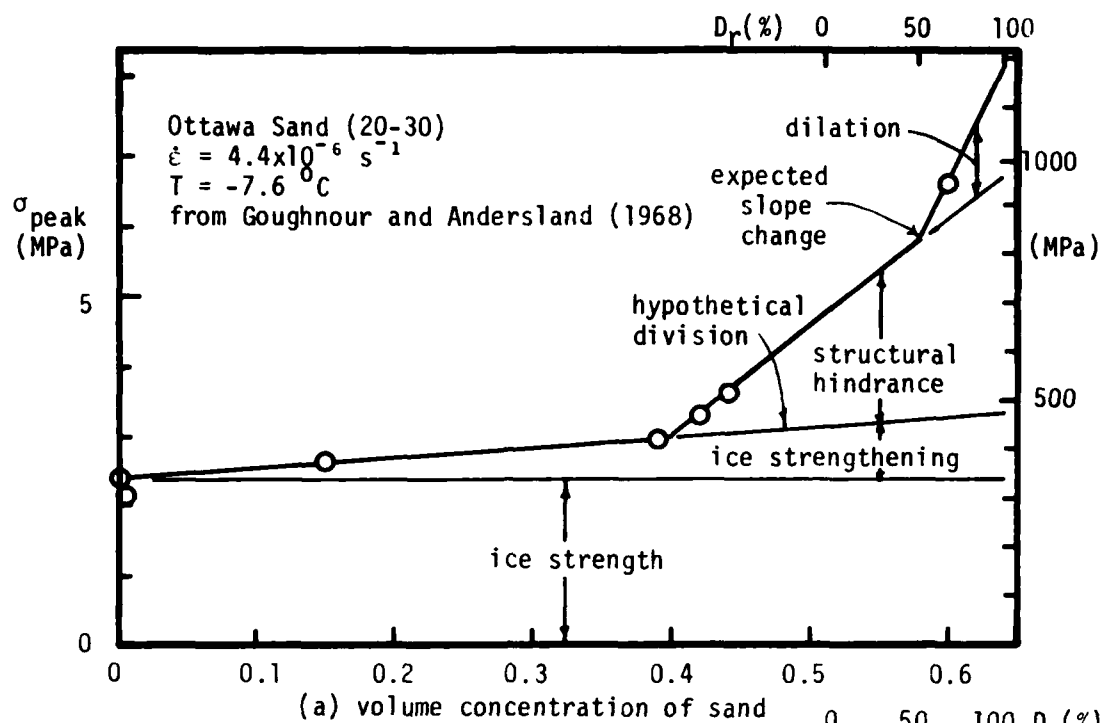


FIGURE 5.11 Tentative mechanism maps for uniaxial compression of frozen sands

one for strength testing based on Goughnour and Andersland's (1968) data; the other for creep testing based on data from Hooke et al. (1972) and the current testing program on MFS. In each case, simple linear projections were used to separate the total measured strength (and strain rate) into the components attributed to the proposed mechanisms.

For the strength data in Figure 5.11(a), the ice strength component is measured at 2.4 MPa at zero sand concentration, while the component attributed to ice strengthening is assumed to increase linearly with increasing concentration for all levels of sand concentration. Structural hindrance accounts for the component of strength over and above this ice strengthening component. An anticipated change in total measured strength due to dilatancy effects at 50% relative density is also shown. The relative densities for the Ottawa sand were computed based on assumed values of maximum and minimum density for 20-30 mesh sand from Winterkorn and Fang (1975).

For the analogous creep plot (Figure 5.11(b)), the data for Manchester Fine Sand at an applied stress of 10.9 MPa and -15.4°C are first plotted using a bilinear curve to fit the data above 40% sand concentration. Then, a line with a slope similar to that for Hooke et al.'s (1972) data on sand-ice between zero and 0.35 sand concentration was projected back to zero sand concentration, yielding an estimated $\dot{\epsilon}_m$ for pure ice. A test on polycrystalline ice at the same test conditions as the MFS yielded a $\dot{\epsilon}_m$ too fast to record; however, based on a

test carried out at a slightly lower stress, the estimated value 10^{-2} /s for pure ice at 10.9 MPa and -15.4°C is not unreasonable. From this construction, the various mechanisms of strength may be obtained, as for the strength data in 5.11(a). For the creep data, the projected lines indicate the minimum strain rate which would exist in the sand-ice system without the components of strength shown below the lines.

The bulk of the behavior of frozen soils may be explained consistently from a knowledge of these mechanisms and unfrozen soil behavior. Details of these explanations have been presented in the previous sections, and may be summarized as follows:

(1) for very low confining stresses, the ice matrix is responsible for most of the strength, both by directly carrying the applied load and due to mechanical interaction with the soil;

(2) the ice matrix controls the strength and deformation behavior of the frozen sand system at low strains and confining stresses; at greater strains (say above 1% for medium-dense sands), the mechanisms attributed to soil strength and interaction become more important;

(3) significant adhesional strength between ice and soil exists; hence, the mechanical interaction between the soil and ice is probably synergistic at low confining stresses, and is partly responsible for the high "cohesion" intercept;

(4) as the confining stress increases, strengthening of the pore ice occurs due to crack inhibition and closure; if the pore ice is partially saturated such that Skempton's B parameter

is less than unity, a portion of the confining stress may increase the effective stress acting on the soil skeleton and hence lead to increased frictional resistance between the sand grains; for soils above about 40 MPa, local pressure melting of the ice results in a decreased ability of the ice to resist soil skeleton deformations and hence a decreased overall measured strength; above about 110 MPa, essentially global pressure melting exists; an observed slight increase in strength with increased confinement above this level is due to a decreased soil skeleton compressibility, with a resulting B value less than one;

(5) for slow loading rates or for longterm creep loading, the ice matrix undergoes large deformations under the applied load, and hence more of the applied load is transferred from the ice matrix to the soil skeleton; this effect is analogous to partially drained loading in unfrozen soil;

(6) an increase in relative density in the sand results in rapidly increasing frozen soil strength and decreasing creep behavior; even greater strengthening of the frozen soil system probably occurs in the range of dilatant soil behavior;

(7) an increasing ice saturation results in an increased overall strengthening of the frozen soil system due to a greater load carrying capacity in the ice and increased resistance to sand deformation;

(8) a decreasing temperature results in increasing strength due to a strengthening of the ice matrix;

(9) the temperature dependence of strength and creep behavior decreases with increasing confining stress level; this must be due to the decreased effect of the ice matrix component of strength at the higher confining stresses;

(10) the linear relationship between the logarithm of the minimum strain rate and the logarithm of the time to this minimum is due to an approximately constant strain at the minimum strain rate and the relative insensitivity of this log-log plot to small deviations from a constant strain at minimum.

5.4. Conclusions

In order to obtain a better qualitative understanding of the mechanical behavior of frozen soil, a thorough literature review of the nature and mechanics of ice, soil and frozen soil was undertaken. Based on this review, and various results from the testing program on Manchester Fine Sand and ice reported by Martin, Ting and Ladd (1981), possible physical mechanisms controlling the strength and deformation of frozen sand were proposed and discussed. The relative importance, implications and probable existence of each mechanism were also presented. These probable mechanisms included: ice strength, soil strength, ice strengthening, effective stress increase due to dilatancy effects, effective stress increase due to tension in the unfrozen water film, and mechanical interaction through structural hindrance.

From this study, it was concluded that a need existed to clarify the nature of the adhesional bond and mechanical interaction between the ice and soil. From the testing program on wetting and nonwetting glass beads, including uniaxial creep testing on frozen saturated samples, unfrozen drained triaxial compression tests, pulsed NMR unfrozen water content determinations and scanning electron microscopy, various inferences into the nature of the adhesion between ice and soil were made. The results, summarized in Table 5.1, indicate that the nonwetting surface treatment was successful in decreasing the adhesional bond between the ice and the beads. The minimum creep rate

of the wetting beads was much smaller than for the nonwetting beads, which implies that sufficient adhesional tensile strength exists in the wetting bead system to significantly affect the creep behavior. Since the "coarse" and "fine" wetting beads are similar to natural sands in gradation and mineralogy, this conclusion should apply to natural frozen sands.

The nature of the interaction between ice and soil was further evaluated by carrying out creep tests on frozen MFS at varying relative density. These data suggest that dilatancy causes a significant reduction in the creep of the frozen soil for medium-to-dense sands.

From these inferences, a better understanding of the mechanisms of strength, and ultimately the behavior of frozen soils, results. The important mechanisms controlling frozen soil behavior consist of the following:

- (1) a pore ice strength that is lightly greater than for normally tested ice;
- (2) a soil strength that consists of interparticle friction, interference and dilatancy effects;
- (3) a mechanical interaction between the soil and ice through structural hindrance, which depends on the adhesional tensile and shear strength developed at the ice/unfrozen water/soil grain interface;
- (4) a mechanical interaction through dilatancy effects wherein any tendency of the soil skeleton to dilate is resisted by an adhesional tensile strength at the ice/unfrozen water/

soil grain interface which results in a positive increment of effective confining stress acting on the soil skeleton.

Section 5.3 summarizes these mechanisms, and presents a comprehensive model for frozen soil behavior. Figure 5.11 presents an estimate of the relative importance of these mechanisms for uniaxial compressive loading of frozen sands during strength and creep testing. Construction of such mechanism maps aid in providing a conceptual picture of the behavior of the system. However, "fine-tuning" of this Figure is necessary. Additional strength data are required at varying relative density to more precisely determine the nature of the dilational component of the strength. Creep data at various degrees of sand concentration at one testing condition are necessary to confirm the relative effect of ice strengthening. To make such maps more general, the effect of varying temperature and confining stress need to be examined; for strength testing, varying $\dot{\epsilon}$ levels and for creep testing, varying applied stress levels should be incorporated.

While this model is useful from a qualitative view, it is desirable to have a theoretically based quantitative model of behavior, able to predict strength-deformation-time behavior as a function of the applied stress state, temperature and structural parameters. One possible approach would include formulating mathematical mechanistic models of behavior, based on the mechanical interaction between the ice matrix and soil grains. Initial attempts at modifying existing models devel-

oped for asphalt, concrete, fiber- and inclusion-reinforced composites did not prove useful, as they were not applicable to the frozen soil system. Instead, the bulk of the quantitative modelling for this Report concentrated on developing simple empirical models for describing and predicting creep behavior.

Ultimately, it is hoped that a quantitative model will emerge which can theoretically account for the interaction of the components in the frozen soil system. Then, one need only input data on the individual components of the system in order to determine the system behavior. It is currently not feasible to obtain such a model. However, it is hoped that the forgoing presentation of the physical mechanisms of strength and deformation in frozen soils represents a positive step in that direction.

CHAPTER 6 QUANTITATIVE MODELS FOR THE CREEP OF FROZEN SAND

The engineer is often required to predict the deformation-time behavior of a system, first for simple testing conditions to obtain constitutive relationships and then for more complex loading conditions. For frozen sand loaded uniaxially under unconfined compression, the pertinent test parameters are temperature and applied load, while the sample structure may often be described by the relative density of the soil and the degree of saturation of the pores. Though it is desirable to predict the entire deformation-time behavior, it is also useful to know if and when the creep of the system will accelerate, changing from primary to tertiary creep.

This Chapter presents simple empirical methods which have been developed by the author for predicting various aspects of the creep, as well as the entire deformation-time behavior for uniaxially loaded frozen sands. Relatively simple procedures for evaluating the required model parameters for prediction are also summarized. Details of the derivations and computations for this Chapter are found in Appendix B.

To determine if a frozen material under constant load will exhibit tertiary creep, and ultimately, creep rupture, some researchers refer to a limiting long term strength (LLTS) (Vyalov 1973, Rein et al. 1975). While the existence of such a quantity is hypothetical at present for uniaxially loaded frozen sand, some data strongly suggest that there is a level of applied stress below which extremely low creep rates are

experienced. It is not clear whether this low creep behavior is actually indicative of a limiting longterm strength; it may be that tertiary creep would result if the tests were carried out for sufficiently long times. However, due to experimental problems with long term testing and equipment maintenance at sub-freezing temperatures, the existence of a true LLTS has not been proven.

Some data from the testing program of Martin et al. (1981) on MFS appear to support the belief that there is a stress level below which extremely reduced creep behavior occurs. This critical stress level, expressed as a fraction (σ/σ_{ult}) of the ultimate strength presented in Appendix A.5, is approximately 0.3 for 40% ice saturated 55% relative density MFS, while for saturated MFS it is about 0.2. One partially saturated sample was loaded at -14.8°C with 3.04 MPa (0.33 stress level), and should have exhibited a minimum strain rate $\dot{\epsilon}_m$ of about 9×10^{-8} /s at a t_m of 1110 min, based on the (σ/σ_{ult}) correlations for $\dot{\epsilon}_m$ and t_m to be described later in this Section. Instead, the test exhibited a marked drop in strain rate after about 250 minutes, at a strain of about 0.6%, as shown in Figure 6.1. After a period of creep at a minimum creep rate of about 2×10^{-10} /s between 7500 and 25000 min., tertiary creep ensued.

While this tends to suggest that there may be merit to the hypothesis of a LLTS, or at least a stress level below which very low creep is observed, the current testing program

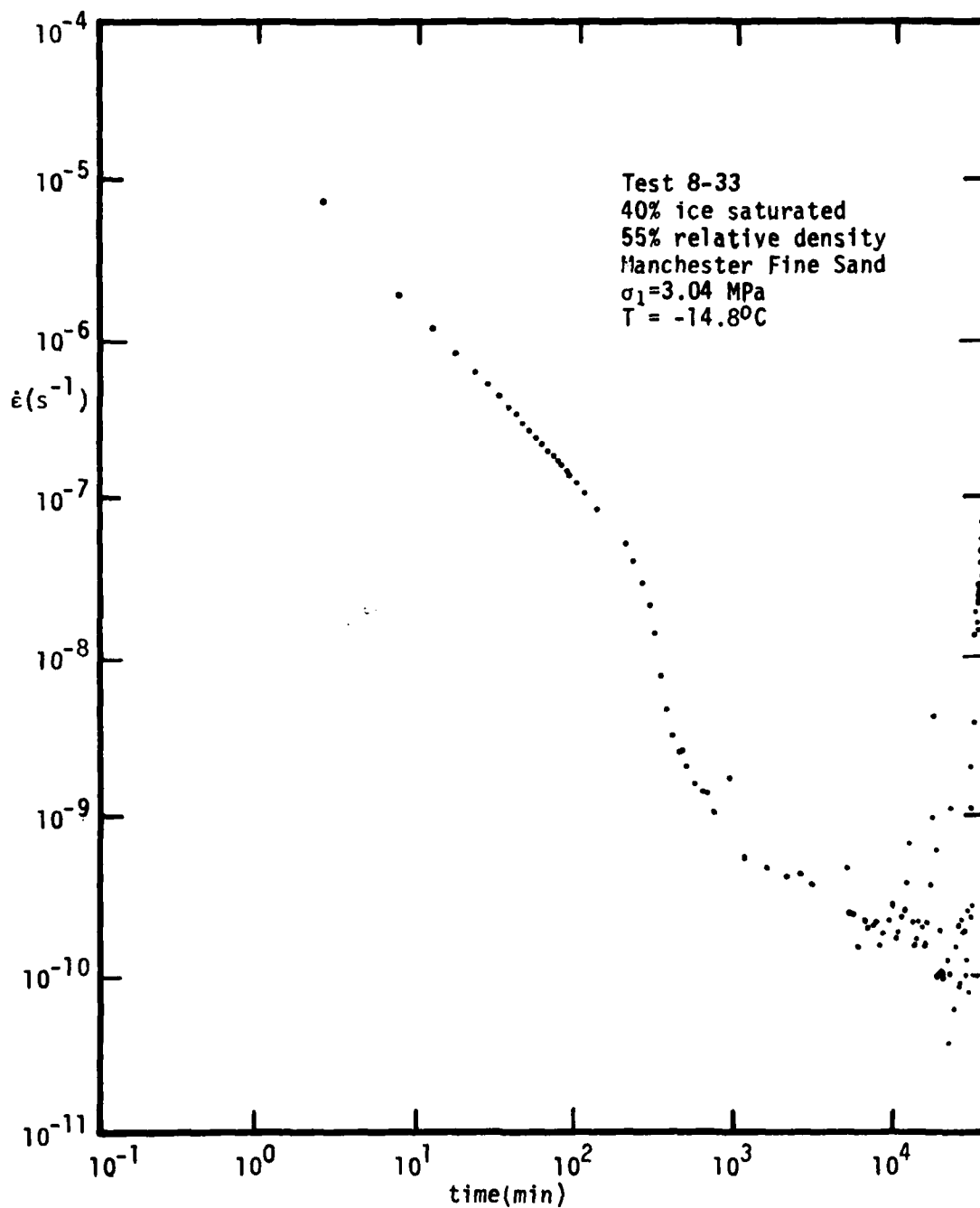


FIGURE 6.1 Results of creep test on 40% S_f MFS at 0.3 stress level

was not designed to investigate these possibilities. Consequently this subject is not discussed further.

Based on the wealth of uniaxial compressive creep data presented in Appendix A.5, Figure 6.2 summarizes the characteristic creep behavior for medium-dense MFS. For saturated MFS at high stress levels and for partially saturated MFS, a $\log \dot{\epsilon} - \log t$ plot similar to curve I results. For intermediate stresses, saturated MFS exhibits behavior similar to curve II, with a downward change in slope of the curve in the primary creep stage occurring at about 1% strain. At very low stress levels, a sharply decreased creep is observed in the form of a drop in strain rate, as in Curve III. This may be indicative of a limiting longterm strength, as already described.

For a given creep loading situation, it is common to refer to failure as the point at which creep starts to accelerate, i.e. $\dot{\epsilon}_m$. In order to predict the minimum creep of a system, three quantities are usually used: the minimum strain rate, $\dot{\epsilon}_m$, the time to the minimum strain rate, t_m , and the strain at the minimum strain rate, ϵ_m . Of these, the strain at the minimum strain rate is approximately constant at all stress levels, exhibiting only a slight decrease with decreasing minimum strain rate. This trend has been described in Section 5.1 and Appendix B.1, and is plotted in Figure B.1.5 in Appendix B.1. The ϵ_m also decreases with decreasing ice saturation S_i and increasing relative density D_r , as indicated in Tables A.5.3 and A.5.4 in Appendix A.5.

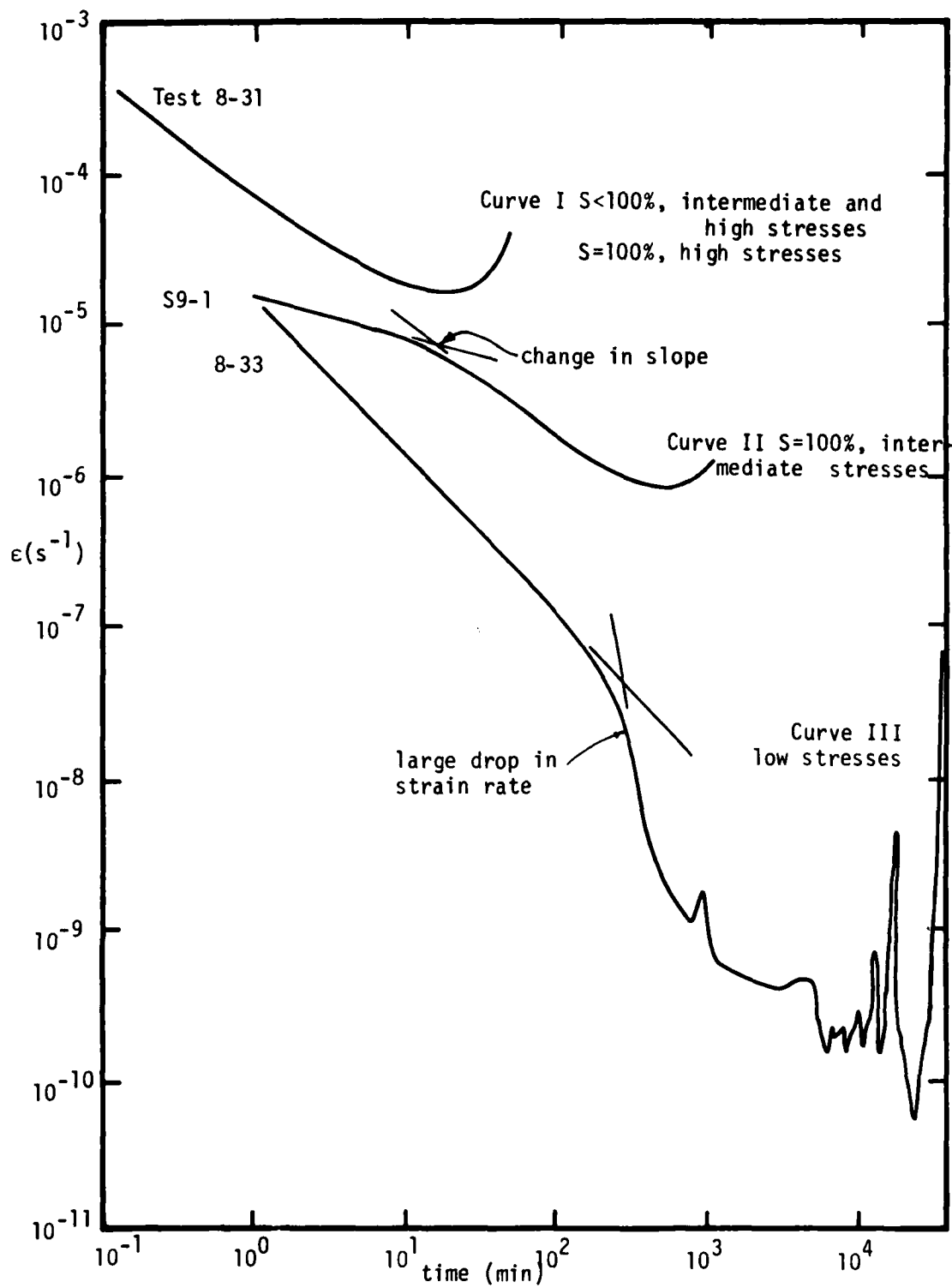


FIGURE 6.2 Typical uniaxial (unconfined) creep behavior for frozen sand

6.1 Prediction of the Minimum Strain Rate

The minimum strain rate $\dot{\epsilon}_m$ will be predicted using three different methods. The first is very loosely based on Rate Process Theory (RPT), using data only from single stage creep tests. This method employs the following empirical equation to fit the $\dot{\epsilon}_m$ data for samples at a particular Dr and Si:

$$\dot{\epsilon}_m = A T \sigma_1^n \exp\left(-\frac{E}{RT}\right) \quad (6.1)$$

where T = temperature ($^{\circ}$ K)

σ_1 = applied stress (MPa)

R = Universal Gas constant

A,n,E = experimentally determined constants

Equations similar to (6.1) have been used by various workers to describe the creep of ice, notably Glen (1955), Weertman (1973), Langdon (1973), Gold (1978) and Homer and Glen (1978). These equations employ Rate Process Theory only in that they contain a $\exp(-E/RT)$ term to describe the temperature dependence of the creep. Whereas RPT uses the variation in the apparent activation energy E to describe the stress dependence, equation (6.1) includes an empirical σ_1^n term since the RPT is grossly inadequate for predicting the variation of $\dot{\epsilon}_m$ with stress for frozen soils. Details of this equation and procedures for determining the "modified RPT" model parameters are found in Appendix B.2.

The model parameters determined by applying these procedures to all of the 20, 40 and 100% ice saturated MFS

constant load creep data are found in Table 6.1. Figure 6.3 plots the frequency histograms of the ratio of the fitted and actual $\dot{\epsilon}_m$ for each dataset.

By using one value of n for all levels of ice saturation, new A parameters may be computed. These new A coefficients may then be correlated with degree of saturation using an equation of the form:

$$\dot{\epsilon}_m = A \exp\left(\frac{\beta}{S_i + \alpha}\right) T \sigma_1^n \exp\left(-\frac{E}{RT}\right) \quad (6.2)$$

where α and β may be determined by iterative regression of the new A parameters.

Then, noting that the change in strain rate with relative density is approximately the same for medium-dense ($Dr > 60\%$) sand at various ice saturations, it is possible to use an equation of the following form to fit the creep data for all values of σ_1 , T , Dr and S_i :

$$\dot{\epsilon}_m = A \exp(\gamma Dr) \exp\left(\frac{\beta}{S_i + \alpha}\right) T \sigma_1^n \exp\left(-\frac{E}{RT}\right) \quad (6.3)$$

where A , α , β , γ , n and E are experimentally determined coefficients, and for MFS,

$$\dot{\epsilon}_m = 1.85 \times 10^{31} \exp(-12.4 Dr) \exp\left(\frac{12.54}{S_i + 0.30}\right) T \sigma_1^{10} \exp\left(-\frac{30000}{T}\right) \quad (6.4)$$

The comparison of the fitted and actual $\dot{\epsilon}_m$ using this equation is found in Figures 6.4 and B.2.7. From these Figures, it can be seen that 95% of the fitted data are within ± 5 times the actual $\dot{\epsilon}_m$.

The second method for predicting $\dot{\epsilon}_m$ uses stress ratios based on the ultimate strengths presented in Appendix A.5. These ultimate strengths are the peak strengths measured in

Si(%)	A (s ⁻¹)	n	- E/R (°K)
20	1.79x10 ⁴⁷	9.21	34358
40	2.03x10 ³⁵	10.41	29781
100	1.09x10 ²⁵	9.97	25690

TABLE 6.1

Summary of Modified RPT model parameters for MFS:

$$\dot{\epsilon}_m = A T \sigma_1^n e^{-E/RT}$$

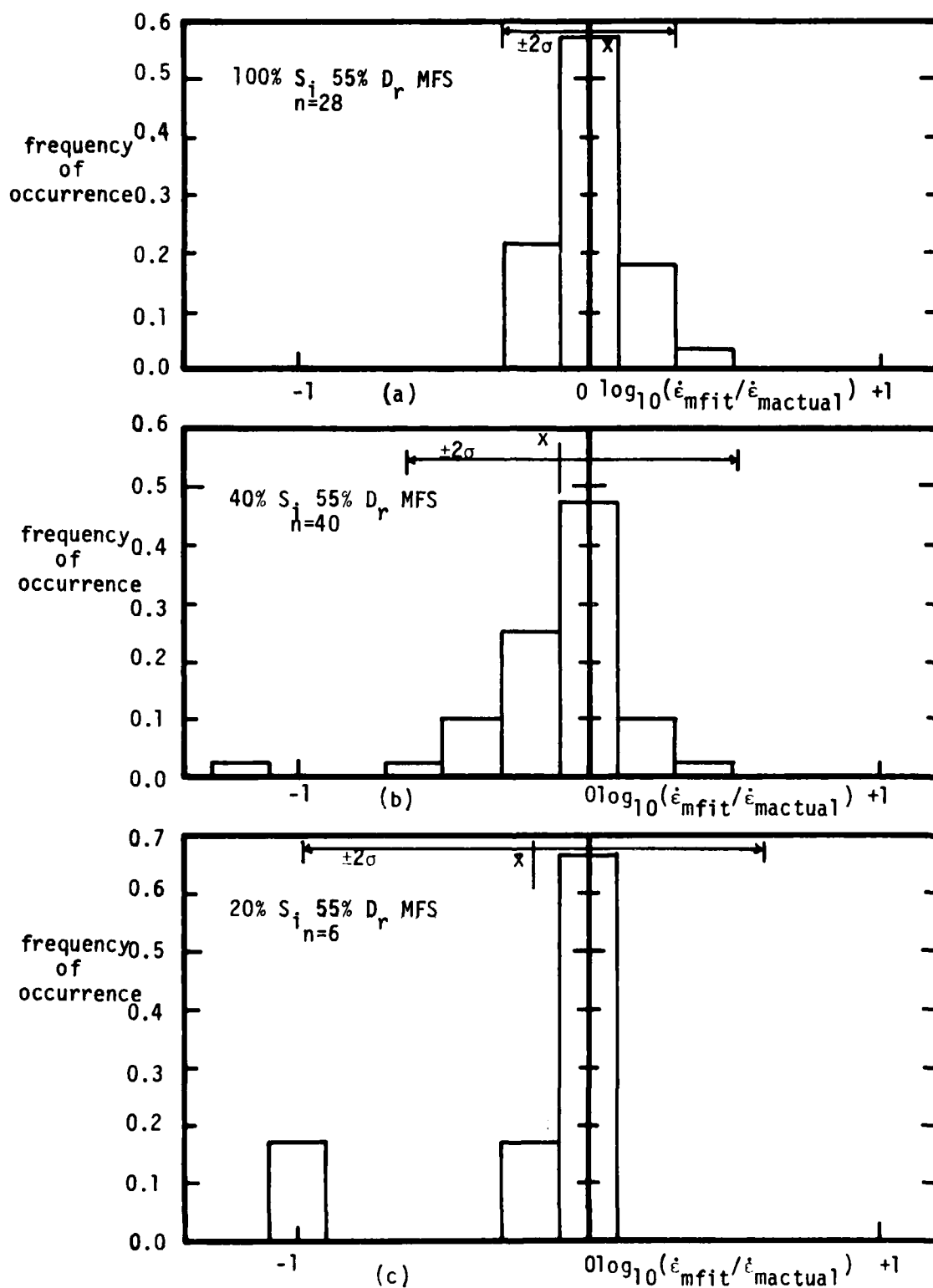


FIGURE 6.3 Comparison of fitted and actual $\dot{\epsilon}_m$ using the modified RPT equation for 55% D_r MFS at various levels of saturation

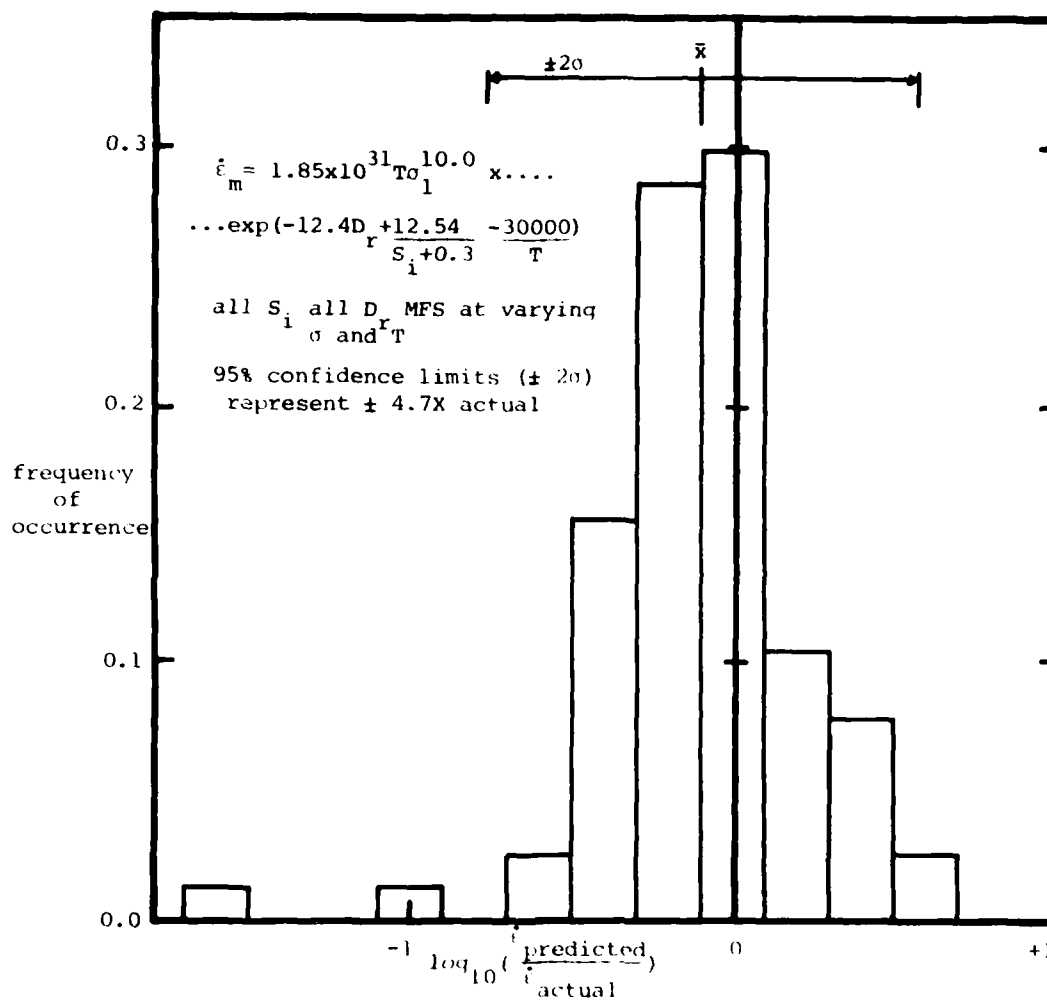


FIGURE 6.4 Frequency histogram indicating quality of fit using one modified RPT equation for describing S_1 , D_1 , σ and T variation

strain rate controlled tests at the (observed) ductile-to-brittle transition point. This ductile-to-brittle transition was determined visually by running a sequence of tests at varying strain rates and temperatures. The results of such test sequences on 40 and 100% Si MFS are plotted in Figures A.5.13 and A.5.12 in Appendix A.5, respectively. This ultimate strength may be approximately represented by:

$$\sigma_{ult} = 10.1 + 1.5\theta \quad (\text{MPa}) \text{ for } 100\% \text{ Si } 55\% \text{ Dr MFS} \quad (6.5)$$

$$\sigma_{ult} = 2.38 + 0.46\theta \quad (\text{MPa}) \text{ for } 40\% \text{ Si } 55\% \text{ Dr MFS}$$

where $\theta = -T(^{\circ}\text{C})$. Note that these relationships are based on a limited number of strength tests. A more refined estimate of the ultimate strength and its temperature dependence would require a more comprehensive testing program.

By expressing the loading condition in terms of a stress ratio, both the applied load and temperature are quantified in one variable. Then, one simple empirical equation of the following form may be used for predicting $\dot{\epsilon}_m$:

$$\dot{\epsilon}_m = A \left(\frac{\sigma}{\sigma_{ult}} \right)^n \quad (6.6)$$

For MFS, the following equations result:

$$\dot{\epsilon}_m = 0.196 \left(\frac{\sigma}{\sigma_{ult}} \right)^{9.95} \quad (/s) \quad , r^2 = 0.98 \text{ for } 100\% \text{ Si} \quad (6.7)$$

$$\dot{\epsilon}_m = 3.46 \times 10^{-3} \left(\frac{\sigma}{\sigma_{ult}} \right)^{9.53} \quad (/s) \quad , r^2 = 0.92 \text{ for } 40\% \text{ Si}$$

The quality of these fits is shown in Figures 6.5 and 6.6 which indicate that use of this method gives a fit slightly better than that from using the previously described modified RPT method.

By averaging the exponent n and using an exponential term

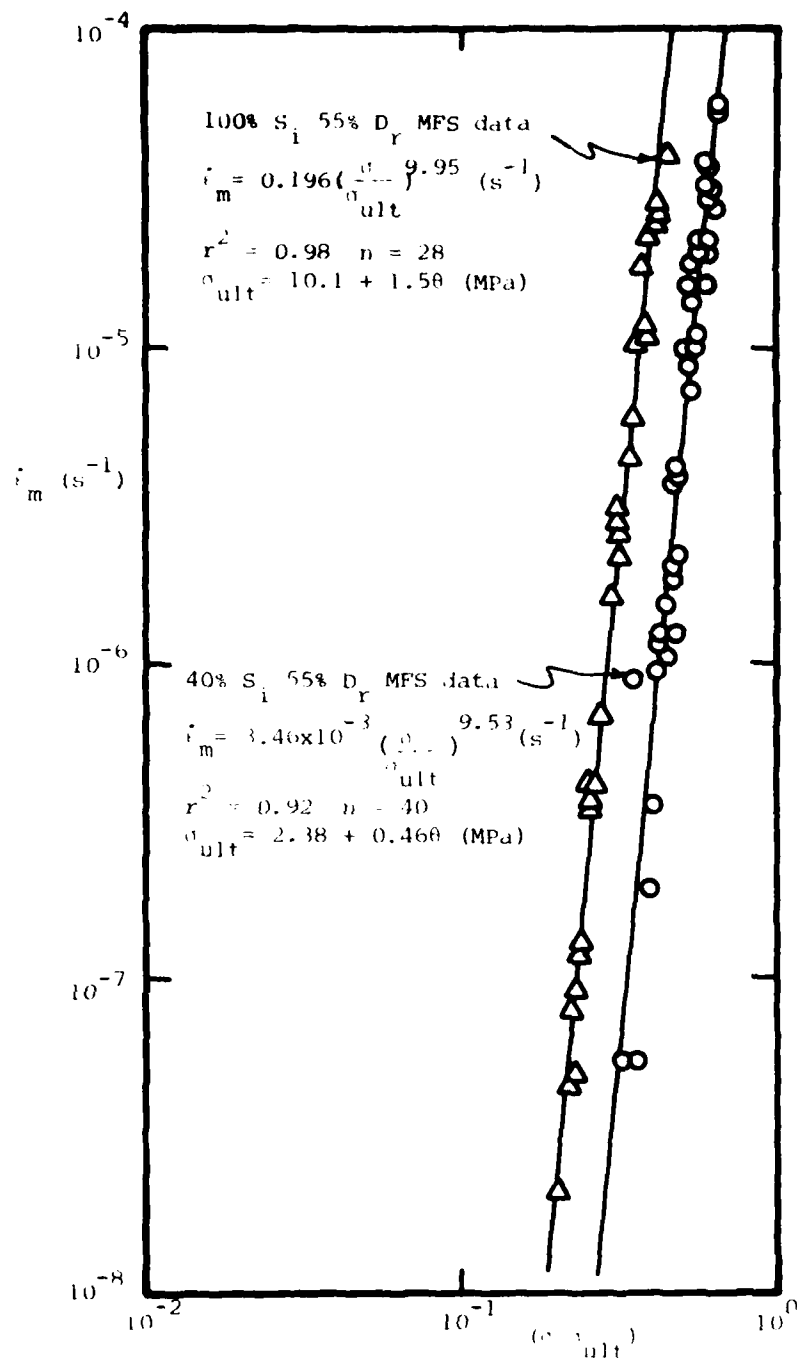


FIGURE 6.5 Use of ultimate strength for fitting constant load creep data for 40% S_i and 100% S_i MFS

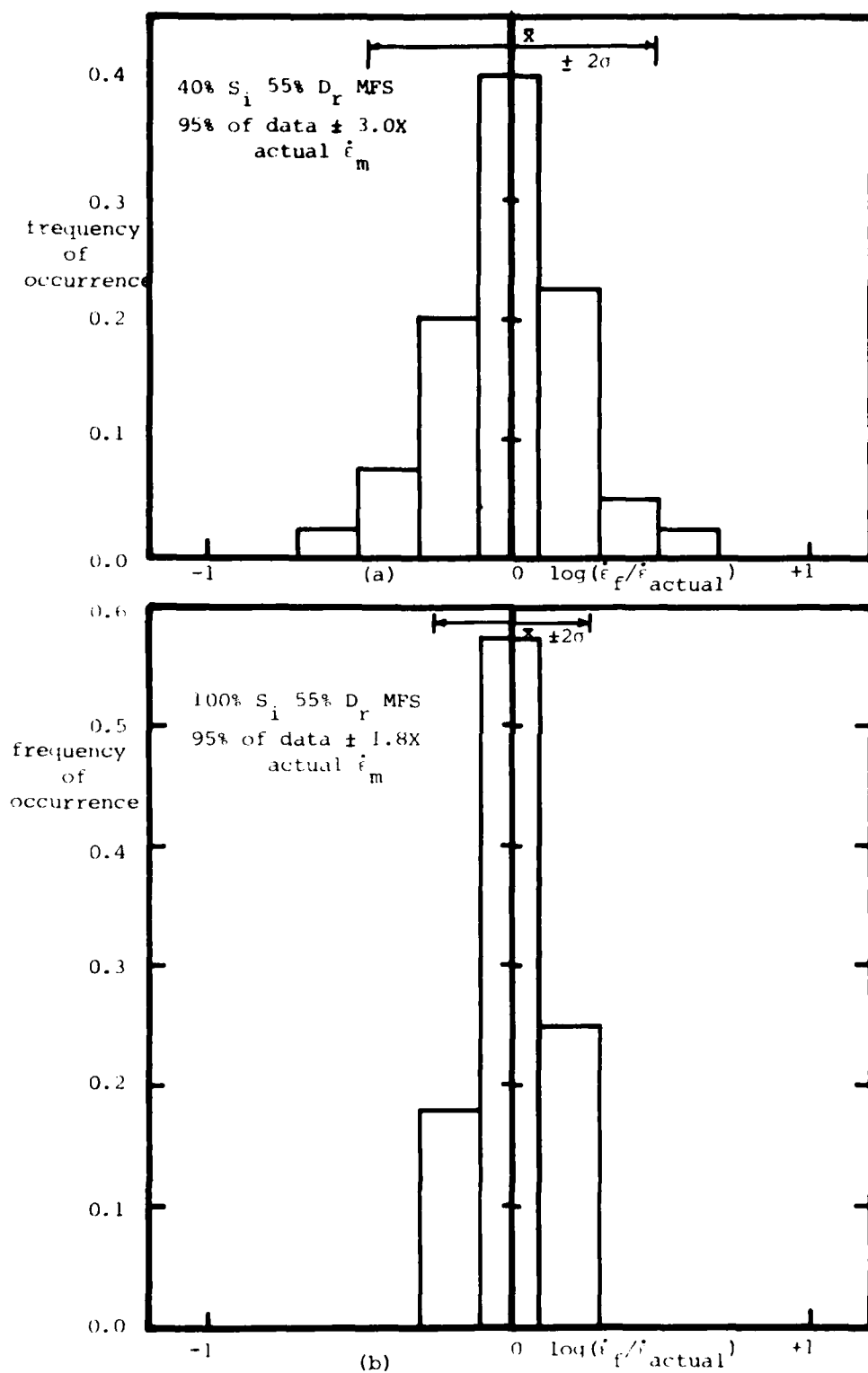


FIGURE 6.6 Frequency histogram of data fits using ultimate strength

to describe the effect of saturation, the following equation results:

$$\dot{\epsilon}_m = 3.49 \times 10^{-4} \exp(6.1Si) \left(\frac{\sigma}{\sigma_{ult}} \right)^{9.74} \quad (6.8)$$

where σ_{ult} may be expressed as:

$$\sigma_{ult} = -2.76 + 12.87Si - 0.233\theta + 1.73\theta Si \text{ (MPa)}$$

Since data are available from only two levels of saturation, equation (6.8) is an "exact" fit for the data. The quality of the fit using this equation is shown in Figure 6.7, and indicates that 95% of the fitted $\dot{\epsilon}_m$ are within $\pm 3X$ of the actual $\dot{\epsilon}_m$. Note that direct comparison with equation (6.4) and Figure 6.4 is inappropriate, since equation (6.8) and Figure 6.7 do not account for changes in relative density and include only two levels of saturation.

In general, equation (6.6) is a far simpler mathematical expression than the "modified RPT" method using equation (6.1). The coefficients for the stress ratio equation are easier to obtain, the resulting fit is slightly better than for equation (6.1) and is always centered. However, the modified RPT method requires only creep test data to evaluate its parameters. For the stress ratio method, a fairly elaborate strength testing program is required in order to determine the ultimate strength at the ductile-to-brittle transition point at several temperatures in addition to creep tests. Consequently, the use of each method depends on the available testing apparatus and individual preference.

It may be possible to use an alternate reference strength

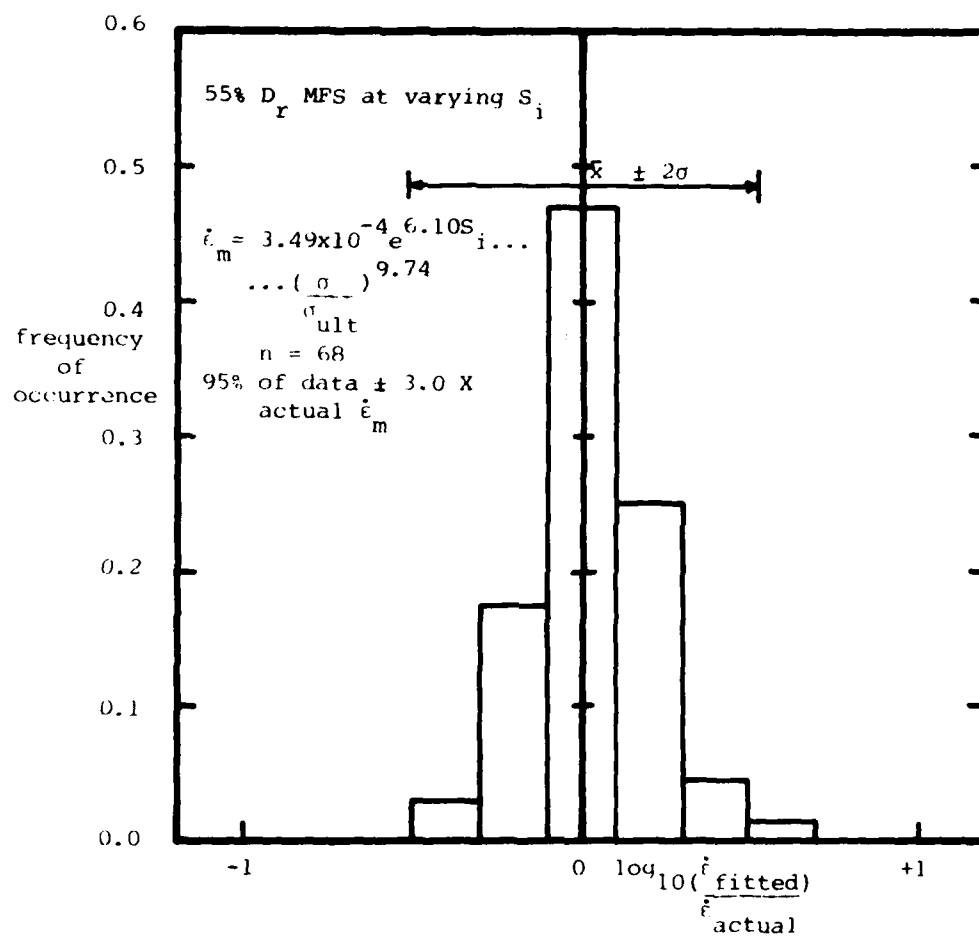


FIGURE 6.7 Frequency histogram of quality of fit using ultimate strength to account for temperature dependence, data at varying degrees of ice saturation S_i

in the stress ratio method. While the ultimate strengths given by equation (6.5) are supposedly measured strengths at an observed ductile-to brittle transition, in reality this transition was observed at only one temperature for one saturation level. The values of strength given by equation (6.5) for both degrees of saturation are based on an assumed constant applied strain rate of 0.02 /s at the transition. Consequently, it may be possible to use a standard strain rate for determining the "ultimate" strength. This needs to be checked by careful evaluation of the strength at the ductile-to-brittle transition, compared with the strength at constant rates of strain. If the latter yield equally satisfactory correlations when applying equation (6.6), then the strength testing for the stress ratio method would be greatly simplified, making the stress ratio method much more attractive as a predictive tool.

By using data from a fraction of the total number of tests, the above two methods were also used to "predict" the minimum creep rate for the remainder of the tests. The tests used for determining the model parameters in each case are summarized in Table B.2.3. Six tests at 20% Si, 8 tests at 40% Si and 10 tests at 100% Si were selected, all at 55% relative density, plus one 40% Si sample at 80% relative density. The tests at each degree of saturation were chosen impartially according to the needs of the modified RPT model, a represent a small, but not minimum, number of tests. In each case, the quality of the "predictions" using only a portion of the data for deter-

mining the model parameters was similar to the quality of the fit using all of the data, as indicated in Figure 6.8. Consequently, it appears that fairly good quality $\dot{\epsilon}_m$ predictions may be made using either method based on a relatively few number of tests. The exact number necessary depends on on sample and test reproducibility. Table 6.2 provides an indication of the minimum number of tests required and considered necessary for reliable prediction, together with a summary of the procedures required for each method.

A third method for $\dot{\epsilon}_m$ prediction arises from the author's proposed creep model. This will be discussed in Section 6.3.

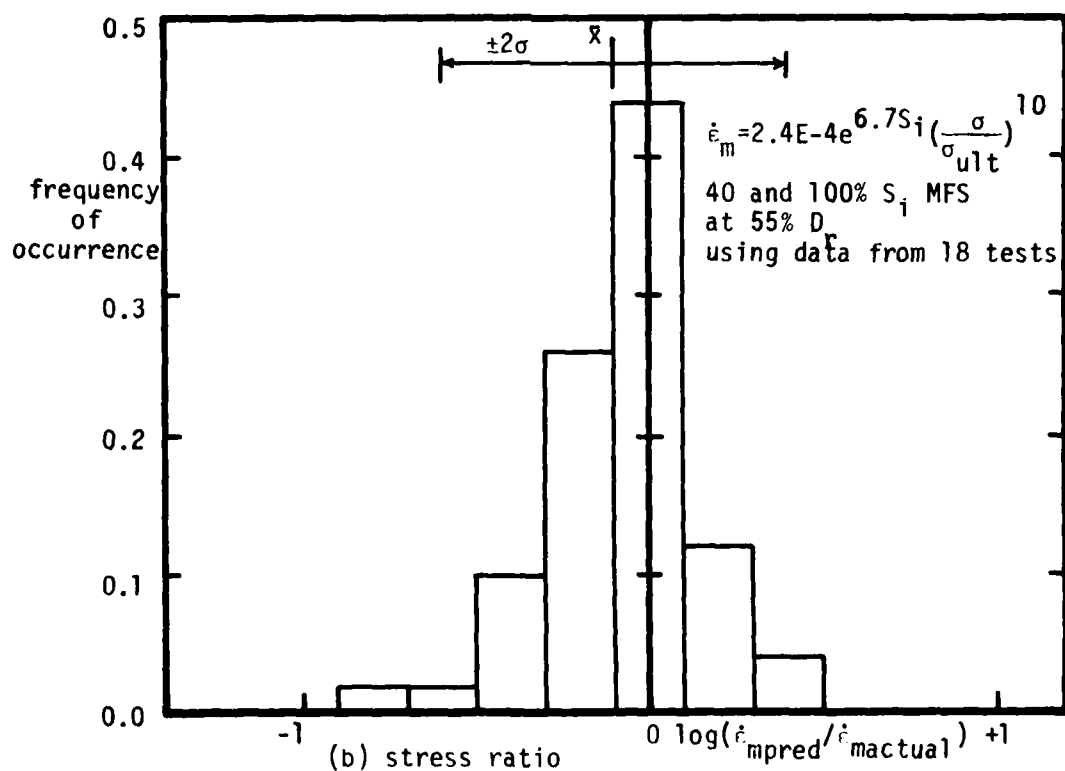
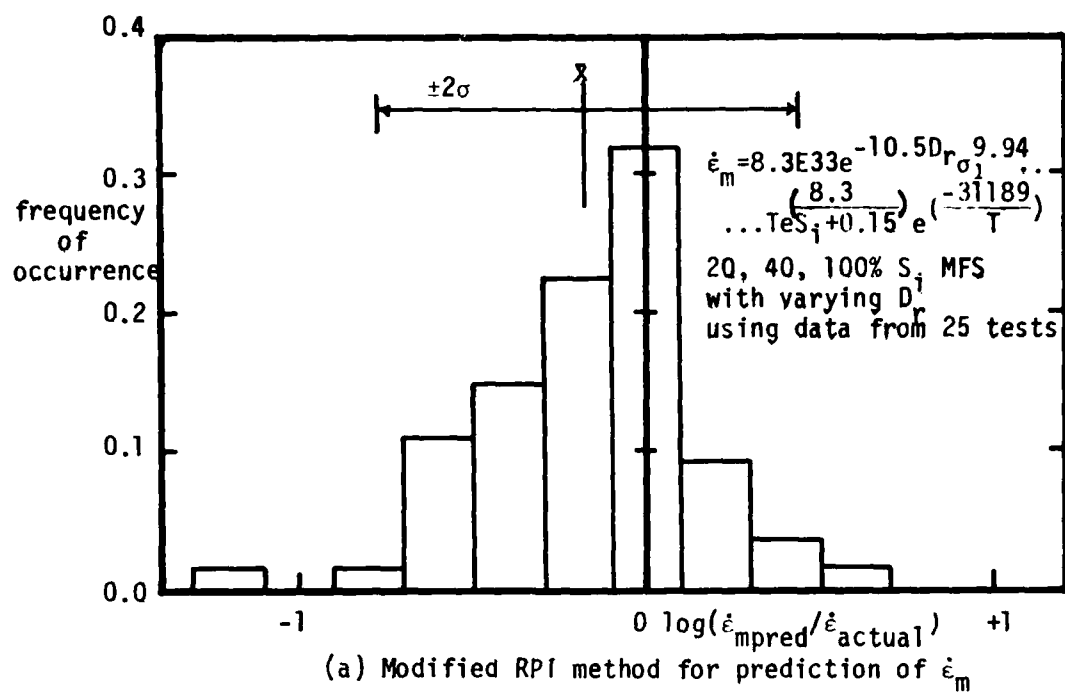


FIGURE 6.8 Comparison of predicted and actual $\dot{\epsilon}_m$ using modified RPT and stress ratio methods

Method	Modified RPT $\frac{\sigma}{\sigma_1}$	Stress Ratio
Generalized equation	$\dot{\epsilon}_m = A e^{D_{re} \frac{\sigma_1}{\sigma_1}} T_1^n e^{-\frac{E}{RT}}$	$\dot{\epsilon}_m = A e^{(S_1 \frac{\sigma_1}{\sigma_{ult}})^n}$
Test parameters	σ_1, T, D_r, S_1	$\sigma_{ult} = f(S_1, T)$
Minimum tests required for one soil condition	3 creep	σ_1, T, S_1
Test conditions	$(\sigma_1, T), (\sigma_1, T_2), (\sigma_2, T_1)$	2 creep, 3-5 strength creep: $(\sigma/\sigma_{ult})^1, (\sigma_1/\sigma_{ult})^2$
number of tests required for reliable prediction, 1 soil condition	8 \pm 2	strength: vary $\dot{\epsilon}$ to determine ductile to brittle transition, vary T to determine dependence of σ_{ult} (T)
quality of fit for one soil condition	± 2 to 4x actual, approx. centered fit	4 creep, 6-8 strength ± 2 to 3x actual, exactly centered fit
procedures for evaluating parameters	<ul style="list-style-type: none"> - plot $\dot{\epsilon}_m/T$ vs $1/T$ to determine E - choose central T, get fitted $\dot{\epsilon}_m$ vs σ - determine n from $\dot{\epsilon}_m - \sigma$ - choose central $\sigma, T, \dot{\epsilon}_m$ for A - for varying S_1, use avg. n, E, -refit $\dot{\epsilon}_m$ for new A(S_1) - iterate for n, E - for varying D_r, compute avg. $\frac{30n\dot{\epsilon}_m}{3D_r}$ to fit new A. 	<ul style="list-style-type: none"> - correlate $\dot{\epsilon}_m$ with $(\sigma_1/\sigma_{ult})^m$ - for varying S_1, use avg n, - establish general $\sigma_{ult} = f(T, S_1)$ - recompute A(S_1)

TABLE 6.2
Summary of $\dot{\epsilon}_m$ prediction methods

6.2 Prediction of t_m

Three methods were used in attempting to predict the time to the minimum strain rate t_m . These are discussed in detail in Appendix B.3 and are summarized here. The first two methods combine the linear $\log \dot{\epsilon}_m - \log t_m$ correlation for MFS with each of the two $\dot{\epsilon}_m$ prediction methods described above.

For 40% Si 55% Dr MFS,

$$\dot{\epsilon}_m = 4.20 \times 10^{-4} t_m^{-1.21} \quad (6.9)$$

from Table A.5.9 in Appendix A.5. From the modified RPT method,

$$\dot{\epsilon}_m = 2.03 \times 10^{35} T \sigma_1^{10.4} \exp\left(-\frac{29781}{T}\right) \quad (6.10)$$

from equation (6.1) and Table 6.1. Combining leads to:

$$t_m = 7.89 \times 10^{-33} T^{-.83} \sigma_1^{-8.6} \exp\left(\frac{24714}{T}\right) \quad (6.11)$$

where t_m is in min, $\dot{\epsilon}_m$ is in /s, σ_1 is in MPa, and T is in $^{\circ}\text{K}$. The quality of this fit is shown in Figure 6.9(a) and in Figure B.3.1(a) in Appendix B.3, and indicates that 95% of the fitted t_m are within $\pm 3.3X$ the actual t_m .

Combining the stress ratio method for $\dot{\epsilon}_m$ prediction (equation 6.7) with the $\log \dot{\epsilon}_m - \log t_m$ correlation (equation 6.9) for 40% Si 55% Dr MFS leads to:

$$t_m = 0.174 \left(\frac{\sigma}{\sigma_{ult}}\right)^{-7.91} \quad (6.12)$$

where σ_{ult} is the ultimate strength from equation (6.5). This fit is very well-centered, with 95% of the fitted t_m within $\pm 2.5X$ the actual t_m , as shown in Figure 6.9(b).

A direct correlation between (σ/σ_{ult}) and t_m gives:

$$t_m = 0.170 \left(\frac{\sigma}{\sigma_{ult}}\right)^{-7.91}, r^2 = 0.92 \quad (6.13)$$

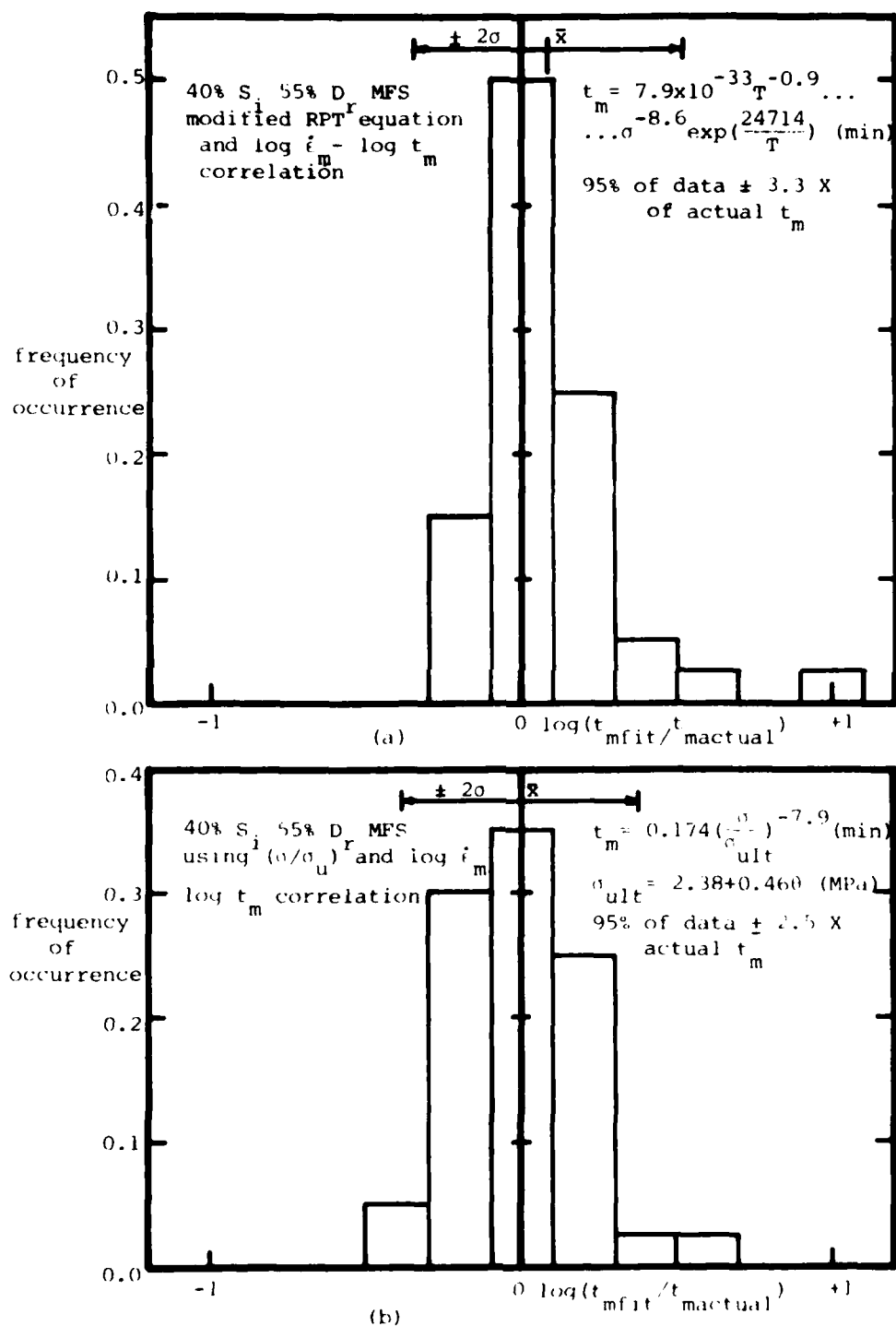


FIGURE 6.9 Histograms of fitted t_m using $\log i_m - \log t_m$ correlation

which is essentially identical to equation (6.12). Hence, these two procedures for obtaining t_m in terms of (σ/σ_{ult}) are completely analogous.

From Figure 6.9, it can be seen that both equations (6.10) and (6.12) yield fairly good results, with the method based on stress ratios providing a marginally better fit.

A third method for predicting t_m was also tried. This method is primarily based on the premise that the linear $\log \dot{\epsilon}_m - \log t_m$ correlation is due to an approximately constant strain at the minimum strain rate, and the relative insensitivity of the $\log \dot{\epsilon}_m - \log t_m$ plot to minor deviations from this "constant" value, as discussed in Section 5.1 and explained in Appendix B.1. By using an estimate of ϵ_m and a simple three-parameter (Singh and Mitchell 1968) creep model, an alternate relationship between $\dot{\epsilon}_m$ and t_m was obtained. This relationship was then combined with a $\dot{\epsilon}_m$ prediction method to yield predictions of t_m . As outlined in greater detail in Appendix B.3, this procedure yields results which are similar but slightly inferior to those based on the direct $\log \dot{\epsilon}_m - \log t_m$ correlation. This method is more pleasing from a fundamental viewpoint as it utilizes the very basis of the linear correlation to obtain the $\dot{\epsilon}_m - t_m$ relation. However, from an engineering viewpoint, the direct $\log \dot{\epsilon}_m - \log t_m$ correlation provides a far simpler and more reliable estimate of t_m .

The use of the $\log \dot{\epsilon}_m - \log t_m$ correlation in conjunction with a $\dot{\epsilon}_m$ prediction method was evaluated as a predictive tool

by using only a portion of the total dataset to obtain the model parameters. Using the results from only eight of the creep tests on 40% Si 55% Dr MFS, and ultimate strength evaluations from equation (6.5) based on numerous strength tests, both the modified RPT and stress ratio based $\dot{\epsilon}_m$ predictors and the $\log \dot{\epsilon}_m - \log t_m$ correlation were obtained. Then, the $\dot{\epsilon}_m$ predictors were used together with the $\log \dot{\epsilon}_m - \log t_m$ correlation to obtain predictions of t_m . The resulting comparison of the predicted and actual t_m are shown in Figure B.3.4 in Appendix B.3, and indicate that both methods predict t_m to within $\pm 3.7X$ the actual t_m for 95% of the data.

From this presentation, it can be seen that use of the linear $\log \dot{\epsilon}_m - \log t_m$ correlation in combination with one of the $\dot{\epsilon}_m$ prediction methods (modified RPT or stress ratio) does a fairly good job of fitting the t_m data as a function of the loading parameters. For the testing program on MFS, use of a relatively few tests (eight in the case of 40% Si 55% Dr MFS) were sufficient to ensure reliable prediction of t_m . Since a linear $\log \dot{\epsilon}_m - \log t_m$ correlation typically exists for individual degrees of ice saturation, these fitting and prediction methods for t_m are certainly applicable for different saturation levels. However, since this correlation does not appear to exist for varying relative density samples (see Figures A.5.9 and A.5.10 in Appendix A.10), this method is not easily generalized to include such a parameter.

6.3 Proposed Creep Models

While it is useful to be able to easily predict $\dot{\epsilon}_m$, and t_m , it is also desirable to be able to describe the entire strain-time or strain rate-time creep curves for a given material under specific loading conditions. While several creep models can describe primary creep behavior, such as the Singh-Mitchell (1968), Vyalov (1963) or Andrade $t^{1/3}$ (1910) models, few can describe the complete creep curve from primary through tertiary creep. Among the few that can model tertiary creep is one presented by Goughnour and Andersland (1968) for the creep of sand-ice materials. However, this model is rather complex with parameters not easily determined. A simple creep model that can accurately describe the entire creep curve over a wide range of loading conditions, and whose parameters can easily be determined experimentally is obviously desirable.

For partially saturated MFS, the following equation was found to fit the individual test data quite well:

$$\dot{\epsilon} = A t^{-m} e^{\beta t} \quad (6.14)$$

where A , m , β are experimentally determined. A similar equation was recently developed independently for ice by Assur (1979). For simplicity, this model (equation 6.14) is henceforth referred to as the "Assur-Ting" (AT) model. However, all of the proposed integrations and techniques for model parameter evaluation were developed solely by the author.

Integrating (6.14) for strains,

$$\epsilon = \epsilon_0 + A e^{\frac{\beta t}{i+1}} t^{1-m} S(t) - A e^{\beta} S(t_0) \quad (6.15)$$

where $S = \sum_{i=1}^{\infty} \frac{(-1)^i (\beta t)^i}{\prod_{j=1}^i (j-m)}$, $t_0 = 1$, $m \neq 1, 2, 3, \dots$

Details of this integration, together with the development and analysis of this model are found in Appendix B.4.

The following simplified procedure was developed to obtain the model parameters needed to fit data for an actual creep test. Using $t_0 = 1$ min.,

$$A = \dot{\epsilon}_0 / e^{\beta} \quad (6.16)$$

For the initial slope m_0 of the $\log \dot{\epsilon} - \log t$ curve,

$$m_0 = - \left. \frac{\partial \ln \dot{\epsilon}}{\partial \ln t} \right|_{t_0} = m - \beta t_0$$

$$\Rightarrow m = m_0 + \beta \quad (6.17)$$

At the minimum strain rate,

$$\ddot{\epsilon} = A t_m^{-m-1} e^{\beta t_m} [-m + \beta t_m] = 0$$

$$\Rightarrow m = \beta t_m \quad (6.18)$$

Combining (6.17) and (6.18),

$$\beta = \frac{m_0}{t_m - 1} \quad (6.19)$$

Then, by knowing $\dot{\epsilon}_0$ and m at t_0 and t_m for a given testing condition, the creep model parameters may be easily determined from equations (6.19), (6.18) and (6.16). This procedure is outlined in Figure 6.10. By using equation (6.14), the $\dot{\epsilon} - t$ curve may be readily obtained. By also knowing ϵ_0 at t_0 , the entire strain-time curve may be computed from equation (6.15) by evaluating the series S at each time. For typical creep tests carried well into the tertiary zone, between two and twenty terms of this series were required for three-digit

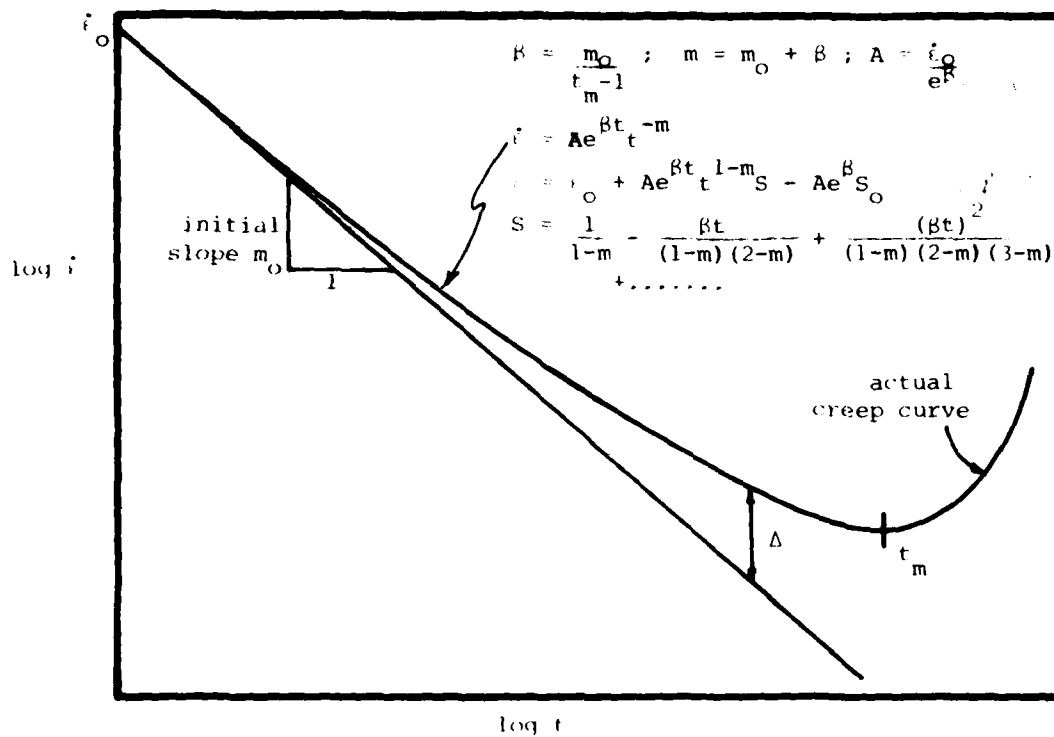


FIGURE 6.10 Proposed determination of parameters for Arrhenius-Ting model

accuracy of the series, with the larger number of terms being required at larger times. During the primary stage, only 4 or 5 terms were necessary; at the minimum strain rate, about 10 were used.

This technique for determining the "Assur-Ting" model parameters was applied to all of the 40% Si MFS constant load data. The resulting individually fitted parameters are summarized in Table B.4.1 of Appendix B.4. The actual and fitted $\log \dot{\epsilon}$ - $\log t$ curves for a series of creep tests at one stress and various temperatures are plotted in Figure 6.11. The resulting integrated strain-time curves are plotted in Figure 6.12 together with the actual data. While excellent agreement exists between the individually fitted creep models and the data for each test, remember that this procedure for obtaining the model parameters does not yield a least squares fit of the data. Instead, the model parameters were determined from a very simple method based on information at only two times, t_0 and t_m .

A comparison was made between the Assur-Ting creep model and the Singh-Mitchell creep model for one test. The resulting strain rate-time and strain-time curves are plotted in Figure 6.13 and show that while the Singh-Mitchell (SM) model does a good job of fitting the first portion of each curve, it is clearly inadequate for larger times. Note that in the $\log \dot{\epsilon}$ - $\log t$ curve, the length over which the SM model appears to fit the data is exaggerated by the log scale since the strain-time

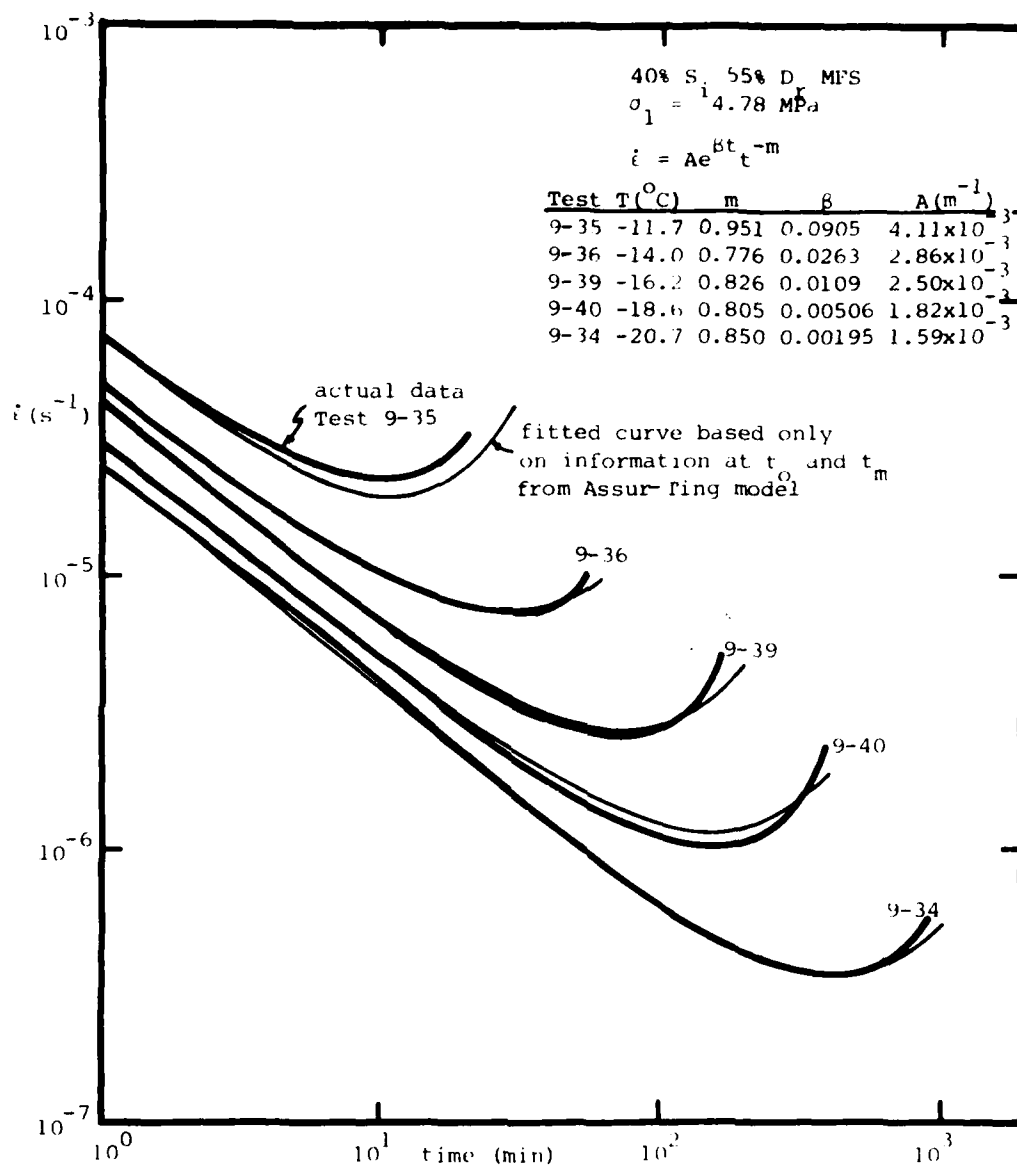


FIGURE 6.11 Comparison of actual and fitted creep curves for 40% S, 55% D, MFS data at $\sigma_1 = 4.8 \text{ MPa}$ from Assur-Ting model

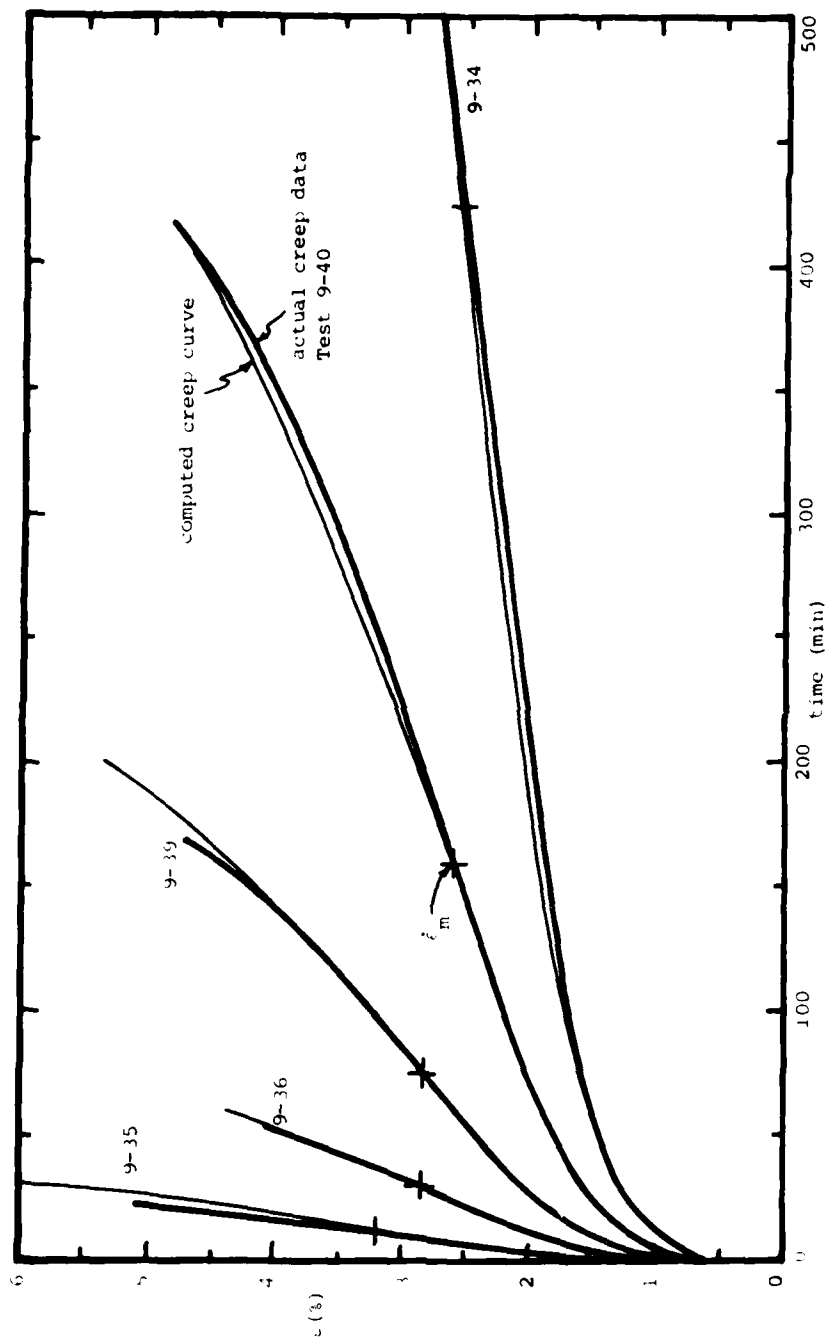


FIGURE 6.12 Comparison of actual and computed strain-time curves for 40% S₁ 55% D_{1r} MFS at $\sigma_1 = 4.78$ MPa

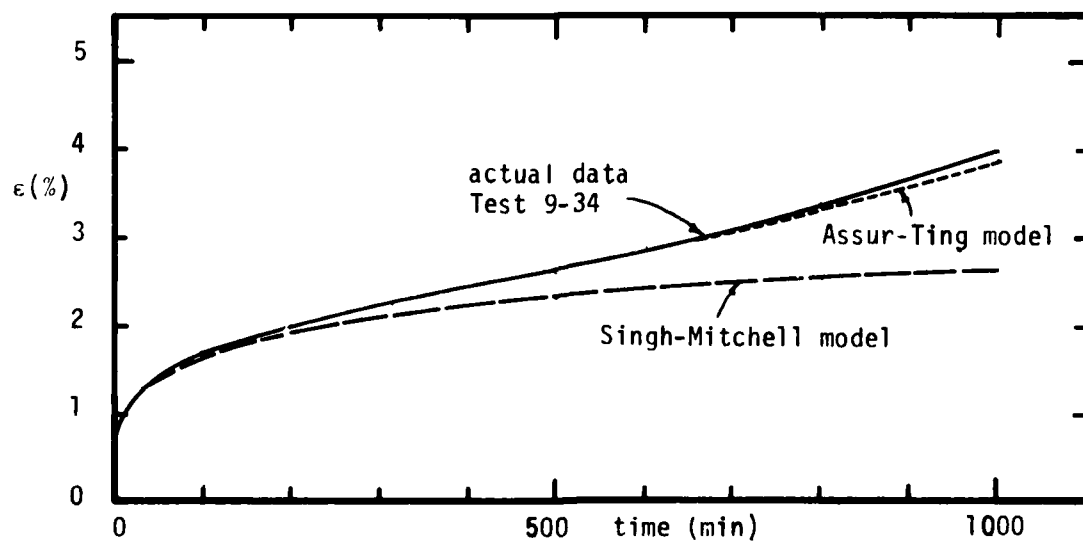
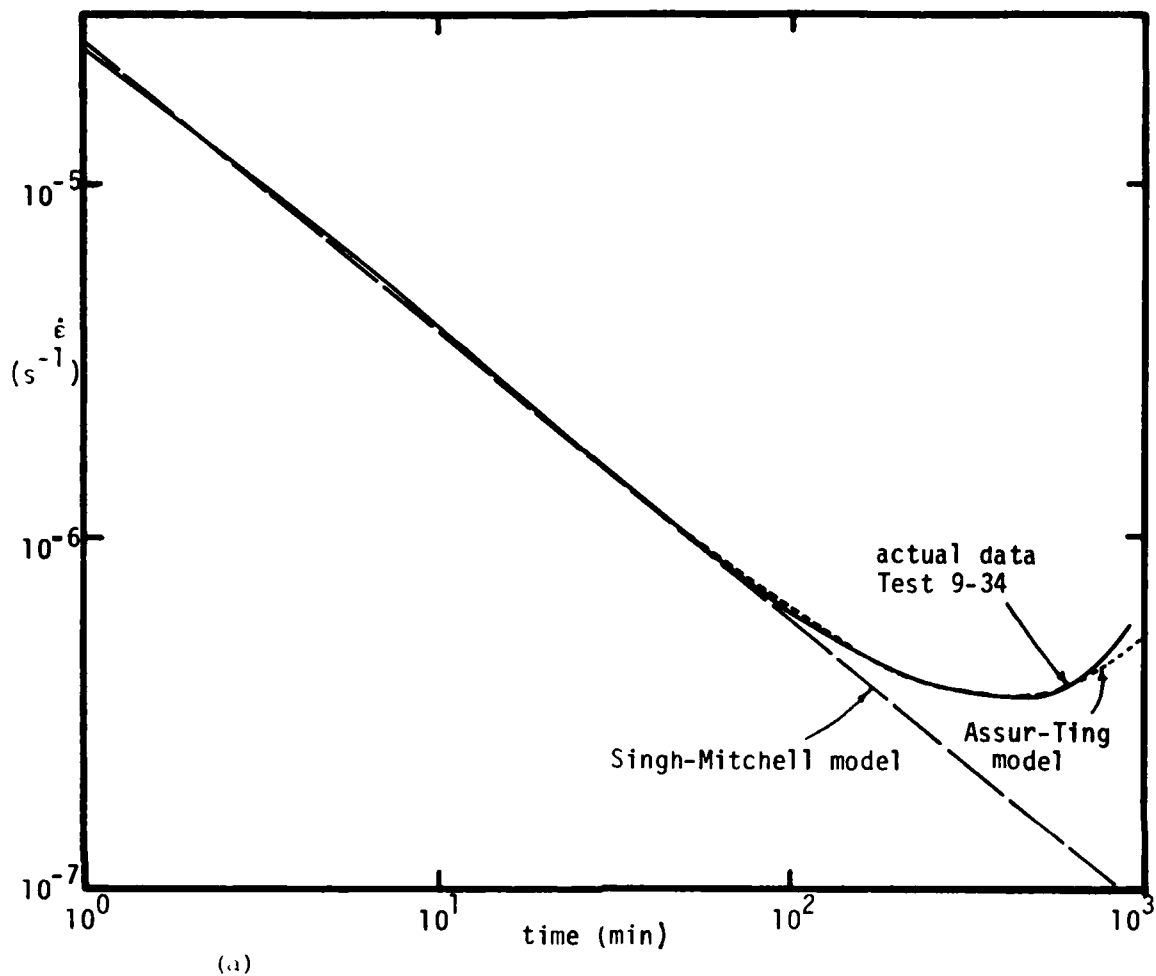


FIGURE 6.13 Comparison of Assur-Ting, Singh-Mitchell creep models with actual test data

plot shows that the SM model actually only accurately fits the data for the first tenth of the test.

Attempts were made to use the AT model for fitting and predicting the creep behavior of partially saturated MFS at varying stress and temperature. Extensive use was made of stress ratios based on the ultimate strength, as described by equation (6.15) and Appendix A.5. Although explicit use of σ_1 and T rather than stress ratios should yield comparable results, stress ratios were used exclusively due to the increased ease in fitting and plotting the data with one parameter rather than two.

Data from eight of the 40% Si 55% Dr MFS constant load creep tests gave the following correlations:

$$\begin{aligned}\dot{\epsilon}_O &= 0.019 \left(\frac{\sigma}{\sigma_{ult}} \right)^{2.96} & (/m) \\ m_O &= 0.78 \\ \epsilon_O &= -0.013 + 0.0426 \left(\frac{\sigma}{\sigma_{ult}} \right) & (6.20) \\ t_m &= 0.118 \left(\frac{\sigma}{\sigma_{ult}} \right)^{-8.78} & (m)\end{aligned}$$

These correlations very closely match the correlations obtained from using all 40 tests in the dataset. Combining equations (6.20) to obtain the creep model parameters leads to:

$$\begin{aligned}\beta &= 6.57 \left(\frac{\sigma}{\sigma_{ult}} \right)^{8.78} \\ m &= 0.78 + \beta & (6.21) \\ A &= \frac{0.0194 \left(\sigma / \sigma_{ult} \right)^{2.96}}{\exp(6.57 (\sigma / \sigma_{ult})^{8.78})}\end{aligned}$$

The fitted and predicted parameters and resulting predictions of $\dot{\epsilon}_m$ and $\dot{\epsilon}$ are summarized in Table B.4.2 in Appendix

B.4. Frequency histograms of the comparison between the predicted and actual $\dot{\epsilon}_m$ and ϵ_m are found in Figure 6.14, and indicate a scatter in $\dot{\epsilon}_m$ not too dissimilar from direct prediction using equation (6.1) or (6.6), and a fairly good prediction for ϵ_m . To provide a better indication of the quality of this fit, three predicted tests are plotted in Figures 6.15 and 6.16. These were chosen as they are indicative of a good fit, a large underestimation and a large overestimation of the $\dot{\epsilon}_m$ and the ϵ_m . The two extreme cases plotted represent approximately the worst predictions made by this model with the data used for parameter determination.

As can be seen from the results, the new creep model does fairly well as a predictive model. Although considerable over- and underestimation of the creep can occur for a given test condition, just as with the direct $\dot{\epsilon}_m$ and t_m predictions, such fluctuations may be due to sample variability rather than model deficiencies.

For saturated MFS, the $\log \dot{\epsilon}_m - \log t_m$ curve typically does not exhibit continuous upward concavity like the partially saturated MFS, as shown in Figure 6.17. Instead, a change in slope of the $\log \dot{\epsilon}_m - \log t_m$ curve exists during primary creep, typically at about 1.2% axial strain. This happens to coincide with the ϵ_m for polycrystalline ice, and supports the hypothesis that a change in the strength/deformation mechanism occurs in the frozen soil, as proposed in Section 5.3. Below this strain level, creep is probably more a function of the pore

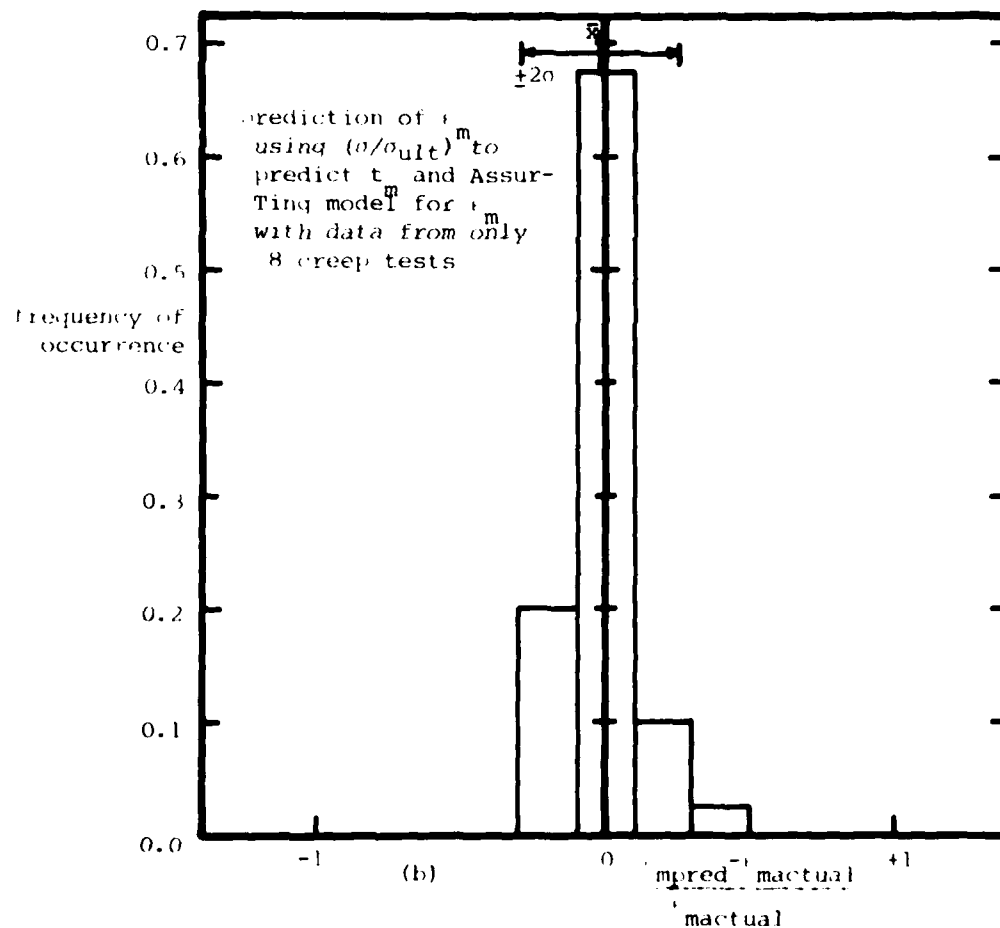
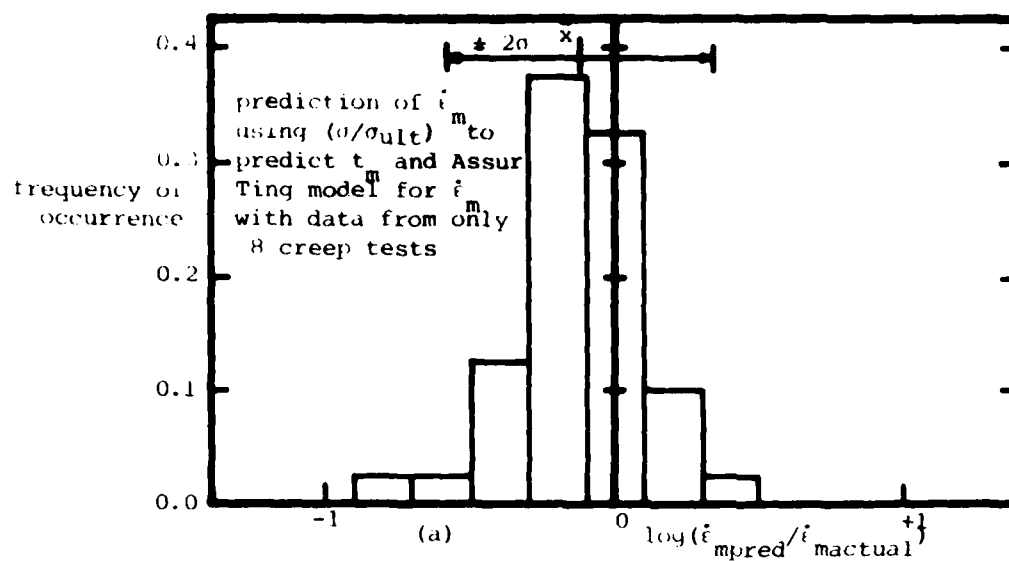


FIGURE 6.14 Comparison of predicted and actual $\dot{\epsilon}_m$ and $\dot{\epsilon}_m$ using Assur-Ting Model for 40% S_i 55% D_r MFS using data from 8 creep tests

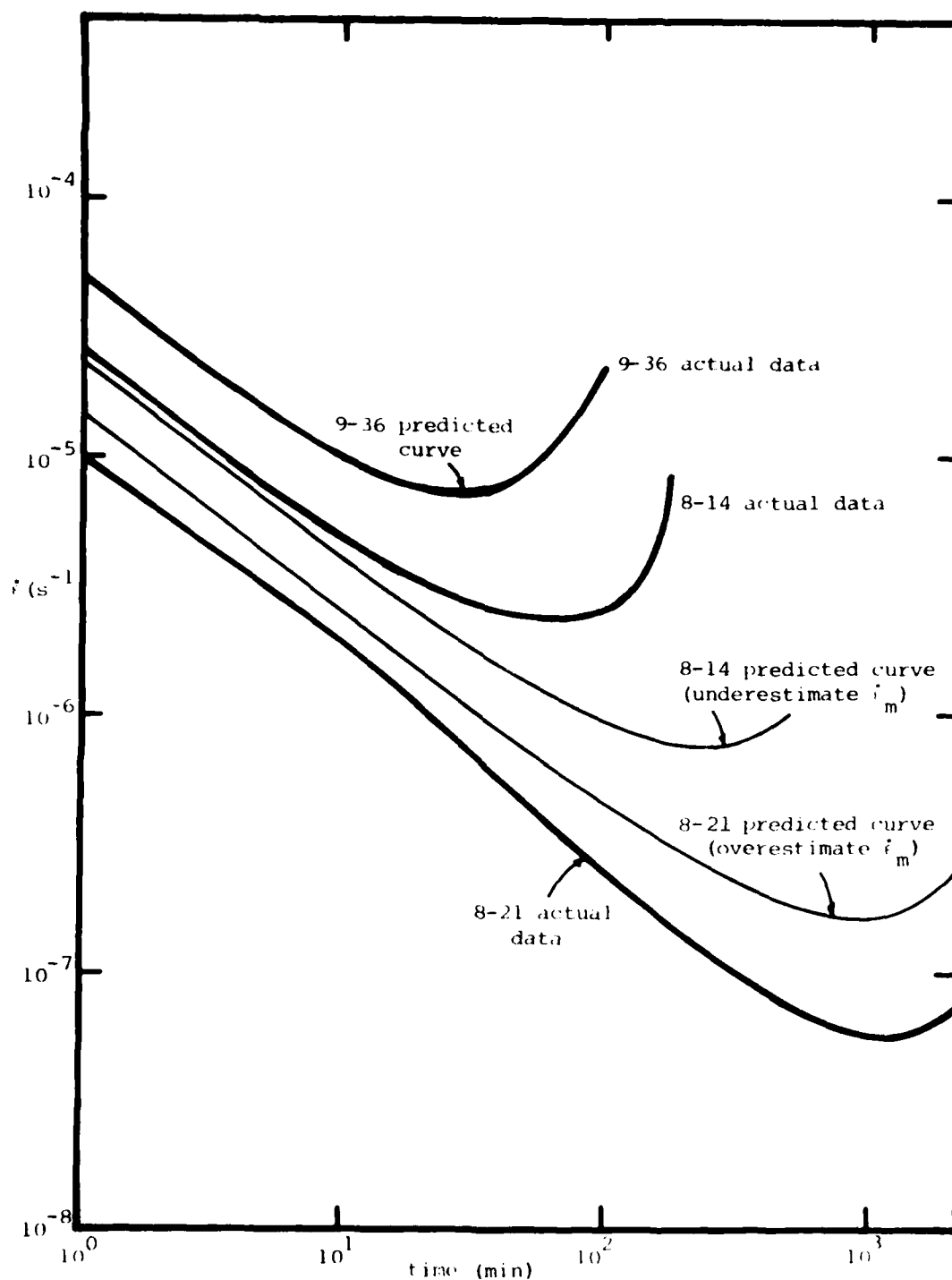


FIGURE 6.15 Comparison of $\log i - \log t$ curves from Assur-Ting model predictions and actual data

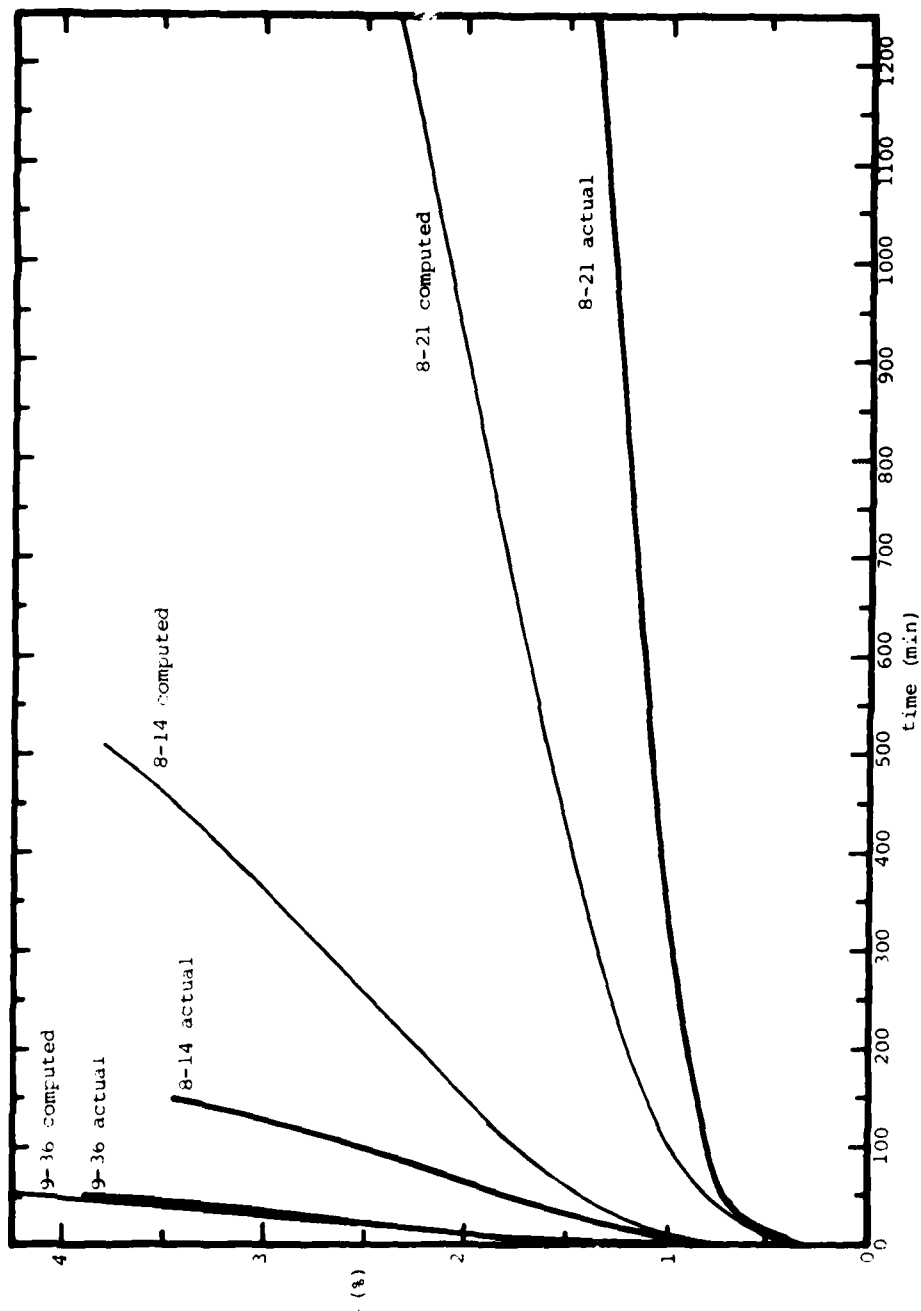


FIGURE 6.16 Comparison of strain-time curves from predictions and actual data

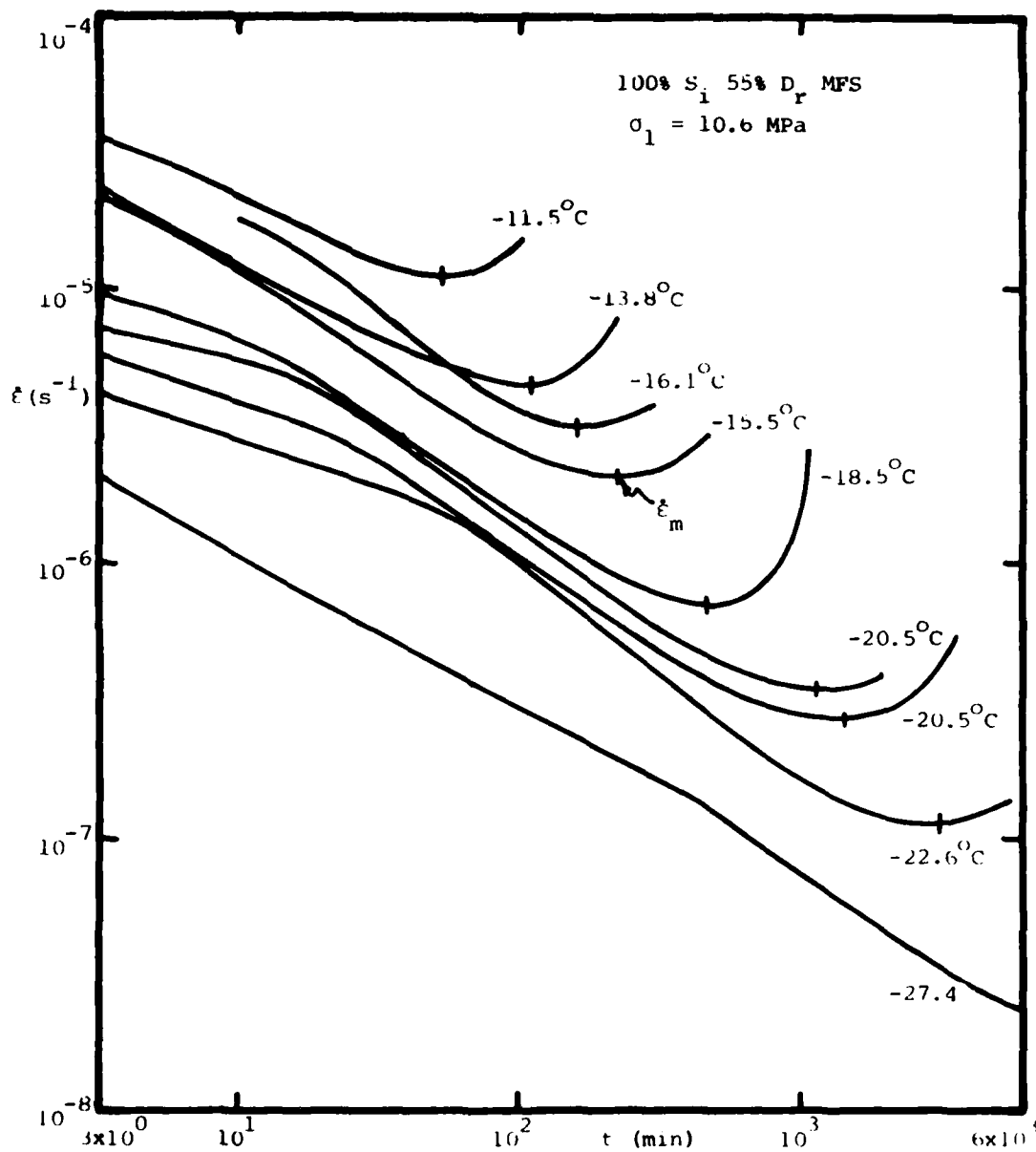


FIGURE 6.17 Results of creep testing on saturated 55 % D_r MFS at $\sigma_1 = 10.6 \text{ MPa}$, various temperatures

ice deformation (hence the low m value, similar to that for ice). At the larger strains where the ice can no longer supply as much resistance, the frictional strength of the sand skeleton is more fully mobilized, resulting in a steeper $\log \dot{\epsilon}$ - $\log t$ curve.

To model the saturated sand data, a modified creep model was developed. A Singh-Mitchell primary creep model is used for the initial 1% strain, then the previously described AT creep model fits the remainder of the curve:

$$\begin{aligned}\dot{\epsilon} &= A_1 t^{-m_1} & t_0 < t < t_\Delta \\ \dot{\epsilon} &= A_2 t^{-m_2} e^{\beta t} & t > t_\Delta\end{aligned}\quad (6.22)$$

as shown in Figure 6.18.

For the strain,

$$\begin{aligned}\epsilon &= \epsilon_0 + \frac{A_1}{1+m_1} (t^{1-m_1} - 1) \quad \text{for } t_0 = 1, m_1 \neq 1 \\ \epsilon &= \epsilon_\Delta + A_2 e^{\beta t} t^{1-m_2} S(t) - A_2 e^{\beta t_\Delta} t_\Delta^{1-m_2} S(t_\Delta)\end{aligned}\quad (6.23)$$

where S is defined in equation (6.15).

A simple procedure for obtaining the experimental parameters based on information at three times, t_0 , t_Δ and t_m is described in Appendix B.4. Table B.4.4 summarizes the individually fitted modified model parameters. The individual fit of one test is plotted in Figures 6.19 and 6.20. From these figures, it can be seen that the modified creep model does a very effective job of fitting both the $\dot{\epsilon}$ - t and ϵ - t data.

Fitting and prediction of the creep data for all values of σ_1 and T were made using all of the data. The correlations based on a portion of the data differed only slightly from

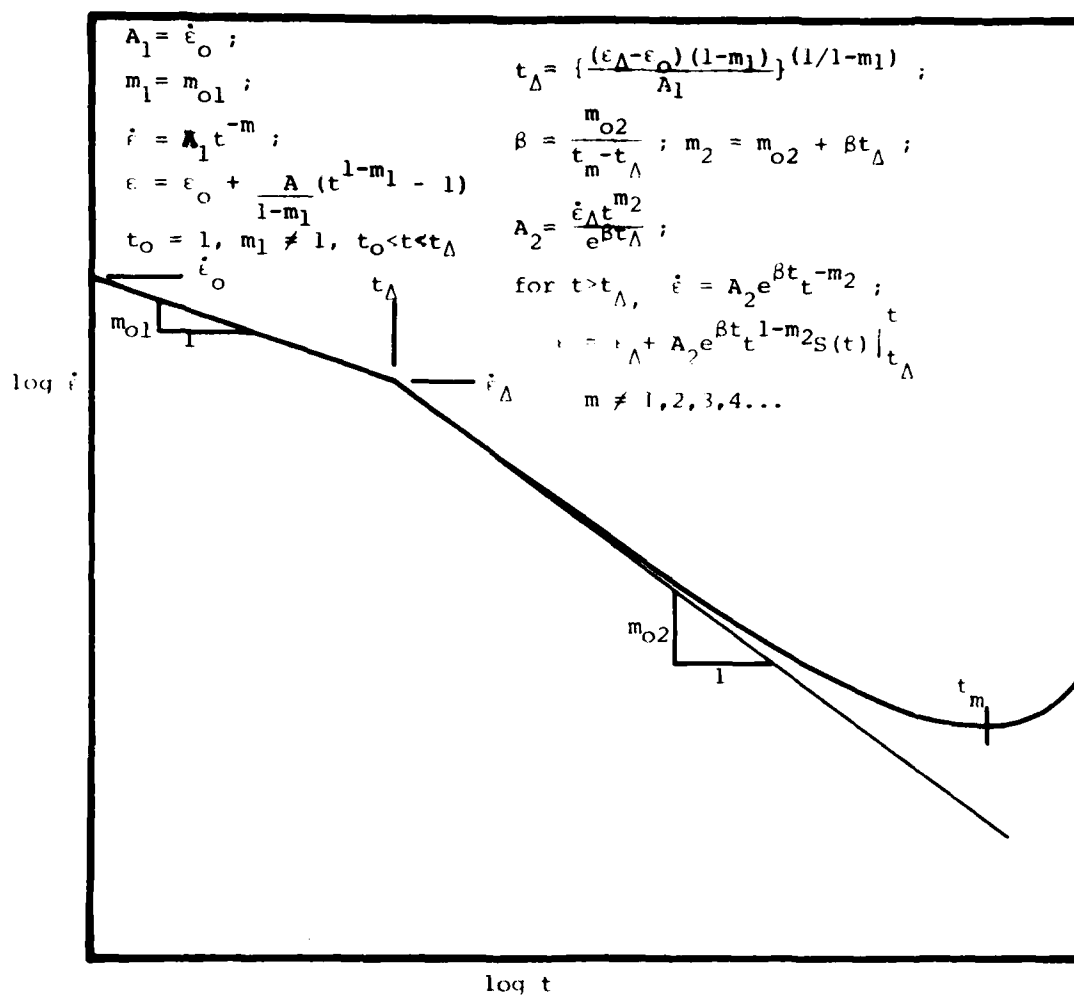


FIGURE 6.18 Determination of parameters for modified creep model for saturated frozen MFS

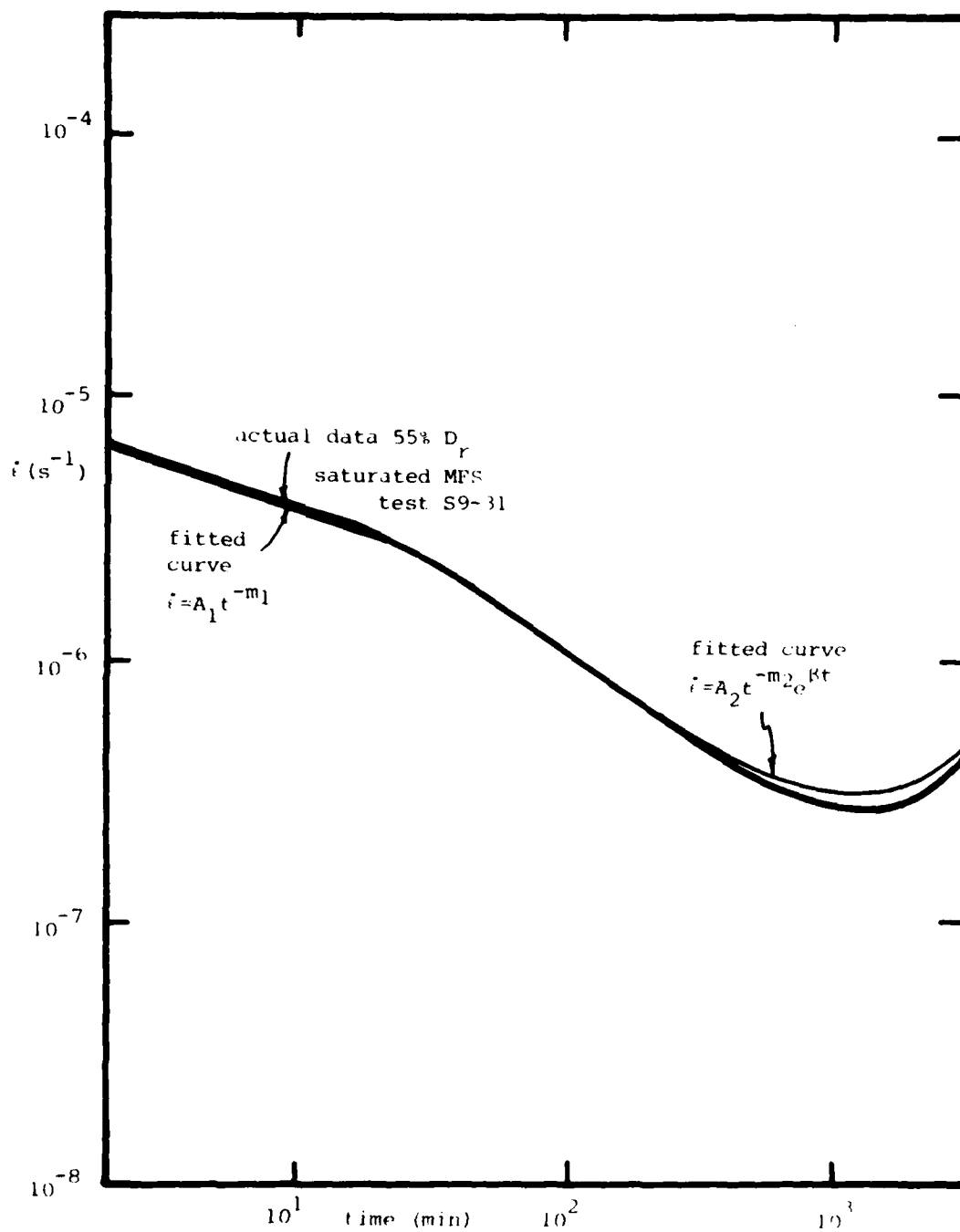


FIGURE 6.19 Comparison of modified creep model and actual data for saturated Manchester Fine Sand

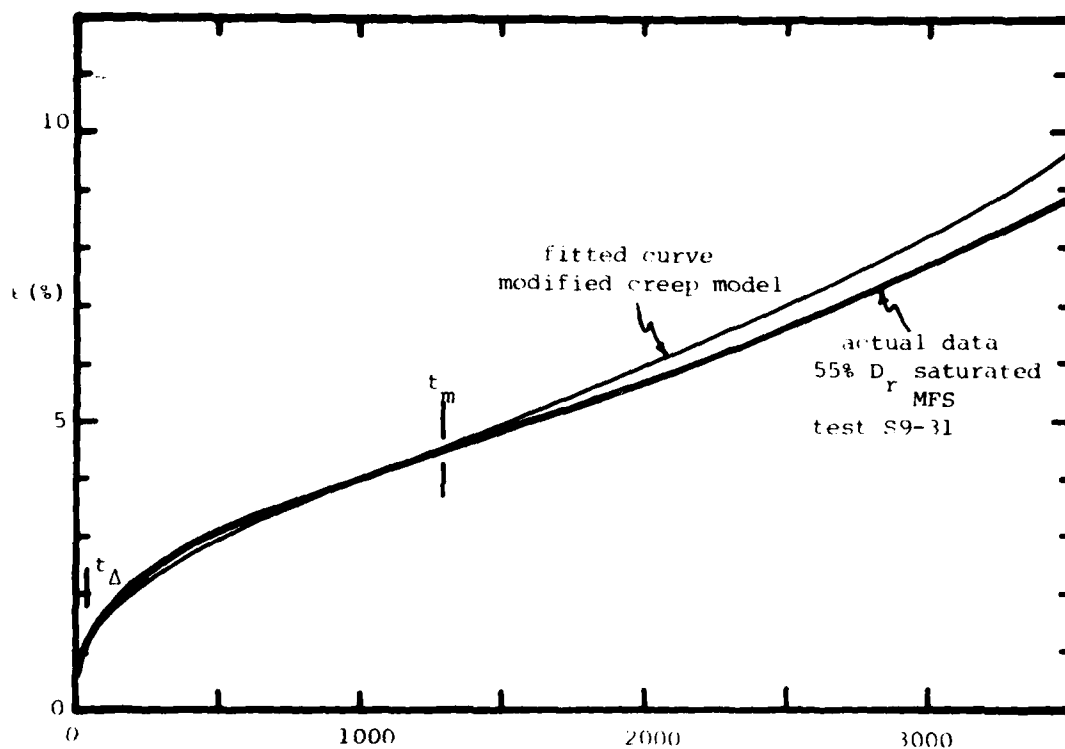


FIGURE 6.20 Comparison of strain-time curve from modified creep model with actual test for saturated MFS

those using all of the data. By using data from only 10 tests, the following correlations were obtained:

$$\begin{aligned}
 \epsilon_o &= -0.0065 + 0.0362\left(\frac{\sigma}{\sigma_{ult}}\right) & , r^2 &= 0.72 \\
 \dot{\epsilon}_o &= 0.139\left(\frac{\sigma}{\sigma_{ult}}\right) & (/m) & , r^2 = 0.97 \\
 m_{o1} &= 0.73 - 1.15\left(\frac{\sigma}{\sigma_{ult}}\right) & , r^2 &= 0.44 \\
 m_{o2} &= 1.06 - 1.37\left(\frac{\sigma}{\sigma_{ult}}\right) & , r^2 &= 0.29 \\
 t_m &= 0.0095\left(\frac{\sigma}{\sigma_{ult}}\right)^{-8.78} & (m) & , r^2 = 0.98 \\
 \epsilon_{\Delta} &= 0.0127 + 0.0038 (\pm 1 \text{ std.dev.})
 \end{aligned} \tag{6.24}$$

The details of the fitted and predicted parameters for each test are summarized in Table B.4.5 in Appendix B.4, together with the predicted $\dot{\epsilon}_m$ and ϵ_m . Figure 6.21 plots the frequency histograms of the comparisons between the actual and predicted $\dot{\epsilon}_m$ and ϵ_m , and indicate that the modified model typically overestimates both the minimum strain rate and the strain at the minimum strain rate.

Note that predictions of $\dot{\epsilon}_m$ based on the modified Assur-Ting model result as an additional benefit. Such use of these models constitutes the third method of $\dot{\epsilon}_m$ prediction mentioned earlier in this Chapter.

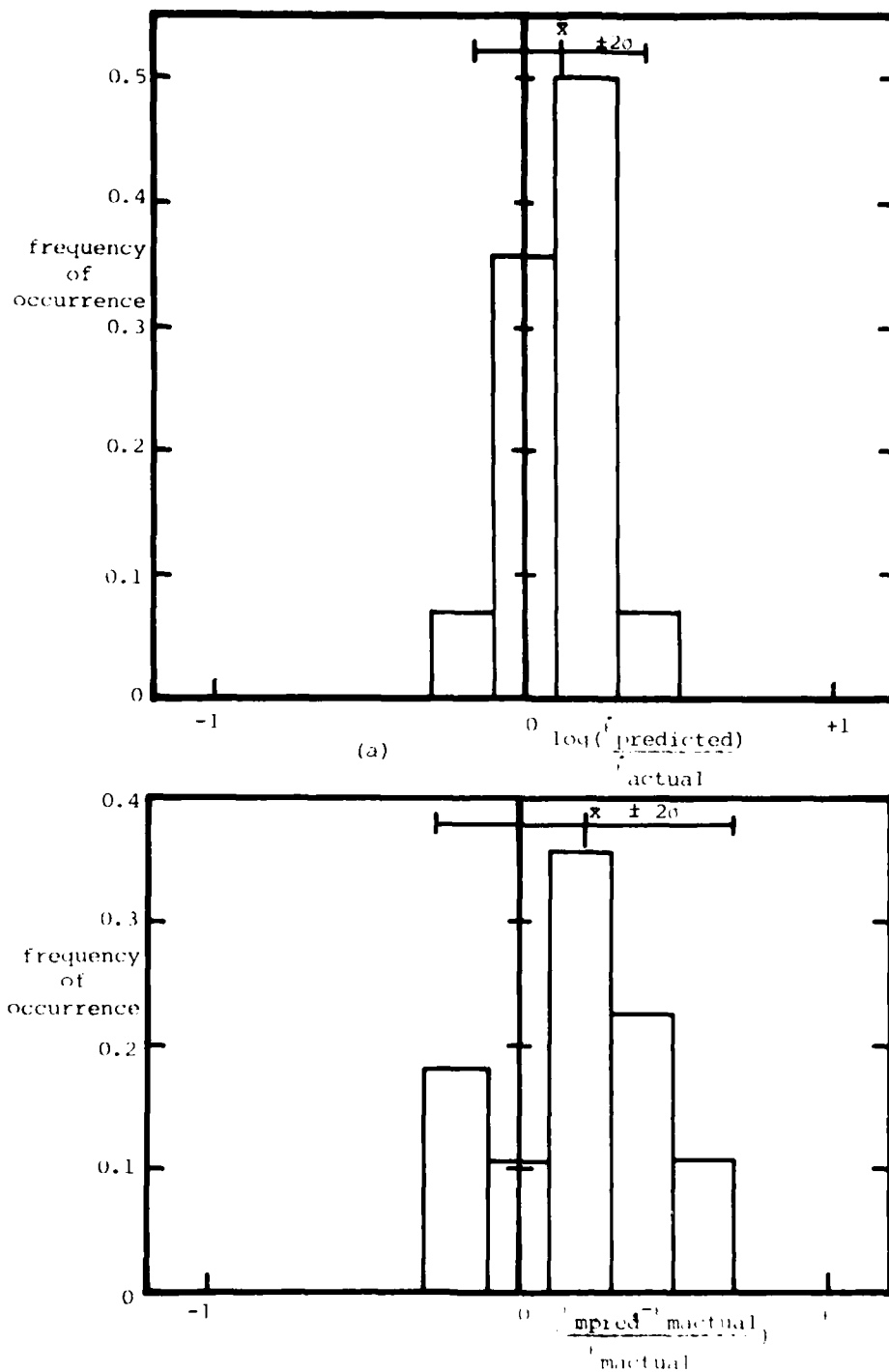


FIGURE 6.21 Comparison of predicted and actual i_m and c_m using modified creep model for saturated MPS using 10 tests to predict others.

6.4 Conclusions

The first five Chapters of this Report sought to understand the behavior of frozen soils from a qualitative viewpoint. By drawing upon the literature in ice, soil and frozen soil mechanics, various possible explanations for the observed behavior were proposed. These explanations were then evaluated through additional creep testing on various types of glass beads, Manchester Fine Sand and ice, allowing development of specific mechanisms controlling the strength and deformation of frozen sands. While such a qualitative model is extremely important conceptually, and allows the extrapolation of known behavior to unknown conditions, it can not serve as an analytical tool.

Chapter 4 summarizes the various available quantitative models for frozen soils. These have tended to be empirical or semi-empirical in nature. For creep, the bulk of available models predict only primary creep or are inordinately complex. Few have attempted to predict the minimum strain rate for frozen soils, which is often considered to be a failure criterion. The thrust of the author's research in the analytical area was first to develop simple empirical models capable of predicting the minimum strain rate and the time to this minimum, and then relatively simple creep models capable of describing all three stages of creep.

Regarding the prediction of the minimum strain rate, it can be seen that the Rate Process Theory (RPT) as described in Chapter

2 is not applicable for the overall creep behavior of frozen soils. By empirically modifying RPT with an additional σ_1^n term to better account for the stress dependence, and using a constant apparent activation energy E (equation 6.1), the creep data for a particular type of frozen soil can be fitted with some degree of success. The various parameters for this model can be easily evaluated from data from a series of constant load creep tests, as summarized in Table 6.2. Typically, the actual $\dot{\epsilon}_m$ differs from the fitted $\dot{\epsilon}_m$ by a factor of 2 to 4 times. When one expression is used to fit all of the MFS data at various degrees of saturation and relative density, this difference may be up to a factor of ± 5 times. By using data from as few as eight to ten creep tests, the modified RPT model can predict the $\dot{\epsilon}_m$ for each soil condition with little loss in reliability.

By establishing the ductile-to-brittle transition strength as a function of temperature through a careful program of strength testing, it is possible to express the stress and temperature dependence of a sample in terms of one parameter, the stress ratio σ/σ_{ult} (equation 6.6). This parameter considerably simplifies the mathematical expressions and procedures involved in making $\dot{\epsilon}_m$ predictions and also results in a slightly better reliability in fitting and predicting $\dot{\epsilon}_m$. The parameters for this model can be obtained from a series of creep tests and strength tests, as summarized in Table 6.2. Although the current procedure requires determining the strength at the ductile-to-brittle transition for different temperatures, it

may be possible that the strength measured at a standard strain rate would suffice. In that case, the stress ratio method for $\dot{\epsilon}_m$ prediction would be extremely attractive. However, additional experimental work is required to check this possibility.

To fit and predict the time to the minimum strain rate t_m , a combination of the linear $\log \dot{\epsilon}_m - \log t_m$ correlation with either the modified RPT or stress ratio $\dot{\epsilon}_m$ prediction methods results in a fairly good prediction of t_m . Use of the stress ratio in this case is particularly attractive as the t_m may be directly correlated with (σ/σ_{ult}) (equation 6.12). The Singh Mitchell creep model can also be used to predict t_m when combined with an $\dot{\epsilon}_m$ prediction method and an estimate of ϵ_m . However, this procedure, while fundamentally pleasing, is unnecessarily complicated.

For creep modelling of partially saturated MFS, a simple empirical tertiary creep model (the "Assur-Ting" model) has been developed which can accurately fit both the $\dot{\epsilon} - t$ and $\epsilon - t$ creep curves at all times for a great variety of testing conditions (equation 6.14). Using the simple procedure for determining the AT model parameters outlined in Figure 6.10, the $\dot{\epsilon} - t$ and $\epsilon - t$ curves may be computed. When this model is used as a fitting tool for all stresses and temperatures using stress ratios, it yields fits with the same fluctuation as for direct $\dot{\epsilon}_m$ or t_m fits, ie. ± 2 to $4X$ for $\dot{\epsilon}_m$. In addition, the model can predict the entire deformation-time behavior for frozen sands by using data from a relatively small

number of tests.

With saturated MFS, a break in the $\log \dot{\epsilon}$ - $\log t$ curve during primary creep probably indicates a change in deformation/strength mechanism for the frozen soil, possibly from ice-controlling to sand-controlling. This behavior can be fitted with the Singh-Mitchell primary creep model in the initial stages of a test, and the new Assur-Ting creep model for the remainder of the test after the break in the curve. This new modified creep model, together with the simple procedure for determining the model parameters outlined in Figure 6.18, can also accurately fit individual $\dot{\epsilon} - t$ and $\epsilon - t$ test data. When it is used as a predicting model for all stresses and temperatures by using stress ratios, however, it typically overestimates both $\dot{\epsilon}_m$ and ϵ_m . Although the parameters for the AT model can be obtained from a few creep tests, supplemental data from strength tests are required to allow the calculation of stress ratios.

The explicit use of stress and temperature in the AT creep models, rather than the stress ratios, is possible by fitting $\dot{\epsilon}_0$ and t_m as with the modified RPT for $\dot{\epsilon}_m$ and t_m . The resulting models would probably be similar in quality to those using stress ratios, but would require no strength testing. However, this approach involves much more complex mathematical expressions and procedures for extracting the model parameters.

The ultimate goal for quantitative modelling of the mechanical behavior of any material is an equation of state

linking strain rate, stress, temperature and various structural parameters. In this Chapter, empirical equations have been advanced which express the strain rate as a function of stress, temperature, relative density and degree of ice saturation. Work needs to be carried out to determine if the equations are indeed empirical equations of state. This requires first rewriting the creep models explicitly in terms of the applied stress and temperature. The resulting "equation of state" could then be experimentally verified with stress stage and temperature stage data. If the correspondence principle between strength and creep data previously described in Chapters 2 and 4 were valid in frozen soil, then strength data could also be compared with the predicted $\dot{\epsilon} - \sigma$ relation from the "equation of state". However, owing to the extremely complex equation of state which results from these models, this verification would not be a trivial task, especially since the qualitative physical mechanisms presented in Chapter 5 suggest different mechanisms as a function of strain level, degree of confinement, etc.

As has been shown, the Assur-Ting models work very well in fitting individual creep test data. However, their application as overall models to predict the influence of stress and temperature will potentially over- and underestimate the actual creep. Since the same variability occurs for all of the various $\dot{\epsilon}_m$, t_m and deformation models, this scatter is attributed primarily to sample variability rather than model error. Con-

sequently, another area requiring additional work involves this apparent scatter. Structural parameters other than relative density and degree of ice saturation are probably needed to define the structure of frozen soil systems, just as it is now well established that fabric and anisotropy play an important role in strength-deformation characteristics of dry sand (Ladd et al. 1977). Improved test conditions (ie. better sample alignment, improved end restraint, reduced sample variability, etc.) may also be warranted.

Model evaluation and development by the author has been restricted to only one state of stress, uniaxial (unconfined) compression. Other stress states must eventually be included, beginning with a much more thorough investigation of strength and creep behavior as a function of confining stress level. In addition, carefully controlled creep and strength testing at temperatures closer to the melting point need to be undertaken to see if the proposed prediction methods and creep models are still applicable above the current test temperature range for MFS, ie. less than -10°C .

CHAPTER 7 - SUMMARY AND CONCLUSIONS

Frozen soil is an exceedingly complicated material, since its major components, ice and soil themselves possess complex behavior and physico-chemical and mechanical interaction. Frozen soil typically possesses large short-term strength compared with its components, particularly at low confining stresses (see Figures 4.3 and 4.8), while exhibiting a large creep susceptibility (see Figure 4.11), and temperature and stress dependence. This Report has sought to provide qualitative explanations for these and other observed mechanical behavior by systematically examining all available data on frozen soil. Specifically, the Report sought to develop and quantify the various physical mechanisms controlling strength and deformational behavior. This Report also sought to develop improved mathematical relationships for modelling and predicting the the creep behavior frozen sands subjected to unconfined compressive loading.

By drawing upon an extensive literature survey of ice and frozen soil, creep and strength test data on frozen Manchester Fine Sand from the Martin et al. (1981) research on Rate Process Theory, and the results of creep tests performed on glass beads made wetting and nonwetting, various mechanisms of strength were proposed, discussed, evaluated and quantified. The physical mechanisms which probably control the mechanics of frozen soil, as summarized in Figure 5.11 for the unconfined compression of frozen sand, are as follows:

(1) an ice strength, which is slightly greater in pore ice than in normally tested bulk ice due to an altered structure, deformational constraints and different stress states and strain rates in the pores; this component accounts for between a third to a half of the total strength of frozen sand at zero total confining stress;

(2) a soil strength, which consists of interparticle friction, particle interference and dilatancy effects; it is mainly a function of the effective (intergranular) stress acting on the soil skeleton, which unfortunately can not be directly measured in frozen soil;

(3) a mechanical interaction between the soil and ice through structural hindrance, which depends on the adhesional tensile and shear strengths developed at the ice/unfrozen water/soil grain interface; this component accounts for a significant portion of the overall frozen soil resistance; and at low confining stresses results in a synergistic response, ie. the composite strength is greater than the sum of the component resistances;

(4) a mechanical interaction through dilatancy effects, in which any tendency of the soil skeleton to dilate results in a positive increment of "effective" confining stress; this component depends on the development of an adhesional tensile strength at the ice/unfrozen water/soil grain interface and contributes to the strength of dense frozen sands.

The above mechanisms of strength provide a qualitative explanation for the observed behavior of frozen soil, as presented

in Section 5.3 and as summarized below:

(1) the ice matrix controls the strength and deformation behavior of the frozen sand system at low strains and confining stresses, both by directly carrying the applied load and due to mechanical interaction with the soil; at greater strains (above about 1% for medium-dense sands), the mechanisms attributed to soil strength and interaction become more important;

(3) significant overall adhesional strength exists between ice and soil, in spite of the unfrozen water film separating the two, sufficient to greatly affect the mechanical behavior of the frozen soil system;

(4) as the confining stress increases, strengthening of the pore ice occurs due to crack inhibition and closure; above about 40 MPa, local pressure melting of the pore ice results in a decreased ability of the ice to resist soil skeleton deformations and hence a decreased overall measured strength; above 110 MPa, essentially global pressure melting occurs; an observed slight increase in strength with increased confinement above 110 MPa is caused by a Skempton "B" parameter less than unity due to a decreased soil skeleton compressibility;

(5) once the sand concentration is sufficient to cause grain/grain contacts, an increasing relative density in the sand results in a rapidly increasing soil strength and decreasing creep susceptibility; even greater strengthening of the frozen soil system occurs due to dilatancy in the medium-to-dense range;

(6) an increasing ice saturation results in an increased

overall strengthening of the frozen soil system due to a greater load carrying capacity in the ice and increased mechanical interaction due to structural hindrance;

(7) a decreasing temperature results in increasing strength due to a strengthening of the ice matrix.

The nature of the linear $\log \dot{\epsilon}_m - \log t_m$ correlation has been examined. By using simple creep models such as the secondary creep and Singh-Mitchell (1968) creep models, this linear correlation is shown to be the result of an apparently constant strain ϵ_m at the minimum strain rate, and the relative insensitivity of a $\log \dot{\epsilon}_m - \log t_m$ plot to small deviations from a constant value of ϵ_m .

Simple quantitative models for describing the uniaxial (unconfined) creep behavior of frozen sands at various temperatures, stresses, degrees of ice saturation and relative densities were developed. This research first concentrated on fitting and predicting the minimum strain rate $\dot{\epsilon}_m$ and the time t_m to this minimum strain rate, and then the entire strain rate-time and strain-time creep curves.

Two main methods for fitting and predicting $\dot{\epsilon}_m$ were used. The first, the "modified RPT method", requires data only from creep tests for parameter evaluation. The second, the "stress-ratio method", uses both creep and strength data. These strength tests define a reference ultimate strength as a function of temperature. In this research project, the reference strength was evaluated at a visually determined ductile-to-

brittle transition point. While both approaches yield fairly reliable fits and predictions of the minimum strain rate (typically ± 2 to 4 times the actual value for a given soil condition), the stress ratio method involves a much simpler equation and fitting procedures since only one parameter accounts for both stress and temperature. Table 6.2 presents the procedures for parameter evaluation, together with guidelines for the number and type of tests required, for both methods.

The modified RPT method can be combined with a linear $\log \dot{\epsilon}_m - \log t_m$ correlation to predict the time t_m to the minimum strain rate. Alternatively, the t_m can be directly correlated with the stress ratio. Each of these t_m procedures yields fits and predictions of similar reliability to the results.

The research developed a new empirical relationship capable of describing the entire strain-time curve, similar to that independently formulated by Assur (1979) for the creep of ice. For partially saturated frozen sand, the "Assur-Ting" model employs the simple relationship:

$$\dot{\epsilon} = A t^{-m} e^{\beta t}$$

where the parameters A , m and β can be easily evaluated from data obtained shortly after load application and the time to the minimum strain rate. Figure 6.10 outlines this procedure, which enable high quality fits of individual test data and/or fairly reliable predictions of the entire $\dot{\epsilon} - t$ and $\epsilon - t$ curves from a relatively limited number of tests. For 40%

ice saturated MFS, these procedures yielded predictions of $\dot{\epsilon}_m$ within ± 3 times and ϵ_m within $\pm 30\%$ of the actual values using data from only 8 creep tests, together with the strength data necessary for evaluation of the "ultimate" strength.

This curve fitting technique was extended to saturated frozen sands by combining the Assur-Ting model with a short segment of the Singh-Mitchell creep model at low strains. As with the partially saturated sand data, a simple parameter evaluation procedure, outlined in Figure 6.18, yields high quality fits of both the strain-time and strain rate-time data for individual tests. By correlating the various parameters and time to the minimum strain rate with the applied stress ratio from a relatively small number of tests, this modified model yields fairly reliable (albeit conservative) predictions of the creep behavior. Using data from 10 creep tests, this modified model yielded predictions of $\dot{\epsilon}_m$ within 3 times and ϵ_m within 70% of the actual values.

APPENDICES

APPENDIX A.1 Properties of Glass Beads

Four types of glass beads were chosen for creep testing in the frozen state. Two different gradations, MS-M and MS-XPX and two different surface treatments, waterproofed (WP) and nonwaterproofed, were used. The MS-M size beads are similar in gradation to Manchester Fine Sand and are manufactured by Ferro Corporation, Cataphote Division, PO Box 2639, Jackson, Mississippi 39205. The manufacturer classifies the beads as "Class III Microbeads Glas-Shot", and makes them from high-grade glass as an abrasive for blasting and cleaning. According to the manufacturer's specifications, the beads are spheroidal in shape, containing not more than fifteen percent irregularly shaped particles and not more than three percent angular particles. The waterproofing consists of an integral molecular film of silicone material applied to the beads at 200°C. Owing to the proprietary nature of the surface treatment, additional details on the nature and type of treatment are not available from the glass bead manufacturer.

Table A.1.1 summarizes the results of tests performed to establish the reference characteristics and mechanical behavior of the unfrozen beads. Grain size curves are found in Figure A.1.1. CIDC loading triaxial tests were carried out on MS-M and MS-M WP samples prepared by dry vibration on a shaking table, then sheared at 0.03 % strain/sec in a MIT-modified Wykeham Farrance triaxial cell. Samples sheared wet and dry indicate that the presence of water has little effect on the

frictional characteristics of the unfrozen beads. Also, the effect of varying confining stress in the range 0.2 to 0.6 MPa had relatively little effect on the friction angle for either type of bead. Overall, however, the treated beads possess a lower friction angle than the untreated beads. A summary of these triaxial tests, together with detailed stress-strain curves for each test, are found in Table A.1.2 and Figures A.1.2 and A.2.3.

In order to better examine the particle shape, surface texture and nature of the surface treatment, scanning electron micrographs were taken of each type of bead at various levels of magnification. These are found in Figures A.1.4 through A.1.7. As can be seen from a comparison of the 5000X micrographs of the waterproofed and nonwaterproofed surfaces, the treated (waterproofed) surface has a greater surface roughness due to the coating, although it possesses a lower overall friction angle.

Property	MS-M	MSM WP	MS-XPX	MS-XPX WP
nominal size ranges (US sieve numbers)	60-200	60-200	20-40	20-40
surface treatment	none	waterproof	none	waterproof
specific gravity	2.50	2.47	2.51	2.51
γ_d max (t/m ³) *	1.552	1.585	-	-
γ_d min (t/m ³) **	1.422	1.452	-	-
drained friction angle	36.6°	33.9°	-	-
axial strain at peak stress	2.2%±	2.7%±	-	-
average D_r of samples	81%	70%	-	-

* by dry vibration

** by dry pluviation

TABLE A.1.1 Properties of glass beads

test no.	test run wet or dry	σ'_3 (MPa)	u_f (MPa)	$\frac{\sigma'_1 - \sigma'_3}{2}$ (MPa) peak	$\frac{\sigma'_1 + \sigma'_3}{2}$ (MPa) peak	ϵ_{peak} (%)	ϕ (°)	α (°)	γ_d (t/m ³)
MSM U1	dry	0.199	-	0.296	0.495	2.66	36.7	30.9	-
MSM U2	wet	0.196	0.098	0.291	0.488	2.00	36.8	30.9	-
MSM U3	dry	0.593	-	0.867	1.460	1.78	36.4	30.7	1.502
						Avg.	36.6°		
MSMWP U2	dry	0.585	-	0.746	1.330	2.8±	34.1	29.3	1.555
MSMWP r5	dry	0.198	-	0.237	0.436	2.94±	33.0	28.6	1.551
MSMWT J6	wet	0.196	0.098	0.256	0.452	2.27	34.5	29.5	1.527
							33.9°		

TABLE A.1.2

Summary of CIDC loading triaxial tests on unfrozen glass beads

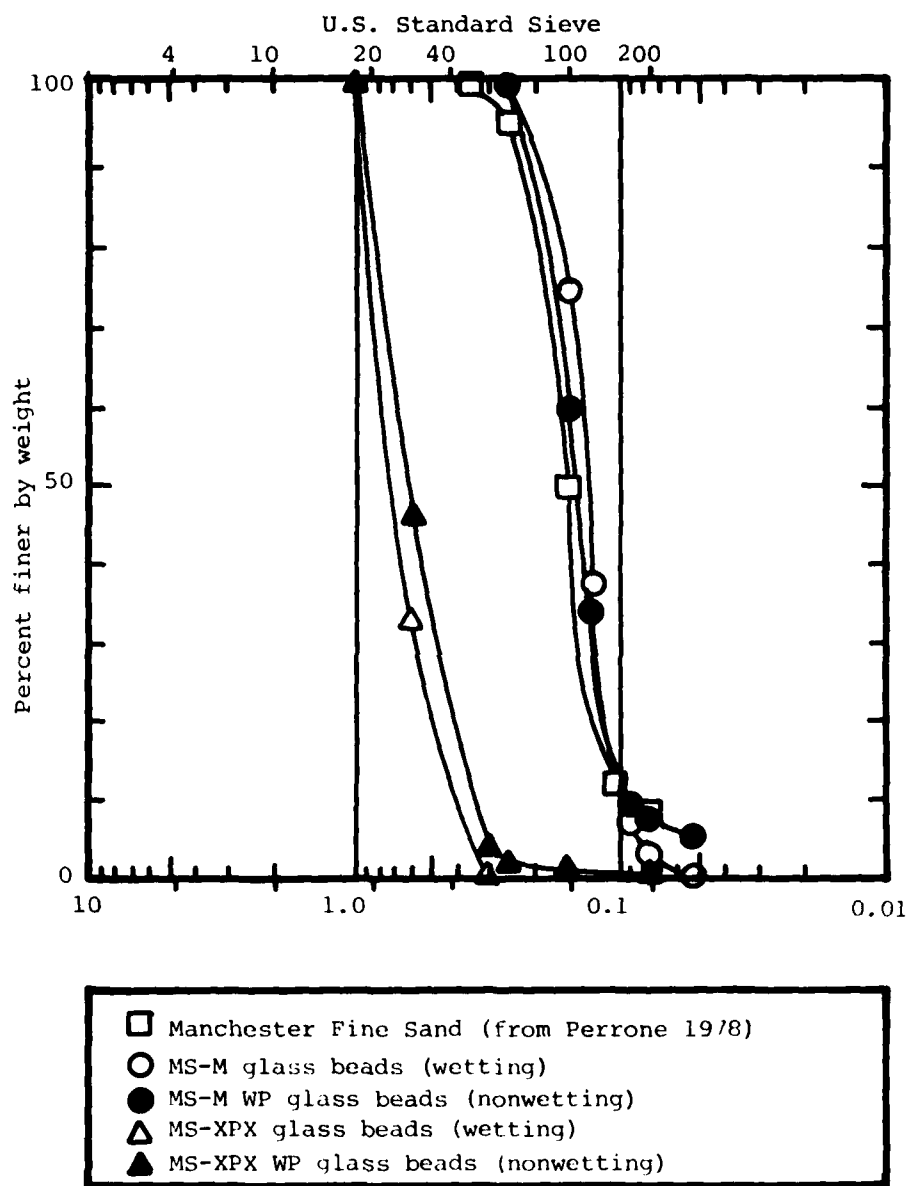


FIGURE A.1.1 Grain sizes of tested materials

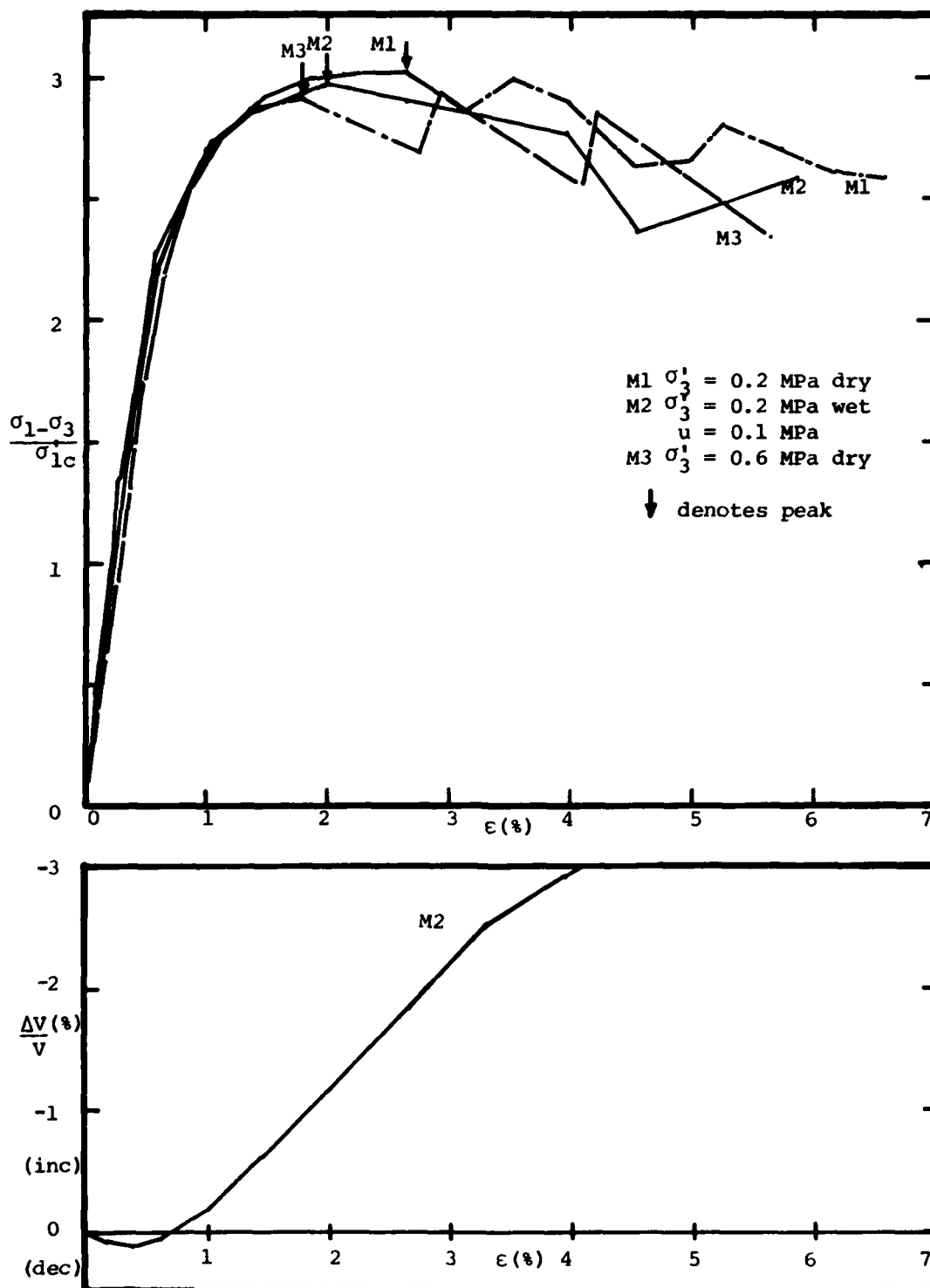


FIGURE A.1.2 Results of CIDC tests on MS-M glass beads

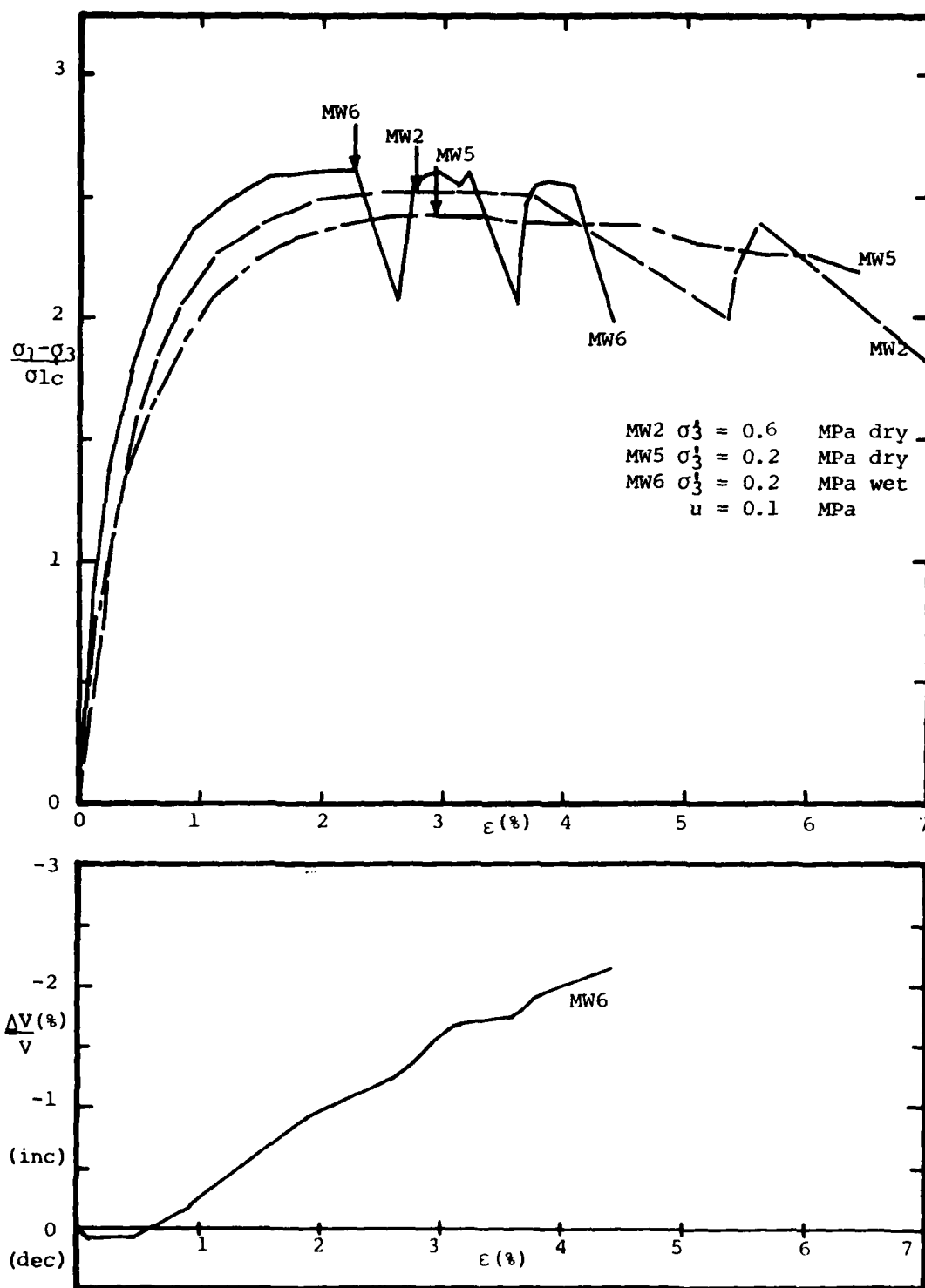


FIGURE A.1.3 Results of CIDC tests on MS-M WP glass beads

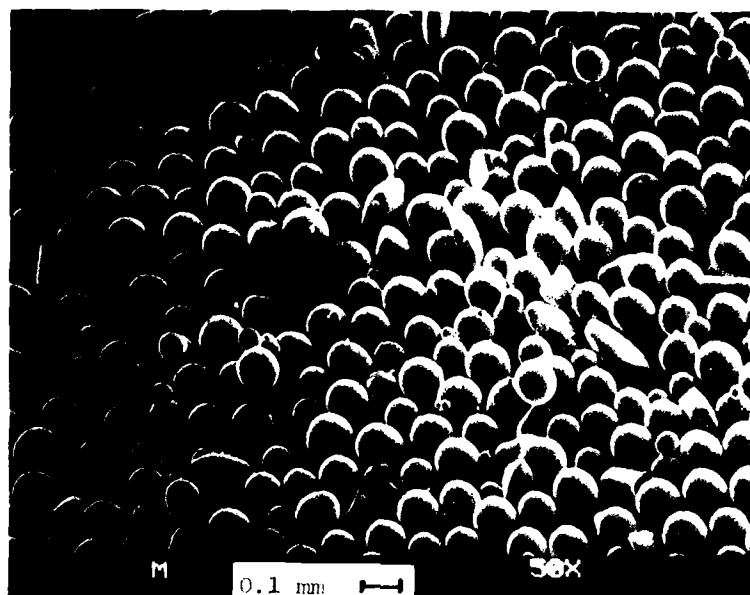


FIGURE A.1.4 Scanning electron micrographs of MS-M glass beads

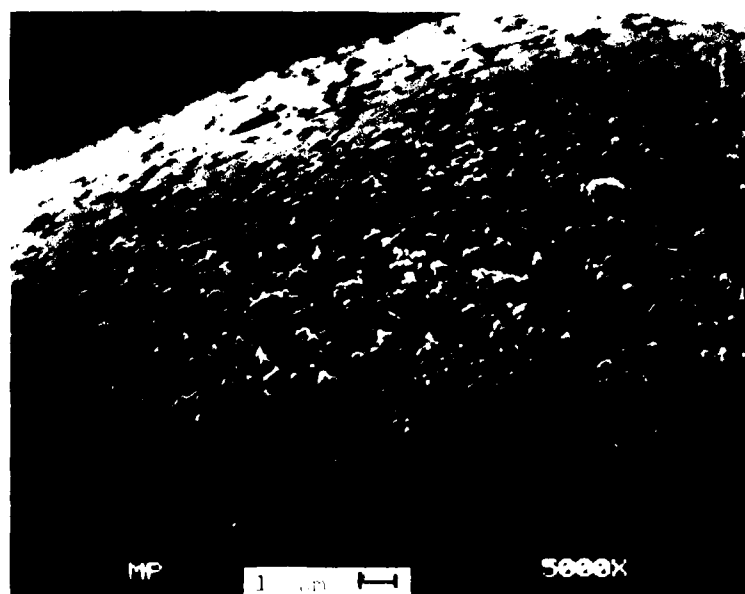
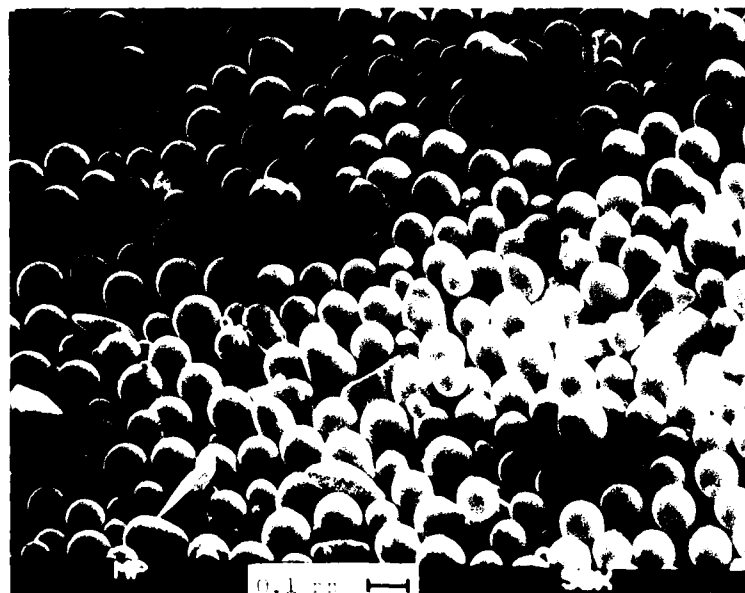


FIGURE A.1.5 Scanning electron micrographs of MS-M WP (nonwetting) glass beads

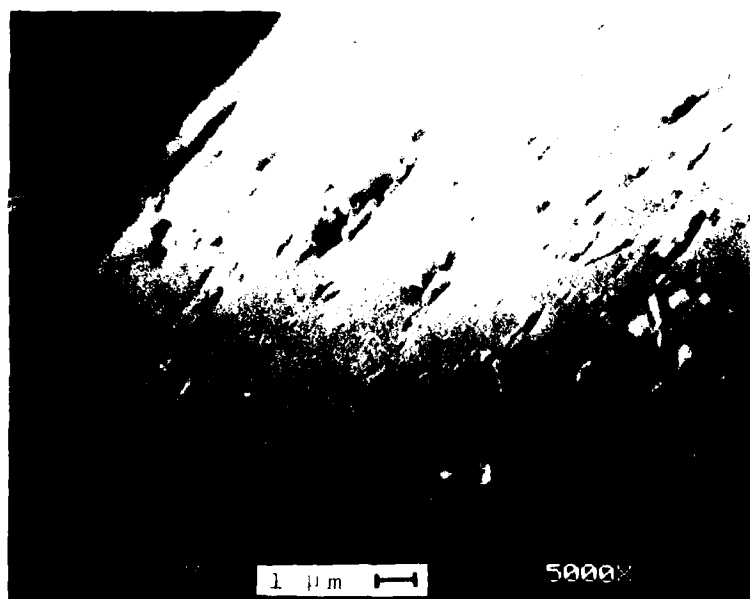
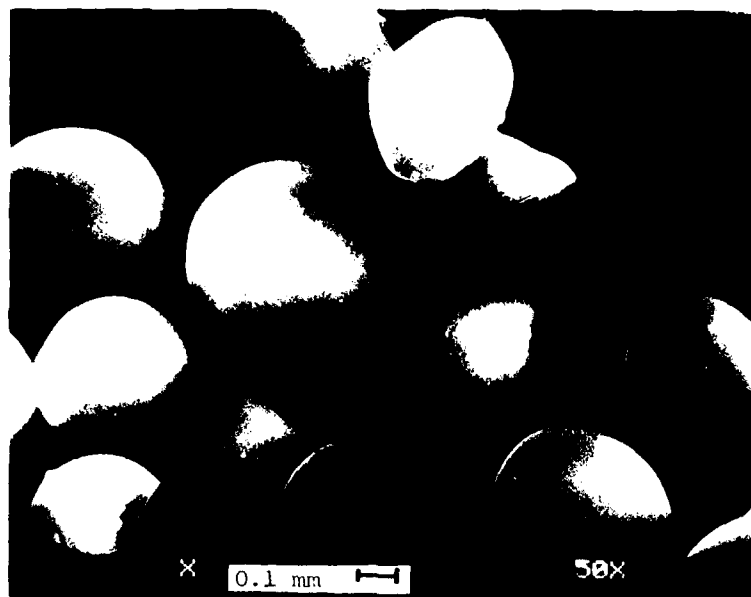


FIGURE A.1.6 Scanning electron micrographs of MS-XPX glass beads

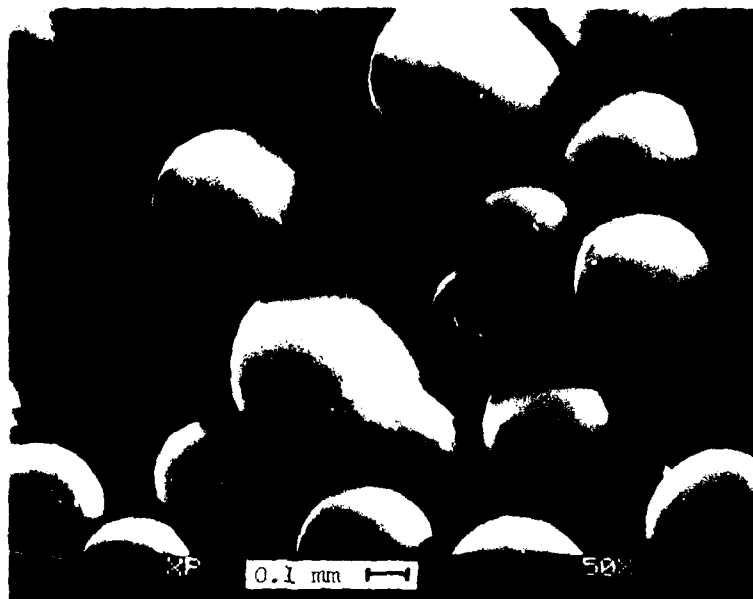


FIGURE A.1.7 Scanning electron micrographs of MS-XPX WP (nonwetting) glass beads

APPENDIX A.2 Sample Preparation and Testing for Unconfined

Creep of Saturated Frozen Glass Beads

The preparation of the frozen saturated glass bead samples for creep testing entailed several stages: (i) dry vibration, (ii) saturation, (iii) freezing, and (iv) ejection. Preparation was carried out in molds designed for the preparation of Manchester Fine Sand samples using the undercompaction method described in Martin, Ting and Ladd (1981). Figure A.2.1 shows a schematic diagram of the mold. During stage (i) of the preparation, parts 2 through 5 were bolted together with four bolts (part 7), as glass beads were poured into the vibrating mold. After the mold was full of vibrated beads, part 2 was unbolted gently, and the top was scraped flat and was cleaned to ensure a squared top. The entire mold was then bolted together with bolts 6 and 7 to ensure a vacuum-tight seal.

The entire mold was then evacuated from the bottom and top through ports 9 and 10, as in Figure A.2.2. After 45 minutes to 1 1/2 hour of evacuation, deaired distilled water was introduced into the mold through the bottom port of the mold while the sample was kept under vacuum. The level of water in the sample was allowed to increase gradually by controlling the the height of hydrostatic head of the water source. Saturation was considered complete after several void volumes of water flowed through the sample, and no bubbles were seen in the tube leading from the top of the sample mold. The ports at both ends were then closed off. The saturation procedure by itself usually

took between 1 1/2 to 10 hours to complete.

The saturated samples were then placed upside down in a freezing cabinet, with the top port connected to a source of free water at $+5^{\circ}\text{C}$. Cork insulation was placed around the mold, leaving the bottom exposed, as in Figure A.2.3. Cooling brine at about -40°C was circulated in the walls of the cabinet, allowing freezing to take place in the sample from bottom to top. Volumetric expansion of the pore material during the phase transition from water to ice was accommodated by pore water expulsion through the drainage tube.

After a minimum of twelve hours in the freezing cabinet, the sample was removed from the cabinet and taken to a cold room with an air temperature less than -4°C . Removal of the sample from the mold was accomplished by dismantling parts 1, 2 and 5 from the Lucite sleeves 3 and 4. The inner sleeve and sample were separated from the outer sleeve by a hydraulic press and the sample was removed from the split inner sleeve, weighed, measured, wrapped in cellophane and stored at -9°C .

Unconfined creep testing was carried out in a test setup as shown in Figure A.2.4. and as described in Martin et al. (1981). The entire setup was located in a cold room set at -9°C . An air jack equipped with a frictionless rolling diaphragm and a linear ball bushing, manufactured by Bellofram Corp. of Burlington, MA, applied the load. A Bellofram bleed-type regulator controlled the air pressure to within ± 0.069 kPa (0.01 psi), which translates to a sample stress variability

of about 2.8 kPa (0.4 psi). For tests conducted during the summer months, icing in the pressure lines was a problem. A cold stage setup as illustrated in Figure A.2.5 was used, and the pressure lines were blown or melted clear of ice periodically.

A circulating coolant bath controlled the sample temperature. Circulation and temperature control of the coolant was accomplished with a Lauda K4R bath and controller built by Brinkman Instruments. Temperature variation of the glycol bath around the sample in the test cell was typically $\pm 0.02^{\circ}\text{C}$, when the unit was functioning properly. Icing of the refrigeration coils and low coolant level in the bath resulted in poor temperature control. Periodical warming of the bath to above melting and checking of the bath level were required. For temperature stage tests, an auxiliary heater was used in the bath to effect a more rapid temperature change in the bath.

A Collins type SS-103 linear motion transducer (DCDT) with a maximum stroke of 6.35 mm (1/4 in.) measured the axial deformation of the sample near the top of the sample. This transducer, manufactured by G.L. Collins Corp., Long Beach CA, was chosen for its high sensitivity and low temperature coefficient. The lower bound of strain rate measurement was approximately $10^{-10}/\text{s}$, based on the assumption that a deformation equal to ten times the zero stability took place per day.

Temperature measurements were made on thermistors which together with the data acquisition system could detect a tem-

AD-A097 668

MASSACHUSETTS INST OF TECH CAMBRIDGE DEPT OF CIVIL E--ETC F/G 8/13
THE CREEP OF FROZEN SANDS: QUALITATIVE AND QUANTITATIVE MODELS.(U)

MAR 81 J M TING

DAAG29-77-C-0016

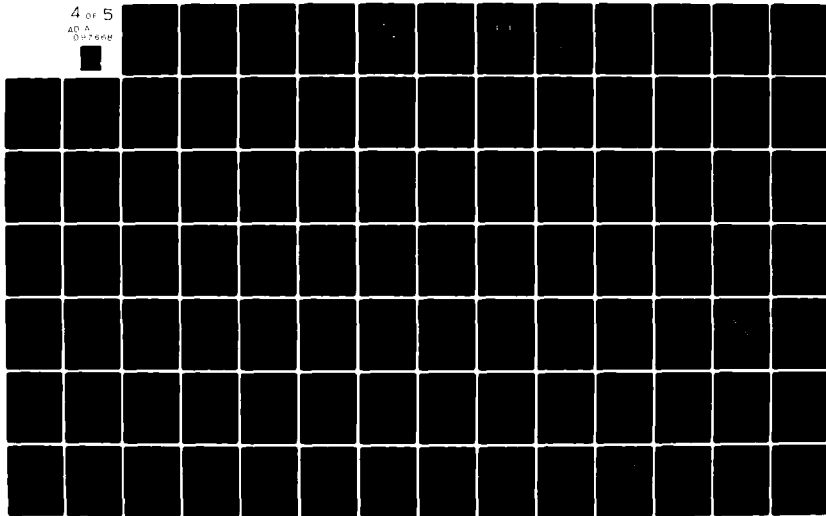
UNCLASSIFIED

R81-5

ARO-14725.2-65

NL

4 of 5
AD A
0-7668



perature change of 0.005°C . Thermistors were located in the Lauda bath, in the test cell near the sample, and in the room near the loading jack.

Sample setup was carried out by first encapsulating the sample and endcaps with a thin latex membrane. Several O-rings provided a fluid-tight seal between the endcaps and the membrane. The sample and endcaps were then placed in the test cell, which in turn was placed in the load frame. The alignment pin at the base of the load frame assured precise alignment between the loading piston and the test cell. Alignment between the sample and the endcaps was done visually as the loading piston was gradually lowered into contact with the steel ball resting on the topcap. After ensuring proper alignment, a small seating load of $0.50 \pm \text{MPa}$ was applied to the sample, and the glycol bath was circulated for a minimum of six hours prior to creep testing to allow for complete thermal equilibration at the test temperature.

To initiate a creep test, the valve in the air supply line between the regulator and the air jack was closed, the regulator adjusted to the required level, and the valve opened. The first data point after the opening of the valve, usually within five seconds, signifies time zero for each test. Stress stage tests used the same procedure as for initial load application. For temperature stage tests, the temperature was usually increased in the bath. The temperature controller was first turned to the appropriate level, then an auxiliary heater was

placed in the bath until the desired temperature was reached. The heater was then removed from the bath. For a typical temperature stage of about 2.5°C , the temperature of the bath could be changed in less than 3 minutes. However, this temperature change does not reach to the core of the sample immediately. Based on data on partially saturated Manchester Fine Sand from Martin et al. (1981), at least five more minutes are required before the temperature change reaches the center of the sample. Consequently, a total of 8 minutes elapses for a typical temperature stage of 2.5°C to be fully effected.

All measurements of deformation and temperatures were recorded electronically by a Kaye Instruments System 8000 data logger, and were converted to punched paper tape on a Facit paper tape puncher. The minimum data interval used was about six seconds, with typical data intervals being 1 to 60 minutes, depending on the test duration and testing conditions. The data from the punch paper tape were fed into a PRIME computer at the CRREL computer facility for manipulation and plotting of the results.

Strains were computed from the displacement transducer information based on the initial sample length. Due to the relatively small axial strains involved, stresses were computed based on the initial cross-sectional area. Strain rates were computed based on the slope between adjacent points. Where the data interval was so small compared to the creep rate that distinct strain rate jumps were observed, a larger data inter-

val was used. For the extremely low creep rates (10^{-8} to 10^{-10} /s), a linear least squares regression was used to fit segments of data in order to accurately determine the strain rate.

Plots of strain-time, log strain rate-log time and $\log \dot{\epsilon}$ - $\log \epsilon$ were made directly from the data. Due to the typically small time intervals between data readings, almost continuous lines are formed, as shown in Figure A.2.6. Note that all plots of creep test data in this Report are not smoothed curves through the data, but are accurate representations of the actual data.

After testing, each sample was recovered and cut into five slices for individual water content determinations. From these data, water content profiles were made for each bead type. As can be seen from the data plotted in Figure A.2.7, all bead samples had a lower water content in the middle than at the ends. This general trend is similar to that observed for frozen Manchester Fine Sand, and is attributed to moisture migration to the ends during freezing, since the same profiles were measured for samples cut after freezing and storage, without testing. The moisture content is in general more uniform for the glass beads than for the MFS, however. For the MS-M beads, no noticeable difference can be detected between the profiles of the treated and nontreated beads.

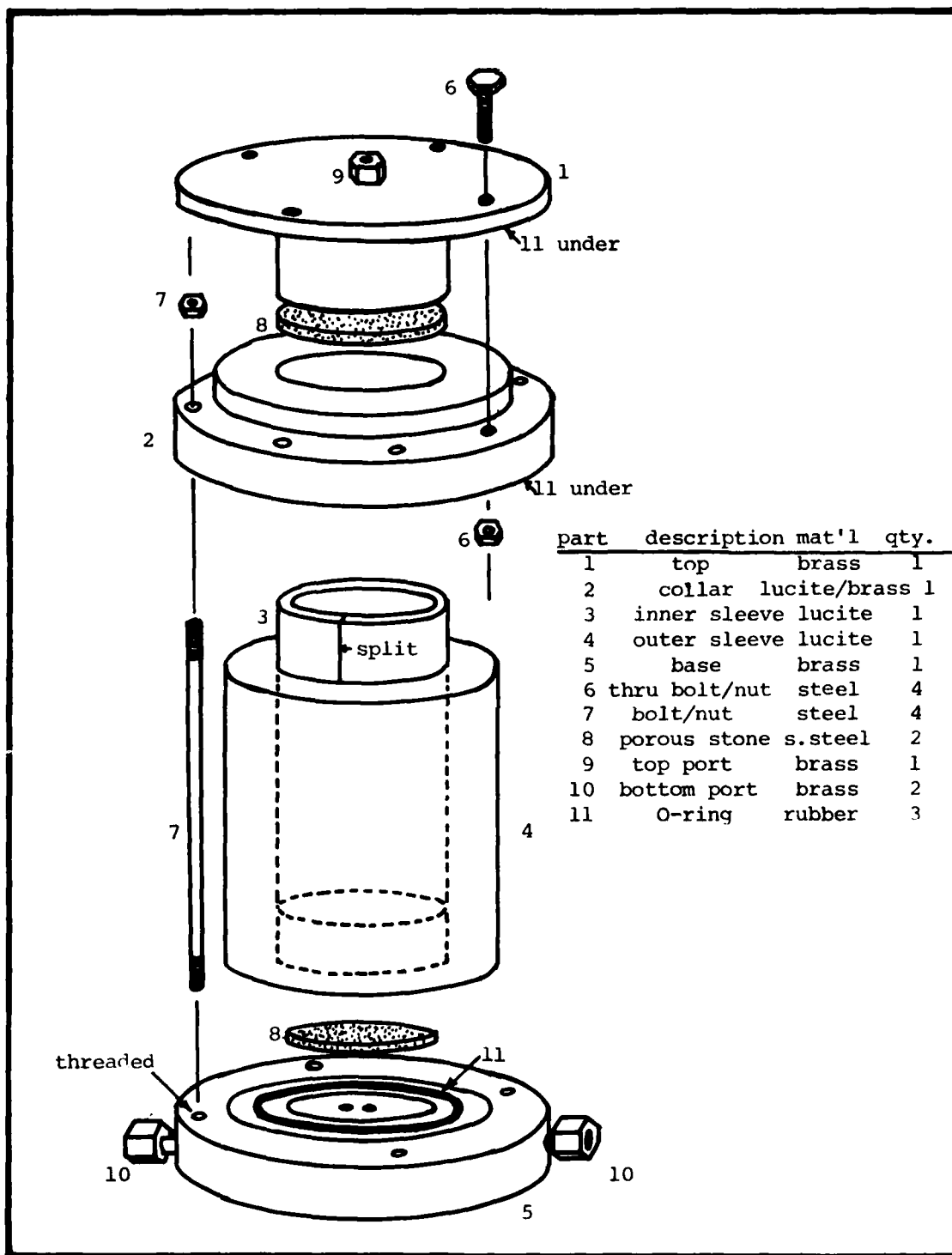


FIGURE A.2.1 Schematic of compaction mold

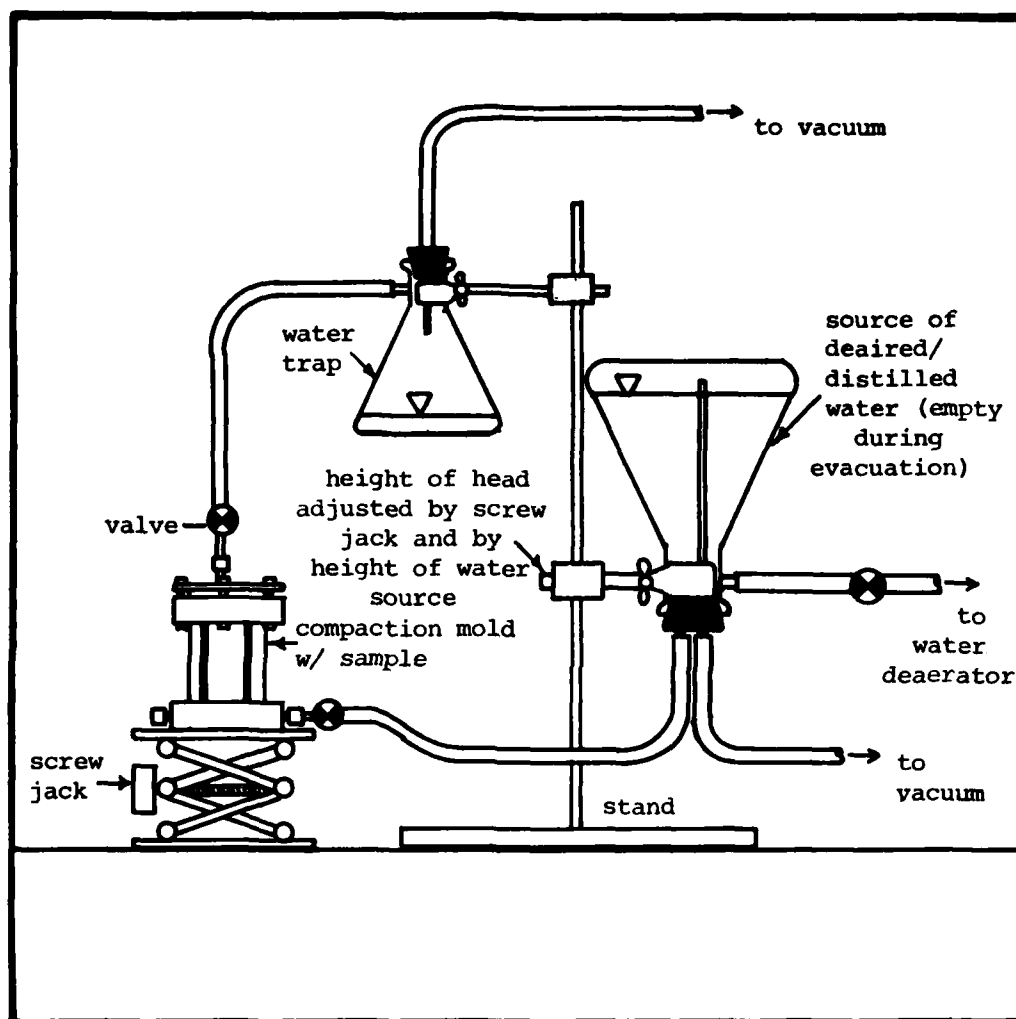


FIGURE A.2.2 Schematic of evacuation/saturation apparatus

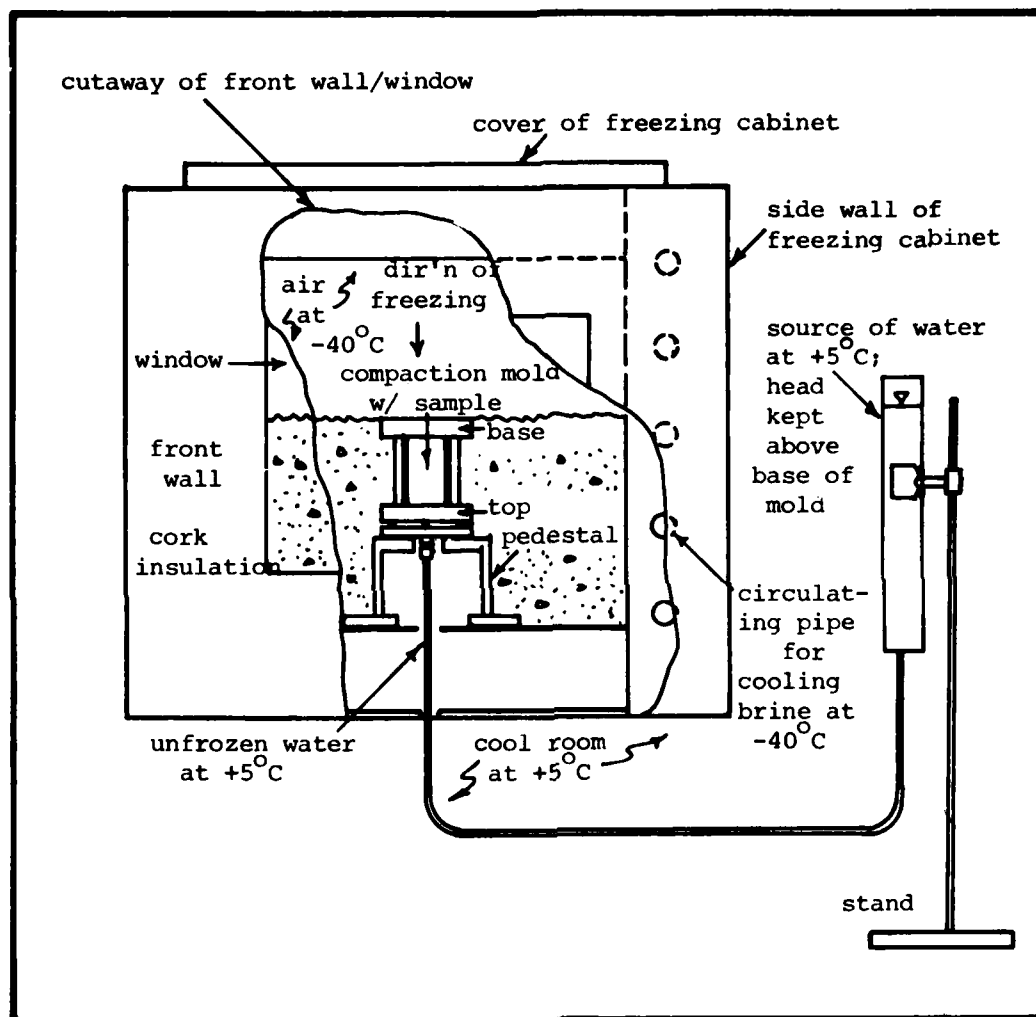


FIGURE A.2.3 Schematic of apparatus for freezing samples

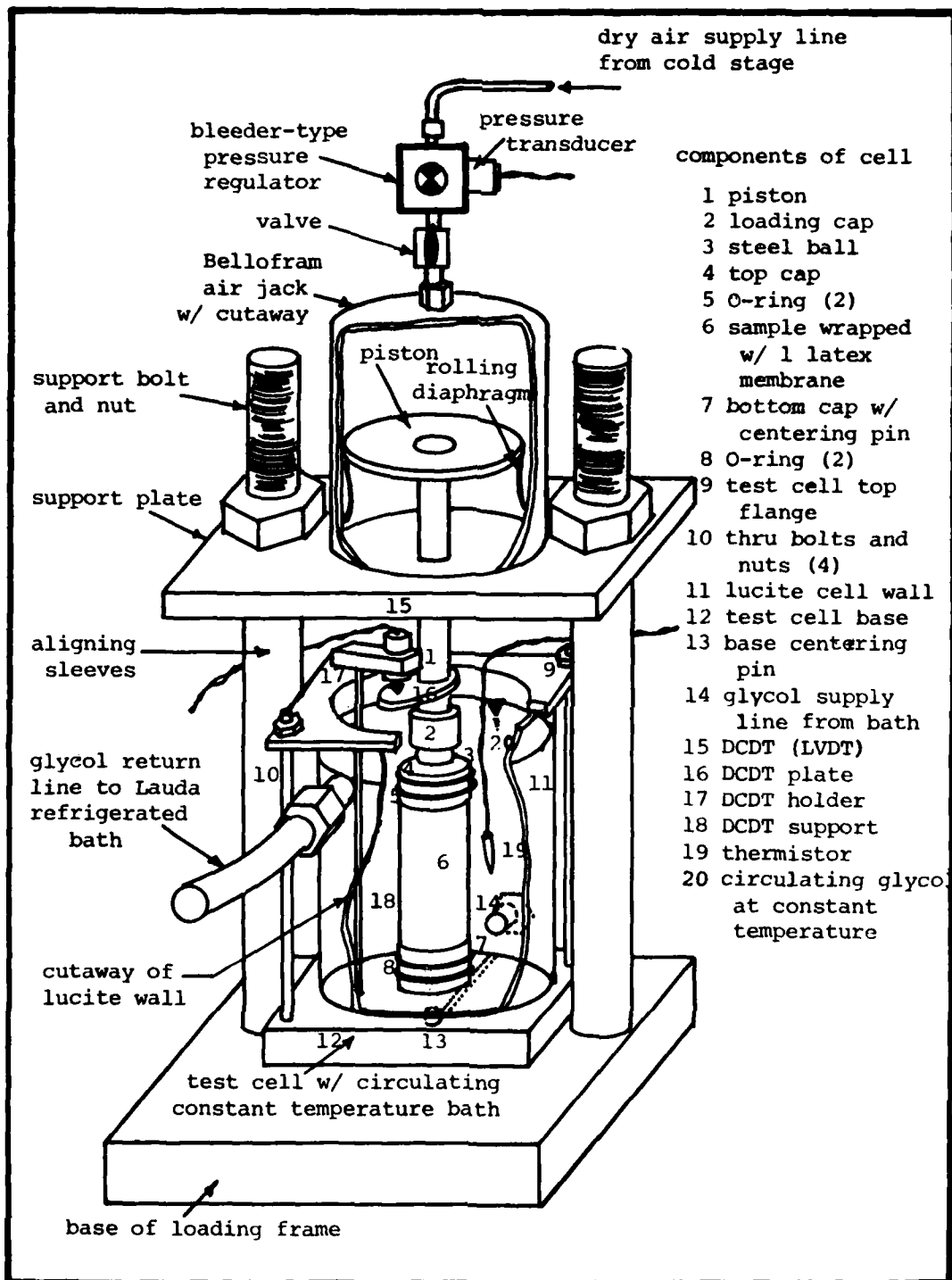


FIGURE A.2.4 Schematic of creep testing apparatus

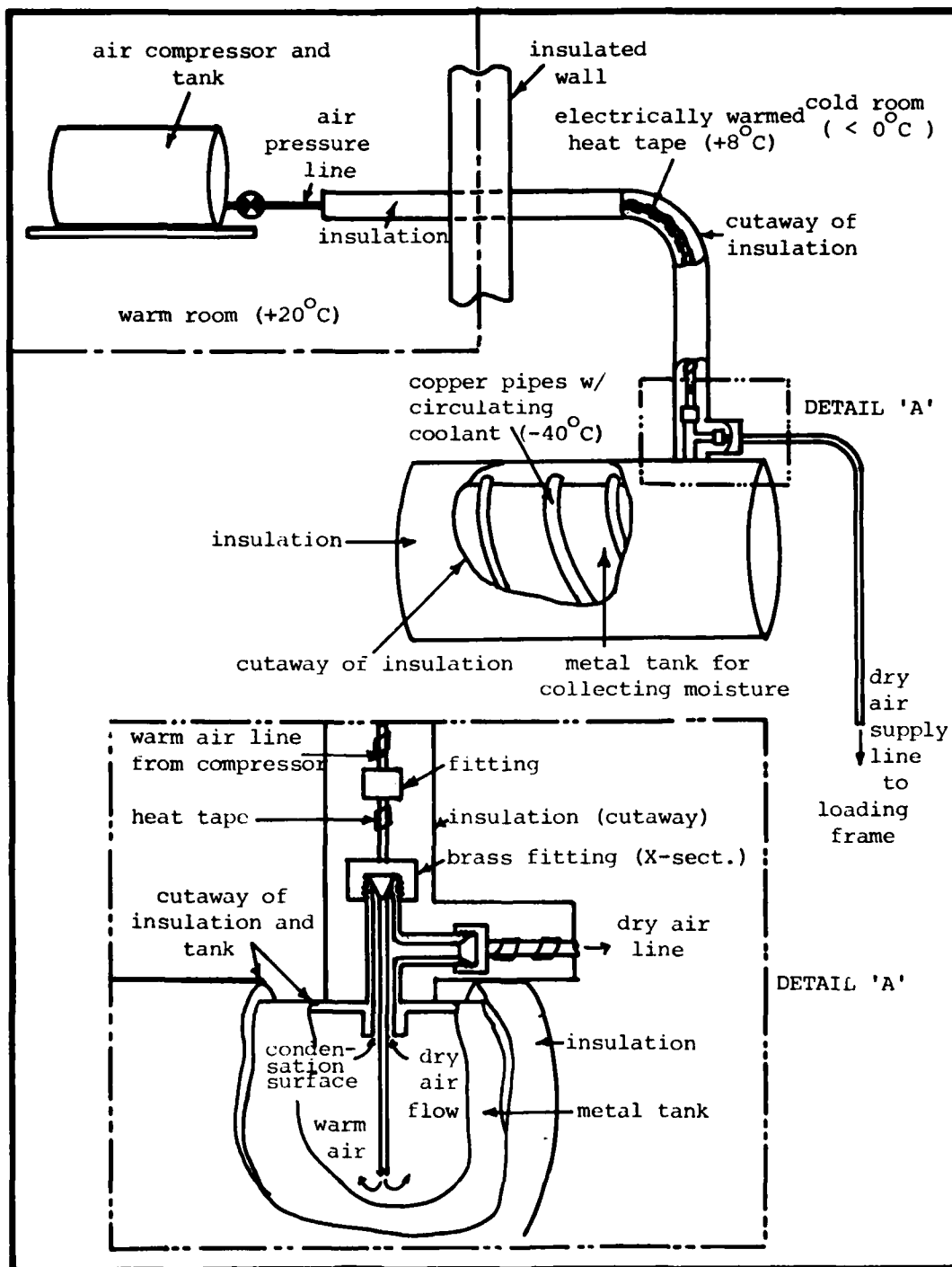


FIGURE A.2.5 Schematic of cold stage apparatus

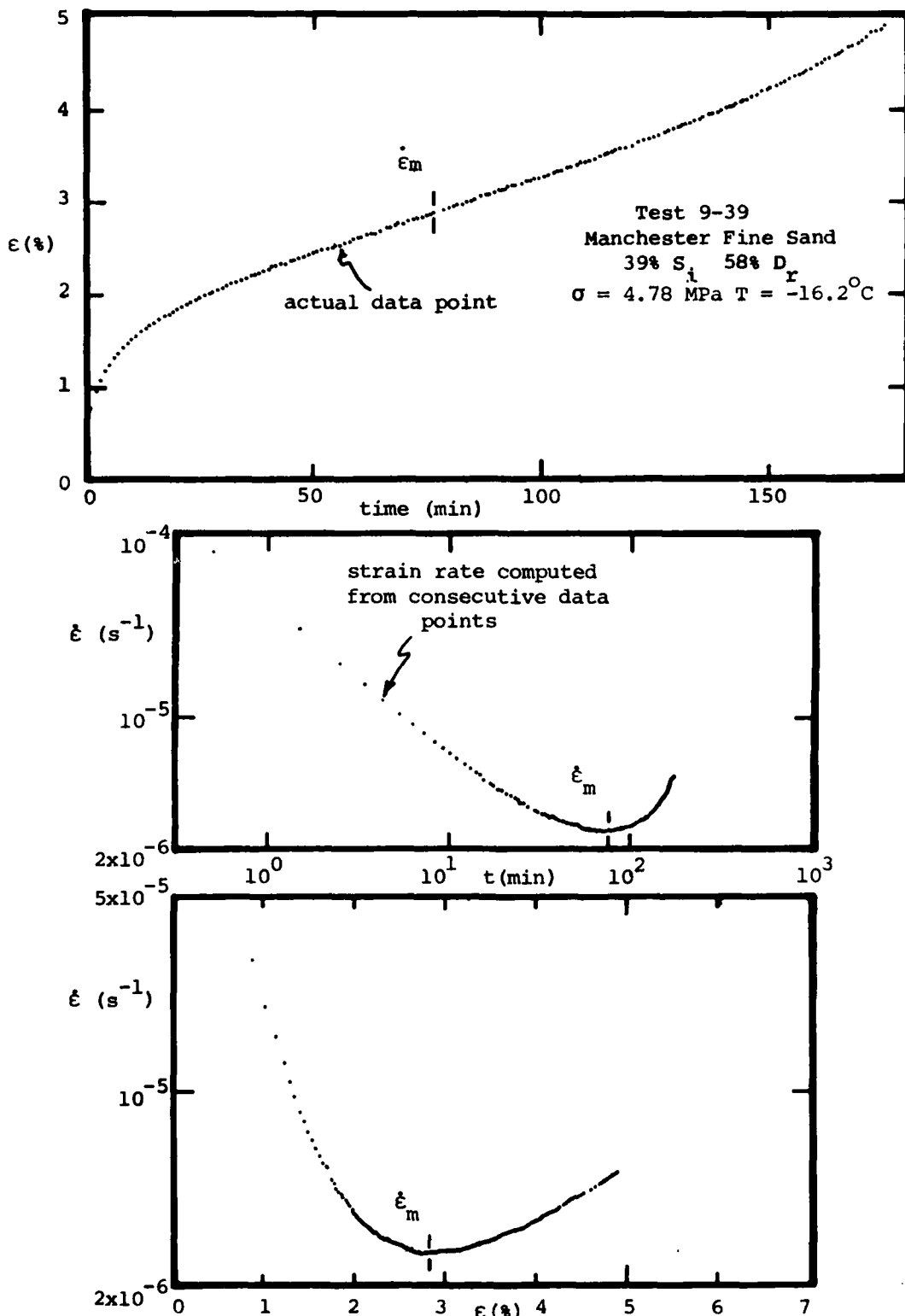


FIGURE A.2.6 Typical plots of creep data from one test

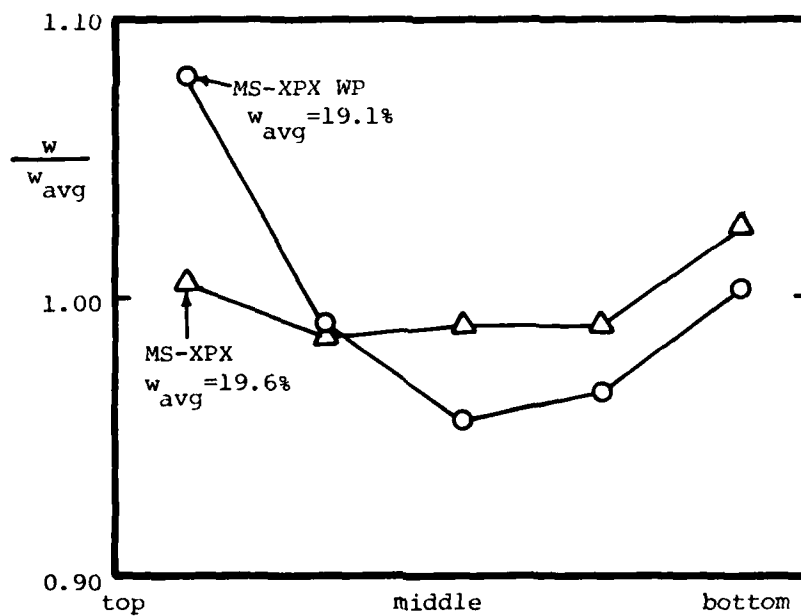
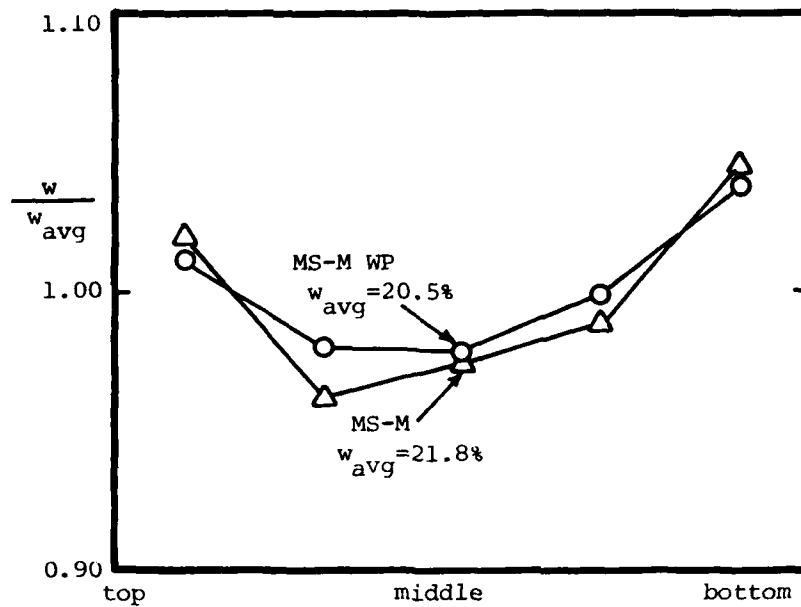


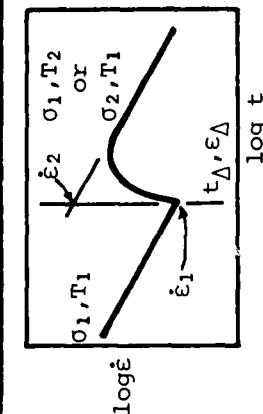
FIGURE A.2.7 Water content profiles of frozen glass bead samples

APPENDIX A.3 Results of Creep Tests on Glass Beads

Unconfined creep tests were carried out on each of the four types of glass beads ($D_r = 100\%$) at various temperatures and stresses. Constant load, stress stage and temperature stage tests were performed in the manner previously described in Appendix A.2 and in Martin et al. (1981). The purpose of each test sequence was to establish the general creep behavior and stress and temperature dependence of creep for each bead type. Comparisons were desired between beads of the same gradation with different surface treatments. Also, it was possible to assess the effect of particle size and the effect of surface roughness by comparing the MS-M and MS-XPX bead tests, and the MS-M beads and Manchester Fine Sand results, respectively.

The test conditions and results for each test are tabulated in Tables A.3.1 and A.3.2. and are plotted in Figures A.3.1 through A.3.9. Note that owing to the difficulty in ensuring proper evacuation and saturation during sample preparation, some of the samples which were made and tested are not considered to be representative tests. The tests summarized in Tables A.3.1 and A.3.2 are those which were carefully controlled during sample preparation, and are considered to be valid and representative tests. Table A.3.3 summarizes the results derived from these tests.

test no.	γ_d (t/m)	w_f (%)	S_i (%)*	σ_a (MPa)	T(°C)	$\dot{\epsilon}_1$ or $\dot{\epsilon}_{(s-1)m}$	$\dot{\epsilon}_2$ (after stage)	t_m or t_Δ (m)	ϵ_m or ϵ of Δ (%)
SM-1	1.566	21.11	96.8	7.02 8.25 10.40	-15.03	4.03×10^{-7} 2.57×10^{-7}	9.77×10^{-7} 8.18×10^{-7}	160	1.02 1.06
SM-3	1.528	22.79	98.0	10.38	-15.20 -12.88	2.91×10^{-6}	4.91×10^{-6}	23	0.99
SM-4	1.526	22.77	97.6	10.46	-15.37	3.41×10^{-7}		900±110	3.77±0.23
SM-7	1.571	-	-	13.41±	-12.65	immediate rupture	(<15 sec)		
SM-11	1.573	21.07	97.8	7.50	-15.35	2.16×10^{-8}		3305±150	2.09±0.02
SM-12	1.559	21.40	97.0	7.55	-12.41	7.29×10^{-8}		2314±180	3.39±0.10
SMWP4	1.563	21.43	97.8	5.62 6.54 7.55	-15.29	3.81×10^{-7} 3.10×10^{-7}	7.10×10^{-7} 6.03×10^{-7}	50	0.45 0.74
SMWP6	1.574	20.45	95.1	7.52	-15.08	1.83×10^{-6}		74±3	1.46
SMWP7	1.598	20.14	97.6	6.91	-14.93 -12.50	1.68×10^{-6}	2.83×10^{-6}	28	0.70
SMWP9	-	-	-	11.27	-15.10	$2. \times 10^{-3}$	immediate rupture	(<15 sec)	
SMWPI3	1.600	20.05	97.5	7.53	-12.38	4.07×10^{-6}		28±6	1.28±0.16
SMWPI4	1.589	-	-	10.50	-15.23	6.22×10^{-6}		27±2	2.11±0.07



* S_i = degree of ice saturation = $\frac{\rho_{\text{water}}}{\rho_{\text{ice}}} = 1.093 \frac{G_w}{e}$

→ $S_i = \frac{1.093(G_w)}{G_y \left(\frac{\gamma_w}{\gamma_d} - 1 \right)}$ where $G = 2.50$ for glass beads
 $\rho_{\text{ice}} = 0.915$
 $\gamma_w = 1.00$

TABLE A.3.1

Results of Creep testing - MS-M Series glass beads

test no.	$\gamma_d (t/m^3)$	w (%)	S_i (%)	σ_1 (MPa)	T (°C)	ϵ_1' or ϵ_1' min (s ⁻¹)	ϵ_2' after Δ (s ⁻¹)	t_1 or t_Δ (m)	ϵ min or ϵ_Δ (%)
SX-4	1.624	-	-	10.48	-15.43	ruptured	-	<10 sec.	-
SX-5	1.603	-	-	7.47	-12.58	1.23×10^{-7}	-	1120±250	1.89±0.17
SX-7	1.619	19.31	96.5	3.45	-15.40	2.50×10^{-7}	2.82×10^{-6}	122	0.202
				7.56	-12.61	1.80×10^{-7}	4.90×10^{-7}	236	0.550
SX-8	1.604	19.65	95.7	4.87	-12.65	1.61×10^{-8}	-	8420±720	2.15±0.03
SX-9	1.616	19.82	98.6	7.50	-15.33	2.06×10^{-8}	-	3740±720	1.51±0.09
SXWP1	1.647	-	-	7.52	-15.56	ruptured	-	<5 sec.	-
SXWP2	1.628	-	-	4.83	-12.71	ruptured	-	<5 sec.	-
SXWP4	1.638	18.87	97.5	3.45	-15.53	5.84×10^{-8}	-	3345±480	2.68±0.17
SXWP5	1.628	18.82	96.1	4.14	-15.23	7.94×10^{-7}	2.40×10^{-7}	8	0.50
				3.46	-12.52	8.41×10^{-8}	1.76×10^{-7}	94	0.57
SXWP6	1.618	19.64	98.0	3.43	-12.66	2.25×10^{-7}	-	1215±120	0.95±0.07
SXWP7	1.657	-	-	4.83	-12.66	ruptured	-	<1 min.	-
SXWP8	1.645	19.02	99.5	4.13	-12.54	1.19×10^{-6}	-	50±5	1.29±0.04

TABLE A.3.2

Results of Creep testing - MS-XPX series glass beads

quantity		MS-M	MS-M WP	MS-XPX	MS-XPX WP
γ_d	(t/m ³)	1.554	1.585	1.613	1.637
± 1 std.		± 0.021	± 0.016	± 0.009	± 0.013
ϵ_m	(%)	3.08	1.62	1.52	1.64
± 1 std.		± 0.88	± 0.44	± 0.63	± 0.92
from	$\frac{\partial \ln \dot{\epsilon}}{\partial \sigma} m$ (s ⁻¹ MPa ⁻¹)	0.93	3.26	0.78	2.38
$\dot{\epsilon}$ min	$E = \frac{-R \partial \ln(\dot{\epsilon}/T)}{\partial (1/T)}$ (kcal/mole)	54.8	39.1	86.2	62.1
data	(kJ/mole)	229	164	361	260
from	$\frac{\partial \ln \dot{\epsilon}}{\partial \sigma}$ (MPa ⁻¹)	0.63	0.67	1.15	1.76
stage	$E = \frac{-R \partial \ln \dot{\epsilon}/T}{\partial (1/T)}$ (kcal/m)	29.6	28.2	47.4	35.9
tests	E_2 (kJ/m)	124	118	199	150

TABLE A.3.3

Summary of creep testing on glass beads

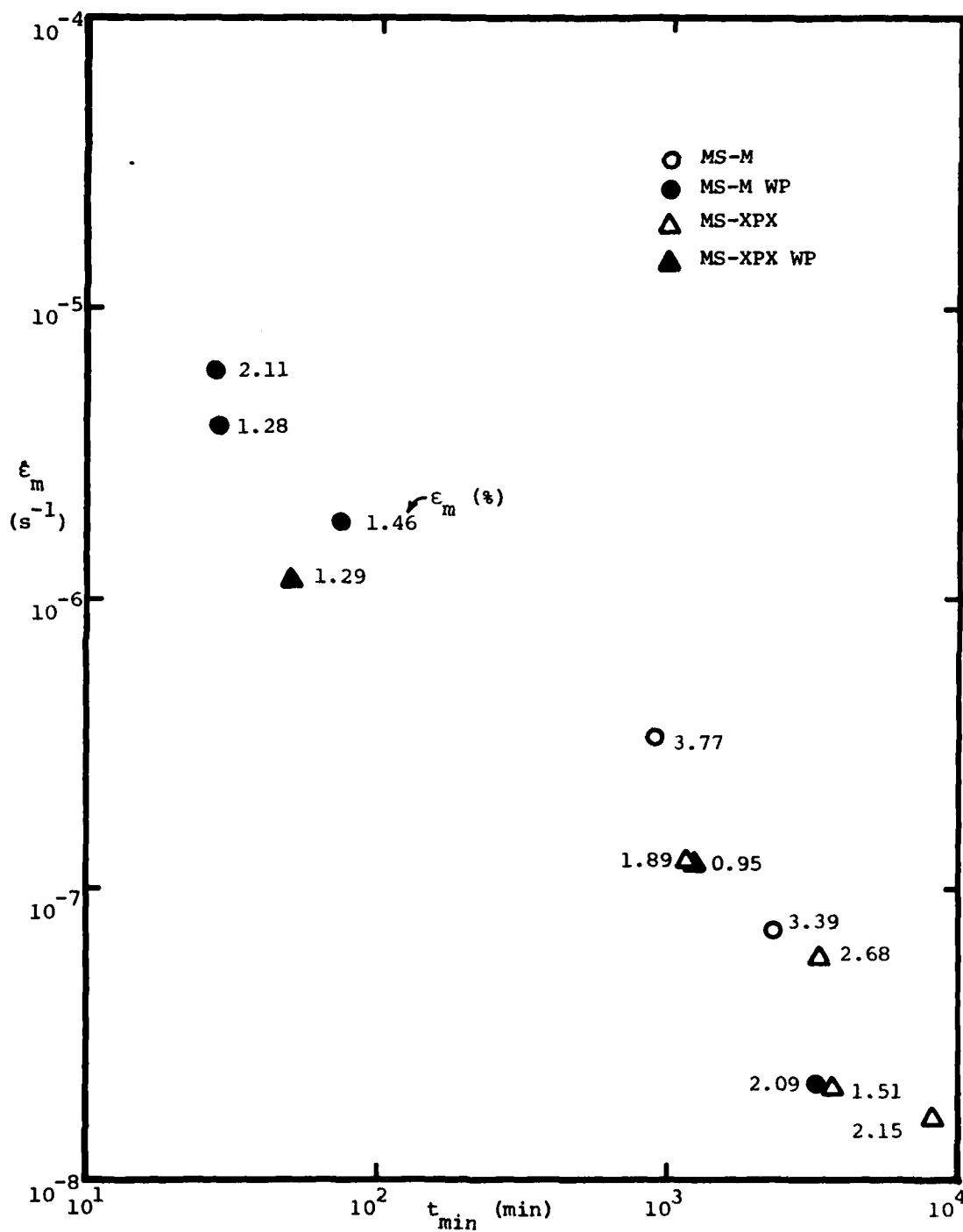


FIGURE A.3.1 Results of constant load creep testing on glass beads

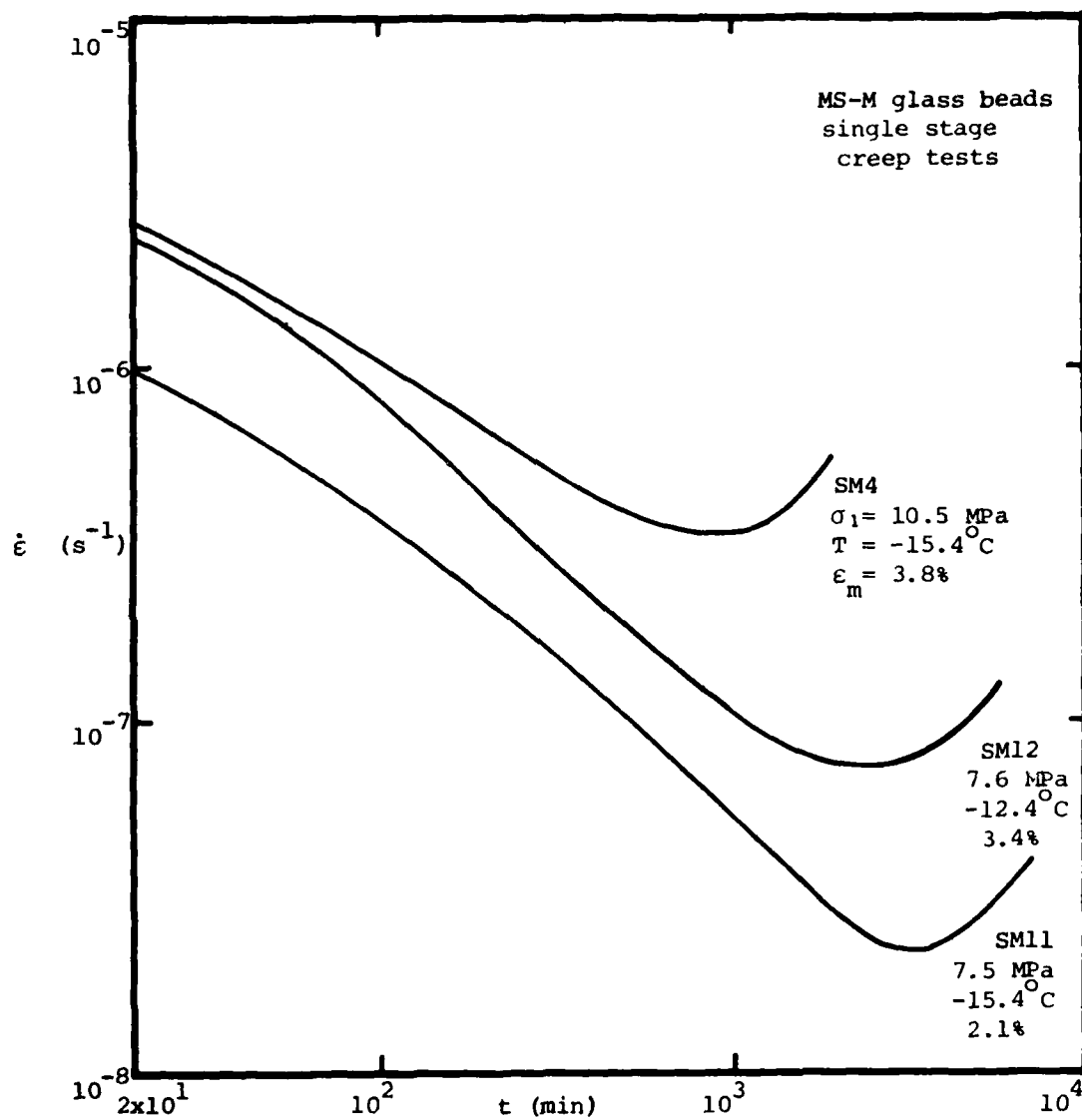


FIGURE A.3.2 Results of creep testing on MS-M (wetting) glass beads

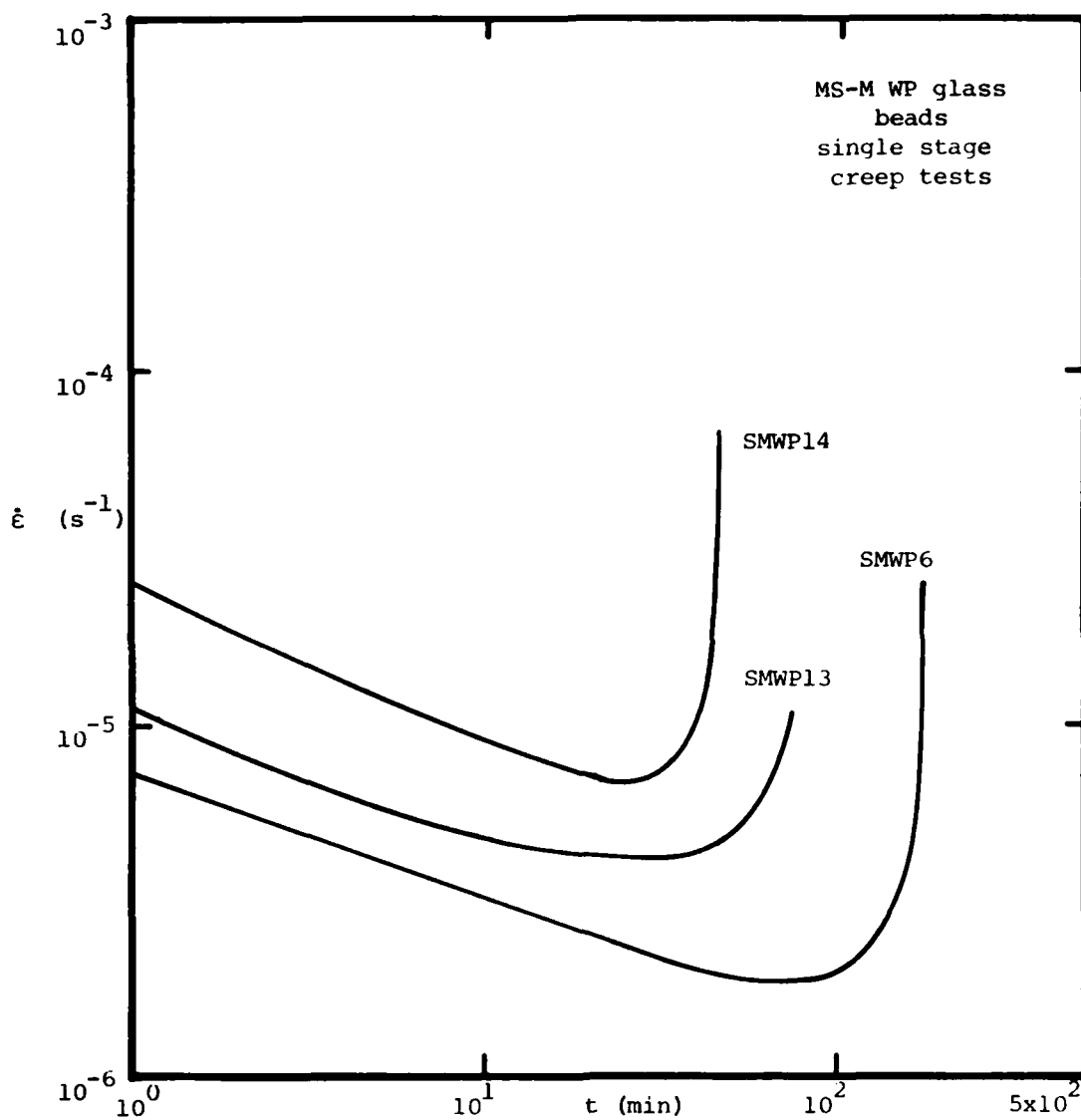


FIGURE A.3.3 Results of creep testing on MS-M WP (nonwetting) glass beads

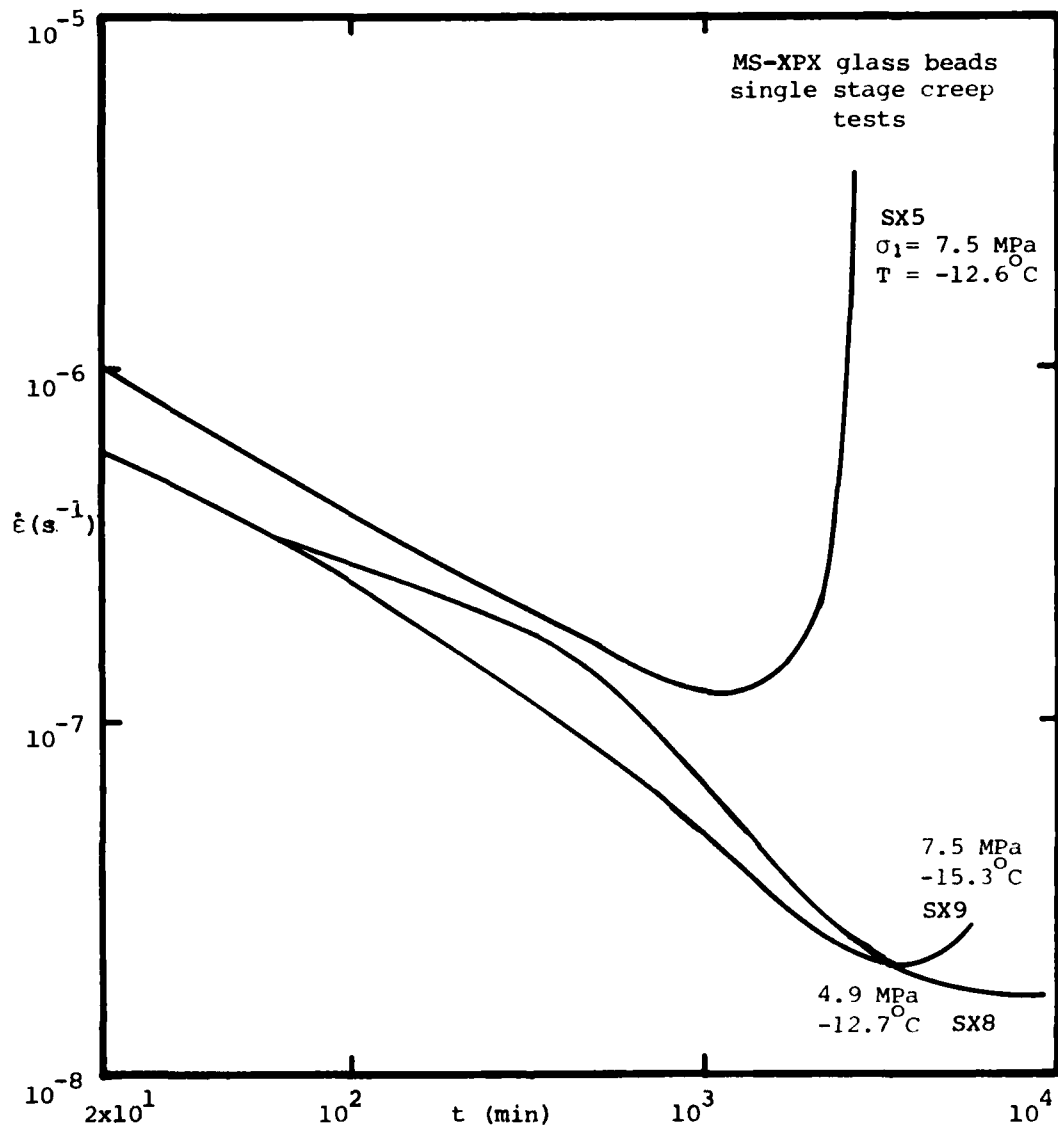


FIGURE A.3.4 Results of creep testing on MS-XPX (wetting) glass beads

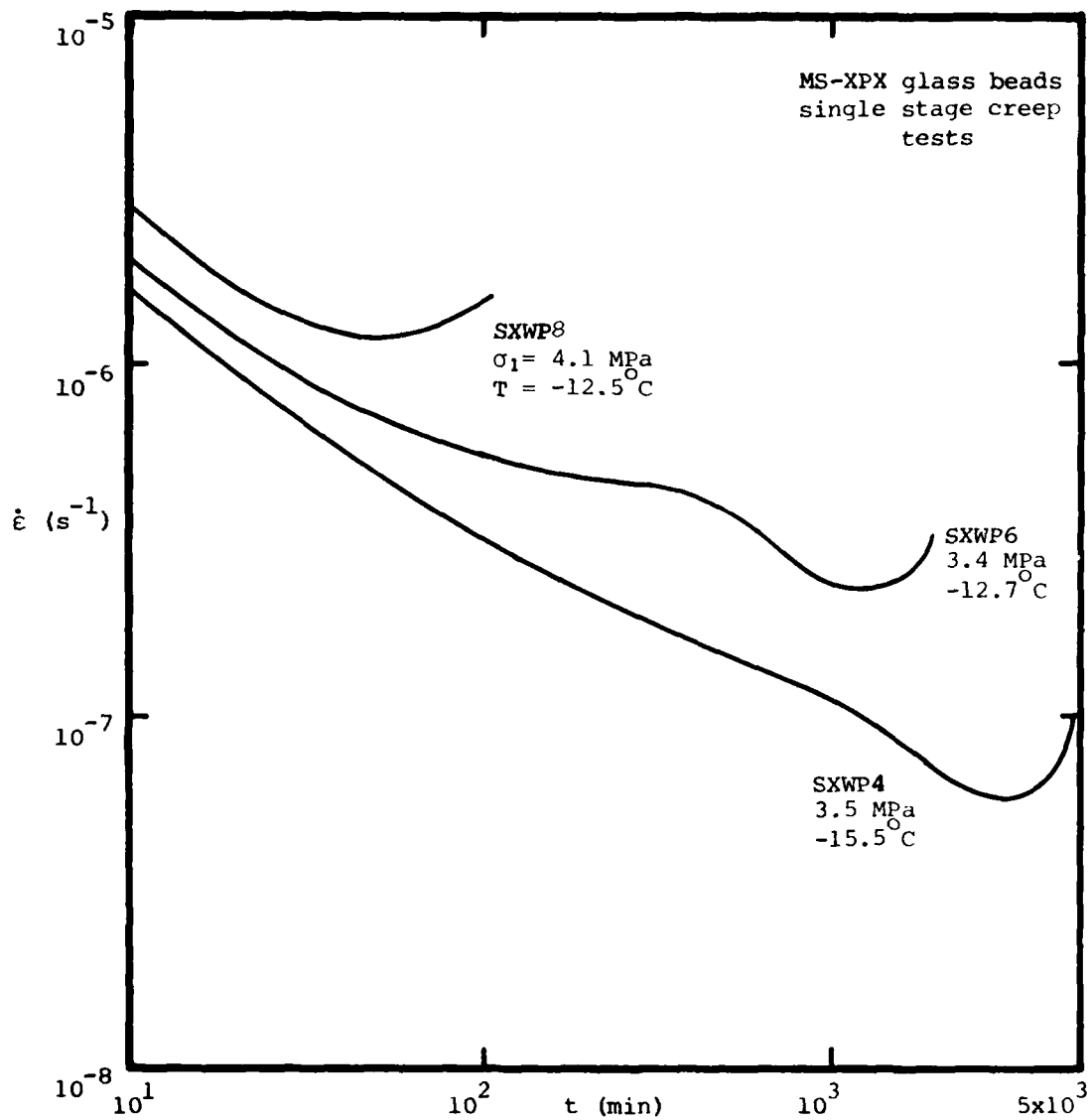


FIGURE A.3.5 Results of creep testing on MS-XPX WP (nonwetting)
glass beads

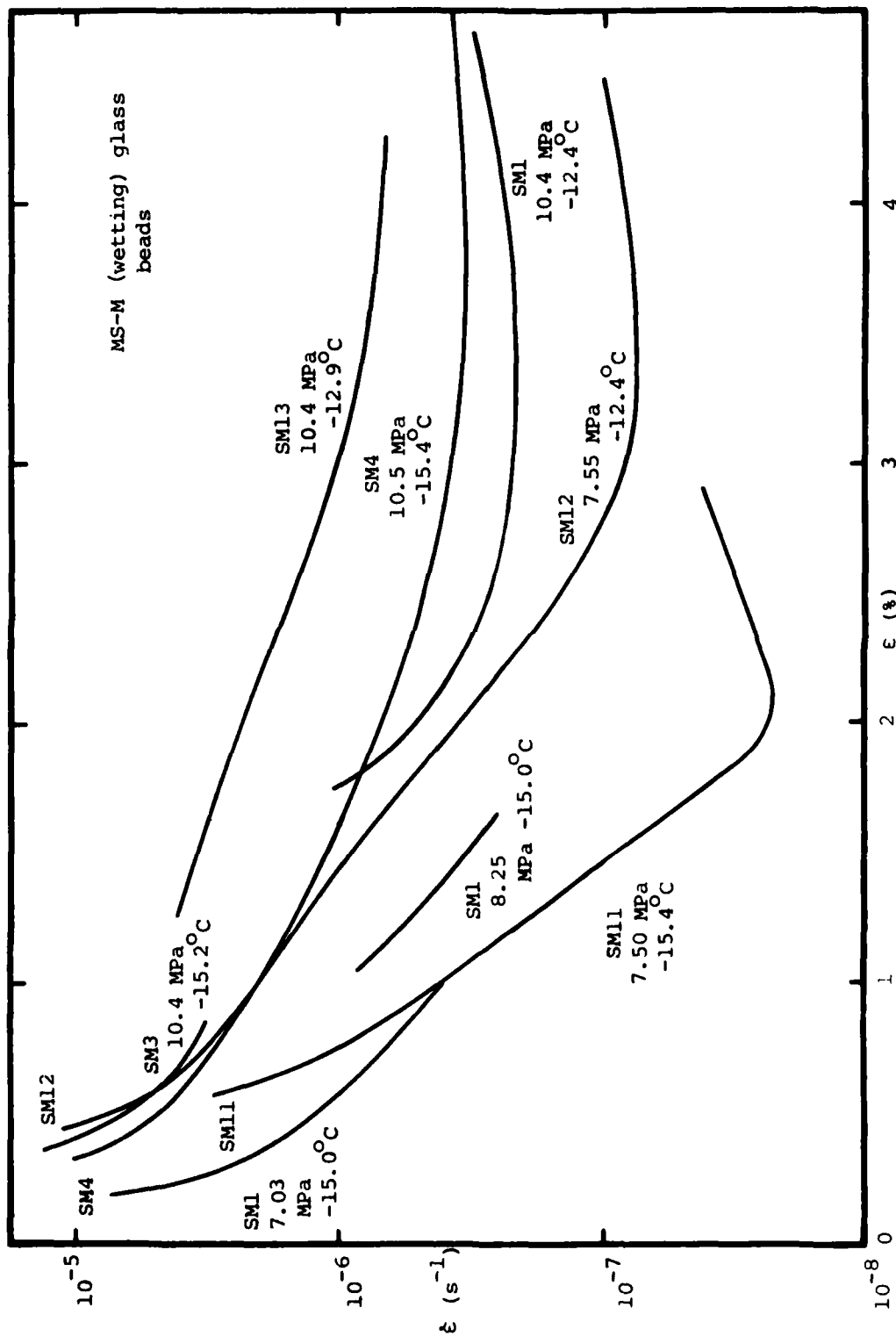


FIGURE A.3.6 Results of creep testing on MS-M (wetting) glass beads

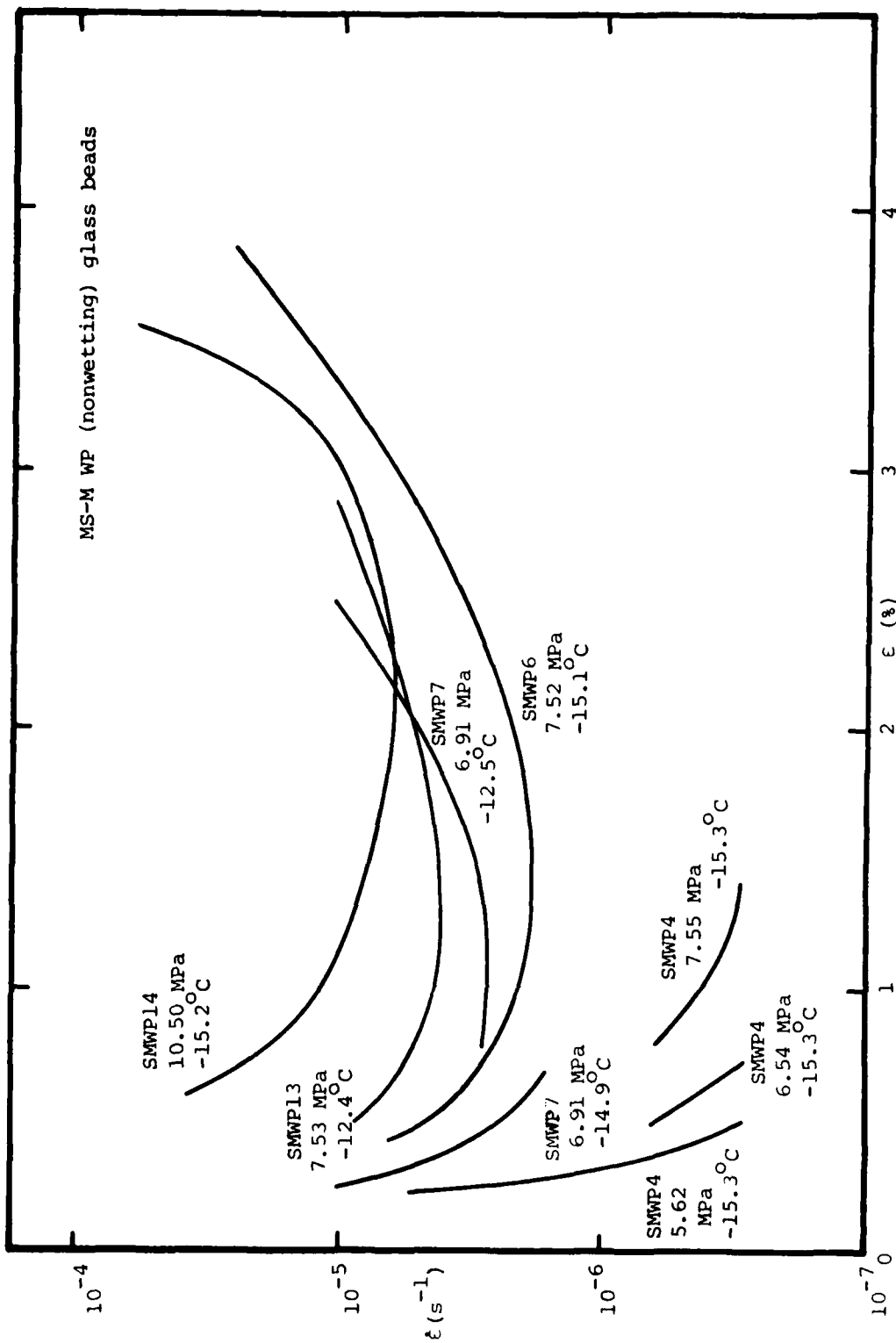


FIGURE A.3.7 Results of creep testing on MS-M WP (nonwetting) glass beads

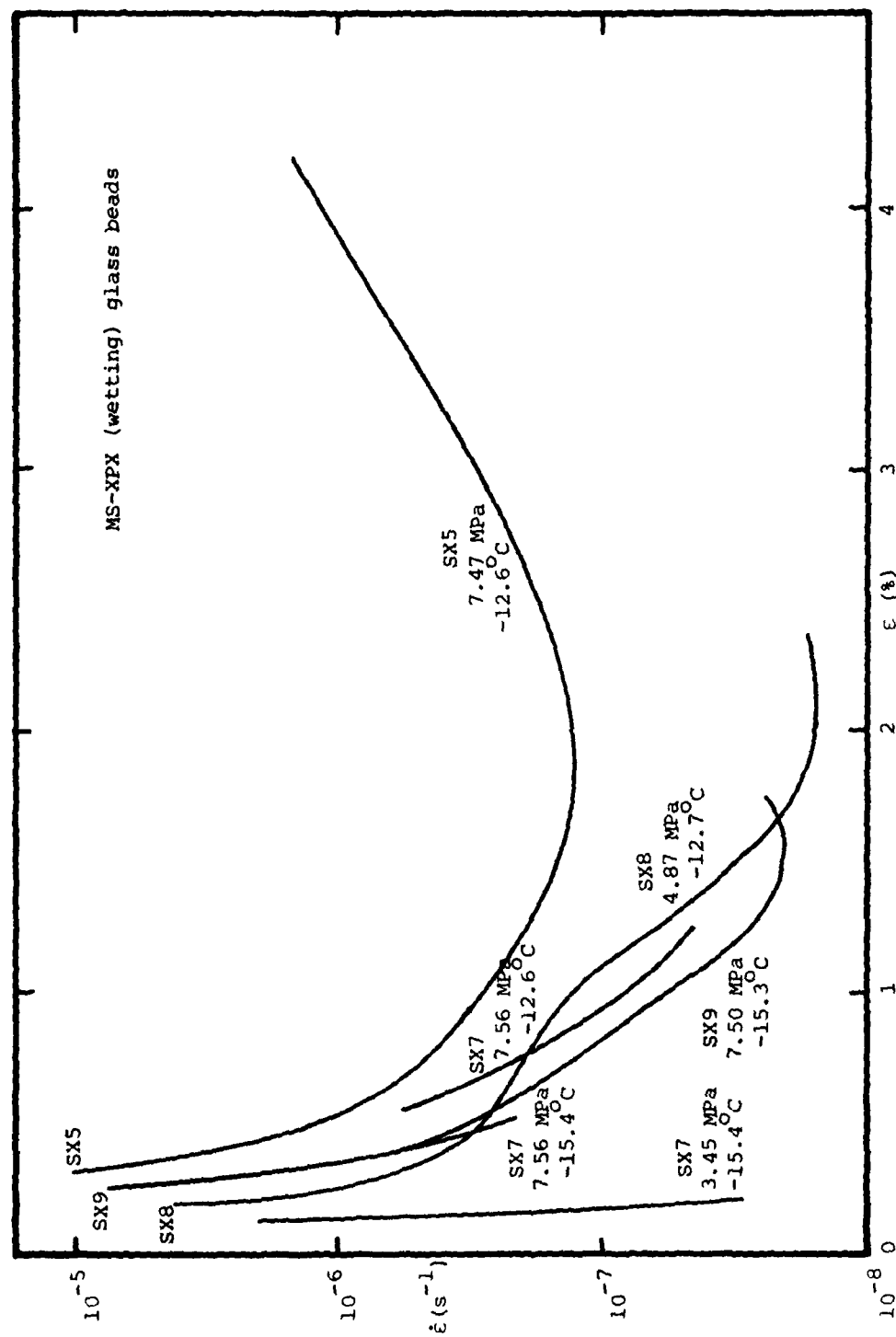


FIGURE A.3.8 Results of creep testing on MS-XPX (wetting) glass beads

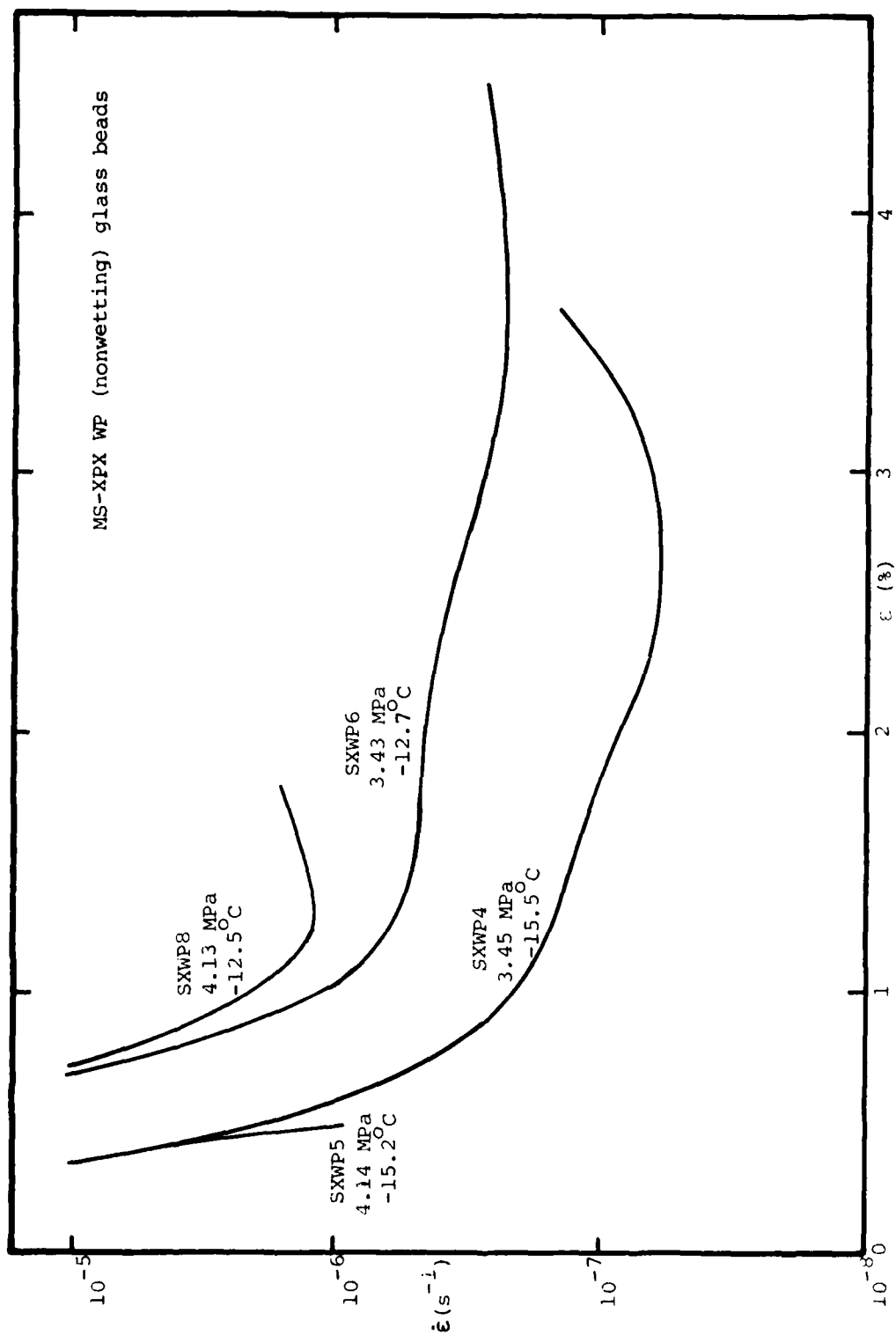


FIGURE A.3.9 Results of creep testing on MS-XPX WP (nonwetting) glass beads

APPENDIX A.4 Results of Unfrozen Water Content Determinations of MS-M Series Glass Beads

Unfrozen water contents were determined by A. Tice of CRREL by nuclear magnetic resonance (NMR) in the manner described by Tice, Burrous and Anderson (1978) using a Praxis model PR103 pulsed NMR analyzer operated in the 90 degree mode with a 0.1 s clock. Unfrozen water contents (w_u = weight of unfrozen water/weight of solids) were determined from the first pulse amplitude. Each sample was taken through one warming and cooling cycle, and exhibited very little hysteresis, as shown in Figure A.4.1.

A total of eight frozen glass bead samples were prepared, 4 each from MS-M and MS-M WP beads. For each type of bead, samples were prepared by mixing, tamping and freezing beads at 10 and 20% water content, trimming an intact portion from a frozen saturated sample prepared for creep testing, and by pulverizing a portion from a frozen saturated sample prepared for creep testing.

Essentially no difference in unfrozen water content existed between the pulverized and intact samples cut from the sample prepared for creep testing, as can be seen from Figure A.4.2. Since such low unfrozen water contents exist for these beads, it is difficult to completely analyze the unfrozen water content data in the manner suggested by Martin et al. (1981). However, there is sufficient resolution in the NMR data to show that the treated, hydrophobic (MS-M WP) beads uniformly possess a lower unfrozen water content than the untreated, hydrophilic

(MS-M) beads. For temperatures below about -3°C , saturated MS-M beads possess about 1.9 % unfrozen water, while saturated MS-M WP beads possess about 1.3 % unfrozen water. For the MS-M (untreated) beads, about 1 % of the total unfrozen water may be attributed to the solid bead surface, while the remainder may be attributed to the ice phase, as can be seen in Figure A.4.3. The 1 % value is inferred from the observation that the unfrozen water content remains essentially constant below -8°C . However, due to the low unfrozen water content in the MS-M WP beads, it is not possible to separate the total unfrozen water content in portions attributable to the solid and ice phases.

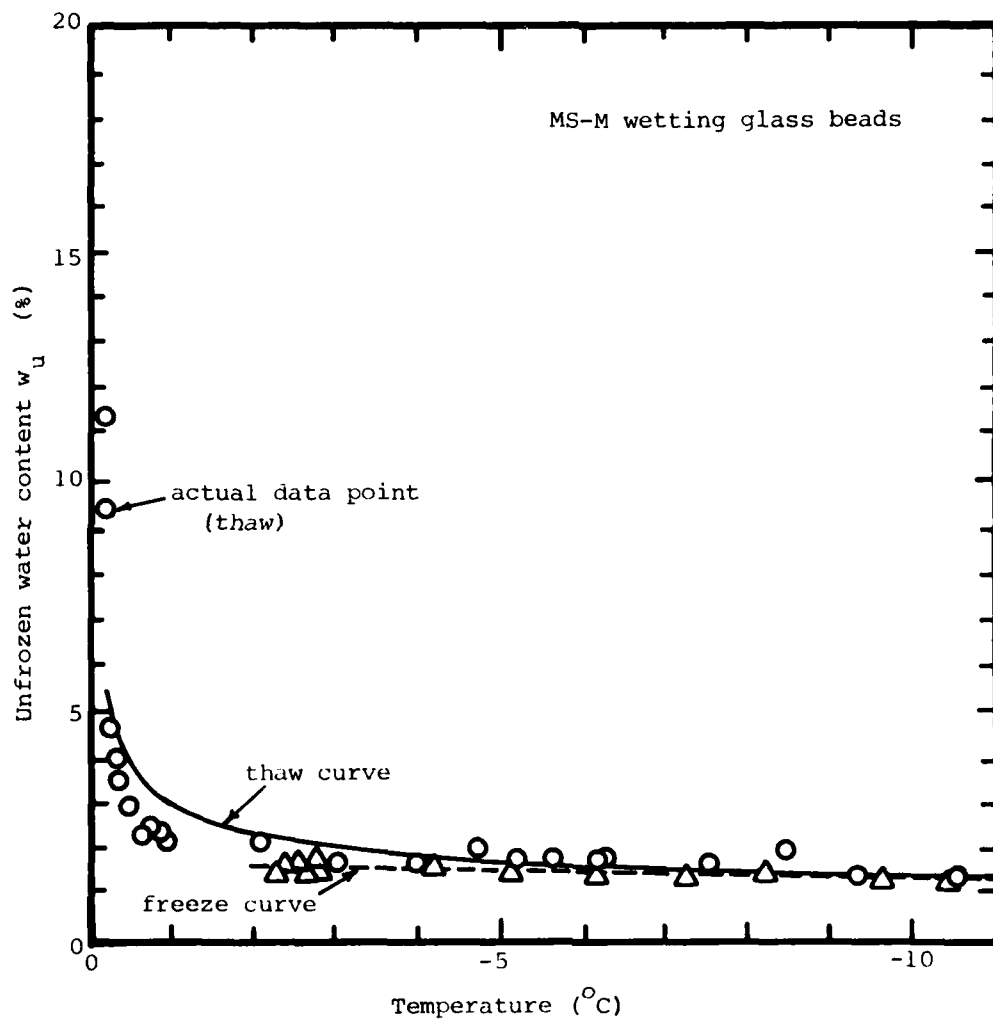


FIGURE A.4.1 Unfrozen water contents of MS-M glass beads from pulsed NMR

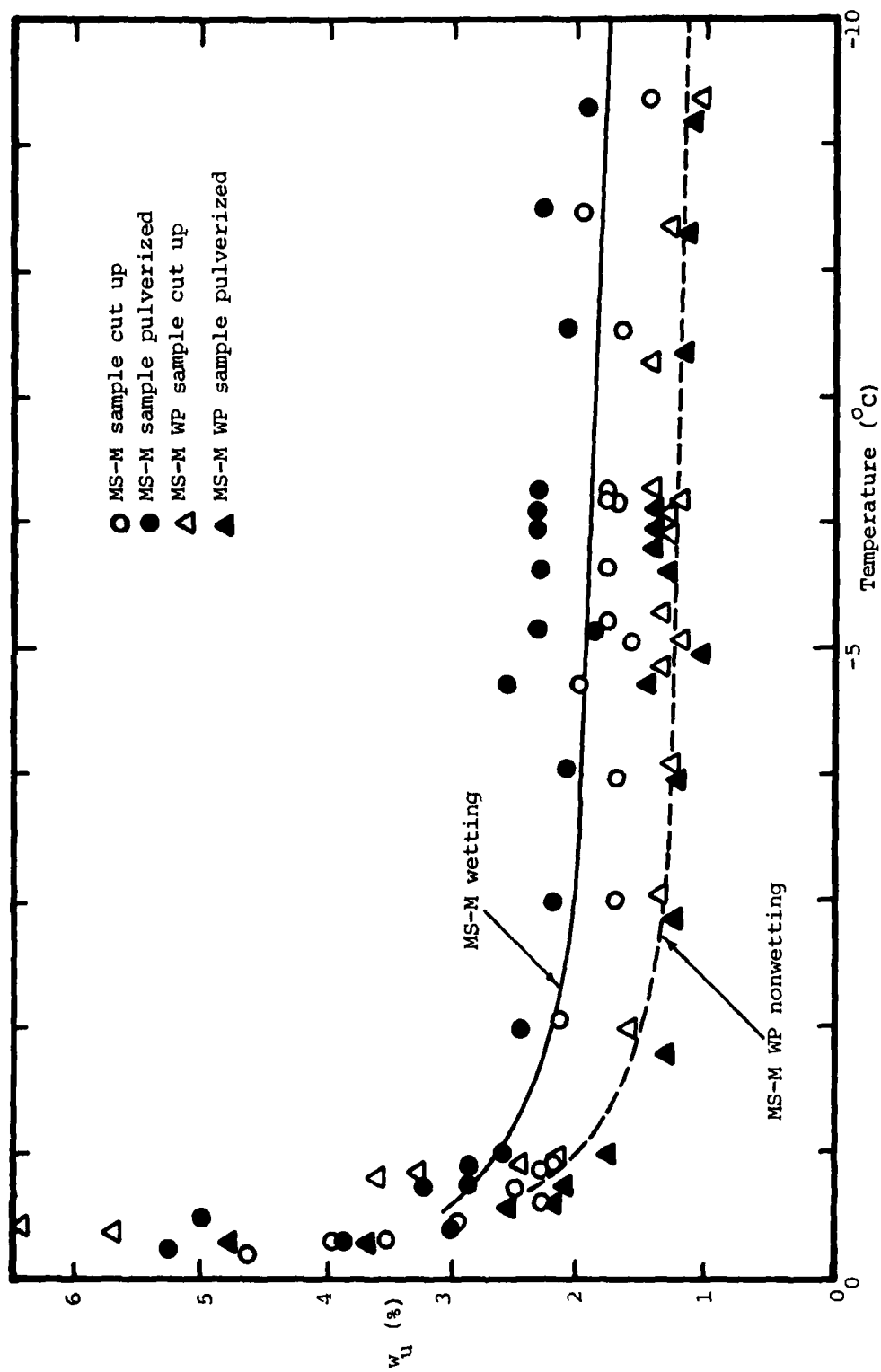


FIGURE A.4.2 Unfrozen water contents of MS-M wetting and MS-M WP nonwetting glass beads from pulsed NMR (warming curves)

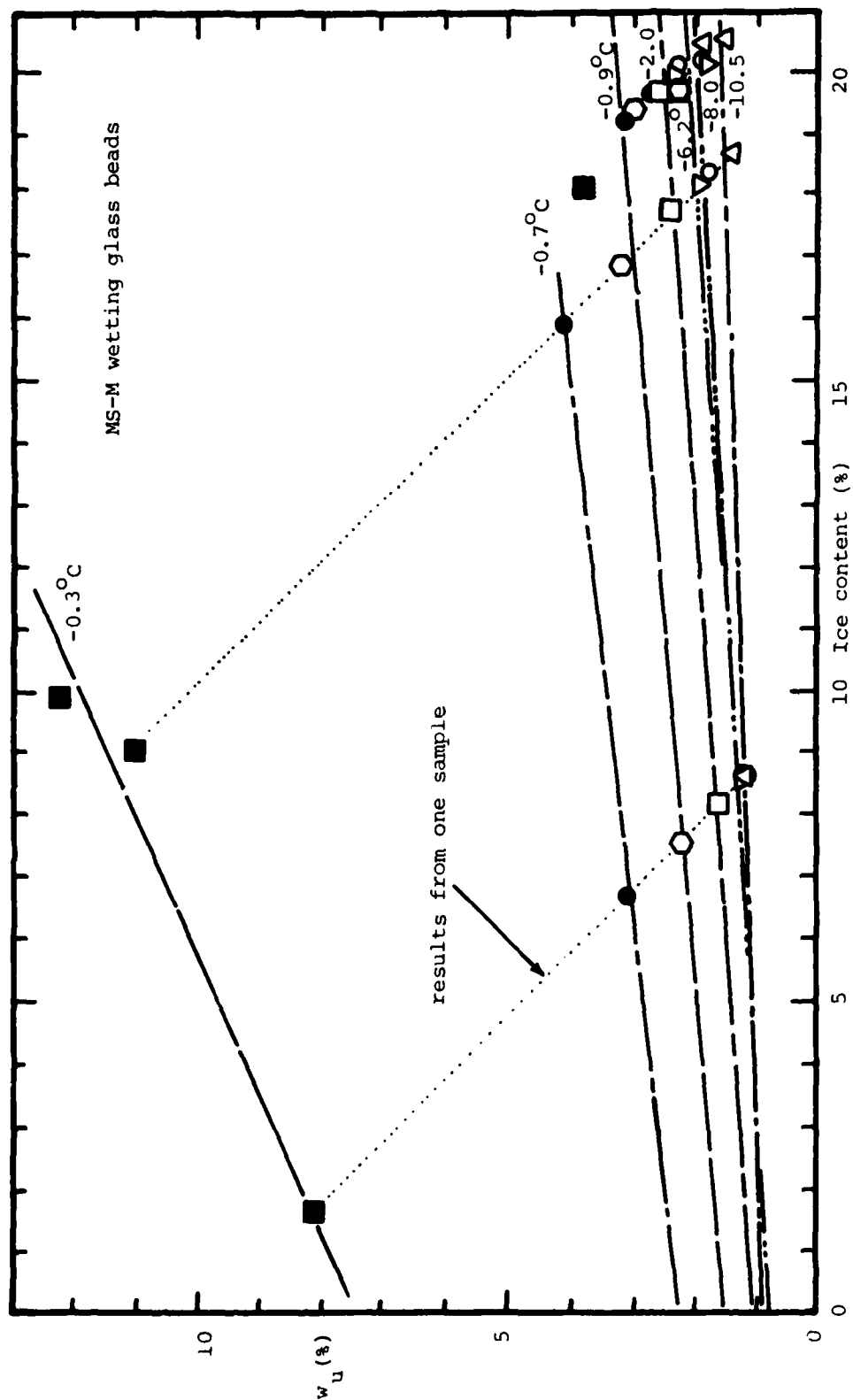


FIGURE A.4.3 Unfrozen water content as a function of ice content for MS-M wetting glass beads

APPENDIX A.5 Results of Testing on Frozen Manchester Fine Sand

A comprehensive program of unconfined creep testing was carried out on frozen Manchester Fine Sand (MFS) as part of the joint MIT-CRREL research project on the evaluation of the Rate Process Theory (RPT), as reported in Martin, Ting and Ladd (1981). Extensive sequences of constant load, temperature stage and stress stage creep testing were carried out on 40 and 100 % ice saturated (Si) MFS samples at 55 % relative density (Dr). A smaller test program was performed on 12 and 20 % ice saturated samples at 55 % Dr, and on 40 and 100 % ice saturated samples at varying relative density. Tables A.5.1 through A.5.4 tabulate constant load creep data, while temperature stage tests are summarized in Tables A.5.4 through A.5.7. Table A.5.8 tabulates stress stage test data. The values of relative density reported in these tables were computed using maximum and minimum dry densities of 1.707 t/m^3 and 1.370 t/m^3 , respectively (Perrone 1978).

Typical stress-strain data are plotted in Figure A.5.1 for a family of tests carried out on 40 % Si, 55 % Dr MFS at an applied axial stress of 4.78 MPa (693 psi) and varying temperatures. Figure A.5.2 shows the corresponding $\log \dot{\epsilon} - \log t$ data. A family of creep curves for 40 % Si at one temperature and varying stress levels is plotted in Figure A.5.3. Similarly, families of creep curves for saturated, 55 % Dr MFS at constant stress levels and constant temperature are found

in Figures A.5.4 and A.5.5, respectively. Note that the shapes of the $\log \dot{\epsilon} - \log t$ curves for the 40 % and 100 % Si samples are different; whereas the partly saturated samples exhibit a constantly increasing second derivative of strain with respect to time (ie. $d^3\epsilon / dt^3 > 0$), the saturated samples possess a break in their creep curves during "primary" creep, where an increasing negative change in slope of the $\log \dot{\epsilon} - \log t$ curve is observed. However, fairly good reproducibility of test results is observed for both cases.

For the partially saturated samples subjected to single stage constant loads, Tables A.5.2 through A.5.4 tabulate the initial slope m_0 , the strain ϵ_0 and strain rate $\dot{\epsilon}_0$ after one minute of load application. For the saturated MFS samples, the initial slope m_{01} and slope m_{02} after the break in the $\log \dot{\epsilon} - \log t$ curve are tabulated in Tables A.5.1 and A.5.4 together with the strain ϵ_0 and strain rate $\dot{\epsilon}_0$ one minute after load application, and strain ϵ_Δ and strain rate $\dot{\epsilon}_\Delta$ at the break in the curve.

The constant load creep data for 55 % relative density MFS samples show excellent $\log \dot{\epsilon}_m - \log t_m$ correlations, as can be seen from Figure A.5.6. These correlation coefficients, together with other observed and computed parameters for MFS MFS at 55 % Dr are found in Table A.5.9.

The effect of varying relative density for 40 and 100 % Si Manchester Fine Sand at constant stress and temperature is found in Figures A.5.7 through A.5.10. Note the change in rate of

decrease in minimum strain rate with increasing D_r for the saturated MFS at about 60 % relative density.

After creep testing, each sample was cut into five slices for individual water contents. Results of these water content profile data for 20, 40 and 100 % Si MFS at 55 % D_r MFS are found in Figure A.5.11. For the 40 % saturated samples, which were frozen from both ends, significant moisture migration is evident due to the mode of freezing. For the 20 % Si samples, far less migration occurred, probably due to a lack of availability of free water in the pores. For the saturated samples, which were frozen from the bottom end first, some moisture migration occurred towards the bottom end.

Numerous attempts were made to obtain an "instantaneous" reference strength for the Manchester Fine Sand at 55 % relative density. By carrying out rapid strain-rate controlled unconfined strength tests, it was hoped that the strength corresponding to the "ductile to brittle transition" could be obtained. By using a special set of aligning jigs in an MTS testing facility equipped with an environmental chamber, good reproducibility in observed strengths was obtained for observed strengths for each strain rate. Details on the testing facility and procedure are found in Martin et al. (1981).

By varying the applied strain rate, ductile or brittle fracture modes could be induced. Visual inspection of each sample after testing ascertained whether brittle fracture or ductile ductile failure had occurred. The results of this testing pro-

program for 40 and 100 % ice saturation are found in Tables A.5.10 and are plotted in Figures A.5.10 and A.5.11. Based on these data, the following estimates of "instantaneous strength" for MFS at 55 % relative density were used:

$$\sigma_{ult} = 10.1 + 1.5 \theta \quad \text{MPa for 100 \% Si}$$

$$\sigma_{ult} = 2.38 + 0.46 \theta \quad \text{MPa for 40 \% Si.}$$

where $\theta = -T$ ($^{\circ}\text{C}$)

Note that the estimate of ultimate strength for the 40% Si MFS differs somewhat from that provided by Martin et al.(1981). Martin et al. fitted one line through both 40 and 60% Si data at strain rates of 0.18 and 1.6 /s, respectively. The estimate provided here is based on only 40% Si data, "adjusted" empirically to a strain rate of 0.02 /s by using the saturated MFS data, where a visually observed ductile-to-brittle transition was observed at this strain rate.

test no.	S ₁ (%)	D _r (%)	γ_1 (MPa)	T (°C)	$\dot{\epsilon}_m$ (s ⁻¹)	ϵ_m (%)	ϵ_0 (%)	at t = 1 m	m ₀₁	$\dot{\epsilon}_0$ (s)	at break Δ	ϵ_Δ (m)	t _m (m)	m ₀₂
58-45	99	57	6.66	-12.82	7.80x10 ⁻⁸	2330	3.04	0.26	4.93x10 ⁻⁴	0.51	0.93	6.70x10 ⁻⁵	50	0.75
58-31	100	57	7.54	-12.65	1.99x10 ⁻⁷	900	4.18	0.40	8.09x10 ⁻⁴	0.44	1.00	2.21x10 ⁻⁴	19	0.73
58-28	99	56	7.87	-14.68	1.29x10 ⁻⁷	2195	4.33	-	-	-	-	-	-	0.80
58-46	99	58	7.87	-12.62	4.0 x10 ⁻⁸	970	4.88	0.38	1.13x10 ⁻³	0.55	1.25	1.74x10 ⁻⁵	30	0.71
58-71	93	56	8.75	-16.67	9.1 x10 ⁻⁸	3200	4.8	0.29	5.47x10 ⁻⁴	0.44	1.18	9.78x10 ⁻⁵	50	0.77
58-2	97	58	8.57	-16.82	4.73x10 ⁻⁷	3800	3.0	0.39	4.06x10 ⁻⁴	0.55	1.10	2.84x10 ⁻⁵	126	0.75
58-55	100	59	9.36	-15.27	4.10x10 ⁻⁷	884	4.61	0.23	7.04x10 ⁻³	0.44	1.11	2.04x10 ⁻⁴	20	0.67
58-59	101	57	9.08	-12.31	2.81x10 ⁻⁶	120	3.88	0.50	1.69x10 ⁻³	0.39	0.98	9.24x10 ⁻⁴	4.7	0.59
58-1	-	58	10.57	-18.55	6.87x10 ⁻⁷	465	4.3	0.31	1.07x10 ⁻³	0.44	1.00	3.25x10 ⁻⁴	15	0.67
58-31	100	64	10.61	-20.54	3.41x10 ⁻⁷	1290	4.6	0.30	4.93x10 ⁻⁴	0.34	0.93	1.61x10 ⁻⁴	27	0.73
58-43	101	65	10.61	-22.49	3.50x10 ⁻⁷	1140	4.9	0.31	5.80x10 ⁻⁴	0.51	1.17	2.60x10 ⁻⁴	22	0.77
58-3	101	63	10.61	-16.12	3.08x10 ⁻⁶	165	6.6	0.48	1.77x10 ⁻⁴	0.20	1.9	1.08x10 ⁻⁴	12	0.77
58-77	101	65	10.62	-22.57	1.13x10 ⁻⁷	3100	4.7	0.38	4.25x10 ⁻⁴	0.33	1.10	1.09x10 ⁻⁴	62	0.82
58-13	-	58	10.62	-27.43	2.15x10 ⁻⁸	10000	2.9	0.31	3.01x10 ⁻⁴	0.53	1.05	1.34x10 ⁻⁵	-	0.71
58-42	99	57	10.63	-15.52	4.18x10 ⁻⁶	225	4.8	0.60	1.73x10 ⁻³	0.24	1.08	1.19x10 ⁻³	4.8	0.69
58-4	100	58	10.63	-11.48	1.12x10 ⁻⁵	51.5	5.5	0.60	3.19x10 ⁻³	0.35	1.60	1.76x10 ⁻³	5.5	0.50
58-44	-	63	10.64	-13.90	4.53x10 ⁻⁶	110	4.8	0.62	2.33x10 ⁻⁴	0.19	0.84	1.87x10 ⁻³	3.2	0.59
58-126	100	61	11.35	-16.24	1.62x10 ⁻⁶	283	4.95	0.43	8.98x10 ⁻⁴	0.29	1.06	4.81x10 ⁻⁴	8.6	0.59
58-68	99	58	14.07	-18.35	1.04x10 ⁻⁵	45	6.37	0.68	-	-	-	-	-	0.77
58-11	90	58	14.17	-20.57	5.46x10 ⁻⁶	75	5.0	0.60	1.73x10 ⁻³	0.23	1.24	1.12x10 ⁻³	6.5	0.35
58-41	99	62	14.22	-16.46	1.06x10 ⁻⁵	60	5.8	-	-	0.34	-	-	-	0.34
58-1	100	59	15.46	-18.07	2.85x10 ⁻⁵	16.5	4.5	0.73	-	0.37	-	-	-	0.37
58-114	99	62	15.51	-20.55	2.24x10 ⁻⁵	30	6.61	0.88	4.40x10 ⁻³	0.17	2.0	3.49x10 ⁻³	3.9	0.60
58-134	96	58	16.54	-27.56	2.55x10 ⁻⁶	165	4.29	0.48	9.08x10 ⁻⁴	0.29	1.38	3.94x10 ⁻⁴	17.8	0.51
58-138	99	64	16.64	-19.63	2.47x10 ⁻⁵	17	3.70	0.91	-	0.27	-	-	-	0.27
58-13	97	64	16.65	-19.37	3.94x10 ⁻⁵	14.4	5.0	1.26	-	-	-	-	-	-
58-13	101	58	16.81	-23.63	1.95x10 ⁻⁵	42	3.73	0.50	-	0.31	-	-	-	0.31
58-13	97	56	17.53	-20.73	2.65x10 ⁻⁵	13	3.29	0.90	-	-	-	-	-	-

TABLE A.5.1
Results of constant load creep testing on saturated MFS samples,
nominal w = 25%

nominal applied axial stress
Temperature
minimum strain rate
time to failure
failure stress

test no.	S_1 (%)	D_r (%)	σ_1 (MPa)	T (°C)	$\dot{\epsilon}_m$ (s ⁻¹)	t_m (m)	ϵ_m (%)	at $t=1m$		
								ϵ_o	$\dot{\epsilon}_o$ (/m)	m
8-29	40	56	2.62	-10.93	8.91×10^{-7}	168	2.30	0.71	1.61×10^{-3}	0.83
9-53	44	72	3.45	-13.91	1.90×10^{-7}	570	1.83	0.40	1.42×10^{-3}	1.03
9-48	41	64	3.45	-18.43	6.2×10^{-8}	1200	1.60	0.45	1.01×10^{-3}	0.93
8-22	38	56	3.91	-11.13	4.36×10^{-6}	42	2.18	0.61	1.81×10^{-3}	0.71
8-26	39	55	3.92	-14.92	7.0×10^{-7}	182	1.88	0.47	1.09×10^{-3}	0.74
8-14	40	54	4.02	-15.52	2.42×10^{-6}	65	2.02	0.58	1.56×10^{-3}	0.78
8-21	38	54	3.98	-18.79	5.62×10^{-8}	1190	1.33	0.28	7.56×10^{-4}	0.87
8-73	39	56	4.58	-18.81	9.52×10^{-7}	159	2.31	0.50	1.42×10^{-3}	0.77
9-35	39	56	4.78	-11.69	2.26×10^{-5}	10.5	3.20	1.40	4.50×10^{-3}	0.86
9-36	39	56	4.78	-14.02	7.28×10^{-6}	29.5	2.85	0.95	2.94×10^{-3}	0.75
9-39	39	58	4.78	-16.22	2.66×10^{-6}	76	2.85	0.78	2.53×10^{-3}	0.82
9-40	39	57	4.78	-18.57	1.07×10^{-6}	159	2.60	0.64	1.83×10^{-3}	0.80
9-34	39	55	4.78	-20.69	3.52×10^{-7}	422	2.55	0.56	1.59×10^{-3}	0.85
9-12	38	57	4.87	-18.65	1.26×10^{-6}	145	2.71	0.62	1.85×10^{-3}	0.80
9-8	38	57	4.88	-19.20	1.84×10^{-6}	95	2.53	0.65	1.94×10^{-3}	0.73
8-64	39	56	4.92	-18.85	1.54×10^{-6}	113	2.48	0.71	2.01×10^{-3}	0.86
9-13	38	55	5.17	-18.70	2.02×10^{-6}	100	2.96	0.61	2.56×10^{-3}	0.75
8-42	40	66	5.22	-16.51	1.39×10^{-5}	18.5	3.50	1.37	2.87×10^{-3}	0.66
8-58	39	55	5.27	-18.62	4.26×10^{-6}	42	2.50	0.82	2.01×10^{-3}	0.70
8-66	38	48	5.26	-18.69	3.80×10^{-6}	60	2.96	0.94	2.53×10^{-3}	0.79
8-54	40	55	5.34	-18.55	3.89×10^{-6}	58	2.88	0.79	3.15×10^{-3}	0.83
8-53	38	55	5.57	-18.84	9.97×10^{-6}	23	2.78	1.00	3.92×10^{-3}	0.84
8-51	41	60	5.69	-18.23	8.62×10^{-6}	29	3.10	0.90	2.88×10^{-3}	0.68
8-65	40	55	5.91	-18.83	1.85×10^{-5}	13	2.84	0.69	3.58×10^{-3}	0.69
8-52	39	55	6.03	-18.28	1.12×10^{-5}	24	2.80	0.94	3.23×10^{-3}	0.66
8-49	40	58	5.79	-20.21	2.26×10^{-6}	87	2.70	0.72	1.90×10^{-3}	0.72
8-50	40	57	6.24	-18.84	2.04×10^{-5}	11	2.80	1.15	4.20×10^{-3}	0.68
8-56	39	54	6.41	-18.53	2.17×10^{-5}	11.6	3.03	1.18	3.85×10^{-3}	0.62
8-67	39	55	6.42	-18.52	2.03×10^{-5}	13	3.07	1.18	4.25×10^{-3}	0.77
8-69	39	56	6.50	-20.68	1.1×10^{-5}	22	2.93	0.96	3.04×10^{-3}	0.73
8-48	40	61	6.51	-16.52	5.62×10^{-5}	4.2	2.90	1.59	6.21×10^{-3}	0.70
8-47	41	62	6.50	-18.59	3.28×10^{-5}	7.5	3.02	1.40	5.05×10^{-3}	0.79
8-39	41	59	6.52	-18.47	2.89×10^{-5}	8.4	3.00	0.78	4.85×10^{-3}	0.65
8-19	39	52	6.55	-18.88	3.98×10^{-5}	7	3.00	1.48	5.66×10^{-3}	0.80
8-31	40	58	6.57	-18.80	1.64×10^{-5}	15	2.86	0.48	3.74×10^{-3}	0.74
8-63	39	56	6.61	-18.84	3.83×10^{-5}	6.5	3.04	1.20	5.66×10^{-3}	0.82
8-57	39	56	6.70	-18.36	3.25×10^{-5}	9	2.97	1.10	4.77×10^{-3}	0.58
8-70	39	54	7.02	-18.58	2.76×10^{-5}	9.3	3.18	1.18	5.47×10^{-3}	0.71
8-40	41	59	7.03	-20.59	2.19×10^{-5}	11.2	2.97	1.18	4.01×10^{-3}	0.61
9-1	38	57	7.08	-18.66	5.89×10^{-5}	4.3	2.63	1.15	5.73×10^{-3}	0.55

TABLE A.5.2

Results of constant load creep testing on partially saturated MFS samples,
nominal $\sigma_3 = 10\%$

test no.	S_i (%)	D_r (%)	σ_l (MPa)	T (°C)	$\dot{\epsilon}_m$ (s ⁻¹)	t_m (m)	ϵ_m (%)	at $t = t_m$ ϵ_o	ϵ_o (/m)	m_o
8-05-3	20	57	1.382	-19.09	1.63×10^{-7}	390	1.29	0.43	8.98×10^{-4}	0.92
9-05-2	18	57	2.166	-20.09	6.34×10^{-7}	200	2.52	0.75	1.73×10^{-3}	0.88
9-05-1	20	56	2.168	-18.78	1.27×10^{-6}	100	1.90	0.58	1.39×10^{-3}	0.85
8-05-2	20	55	3.064	-19.14	2.74×10^{-5}	6.5	2.18	1.04	4.19×10^{-3}	0.57
9-05-5	19	54	3.146	-18.56	4.92×10^{-5}	3.2	1.98	1.23	4.55×10^{-3}	0.59
9-05-3	19	54	3.149	-20.42	1.64×10^{-5}	13	2.51		3.30×10^{-3}	0.72
8-05-1	21	56	4.348	-19.02	2×10^{-4}	1.5	2.5	-	-	-
8-03-1	12	55	1.38	-18.59	7.26×10^{-5}	1.5	1.41	1.25	4.62×10^{-3}	0.70

TABLE A.5.3

Results of constant load creep testing on partially saturated MFS
nominal $w = 5, 3\%$

test no.	S_1 (%)	w (%)	D_r (%)	σ_1 (MPa)	T (°C)	$\dot{\epsilon}_m$ (%)	t_m (m)	ϵ_m (%)	at $t = 1$ m		at break Δ	
									ϵ_o	ϵ_o (m)	ϵ_Δ (%)	ϵ_Δ (m)
80-20-1	33	10.0	18.5	4.83	-18.96	6.62×10^{-5}	550	3.73	1.63	7.38×10^{-3}	0.50	-
80-40-1	37	10.0	42.4	4.83	-18.62	5.66×10^{-6}	49	3.14	0.51	3.96×10^{-3}	0.95	-
80-80-1	43	9.5	79.2	4.82	-18.97	1.07×10^{-7}	859	1.65	0.71	9.29×10^{-4}	0.88	-
S80-20-2	100	29.7	21.6	10.47	-15.32	1.02×10^{-5}	120	9.3	0.70	1.56×10^{-3}	0.17*	9.19×10^{-4}
S80-20-1	100	28.4	30.6	10.49	-15.42	3.68×10^{-6}	140	4.58	0.38	9.96×10^{-4}	0.24	5.35×10^{-4}
S80-40-1	99	26.2	45.9	10.49	-15.42	5.46×10^{-6}	50	2.91	0.60	1.23×10^{-3}	0.30	5.80×10^{-4}
S80-80-1	99	20.9	86.6	10.48	-15.46	1.12×10^{-7}	1360	2.88	0.62	7.13×10^{-4}	0.54	1.35×10^{-4}
S80-90-1	-	-	$90_{(nom.)}$	10.50	-15.46	1.05×10^{-7}	1375	2.78	0.49	8.48×10^{-4}	0.54	1.96×10^{-4}
												20*
												0.37*
												0.45
												7.1
												0.42
												18.8
												0.88
												13.3
												0.89

TABLE A.5.4

Results of constant load creep testing on varying D_r MFS samples

test no.	S_1 (V)	D_1 (V)	σ_1 (MPa)	T (°C)	$\dot{\epsilon}_1$ before Δ (s ⁻¹)	$\dot{\epsilon}_2$ after Δ (s ⁻¹)	t_{Δ} (s)	σ_2 (V)	E (KJ/m)
S8-51	101	57	5.33	-19.17	3.63×10^{-8}	1.14×10^{-7}	128	0.31	460
				-17.84					
				-20.39	6.08×10^{-10}	2.02×10^{-9}	1415	0.36	344
S8-49	100	53	6.54	-18.53					
				-18.76	2.69×10^{-7}	4.84×10^{-7}	137	0.72	233
				-17.40	2.41×10^{-7}	1.32×10^{-7}	333	1.09	227
S8-26	99	54	6.72	-18.82					
				-14.87	1.82×10^{-6}	5.79×10^{-6}	60	1.38	114
				-11.87					
S8-50	101	51	7.86	-18.46	8.62×10^{-7}	1.31×10^{-6}	114	1.12	183
				-17.24	1.72×10^{-7}	9.55×10^{-8}	1214	3.84	284
				-18.40					
S8-55	101	57	8.02	-14.86	9.77×10^{-7}	2.08×10^{-7}	122	1.42	230
				-13.04					
S8-56	100	57	8.15	-15.11	6.68×10^{-7}	2.21×10^{-6}	137	1.28	216
				-12.03	8.08×10^{-7}	1.76×10^{-7}	312	2.53	271
				-15.15					
S8-60	99	55	8.61	-18.59	1.41×10^{-7}	3.43×10^{-7}	1484	6.38	190
				-16.07					
S8-52	101	56	9.04	-10.70	7.41×10^{-7}	1.18×10^{-6}	121	0.53	186
				-18.37	4.60×10^{-7}	2.71×10^{-7}	368	2.44	219
				-19.66	1.57×10^{-7}	2.90×10^{-7}	1332	3.61	228
S8-57	101	51	9.24	-18.23	2.60×10^{-7}	1.44×10^{-7}	1511	3.90	219
				-19.67					
S8-57	101	51	9.24	-15.08	2.97×10^{-6}	5.40×10^{-6}	59	2.58	174
				-13.06	2.21×10^{-6}	1.09×10^{-6}	167	4.58	188
				-15.13					
S8-63	101	53	9.25	-15.07	2.35×10^{-6}	4.49×10^{-6}	65	2.70	178
				-13.07	2.26×10^{-6}	1.04×10^{-6}	187	4.82	216
				-15.06	1.02×10^{-6}	2.27×10^{-6}	281	6.44	220
S8-71	99	52	10.61	-13.05					
				-18.66	2.29×10^{-6}	4.27×10^{-7}	100	4.02	146
				-16.29					
S8-73	100	54	10.61	-16.28	5.89×10^{-6}	2.85×10^{-6}	42	3.95	164
				-18.65					
S8-74	99	59	10.61	-18.62	1.63×10^{-6}	3.3×10^{-6}	105	2.47	162
				-16.28					
S9-127	99	61	11.52	-18.19	1.73×10^{-6}	3.55×10^{-6}	121	2.94	153
				-15.69					
S9-112	100	59	12.82	-18.29	1.63×10^{-5}	2.59×10^{-5}	14	2.20	93.2
				-15.64					
S9-22	101	61	14.15	-18.04	2.16×10^{-5}	3.58×10^{-5}	13	2.78	126
				-15.85					
S9-19	100	61	14.17	-18.18	1.64×10^{-5}	2.38×10^{-5}	11	2.77	86.2
				-15.91					
S9-67	99	55	14.20	-18.61	1.39×10^{-5}	1.32×10^{-5}	40	3.78	164
				-16.14					
S9-8	101	60	14.20	-18.32	1.18×10^{-5}	1.09×10^{-5}	34	4.16	140
				-16.11					
S9-33	99	57	14.20	-18.17	1.47×10^{-7}	2.10×10^{-7}	21	3.30	106
				-16.01					
S9-68	100	62	14.22	-18.10	1.30×10^{-7}	2.30×10^{-7}	11	3.80	100
				-15.93					
S9-5	98	58	14.24	-18.02	2.40×10^{-7}	3.09×10^{-7}	7	3.60	100
				-15.84					
S9-27	100	60	15.46	-18.75	3.89×10^{-7}	1.59×10^{-7}	4	4.07	100
				-20.61					
S9-128	100	64	15.56	-24.66	1.19×10^{-7}	1.00×10^{-7}	6	4.99	100
				-22.88					
S9-113	99	64	15.56	-22.60	1.10×10^{-7}	2.00×10^{-7}	1	4.81	100
				-20.74					
S9-111	98	54	15.53	-20.52	3.40×10^{-7}	4.61×10^{-7}	12	4.10	100
				-18.11					

Δ = time to failure

Δ = time before failure

TABLE A.2.2

Results of temperature-time creep tests on saturated MBS
with computed experimental activation energies

test no.	S_1 (%)	D_r (%)	σ_1 (MPa)	T (°C)	$\dot{\epsilon}_1$ before Δ (s ⁻¹)	$\dot{\epsilon}_1$ after Δ (s ⁻¹)	t_{Δ} (m)	ϵ_{Δ} (%)	E (kJ/m)
9-38	37	59	2.49	-18.73 -16.32	1.7×10^{-9}	2×10^{-8}	327	0.26	347
9-41	38	55	3.13	-18.48 -16.04	1.81×10^{-7}	8.2×10^{-7}	90	0.65	326
9-44	39	56	3.13	-18.56 -16.15	6.83×10^{-8}	4.13×10^{-7}	190	0.62	402
9-37	39	56	3.15	-18.72 -16.22	2.33×10^{-4}	1.68×10^{-7}	361	0.75	456
9-25	39	57	3.15	-18.71 -16.29	7.00×10^{-7}	1.90×10^{-6}	36	0.36	225
8-35	40	55	3.91	-18.85 -14.53	2.41×10^{-7}	2.51×10^{-6}	374	1.62	294
9-28	39	58	4.09	-20.60 -18.25	8.37×10^{-7}	1.40×10^{-6}	64	1.05	216
9-43	39	54	4.67	-18.31 -16.18	1.84×10^{-6}	4.25×10^{-6}	41	1.77	211
9-42	39	56	4.67	-18.09 -15.84	1.05×10^{-7}	2.61×10^{-6}	79	2.00	224
9-40	38	56	4.73	-18.39 -16.14	9.49×10^{-7}	2.40×10^{-6}	120	1.96	222
9-10	33	57	3.08	-20.40 -18.24	2.86×10^{-5}	5.56×10^{-6}	25	1.50	150
9-24	33	56	5.12	-18.75 -16.39	5.3×10^{-6}	1.0×10^{-5}	12	1.48	139
9-14	33	57	5.14	-20.44 -18.26	2.79×10^{-6}	5.56×10^{-6}	20	1.03	172
9-46	41	53	3.21	-18.76 -16.39	5.79×10^{-6}	9.55×10^{-6}	13	1.49	139
9-20	33	54	3.49	-20.41 -18.18	9.28×10^{-6}	9.60×10^{-6}	14	1.53	149
9-2	33	56	3.3	-20.67 -18.22	5.10×10^{-6}	9.23×10^{-6}	20	1.98	140
9-1	33	57	3.13	-20.69 -18.32	7.94×10^{-6}	1.41×10^{-5}	10	1.70	128
9-36	4	53	3.78	-18.48 -16.29	8.04×10^{-6}	1.3×10^{-5}	19	2.33	123
9-7	40	53	3.78	-20.63 -18.19	1.95×10^{-6}	4.62×10^{-6}	31	1.44	218
9-12	33	57	3.79	-20.71 -18.34	5.75×10^{-6}	1.15×10^{-5}	30	2.35	154
9-4	33	58	3.94	-20.46 -18.26	7.33×10^{-6}	1.25×10^{-5}	20	2.87	126
9-11	33	56	3.14	-20.41 -18.26	7.76×10^{-6}	1.22×10^{-5}	20	1.05	11
9-16	33	56	3.18	-20.43 -18.26	1.05×10^{-5}	1.71×10^{-5}	9	1.09	12

t_{Δ} = time of change

$\dot{\epsilon}_1$ = strain before change

TABLE A.1.1.1

Stress-strain curves for partially saturated MS
with different experimental conditions

test no.	S_i (%)	D_r (%)	σ_1 (MPa)	T (°C)	$\dot{\epsilon}_1$ before Δ (s ⁻¹)	$\dot{\epsilon}_2$ after Δ (s ⁻¹)	t_Δ (m)	ϵ_Δ (%)	E (kJ/m)
9-05-8	19	54	1.99	-20.43	1.74×10^{-6}	4.14×10^{-6}	15	0.81	211
				-18.26	1.23×10^{-6}	2.82×10^{-7}	60	1.31	350
9-05-10	19	54	2.01	-20.50					
				-18.24	2.46×10^{-6}	6.43×10^{-6}	14	0.46	222
9-05-7	19	55	2.17	-15.90					
				-20.48	1.30×10^{-6}	3.53×10^{-6}	30	0.78	231
9-05-9	18	54	2.32	-18.20					
				-20.42	3.97×10^{-6}	7.84×10^{-6}	16	1.27	166
9-05-11	20	54	2.68	-18.25					
				-20.86	4.54×10^{-6}	8.23×10^{-6}	17	1.52	154
				-18.83					

t_Δ = time to change Δ
 ϵ_Δ = strain at change Δ

TABLE A.5.7

Results of temperature stage creep tests on partially saturated MFS
with computed experimental activation energy

test no.	$S_L(\%)$	$L_L(\%)$	σ_L (MPa)	$T(^{\circ}\text{C})$	$\dot{\epsilon}_1$ before Δ (s ⁻¹)	$\dot{\epsilon}_2$ after Δ (s ⁻¹)	L_c (mm)	$\epsilon_c(\%)$	$\dot{\epsilon} = \frac{\dot{\epsilon}_2 - \dot{\epsilon}_1}{\Delta t}$ (MPa ⁻¹ s ⁻¹)
S8-41	100	57	7.05	-12.81	1.91×10^{-6}	9.5×10^{-7}	50	1.05	1.356
			6.53		9.1×10^{-6}	3.6×10^{-7}	4500	3.14	1.625
			7.29						
S9-39	101	58	8.17	-18.62	1.16×10^{-6}	1.74×10^{-6}	31	3.6	0.896
			9.54		8.13×10^{-7}	2.42×10^{-6}	156	1.74	0.803
			10.30						
S9-9	101	59	9.60	-18.82	1.73×10^{-6}	4.26×10^{-6}	68	1.47	0.827
			11.14		1.76×10^{-6}	2.94×10^{-6}	151	2.80	0.619
			11.97						
S9-115	100	64	10.06	-18.22	3.13×10^{-6}	8.77×10^{-6}	63	2.4	0.729
			11.48		3.06×10^{-6}	6.61×10^{-6}	120	3.95	0.578
			12.81						
S9-129	100	59	11.43	-18.07	4.04×10^{-6}	8.25×10^{-6}	44	2.31	0.524
			12.87		5.31×10^{-6}	1.00×10^{-5}	59	3.97	0.510
			14.15						
S9-139	100	57	11.43	-18.22	3.06×10^{-6}	6.58×10^{-6}	80	3.09	0.507
			12.86		4.36×10^{-6}	8.32×10^{-6}	160	5.33	0.441
			14.20						
S9-118	101	59	12.82	-18.16	6.64×10^{-6}	1.66×10^{-5}	24	2.64	0.477
			14.19		1.08×10^{-5}	1.85×10^{-5}	55	4.87	0.399
			15.54						
S9-24	99	56	13.67	-26.58	3.06×10^{-6}	5.82×10^{-6}	16	3.81	0.466
			15.06		3.82×10^{-6}	6.41×10^{-6}	54	2.38	0.377
			16.23						
S9-14	1	65	14.21	-13.23	1.84×10^{-6}	2.60×10^{-5}	15	3.06	0.328
			15.52		2.54×10^{-5}	3.97×10^{-5}	31	5.62	0.325
			16.89						
9-7	99	58	4.09	-18.36	1.41×10^{-6}	5.01×10^{-6}	29	0.82	1.88
			4.76		1.45×10^{-6}	4.79×10^{-7}	75	1.62	1.76
			4.08		4.79×10^{-6}	3.39×10^{-6}	103	1.58	1.91
9-10	99	57	5.11	-18.36	1.76×10^{-6}	1.74×10^{-6}	141	2.11	2.25
			4.98		1.74×10^{-6}	2.34×10^{-6}	194	2.17	2.54
			5.13						
9-15	99	57	4.77	-18.51	3.61×10^{-6}	8.81×10^{-6}	19	1.35	1.43
			5.46		3.63×10^{-6}	1.20×10^{-6}	51	2.36	1.67
			4.78						
9-17	99	56	4.78	-18.61	2.78×10^{-6}	9.73×10^{-6}	24	1.50	1.75
			5.47		3.90×10^{-6}	1.20×10^{-6}	44	2.15	1.77
			4.78						
9-23	99	55	4.78	-18.66	6.03×10^{-6}	1.62×10^{-6}	9	3.99	1.44
			5.47		3.83×10^{-6}	1.23×10^{-6}	47	2.14	1.64
			4.78						
9-27	99	56	4.78	-18.76	1.64×10^{-6}	1.0×10^{-4}	7	3.96	1.32
			5.16		1.74×10^{-6}	1.78×10^{-6}	17	2.07	1.41
			4.78						
9-13	99	57	5.47	-18.66	6.92×10^{-6}	1.96×10^{-5}	13	1.69	1.52
			4.78						
			5.47						
9-21	98	55	5.47	-18.68	6.89×10^{-6}	1.75×10^{-6}	14	1.82	1.35
			5.16		1.91×10^{-6}	3.89×10^{-6}	24	2.05	1.33
			5.4						
9-26	98	56	5.16	-18.44	4.84×10^{-6}	1.75×10^{-6}	14	1.7	1.34
			4.78		2.78×10^{-6}	2.09×10^{-6}	23	1.75	1.48
			5.16						

Δ = time of change

$\dot{\epsilon}_1$ = strain rate before change

TABLE A.5.2b

Results of three-stage creep test on saturated and partially saturated M

quantity	MFS 20% Si	MFS 40% Si	MFS 100% Si
ϵ_m (%)	2.13	2.69	4.61
± 1 st. dev.	± 0.45	± 0.46	± 0.99
$\epsilon_m = B t_m^\gamma$			
B (s^{-1})	2.78×10^{-4}	4.20×10^{-4}	8.10×10^{-4}
γ	-1.194	-1.205	-1.129
γ^2	0.991	0.993	0.987
no. of data pts.	7	40	28
RPT parameters:			
$E = \Delta F - \beta \sigma$			
ΔF (kJ/mole)	455	488	316
β (MPa^{-1})	114	62	14.5

TABLE A.5.9

Summary of observed and computed quantities for MFS at 55% D_r

test no.	$S_i(\%)$	$D_r(\%)$	$T(^{\circ})$	σ_{peak} (MPa)	$\epsilon_f(\%)$	$\dot{\epsilon}(s^{-1})$	mode of failure	comments
8-11	40	56	-18.0	12.73	1.03	0.16	brittle	
8-12	40	56	-18.1	12.73	1.28	0.19	"	
8-5	39	56	-14.6	10.74	1.03	0.14	brittle	
8-17	39	56	-14.6	9.72	1.44	0.19	"	
8-18	40	56	-14.7	10.34	0.85	0.13	"	
8-6	39	57	-10.8	9.76	2.06	0.15	brittle	
8-7	40	56	-10.6	8.88	1.40	0.23	"	
8-9	41	58	-10.5	9.50	1.76	0.24	"	
8-10	41	58	-10.3	8.61	1.50	0.16	"	
8-8	100*	55*	-19.6	43.49	1.85	0.22	brittle	
8-14	100*	55*	-18.1	42.82	3.52	0.29	brittle	
8-15	100*	55*	-18.1	42.96	2.70	0.22	"	
8-16	100*	55*	-18.1	44.83	3.18	0.27	"	
8-7	100*	55*	-14.8	40.05	-	-	brittle	
8-11	100*	55*	-14.6	39.60	-	-	"	
8-19	100*	55*	-14.6	39.36	3.81	0.29	"	
8-13	100*	55*	-10.6	31.99	3.81	0.28	brittle	
8-21	100*	55*	-10.6	32.52	-	-	"	
8-22	100*	55*	-10.8	31.95	2.42	0.24	"	
8-32	100*	55*	-14.5	36.40	1.22	0.109	brittle	w/special jig
8-33	100	56	-14.5	36.29	1.18	0.105	"	"
8-34	99	54	-14.6	36.36	1.17	0.105	"	"
8-35	100	56	-14.8	29.55	1.32	0.0113	ductile	w/special jig
8-36	96	53	-14.7	29.84	1.17	0.0109	"	"
8-37	100	59	-14.6	29.59	1.12	0.0104	"	"
8-38	100	53	-14.6	31.95	1.17	0.0200	ductile/brittle	w/special jig

*nominal values

ϵ_f = strain at peak stress

$\dot{\epsilon}$ = applied strain rate

TABLE A.5.10

Summary of unconfined strength testing on MFS at 55% Dr

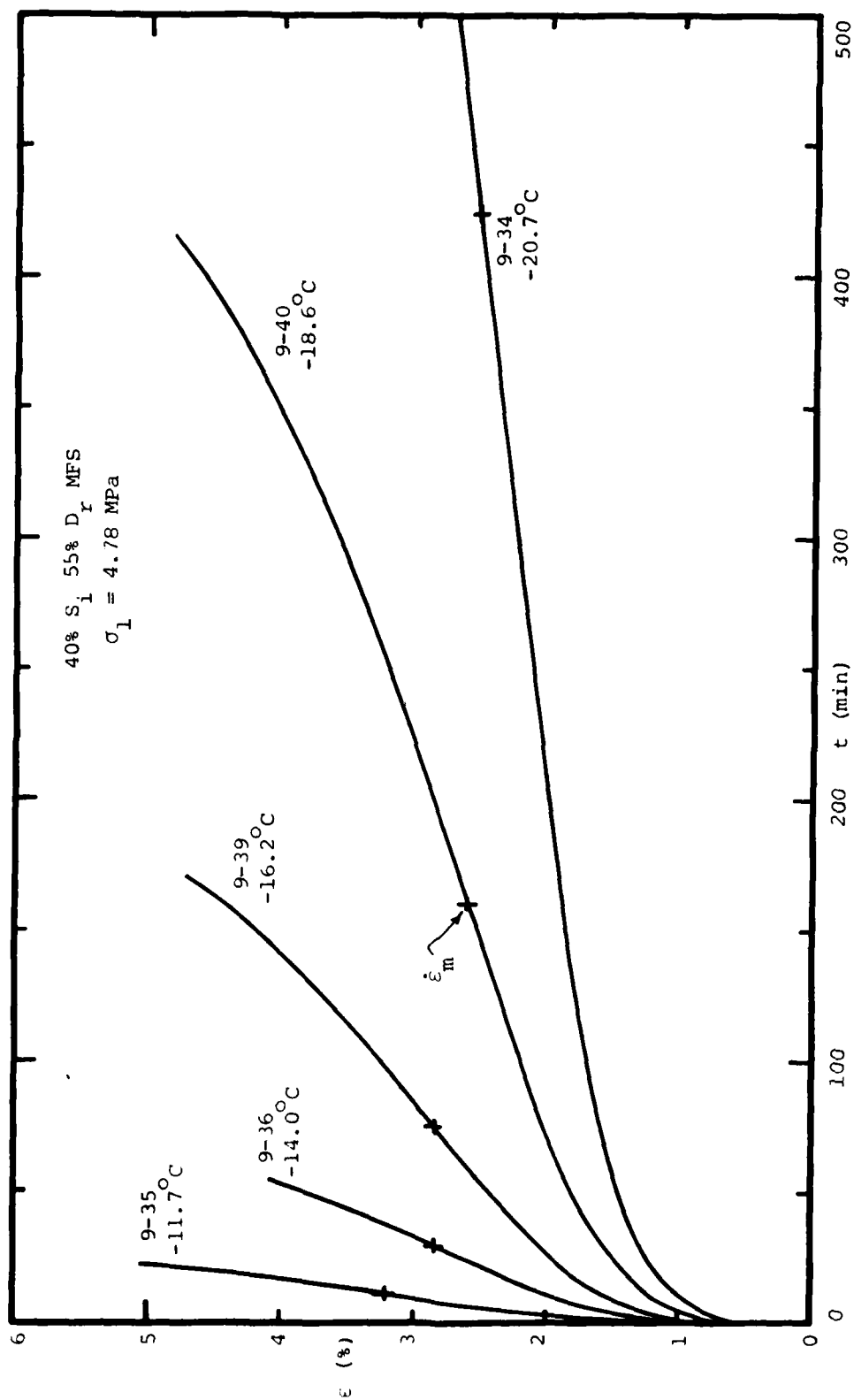


FIGURE A.5.1 Results of creep testing on 40% S_i 55% D_r MFS at $\sigma_1 = 4.78$ MPa, various temperatures

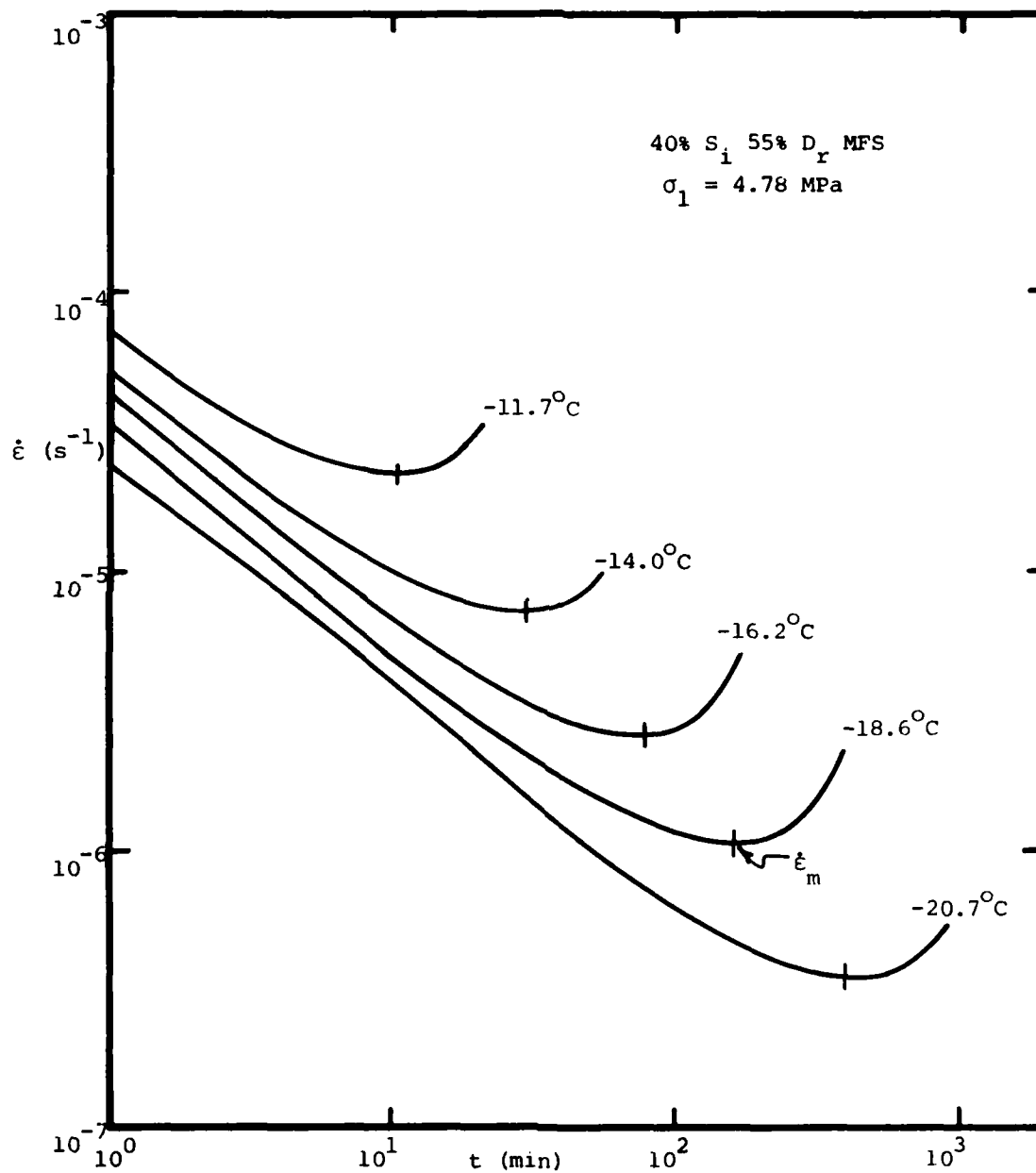


FIGURE A.5.2 Results of creep testing on 40% S_i 55% D_r MFS at $\sigma_1 = 4.78$ MPa, various temperatures

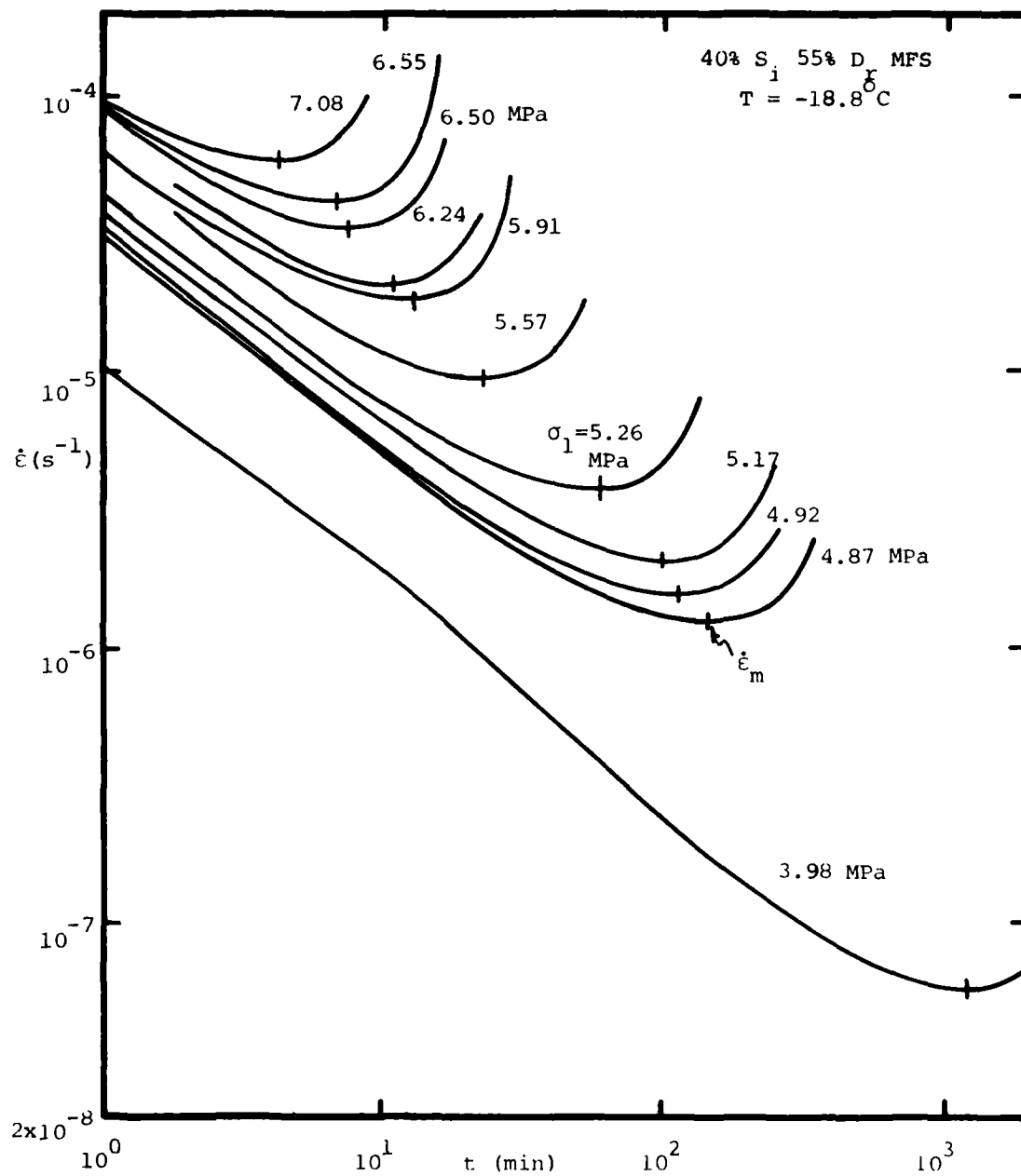


FIGURE A.5.3 Results of creep testing on 40% S_i 55% D_r MFS at -18.8°C, various stresses

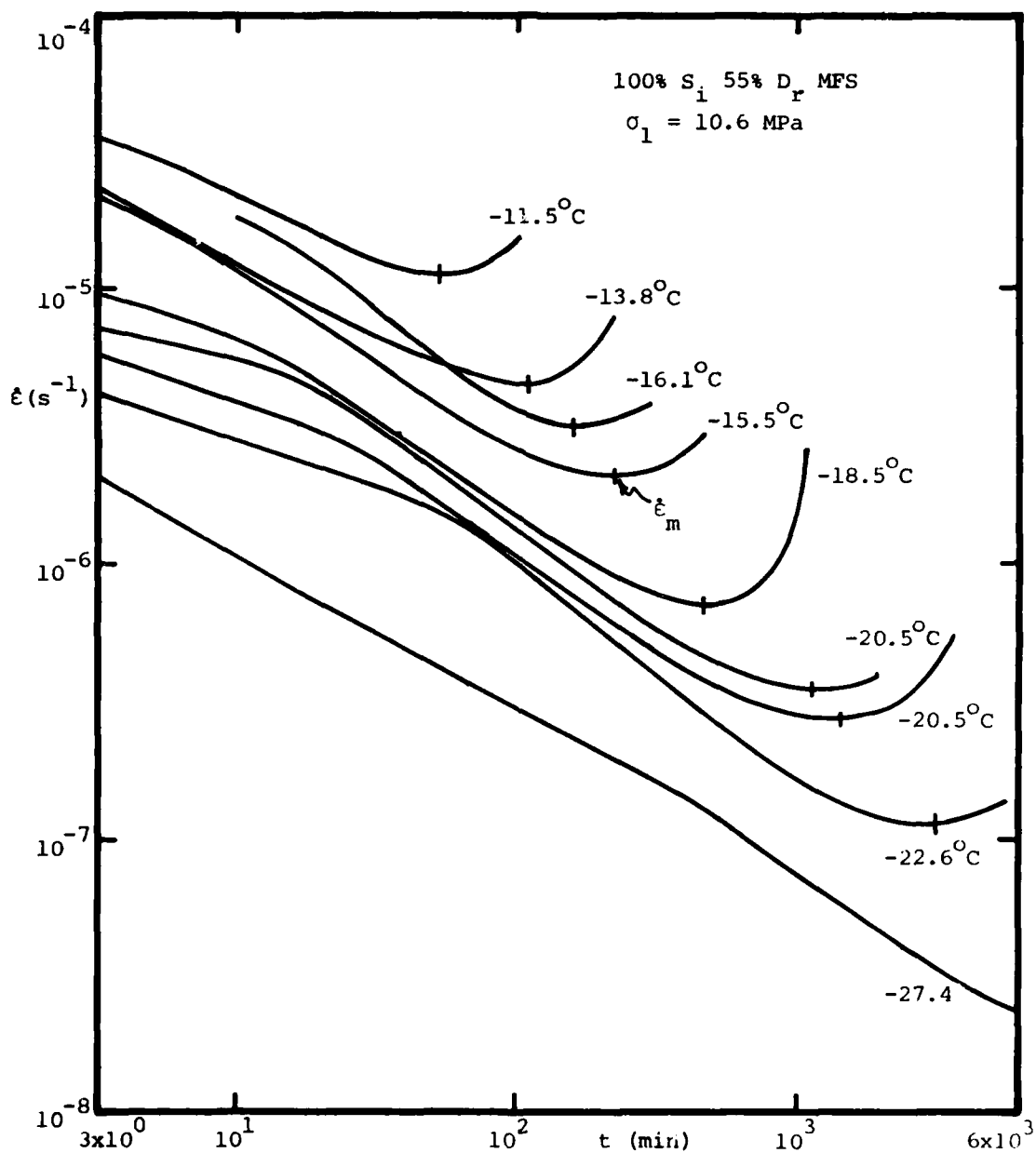


FIGURE A.5.4 Results of creep testing on saturated 55 % D_r MFS
 at $\sigma_1 = 10.6 \text{ MPa}$, various temperatures

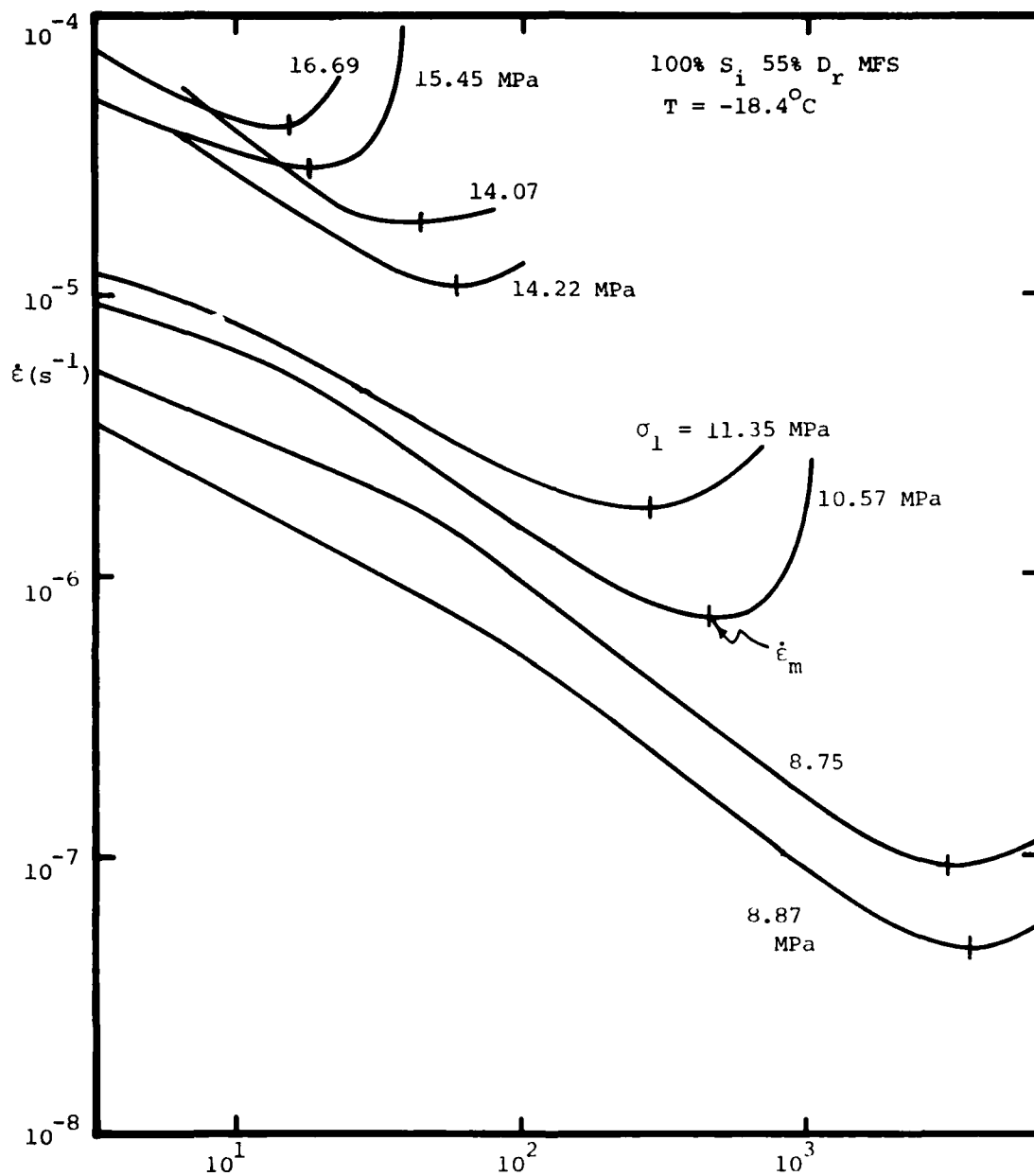


FIGURE A.5.5 Results of creep testing on saturated 55% D_r MFS at
T = -18.4°C, various stresses

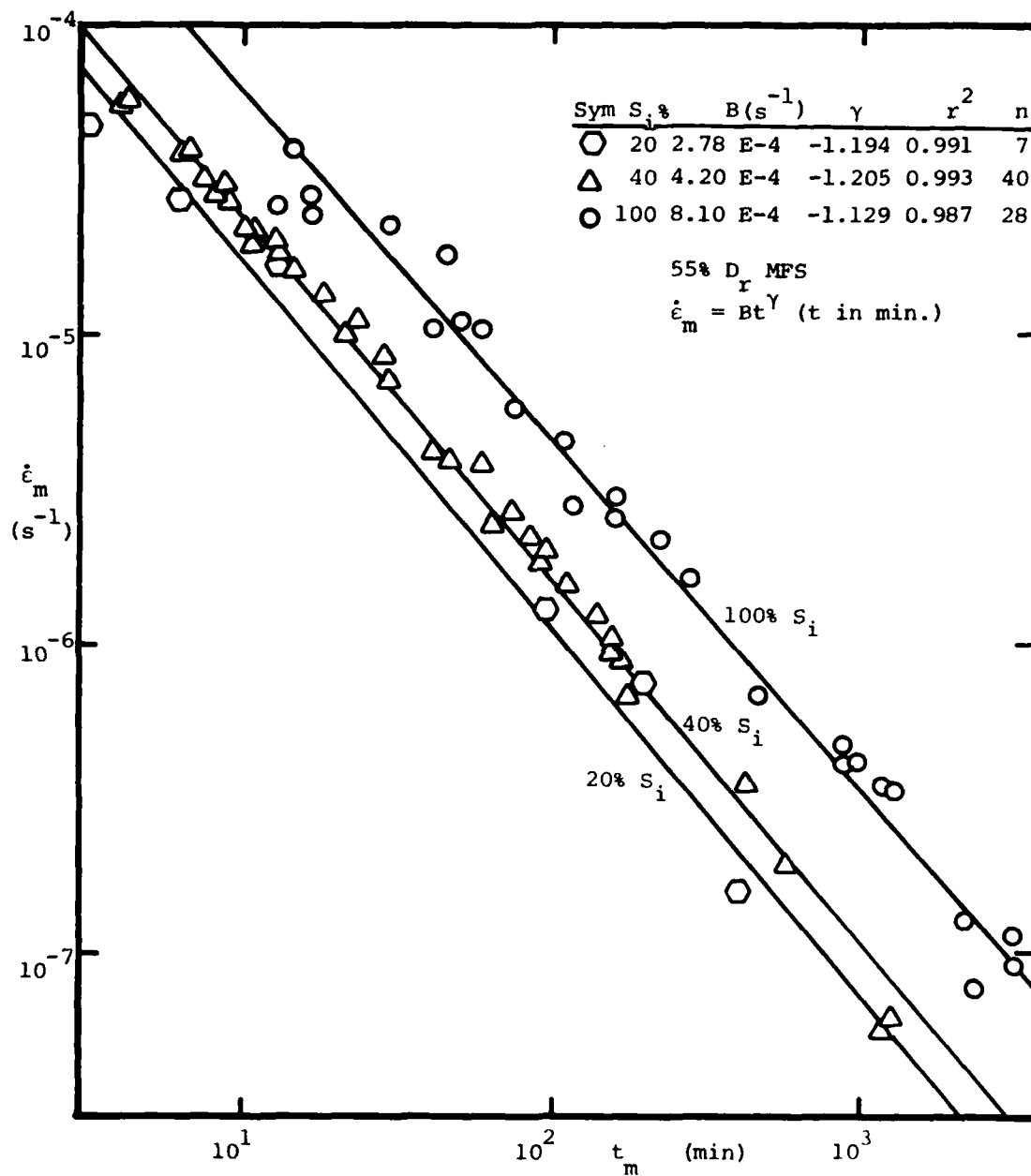


FIGURE A.5.6 Summary of minimum creep data for 55% relative density Manchester Fine Sand at various degrees of ice saturation

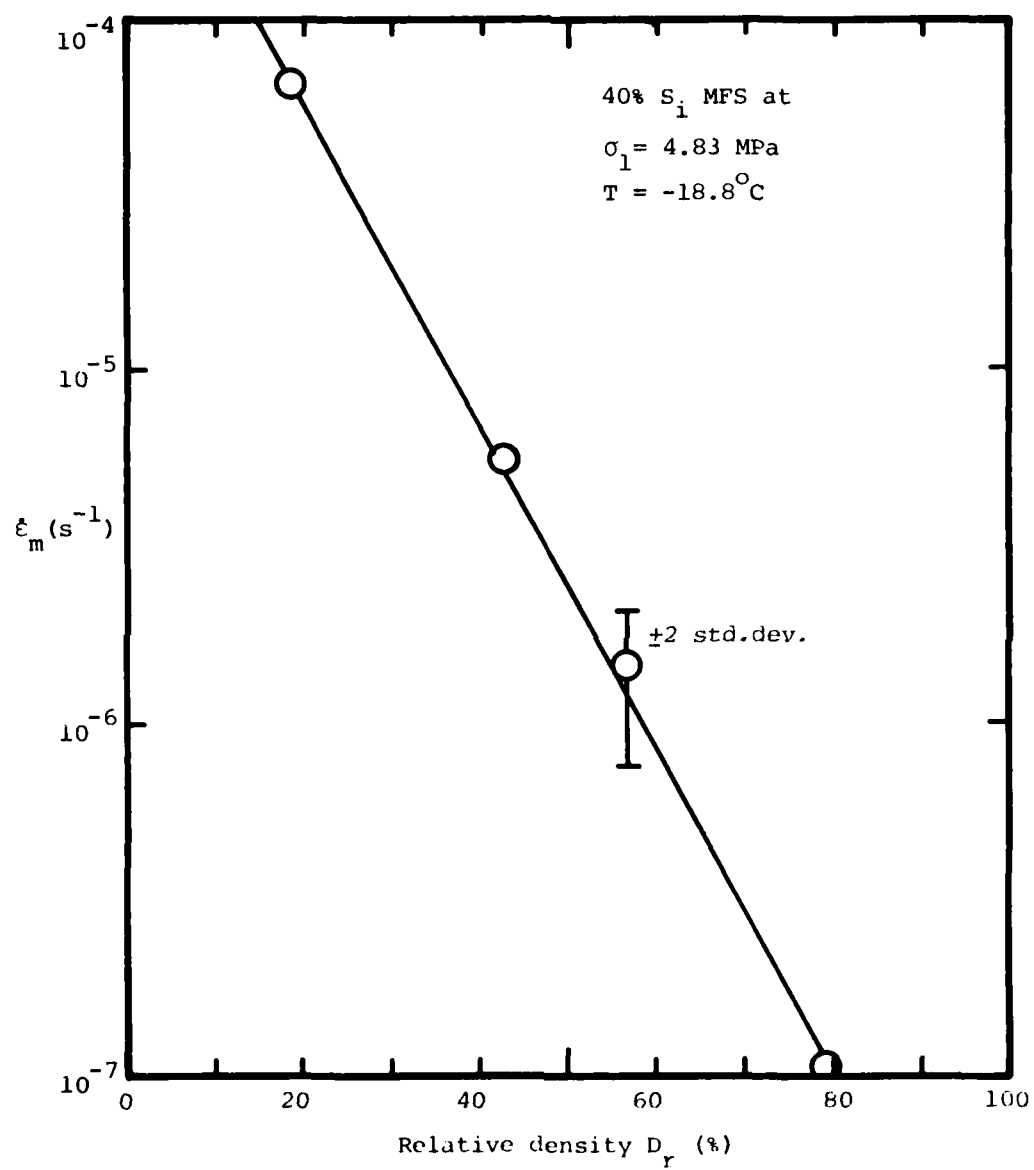


FIGURE A.5.7 Results of creep testing on 40% S_i MFS at varying D_r .

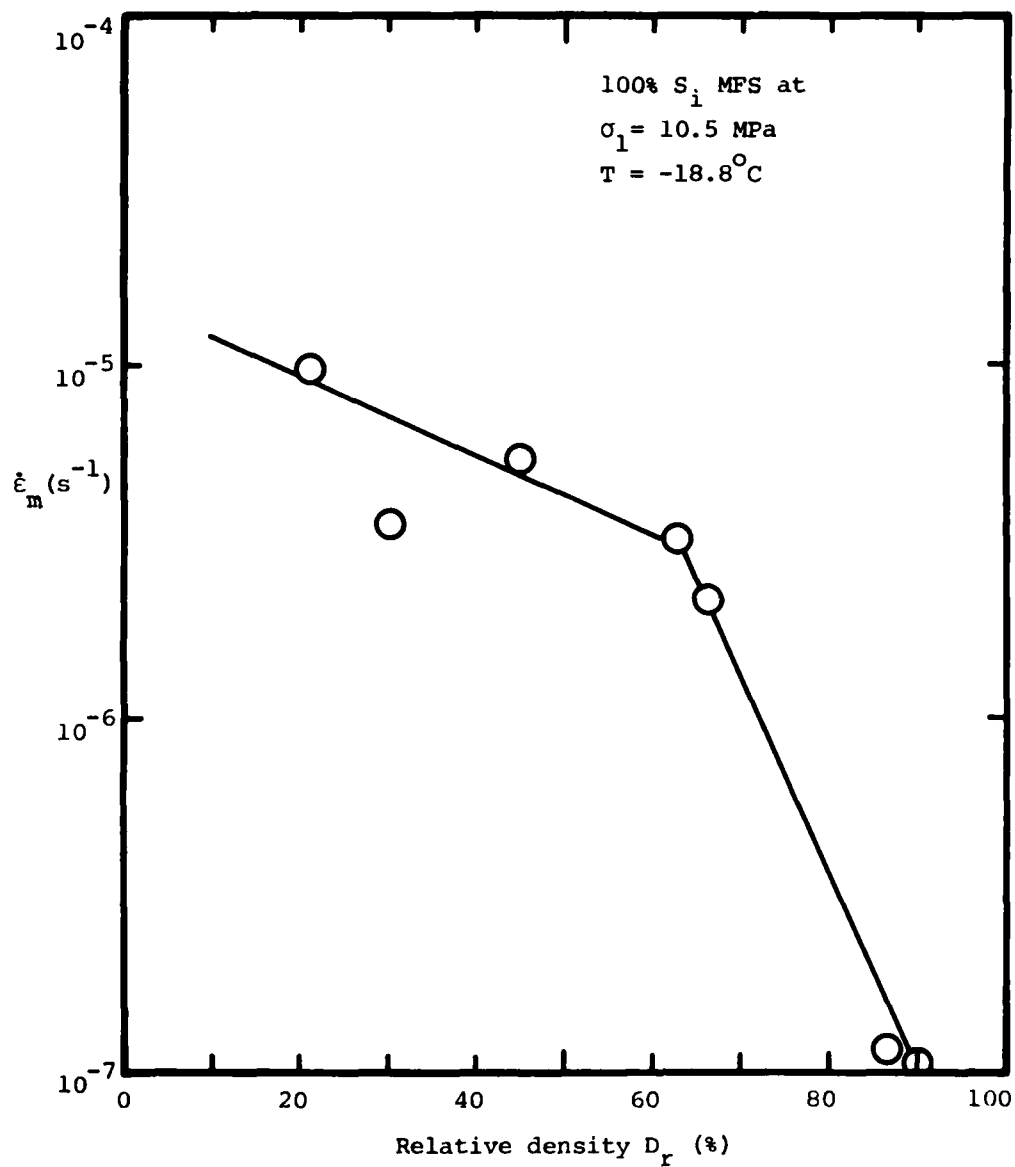


FIGURE A.5.8 Results of creep testing on saturated MFS at varying D_r

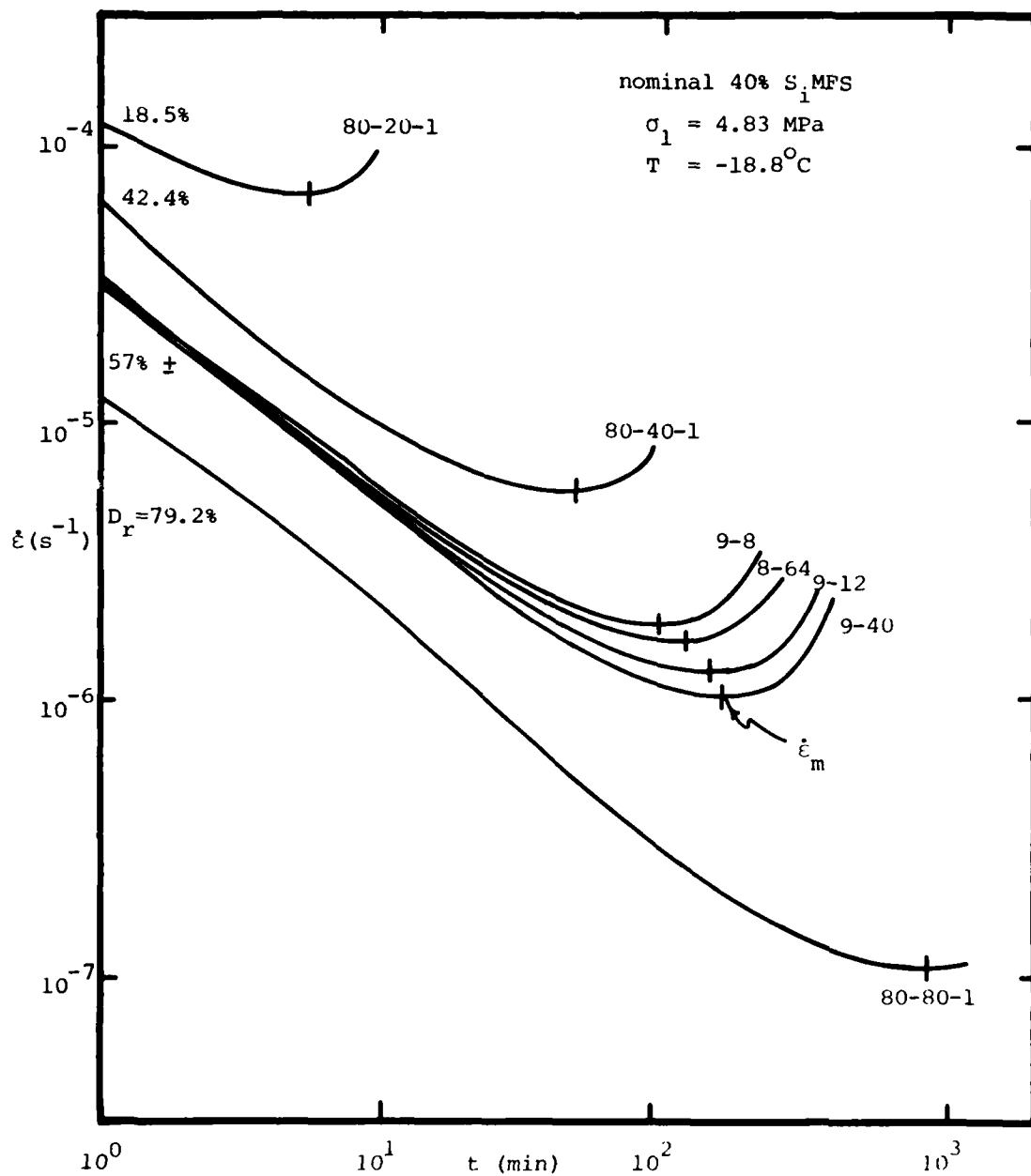


FIGURE A.5.9 Results of creep testing on 40% S₁ MFS at varying D_r

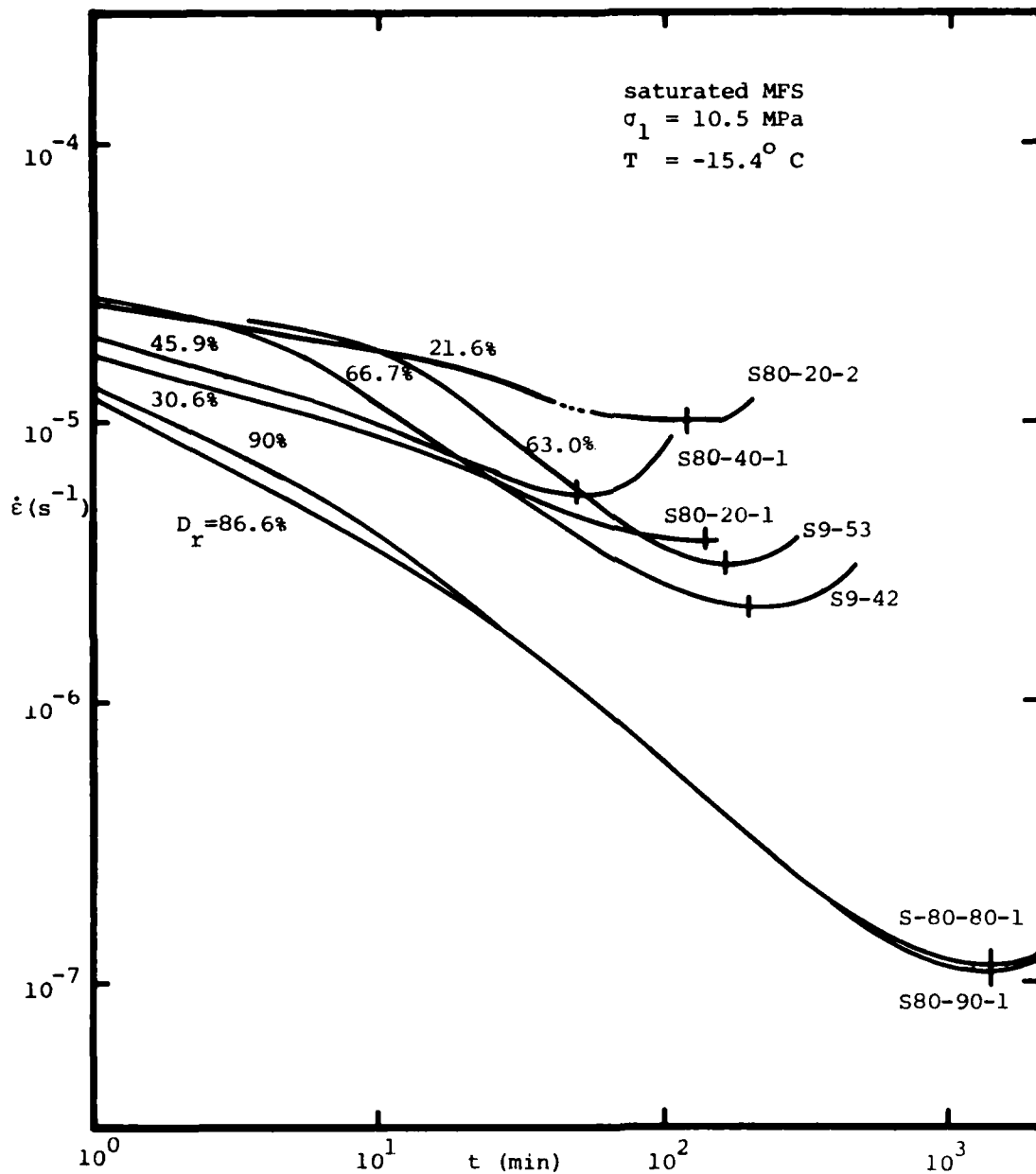


FIGURE A.5.10 Results of creep testing on saturated MFS at varying relative density

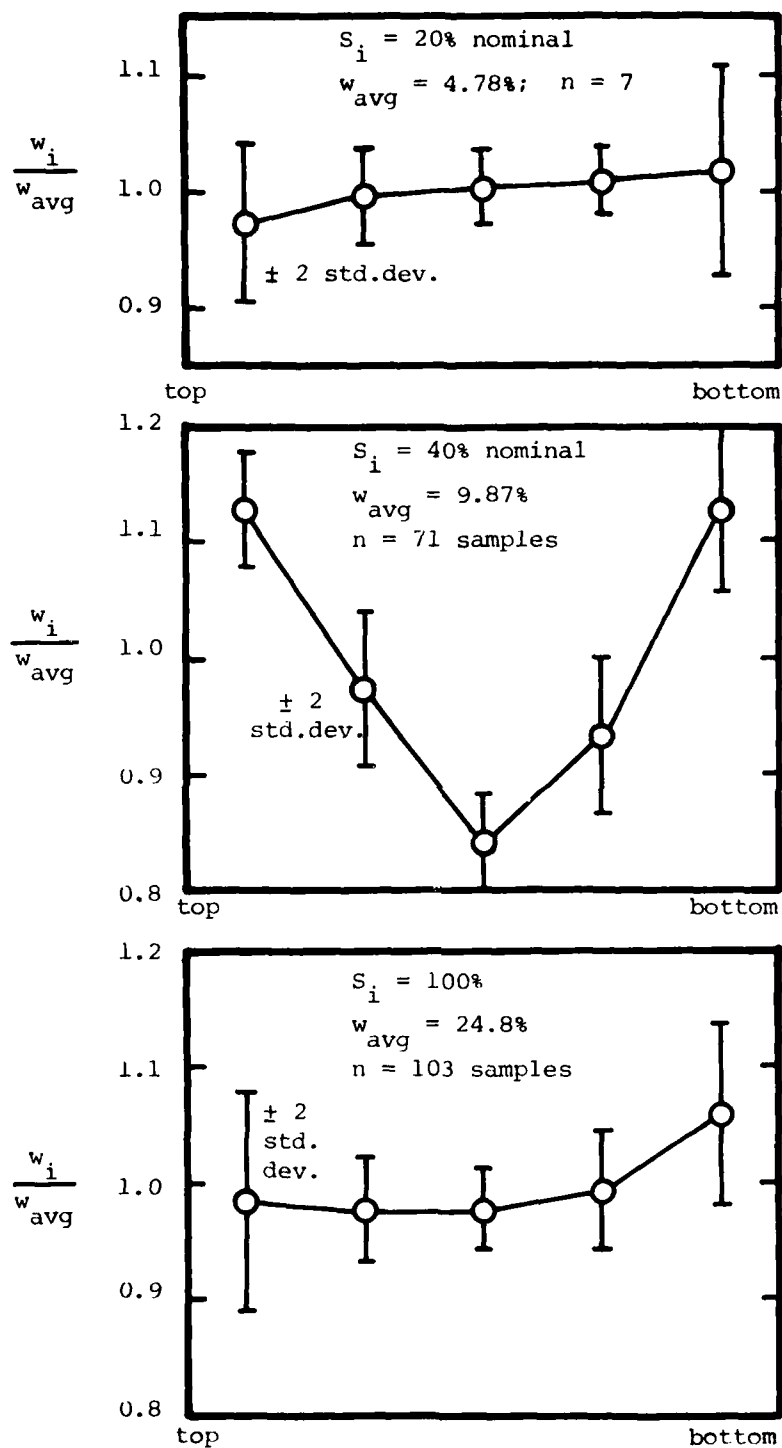


FIGURE A.5.11 Water content profiles of MFS at 55% relative density

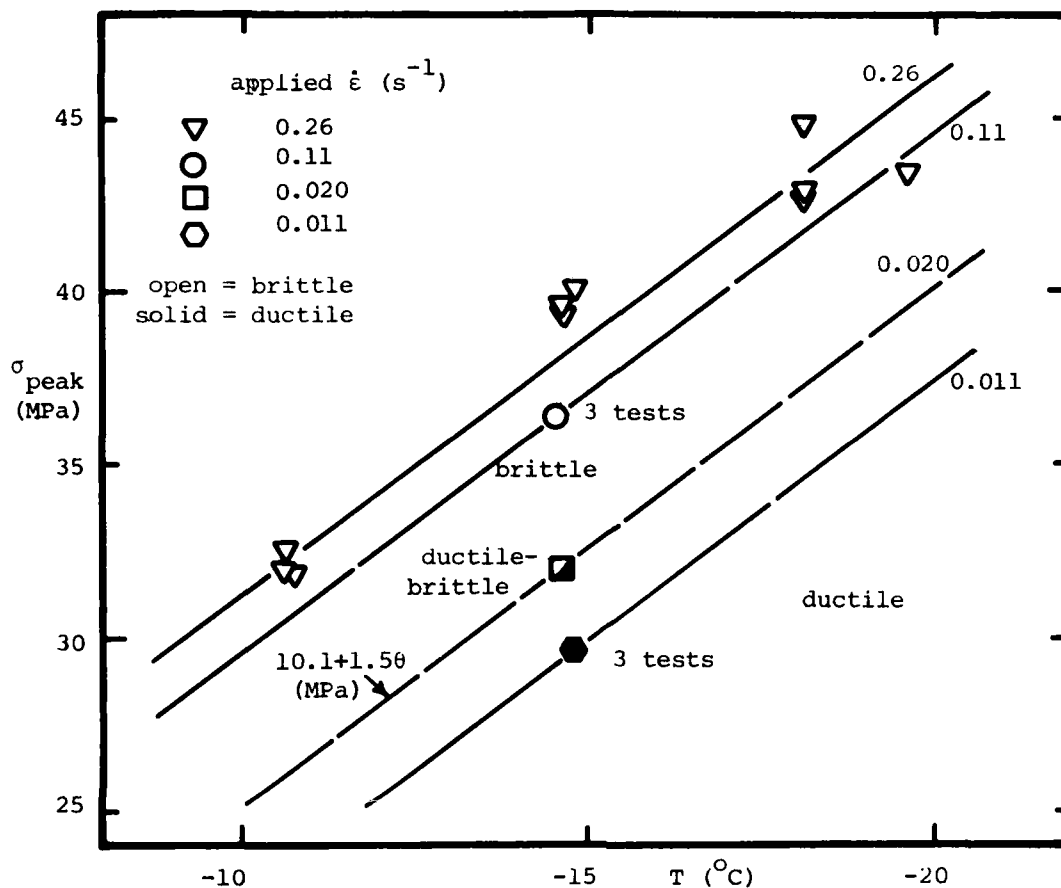


FIGURE A.5.12 Unconfined strength tests on saturated MFS at 55% relative density

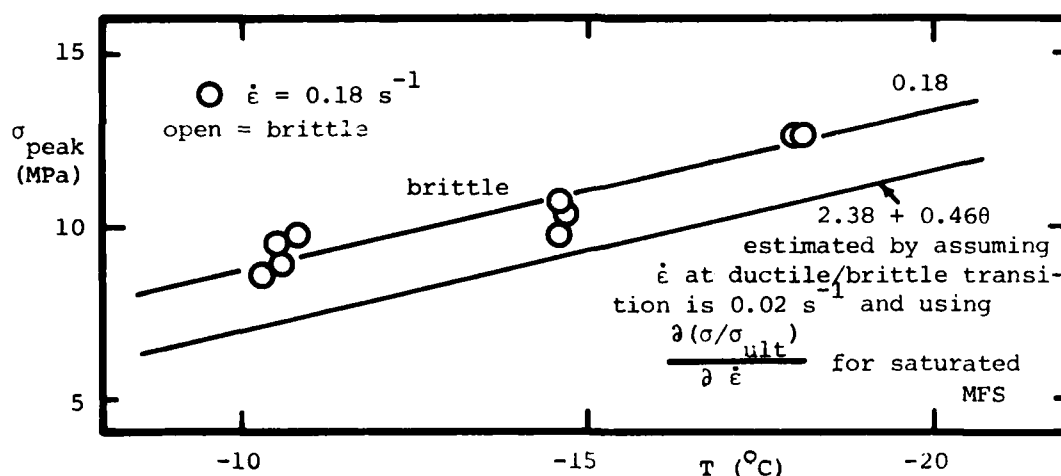


FIGURE A.5.13 Unconfined strength tests on 40% S_i 55% D_r MFS

APPENDIX A.6 Results of Creep Testing on Ice

A series of unconfined creep tests was conducted on fine polycrystalline granular ice as part of the MIT-CRREL research on the evaluation of the Rate Process Theory. Some tests were also performed as part of the author's study of the mechanisms of strength in frozen soil. The ice samples, supplied by D. Cole, were prepared using either of two methods developed at CRREL (Cole 1979). The first technique involved the preparation of a compact of dry ice grains which was initially flushed with carbon dioxide (CO_2) and then was flooded with deaired distilled water at 0°C at a fairly slow flow rate. The other technique involved the evacuation and subsequent flooding of the ice grain compact with deaired distilled water under vacuum. Both techniques yielded relatively bubble-free fine-polycrystalline granular (snow) ice samples.

Prior to testing, the samples were removed from the -30°C storage cold room and allowed to equilibrate for at least 8 hours at -10°C . The samples were then trimmed to size using a lathe, and the ends squared using a squaring jig. The final sample dimensions were similar to those for the MFS samples, but were limited by the trimming process and by the nature and location of any imperfections in the original ice samples. The final sample dimensions averaged 35.8 mm in diameter and 82.2 mm in height. The trimmed samples were then set up in the creep test apparatus previously described in Appendix A.2. The test procedures followed for the ice samples were the same

as for creep testing of frozen glass beads and MFS samples.

Three basic types of unconfined compressive creep tests were carried out: single stage constant load tests, temperature stage tests and stress stage tests. The results of the tests on the ice samples are summarized in Table A.6.1. For the range of test conditions imposed, the data indicate that the strain at minimum strain rate, ϵ_m , is between 1 and 2 % for ice. Also, for these test conditions, ice possesses an apparent activation energy between 30 and 50 kJ/m, based on temperature stage tests. These values of apparent activation energy, E , are much lower than the values similarly obtained for saturated and partially saturated Manchester Fine Sand and wetting and non-wetting glass beads of different gradations. The values of the ϵ_m for ice are also generally lower than MFS and wetting (non-treated) glass beads, but are about the same as for the nonwetting (treated) beads.

sample	γ (g/cc)	σ_1 (MPa)	T (°C)	$\dot{\epsilon}_m$ or $\dot{\epsilon}_1$ (s ⁻¹)	$\dot{\epsilon}_2$ after $\dot{\epsilon}_\Delta$ (s ⁻¹)	t min or t_Δ (m)	ϵ min or ϵ_Δ (%)	E (kJ/m)	$\alpha = \frac{\partial \ln \dot{\epsilon}}{\partial \sigma}$ (MPa ⁻¹)
I9-1	0.915	3.45	-15.93	2.44×10^{-6}		82	1.89		
I9-4	0.916	3.70	-13.71	3.31×10^{-6}		41	1.34		
I9-7	0.915	10.49	-15.53	rupture in	<18 sec.				
I9-8	0.916	7.52	-15.49	$1.8 \times 10^{-4} \pm$		12 sec \pm	0.38		
I9-2	0.915	3.53	-15.90	2.99×10^{-6}	3.82×10^{-6}	20	0.94	41.8	
			-13.50						
I9-5	0.918	3.46	-15.73	3.90×10^{-6}	4.44×10^{-6}	16	0.66	29.5	
			-13.41						
I9-6	0.916	2.67	-15.84	1.55×10^{-6}	1.97×10^{-6}	31	0.65	50.7	
			-13.33						
I9-3	0.915	2.80	-15.90	2.80×10^{-6}	6.48×10^{-6}	19	0.58		1.23
		3.48		3.22×10^{-6}	6.20×10^{-6}	42	1.19		0.98
		4.15							

TABLE A.6.1

Results of creep testing on fine polycrystalline snow ice,

$$\bar{\phi} \approx 0.6 \text{ mm}$$

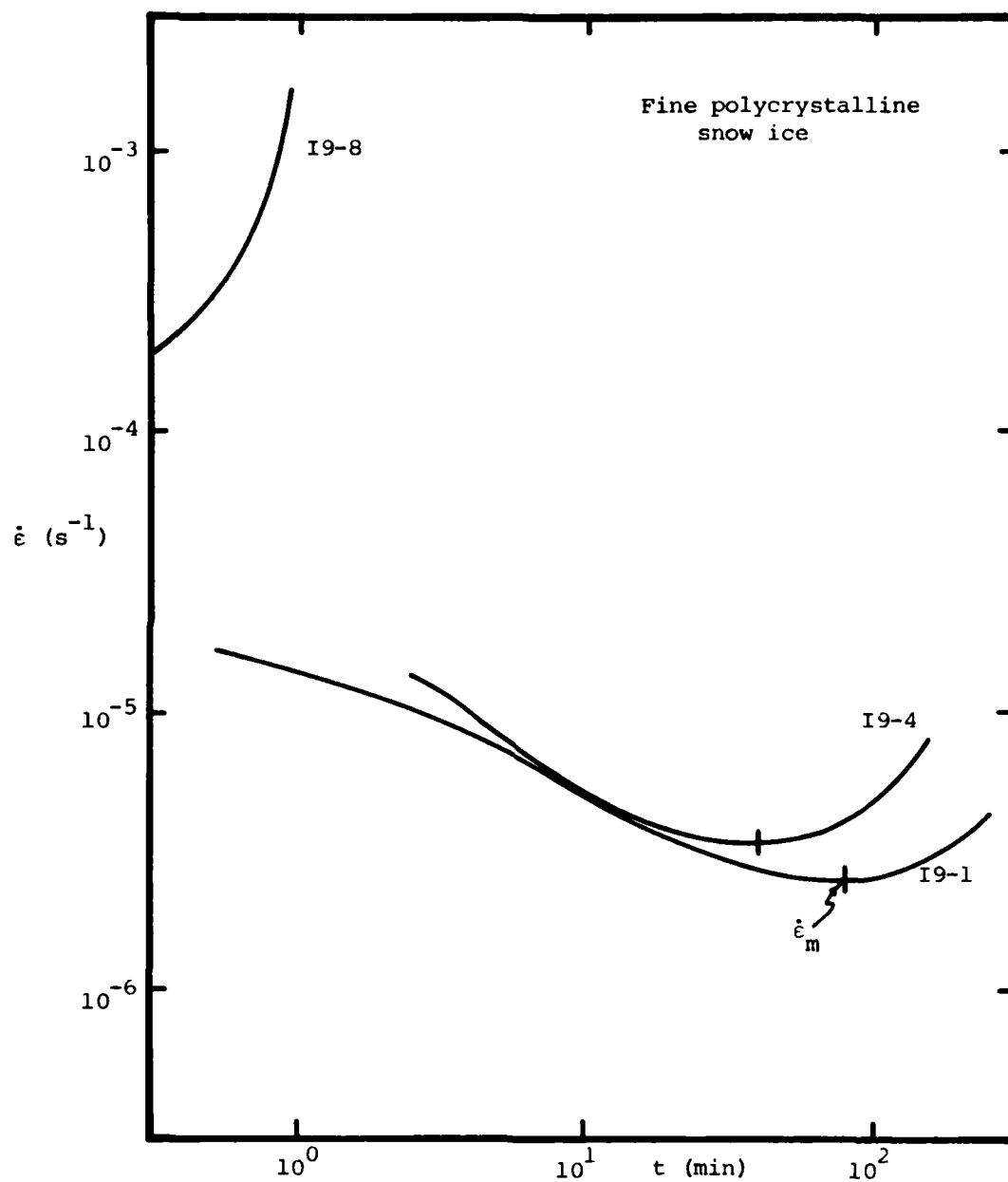


FIGURE A.6.1 Results of creep testing on fine polycrystalline snow ice

APPENDIX B.1 Details on the Nature of the Linear $\log \dot{\epsilon}_m - \log t_m$ Correlation

A log linear correlation between the minimum strain rate, $\dot{\epsilon}_m$, and the time to minimum, t_m , has been observed for many engineering materials. These observations have been mentioned in Chapter 2 and Appendix A.5, and are summarized in Figure B.1.1. This Appendix examines the underlying reasons for this apparent linearity in the hope that such an understanding will lead to better qualitative and quantitative models for creep, especially for frozen soils.

A secondary creep model such as proposed by Ladanyi (1972) was initially used to study the implications of such a linear $\log \dot{\epsilon}_m - \log t_m$ correlation. According to this model,

$$\epsilon = \dot{\epsilon}_m t + \epsilon_i \quad (\text{B.1.1})$$

where $\dot{\epsilon}_m$ is a constant secondary strain rate, and ϵ_i is the initial strain. This leads to:

$$t = \frac{\epsilon_m - \epsilon_i}{\dot{\epsilon}_m} \quad (\text{B.1.2})$$

where for $\epsilon_m \gg \epsilon_i$,

$$t_m \approx \frac{\epsilon_m}{\dot{\epsilon}_m} \quad (\text{B.1.3})$$

This model is illustrated in Figure 4.19.

Then, the contours of constant strain based on this model are given by:

$$\begin{aligned} \log t &= \log \epsilon - \log \dot{\epsilon}_m \\ \Rightarrow \frac{d \log \dot{\epsilon}_m}{d \log t} &= -1 \end{aligned} \quad (\text{B.1.4})$$

This equation describes a family of straight lines with slope -1 as shown in Figure B.1.2 (drawn for $\epsilon_i = 0$). Notice that

for the larger strains, relatively little separation exists between the strain contours.

Since the materials which are plotted in Figure B.1.1 have a slope of between -0.8 and -1.2, the secondary creep model suggests that the strain at the minimum strain rate is approximately a constant for each material. However, the slope of the $\log \dot{\epsilon}_m - \log t_m$ line is not exactly -1, and the strain at $\dot{\epsilon}_m$ is not absolutely constant. Instead, for frozen MFS, the slope is -1.2, and the strain at $\dot{\epsilon}_m$ typically decreases with decreasing minimum strain rate. This trend is predicted by this secondary creep model as plotted in Figure B.1.2. For unfrozen Haney clay, with a slope greater than -1, the strain at the minimum strain rate increases slightly with decreasing minimum strain rate. This trend is also consistent with the secondary creep model.

The actual shape of the $\dot{\epsilon} - t$ creep curves bears no resemblance to the secondary creep model. Consequently, if the actual $\dot{\epsilon}_m - t_m$ points for each test are plotted in Figure B.1.2, the actual data do not fit within the strain contours predicted by the secondary creep model.

A more refined creep model, the Singh-Mitchell (1968) three-parameter primary creep model, was also used to examine the linear $\log \dot{\epsilon}_m - \log t_m$ correlation. This model states:

$$\dot{\epsilon} = A e^{\alpha D} \left(\frac{t_1}{t} \right)^m \quad (B.1.5)$$

where D = stress in dimensional or dimensionless form

t_1 = some initial time

A, α, m = experimentally determined coefficients

Then, for $m \neq 1$, $\epsilon = \epsilon_1$ at $t = t_1$, $t_1 = 1$,

$$\epsilon = \epsilon_1 + \frac{A}{1-m_1} e^{\alpha D} (t^{1-m} - 1) \quad (B.1.6)$$

where ϵ is the strain at time t .

Combining these two equations,

$$\epsilon = \epsilon_1 + \frac{\dot{\epsilon}}{1-m} (t - t^m) \quad (B.1.7)$$

where $\dot{\epsilon}$ is the strain rate at strain ϵ .

For $\epsilon \gg \epsilon_1$, $t \gg t_1$ and $m \leq 0.6$,

$$\epsilon \cong \frac{\dot{\epsilon}}{1-m} t \quad (B.1.8)$$

Combining equations (B.1.6) and (B.1.8), the contours of constant strain may be plotted for any given m . This has been done for $m = 0.6$ in Figure B.1.3. The slope of these constant strain lines is obtained by manipulating equation (B.1.7):

$$\begin{aligned} \log \epsilon &= \log \epsilon_1 + \log \dot{\epsilon} + \log[t(1-t^{m-1})] - \log(1-m) \\ \frac{d \log \dot{\epsilon}}{d \log t} &= \text{slope} = -1 - \frac{d \log(1-t^{m-1})}{d \log t} \end{aligned} \quad (B.1.9)$$

For large t and $m < 1$, t^{m-1} approaches 0, and the slope of the constant strain contours approaches -1. Also, at the larger strains relatively little separation exists between the contours. These two features are also predicted by the secondary creep model. However, the actual locations of the contours are different for the two models.

Actual creep data on frozen Manchester Fine Sand are plotted together with the strain contours from the Singh-Mitchell model in Figure B.1.4. Most of the data fall within the contours predicted by the model for $m=0.6$. However, at the higher strain rates, the strains indicated by the model are slight-

ly higher than the actual. This trend may be quantified by combining the equation for a linear $\log \dot{\epsilon}_m - \log t_m$ correlation,

$$\dot{\epsilon}_m = B t_m^\gamma \quad (\text{B.1.10})$$

with equation (B.1.8):

$$\epsilon = \frac{\dot{\epsilon}}{1-m} \left(\frac{\dot{\epsilon}}{B} \right)^{1/\gamma} \quad (\text{B.1.11})$$

where B is in units consistent with $t_1 = 1$ sec.

For 40% Si 55% Dr MFS,

$$\begin{aligned} \dot{\epsilon}_m &= 4.20 \times 10^{-4} t_m^{-1.21}, t \text{ in min,} \\ \text{or } \dot{\epsilon}_m &= 0.0583 t_m^{-1.21}, t \text{ in sec.} \end{aligned} \quad (\text{B.1.12})$$

Then for $m = \frac{0.6}{0.170}$,

$$\epsilon_m = \frac{\dot{\epsilon}_m}{4.23} \quad (\text{B.1.13})$$

This is plotted in Figure B.1.5 together with the actual data for 40% Si 55% Dr MFS.

While the fit is fairly good for the lower strain rates, the overestimation of ϵ_m for $\dot{\epsilon}_m > 10^{-5}$ /sec is again evident. This overestimation is probably due to two factors. Firstly, the $\log \dot{\epsilon}_m - \log t_m$ data are not really linear for the higher strain rates, but certainly exhibit curvature. Consequently, the intersection of the fitted $\log \dot{\epsilon}_m - \log t_m$ correlation with the Singh-Mitchell model results in a higher predicted ϵ_m . The second reason is related to a change in the value of m with varying $\dot{\epsilon}_m$. Since the Singh-Mitchell model is only an approximation of the actual creep curve, an average slope m is used, as shown in Figure B.1.6. For the MFS tests, $m = 0.6$ was used in preparing Figure B.1.4. However, at the higher strain rates, the average value of m decreases. The use of a high m value in

this strain rate range also results in a higher predicted ϵ_m . If an m of 0.45 were used, consistent with an $\dot{\epsilon}_m = 10^{-4}$, then a more realistic prediction of ϵ_m results, as illustrated in Figure B.1.5.

From this presentation, it can be seen that the linear $\log \dot{\epsilon}_m - \log t_m$ correlation for the creep of engineering materials is due primarily to the existence of an approximately constant strain at the minimum strain rate, and the relative insensitivity of the $\log \dot{\epsilon}_m - \log t_m$ correlation to small deviations from this constant ϵ_m . For materials with relatively large ϵ_m , this insensitivity to small deviations is increased. Deviations from linearity at the higher strain rates and trends in the strain with varying strain rate may be explained by using simple creep models, such as the secondary creep and Singh-Mitchell models.

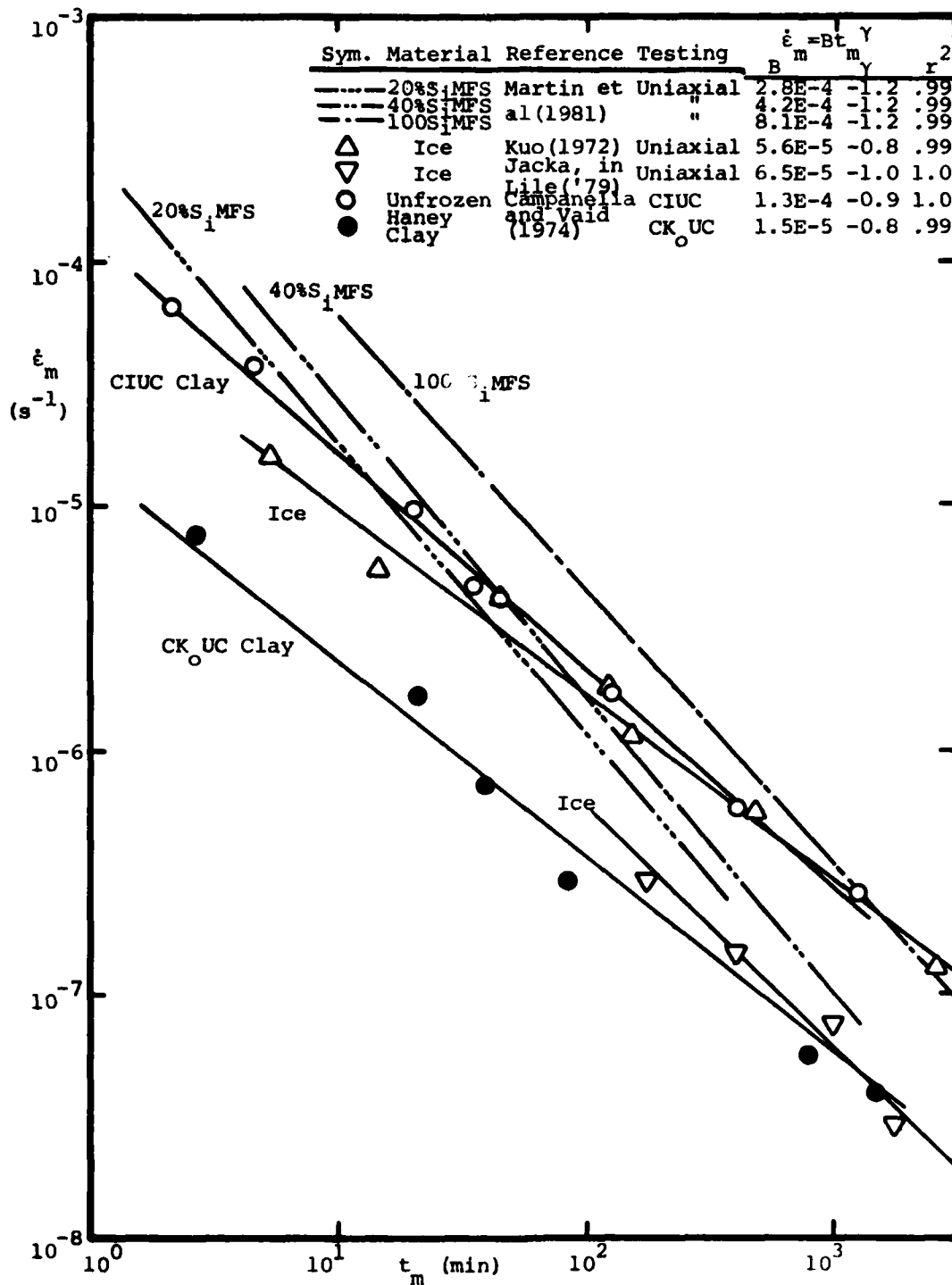


FIGURE B.1.1 Summary of $\dot{\epsilon}_m - t_m$ correlations for various materials

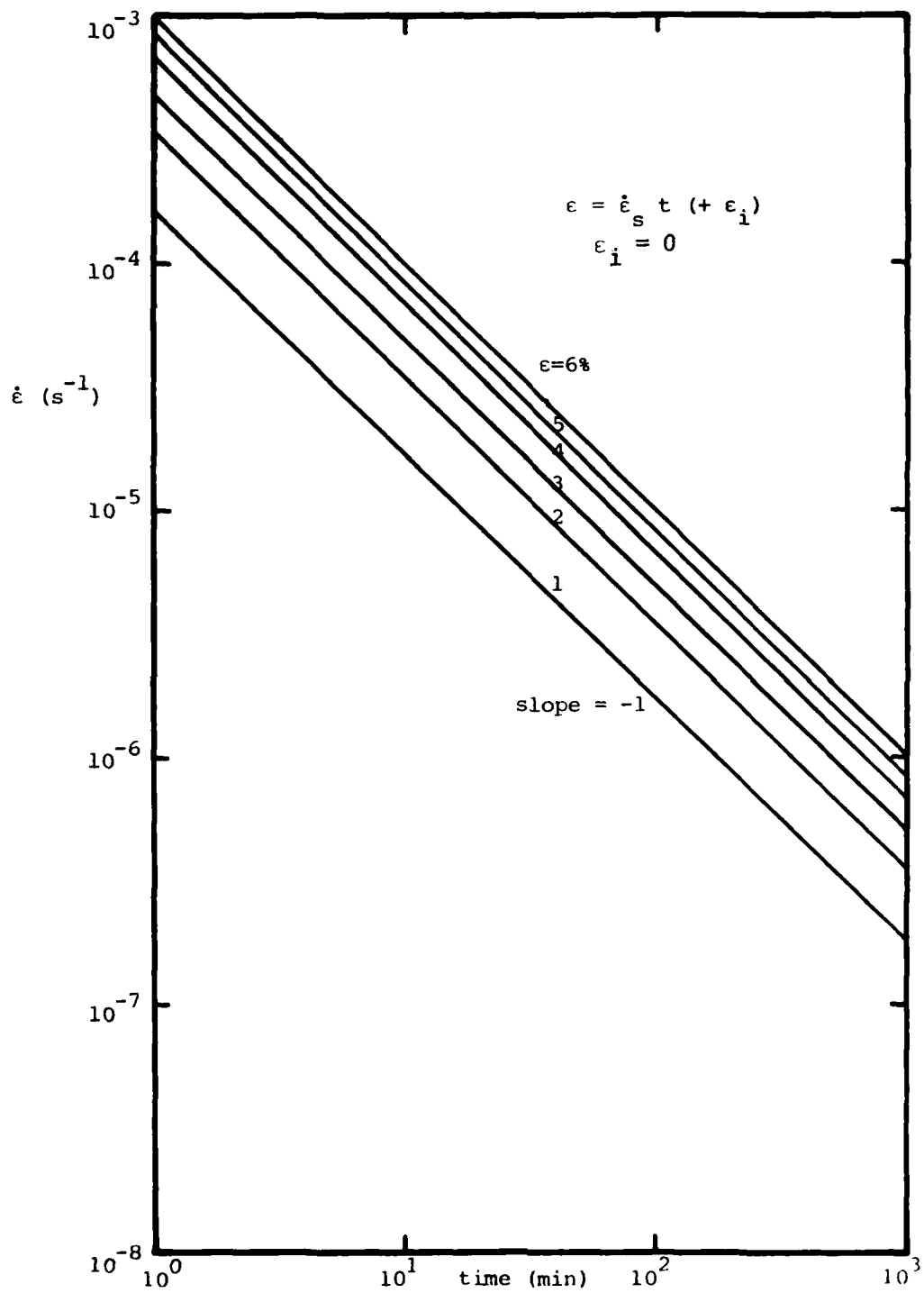


FIGURE B.1.2 Lines of constant strain based on secondary creep model

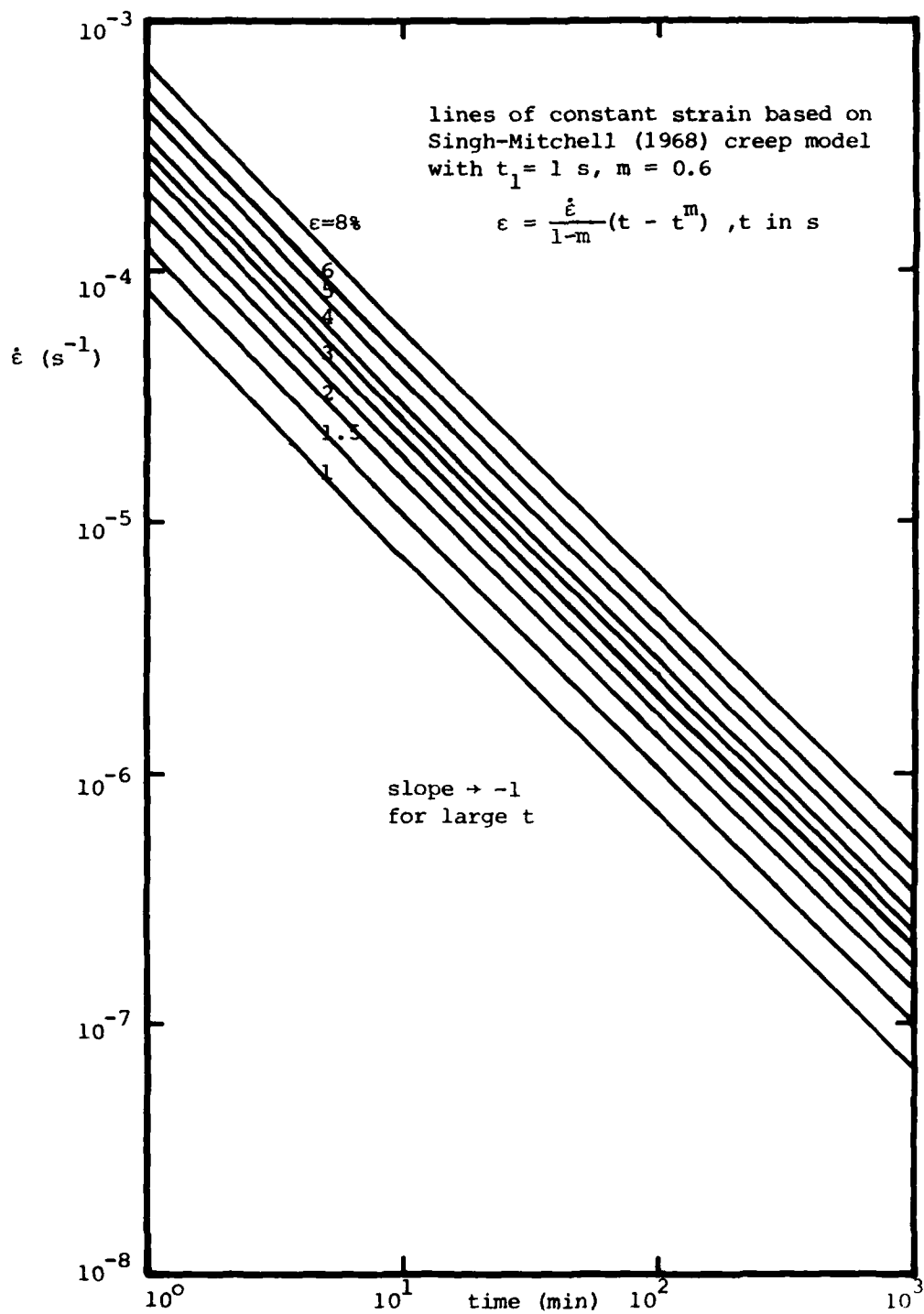


FIGURE B.1.3 Lines of constant strain based on Singh-Mitchell (1968) creep model

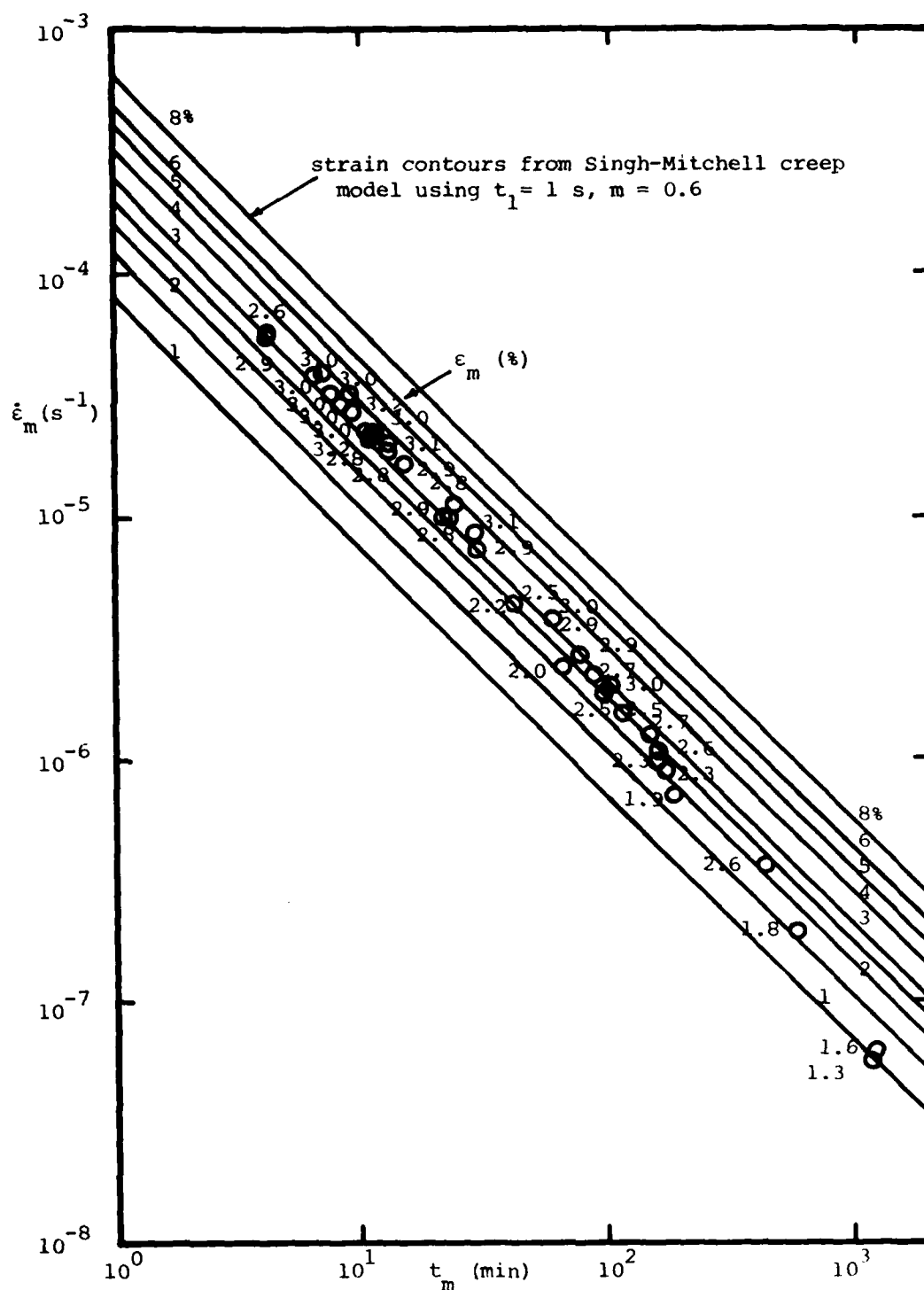


FIGURE B.1.4 Minimum creep data for 40% Si, 55% D, MFS with constant strain contours from Singh-Mitchell creep model

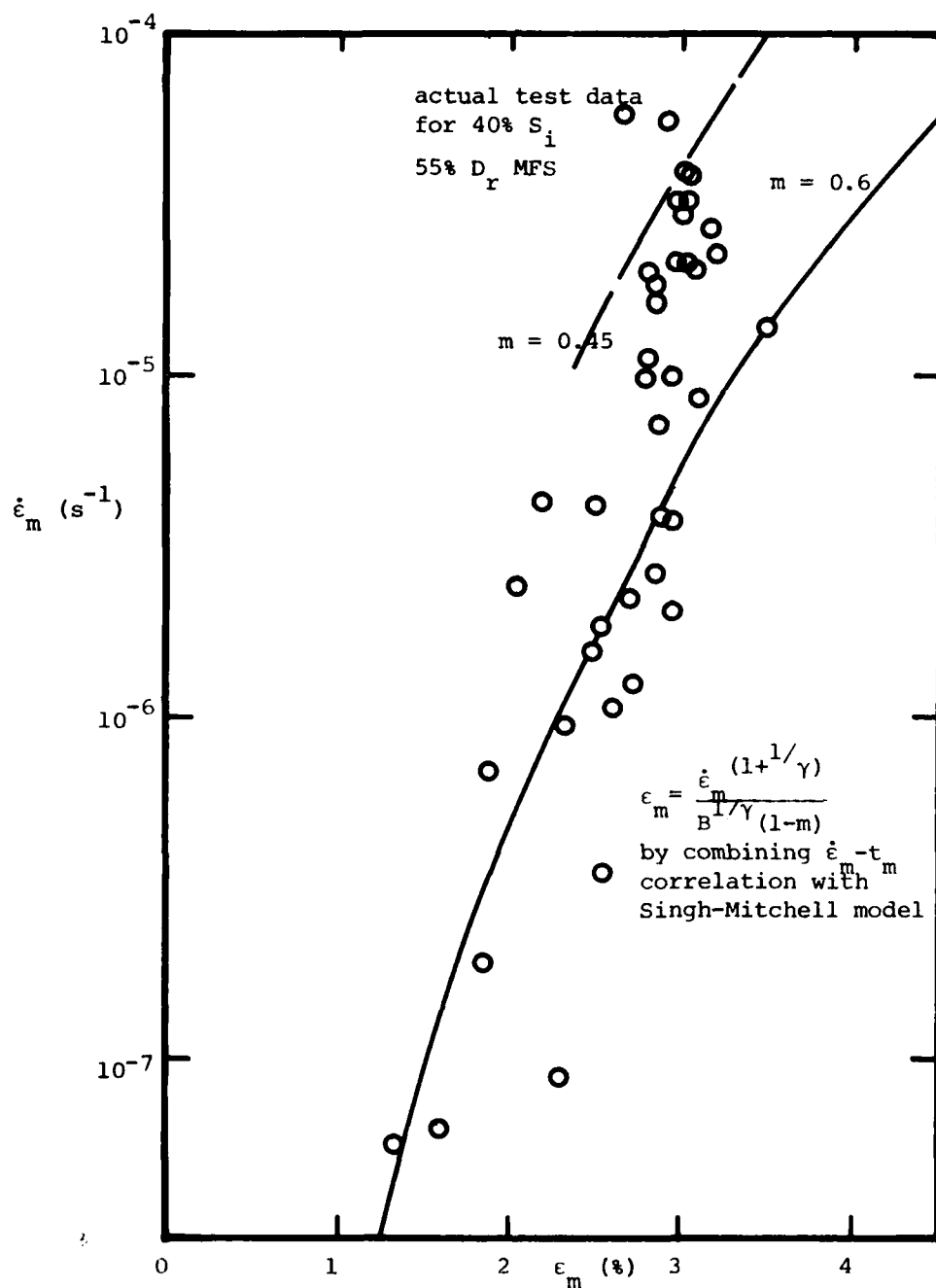


FIGURE B.1.5 Comparison of actual creep data with ϵ_m prediction using $\dot{\epsilon}_m - t_m$ correlation and Singh-Mitchell creep model

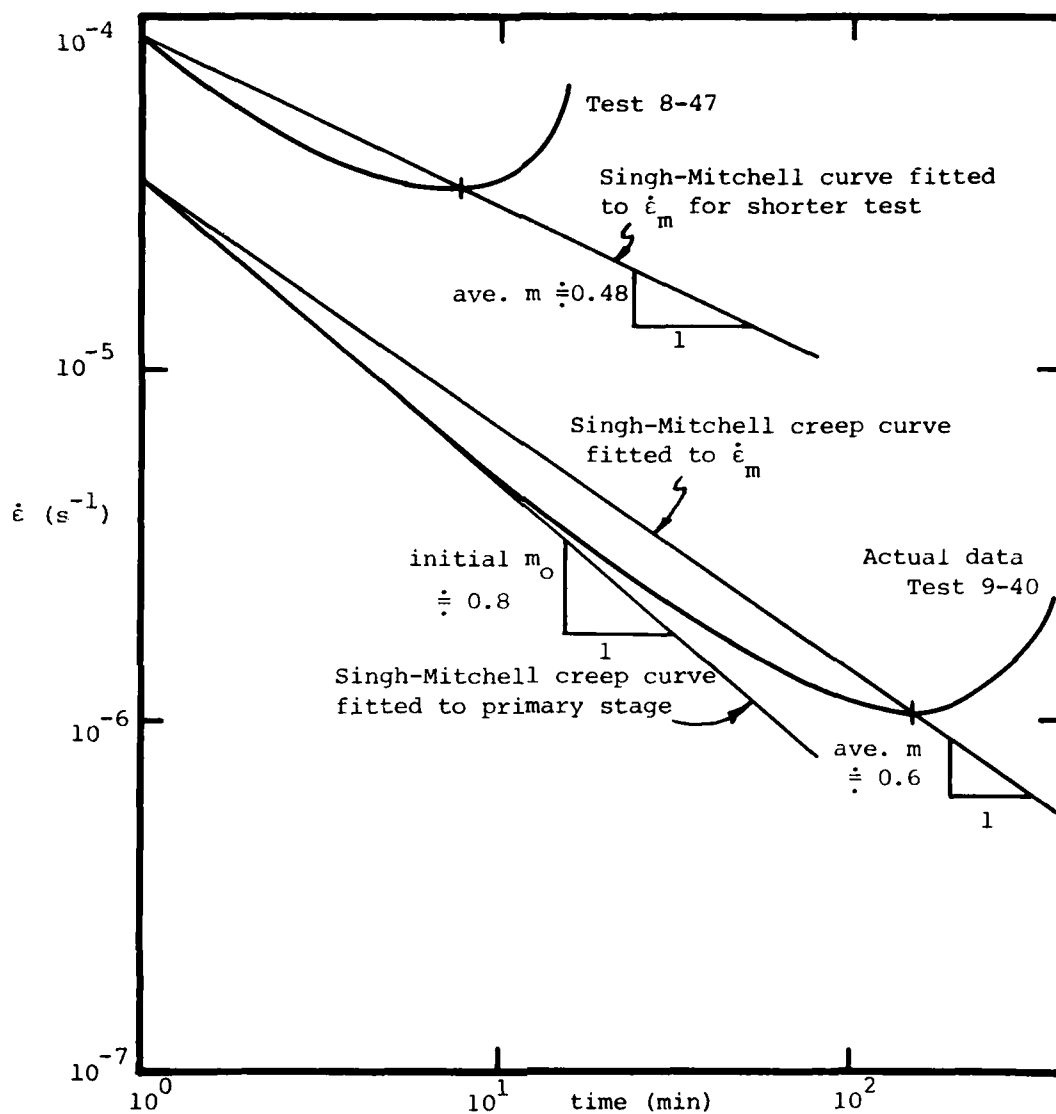


FIGURE B.1.6 Use of the Singh-Mitchell creep model for fitting actual creep data

APPENDIX B.2 Details of $\dot{\epsilon}_m$ Prediction for Manchester Fine Sand

A variety of methods were used for fitting and predicting the minimum strain rate, $\dot{\epsilon}_m$ for the undrained creep of frozen MFS. These methods may be categorized into two groups, one which is loosely based on Rate Process Theory (RPT) and uses data only from single stage creep tests, and another which uses stress ratios based on the ultimate strengths determined in Appendix A.5.

As presented in Section 2.2.5, RPT states that:

$$\dot{\epsilon}_m = \frac{2XkT}{h} \exp\left(-\frac{\Delta F}{RT}\right) \sinh\left(\frac{f\lambda}{2kT}\right) \quad (B.2.1)$$

where for sufficiently large stresses,

$$\dot{\epsilon}_m \cong XkT \exp\left(-\frac{E}{RT}\right) \quad (B.2.2)$$

where $E = \Delta F - \frac{f\lambda N}{2}$ = apparent activation energy

T = temperature ($^{\circ}\text{K}$)

f = measure of applied shear stress = $\sigma/2S$

N = Avogadro's number (6.02×10^{23})

R = Universal Gas constant ($8.30 \text{ joule}/^{\circ}\text{K-mole}$)

S = number of flow units per unit area

k = Boltzmann's constant ($1.38 \times 10^{-23} \text{ j}/^{\circ}\text{K}$)

h = Planck's constant ($6.624 \times 10^{-34} \text{ j-s}$)

F = free energy of activation

λ = displacement of flow unit

X = some "structure factor", supposedly independent of T
and shear stress

From temperature stage creep tests at different stresses, the apparent activation energy may be obtained, yielding:

$$\Delta F = E + \beta \sigma_1 \quad (\text{B.2.3})$$

where σ_1 = applied deviator stress.

From stress stage creep tests, the stress dependence may be assessed:

$$\alpha = \frac{\partial \ln \dot{\epsilon}}{\partial \sigma_1} \quad (\text{B.2.4})$$

$$\text{where } \frac{\alpha}{\beta} = \frac{1}{RT} \quad (\text{B.2.5})$$

By assuming the "structure factor" X is constant at the minimum strain rate, then ΔF , α and β can also be obtained from constant stress or load creep tests at different stresses and temperatures. By plotting $\log \dot{\epsilon}_m/T$ against $1/T$ as in Figure B.2.1 for 40% Si 55% Dr MFS, the values of E can be obtained at each level of stress. The free energy of activation, ΔF , can be evaluated by extrapolating the value of E to $\sigma_1 = 0$. Using the appropriate value of E , and assuming X is a constant at the minimum strain rate, then equation B.2.2 should predict the temperature and stress dependence of the minimum strain rate.

However, if a value of X is determined for a given test condition, equation B.2.2 still does not adequately "predict" the $\dot{\epsilon}_m$ for other stresses and temperatures. Martin et al. (1981) concluded that the value of X must vary by several orders of magnitude in order to adequately fit the MFS creep data. Since RPT is supposed to predict the variation of the $\dot{\epsilon}_m$ with stress and temperature, it is clear that it is inadequate for fitting the $\dot{\epsilon}_m$ data for frozen sand.

In their work, Martin et al. expressed the shear stress

level in dimensional form. For unfrozen soils, a stress ratio, rather than the absolute magnitude, is commonly used. When the stress level in frozen soils was expressed in terms of a ratio of stress using the ultimate strength, no improvement resulted. Consequently, regardless of whether the stress level is expressed in terms of dimensional or dimensionless quantities, RPT as expressed in equation (B.2.2) is clearly inadequate for fitting the $\dot{\epsilon}_m$ data for frozen sand.

Instead, a method based loosely on the Rate Process Theory was then developed for fitting the minimum strain rate data. A constant value of the experimental activation energy was used for all of the data at a given degree of ice saturation and relative density, such as illustrated in Figure B.2.2 for the 40% Si, 55% Dr MFS data. At a given temperature, the fitted $\dot{\epsilon}_m/T$ was evaluated for each level of stress. Figures B.2.3 and B.2.4 present these data, together with the accompanying least squares exponential and power fits. These equations are of the form:

$$\dot{\epsilon}_m = A_1 T \exp(\gamma \sigma_1) \exp\left(-\frac{E}{RT}\right) \quad (B.2.6)$$

$$\text{and } \dot{\epsilon}_m = A_2 T \sigma_1^n \exp\left(-\frac{E}{RT}\right) \quad (B.2.7)$$

where the values of A_1 and A_2 were obtained from fitting the observed data at a given stress and temperature. This procedure yields the following parameters for all of the 40% Si 55% Dr MFS data:

$$\dot{\epsilon}_m = 1.47 \times 10^{38} T \exp(2.03 \sigma_1) \exp\left(-\frac{29781}{T}\right) \quad (B.2.8)$$

$$\text{and } \dot{\epsilon}_m = 2.03 \times 10^{35} T \sigma_1^{10.4} \exp\left(-\frac{29781}{T}\right) \quad (B.2.9)$$

By comparing the logarithm of the actual minimum strain rate with the fitted $\dot{\epsilon}_m$, a measure of the reliability of the two equations was obtained. The resulting frequency histograms are plotted in Figure B.2.5, and indicate that both methods yielded reasonably centered fits with approximately 95% of the data within $\pm 4X$ the actual $\dot{\epsilon}_m$.

Similar fitting carried out on 100% Si 55% Dr MFS also yielded fairly well centered fits with 95% of the data within $\pm 2X$ for the power fit compared with $\pm 4X$ for the exponential fit (see Figure B.2.6). Consequently, the power fit for stress was used for all subsequent analyses. Note that the form of the power fit is similar to that used by a variety of workers in ice, notably Glen (1955), Weertman (1973), Langdon (1973), Gold (1973) and Homer and Glen (1978).

A similar procedure was performed on the rather limited 20% Si 55% Dr MFS data. The resulting coefficients for this fit, together with the coefficients from the fits at other levels of ice saturation are summarized in Table B.2.1 along with the pertinent data on the quality of each fit.

Using an average value of n and E/R , new "A" parameters were computed by fitting the actual data for a given stress and temperature, as tabulated in Table B.2.2. Then, a three-parameter exponential equation was used to fit the variation of A with respect to the degree of ice saturation:

$$\dot{\epsilon}_m = 1.54 \times 10^{28} \exp\left(\frac{12.54}{S_i + 0.30}\right) T^{10.0} \exp\left(-\frac{30000}{T}\right) \quad (B.2.10)$$

Note that iteration was required to obtain the three parameters

in the degree of saturation term.

To account for the variation of $\dot{\epsilon}_m$ with relative density, the rather limited data from Figures A.5.7 and A.5.8 were used. Noting the similarity in the change in log strain rate with relative density in the medium to dense range for both the 40 and 100% saturated samples ($>60\%$ Dr), a single exponential term was introduced into equation (B.2.10). The resulting equation which fitted the MFS data at all degrees of ice saturation, relative density, stress level and temperature, is:

$$\dot{\epsilon}_m = A \exp(\gamma Dr) \exp\left(\frac{\beta}{Si + \alpha}\right) T \sigma_I^n \exp\left(-\frac{E}{RT}\right) \quad (B.2.11)$$

for Dr $> 60\%$, where $A = 1.85 \times 10^{31}$

$$\gamma = -12.4$$

$$\beta = 12.54$$

$$\alpha = 0.30$$

$$\frac{E}{R} = -30000 \quad (^{\circ}\text{K})$$

$$n = 10.0$$

Figure B.2.7 plots the resulting comparison of the fitted and actual minimum strain rates. Again, equation (B.2.11) yielded a reasonably centered fit with 95% of the data within $\pm 5X$ of the mean predicted strain rate, which is $+4X$ and $-6X$ the actual. While the fit is not too bad, there is not sufficient data at varying Dr to thoroughly test the validity of equation (B.2.11) with respect to this parameter. Note that use of equation (B.2.11) assumes the separability of the individual parameters, Dr, Si, T and σ .

The fits presented thusfar were made using the entire data

sets available. In order to see whether an equation of the form given by equation (B.2.11) is useful as a predictor of minimum strain rate, an arbitrary set of data were taken from the overall data set to determine the values of the parameters in the equation. These tests were selected to provide a large range of stress as well as temperature, with several tests run at the same stress level at different temperatures in order to obtain values of the apparent activation energy. Using the test data tabulated in Table B.2.3, these parameters were determined, as shown in Figures B.2.8 through B.2.11. The resulting equation based on 25 tests is:

$$\dot{\epsilon}_m = 8.3 \times 10^{33} \exp(-10.5Dr) \exp\left(\frac{8.28}{S_i + 0.15}\right) T_o^{9.94} \exp\left(\frac{-31189}{T}\right) \quad (B.2.12)$$

The histogram of the reliability of the fit is plotted in Figure B.2.12 and indicates that this fit, based on about one-third of the total data base, is as reliable as the fit using all of the data.

The fits have thusfar assumed a constant value of the experimental activation energy. From Martin et al. (1981) and Appendix A.5, it is observed that E is a function of the stress level, as well as the degree of ice saturation. Since the effect on the predicted creep rate due to a variation in E with stress is small compared to the effect of the stress alone, the assumption of a constant E is probably not too bad. Some work was done to examine the effect of the variation of the average E for different S_i . By fitting the $E/R - S_i$ relation with a straight line, then computing the resulting degree of

saturation coefficients and new "A" coefficients, the following equation was obtained for 55% Dr data:

$$\dot{\epsilon}_m = 3.5 \times 10^{-15} \exp\left(\frac{206}{S_i + 1.30}\right) T \sigma_1^{10.0} \exp\left(-\frac{35227 + 9908S_i}{T}\right) \quad (\text{B.2.13})$$

The resulting fit, however, is not significantly better than for the fit assuming a constant E, with a reasonably centered mean and 95% of the data within $\pm 4X$ on the actual $\dot{\epsilon}_m$. Consequently, the slight improvement in reliability gained with a variable E over the constant E fit is probably not worth the extra effort required.

Attempts were also made at using temperature stage and stress stage data for assessing the temperature and stress dependence of the minimum strain rate. However, the stage tests tended to uniformly and significantly underestimate both the temperature and stress dependence of the $\dot{\epsilon}_m$. Consequently, the data from the stage tests were not used in further attempts at fitting the minimum strain rate.

The second "method" for predicting the minimum strain rate uses stress ratios based on the ultimate strengths determined in Appendix A.5. As already mentioned, the use of stress ratios in conjunction with the RPT proved to be nonproductive. Here, a more empirical and simpler approach was developed to fit the creep data:

$$\dot{\epsilon}_m = A \left(\frac{\sigma}{\sigma_{ult}} \right)^n \quad (\text{B.2.14})$$

where $\sigma_{ult} = \sigma(\theta)$ as determined in Appendix A.5,

$$\sigma_{ult} = 10.1 + 1.5 \theta \quad (\text{MPa}) \quad \text{for } 100\% \text{ Si}$$

$$\sigma_{ult} = 2.38 + 0.46 \theta \quad (\text{MPa}) \quad \text{for } 40\% \text{ Si}$$

based on $\dot{\epsilon} = 0.02$ /s at the "ductile-brittle" transition. The temperature dependence of the creep rate was assumed to be accounted for by the variation in the ultimate strength with temperature.

The resulting linear least squares fits for 40% and 100% Si 55% Dr MFS creep data are shown in Figure B.2.13, with the resulting histograms of comparisons shown in Figure B.2.14. Notice that these fits have slightly smaller standard deviations than the corresponding fits using the first method, based loosely on RPT. Also, since these are least squares fits, they are centered exactly about the actual $\dot{\epsilon}_m$.

By combining the equations for the 40% and 100% Si fits with a common n and an exponential term to account for the Si, the following equation results:

$$\dot{\epsilon}_m = 3.5 \times 10^{-4} \exp(6.10Si) \left(\frac{\sigma}{\sigma_{ult}} \right)^{9.74} \quad (B.2.15)$$

where σ_{ult} may be expressed as:

$$\sigma_{ult} = -2.767 + 12.867Si - 0.233 \theta + 1.733 \theta Si \text{ (MPa)} \quad (B.2.16)$$

Since data are available from only two different levels of saturation, equation (B.1.16) is exact for our data.

The quality of this fit is shown in Figure B.2.15, and indicates a well-centered fit with 95% of the data within $\pm 2.5X$ of the actual. While this is much better than the fit shown in Figure B.2.7 using the modified RPT method, note that this fit uses only data from one relative density and two Si. Regardless of that fact, however, it can be seen that this method, using stress ratios, is slightly better than the previous fit-

ting method, and certainly seems to be able to adequately account for the temperature and stress dependence.

As with the first method, this second method was checked to determine whether it could be effective as a predictive tool. By using the same eighteen 40 and 100% Si 55% Dr MFS tests from Table B.2 as before, and with the ultimate strengths determined from a series of unconfined strength tests as in Appendix A.5, the following equation was determined:

$$\epsilon_m = 2.4 \times 10^{-4} \exp(6.74Si) \left(\frac{\sigma}{\sigma_{ult}} \right)^{10.0} \quad (B.2.17)$$

where σ_{ult} is as in equation B.2.16.

Figure B.2.16 shows the results of the use of this equation as a fitting and predictive equation. As can be seen in this Figure, this equation based on about one-third of the entire data base yields predictions which are just as good as when all of the data are used and fitted.

S_i (%)	A	n	-E/R	$\log \left[\frac{\dot{\epsilon}_m^{\text{predicted}}}{\dot{\epsilon}_m^{\text{actual}}} \right]$	avg	st. dev. $\log \left[\frac{\dot{\epsilon}_m^{\text{pred}}}{\dot{\epsilon}_m^{\text{actual}}} \right]$	no. of tests
20	1.79×10^{47}	9.21	-34358	-0.09		0.45	6
40	2.03×10^{35}	10.41	-29781	-0.11		0.26	40
100	1.09×10^{25}	9.97	-25690	0.00		0.15	28

TABLE B.2.1

Parameters for Equation B.2.7 for 55% D_r MFS

S_i (%)	A
20	1.38×10^{39}
40	9.38×10^{35}
100	2.55×10^{32}

TABLE B.2.2

A Parameters for 55% Dr MFS using avg. $n = 10$, $\frac{-E}{R} = 30000$

test no.	D _r (%)	S _i (%)	σ (MPa)	T (°C)	$\dot{\epsilon}_m^{act} (s^{-1})$	ϵ_m
8-22	56	38.8	3.91	-11.13	4.36x10 ⁻⁶	2.18
8-26	55	39.6	3.92	-14.92	7.0 x10 ⁻⁷	1.88
9-35	56	38.8	4.78	-11.69	2.26x10 ⁻⁵	3.20
9-40	57	38.8	4.78	-18.57	1.07x10 ⁻⁶	2.60
9-34	55	39.6	4.78	-20.69	3.52x10 ⁻⁷	2.55
8-54	55	40.0	5.34	-18.55	3.89x10 ⁻⁶	2.88
8-69	56	38.8	6.50	-20.68	1.0 x10 ⁻⁵	2.93
8-48	61	39.2	6.51	-16.52	5.62x10 ⁻⁵	2.90
S8-28	58	100	7.87	-14.88	1.29x10 ⁻⁷	4.33
S8-58	59	100	9.06	-15.27	4.10x10 ⁻⁷	4.61
S8-59	56	100	9.08	-12.31	2.81x10 ⁻⁶	3.88
S9-1	56	100	10.57	-18.50	6.87x10 ⁻⁷	4.3
S9-53	63	100	10.61	-16.12	3.08x10 ⁻⁶	6.6
S9-137	55	100	10.62	-27.40	2.10x10 ⁻⁸	2.9
S8-68	53	100	14.07	-18.35	1.84x10 ⁻⁵	6.37
S8-80	55	100	10.63	-11.48	1.12x10 ⁻⁵	5.5
S8-79	54	100	16.69	-18.37	3.98x10 ⁻⁵	5.0
S9-135	58	100	16.81	-23.63	1.05x10 ⁻⁵	3.73
9-05-2	57	18.4	2.17	-20.09	6.34x10 ⁻⁷	2.52
9-05-1	58	18.8	2.17	-18.78	1.27x10 ⁻⁶	1.90
9-05-5	54	19.6	3.15	-18.56	4.92x10 ⁻⁵	1.98
9-05-3	54	19.6	3.15	-20.42	1.64x10 ⁻⁵	2.51
8-05-1	56	19.6	4.35	-19.02	2. x10 ⁻⁴	2.50
8-05-3	57	20.0	1.38	-19.09	1.63x10 ⁻⁷	1.29
80-80-1	79	43	4.82	-18.97	1.07x10 ⁻⁷	1.65

TABLE B.2.3

Summary of tests used for determining model parameters for predictions

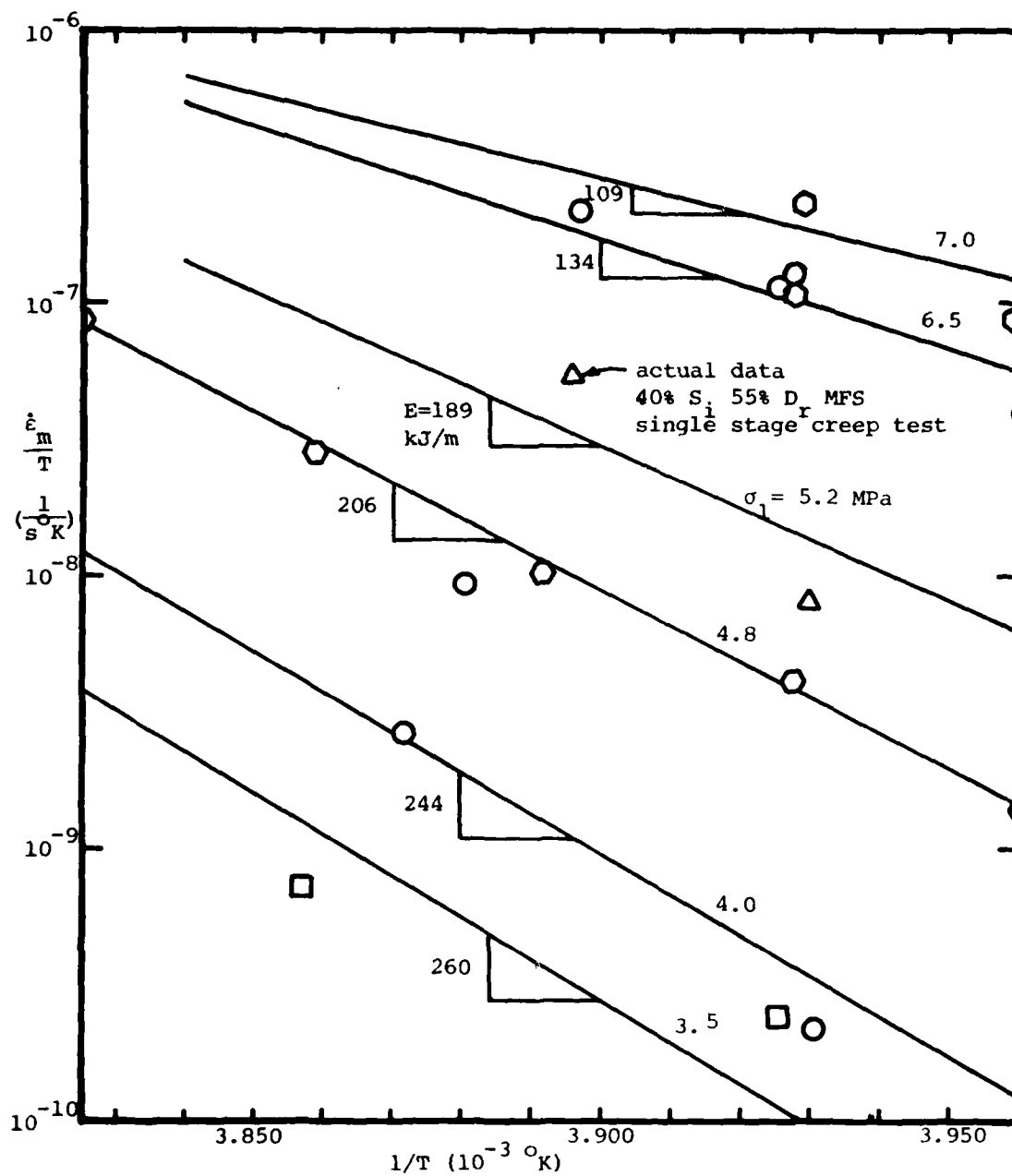


FIGURE B.2.1 Fit of constant load single stage creep test data for 40% S_i 55% D_r MFS with variable apparent activation energy E fits

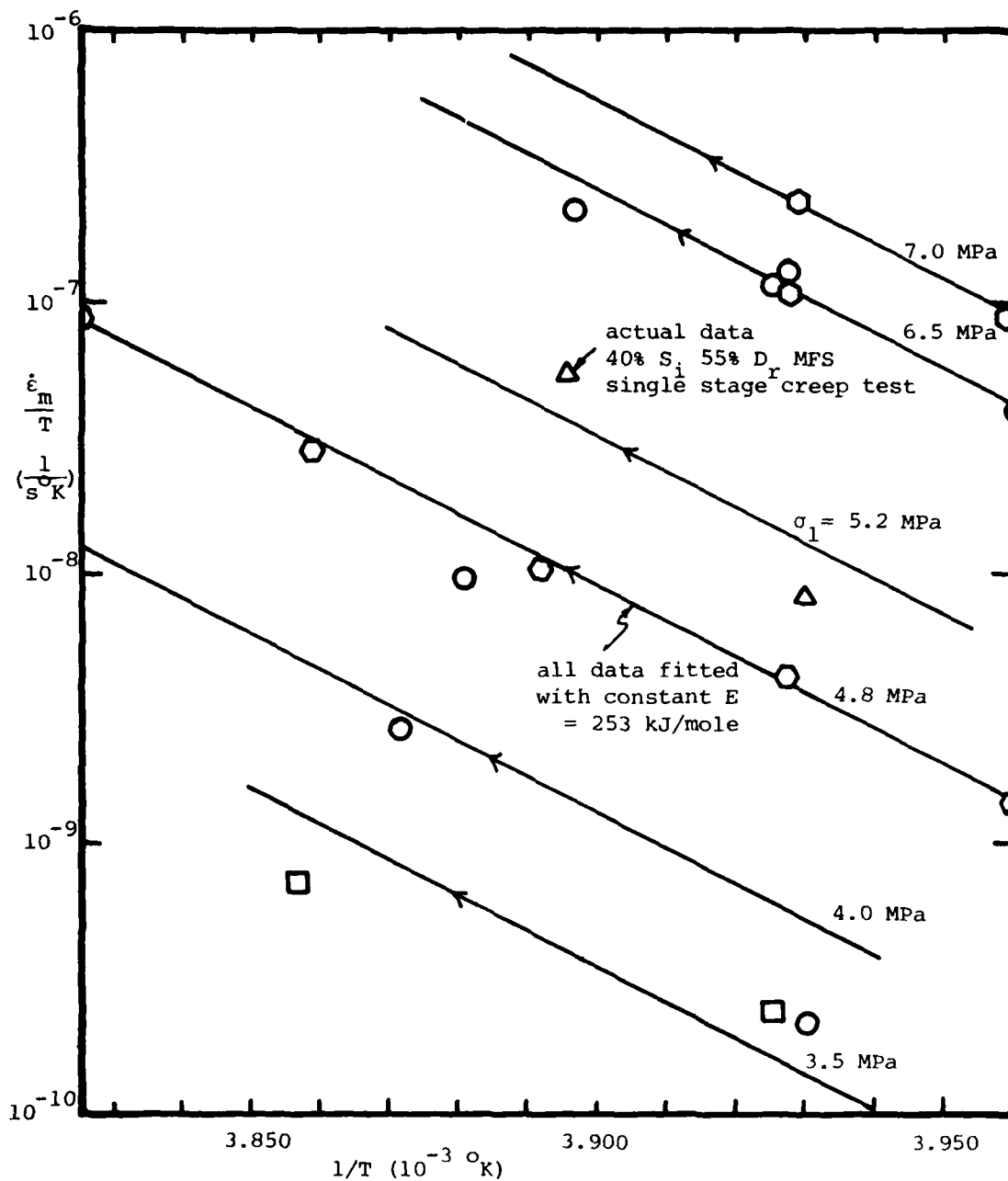


FIGURE B.2.2 Fit of constant load single stage creep test data for 40% S_i 55% D_r MFS with constant apparent activation energy E

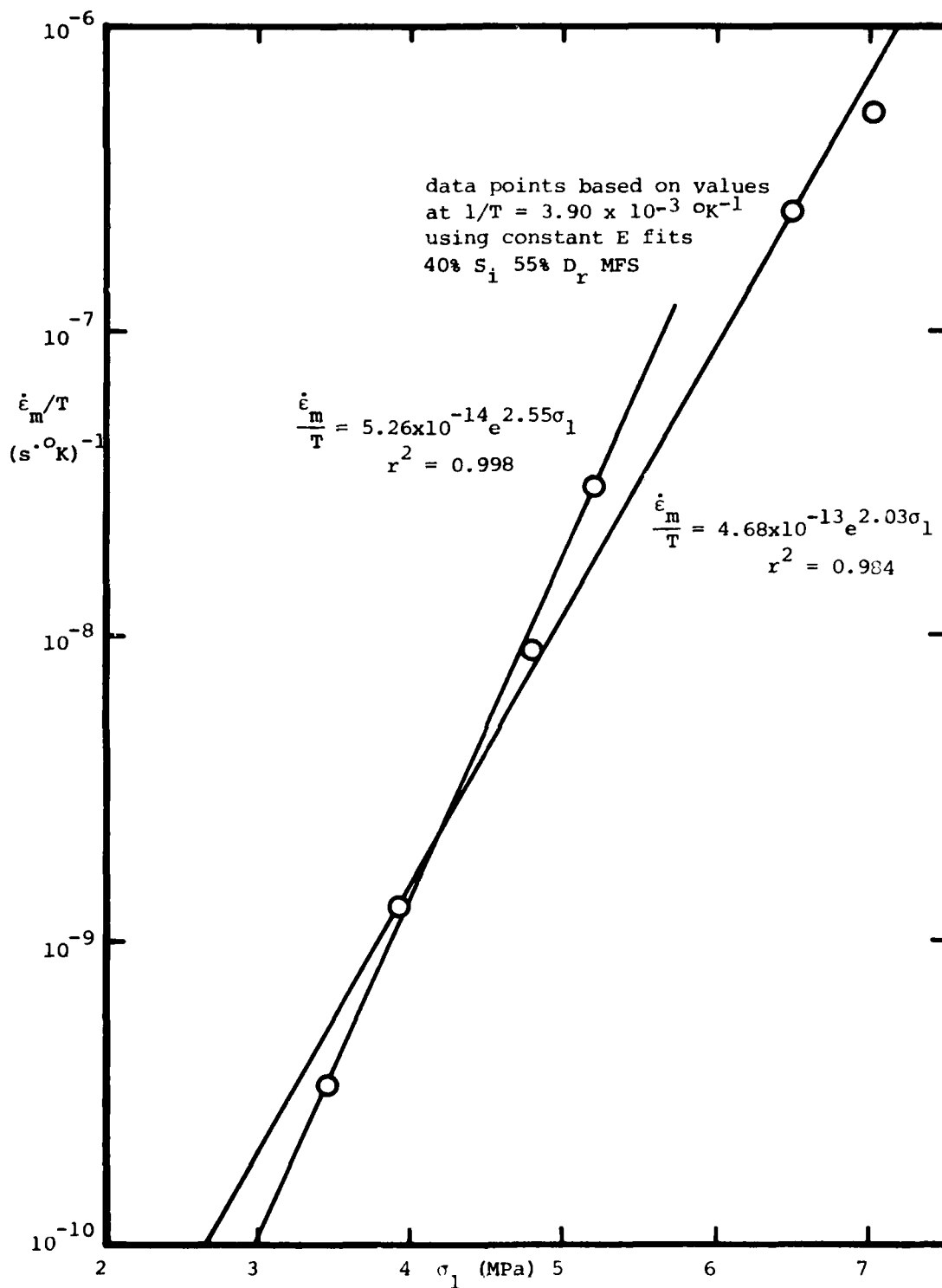


FIGURE B.2.3 Use of exponential function to describe stress dependence

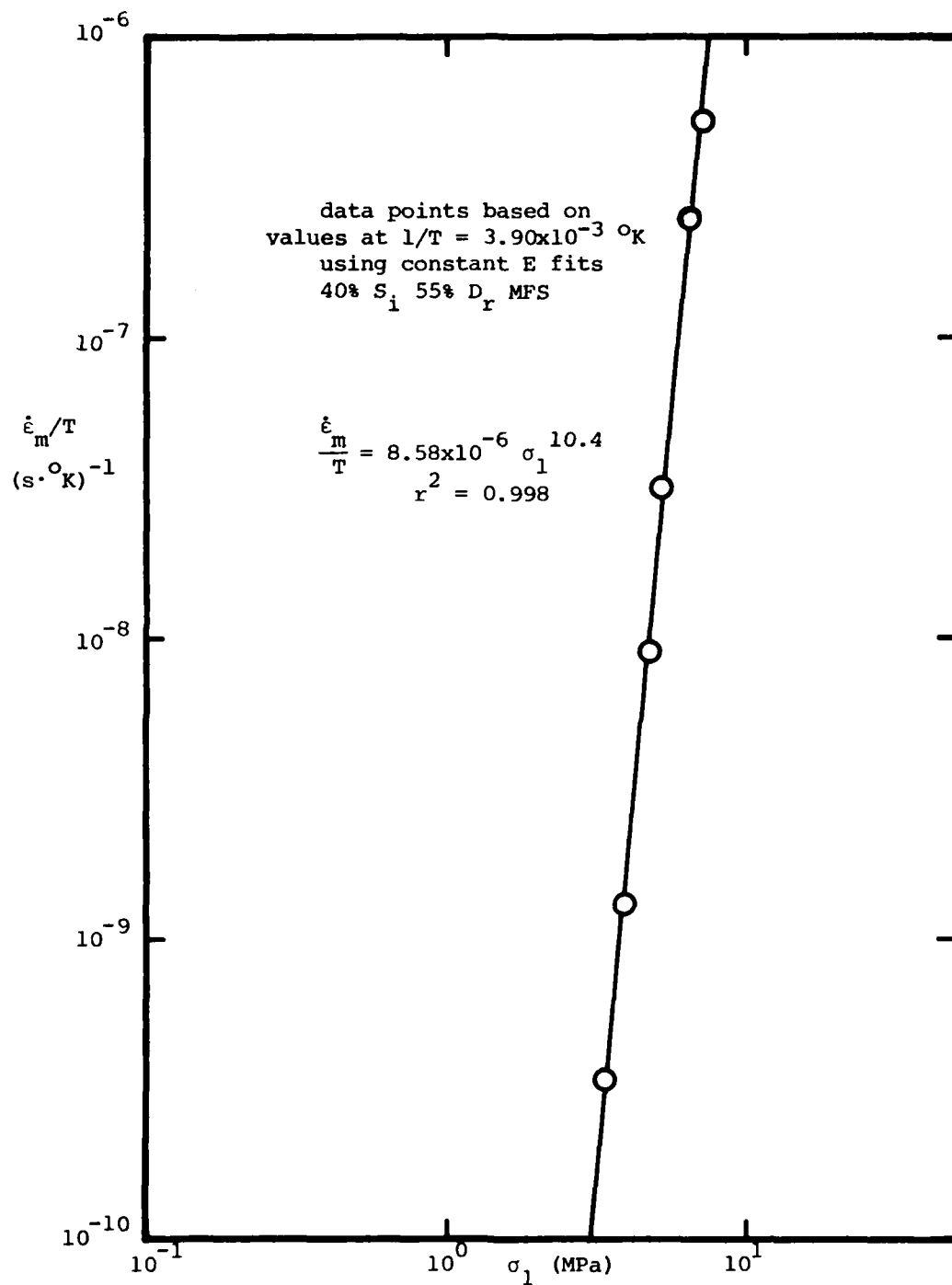


FIGURE B.2.4 Use of power function to describe stress dependence

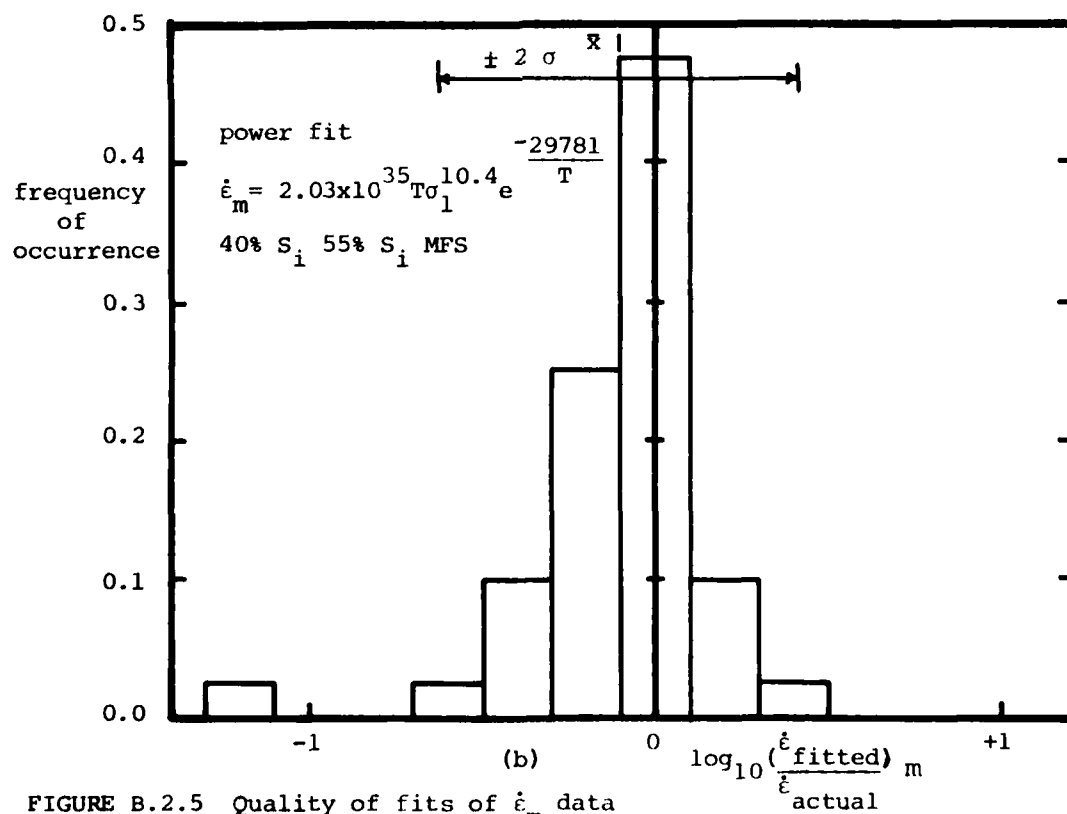
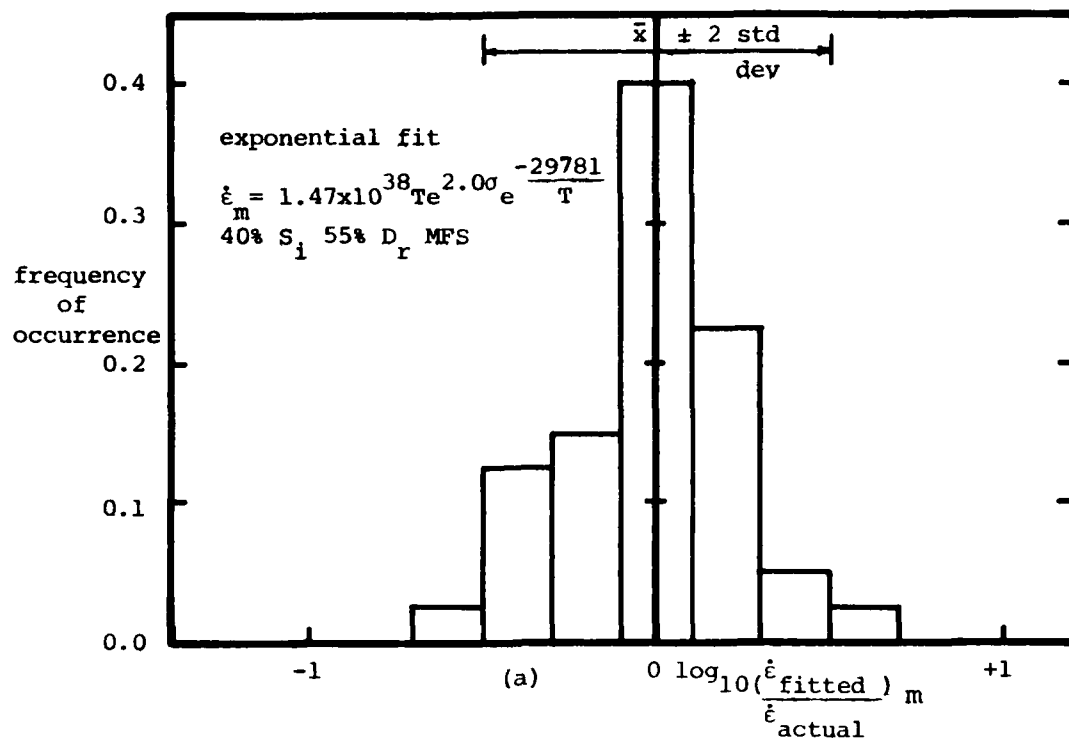


FIGURE B.2.5 Quality of fits of $\dot{\epsilon}_m$ data

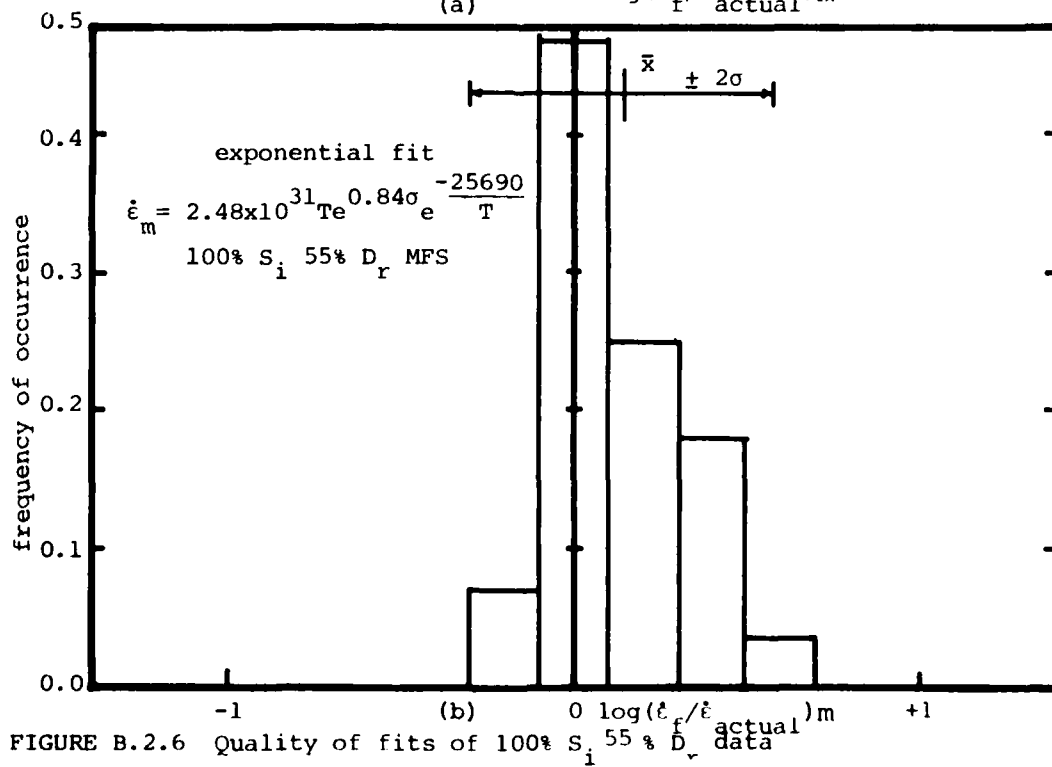
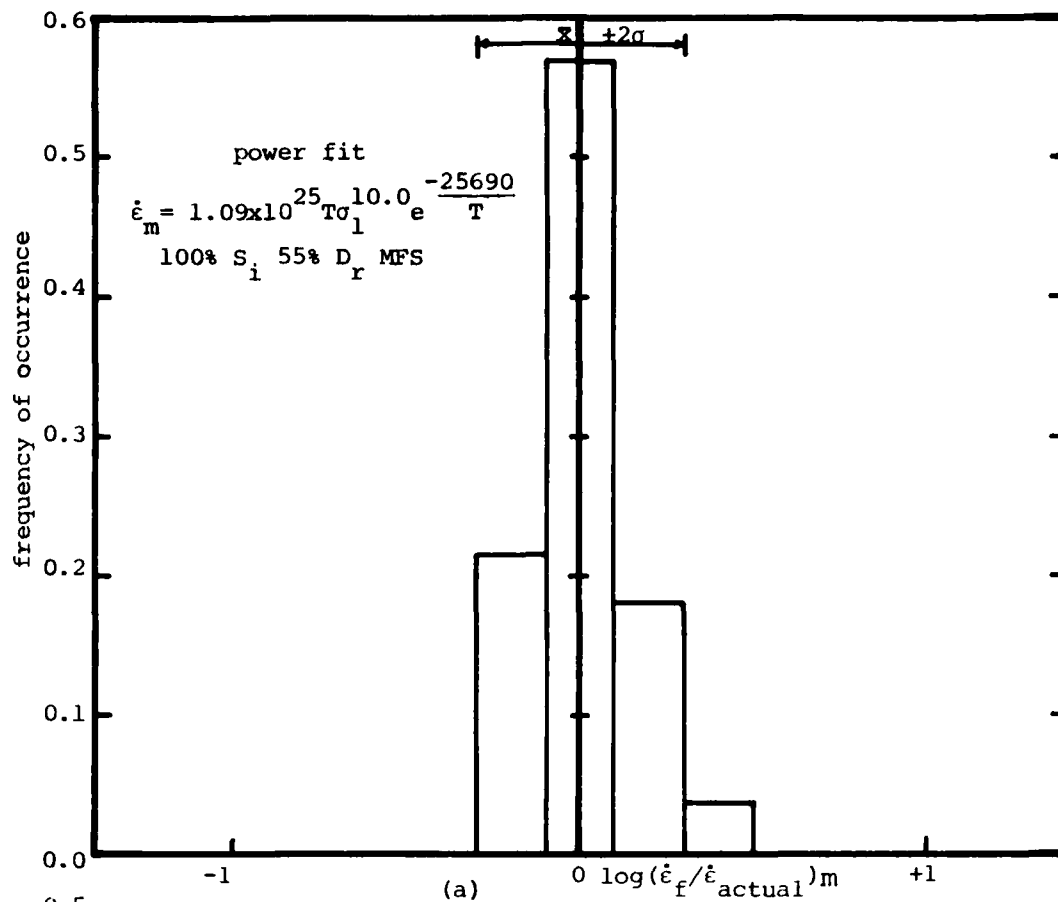


FIGURE B.2.6 Quality of fits of 100% S_i 55% D_r data

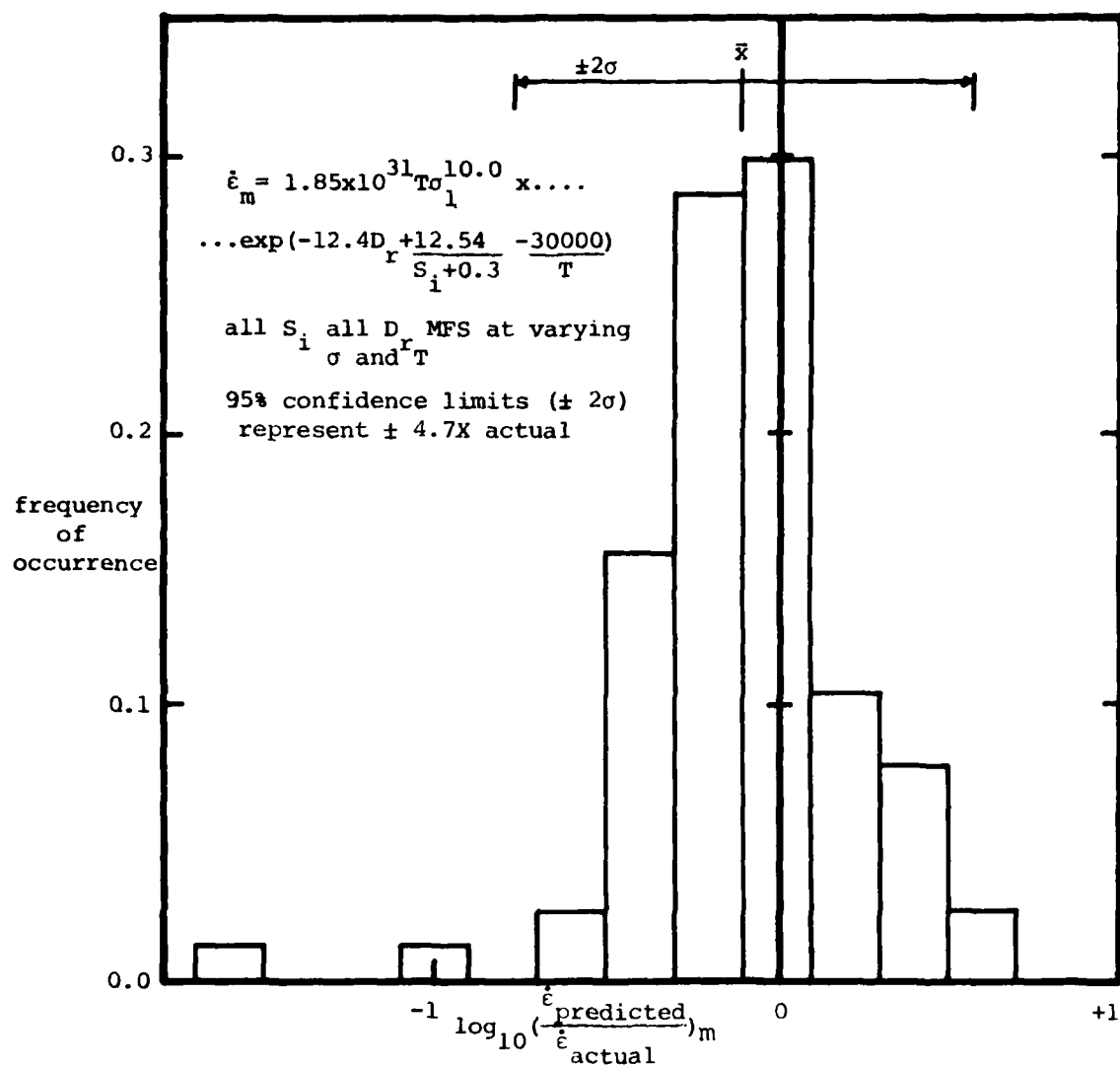


FIGURE B.2.7 Frequency histogram indicating quality of fit using one modified RPT equation for describing S_i , D_r , σ and T variation

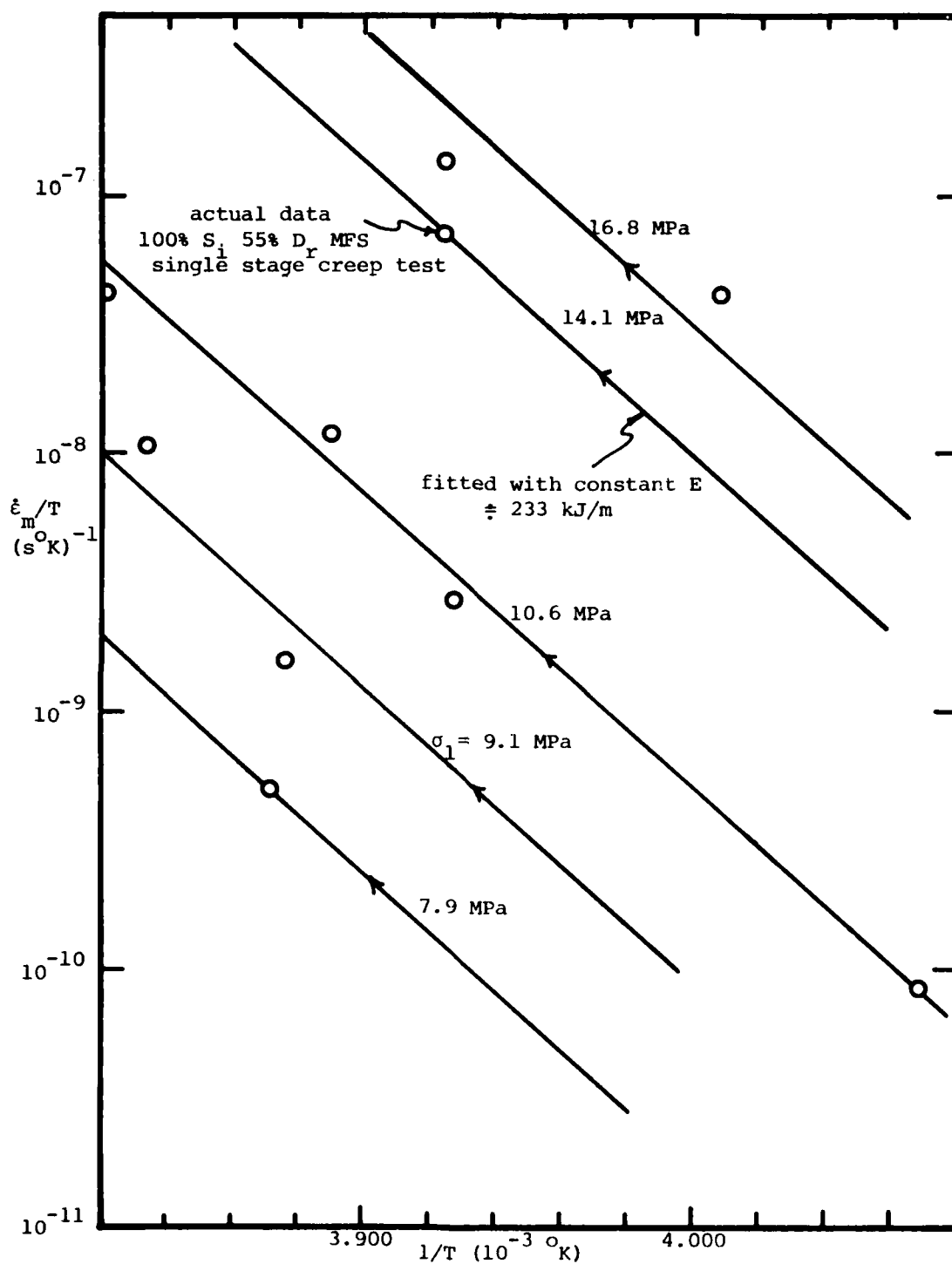


FIGURE B.2.8 Fit of selected constant load single stage creep test data for 100% S_i 55% D_r MFS with constant apparent activation energy

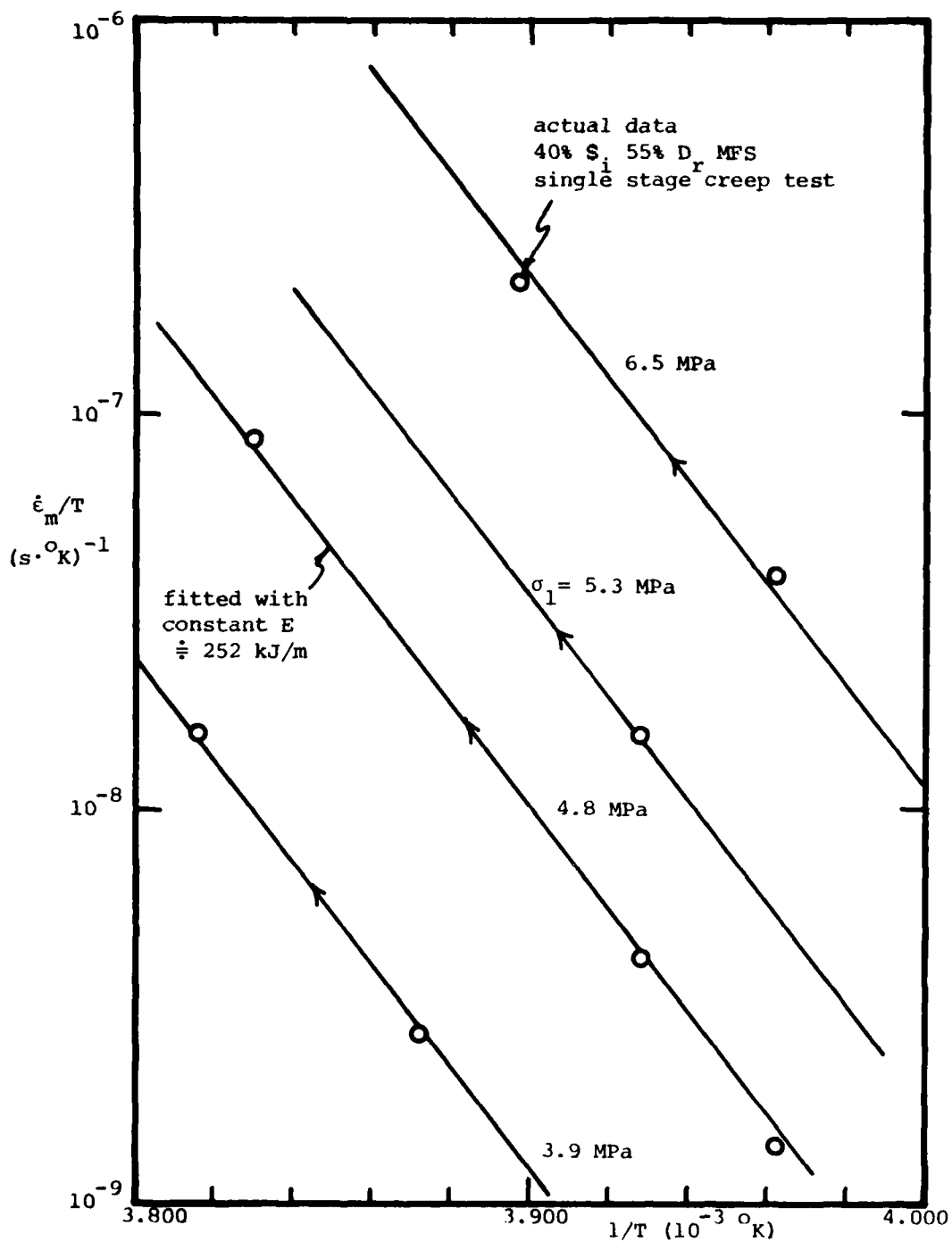


FIGURE B.2.9 Fit of selected constant load single stage creep test data for 40% S_i 55% D_r MFS with constant apparent activation energy

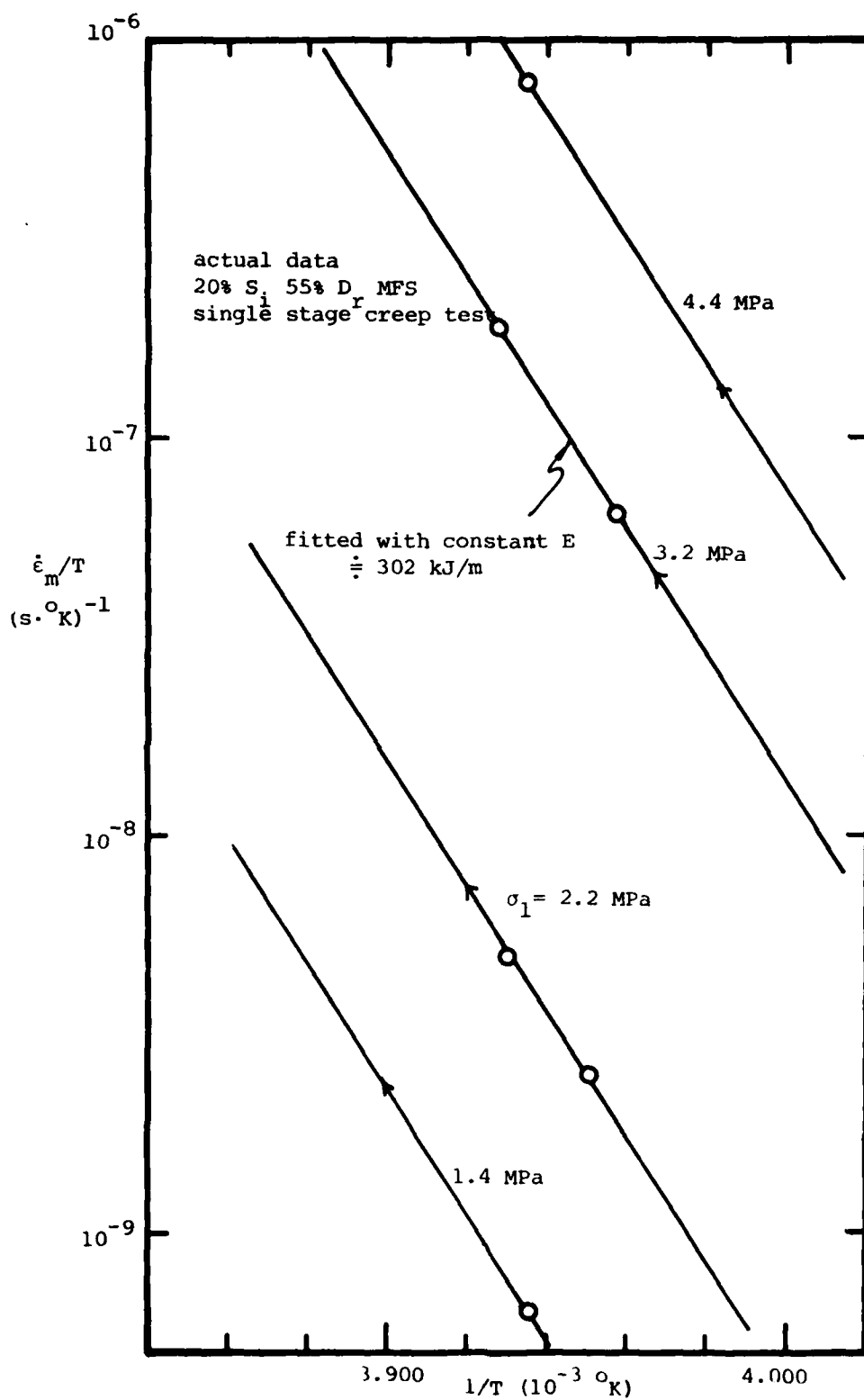


FIGURE B.2.10 Fit of selected constant load single stage creep test data for 20% S_i 55% D_r MFS with constant apparent activation energy

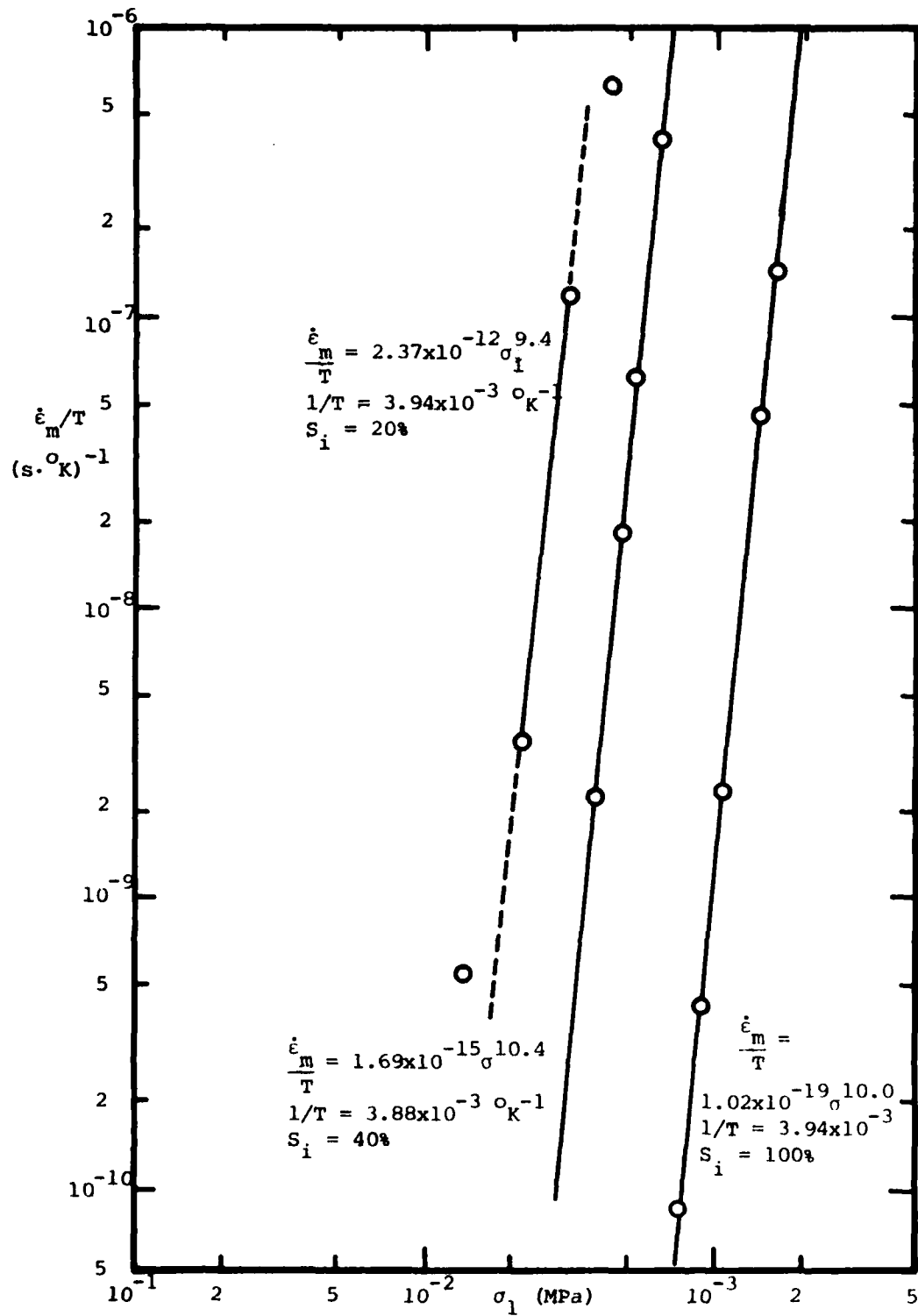


FIGURE B.2.11 Summary of stress dependence of creep for selected constant load creep tests at varying degrees of saturation S_i

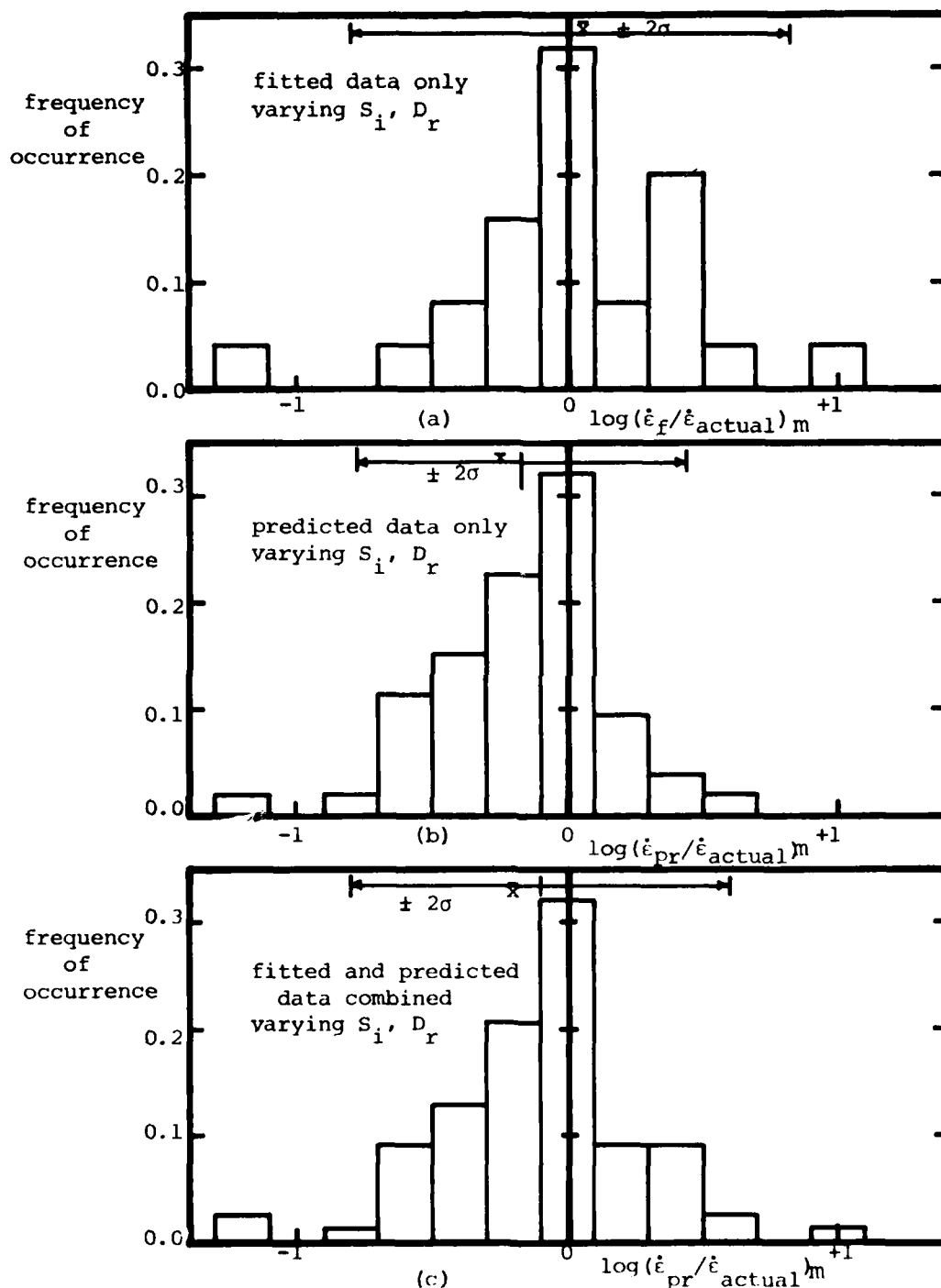


FIGURE B.2.12 Frequency histogram of quality of predictions using one modified RPT equation and the results from 25 tests to predict all single stage constant load creep test data

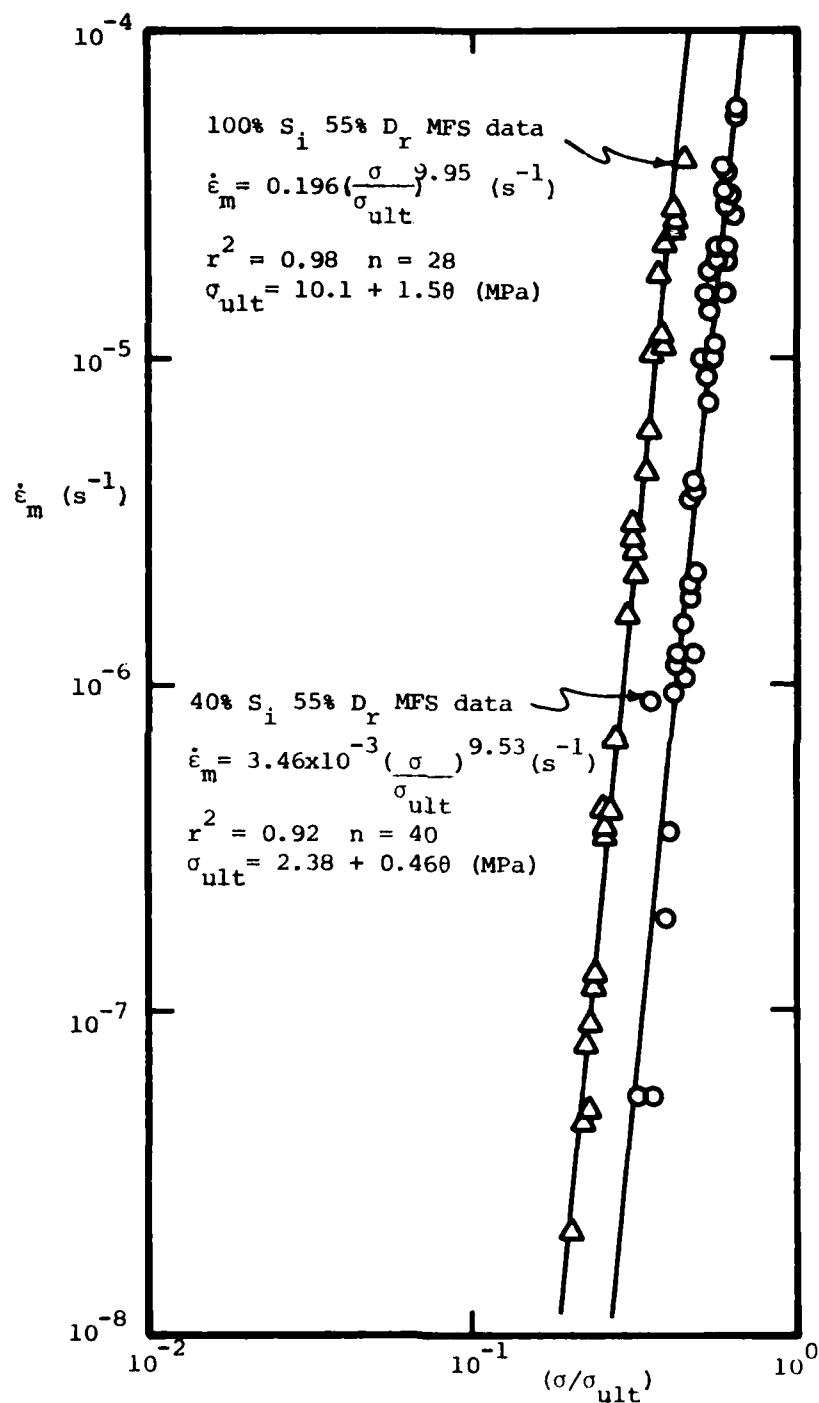


FIGURE B.2.13 Use of ultimate strength for fitting constant load creep data for 40% S_i and 100% S_i MFS

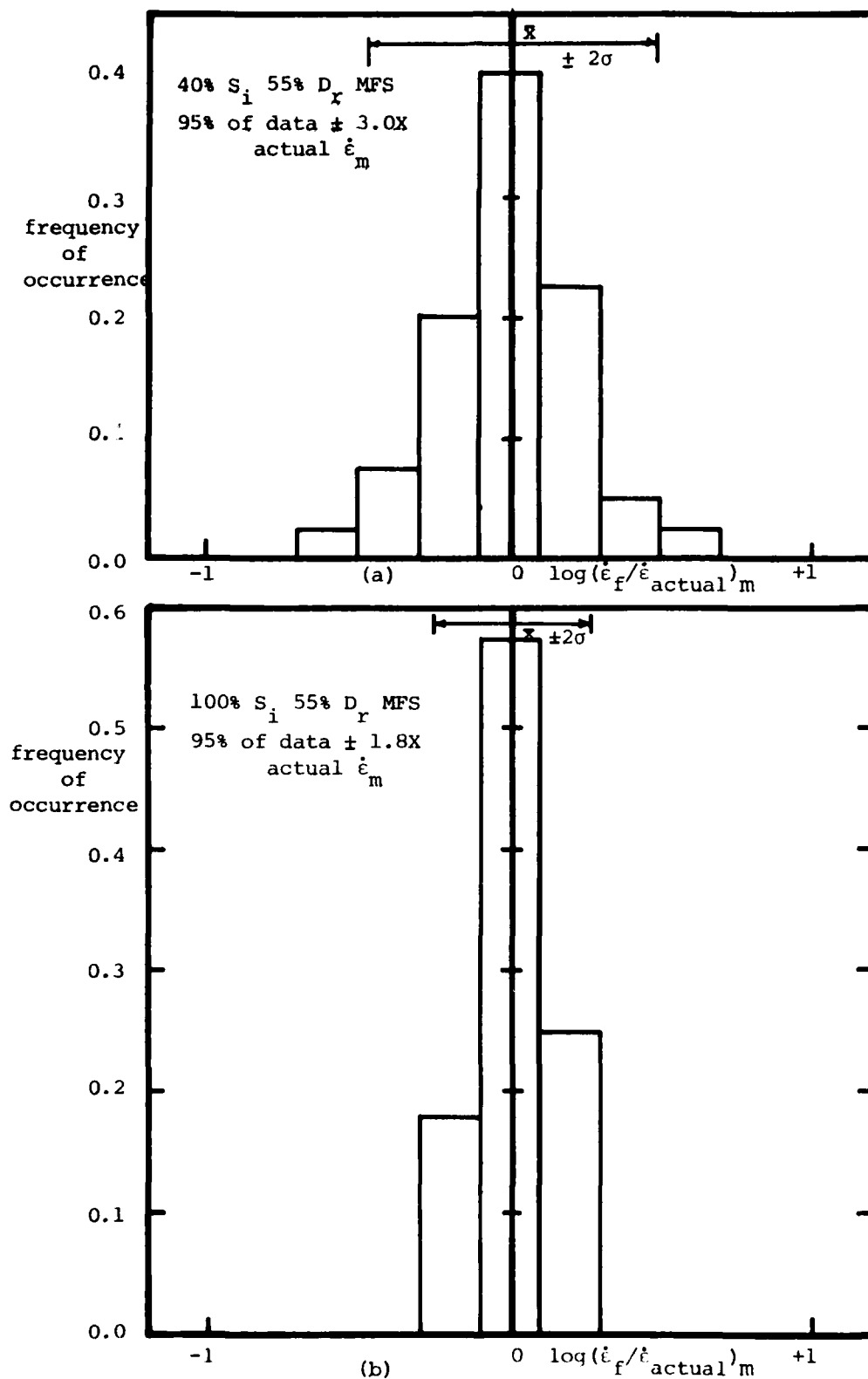


FIGURE B.2.14 Frequency histogram of data fits using ultimate strength

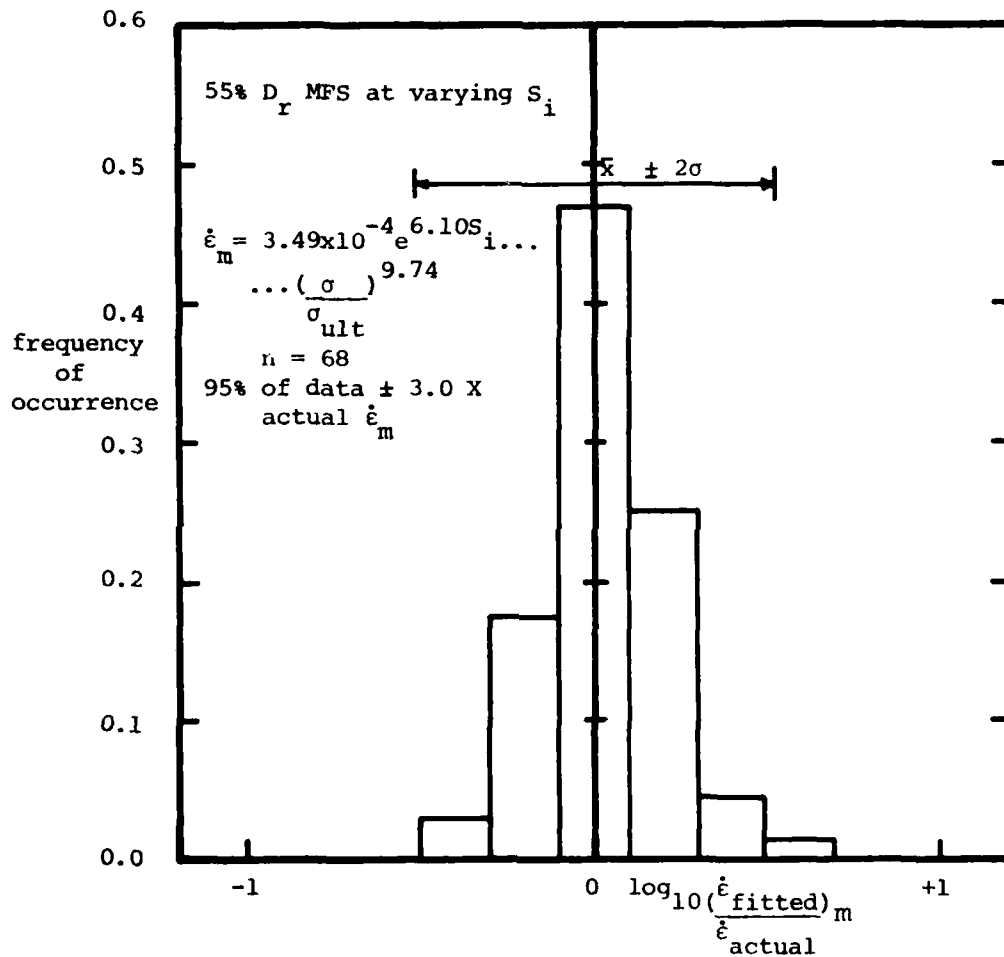


FIGURE B.2.15 Frequency histogram of quality of fit using ultimate strength to account for temperature dependence, data at varying degrees of ice saturation S_i

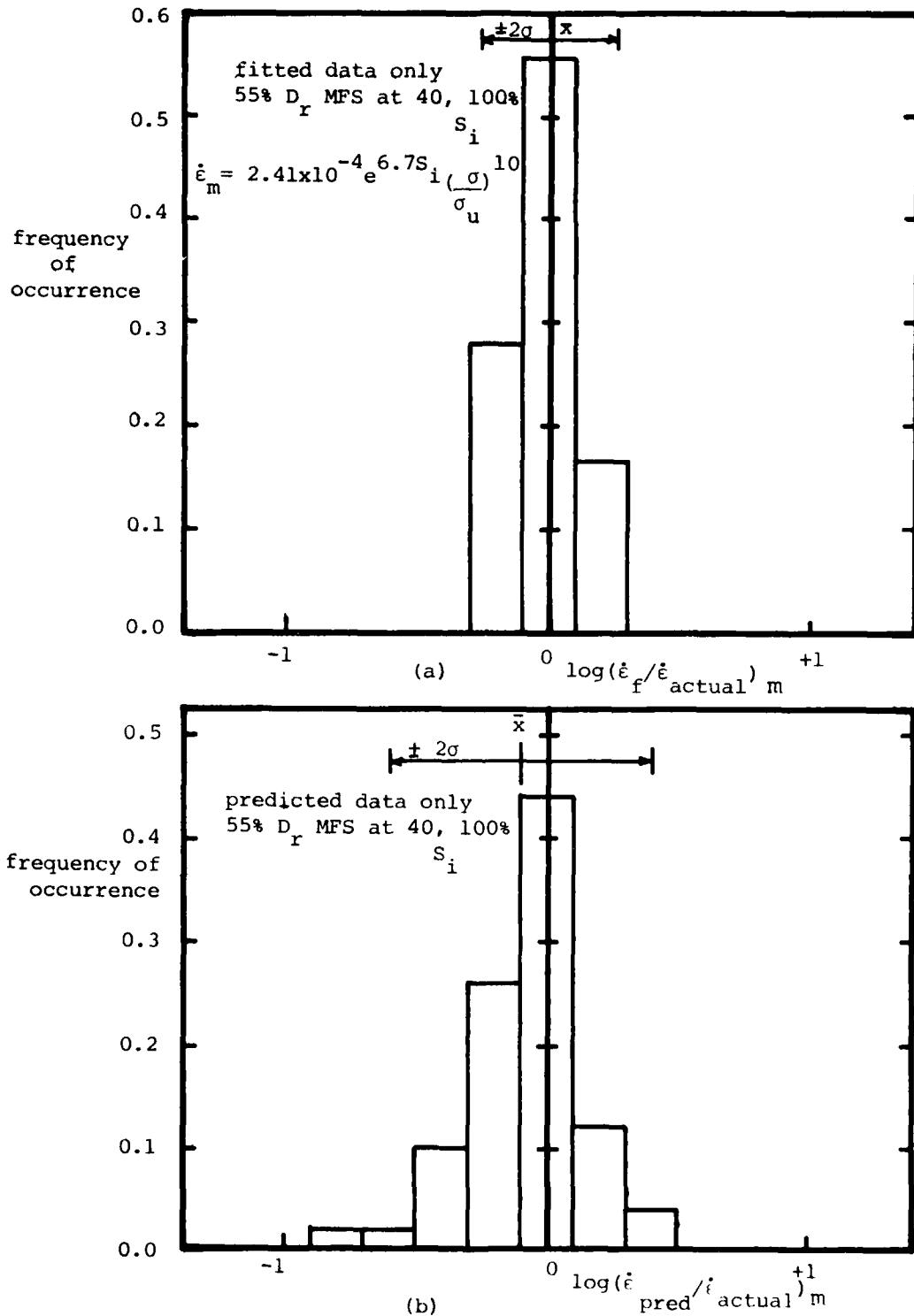
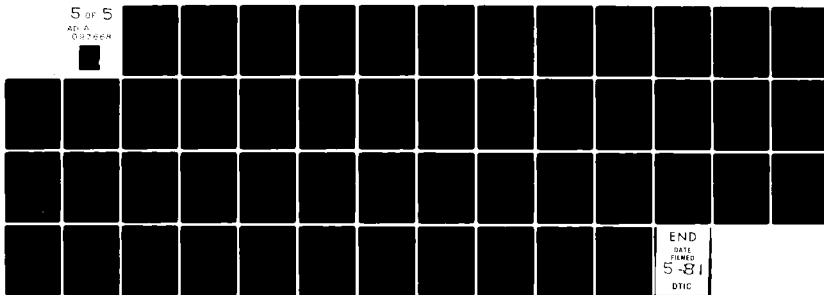


FIGURE B.2.16 Frequency histogram of quality of fit using σ_{ult} and results from 18 creep tests to predict all MFS data

AD-A097 668 MASSACHUSETTS INST OF TECH CAMBRIDGE DEPT OF CIVIL E--ETC F/G 8/13
THE CREEP OF FROZEN SANDS; QUALITATIVE AND QUANTITATIVE MODELS.(U)
MAR 81 J M TING DAA629-77-C-0016
UNCLASSIFIED R81-5 ARO-14725.2-6S NL

5 of 5

AD-A
087668



END
DATE
FILMED
5-81
DTIC

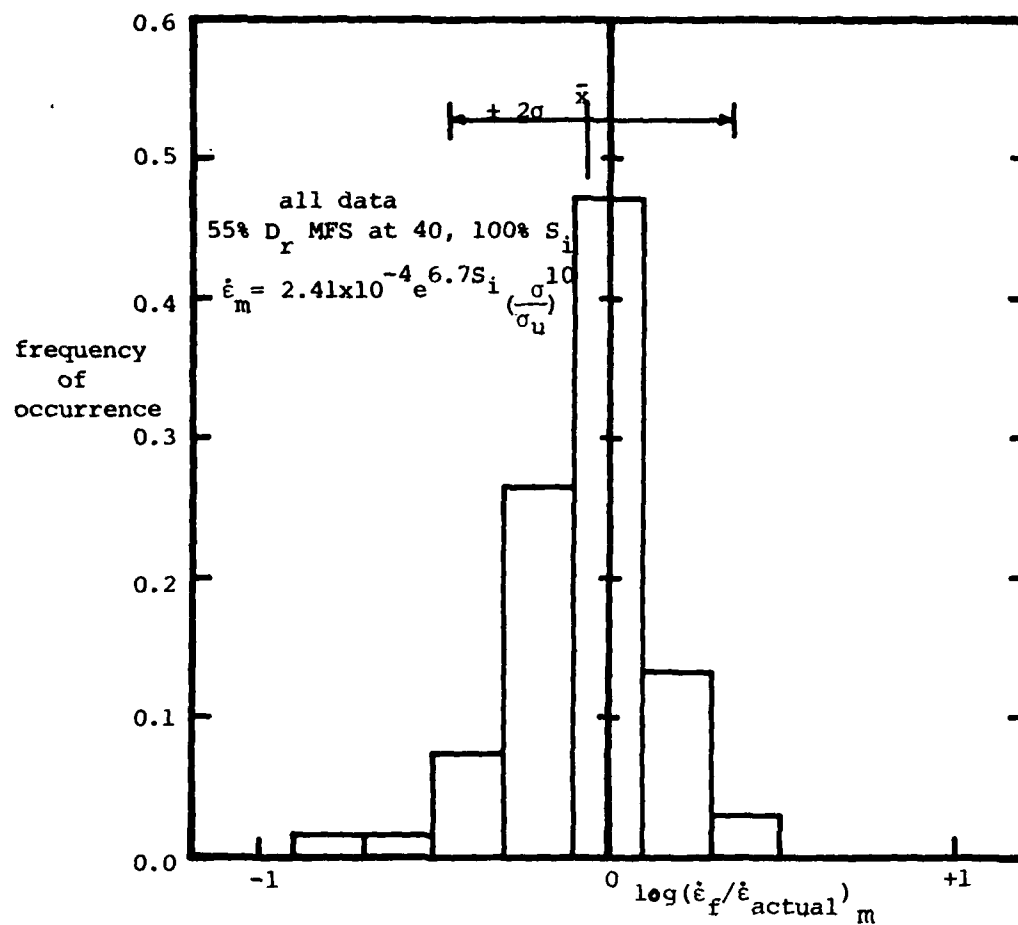


FIGURE B.2.16(c) Frequency histogram of quality of fit using σ_{ult} and results from 18 creep tests to predict all MFS data

APPENDIX B.3 Details of Prediction of t_m for Manchester Fine Sand

Two basic methods were used to predict the time to minimum strain rate for constant load creep tests on MFS. The first method uses the linear $\log \dot{\epsilon}_m - \log t_m$ correlation which has been observed to be quite common in engineering materials, in conjunction with the predictive methods presented in Appendix B.2 for the minimum strain rate. The second method in effect replaces the $\dot{\epsilon}_m - t_m$ correlation with a $\epsilon_m - \log \dot{\epsilon}_m$ correlation and a creep model.

The linear relation between the $\log \dot{\epsilon}_m$ and $\log t_m$ has been mentioned in previous Sections and in Appendix B.1. For 20, 40 and 100 % saturated MFS, the coefficients for this correlation are found in Table A.5.9, for tests at various temperatures and stresses. By taking this correlation in conjunction with a predictive method for $\dot{\epsilon}_m$, the t_m may be estimated.

This was done for 40% Si 55% Dr MFS using the constant E modified RPT method and the stress-ratio based fits. For this material,

$$\dot{\epsilon}_m = 4.20 \times 10^{-4} t_m^{-1.21} \quad (B.3.1)$$

from Table A.5.9. From Appendix B.2,

$$\dot{\epsilon}_m = 2.03 \times 10^{35} T \sigma_1^{10.4} \exp\left(-\frac{29781}{T}\right) \quad (B.3.2)$$

Combining the two equations leads to:

$$t_m = 7.89 \times 10^{-33} T^{-0.83} \sigma_1^{-8.6} \exp\left(\frac{24714}{T}\right) \quad (B.3.3)$$

where T is in $^{\circ}K$, σ_1 is in MPa, t_m is in minutes and $\dot{\epsilon}_m$ is in /s. The quality of the fit is shown in Figure B.3.1(a), and indic-

ates that 95% of the data fitted are within $\pm 3.3X$ the actual t_m .

Alternatively, using the "stress ratio method" for $\dot{\epsilon}_m$ prediction:

$$\dot{\epsilon}_m = 3.46 \times 10^{-3} \left(\frac{\sigma}{\sigma_{ult}} \right)^{9.53} \quad (B.3.4)$$

Combining with (B.3.1) leads to:

$$t_m = 0.174 \left(\frac{\sigma}{\sigma_{ult}} \right)^{-7.91} \quad (B.3.5)$$

where σ_{ult} is the ultimate strength as computed in Appendices A.5 and B.2. The results of this fit are shown in Figure B.3.1(b), and indicate that the fit is very well-centered, with 95% of the fitted t_m within $\pm 2.5X$ of the actual t_m . Both equations (B.3.3) and (B.3.5) yield fairly good results, with the method based on stress ratios yielding marginally less scatter in the fit.

The second method is based primarily on the premise that the linearity of the $\log \dot{\epsilon}_m - \log t_m$ correlation is due to the fact that the strain at the minimum strain rate is approximately constant, and that the linear correlation is relatively insensitive to small deviations from constant ϵ_m . This premise was thoroughly examined in Appendix B.1. By using an estimate of the ϵ_m and the Singh-Mitchell (1968) three-parameter primary creep model, an alternate relation between $\dot{\epsilon}_m$ and t_m can be obtained. This has been done for 40% Si 55% Dr MFS creep data. By correlating the strain at minimum strain rate to the minimum creep rate, the following results:

$$\ln \dot{\epsilon}_m = -20.77 + 319 \epsilon_m, \quad r^2 = 0.66 \quad (B.3.6)$$

which is plotted in Figure B.3.2. In spite of the tremendous

scatter, a definite trend exists. From the Singh-Mitchell three-parameter creep model, as derived in Appendix B.1,

$$\epsilon_m = \frac{\dot{\epsilon}_m}{1-m} (t_m - t_m^m) \quad (\text{B.3.7})$$

where t_m is in seconds, $\dot{\epsilon}_m$ is in /sec, and $m = -\partial \ln(\dot{\epsilon}) / \partial \ln(t)$.

For $t_m < 5$ min and $m = 0.6$, less than 10% error is incurred by writing:

$$\begin{aligned} t_m &\approx t_m - t_m^m \\ \Rightarrow t_m &= \frac{(1-m)\epsilon_m}{\dot{\epsilon}_m} = \frac{(1-m)(\ln \dot{\epsilon}_m + 20.77)}{319 \dot{\epsilon}_m} \end{aligned} \quad (\text{B.3.8})$$

where m is an average value during primary creep, approximately 0.6 for 40% Si 55% Dr MFS.

When equation (B.3.8) is used in conjunction with a $\dot{\epsilon}_m$ prediction method, such as equation (B.3.2) or (B.3.4), then t_m can be predicted. This has been carried out for the 40% Si 55% Dr MFS, the results being plotted in Figure B.3.3 for two $\dot{\epsilon}_m$ prediction methods. Again, this Figure indicates that 95 % of the data may be fitted within about $\pm 3X$ the actual t_m , as for the $\log \dot{\epsilon}_m - \log t_m$ correlation.

Since the Singh-Mitchell equation is only an approximation of the actual creep behavior up to and including the secondary creep rate, an average m value is necessary. Its value obviously affects the t_m predicted. For example, if a value of m equal to 0.7 based on the initial stages of primary creep is used instead of a more average value of 0.6, the prediction of t_m is about 30% too low. What really needs to be used is a different creep model which accounts for secondary creep.

The use of the $\log \dot{\epsilon}_m - \log t_m$ correlation as a predictive tool was examined using the same portion of the dataset as before for 40% Si 55% Dr. MFS. Using only the results from eight constant load creep tests and numerous strength tests, the RPT-based and stress ratio-based predictors for $\dot{\epsilon}_m$ and the $\log \dot{\epsilon}_m - \log t_m$ correlation were determined. These methods were then used to predict the time to minimum strain rate, t_m , the results of which are plotted in Figure B.3.4. As can be seen, both yield predictions of t_m which have 95% of the predicted t_m within $\pm 3.7X$ the actual t_m .

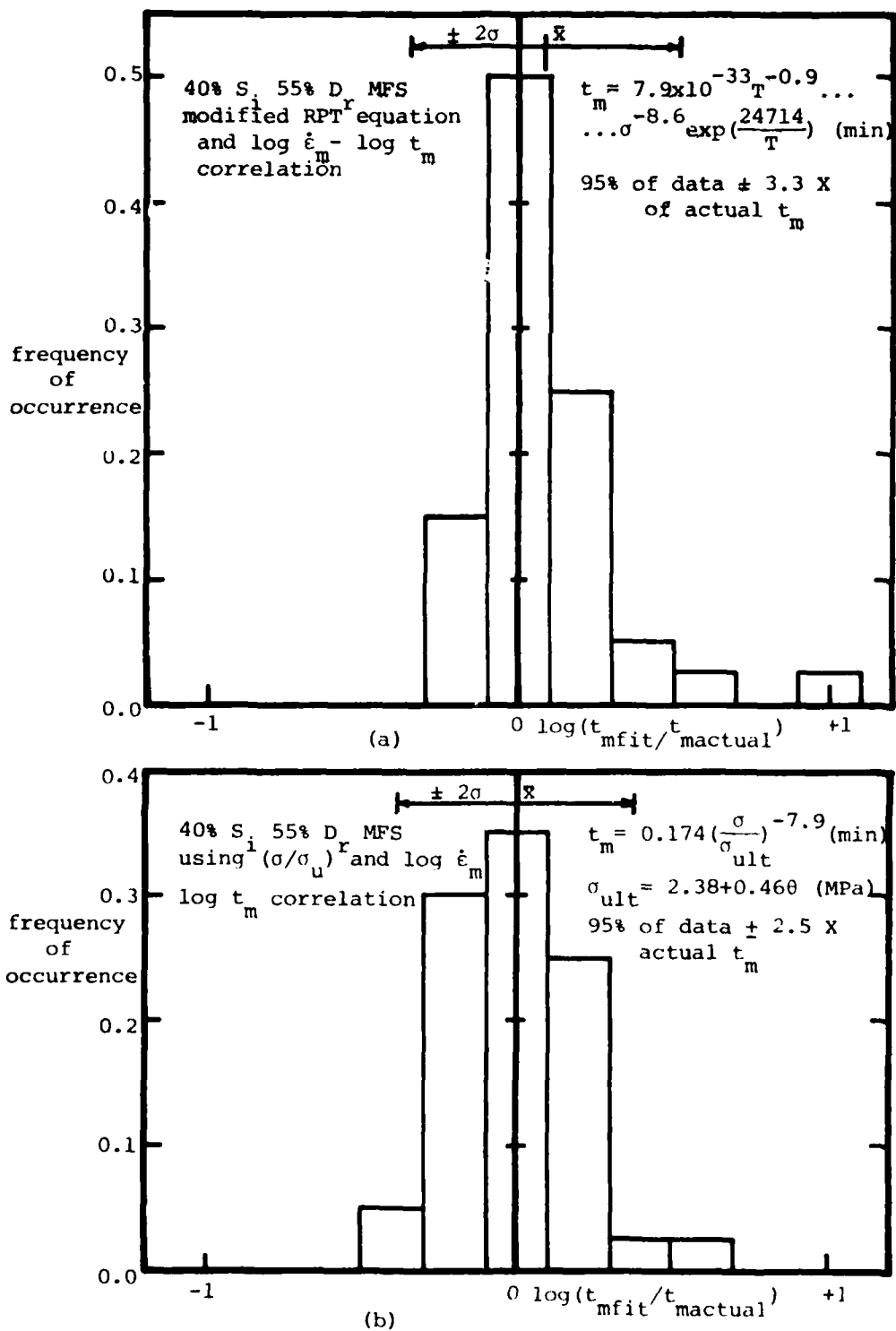


FIGURE B.3.1 Histograms of fitted t_m using $\log \dot{\epsilon}_m - \log t_m$ correlation

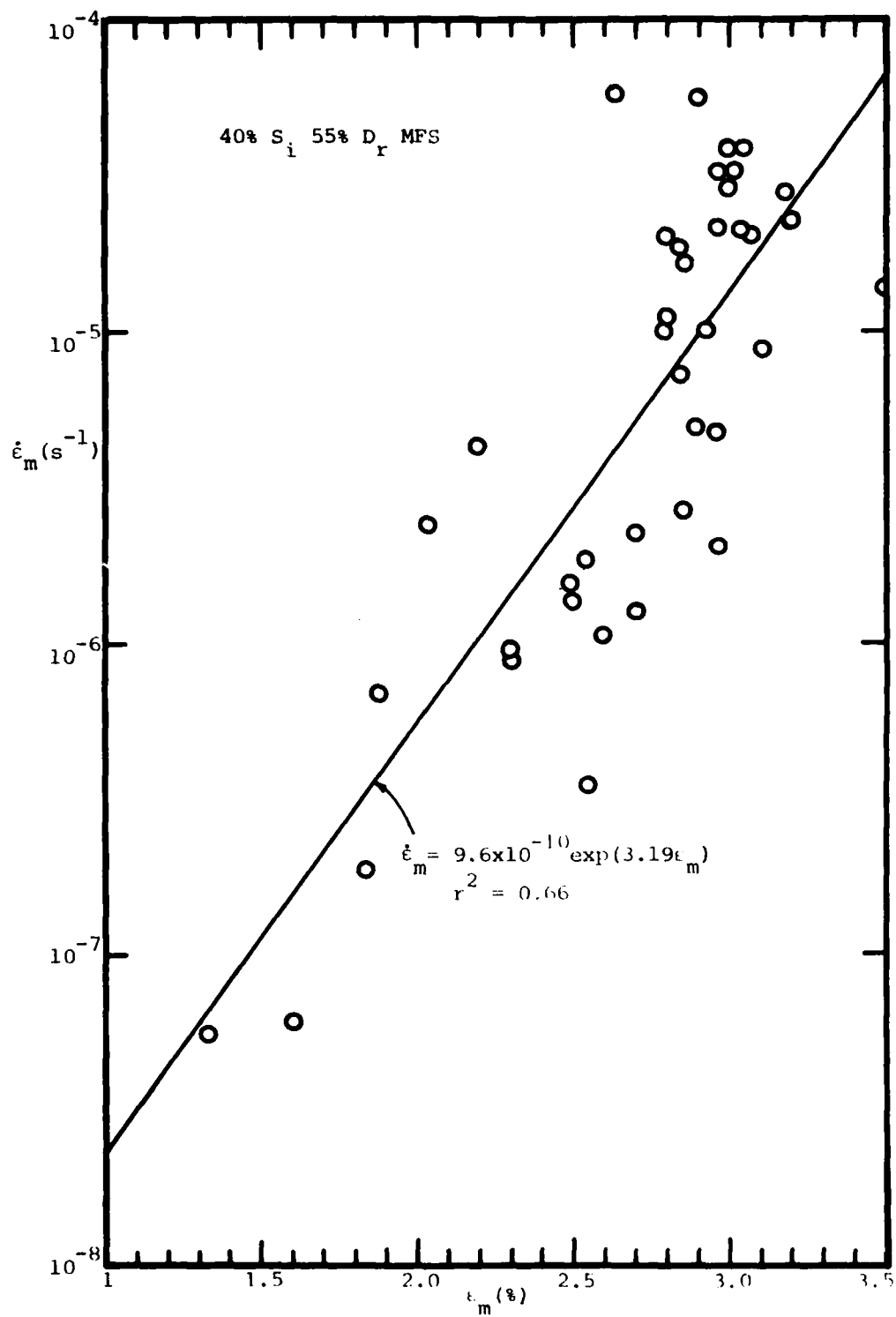


FIGURE B.3.2 Correlation between $\dot{\epsilon}_m$ and ϵ_m

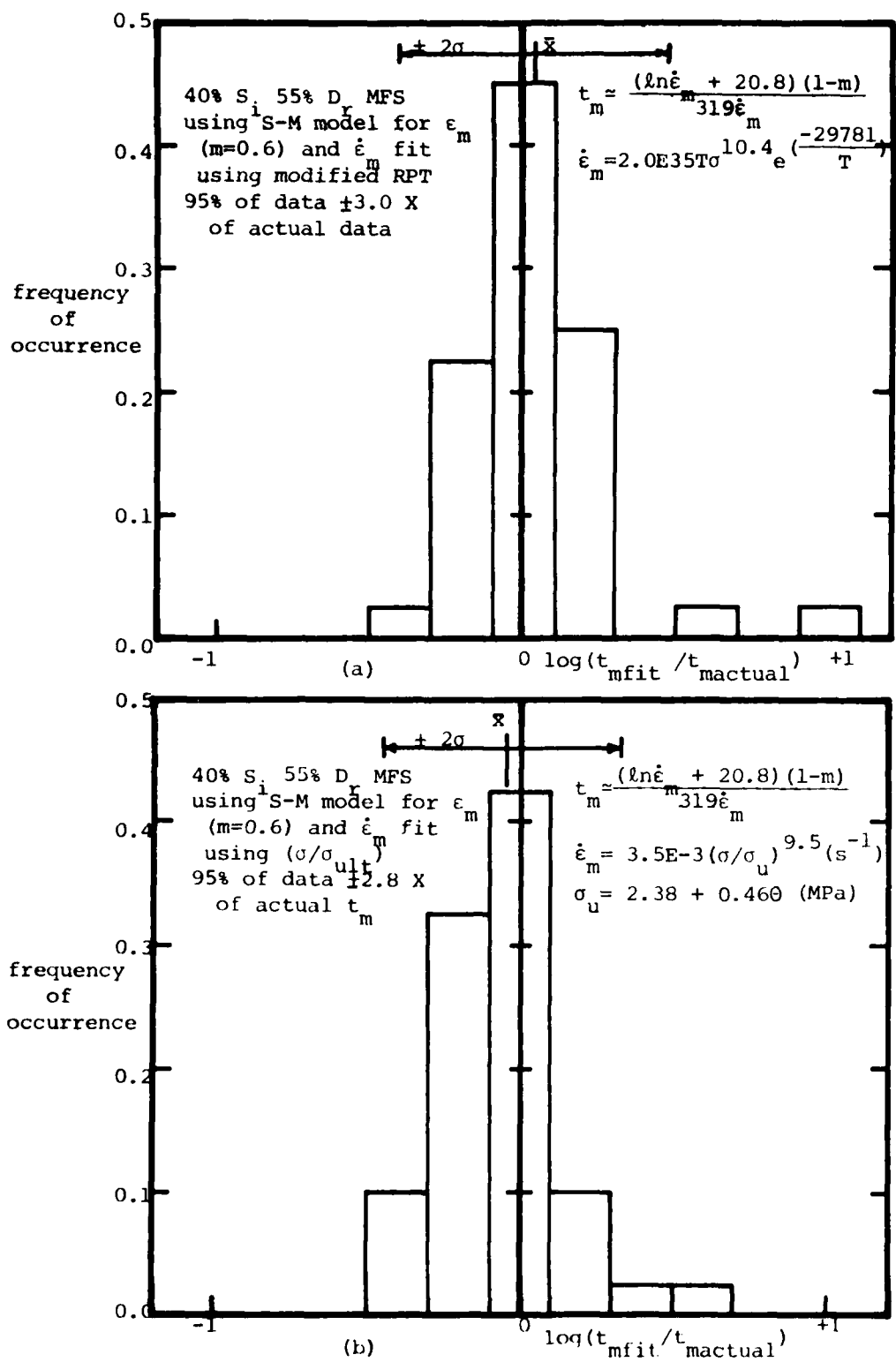


FIGURE B.3.3 Histograms of t_m fit using ϵ_m model with $\dot{\epsilon}_m$ fits

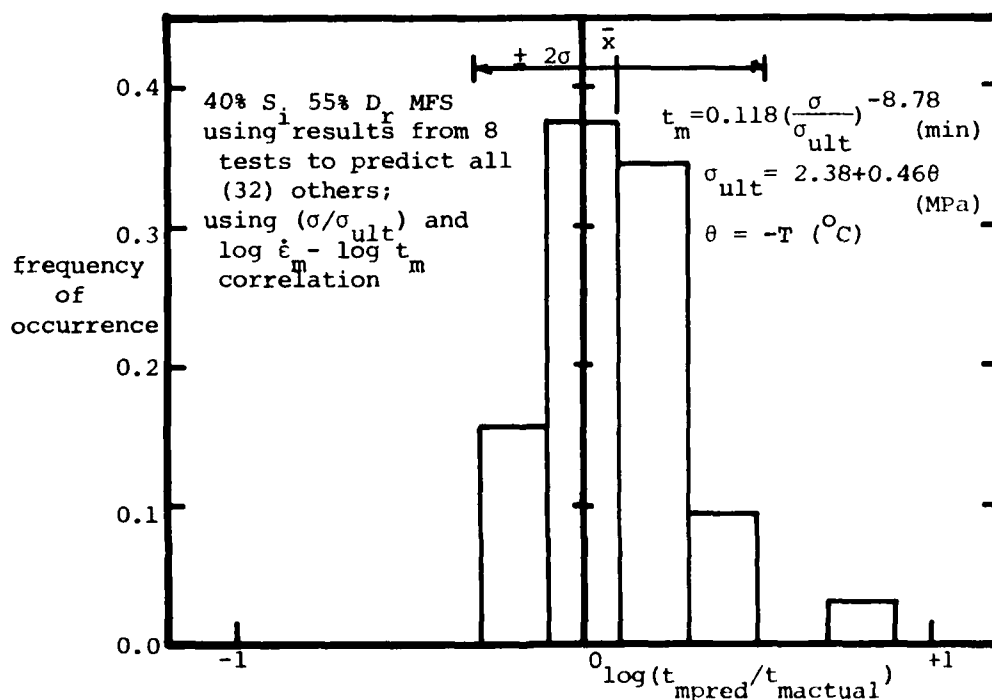
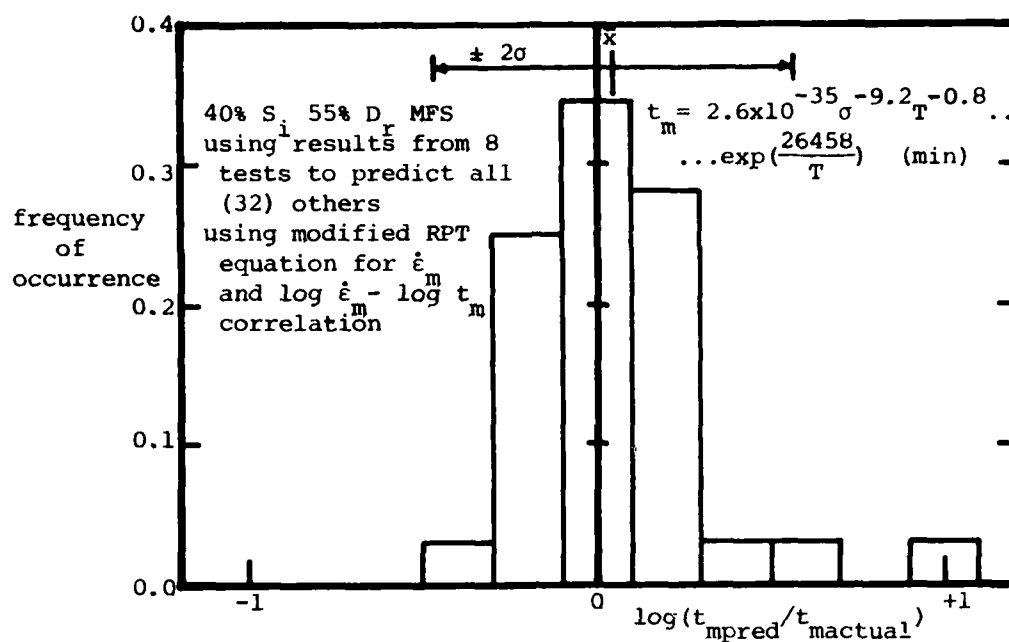


FIGURE B.3.4 Histograms of t_m prediction using results from 8 tests to predict others, with $\log \dot{\epsilon}_m - \log t_m$ correlation

APPENDX B.4 Details on the Proposed Creep Models

This Appendix develops new creep models capable of representing the deformation-time behavior of frozen MFS through all three stages of creep. In order to find a unifying shape for all of the creep curves, the $\log \dot{\epsilon} - \log t$ plots for the 40% ice saturated MFS were normalized to $\dot{\epsilon}_m$ and t_m , as demonstrated in Figure B.4.1. From such a plot, it was noted that the deviation Δ of the creep curve from a "linear" primary creep relationship such as the Singh-Mitchell (1968) model could be expressed quite well as (see Figure B.4.2):

$$\Delta = \beta t^n, \text{ where } n = 0.88 \text{ for 40\% Si MFS} \quad (\text{B.4.1})$$

Combining this with the form of the Singh-Mitchell model, the complete creep curve may be described by:

$$\begin{aligned} \ln \dot{\epsilon} &= \ln A - m \ln t + \beta t^n \\ \text{or } \dot{\epsilon} &= A t^{-m} e^{\beta t^n} \end{aligned} \quad (\text{B.4.2})$$

where A , m , β , n are experimentally determined parameters.

For 40% Si MFS, $n = 0.88$ and m is between about 0.6 and 0.9.

Simplifying for $n = 1$,

$$\dot{\epsilon} = A t^{-m} e^{\beta t} \quad (\text{B.4.3})$$

This simplified form of the creep model was independently developed for ice by Assur (1979). For simplicity, this model (equation B.4.3) is referred to as the "Assur-Ting" model herein. Note, however, that all of the proposed integrations and techniques for parameter determination were developed solely by the author.

Integrating for strains,

$$\epsilon = \int_{t_0}^t \dot{\epsilon} dt + \epsilon_0 = A \int_{t_0}^t t^{-m} e^{\beta t} dt + \epsilon_0$$

Using integration by parts,

$$\epsilon = \epsilon_0 + \frac{A e^{\beta t} t^{1-m}}{1-m} - A \int_{t_0}^t \frac{e^{\beta t} t^{-(m-1)}}{(1-m)} dt$$

where $m \neq 1, 2, 3, \dots$

$$\begin{aligned} \Rightarrow \epsilon &= \epsilon_0 + \frac{A e^{\beta t} t^{1-m}}{1-m} - \frac{A \beta}{1-m} \left[\frac{e^{\beta t} t^{1-(m-1)}}{1-(m-1)} - \frac{\beta}{1-(m-1)} \left[\frac{e^{\beta t} t^{1-(m-2)}}{1-(m-2)} \right. \right. \\ &\quad \left. \left. - \frac{\beta}{1-(m-2)} \left[\frac{e^{\beta t} t^{1-(m-3)}}{1-(m-3)} \dots \dots \dots \right] \right] \right] \Bigg|_{t_0}^t \\ \Rightarrow \epsilon &= \epsilon_0 + A e^{\beta t} t^{1-m} \left[\frac{1}{1-m} - \frac{(\beta t)}{(1-m)(2-m)} - \frac{(\beta t)^2}{(1-m)(2-m)(3-m)} \right. \\ &\quad \left. - \frac{(\beta t)^3}{(1-m)(2-m)(3-m)(4-m)} + \dots \dots \dots \right] \Bigg|_{t_0}^t \\ \Rightarrow \epsilon &= \epsilon_0 + A e^{\beta t} t^{1-m} S \Big|_{t_0}^t \end{aligned} \quad (B.4.4)$$

$$\text{where } S = \frac{1}{1-m} - \frac{\beta t}{(1-m)(2-m)} + \frac{(\beta t)^2}{(1-m)(2-m)(3-m)} \dots + \frac{(-1)^{i+1} (\beta t)^{i-1}}{\prod_{k=1}^i (k-m)}$$

$$\Rightarrow S = \sum_{i=1}^{\infty} \frac{(-1)^{i+1} (\beta t)^{i-1}}{\prod_{k=1}^i (k-m)}$$

Since $m < 1$, $\beta > 0$, $t > 0$, the value of each term of the series is positive, and hence the series is alternating.

The following presents a simple procedure developed to determine the parameters necessary for modelling an actual test.

Using $t_0 = 1 \text{ min}$,

$$\dot{\epsilon}_0 = A t_0^{-m} e^{\beta t_0} = A e^{\beta} \quad (/m) \quad (B.4.5)$$

At the minimum strain rate,

$$\ddot{\epsilon}_m = A t_m^{-m-1} e^{\beta t_m} [-m + \beta t_m] = 0$$

$$\Rightarrow m = \beta t_m \quad (B.4.6)$$

Knowing the initial slope m_0 of the $\log \dot{\epsilon} - \log t$ creep curve at time t_0 ,

$$m_0 = - \left. \frac{\partial \ln \dot{\epsilon}}{\partial \ln t} \right|_{t_0} = m - \beta \left. \frac{\partial t}{\partial \ln t} \right|_{t_0} = m - \beta t_0$$

$$\Rightarrow m = m_0 + \beta \quad \text{for } t_0 = 1 \quad (B.4.7)$$

Combining equations (B.4.6) and (B.4.7),

$$\beta = \frac{m_0}{t_m - 1} \quad (B.4.8)$$

Then, by using equations (B.4.5), (B.4.7) and (B.4.8), the parameters of the proposed creep model can be easily determined from m_0 , $\dot{\epsilon}_0$, at t_0 and from t_m . Figure B.4.2 illustrates this procedure. The entire strain - time creep curve can be determined after knowing the strain ϵ_0 at t_0 and by evaluating the series S at each time. For typical creep tests carried well into tertiary creep, between 2 and 20 terms of the series are required for three-digit accuracy of the series, with the larger number of terms required at the larger times. For times during the primary stage, only 4 or 5 terms were required; however, about ten terms were used at the minimum strain rate.

Application of the above techniques to all of the 40% Si MFS constant load creep data yielded the results summarized in Table B.4.1. The actual and fitted $\log \dot{\epsilon} - \log t$ curves for a family of creep tests at one stress and various temperatures are plotted in Figure B.4.3. Figure B.4.4 plots the resulting integrated strain-time curve together with the actual data.

Note that when the proposed creep model is individually fitted to each test, excellent agreement exists for both the

$\log \dot{\epsilon} - \log t$ curve and integrated $\epsilon - \text{time}$ curves, except during the latter stages of tertiary creep. This occurs primarily due to the simplified assumption of $n = 1$ shown in Figure B.4.2. Also, the curves plotted in Figure B.4.3 are not least squares fits of the $\log \dot{\epsilon} - \log t$ data, since the model parameters were determined from a very simple method using information at only two points, t_0 and t_m .

Figure B.4.5 compares the fits provided by the "Assur-Ting" and Singh-Mitchell (1968) models. The Singh-Mitchell model does a good job of fitting the data for the first 100 minutes of the test, but is clearly inadequate at larger times after the $\log \dot{\epsilon} - \log t$ curve deviates from "linear" behavior.

The Assur-Ting model was also extended to act as a unifying relationship for fitting and predicting the creep behavior of partially saturated MFS at varying stresses and temperatures. Extensive use was made of the stress ratio, σ/σ_{ult} , in quantifying the stress and temperature dependence of the creep. Based on the results from Appendix B.2 and B.3 on the prediction of $\dot{\epsilon}_m$ and t_m using stress ratios and strength tests compared with σ_1 and T and creep data using the modified RPT equation, it is expected that the either method for describing stress and temperature should yield fits and predictions similar in quality. However, due to increased ease in fitting and plotting the data with only one test parameter, stress ratios are used exclusively in this Appendix.

Using all 40 constant load creep tests at 40% Si to deter-

mine the model parameters, the following correlations resulted:

$$\begin{aligned}\dot{\epsilon}_O &= 0.018 \left(\frac{\sigma}{\sigma_{ult}} \right)^{2.77} (/m) & r^2 &= 0.86 \\ m_O &= 0.78 \pm 0.09 (\pm 1 \text{ std. dev.}) \\ \epsilon_O &= -0.0065 + 0.0297 \left(\frac{\sigma}{\sigma_{ult}} \right) & r^2 &= 0.63 \\ t_m &= 0.170 \left(\frac{\sigma}{\sigma_{ult}} \right)^{-7.94} (m) & r^2 &= 0.91\end{aligned} \quad (B.4.9)$$

Data from eight tests were also used to predict the behavior of the other 32 constant load creep tests. Based on the experience with the prediction of $\dot{\epsilon}_m$ and t_m , use of more test data for determining the model parameters should affect the overall predictions only marginally. The data from these eight tests (the same ones used for prediction in Appendices B.2 and B.3) yielded the following correlations:

$$\begin{aligned}\dot{\epsilon}_O &= 0.019 \left(\frac{\sigma}{\sigma_{ult}} \right)^{2.96} (/m) & r^2 &= 0.80 \\ m_O &= 0.775 \pm 0.068 (\pm 1 \text{ std. dev.}) & & \\ \epsilon_O &= -0.0130 + 0.0426 \left(\frac{\sigma}{\sigma_{ult}} \right) & r^2 &= 0.88 \\ t_m &= 0.118 \left(\frac{\sigma}{\sigma_{ult}} \right)^{-8.78} \text{ from correlating } \dot{\epsilon}_m - t_m \text{ and } \dot{\epsilon}_m - \sigma/\sigma_{ult}.\end{aligned} \quad (B.4.10)$$

Note that these correlations are very similar to (B.4.9) using all of the data. Combining equations (B.4.10),

$$\begin{aligned}\beta &\cong 6.57 \left(\frac{\sigma}{\sigma_{ult}} \right)^{8.78} \\ m &= 0.775 + \beta \\ A &= \frac{0.0194 (\sigma/\sigma_{ult})^{2.96}}{\exp(6.57 (\sigma/\sigma_{ult})^{8.78})} (/m)\end{aligned} \quad (B.4.11)$$

The fitted and predicted parameters and resulting predicted $\dot{\epsilon}_m$ and ϵ_m are summarized and compared in Table B.4.2. The frequency histograms of these comparisons are plotted in Figure B.4.6. These indicate a scatter for the $\dot{\epsilon}_m$ not too different from Ap-

pendix B.2, and a fairly good prediction of the ϵ_m . To provide an idea of the typical quality of these fits, three predicted tests are plotted in Figures B.4.7 and B.4.8. These are indicative of a good fit, a large overestimation, and a large underestimation of the $\dot{\epsilon}_m$ and the ϵ_m .

For saturated frozen Manchester Fine Sand, the $\log \dot{\epsilon} - \log t$ creep curves typically do not exhibit continuous upward concavity, as seen in Figures A.6.4 and A.6.5. Instead, a change in slope of the $\log \dot{\epsilon} - \log t$ curve exists during primary creep. This change in slope occurs at about 1.2 % axial strain, and is possibly indicative of a change in the mechanisms controlling deformation behavior. Below this strain level, the creep is possibly more a function of pore ice deformation (hence the lower m value), while at the higher strains the frictional strength of the sand structure is more fully mobilized, resulting in a steeper $\log \dot{\epsilon} - \log t$ creep curve. The details of the actual strain at the slope change for each test are found in Table B.4.3, together with other pertinent test information.

In order to model these data, a modified creep model consisting of a combination of the Singh-Mitchell and Assur-Ting creep models is used. As shown in Figure B.4.9, the strain rate can be represented by:

$$\begin{aligned} \dot{\epsilon} &= A_1 t^{-m_1} & \text{for } t_1 < t < t_\Delta & \quad (B.4.12) \\ \text{and } \dot{\epsilon} &= A_2 t^{-m_2} e^{\beta t} & \text{for } t > t_\Delta \end{aligned}$$

Integrating for strain,

$$\epsilon = \epsilon_o + \frac{A_1}{1-m_1} (t^{1-m_1} - 1) \quad \text{for } t_o = 1 \text{ min, } m \neq 1$$

$$\text{and } 1 < t < t_{\Delta} \quad (B.4.13)$$

$$\text{and } \epsilon = \epsilon_{\Delta} + A_2 e^{\beta t} t^{1-m_2} S(t) - A_2 e^{\beta t_{\Delta}} t_{\Delta}^{1-m_2} S(t_{\Delta})$$

where S is defined by equation (B.4.4), and $t > t_{\Delta}$.

By using $t_0 = 1 \text{ min}$,

$$\begin{aligned} A_1 &= \dot{\epsilon}_0 \\ m_1 &= m_{01} \\ \dot{\epsilon}_{\Delta} &= A_1 t_{\Delta}^{-m} \end{aligned} \quad (B.4.14)$$

At the break in the curve,

$$t_{\Delta} = \left[\frac{(\epsilon_{\Delta} - \epsilon_0)(1-m)}{A_1} + 1 \right]^{1/1-m_1} \quad (B.4.15)$$

$$\text{and } \dot{\epsilon}_{\Delta} = A_2 e^{\beta t_{\Delta}} t_{\Delta}^{-m_2}$$

$$\Rightarrow A_2 = \frac{\dot{\epsilon}_{\Delta} t_{\Delta}^{m_2}}{e^{\beta t_{\Delta}}} \quad (B.4.16)$$

By differentiating (B.4.12),

$$\ddot{\epsilon} = A_2 e^{\beta t} t^{-m_2} [\beta - m_2 t^{-1}] \quad (B.4.17)$$

At the minimum strain rate,

$$\ddot{\epsilon}_m = 0 \text{ and}$$

$$\Rightarrow \beta = \frac{m_2}{t_m} \text{ as before in equation (B.4.6)} \quad (B.4.18)$$

$$\text{At } t_{\Delta}, \text{ the initial slope } m_{02} = -\frac{\partial \ln \dot{\epsilon}}{\partial \ln t} = -m_2 + \beta t_{\Delta} \quad (B.4.19)$$

Combining,

$$\beta = \frac{m_{02}}{t_m - t_{\Delta}} \quad (B.4.20)$$

Using equations (B.4.14), (B.4.16), (B.4.19) and (B.4.20), all of the parameters of the modified creep model may be determined. Table B.4.4 presents the results of applying this model to all of the saturated constant load creep tests on MFS.

The $\log \dot{\epsilon}$ - $\log t$ and integrated strain - time curves for a typical test are plotted in Figures B.4.10 and B.4.11. As can be seen, this modified model does a very effective job of fit-

ting both the $\log \dot{\epsilon} - \log t$ and $\epsilon - t$ data.

This modified model was also extended to act as a unifying relationship for fitting and predicting the creep behavior of saturated MFS at varying loads and temperatures. The various parameters of the modified creep model may be correlated to the stress ratio as follows, using all 28 creep tests:

$$\begin{aligned}
 \epsilon_0 &= -0.0047 + 0.0317 \left(\frac{\sigma}{\sigma_{ult}} \right) & r^2 &= 0.79 \\
 &\text{(see Figure B.4.12)} \\
 \dot{\epsilon}_0 &= 0.126 \left(\frac{\sigma}{\sigma_{ult}} \right)^{3.86} \quad (/m) & r^2 &= 0.89 \\
 m_{01} &= 0.69 - 1.10 \left(\frac{\sigma}{\sigma_{ult}} \right) & r^2 &= 0.36 \\
 m_{02} &= 1.26 - 2.19 \left(\frac{\sigma}{\sigma_{ult}} \right) & r^2 &= 0.56 \\
 &\text{(see Figure B.4.13)} \\
 t_m &= 0.0097 \left(\frac{\sigma}{\sigma_{ult}} \right)^{-8.56} \quad (m) & r^2 &= 0.92 \\
 &\text{using direct correlation}
 \end{aligned} \tag{B.4.21}$$

$$\epsilon_{\Delta} = 0.0120 \pm 0.0031 \quad (\pm 1 \text{ std. dev.})$$

Using the data from only 10 tests yielded the following parameters:

$$\begin{aligned}
 \epsilon_0 &= -0.0065 + 0.0362 \left(\frac{\sigma}{\sigma_{ult}} \right) & r^2 &= 0.72 \\
 \dot{\epsilon}_0 &= 0.139 \left(\frac{\sigma}{\sigma_{ult}} \right)^{3.88} \quad (/m) & r^2 &= 0.97 \\
 m_{01} &= 0.73 - 1.15 \left(\frac{\sigma}{\sigma_{ult}} \right) & r^2 &= 0.44 \\
 m_{02} &= 1.06 - 1.37 \left(\frac{\sigma}{\sigma_{ult}} \right) & r^2 &= 0.29 \\
 t_m &= 0.0095 \left(\frac{\sigma}{\sigma_{ult}} \right)^{-8.64} \quad (m) & r^2 &= 0.98 \\
 \epsilon_{\Delta} &= 0.0127 \pm 0.0038 \quad (\pm 1 \text{ std. dev.})
 \end{aligned} \tag{B.4.22}$$

Notice that these correlations are very similar to those based on the entire dataset (B.4.21), as expected.

The results of the fitted and predicted parameters for each

test are summarized in Table B.4.5, including the predicted $\dot{\epsilon}_m$ and ϵ_m . The frequency histogram of the comparisons between the actual and predicted $\dot{\epsilon}_m$ and ϵ_m are plotted in Figure B.4.14. Notice that the modified model in this case typically overestimates the minimum strain rate and strain at the minimum strain rate.

test no.	ϵ_c at $t=t_m$	ϵ_c at $t=t_m$	m_c (actual)	t_m (m)	ϵ_c at $t=t_m$	r	m	A (/m)
8-29	0.354	1.61×10^{-3}	0.825	168	0.71	4.94×10^{-3}	0.830	1.60×10^{-3}
9-53	0.393	1.42×10^{-3}	1.030	576	0.40	1.81×10^{-3}	1.332	1.42×10^{-3}
9-48	0.318	1.01×10^{-3}	0.930	1280	0.45	7.27×10^{-4}	0.931	1.01×10^{-3}
8-22	0.521	1.81×10^{-3}	1.705	42	0.61	1.72×10^{-3}	0.722	1.78×10^{-3}
8-26	0.424	1.09×10^{-3}	0.715	182	0.47	4.00×10^{-3}	0.739	1.09×10^{-3}
8-14	0.422	1.56×10^{-3}	0.786	85	0.58	1.22×10^{-3}	0.792	1.54×10^{-3}
8-21	0.361	7.56×10^{-4}	0.865	1193	0.28	7.27×10^{-4}	0.866	7.56×10^{-4}
8-73	0.415	1.42×10^{-3}	0.70	150	0.50	4.87×10^{-3}	0.775	1.42×10^{-3}
9-35	0.616	4.50×10^{-3}	0.860	10.5	1.40	9.05×10^{-2}	0.951	4.11×10^{-3}
9-36	0.541	2.94×10^{-3}	0.750	29.5	0.95	2.64×10^{-2}	0.776	2.86×10^{-3}
9-39	0.486	2.54×10^{-3}	0.815	76	0.78	1.09×10^{-2}	0.826	2.50×10^{-3}
9-40	0.438	1.83×10^{-3}	0.800	159	0.64	5.06×10^{-3}	0.805	1.82×10^{-3}
9-34	0.402	1.59×10^{-3}	0.850	422	0.56	1.95×10^{-3}	0.850	1.59×10^{-3}
9-12	0.444	1.85×10^{-3}	0.800	145	0.62	6.56×10^{-3}	0.806	1.84×10^{-3}
9-8	0.440	1.94×10^{-3}	0.730	95	0.65	7.72×10^{-3}	0.738	1.94×10^{-3}
8-64	0.440	2.01×10^{-3}	0.895	113	0.71	7.64×10^{-3}	0.867	1.99×10^{-3}
9-13	0.471	2.56×10^{-3}	0.745	100	0.64	7.54×10^{-3}	0.753	2.54×10^{-3}
8-42	0.423	1.90×10^{-3}	0.695	160.5	1.17	6.74×10^{-3}	0.692	1.79×10^{-3}
8-58	0.401	2.01×10^{-3}	0.697	82	0.62	1.70×10^{-2}	0.712	1.98×10^{-3}
8-66	0.479	2.50×10^{-3}	0.790	60	0.94	1.34×10^{-2}	0.803	2.50×10^{-3}
8-63	0.489	3.11×10^{-3}	0.833	58	0.79	1.46×10^{-2}	0.845	3.10×10^{-3}
8-65	0.504	3.02×10^{-3}	0.843	23	1.20	1.82×10^{-2}	0.878	3.01×10^{-3}
8-51	0.529	3.64×10^{-3}	0.675	29	0.90	2.41×10^{-2}	0.699	3.64×10^{-3}
8-67	0.500	3.01×10^{-3}	0.700	24	0.79	3.75×10^{-2}	0.748	3.01×10^{-3}
8-52	0.500	3.11×10^{-3}	0.662	24	0.94	2.88×10^{-2}	0.691	3.11×10^{-3}
8-49	0.476	1.90×10^{-3}	0.715	97	0.72	6.31×10^{-3}	0.723	1.88×10^{-3}
8-55	0.460	4.01×10^{-3}	0.675	11	1.15	6.75×10^{-3}	0.743	4.01×10^{-3}
8-56	0.460	3.69×10^{-3}	0.624	13.0	1.18	5.89×10^{-3}	0.693	3.69×10^{-3}
8-57	0.460	4.01×10^{-3}	0.715	14	1.18	6.42×10^{-3}	0.834	4.01×10^{-3}
8-59	0.460	4.01×10^{-3}	0.715	12	0.96	6.45×10^{-3}	0.760	4.01×10^{-3}
8-18	0.460	6.01×10^{-3}	0.695	4.0	1.89	1.17×10^{-2}	0.911	6.01×10^{-3}
8-4	0.460	8.01×10^{-3}	0.715	7.0	1.49	1.22×10^{-2}	0.912	8.01×10^{-3}
8-19	0.500	4.00×10^{-3}	0.693	8.4	0.78	6.82×10^{-3}	0.741	4.44×10^{-3}
8-19	0.500	6.00×10^{-3}	0.693	7	1.48	1.33×10^{-2}	0.933	6.00×10^{-3}
8-53	0.500	6.00×10^{-3}	0.693	15	0.48	8.25×10^{-3}	0.768	6.00×10^{-3}
8-53	0.500	6.00×10^{-3}	0.693	15	0.20	1.48×10^{-2}	0.963	6.00×10^{-3}
8-53	0.500	1.00×10^{-3}	0.693	15	1.17	7.25×10^{-3}	0.888	1.00×10^{-3}
8-53	0.500	4.00×10^{-3}	0.693	15	1.18	1.11×10^{-2}	1.020	4.00×10^{-3}
8-53	0.500	4.00×10^{-3}	0.693	15	1.18	5.93×10^{-3}	0.964	1.78×10^{-3}
8-53	0.500	4.00×10^{-3}	0.693	15	1.18	1.67×10^{-3}	0.717	4.00×10^{-3}

400 MPa

TABLE B.4.1

Test results for individual specimens and load versus time for 400 MPa

test no.	n	m	$A (/m)$	ϵ_o (%)	$\dot{\epsilon} (/m)$ m fitted	$\dot{\epsilon}$ (%) m fitted	$\log(\frac{m_{fit}}{m_{act}})$	$\frac{m_{fit}-m_{act}}{m_{act}}$
8-29	7.18×10^{-4}	0.776	8.47×10^{-4}	0.21	8.14×10^{-6}	1.97	-0.82	-0.14
9-53	1.78×10^{-3}	0.777	1.15×10^{-3}	0.37	2.22×10^{-5}	2.20	+0.29	0.20
9-48	2.80×10^{-4}	0.775	6.16×10^{-4}	0.05	2.87×10^{-6}	1.70	-0.11	0.06
8-22	2.14×10^{-2}	0.796	2.61×10^{-3}	0.92	3.25×10^{-4}	2.73	+0.09	0.25
8-26	3.50×10^{-3}	0.779	1.44×10^{-3}	0.51	4.66×10^{-5}	2.38	+0.05	0.27
8-34	1.3×10^{-3}	0.777	1.42×10^{-3}	0.53	4.51×10^{-5}	2.54	-0.51	0.23
8-31	3.7×10^{-4}	0.776	3.97×10^{-4}	0.24	3.36×10^{-5}	2.01	+0.47	0.51
8-37	2.9×10^{-3}	0.778	1.75×10^{-3}	0.57	3.79×10^{-5}	2.34	-0.38	0.02
8-35	0.32×10^{-2}	0.763	3.99×10^{-3}	1.32	1.38×10^{-3}	2.71	+0.01	-0.15
8-36	2.02×10^{-3}	0.705	3.39×10^{-3}	1.39	1.55×10^{-3}	2.75	+0.02	-0.04
8-37	1.7×10^{-2}	0.737	2.7×10^{-3}	0.77	1.70×10^{-4}	2.65	+0.03	-0.07
8-37	1.6×10^{-3}	0.773	1.59×10^{-3}	0.57	5.39×10^{-5}	2.47	-0.30	-0.05
8-34	2.1×10^{-3}	0.777	1.23×10^{-3}	0.41	2.79×10^{-5}	2.27	+0.12	-0.11
8-32	5.23×10^{-3}	0.793	1.74×10^{-3}	0.59	7.23×10^{-5}	2.29	-0.01	-0.02
8-34	4.3×10^{-3}	0.779	1.55×10^{-3}	0.55	5.98×10^{-5}	2.43	-0.27	-0.02
8-64	5.3×10^{-3}	0.780	1.66×10^{-3}	0.60	7.44×10^{-5}	2.33	-0.09	0.02
9-13	8.8×10^{-3}	0.784	1.96×10^{-3}	0.71	1.27×10^{-4}	2.60	+0.02	-0.12
8-42	2.21×10^{-2}	0.797	2.64×10^{-3}	0.93	3.36×10^{-4}	2.71	-0.39	-0.22
8-58	1.06×10^{-2}	0.786	2.08×10^{-3}	0.75	1.95×10^{-4}	2.61	-0.22	0.04
8-66	1.02×10^{-2}	0.785	2.06×10^{-3}	0.74	1.49×10^{-4}	2.63	-0.18	-0.11
8-54	1.23×10^{-2}	0.787	2.18×10^{-3}	0.78	1.82×10^{-4}	2.65	+0.11	-0.08
8-53	1.60×10^{-2}	0.791	2.38×10^{-3}	0.85	2.40×10^{-4}	2.69	-0.40	-0.23
8-51	2.45×10^{-2}	0.799	2.72×10^{-3}	0.95	3.74×10^{-4}	2.76	-0.14	-0.11
8-65	2.70×10^{-2}	0.802	2.80×10^{-3}	0.99	4.11×10^{-4}	2.76	-0.43	-0.23
8-52	3.97×10^{-2}	0.815	3.14×10^{-3}	1.08	6.07×10^{-4}	2.77	-0.04	-0.01
8-43	1.39×10^{-2}	0.789	2.27×10^{-3}	0.81	2.06×10^{-4}	2.68	+0.18	-0.1
8-50	4.36×10^{-2}	0.819	3.24×10^{-3}	1.11	6.66×10^{-4}	2.77	-0.26	-0.11
8-56	6.19×10^{-2}	0.837	3.58×10^{-3}	1.23	9.37×10^{-4}	2.76	-0.14	-0.09
8-67	6.28×10^{-2}	0.838	3.60×10^{-3}	1.21	9.52×10^{-4}	2.75	-0.11	-0.1
8-69	3.28×10^{-2}	0.808	2.98×10^{-3}	1.03	5.02×10^{-4}	2.78	-0.08	-0.02
8-48	1.53×10^{-1}	0.928	4.44×10^{-3}	1.48	2.14×10^{-3}	2.81	-0.27	-0.12
8-47	6.87×10^{-2}	0.844	3.69×10^{-3}	1.23	1.04×10^{-3}	2.76	-0.28	-0.09
8-39	7.29×10^{-2}	0.848	3.75×10^{-3}	1.25	1.10×10^{-3}	2.74	-0.27	-0.09
8-19	6.57×10^{-2}	0.841	3.64×10^{-3}	1.22	9.92×10^{-4}	2.75	-0.36	-0.18
8-31	6.97×10^{-2}	0.845	3.70×10^{-3}	1.24	1.05×10^{-3}	2.76	+0.03	-0.03
8-63	7.18×10^{-2}	0.847	3.73×10^{-3}	1.25	1.08×10^{-3}	2.74	-0.33	-0.12
8-57	9.72×10^{-2}	0.872	4.03×10^{-3}	1.34	1.43×10^{-3}	2.72	-0.13	-0.08
8-70	1.32×10^{-1}	0.907	4.31×10^{-3}	1.43	1.88×10^{-3}	2.64	+0.06	-0.17
8-40	6.67×10^{-2}	0.842	3.66×10^{-3}	1.23	1.01×10^{-3}	2.75	-0.11	-0.07
9-1	1.41×10^{-1}	0.916	4.37×10^{-3}	1.45	2.00×10^{-3}	2.64	-0.25	-0.1
Avg.							-0.12	-0.07

Table B.4.2 Summary of Assur - Tine model parameters using creep data from 8 tests only for 40% S₁ MFS

test no.	$\frac{1}{\sigma_1}$	ϵ_0 at $t=t_{lm}$	m_0	σ_0 at $t=t_{lm}$	ϵ_0 at break	ϵ_0 at break	ϵ_0 at break	ϵ_0 at break	ϵ_0 at break	m_{O_2}	t_m
		(/m)		(%)	(%)	(/m)	(/m)	(/m)	(/m)		(m)
S8-45	0.227	4.93×10^{-4}	0.51	0.26	0.93	6.70×10^{-5}	50	0.75	2330		
S8-30	0.259	8.09×10^{-4}	0.44	0.40	1.00	2.21×10^{-4}	19	0.73	900		
S8-28	0.243	-	-	-	-	-	-	0.80	2195		
S8-46	0.271	1.13×10^{-3}	0.55	0.38	1.25	1.74×10^{-4}	30	0.71	970		
S8-76	0.230	5.47×10^{-4}	0.44	0.29	1.18	9.78×10^{-5}	50	0.77	3200		
S8-2	0.227	4.06×10^{-4}	0.55	0.39	1.10	2.84×10^{-5}	126	0.75	3800		
S8-58	0.275	7.64×10^{-4}	0.44	0.23	1.11	2.4×10^{-4}	20	0.67	884		
S8-59	0.318	1.69×10^{-3}	0.39	0.50	0.98	9.24×10^{-4}	4.7	0.59	120		
S9-1	0.278	1.07×10^{-3}	0.44	0.31	1.00	3.25×10^{-4}	15	0.67	465		
S9-31	0.258	4.93×10^{-4}	0.34	0.27	0.93	1.61×10^{-4}	27	0.73	1290		
S9-45	0.227	5.80×10^{-4}	0.51	0.31	1.17	2.60×10^{-4}	22	0.77	1140		
S9-53	0.310	1.77×10^{-3}	0.20	0.48	1.9	1.08×10^{-3}	12	0.77	165		
S9-39	0.242	4.25×10^{-4}	0.33	0.38	1.10	1.08×10^{-5}	62	0.82	3100		
S9-137	0.207	3.01×10^{-4}	0.53	0.31	1.05	1.34×10^{-3}	-	0.71	10000		
S9-42	0.316	1.73×10^{-3}	0.24	0.60	1.08	1.19×10^{-3}	4.8	0.69	225		
S8-80	0.389	3.19×10^{-3}	0.39	0.60	1.60	1.76×10^{-4}	5.5	0.50	52		
S9-64	0.346	2.33×10^{-3}	0.19	0.62	0.84	1.87×10^{-3}	3.2	0.59	110		
S9-126	0.303	8.98×10^{-4}	0.29	0.43	1.06	4.81×10^{-4}	8.6	0.59	283		
S8-68	0.374	-	-	0.68	-	-	-	0.77	45		
S9-102	0.346	1.73×10^{-3}	0.23	0.60	1.24	1.12×10^{-3}	6.5	0.35	75		
S9-41	0.376	-	0.34	-	-	-	-	0.34	60		
S9-10	0.415	-	0.37	0.73	-	-	-	0.37	17		
S9-114	0.379	4.40×10^{-3}	0.17	0.88	2.0	3.49×10^{-3}	3.9	0.60	30		
S9-134	0.322	9.08×10^{-4}	0.29	0.48	1.38	3.94×10^{-4}	17.8	0.51	165		
S9-138	0.421	-	0.27	0.91	-	-	-	0.27	17		
S8-79	0.443	-	-	1.26	-	-	-	-	14		
S9-135	0.369	-	0.31	0.50	-	-	-	0.31	42		
S9-136	0.426	-	-	0.90	-	-	-	-	13		

$\sigma_{ult} = 10.1 \pm 1.5$ (MPa)

TABLE B.4.3

Summary of modified model parameters for individual constant load creep tests for
100A Si MPS creep data

test no.	($=m_0$) m_1	($=C_0$) A_1 (/m)	(from C-M) ϵ_{Δ} (/m)	β	m_2	A_2 (/m)
S8-45	0.51	4.93×10^{-4}	6.70×10^{-5}	3.29×10^{-4}	0.766	1.32×10^{-3}
S8-30	0.44	8.09×10^{-4}	2.21×10^{-4}	8.29×10^{-4}	0.746	1.96×10^{-3}
S8-28	-	-	-	-	-	-
S8-46	0.55	1.13×10^{-3}	1.74×10^{-4}	7.55×10^{-4}	0.733	2.06×10^{-3}
S8-76	0.44	5.47×10^{-4}	9.78×10^{-5}	2.44×10^{-4}	0.782	2.06×10^{-3}
S8-2	0.55	4.06×10^{-4}	2.84×10^{-5}	2.04×10^{-4}	0.776	1.18×10^{-3}
S8-58	0.44	7.64×10^{-4}	2.04×10^{-4}	7.75×10^{-5}	0.686	1.57×10^{-3}
S8-59	0.39	1.69×10^{-3}	9.24×10^{-4}	5.12×10^{-3}	0.614	2.33×10^{-3}
S9-1	0.44	1.07×10^{-3}	3.25×10^{-4}	1.49×10^{-3}	0.692	2.07×10^{-3}
S9-31	0.34	4.93×10^{-4}	1.61×10^{-4}	5.78×10^{-4}	0.746	1.85×10^{-3}
S9-45	0.26	5.80×10^{-4}	2.60×10^{-4}	6.89×10^{-4}	0.785	2.90×10^{-3}
S9-53	0.20	1.77×10^{-3}	1.08×10^{-3}	5.03×10^{-3}	0.830	8.00×10^{-3}
S9-39	0.33	4.25×10^{-4}	1.09×10^{-4}	2.70×10^{-4}	0.837	3.39×10^{-3}
S9-137	0.53	3.01×10^{-4}	1.34×10^{-5}	7.36×10^{-5}	0.736	9.84×10^{-4}
S9-42	0.24	1.73×10^{-3}	1.19×10^{-3}	3.13×10^{-3}	0.705	3.54×10^{-3}
S8-80	0.35	3.10×10^{-4}	1.76×10^{-4}	1.09×10^{-2}	0.560	4.31×10^{-4}
S9-64	0.19	2.33×10^{-3}	1.87×10^{-3}	5.52×10^{-3}	0.608	3.73×10^{-3}
S9-126	0.29	8.98×10^{-4}	4.81×10^{-4}	2.15×10^{-3}	0.608	1.75×10^{-3}
S8-68	-	-	-	-	-	-
S9-102	0.23	1.73×10^{-3}	1.12×10^{-3}	5.11×10^{-3}	0.383	2.22×10^{-3}
S9-41	-	-	-	-	-	-
S9-10	-	-	-	-	-	-
S9-114	0.17	4.40×10^{-3}	3.49×10^{-3}	2.30×10^{-2}	0.690	8.16×10^{-3}
S9-134	0.29	9.08×10^{-4}	3.94×10^{-4}	3.46×10^{-3}	0.572	1.92×10^{-3}
S9-138	-	-	-	-	-	-
S8-79	-	-	-	-	-	-
S9-135	-	-	-	-	-	-
S9-136	-	-	-	-	-	-

TABLE B.4.4

Summary of modified model parameters for saturated MFS

test no.	t_0 (s)	$(A_1)_{\infty}$ (m)	m_0	t_A (m)	$\dot{\epsilon}_A$ (/m)	m_0	β	m_2	A_2	t_m (m)	$\dot{\epsilon}_m$ (/m)	t_m (s)	Predictions	
													$\log \frac{\epsilon_{mf}^{\text{mact}}}{\epsilon_{mf}^{\text{fit}}}$	$\frac{\epsilon_{mf}^{\text{mact}}}{\epsilon_{mf}^{\text{fit}}}$
S8-45	0.17	4.41x10 ⁻⁴	0.47	149	4.20x10 ⁻⁵	0.749	2.24x10 ⁻⁴	0.782	2.04x10 ⁻³	3491	7.56x10 ⁻⁶	3.83	0.21	0.64
S8-30	0.29	7.36x10 ⁻⁴	0.43	44	1.45x10 ⁻⁴	0.705	6.57x10 ⁻⁴	0.734	2.26x10 ⁻³	1117	2.73x10 ⁻⁵	5.48	0.06	0.31
S8-28	0.23	5.74x10 ⁻⁴	0.45	78	8.08x10 ⁻⁵	0.727	3.91x10 ⁻⁴	0.758	2.13x10 ⁻³	1938	1.46x10 ⁻⁵	5.24	0.28	0.21
S8-46	0.33	8.77x10 ⁻⁴	0.42	30	2.10x10 ⁻⁴	0.689	9.50x10 ⁻⁴	0.717	2.34x10 ⁻³	755	4.14x10 ⁻⁶	5.54	0.24	0.14
S8-76	0.18	4.64x10 ⁻⁴	0.47	131	4.69x10 ⁻⁵	0.745	2.50x10 ⁻⁴	0.778	2.01x10 ⁻³	3117	8.38x10 ⁻⁶	4.95	0.19	0.03
S8-2	0.17	4.41x10 ⁻⁴	0.47	149	4.20x10 ⁻⁵	0.749	2.24x10 ⁻⁴	0.782	2.04x10 ⁻³	3491	7.56x10 ⁻⁶	4.98	0.43	0.66
S8-58	0.35	9.28x10 ⁻⁴	0.41	26.6	2.42x10 ⁻⁴	0.683	1.07x10 ⁻³	0.712	2.43x10 ⁻³	665	4.84x10 ⁻⁵	5.66	0.29	0.23
S8-59	0.50	1.63x10 ⁻³	0.36	8.9	7.42x10 ⁻⁴	0.624	3.46x10 ⁻³	0.655	3.01x10 ⁻³	190	1.87x10 ⁻⁴	5.82	0.05	0.50
S9-1	0.36	9.68x10 ⁻⁴	0.41	24	2.63x10 ⁻⁴	0.679	1.17x10 ⁻³	0.707	2.42x10 ⁻³	606	5.30x10 ⁻⁵	5.62	0.11	0.31
S9-31	0.28	7.25x10 ⁻⁴	0.43	46	1.40x10 ⁻⁴	0.707	6.37x10 ⁻⁴	0.736	2.27x10 ⁻³	1155	2.64x10 ⁻⁵	5.49	0.11	0.19
S9-45	0.29	7.47x10 ⁻⁴	0.43	43	1.48x10 ⁻⁴	0.704	6.79x10 ⁻⁴	0.733	2.27x10 ⁻³	1080	2.82x10 ⁻⁵	5.48	0.13	0.12
S9-53	0.47	1.48x10 ⁻³	0.37	10.6	6.18x10 ⁻⁴	0.635	2.82x10 ⁻³	0.665	2.88x10 ⁻³	236	1.48x10 ⁻⁴	5.83	-0.10	-0.12
S9-39	0.23	5.65x10 ⁻⁴	0.45	8.1	2.20x10 ⁻⁴	0.728	3.64x10 ⁻⁴	0.731	1.01x10 ⁻³	2008	8.08x10 ⁻⁶	4.07	0.08	-0.13
S9-137	0.10	3.08x10 ⁻³	0.49	375	1.69x10 ⁻⁴	0.776	1.05x10 ⁻³	0.816	2.04x10 ⁻³	7747	3.09x10 ⁻⁶	4.57	0.39	0.58
S9-42	0.50	1.63x10 ⁻³	0.36	8.9	7.42x10 ⁻⁴	0.624	3.46x10 ⁻³	0.655	3.01x10 ⁻³	190	1.87x10 ⁻⁴	5.82	0.16	0.21
S8-80	0.75	3.53x10 ⁻³	0.28	2.7	2.67x10 ⁻³	0.528	1.69x10 ⁻²	0.574	4.52x10 ⁻³	34.0	1.06x10 ⁻³	5.36	0.20	-0.03
S9-64	0.60	2.26x10 ⁻³	0.33	5.1	1.32x10 ⁻³	0.586	6.79x10 ⁻³	0.621	3.51x10 ⁻³	91	3.95x10 ⁻⁴	5.74	0.16	0.19
S9-136	0.45	1.35x10 ⁻³	0.38	12.5	5.17x10 ⁻³	0.645	2.34x10 ⁻²	0.674	2.76x10 ⁻³	288	1.19x10 ⁻⁴	5.78	0.09	0.17
S8-68	0.70	3.06x10 ⁻³	0.30	3.3	2.14x10 ⁻³	0.548	1.26x10 ⁻²	0.589	4.15x10 ⁻³	46.7	7.77x10 ⁻⁴	5.50	-0.15	0.11
S9-102	0.60	2.26x10 ⁻³	0.33	5.1	1.32x10 ⁻³	0.586	6.79x10 ⁻³	0.621	3.51x10 ⁻³	91.4	3.95x10 ⁻⁴	5.73	0.04	0.15
S9-41	0.71	3.12x10 ⁻³	0.30	3.2	2.20x10 ⁻³	0.586	6.64x10 ⁻³	0.607	4.37x10 ⁻³	44.6	5.86x10 ⁻⁴	4.91	-0.04	-0.15
S9-10	0.85	4.58x10 ⁻³	0.25	2.0	3.85x10 ⁻³	0.491	2.89x10 ⁻²	0.549	5.32x10 ⁻³	19.0	1.83x10 ⁻³	4.97	0.03	0.10
S9-114	0.72	3.22x10 ⁻³	0.29	3.1	2.32x10 ⁻³	0.541	1.40x10 ⁻²	0.584	4.30x10 ⁻³	41.6	8.73x10 ⁻⁴	5.47	-0.19	-0.17
S9-134	0.52	1.71x10 ⁻³	0.36	8.1	8.05x10 ⁻⁴	0.619	3.82x10 ⁻³	0.650	3.04x10 ⁻³	170	2.07x10 ⁻³	5.78	0.13	0.35
S9-138	0.87	4.84x10 ⁻³	0.25	1.9	4.12x10 ⁻³	0.483	3.25x10 ⁻²	0.545	5.50x10 ⁻³	16.8	2.04x10 ⁻³	4.85	0.14	0.31
S8-79	0.95	5.90x10 ⁻³	0.221	1.6	5.32x10 ⁻³	0.453	4.92x10 ⁻²	0.532	6.31x10 ⁻³	10.8	3.03x10 ⁻³	4.47	0.10	-0.11
S9-135	0.59	2.90x10 ⁻³	0.306	3.5	1.98x10 ⁻³	0.554	1.13x10 ⁻²	0.594	4.00x10 ⁻³	52.4	6.89x10 ⁻⁴	5.55	0.04	0.49
S9-136	0.89	5.07x10 ⁻³	0.240	1.8	4.40x10 ⁻³	0.476	3.57x10 ⁻²	0.541	5.67x10 ⁻³	15.1	2.24x10 ⁻³	4.79	0.15	0.46

TABLE B.4.5

Summary of modified model parameters using creep data from
10 tests only for saturated MFS

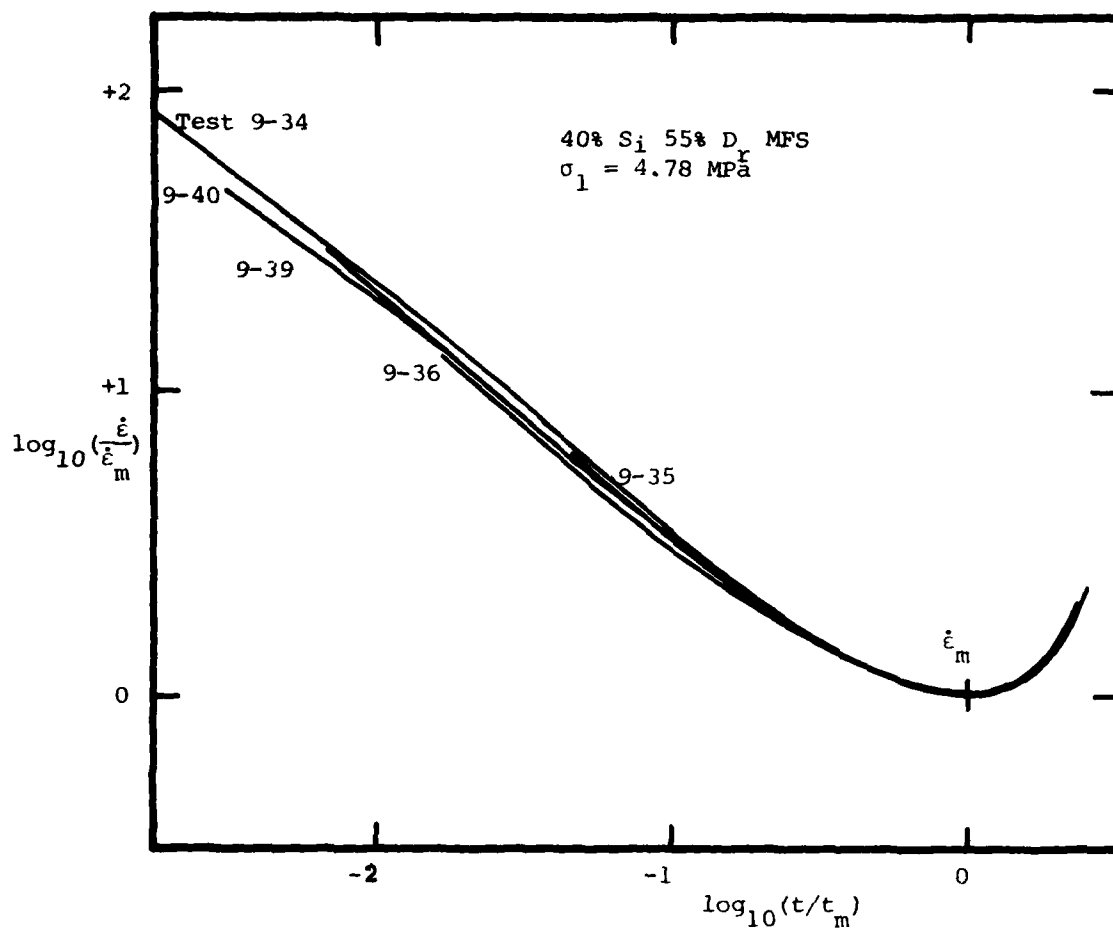


FIGURE B.4.1 Typical normalized creep curves for 40% Si 55% D_r MFS

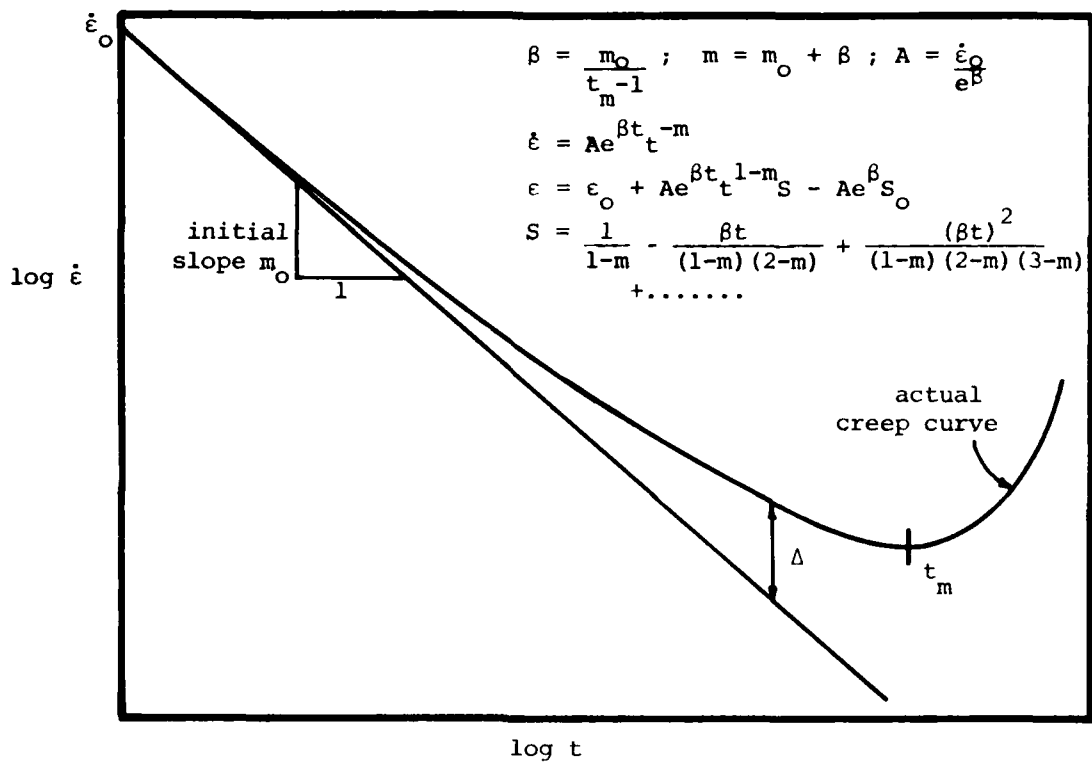


FIGURE B.4.2 Proposed determination of parameters for Assur-Ting model

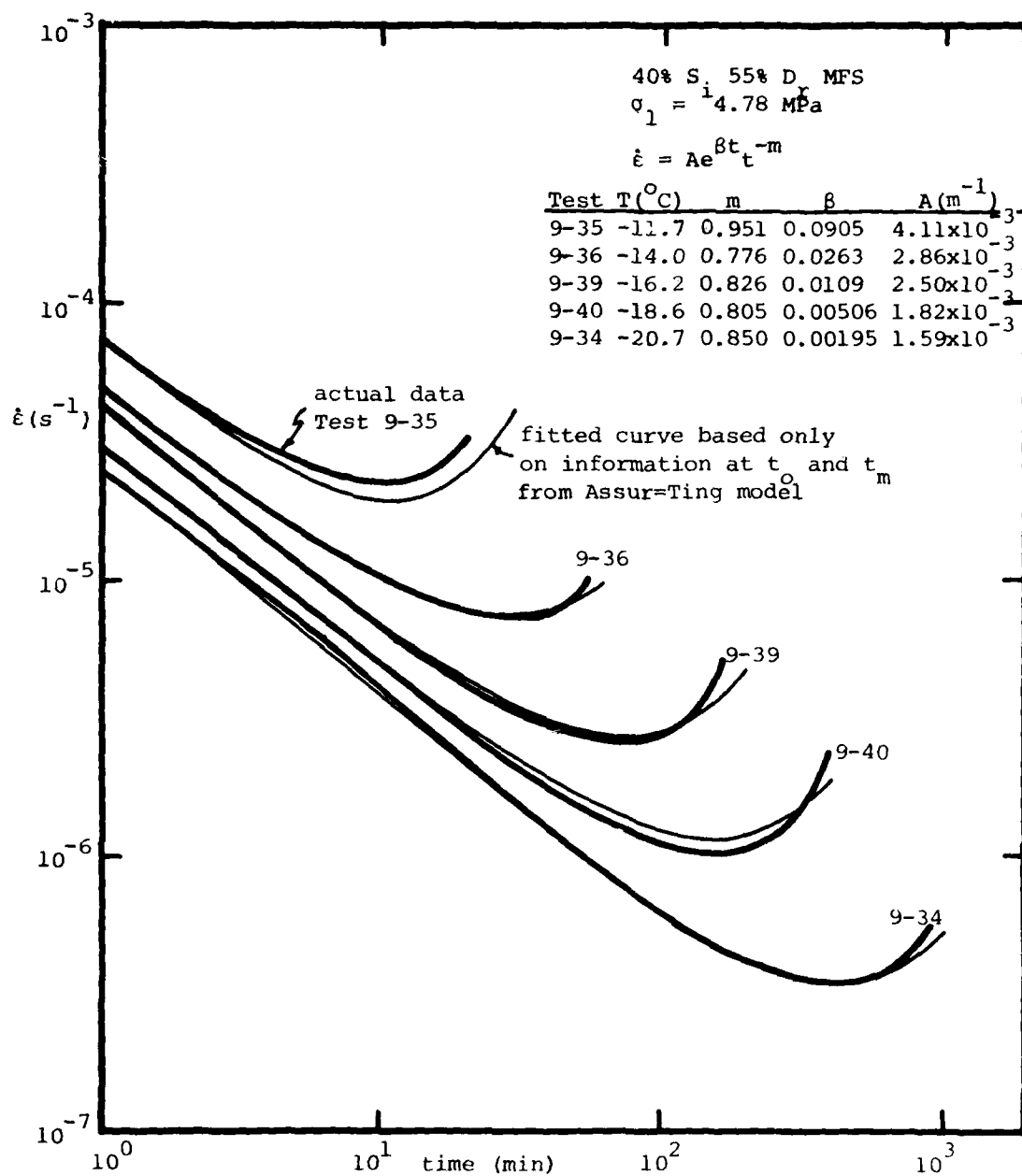


FIGURE B.4.3 Comparison of actual and fitted creep curves for 40% S_i 55% D_r MFS data at $\sigma_1 = 4.8 \text{ MPa}$ from Assur-Ting model

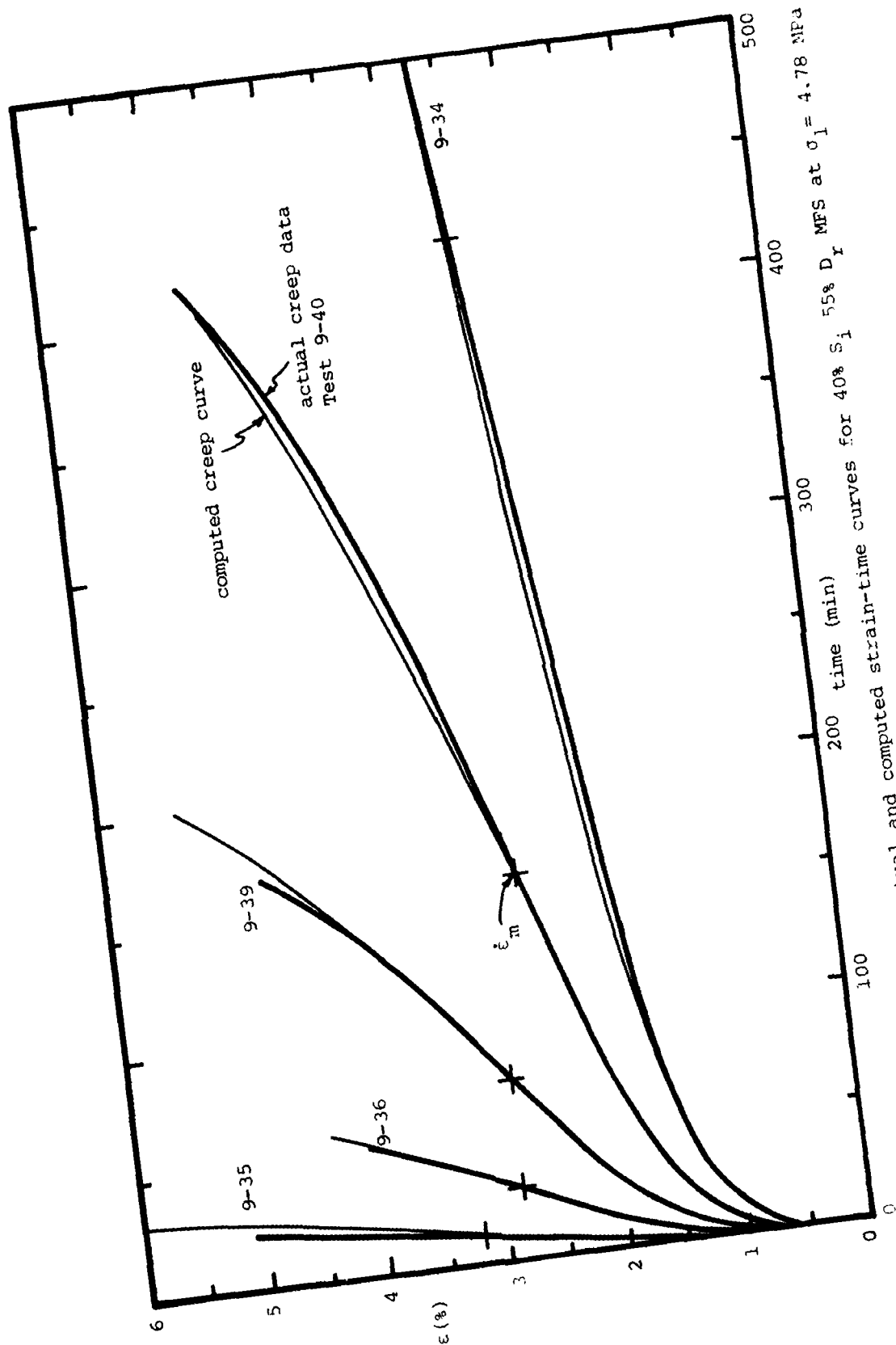


FIGURE B.4.4 Comparison of actual and computed strain-time curves for 40% Si 55% D_r MFS at $\sigma_1 = 4.78$ MPa

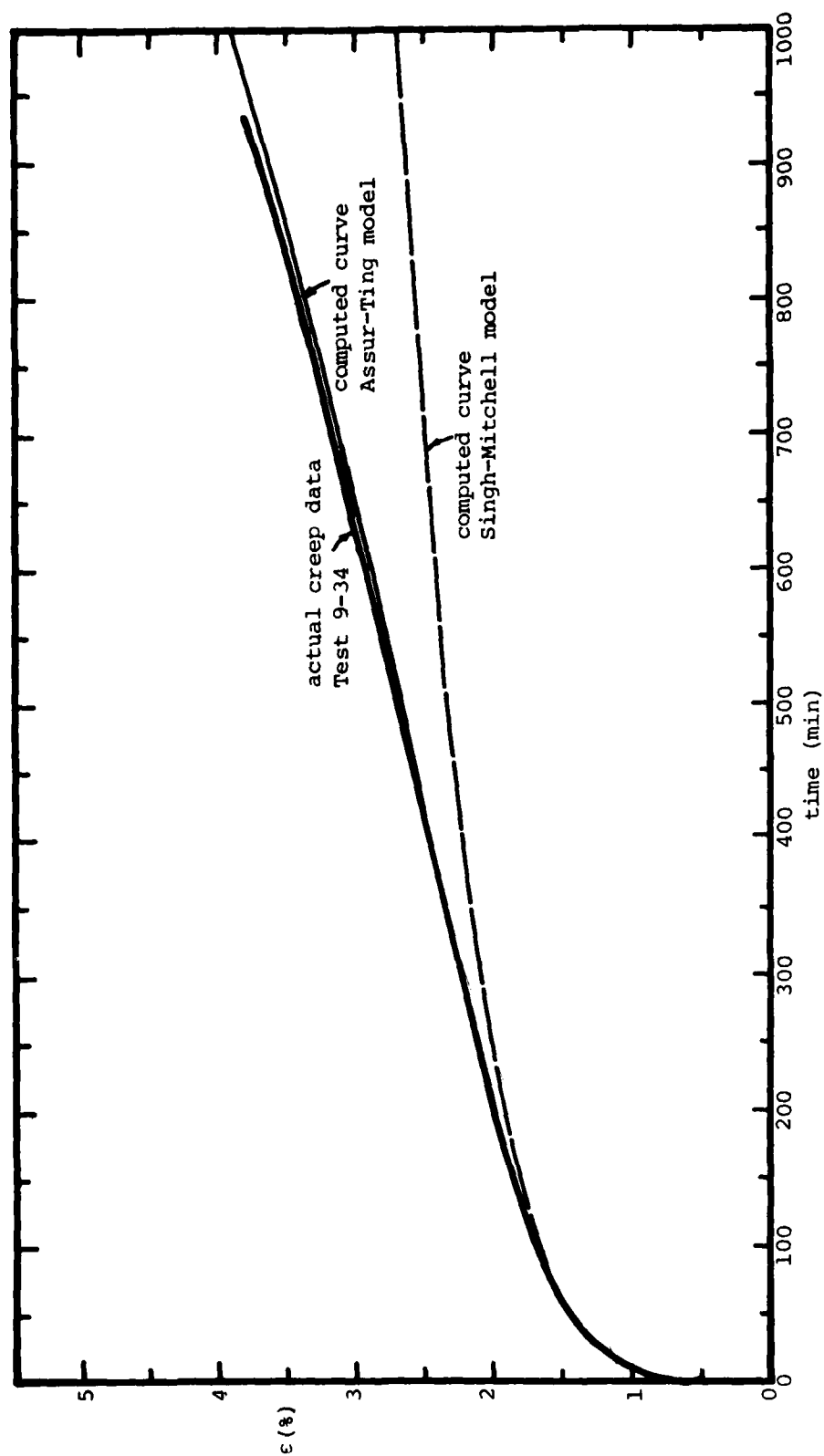


FIGURE B.4.5 Comparison of actual, Singh-Mitchell and Assur-Ting creep curves

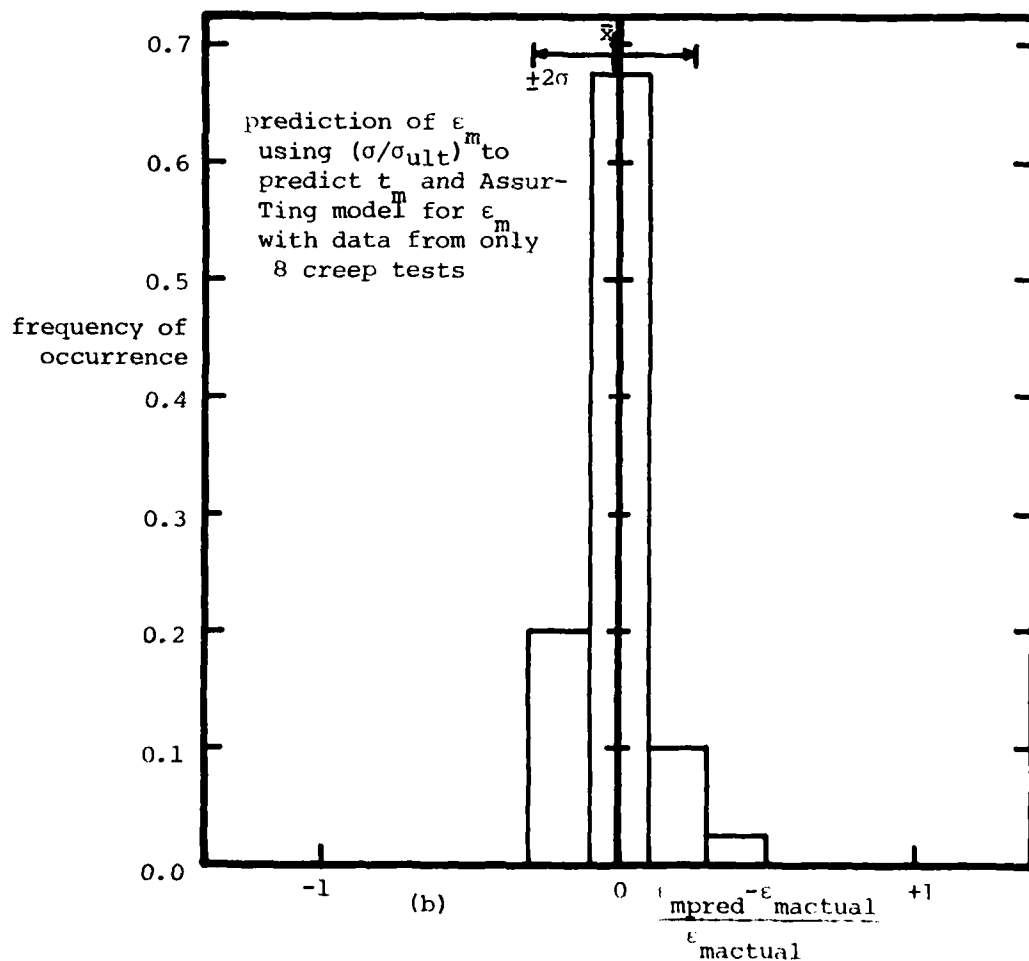
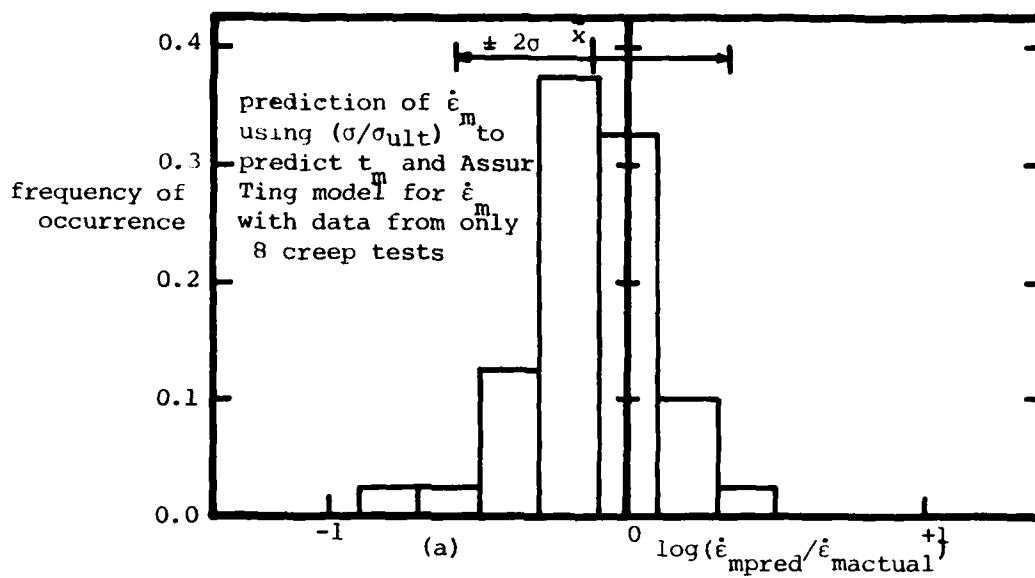


FIGURE B.4.6 Comparison of predicted and actual $\dot{\epsilon}_m$ and ϵ_m using Assuring Model for 40% S_i 55% D_r MFS using data from 8 creep tests

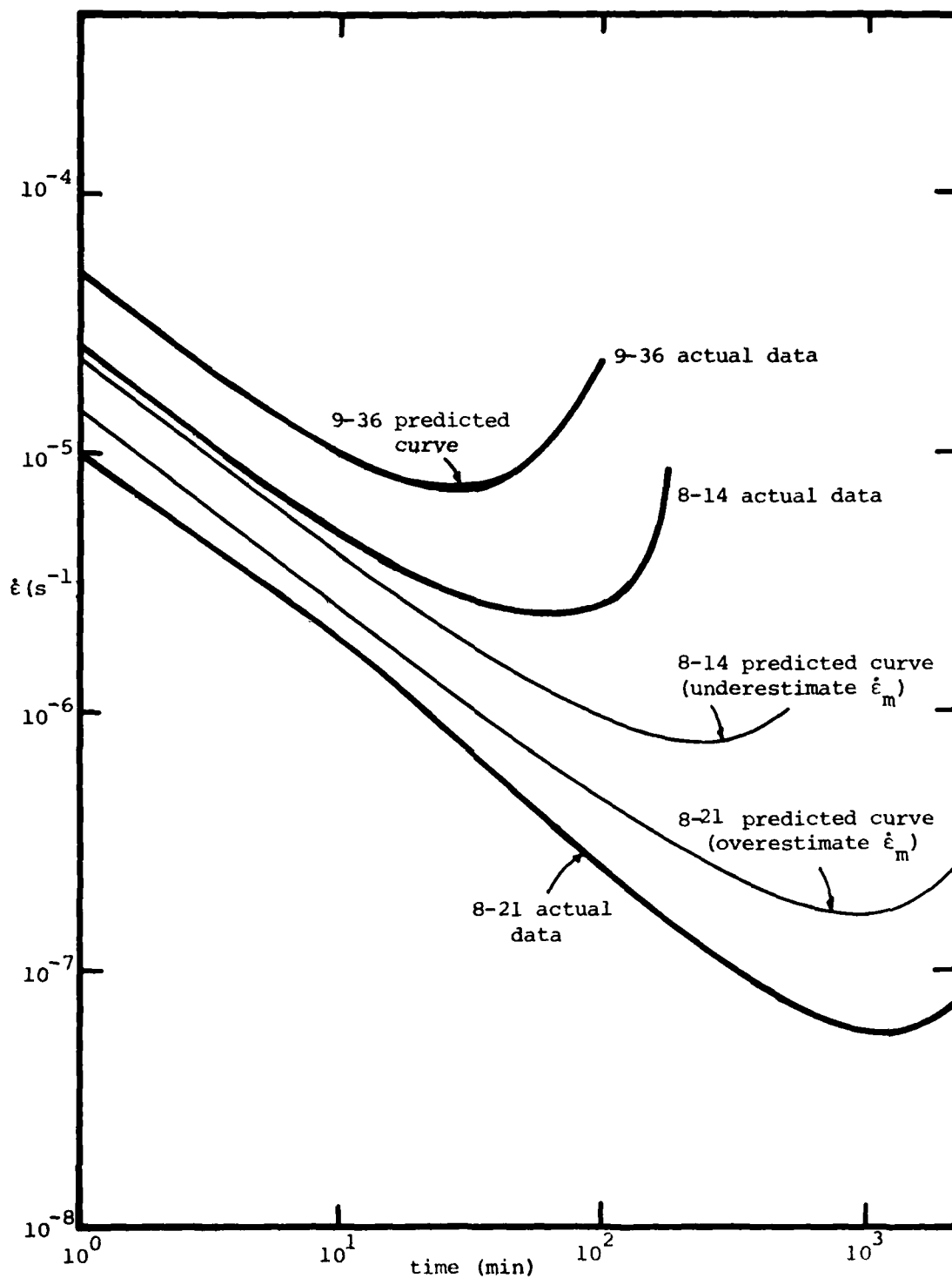


FIGURE B.4.7 Comparison of $\log \dot{\epsilon} - \log t$ curves from Assur-Ting model predictions and actual data

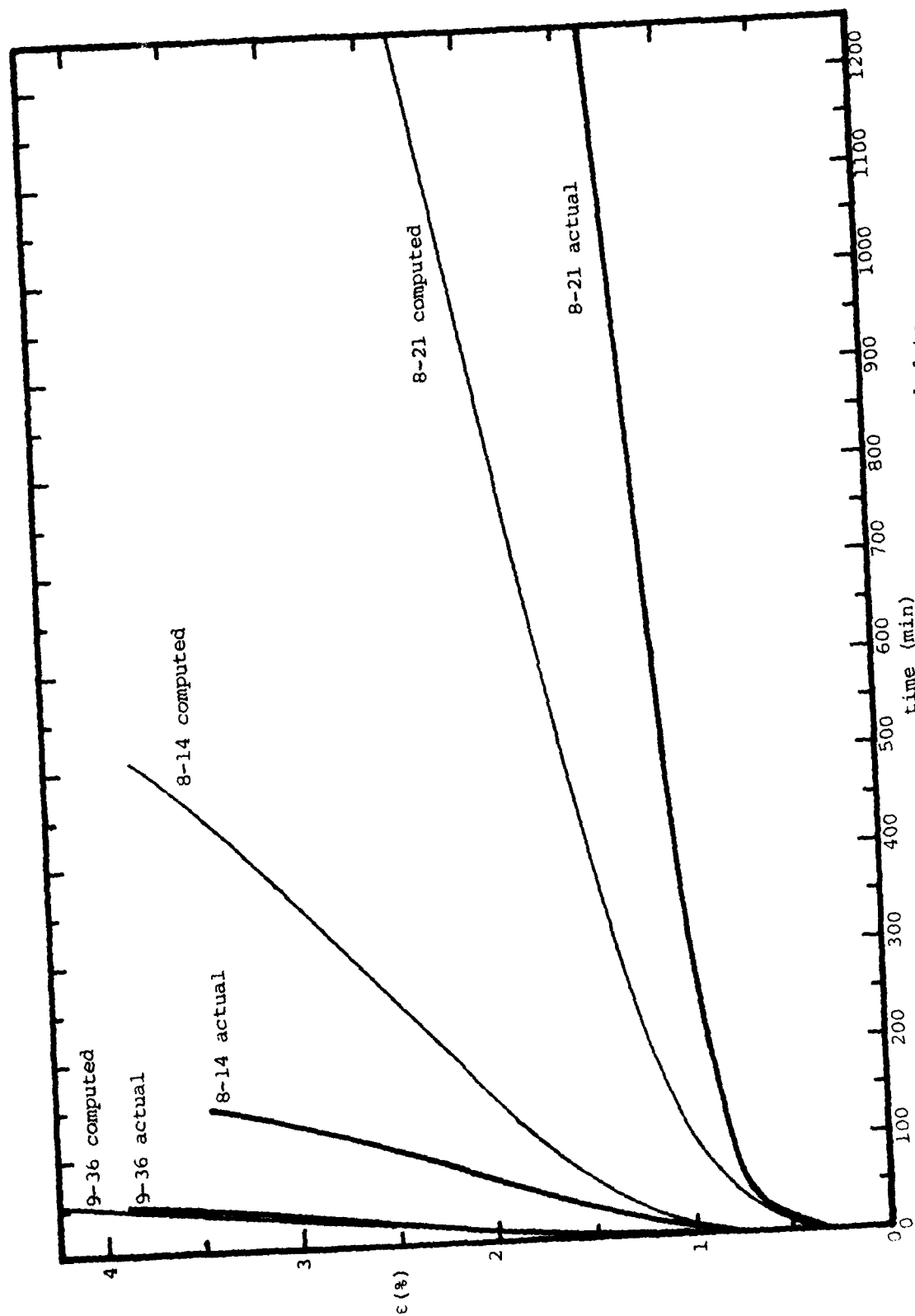


FIGURE B.4.8 Comparison of strain-time curves from predictions and actual data

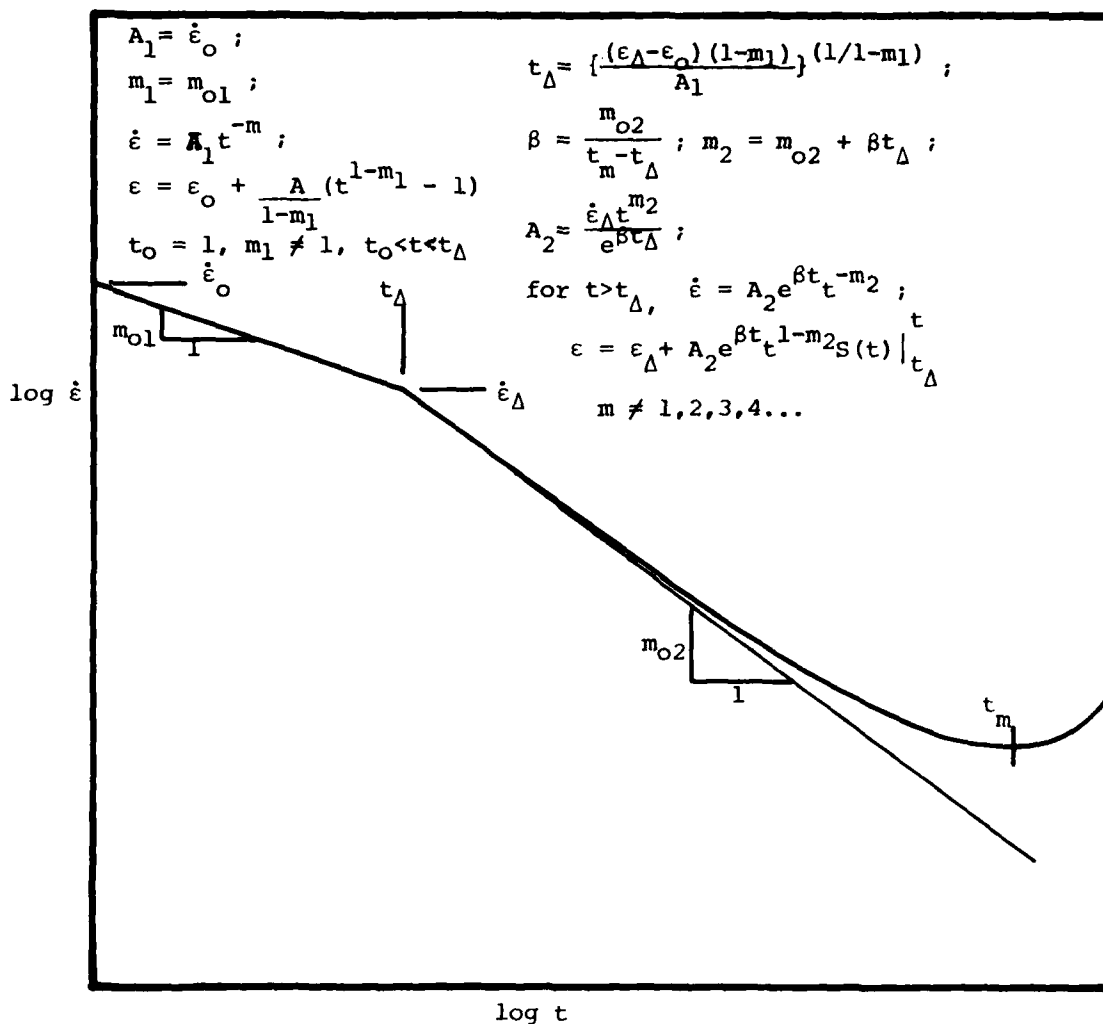


FIGURE B.4.9 Determination of parameters for modified creep model for saturated frozen MFS

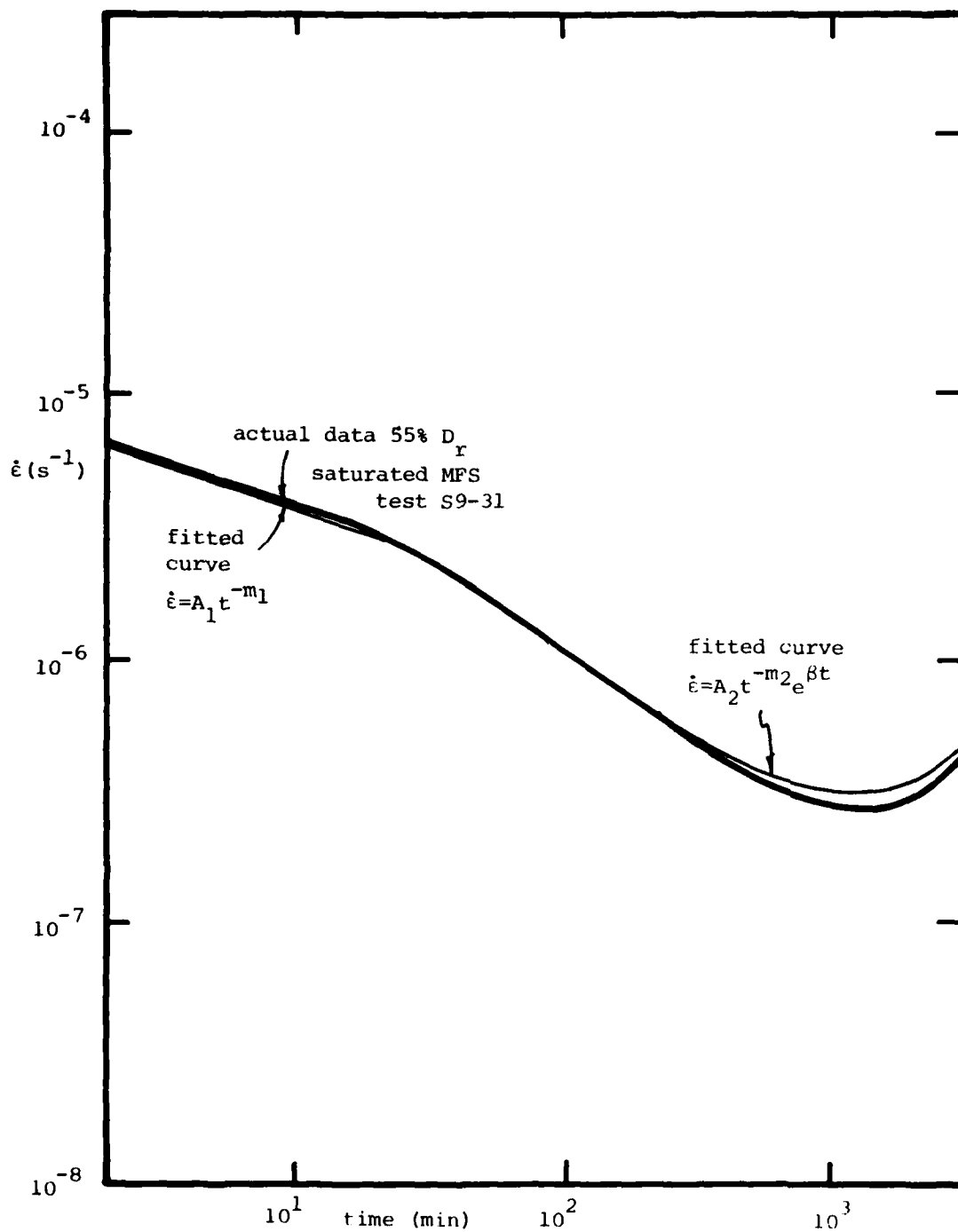


FIGURE B.4.10 Comparison of modified creep model and actual data for saturated Manchester Fine Sand

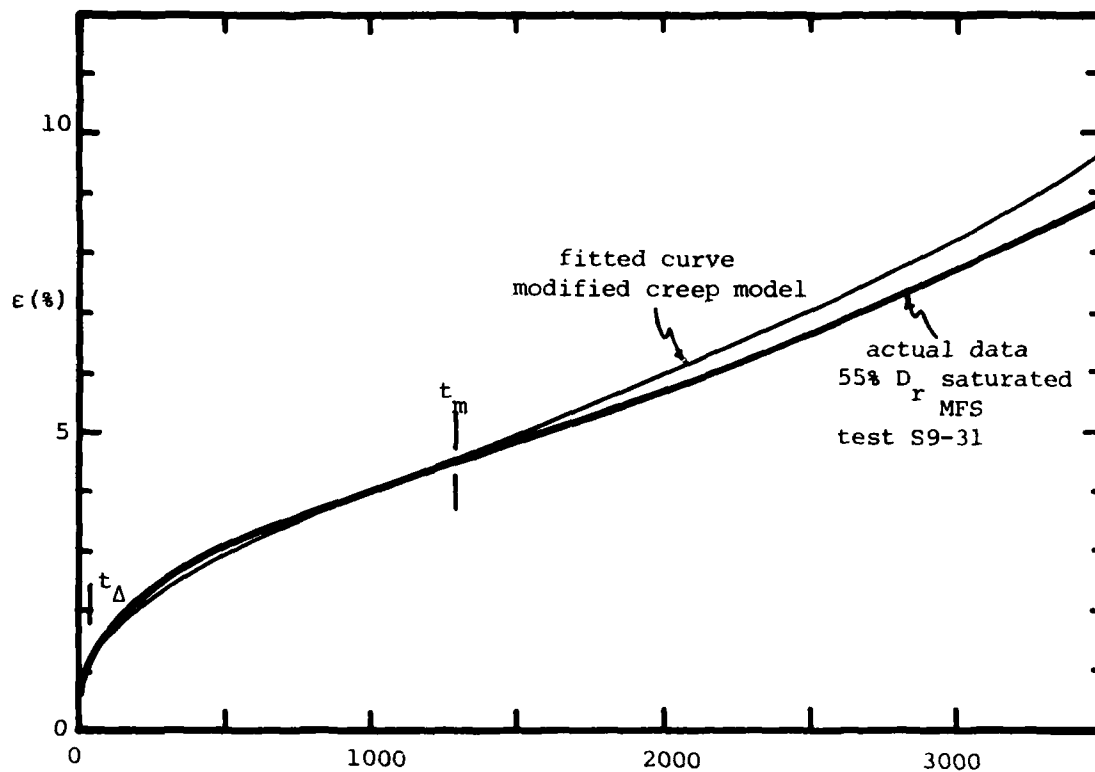


FIGURE B.4.11 Comparison of strain-time curve from modified creep model with actual test for saturated MFS

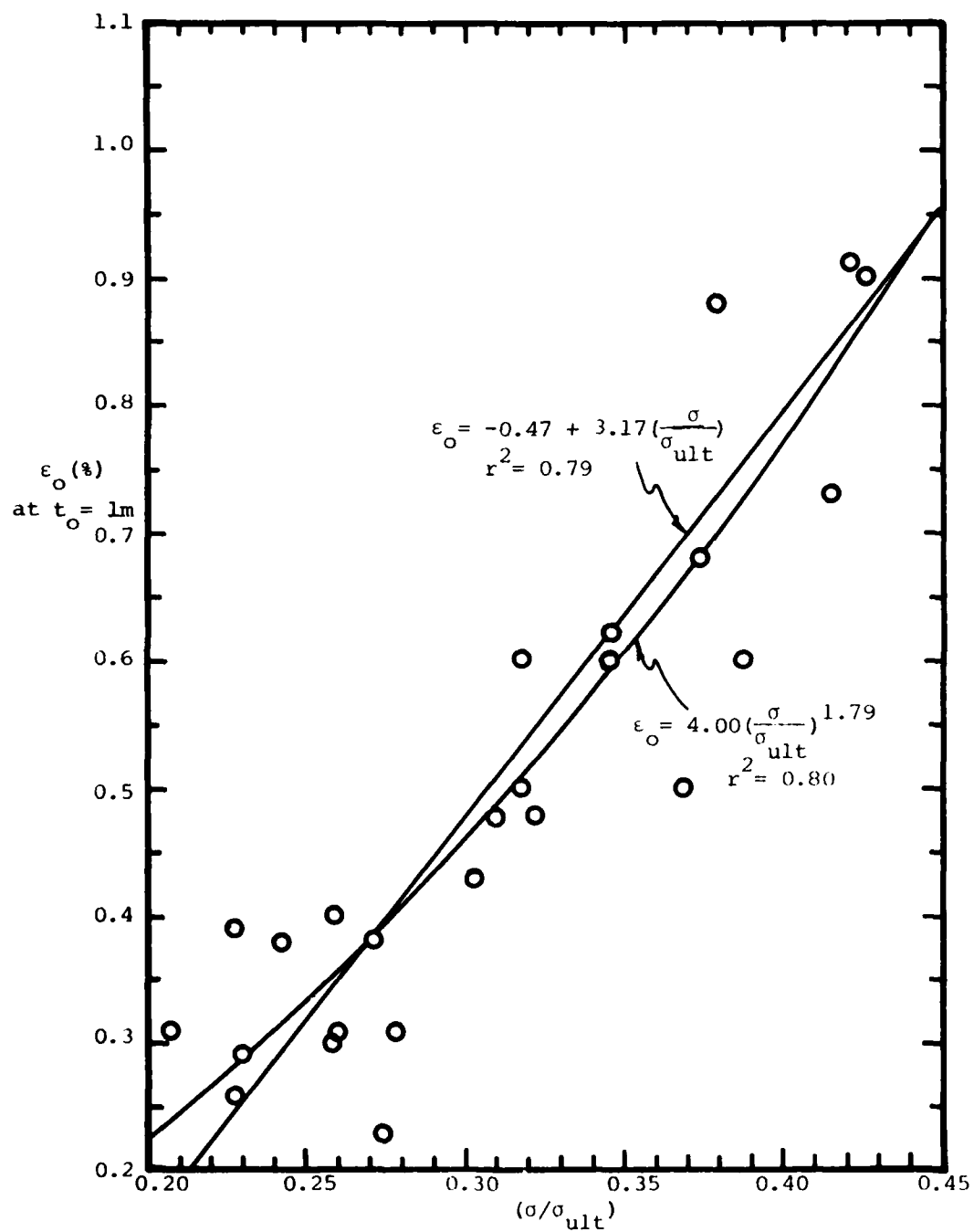


FIGURE B.4.12 Correlations between ϵ_0 and (σ/σ_{ult})

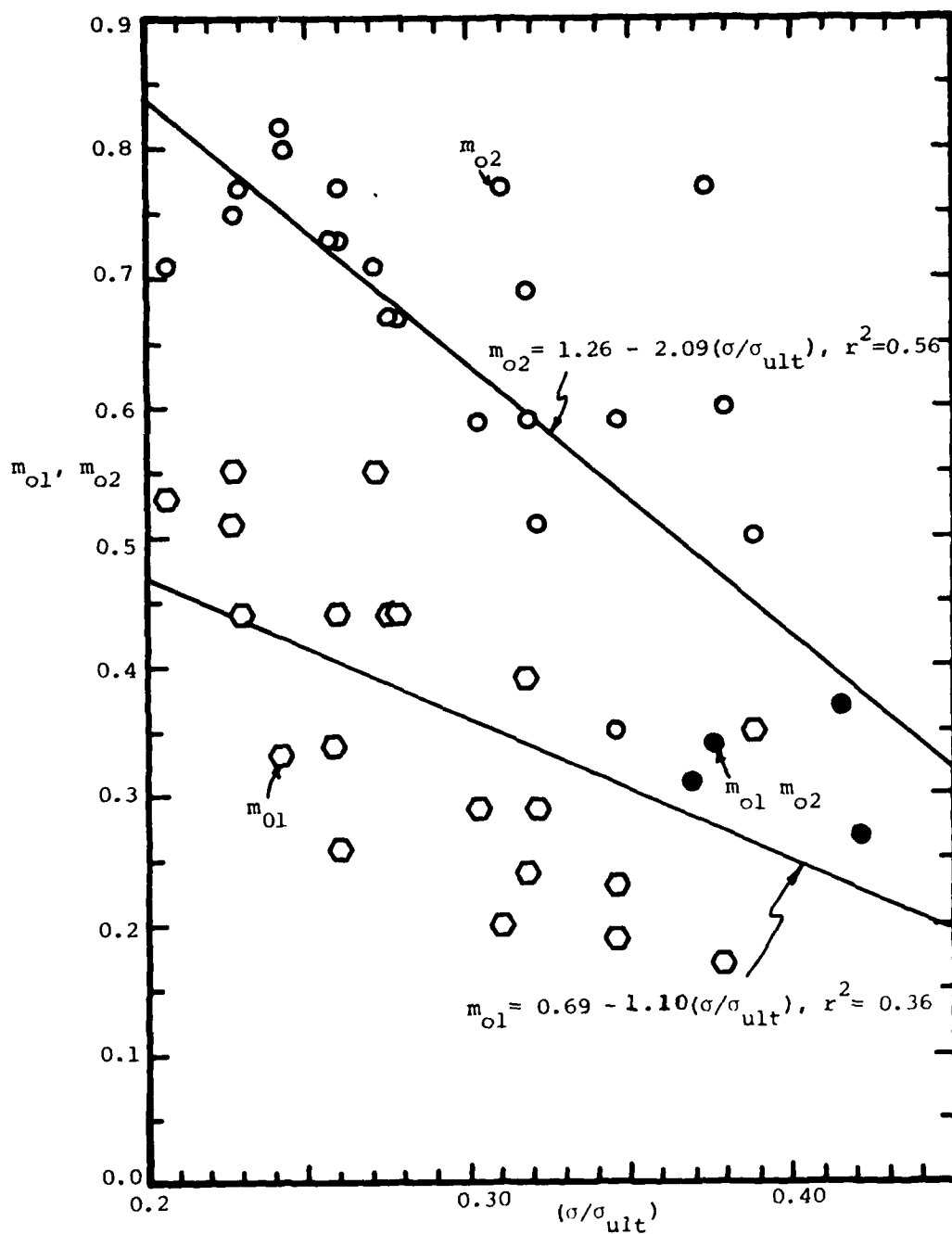


FIGURE B.4.13 Correlations between slopes of $\log \dot{\epsilon} - \log t$ curves for saturated MFS and stress ratio

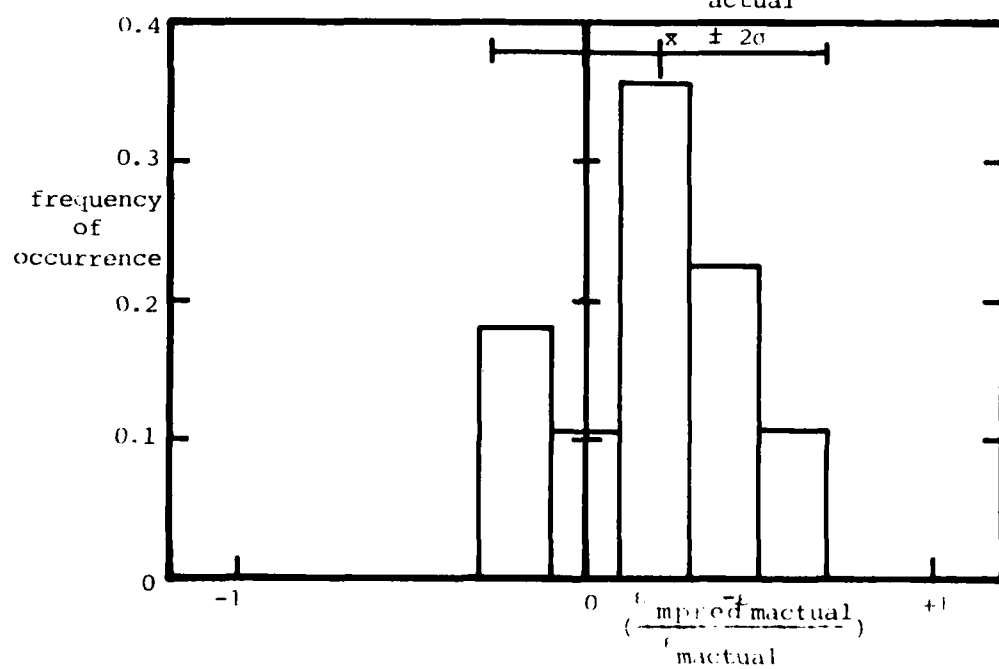
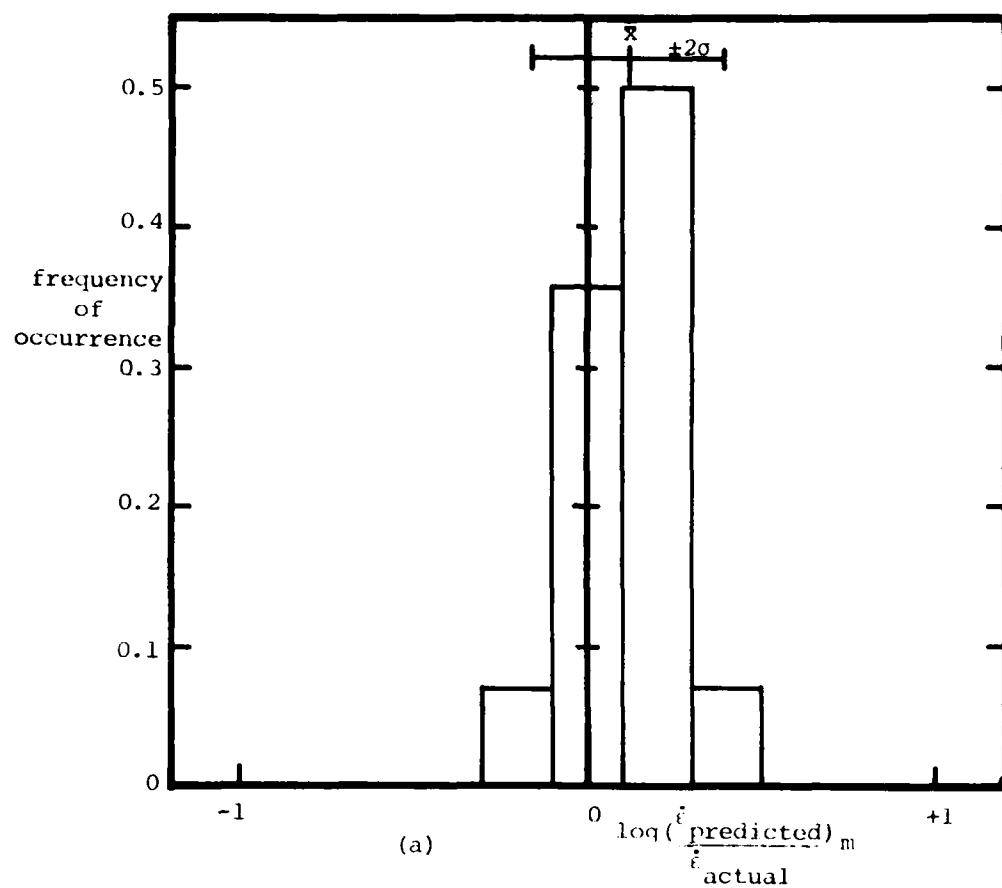


FIGURE B.4.14 Comparison of predicted and actual $\dot{\epsilon}_m$ and ϵ_m using modified creep model for saturated MPS using 10 tests to predict others.

LIST OF REFERENCES

Reference Code:

- ASCE JEMD - American Society of Civil Engineers, Journal of
the Engineering Mechanics Division
- ASCE JGED - American Society of Civil Engineers, Journal of
the Geotechnical Engineering Division
- ASCE JSMFD - American Society of Civil Engineers, Journal of
the Soil Mechanics and Foundations Division
- CGJ - Canadian Geotechnical Journal
- ICSMFE - International Conference on Soil Mechanics and Foun-
ation Engineering
- 1st ICP - 1st Permafrost Conference, Lafayette, U.S.A. 1963.
- 2nd ICP - 2nd International Conference on Permafrost, Yakutsk,
U.S.S.R. 1973.
- 3rd ICP - 3rd International Conference on Permafrost, Edmonton,
Canada 1978.
- Physics of Snow and Ice - Proceedings of the International
Conference on Low Temperature Science, Sapporo,
Japan 1966, edited by H. Oura, 1967.
- Physics of Ice - from the the International Symposium on the
Physics of Ice, Munich 1968, edited by N. Riehl,
B. Bullemer and H. Engelhardt, Plenum Press,
N.Y. 1969.
- Physics and Chemistry of Ice - from the International Symposium
on the Physics and Chemistry of ice, Ottawa,
Canada 1972, edited by E. Whalley, S.J. Jones
and L.W. Gold, Royal Society of Canada 1973.
- USA CRREL - U.S. Army Cold Regions Research and Engineering
Laboratory, Hanover, N.H.
- USA SIPRE - U.S. Army Snow, Ice and Permafrost Research Estab-
lishment, Wilmette, Ill.

REFERENCES - ICE

* literature cited in text

- Ackley, S.F. 1973. Microhardness testing of ice single crystals, Physics and Chemistry of Ice:382-386.
- Ahlborn, G.H. and H.C. Poehlman 1976. Development of a hydrophobic substance to mitigate pavement ice adhesion, EPA Report 600/2-76-242, Cincinnati, Ohio.
- * Andrade, E.N. da C.1910. The viscous flow in metals and allied phenomena, Proc. Royal Society of London A84:1-12.
- * Assur, A. 1979. Some promising trends in ice mechanics, Proc. IUTAM Symposium, Copenhagen.
- Assur, A. 1960. Composition of sea ice and its tensile strength, USA SIPRE RR44.
- Babel, H.W. 1966. Biaxial fracture strength of brittle materials, Air Force Materials Laboratory, Wright-Patterson Air Force Base, TR66-51.
- * Baker, R.W. 1978. The influence of ice-crystal size on creep, J. Glac. 21(85):485-500.
- * Barnes, P., D. Tabor, and J. Walker 1971. The friction and creep of polycrystalline ice, Proc. Royal Society of London A324: 127-155.
- Bascom, W.D., R.L. Cottingham, C.R. Singleterry and R.L. Jones 1966. The adhesion of ice to hydrophobic surfaces, Naval Research Laboratory Report 6350, Washington, D.C.
- * Bromer, D.J. and W.D. Kingery 1968. Flow of polycrystalline ice at low stress and small strains, J. Applied Physics 39: 1688-1691.
- Butkovich, T.R. 1959. Some physical properties of ice from the TUTO tunnel and ramp, Thule, Greenland, USA SIPRE RR47.
- Butkovich, T.R. 1954. Ultimate strength of Ice, USA SIPRE RR11.
- * Butkovich, T.R. and J.K. Landauer 1960. Creep of ice at low stresses, USA SIPRE RR#72, Wilmette, Ill.
- Butkovich, T.R. and J.K. Landauer 1959. The flow law for ice, USA SIPRE RR#56, Wilmette, Ill.
- * Carter, D. and B. Michel 1971. Lois et mecanismes de l'apparente fracture fragile de la glace de riviere et de lac, Rapport S-22, Dept. Genie Civil, Universite Laval, Quebec.
- Colbeck, S.C. and R.J. Evans 1973. A flow law for temperate glacier ice, J. Glac. 12:71-86.
- Cole, D.M. 1979. Preparation of polycrystalline ice specimens for laboratory experiments, Cold Regions Science and Technology 1:153-159.
- * Conway, J.B. 1967. "Numerical methods for creep and rupture analysis", Gordon and Breach, New York, 204 pages.
- * Corte, A.E. 1962. Vertical migration of particles in front of a moving freezing plane, J. Geophysical Research 67(3): 1085-1090 (also USA CRREL RR105, 1963).
- Corte, A.E. 1961. The frost behavior of soils: laboratory and field data for a new concept pt. 1: vertical sorting, USA CRREL RR85

- Edwards, G.R. and L.F. Evans 1962. Effect of surface charge on ice nucleation by silver iodide, *Trans. Faraday Society* 58:1649-1695.
- * Edwards, G.R., L.F. Evans and A.F. Zipper 1970. Two dimensional phase changes in water adsorbed on ice-nucleating substrates, *Trans. Faraday Society* 66:220-234.
- * Eyring, H. 1936. Viscosity, plasticity and diffusion as examples of absolute reaction rates, *J. Chem. Physics* 4(4):283-291.
- Fournier d'Albe, E.M. 1949. Some experiments on the condensation of water vapour at temperatures below 0 C, *Quarterly J. Royal Meteorological Society* 75:1-14.
- Frankenstein, G. 1969. Ring tensile studies of ice, USA CRREL TR172
- * Frederking, R. 1977. Plane strain compressive strength of columnar grained and granular-snow ice, *J. Glac.* 18(80):503-516.
- * Freudenthal, A.M. 1950. "The inelastic behavior of engineering materials and structures", J.Wiley and Sons, Inc., N.Y., 587 pages.
- Fukuta, N. 1966. Activation of atmospheric particles as ice nuclei in cold and dry air, *J. Atmospheric Sciences* 23:741-752.
- Glen, J.W. 1975. The mechanics of ice, USA CRREL Monograph II-C2b
- Glen, J.W. 1974. The physics of ice, USA CRREL Monograph II-C2a.
- * Glen, J.W. 1955. The creep of polycrystalline ice, *Proc. Royal Society of London* A228:519-538.
- Glen, J.W. and S.J. Sowers 1966. The deformation of ice single crystals at low temperatures, *Physics of Snow and Ice*, pt. 1:267-275.
- * Gold, L.W. 1977. Engineering properties of freshwater ice, *J. Glac.* 19(81):197-211.
- * Gold, L.W. 1973. Activation energy for creep of columnar-grained ice, *Physics and Chemistry of Ice* :362-364.
- * Gold, L.W. 1972. The process of failure of columnar grained ice, *Philosophical Magazine 8th Series* 26(2):311-328.
- * Gold, L.W. 1970. Process of failure in ice, *CGJ* 7(4):405-413.
- * Gold, L.W. 1966(a). Time to formation of first cracks in ice, *Physics of Snow and Ice*:359-370.
- * Gold, L.W. 1966(b). Dependence of crack formation on crystallographic orientation of ice, *C.J. Physics* 44:2757-2764.
- Gold, L.W. 1965. The initial creep of columnar-grained ice, *C.J. Physics* 43:1414-1434.
- * Gold, L.W. 1962. Deformation mechanisms in ice, "Ice and Snow", from *Proceedings, Conference on Ice and Snow*, M.I.T., Cambridge, Mass., ed. W.D. Kingery :8-27.
- Gold, L.W. 1958. Some observations on the dependence of strain on stress for ice, *Canadian J. of Physics* 36(10):1265-1275.
- * Gold, L.W. and A.S. Krausz 1971. Investigation of the mechanical properties of St. Lawrence R. ice, *CGJ* 8(23):163-169.

- * Goodman, D.J. 1977. Creep and fracture of ice and surface strain measurements on glaciers and sea ice, Ph.D. thesis, U. of Cambridge; also quoted in discussion to Baker (1978).
- Griggs, D.T. and N.E. Coles 1954. Creep of single crystals of ice, USA SIPRE Rept.#11.
- Haefili, R., C. Jaccard and M. DeQuervain 1968. Deformation of polycrystalline ice under combined uniaxial and hydrostatic pressure. Int'l. Union of Geodesy and Geophysics, XIV General Assembly Publ. 79 de l'Assoc. Int'le d'Hydrologie Scientifique: 341-344.
- Hanley, T.O'D. and A.S. Krausz 1974. Thermally activated deformation. I. Method of analysis, J. Applied Physics 45(4): 2013-2015.
- * Hawkes, I. and M. Mellor 1972. Deformation and fracture of ice under uniaxial stress, J. Glaciology 11(61):103-131.
- * Haynes, F.D. 1978. Effect of temperature on the strength of snow-ice, USA CRREL Report 78-27.
- * Haynes, F.D. 1973. Tensile strength of ice under triaxial stresses, USA CRREL RR 312.
- * Haynes, F.D. unpublished. Effect of temperature and strain rate on the strength of polycrystalline ice, USA CRREL preliminary report, Jan. 1977.
- * Haynes, F.D. and M. Mellor 1977. Measuring the uniaxial compressive strength of ice, J. Glac. 19(81):213-222.
- Higashi, A. 1978. Structure and behaviour of grain boundaries in polycrystalline ice, J. Glac. 21(85):589-605.
- Higashi, A. 1969. Mechanical properties of ice single crystals, Physics of Ice:197-212.
- * Higashi, A. 1966. Mechanisms of plastic deformation in ice single crystals, Ref.I pt.1:277-289.
- Higuchi, K. and N. Fukuta 1966. Ice in the capillaries of solid particles and its effect on their nucleating ability, J. Atmospheric Sciences 23:187-190. Paper presented at the Int'l. Conf. on Cloud Physics, Tokyo 1965.
- Hobbs, P.V. 1974. "Ice Physics", Clarendon Press, Oxford.
- * Homer, D.R. and J.W. Glen 1978. The creep activation energies of ice, J. Glac. 21(85):429-444.
- * Hooke, R.LeB., B.B. Dahlin and M.T. Kauper 1972. "Creep of ice containing dispersed fine sand, J. Glac. 11(63):327-336.
- * Hooke, R.LeB., M. Mellor, S.J. Jones, R.T. Martin, M.F. Meier and J. Weertman unpubl. Mechanical properties of polycrystalline ice: an assessment of current knowledge and priorities for research, Report of the Int'l Committee of Snow and Ice/ N.S.F. working group on ice mechanics, Boulder, Colo., 1979.
- * Hosler, C.L., D.C. Jensen and L. Goldshlak 1957. On the aggregation of ice crystals to form snow, J. Meteorology 14: 415-420.
- * Jellinek, H.H.G. 1970. Ice adhesion and abhesion: a survey, in Proc. Int'l. Symp. on Snow removal and ice control research., NRC-HRB SR115:46-76.
- * Jellinek, H.H.G. 1967. Liquid-like (transition) layer on ice, J. Colloidal and Interface Science 25:192-205.

- * Jellinek, H.H.G. 1962. Ice adhesion, Cdn. J. Physics 40(10): 1294-1309.
- Jellinek, H.H.G. 1960(a). Some frictional properties of thin water films, USA SIPRE SR37.
- * Jellinek, H.H.G. 1960(b). Bonding of flat ice surfaces - some preliminary results, USA SIPRE RR61.
- * Jellinek, H.H.G. 1960(c). Adhesive properties of ice, pt. 2, USA SIPRE RR62.
- * Jellinek, H.H.G. 1957(a). Adhesive properties of ice, pt. 1, USA SIPRE RR38.
- * Jellinek, H.H.G. 1957(b). Tensile strength properties of ice adhering to stainless steel, USA SIPRE RR23.
- Jones, J.R. and M.N. Gardos 1969. Adhesive shear strength of ice to bonded solid lubricants, Proc. 15th Symp. of Aerospace and Process Engineers :1021-1029.
- * Jones, S.J. 1978. Triaxial testing of polycrystalline ice, Proc. 3rd ICP:671-674.
- Jones, S.J. and J.W. Glen 1969(a). The mechanical properties of single crystals of pure ice, J. Glac. 8(54):463-473.
- * Jones, S.J. and J.W. Glen 1969(b). The effect of dissolved impurities on the mechanical properties of ice crystals, Philophical Mag. 19:13-24.
- * Kovacs, A., F. Michitti and J. Kalafut 1977. Unconfined compression tests on snow, a comparative study, USA CRREL SR 77-20.
- * Kuo, S.S. 1972. Stress and time effect on the creep rate of polycrystalline ice, Ph.D. thesis, Michigan State Univ., Lansing Michigan.
- Kvajic, G., V. Brajovic and E.R. Pounder 1969. Rejection of impurities by growing ice from a melt, Physics and Chemistry of Ice :197-212.
- * Langdon, T.G. 1973. Creep mechanisms in ice, Physics and Chemistry of Ice :356-361.
- Law, K.T. 1977. Design of a loading platen for testing ice and frozen soil, CGJ 14:266-271.
- Lawrence, W.F. 1977. A structural theory for the deformation of snow, Ph.D. thesis, Montana State Univ., Bozeman, Montana.
- * Lile, R.C. 1979. Rheology of polycrystalline ice, Ph.D. thesis, Dept. of Meteorology, University of Melbourne, Melbourne.
- Martin, R.J. 1972. Time dependent crack growth in quartz and its application to the creep of rocks, J. Geophysical Research 77(8):1406-1419.
- McClintock, F.A. and J. Walsh 1962. Friction on Griffith cracks in rocks under pressure. Int'l. Congress Appl. Mechanics, Berkeley California.
- Mellor, M. 1979. Mechanical properties of polycrystalline ice, Proc. IUTAM Symposium, Copenhagen.
- Mellor, M. and I. Hawkes 1971. Measurement of tensile strength by diametral compression of discs and annuli, Engineering Geology Reprint 5:194-195.
- * Mellor, M. and J.H. Smith 1966(a). Creep of snow and ice, Physics of Snow and Ice Vol. 1 pt.2:843-855.

- * Mellor, M. and J.H. Smith 1966(b). Creep of snow and ice, USA CRREL RR 220.
- Mellor, M. and J.H. Smith 1966(c). Strength studies of snow, USA CRREL RR 168.
- * Mellor, M. and R. Testa 1969(a). Effect of temperature on the creep of ice, J. Glac. 8(52):131-145.
- * Mellor, M. and R. Testa 1969(b). Creep of ice under low stress, J. Glac. 8(52):147-152.
- Michel, B. 1966. From the nucleation of ice crystals in clouds to the formation of frazil ice in rivers, Physics of Snow and Ice pt. 1:129-136.
- * Michel, B. and R.O. Ramseier 1971. Classification of river and lake ice, CGJ 8:36-45.
- Muguruma, J. 1969. Effects of surface condidtions on the mechanical properties of ice crystals, Brit. J. of Appl. Physics Series 2, 2(11):1517-1525.
- * Nakamura, T. and S.J. Jones 1973. Mechanical properties of impure ice crystals, Physics and Chemistry of Ice:365-369.
- * Nakaya, U. and A. Matsumoto 1953. Evidence of the existence of a liquidlike film on ice surfaces, USA SIPRE RR4.
- * Nevel, D.E. and F.D. Haynes 1976. Interpretation of the tensile strength of ice under triaxial stresses, USA CRREL Report 76-5.
- Offenbacher, E.L., I.C. Roselman and D. Tabor 1973. Friction, deformation and recrystallization of single crystals of ice Ih under stress, Physics and Chemistry of Ice I:377-381.
- * Peyton, H.R. 1966. Sea ice strength, Geophysical Institute, U. of Alaska Report #NR 307-247/7-6-55.
- * Ramseier, R.O. 1971. Growth and mechanical properites of river and lake ice, PhD. thesis, Laval University, Quebec, Canada.
- Raraty, L.E. and D. Tabor 1958. The adhesion and strength properties of ice, Proc. Royal Society A245(241):184-201.
- * Roberts, P. and J. Hallet 1968. A laboratory study of the ice nucleating properties of some mineral particulates, Quarterly J. Royal Meteorological Society 94:25-34.
- Sayward, J.M. 1979(a). Seeking low ice adhesion, USA CRREL SR 79-11.
- Sayward, J.M. 1979(b). Small-scale testing of soils for frost action and water migration, USA CRREL SR 79-17.
- * Sherby, O.D. 1962. Factors affecting the high temperature strength of polycrystalline solids, Acta Metallurgica 10(2):135-147.
- * Shoji, H. and A. Higashi 1978. A deformation mechanism map of ice, J. Glac. 21(85):419-427.
- * Simonson, E.R., A.H. Jones and S.J. Jones 1975. High pressure mechanical properties of three frozen materials, Proc. 4th Int'l. Conf. on High Pressure, Kyoto, 1974:115-121.
- * Sinha, N.K. 1978. Short-term rheology of polycrystalline ice, J. Glac. 21(85):457-473.
- Taylor, G.I. 1938. Plastic strain in metals, J. Inst. Metals 62: 307-324.
- Tegart, W.J.M. 1964. Nonbasal slip as a major deformational

- process in the creep of polycrystalline ice, J. Glac. 5(38): 251-254.
- Tetelman, A.S. 1965. A review of the problem of fracture, ARO contract DA 31-124-ARO-D-251 Tech. Rept. #1, Defence Documentation Center, Cameron Sta., Alexandria, Virginia.
- * Ting, J.M. and R.T. Martin 1979. Application of the Andrade equation to creep data for ice and frozen soil, Cold Regions Science and Technology 1:29-36.
- Traetteberg, A., L.W. Gold and R. Frederking 1975. The strain rate and temperature dependence of Young's modulus of ice, Proc. 3rd Int'l Symposium on Ice Problems, Frankenstein, G.E. ed., Hanover, N.H. 1975:479-486.
- Vinson, T.S. and T. Chaichanavong 1978. Dynamic behavior of ice under cyclic axial loading, ASCE JGED 104(GT7):801-814.
- * Weeks, W.F. and A. Assur 1969. Fracture of lake and sea ice, USA CRREL RR#269.
- * Weertman, J. 1973. Creep of ice, Physics and Chemistry of Ice :320-337.
- * Whalley, E., J.B.R. Heath and D.W. Davidson 1968. Dielectric properties of ice VII. J. Chem. Physics 45(11):3976-3982.

REFERENCES - UNFROZEN SOIL AND PARTICULATE COMPOSITES

* literature cited in text

- Brace, W.F. 1963. Behavior of quartz during indentation, J. of Geology 71(5):581-595.
- Buyukozturk, O., A.H. Nilson and F.O. Slate 1971. Deformation and fracture of particulate composite, ASCE JEMD 98(EM3): 581-593.
- Campanella, R.G. and V.P. Vaid 1974. Triaxial and plane strain creep rupture of an undisturbed clay, CGJ 11(1):1-10.
- * Campanella, R.G. and V.P. Vaid 1972. Creep rupture of a saturated natural clay, Proc. 6th Int. Congress on Rheology, Soil Mechanics Series No. 16, University of British Columbia, Vancouver.
- Carino, N.J. and F.O. Slate 1976. Limiting tensile strain criterion for failure of concrete, American Concrete Institute Journal 73(March):160-165.
- Cundall, P.A. and O.D.L. Strack 1979. A discrete numerical model for granular assemblies, Geotechnique 29(1):47-65.
- Darwin, D. and F.O. Slate 1970. Effect of paste-aggregate bond strength on behavior of concrete, J. Materials 5(March): 86-98.
- Deresiewicz, H. 1958. Stress strain relations for a simple model of a granular medium, ASME J. Applied Mechanics 25: 402-406.
- DiMaggio, F.L. and I.S. Sandler 1971. Material model for granular soils, ASCE JEMD 97(EM3):935-949.
- Duffy, J. 1959. A differential stress-strain relation for the hexagonal close-packed array of elastic spheres, ASME J. Applied Mechanics 26(1):88-94.
- * Edgers, L., C.C. Ladd and J.T. Christian 1973. Undrained creep of Atchafalaya Levee foundation clays, Report R73-16, No. 319, Dept. of Civil Eng., M.I.T., Cambridge, Mass.
- * Hofmann, U. 1952. Neue erkenntnisse auf dem gebiete der thixotrophie insbesondere bei tonhaltigen gelen, Kolloid-Zeischrift 125(2):86-99.
- Horne, M.R. 1969. The behaviour of an assembly of rotund, rigid, cohesionless particles III. Proc. Royal Society of london A310:21-34.
- Horne, M.R. 1965. The behaviour of an assembly of rotund, rigid, cohesionless particles I and II, Proc. Royal Soc. of London A286:62-97.
- Hult, J.A.H. 1966. "Creep in engineering structures", Blaisdell Publ. Co., Waltham, Mass. 115 pages.
- * Ladd, C.C., R. Foott, K. Ishihara, H.G. Poulos and F. Schlosser 1977. Stress deformation and strength characteristics: State of the art report, Proceedings, IXth ICSMFE, Tokyo : 1-74.
- Lade, P.V. and J.M. Duncan 1975. Elastoplastic stress strain theory for cohesionless soil. ASCE JGED 102(GT10):1037-1053.
- * Lambe, T.W. and R.V. Whitman 1969. "Soil Mechanics", J.Wiley

- and Sons, Inc., New York, 553 pages.
- * Lee, K.L. and H.B. Seed 1967. Drained strength characteristics of sands, ASCE JSMFD 23(SM6):117-142.
 - * Martin, R.T. 1960. Adsorbed water on clay: a review, Clays and Clay Minerals 9:28-70.
 - * Mitchell, J.K. 1976. "Fundamentals of soil behavior", J.Wiley and Sons Inc., New York, 422 pages.
 - * Mitchell, J.K., R.G. Campanella and A. Singh 1968. Soil creep as a rate process, ASCE JSMFD 94(SM1):231-253.
 - * Perrone, V.J. 1978. Strength-deformation behavior of Manchester Fine Sand, M.S. thesis, Dept. of C.E., M.I.T., Cambridge, Mass.
 - * Rowe, P.W. 1962. The stress dilatancy relation for static equilibrium of an assembly of particles in contact, Proc. Royal Soc. of London A269:500-527.
 - Scott, R.F. and H.Y. Ko 1969. Stress deformation and strength characteristics: state of the art report, Proc. 7th ICSMFE, Mexico :1-47.
 - Scott, R.F. 1963. "Principles of Soil Mechanics", Addison-Wesley Publ. Co. Inc, Reading, Mass., 550 pages.
 - * Singh, A. and J.K. Mitchell 1968. General stress-strain function for soils, ASCE JSMFD 94(SM1):21-46.
 - * Skempton, A.W. 1954. The pore pressure coefficient A and B, Geotechnique 4:143-147.
 - * Skinner, A.E. 1969. A note on the influence of interparticle forces in the shearing strength of a random assembly of spherical particles, Geotechnique 19:150-157.
 - * Steinfink, H. and J.E. Gebhart 1962. Compression apparatus for powder X-ray diffractometry, Review of Scientific Instruments 33(5):542-544.
 - * Van Olphen, H. 1963. "An introduction to clay colloid chemistry", Interscience publishers, New York, 301 pages.
 - * Whitman, R.V. and K.E. Healy 1963. Shear strength of sands during rapid loading, ASCE Trans. 128:1553-1594..
 - Whitman, R.V. 1957. The behavior of soils under transient loadings, 4th ICSMFE, London, 1957 1:207.
 - * Winterkorn, H.F. and H.Y. Fang 1975. "Foundation Engineering Handbook", Van Nostrand Reinhold Co., N.Y., 751 pages.

REFERENCES - FROZEN SOILS

* literature cited in text

- * Alkire, B.D. and O.B. Andersland 1973. The effect of confining pressure on the mechanical properties of sand-ice materials, *J. Glac.* 12(66):469-481.
- * Andersland, O.B. and W. Akili 1967. Stress effects on creep rates of a frozen clay soil, *Geotechnique* 17:27-39.
- * Andersland, O.B. and I. AlNouri 1970. Time dependent strength behavior of frozen soils, *ASCE JSMFD* 96(SM4):1249-1265.
- * Andersland, O.B. and D.M. Anderson 1978. "Geotechnical Engineering for Cold Regions", McGraw-Hill, N.Y.
- * Andersland, O.B. and A.G. Douglas 1970. Soil deformation rates and activation energies, *Geotechnique* 20(1):1-16.
- * Anderson, D.M. 1968. Undercooling, freezing point depression and nucleation of soil water, *Israel J. Chem.* 6:349-355.
- Anderson, D.M. 1967. The interface between ice and silicate surfaces, *USA CRREL RR219*.
- * Anderson, D.M. and N.R. Morgenstern 1973. Physics, chemistry and mechanics of frozen ground: a review, *Proc. 2nd ICP N. American contribution* :257-288.
- * Anderson, D.M. and A.R. Tice 1972. Predicting unfrozen water contents in frozen soils from surface area measurements, *Highway Research Record* #393:12-18.
- * Baker, T.H.W. 1978. Effect of end conditions on the uniaxial compressive strength of frozen sand, *Proc. 3rd ICP*:609-614.
- Chamberlain, E. 1973. Mechanical properties of frozen ground under high pressure, *Proc. 2nd ICP N.A. contribution*:295-305.
- * Chamberlain, E., C. Groves and R. Perham 1972. The mechanical behaviour of frozen earth materials under high pressure triaxial conditions, *Geotechnique* 22(3):469-483.
- * Chamberlain, E. and P. Hoekstra 1970. The isothermal compressibility of frozen soil and ice to 30 kilobars at -10 C, *USA CRREL TR#225*.
- * Dillon, H.B. and O.B. Andersland 1966. Predicting unfrozen water contents in frozen soils, *CGJ* 3(2):53-60.
- * Everett, D.H. and J.M. Haynes 1965. Capillary properties of some model pore systems with special reference to frost damage, *Reunion internationale des laboratoires d'essais et de recherches sur les matériaux et les constructions (RILEM) Bulletin, New Series* 27:31-38.
- Golparvar, H. 1969. Soil-ice properties of frost-susceptible soils made hydrophobic, Ph.D. thesis, Michigan State Univ., East Lansing, Michigan.
- * Goughnour, R.R. and O.B. Andersland 1968. Mechanical properties of a sand-ice system, *ASCE JSMFD* 94(SM4):923-950.
- * Gow, A.J. 1975. Application of thin section techniques to studies of the internal structure of frozen silts, *USA CRREL Technical note*.
- Haynes, F.D. 1978. Strength and deformation of frozen silt, *Proc. 3rd ICP*:656-661.

- * Haynes, F.D. and J.A. Karalius 1977. Effect of temperature on the strength of frozen silt, USA CRREL Report 77-3.
- * Haynes, F.D., J.A. Karalius and J. Kalafut 1975. Strain rate effect on the strength of frozen silt, USA CRREL RR#350.
- Hoekstra, P. 1969. The physics and chemistry of frozen soils, Highway Research Board Spec. Report 103:78-90.
- Kaplar, C.W. 1970. Phenomenon and mechanism of frost heaving, Highway Research Record 304:1-13.
- Koopmans, R.W.R. and R.D. Miller 1975. Tests of the concept of secondary frost heaving, Proc Soil Science Society of America 39:1036-1041.
- Laba, J.T. and K.A. Aziz 1972. Pressure time relationships in laterally stressed frozen granular soils. Highway Research Record 393:79-87.
- Ladanyi, B. 1975. Bearing capacity of strip footings in frozen soils, CGJ 12(3):393-407.
- * Ladanyi, B. 1972. An engineering theory of creep of frozen soils, CGJ 9(63):63-80.
- Ladanyi, B. and G.H. Johnstone 1973. Evaluation of insitu creep properties of frozen soils with the pressuremeter, Proc. 2nd ICP N.American contribution :310-318.
- Ladanyi, B. and J. Paquin 1978. Creep behaviour of frozen sand under deep circular load, Proc. 3rd ICP:680-686.
- * Martin, R.T. 1959. Rhythmic ice banding in soil, NRC-HRB Bull. 218:11-23.
- Martin, R.T., F.H., Sayles and J.M. Ting 1980. M.I.T. creep data on Manchester Fine Sand, USA CRREL IR 627.
- * Martin, R.T., J.M. Ting and C.C. Ladd 1981. Creep behavior of frozen sand, Research Report R81-4 , Dept. of C. E., M.I.T., Cambridge, Mass.
- McRoberts, E.C. 1975. Some aspects of a simple secondary creep model for deformations in permafrost slopes, CGJ 12 (98):98-105.
- McRoberts, E.C. and N.R. Morgenstern 1975. Pore Water expulsion during freezing, CGJ 12(1):130-141.
- McRoberts, E.C. and N.R. Morgenstern 1974. Stability of slopes in frozen soil, Mackenzie Valley Northwest Territories, CGJ 11(4):554-573.
- McRoberts, E.C., T.C. Law and T.C. Murray 1978. Creep tests in undisturbed ice-rich silt, Proc. 3rd ICP:540-545.
- Miller, R.D. 1972. Freezing and heaving of saturated and unsaturated soils, HRB Record 393:1-11.
- Murrman, R.P. and P. Hoekstra 1968. Ion migration in frozen soil, Proc. 6th Army Science Conference, West Point, N.Y.
- * O'Connor, M.J. and R.J. Mitchell 1978. The energy surface: a new concept to describe the behaviour of frozen soils, Proc. 3rd ICP:120-126.
- Penner, E. 1967. Heaving pressure in soils during unidirectional freezing, CGJ 4:398-408.
- * Perkins, T.K. and R.A. Ruedrich 1973. The mechanical behavior of synthetic permafrost, Soc. Petroleum Engineers Journal 13(4):211-220.

- * Rein, R.G., V.V. Hathi and C.M. Sliepcevich 1975. Creep of sand-ice system, ASCE JGED 101(GT2):115-128.
- * Rein, R.G. and C.M. Sliepcevich 1978. Rheological properties of frozen soils, Univ. of Oklahoma Reprot #1827-1978-FR-1, Norman, Okla.
- * Roggensack, W.D. and N.R. Morgenstern 1978. Direct shear tests on natural fine grained permafrost soils, Proc. 3rd ICP: 729-735.
- Sanger, F.J. 1969. Foundations of structures in cold regions, USA CRREL Monograph III-C4.
- * Sayles, F.H. 1974. Triaxial constant strain rate tests and triaxial creep tests on frozen Ottawa sand, USA CRREL TR#253.
- * Sayles, F.H. 1973. Triaxial and creep tests on frozen Ottawa sand, Proc. 2nd ICP N.American contribution:384-391.
- * Sayles, F.H. 1968. The creep of frozen sands, USA CRREL TR#190.
- * Sayles, F.H. and D.L. Carbee 1980. Strength of frozen silt as a function of ice content and dry unit weight, Proc. 2nd Int'l. Symposium on Ground Freezing, Trondheim, Norway.
- * Sayles, F.H. and D. Haines 1974. Creep of frozen silt and clay, USA CRREL TR#252.
- Scott, R.F. 1969. The freezing process and mechanics of frozen ground, USA CRREL Monograph II-D1.
- * Smith, L.L. and J.B. Cheatham Jr. 1975. Plasticity of ice and sand ice systems, J. of Engineering for industry 97(2): 479-484.
- Sutherland, H.B. and P.N. Gaskin 1973. Pore water and heaving pressures developed in partially frozen soils, Proc. 2nd ICP N.A. contribution:409-419.
- Tagaki, S. 1978(a). The adsorption force theory of frost heaving, USA CRREL Report (in press).
- * Tagaki, S. 1978(b). Segregation freezing as the cause of suction force for ice lens formation, USA CRREL Report 78-6.
- Tagaki, S. 1975. Principles of frost heaving, USA CRREL RR #140
- Thompson, E.G. and F.H. Sayles 1972. Insitu creep analysis of room in frozen soil. ASCE JSMFD 98(SM9):899-915.
- * Tice, A.R., D.M. Anderson and A. Banin 1976. The prediction of unfrozen water contents in frozen soils from liquid limit determinations, USA CRREL Report 76-8.
- * Tice, A.R., C.M. Burrous and D.M. Anderson 1978. Determination of unfrozen water in frozen soil by pulsed nuclear magnetic resonance, Proc. 3rd ICP:150-155.
- * Ting, J.M. 1981. The mechanics of frozen soil: a review. USA CRREL Report (in press).
- * Tsytoich, N.A. 1975. "Mechanics of Frozen Ground", McGraw-Hill, N.Y.
- Vinson, T.S., T. Chaichanavong and R.L. Czajkowski 1978. Dynamic behavior of frozen clay under cyclic triaxial loading, ASCE JGED 104(GT7):779-800.
- * Vyalov, S.S. 1973. Long term rupture of frozen soil as a thermally activated process, Proc. 2nd ICP U.S.S.R. contribution :222-228.

- * Vyalov, S.S. 1963. Rheology of frozen soils, Proc. 1st ICP: 332-342.
- * Vyalov, S.S. 1962. Strength and creep of frozen soils and calculations in ice-soil retaining structures, USA CRREL Translation 76.
- * Vyalov, S.S. 1959. Rheological properties and bearing capacity of frozen soils, USA CRREL Translation #74.
- Vyalov, S.S. and Y.P. Shusherina 1964. Resistance of frozen soils to triaxial compression, Merzlatnye Issledovaniya 4:340-375 (also in USA CRREL TL 173, 1970).
- Williams, P.J. 1972. Use of the surface tension concept in engineering practice, Highway Research Record #393:19-29.
- * Wissa, A.E. and R.T. Martin 1968. Behaviour of soils under flexible pavements; development of rapid frost susceptibility tests, Research Report RR68-77, Soils Publ. 224, Dept. of Civil Eng., M.I.T., Cambridge, Mass.
- Yong, R.N. 1963. Soil freezing considerations in frozen soil strength, Proc. 1st ICP:315-319.

BIOGRAPHICAL NOTE

John Mei-Ming Ting was born on January 5th, 1954 in Taipei, Taiwan to Dr. and Mrs. Paul C.C. Ting. After moving to Canada in 1959, he spent most of his youth in Fredericton, New Brunswick, where he graduated from high school in 1970. He attended McGill University in Montreal, Quebec, specializing in structural engineering, and received his Bachelor of Engineering degree in Civil Engineering with Great Distinction in June 1975. Among his undergraduate awards were: the Ernest Brown Gold Medal for Highest Ability in the Undergraduate Course for the Faculty of Engineering, Robert Forsythe Prize in Structural Engineering, McConnell Memorial Scholar (1970-1975) and Wolvin Memorial Scholar.

Upon graduation, he entered California Institute of Technology in Pasadena, California, working with Prof. R.F. Scott on centrifuge modelling of dynamic soil problems. After graduation in June 1976 with his Master of Science in Civil Engineering, he continued to work at Caltech for a few months before returning to Montreal to start work as a Soils Engineer for Geocon Ltd., a geotechnical consulting firm. He terminated his employment with Geocon in August of 1977 to commence work on his doctorate in geotechnical engineering at M.I.T.

During his stay at M.I.T., he has worked with Dr. Martin at the U.S. Army Cold Regions Research and Engineering Laboratory in Hanover, New Hampshire. Among his publications are:

- Scott, R.F., H.P. Liu and J. Ting 1977. Dynamic pile tests by centrifuge modelling, Proc. Int'l. Conf. Earthquake Engineering, Rorkee, India 4:199-203.
- Ting, J.M. and R.T. Martin 1979. Application of the Andrade equation to creep data for ice and frozen soil, Cold Regions Science and Technology 1:29-36.
- Martin, R.T., J.M. Ting and C.C. Ladd 1981. Creep behavior of frozen sand, M.I.T. Research Report, Dept. of Civil Engineering, Cambridge, Mass.

While at M.I.T., he met and recently married his wife Christine. Upon graduation from M.I.T., they will move to California, where he will assume the position of Research Fellow/part-time Lecturer at Caltech.

L MED
- 8